ADA 278 741

UNITED STATES AIR FORCE

SUMMER FACULTY RESEARCH PROGRAM

1988

PROGRAM TECHNICAL REPORT

UNIVERSAL ENERGY SYSTEMS, INC.

VOLUME II OF IV

Program Director, UES
Rodney C. Darrah

Program Administrator, UES
Susan K. Espy

Program Manager, AFOSR
Lt. Col. Claude Cavender

Submitted to

Air Force Office of Scientific Research

Bolling Air Force Base

Washington, DC

December 1988

94-12298

DTIC QUALITY INSPECTED 8

94

Rtn to Loretta
Reach Apt -
1 7/11 74 Wit Rpt

MEMORANDUM FOR DTIC (Acquisition)
(Attn: Pat Mauby)

SUBJECT: Distribution of USAF (AFOSR Summer Research Program (Air Force Laboratories) and Universal Energy Systems, Inc., and the Research Initiation Program

FROM: AFOSR/XPT
Joan M. Boggs
110 Duncan Avenue, Suite B115
Bolling AFB DC 20332-0001

1. All of the books forwarded to DTIC on the subjects above should be considered Approved for Public Release, distribution is unlimited (Distribution Statement A).

2. Thank you for processing the attached information.

Joan M. Boggs

JOAN M. BOGGS
Chief, Technical Information Division

USAF Graduate Student Research Program (1988)

8 Technical Reports Enclosed

TABLE OF CONTENTS

SECTION	PAGE
Preface	i
List Of Participants	ii
Participant Laboratory Assignment	xxviii
Research Reports	xxxii

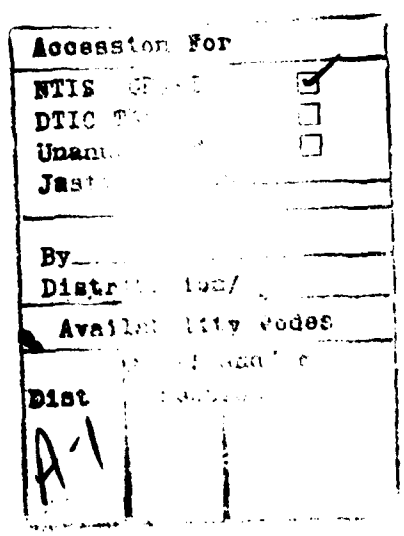

PREFACE

The United States Air Force Summer Faculty Research Program (USAF-SFRP) is designed to introduce university, college, and technical institute faculty members to Air Force research. This is accomplished by the faculty members being selected on a nationally advertised competitive basis for a ten-week assignment during the summer intersession period to perform research at Air Force laboratories/centers. Each assignment is in a subject area and at an Air Force facility mutually agreed upon by the faculty members and the Air Force. In addition to compensation, travel and cost of living allowances are also paid. The USAF-SFRP is sponsored by the Air Force Office of Scientific Research, Air Force Systems Command, United States Air Force, and is conducted by Universal Energy Systems, Inc.

The specific objectives of the 1988 USAF-SFRP are:

(1) To provide a productive means for U. S. Faculty Members to participate in research at Air Force Laboratories/Centers;

(2) To stimulate continuing professional association among the Faculty and their professional peers in the Air Force;

(3) To further the research objectives of the United States Air Force;

(4) To enhance the research productivity and capabilities of the Faculty especially as these relate to Air Force technical interests.

During the summer of 1988, 153-faculty members participated. These researchers were assigned to 23 USAF laboratories/centers across the country. This four volume document is a compilation of the final reports written by the assigned faculty members about their summer research efforts.

LIST OF 1988 PARTICIPANTS

NAME/ADDRESS	DEGREE, SPECIALTY, LABORATORY ASSIGNED
Dr. Ibrahim A. Ahmad Professor and Director Division of Statistics Dept. of Math Sciences Northern Illinois University DeKalb, IL 60115 (815) 753-6739	Degree: Ph.D., Statistics, 1975 Specialty: Statistics and Operations Research Assigned: Armament Laboratory
Dr. Robert J. Arenz Professor Dept. of Mechanical Engineering Gonzaga University Spokane, WA 99258 (509) 328-4220	Degree: Ph.D., Aeronautical Eng., 1964 Specialty: Solid Mech. Assigned: Materials Laboratory
Dr. Lucia M. Babcock Assistant Professor Dept. of Chemistry Louisiana State University Choppin Hall Baton Rouge, LA 70803 (504) 388-3239	Degree: Ph.D., Chemistry, 1978 Specialty: Gas Phase Ion-Molecule Chem. Assigned: Air Force Geophysics Lab.
Dr. Praphulla K. Bajpai Professor Dept. of Biology University of Dayton 300 College Park Dayton, OH 45469 (513) 229-3029	Degree: Ph.D., Animal Physiology, 1965 Specialty: Physiology and Biomaterials Assigned: Harry G. Armstrong Aerospace Medical Research Laboratory
Dr. Stephen D. Baker Professor Dept. of Physics Rice University Houston, TX 77251-1892 (713) 527-8101	Degree: Ph.D., Physics, 1963 Specialty: Nuclear Physics Assigned: Air Force Geophysics Lab.
Dr. Pradip M. Bakshi Research Professor Dept. of Physics Boston College Chestnut Hill, MA 02167 (617) 552-3585	Degree: Ph.D., Theoretical Physics, 1962 Specialty: Quantum Theory Assigned: Air Force Geophysics Lab.

NAME/ADDRESS	DEGREE, SPECIALTY, LABORATORY ASSIGNED
Dr. Shankar S. Bale Professor Dept. of Science and Math Saint Paul's University Lawrenceville, VA 23868 (804) 848-3111	Degree: Ph.D., Genetics, 1971 Specialty: Toxicology-Cytogenetics Assigned: Harry G. Armstrong Aerospace Medical Research Laboratory
Mr. Beryl L. Barber Assistant Professor Dept. of Electronics Eng. Oregon Institute of Technology 3201 Campus Drive Klamath Falls, OR 97601-8801 (503) 882-6890	Degree: MSEE, Electrical Eng., 1961 Specialty: RF/Microwave Components Assigned: Rome Air Development Center
Dr. Bryan R. Becker Assistant Professor Dept. of Aerospace Engineering University of Missouri 600 West Mechanic Independence, MO 64050-1799 (816) 276-1279	Degree: Ph.D., Eng. Science, 1979 Specialty: Computational Fluid Dynamics Assigned: Aero Propulsion Laboratory
Dr. Reuben Benumof Professor Dept. of Applied Sciences College of Staten Island 130 Stuyvesant Pl. Staten Island, NY 10301 (718) 390-7973	Degree: Ph.D., Physics, 1945 Specialty: Semiconductor Physics Assigned: Air Force Geophysics Lab.
Mr. George N. Bratton Associate Professor Dept. of Math and Comp. Science Austin State Peay State Univ. P O Box 8343 Clarksville, TN 37044 (615) 648-7834	Degree: Ed.D., Mathematics Ed., 1977 Specialty: Statistics Assigned: Electronics Systems Division
Dr. Dan R. Bruss Assistant Professor Dept. of Physical Sciences Albany College of Pharmacy 106 New Scotland Avenue Albany, NY 12208 (518) 445-7225	Degree: Ph.D., Chemistry, 1985 Specialty: Physical Organic Chemistry Assigned: Frank J. Seiler Research Lab.

NAME/ADDRESS	DEGREE, SPECIALTY, LABORATORY ASSIGNED
Dr. Ronald Bulbulian Associate Professor Dept. of Health, Physical Education and Recreation University of Kentucky Seaton 100 Lexington, KY 40506 (606) 257-7904	Degree: Ph.D., Physiology, 1980 Specialty: Exercise Physiology Assigned: School of Aerospace Medicine
Dr. Charles M. Bump Assistant Professor Dept. of Chemistry Hampton University P O Box 6483 Hampton, VA 23668 (804) 727-5330	Degree: Ph.D. Organic Chemistry, 1979 Specialty: Organic Synthesis Assigned: Frank J. Seiler Research Lab.
Dr. John A. Burke, Jr. Professor Dept. of Chemistry Trinity University 715 Stadium Drive San Antonio, TX 78284 (512) 736-7316	Degree: Ph.D., Chemistry, 1963 Specialty: Inorganic Compounds Assigned: School of Aerospace Medicine
Mr. Mike Burlakoff Assistant Professor Dept. of Computer Science Southwest Missouri State Univ. 901 S. National Springfield, MO 65804 (417) 836-5930	Degree: MS., Math, Computer Sci., 1965 Specialty: Computer Science Assigned: Avionics Laboratory
Dr. Larry W. Byrd Assistant Professor Dept. of Mechanical Engineering Arkansas State University P O Box 1080 State University, AR 72467-1080 (501) 972-3421	Degree: Ph.D., Mechanical Eng., 1984 Specialty: Mechanical Engineering Assigned: Flight Dynamics Laboratory
Dr. Clarence Calder Associate Professor Dept. of Mechanical Engineering Oregon State University Corvallis, OR 97331 (503) 754-2427	Degree: Ph.D., Mechanical Eng., 1969 Specialty: Stress Wave Propagation Assigned: Astronautics Laboratory

NAME/ADDRESS	DEGREE, SPECIALTY, LABORATORY ASSIGNED
Dr. Richard T. Carlin Assistant Professor Dept. of Chemistry Polytechnic University 333 Jay St. Brooklyn, NY 11201 (718) 260-3339	Degree: Ph.D., Chemistry, 1983 Specialty: Inorganic Chemistry Assigned: Frank J. Seiler Research Lab.
Dr. Gene O. Carlisle Professor Dept. of Chemistry and Physics West Texas State University Canyon, TX 79016 (806) 656-2282	Degree: Ph.D., Inorganic Chem., 1969 Specialty: Coordination Chemistry Assigned: Materials Laboratory
Dr. Patricia Carlson Professor Dept. of Humanities Rose-Hulman Institute of Tech. 5500 Wabash Terre Haute, IN 47803 (812) 877-1511	Degree: Ph.D., Language & Lit., 1973 Specialty: Document Design Assigned: Human Resources Laboratory: Logistics & Human Factors Div.
Dr. David R. Cecil Professor Dept. of Mathematics Texas A&I University Campus Box 172 Kingsville, TX 78363 (512) 592-1839	Degree: Ph.D., Mathematics, 1962 Specialty: Algebra (Finite Fields) Assigned: Wilford Hall Medical Center
Dr. Wayne A. Charlie Associate Professor Dept. of Civil Engineering Colorado State University Fort Collins, CO 80523 (303) 491-8584	Degree: Ph.D., Civil Engineering, 1975 Specialty: Geotechnical Engineering Assigned: Engineering & Services Center
Dr. Steven C. Chiesa Assistant Professor Dept. of Civil Engineering Santa Clara University Santa Clara, CA 95053 (408) 554-4697	Degree: Ph.D., Civil Eng., 1982 Specialty: Biological Waste Treatment Assigned: Occupational and Environment Health Laboratory

NAME/ADDRESS	DEGREE, SPECIALTY, LABORATORY ASSIGNED
Dr. Karen C. Chou Associate Professor Dept. of Civil Engineering Syracuse University Syracuse, NY 13244-1190 (315) 423-3314	Degree: Ph.D., Structural Eng., 1983 Specialty: Structural Engineering Assigned: Flight Dynamics Laboratory
Dr. Phillip A. Christiansen Associate Professor Dept. of Chemistry Clarkson University Potsdam, NY 13676 (315) 268-4099	Degree: Ph.D., Physical Chem., 1978 Specialty: Physical Chemistry Assigned: Astronautics Laboratory
Dr. Keith A. Christianson Assistant Professor Dept. of Electrical Engineering University of Maine Orono, ME 04469 (207) 581-2244	Degree: Ph.D., Materials Science and Engineering, 1985 Specialty: Electronic Materials Assigned: Rome Air Development Center
Dr. Mingking K. Chyu Assistant Professor Dept. of Mechanical Eng. Carnegie Mellon University Pittsburgh, PA 15213 (412) 268-3658	Degree: Ph.D., Heat Transfer, 1986 Specialty: Heat Transfer Assigned: Aero Propulsion Laboratory
Dr. Jerry D. Clark Assistant Professor Dept. of Physics Wright State University 248 Fawcett Hall Dayton, OH 45435 (513) 426-3917	Degree: Ph.D., Physics, 1982 Specialty: Atomic Physics Assigned: Aero Propulsion Laboratory
Dr. Lane Clark Assistant Professor Dept. of Mathematics University of New Mexico Albuquerque, NM 87106 (505) 277-2104	Degree: Ph.D., Mathematics, 1980 Specialty: Graph Theory Assigned: Weapons Laboratory

NAME/ADDRESS	DEGREE, SPECIALTY, LABORATORY ASSIGNED
Dr. Donald F. Collins Faculty in Physics Dept. of Physics Warren Wilson College Swannanoa, NC 28778 (704) 298-3325	Degree: Ph.D., Physics, 1970 Specialty: Optics, Image Processing Assigned: Air Force Geophysics Lab.
Dr. Susan T. Collins Assistant Professor Dept. of Chemistry California State University 18111 Nordhoff Street Northridge, CA 91330 (818) 885-3367	Degree: Ph.D., Physical Chem., 1981 Specialty: Matrix Isolation Spectroscopy Assigned: Astronautics Laboratory
Dr. Charles D. Covington Assistant Professor Dept. of Electrical Engineering University of Arkansas Bell Engineering Center 3217 Fayetteville, AR 72701 (501) 575-6583	Degree: Ph.D., Electrical Eng., 1984 Specialty: Digital Signal Processing Assigned: Harry G. Armstrong Aerospace Medical Research Laboratory
Dr. Parvis Dadras Professor Dept. of Mech. Systems Eng. Wright State University Dayton, OH 45435 (513) 873-2944	Degree: Ph.D., Mechanical Eng., 1972 Specialty: Mechanics of Materials Assigned: Materials Laboratory
Dr. John F. Dalphin Professor Dept. of Computer Science Towson State University Baltimore, MD 21204 (301) 321-3701	Degree: Ph.D., Mathematics, 1973 Specialty: Computer Science Assigned: Electronics Systems Division
Mr. Darin S. DeForest Research Associate Dept. of Computer Science Arizona State University Tempe, AZ 85287 (602) 965-3664	Degree: B.Sc., Computer Science, 1984 Specialty: Programming Language Design Assigned: Rome Air Development Center

NAME/ADDRESS	DEGREE, SPECIALTY, LABORATORY ASSIGNED
Dr. David H. DeHeer Associate Professor Dept. of Biology Calvin College 3201 Burton Street, S.E. Grand Rapids, MI 49506 (616) 957-6083	Degree: Ph.D., Molecular Biology, 1972 Specialty: Molecular Biology Assigned: Engineering & Services Center
Dr. Eustace L. Dereniak Associate Professor Dept. of Optical Science University of Arizona 528 N. Martin Tucson, AZ 85719 (602) 621-1019	Degree: Ph.D., Optics, 1976 Specialty: Infrared Physics Assigned: Arnold Engineering Development Center
Prof. Paul T. Dingman Assistant Professor Dept. of Electronics Eng. Tech. Oregon Institute of Technology 3201 Campus Drive Klamath Falls, OR 97601-8801 (503) 882-6890	Degree: MSEE., Electrical Eng., 1974 Specialty: Digital, Microprocessors Assigned: Rome Air Development Center
Dr. David A. Dolson Assistant Professor Dept. of Chemistry Murray State University Murray, KY 42071 (502) 762-4490	Degree: Ph.D., Physical Chem., 1981 Specialty: Laser Spectroscopy Assigned: Weapons Laboratory
Dr. Hugh K. Donaghy Assistant Professor Dept. of Computer Science Rochester Inst. of Technology 1 Lomb-Memorial Drive Rochester, NY 14623 (716) 475-2994	Degree: Ph.D., Philosophy, 1972 Specialty: Natural Language Processing Assigned: Rome Air Development Center
Dr. Stephen J. Dow Assistant Professor Dept. of Math and Statistics Univ. of Alabama in Huntsville Huntsville, AL 35899 (205) 895-6252	Degree: Ph.D., Mathematics, 1982 Specialty: Discrete Mathematics Assigned: Armament Laboratory

NAME/ADDRESS	DEGREE, SPECIALTY, LABORATORY ASSIGNED
Dr. Derek Dunn-Rankin Assistant Professor Dept. of Mechanical Engineering University of California 616 Engineering Irvine, CA 92717 (714) 854-0460	Degree: Ph.D., Mechanical Eng., 1985 Specialty: Laser Diagnostics (combustion) Assigned: Aero Propulsion Laboratory
Dr. Deanna S. Durnford Assistant Professor Dept. of Agric. & Chem. Eng. Colorado State University Ft. Collins, CO 80523 (303) 491-5252	Degree: Ph.D., Civil Eng., 1982 Specialty: Groundwater Assigned: Engineering & Services Center
Dr. Suren N. Dwivedi Associate Professor Dept. of Mechanical Eng. University of North Carolina Charlotte, NC 28223 (704) 547-2303	Degree: Ph.D., Engineering, 1976 Specialty: Material Processing Assigned: Materials Laboratory
Dr. Wayne A. Eckerle Associate Professor Dept. of Mech. & Ind. Eng. Clarkson University Potsdam, NY 13676 (315) 268-2203	Degree: Ph.D., Fluid Mech., 1985 Specialty: Experimental Fluid Mechanics Assigned: Aero Propulsion Laboratory
Dr. J. Kevin Ford Assistant Professor Dept. of Psychology Michigan State University East Lansing, MI 48824 (517) 353-5006	Degree: Ph.D., Philosophy, 1983 Specialty: Industrial/Organ. Psychology Assigned: Human Resources Laboratory: Training Systems
Prof. Michael E. Frantz Assistant Professor Dept. of Math and Physics University of LaVerne 1950 Third Street LaVerne, CA 91750 (714) 593-3511	Degree: M.S., Mathematics, 1978 Specialty: Partial Differential Equations Assigned: Air Force Geophysics Lab.

NAME/ADDRESS	DEGREE, SPECIALTY, LABORATORY ASSIGNED
Dr. Barry K. Fussell Assistant Professor Dept. of Mechanical Engineering University of New Hampshire Kingsbury Hall Durham, NH 03824 (603) 862-1352	Degree: Ph.D., Mechanical Eng., 1987 Specialty: Systems Modeling & Controls Assigned: Materials Laboratory
Dr. Hugh. P. Garraway, III Associate Professor Dept. of Computer Science Univ. of Southern Mississippi Box 5106 Hattiesburg, MS 39406 (601) 266-4949	Degree: Ph.D., Instruc. Tech., 1980 Specialty: Computer Based Learning Assigned: Human Resources Laboratory: Training Systems
Dr. Christopher P. Godfrey Assistant Professor Dept. of Computer Science Missouri Western State College 4525 Downs Drive St. Joseph, MO 64507 (816) 271-4372	Degree: Ph.D., Physics, 1982 Specialty: High Energy Astrophysics Assigned: Air Force Geophysics Lab.
Dr. Barry P. Goettl Assistant Professor Dept. of Psychology Clemson University 108 Brackett Hall Clemson, SC 29634-1511 (803) 656-2831	Degree: Ph.D., Psychology, 1987 Specialty: Engineering Psychology Assigned: Harry G. Armstrong Aerospace Medical Research Laboratory
Dr. Gerald W. Grams Professor School of Geophysical Sciences Georgia Tech. Atlanta, GA 30332 (404) 894-3628	Degree: Ph.D., Meteorology, 1966 Specialty: Atmospheric Physics Assigned: Avionics Laboratory
Dr. Edward K. Greenwald Assistant Professor Engineering Professional Dev. Univ. of Wisconsin-Madison 432 N. Lake Street Madison, WI 53706 (608) 262-0573	Degree: Ph.D., Physics, 1967 Specialty: Electrical Engineering Assigned: Engineering & Services Center

NAME/ADDRESS	DEGREE, SPECIALTY, LABORATORY ASSIGNED
Prof. William M. Grissom Assistant Professor Dept. of Physics Morehouse College 830 Westview Dr., S.W. Atlanta, GA 30314 (404) 681-2800	Degree: M.S.E., Mechanical Eng., 1978 Specialty: Combustion Diagnostics Assigned: Arnold Engineering Development Center
Dr. David A. Grossie Assistant Professor Dept. of Chemistry Wright State University Dayton, OH 45435 (513) 873-2210	Degree: Ph.D., Chemistry, 1982 Specialty: X-ray Crystallography Assigned: Materials Laboratory
Dr. Vijay K. Gupta Professor Dept. of Chemistry Central State University Wilberforce, OH 45384 (513) 376-6423	Degree: Ph.D., Chemistry, 1969 Specialty: Physical Chemistry Assigned: Materials Laboratory
Dr. Awatef Hamed Dept. of Aerospace Eng. University of Cincinnati Mail Location 70 Cincinnati, OH 45221 (513) 475-5630	Degree: Ph.D., Engineering, 1972 Specialty: Engineering Assigned: Flight Dynamics Laboratory
Dr. Albert A. Heaney Professor Dept. of Electrical Eng. California State University Shaw & Cedar Avenues Fresno, CA 93740-0094 (209) 294-4823	Degree: Ph.D., Electrical Eng., 1972 Specialty: Computer Engineering Assigned: Eastern Space Missile Center
Dr. David Hemmendinger Assistant Professor Dept. of Compt. Sci. & Eng. Wright State University Research Bldg. 317 Research Blvd. Kettering, OH 45420 (513) 259-1345	Degree: Ph.D., Philosophy, 1973 Specialty: Logic Programming Assigned: Avionics Laboratory

NAME/ADDRESS	DEGREE, SPECIALTY, LABORATORY ASSIGNED
Dr. Bennye S. Henderson Associate Professor Dept. of Biology Jackson State University 1325 Lynch Street Jackson, MS 39217 (601) 968-2586	Degree: Ph.D., Physiology, 1979 Specialty: Physiology Assigned: School of Aerospace Medicine
Dr. Darrell E.P. Hoy Assistant Professor Dept. of Mechanical Eng. Tennessee Technological Univ. Box 5014 Cookeville, TN 38505 (615) 372-3732	Degree: M.S.E., Mechanical Eng., 1985 Specialty: Ballistic Impact Shocks Assigned: Arnold Engineering Development Center
Dr. Manuel A. Huerta Professor Dept. of Physics University of Miami P O Box 248046 Coral Gables, FL 33124 (305) 284-2323	Degree: Ph.D., Physics, 1970 Specialty: Plasma Physics Assigned: Armament Laboratory
Dr. Randolph B. Huff Professor Dept. of Chemistry Presbyterian College Clinton, SC 29325 (803) 833-2820	Degree: Ph.D., Inorganic Chem., 1969 Specialty: Physical-Inorganic Chemistry Assigned: Occupational and Environment Health Laboratory
Dr. Neil J. Hutzler Associate Professor Dept. of Civil Engineering Michigan Tech. University Houghton, MI 49931 (906) 487-2194	Degree: Ph.D., Environmental Eng., 1978 Specialty: Environmental Engineering Assigned: Engineering & Services Center
Dr. Douglas E. Jackson Professor Dept. of Math Sciences Eastern New Mexico University Portales, NM 88130 (505) 562-2367	Degree: Ph.D., Mathematics, 1969 Specialty: Math/Statistical Information Assigned: Human Resources Laboratory: Manpower & Personnel Division

NAME/ADDRESS	DEGREE, SPECIALTY, LABORATORY ASSIGNED
Dr. Oleg G. Jakubowicz Assistant Professor Dept. of Elect. & Compt. Eng. State University of New York 238 Bell Hall Buffalo, NY 14260 (716) 636-2406	Degree: Ph.D., Physics, 1984 Specialty: Neural Nets Assigned: Rome Air Development Center
Dr. Manjit S. Jawa Professor Dept. of Mathematics Fayetteville State University Fayetteville, NC 28301 (919) 486-1675	Degree: Ph.D., Applied Math., 1967 Specialty: Applied Mathematics Assigned: Arnold Engineering Development Center
Dr. David W. Jensen Assistant Professor Dept. of Aerospace Eng. Pennsylvania State University 233N Hammond Bldg. University Park, PA 16802 (814) 863-1077	Degree: Ph.D., Structures Tech., 1986 Specialty: Advanced Composite Materials Assigned: Astronautics Laboratory
Dr. Eric R. Johnson Associate Professor Dept. of Chemistry Ball State University Muncie, IN 47306 (317) 285-8078	Degree: Ph.D., Biochemistry, 1974 Specialty: Protein Biochemistry Assigned: School of Aerospace Medicine
Dr. William M. Jordan Assistant Professor Dept. of Mech. & Indus. Eng. Lousiana Tech. University P O Box 10348 Ruston, LA 71272 (318) 257-4304	Degree: Ph.D., Intersiciplinary Eng., 1985 Specialty: Composite Materials Assigned: Weapons Laboratory
Dr. Mohammad A. Karim Assistant Professor Dept. of Electrical Eng. University of Dayton KL-241D Dayton, OH 45469 (513) 229-3611	Degree: Ph.D., Electrical Eng., 1982 Specialty: Electro-Optics Assigned: Avionics Laboratory

NAME/ADDRESS	DEGREE, SPECIALTY, LABORATORY ASSIGNED
Dr. Arkady Kheyfets Assistant Professor Dept. of Mathematics North Carolina State Univ. Box 8205 Raleigh, NC 27695-8205 (919) 737-3265	Degree: Ph.D., Physics, 1986 Specialty: Mathematical Physics Assigned: Weapons Laboratory
Prof. Daisy W. Kimble Assistant Professor Dept. of Chemistry Southern University P O Box 11487 Baton Rouge, LA 70813 (504) 771-3734	Degree: M.S., Analytical Chem., 1986 Specialty: Analytical Chemistry Assigned: School of Aerospace Medicine
Dr. Yulian B. Kin Associate Professor Dept. of Engineering Purdue University Calumet Potter Building Hammond, IN 46323 (219) 989-2684	Degree: Ph.D., Fatigue Stress Analysis 1971 Specialty: Stress Analysis Assigned: Flight Dynamics Laboratory
Dr. Samuel P. Kozaitis Assistant Professor Dept. of Electrical Eng. Florida Institute of Tech. Melbourne, FL 32901-6988 (305) 768-8000	Degree: Ph.D., Electrical Eng, 1986 Specialty: Optics, Computer Architecture Assigned: Rome Air Development Center
Dr. Janet U. Kozyra Assistant Research Scientist University of Michigan Space Physics Research Lab. 2455 Hayward Ann Arbor, MI 48109-2143 (313) 747-3550	Degree: Ph.D., Atmospheric Sci., 1986 Specialty: Space Physics Assigned: Air Force Geophysics Lab.
Dr. Charles E. Lance Assistant Professor Dept. of Psychology University of Georgia Athens, GA 30602 (404) 542-3053	Degree: Ph.D., Psychology, 1985 Specialty: Industrial/Organizational Psy. Assigned: Human Resources Laboratory: Manpower & Personnel Division

NAME/ADDRESS	DEGREE, SPECIALTY, LABORATORY ASSIGNED
Dr. Thomas L. Landers Assistant Professor Dept. of Industrial Engineering University of Arkansas 4176 Bell Engineering Ctr. Fayetteville, AR 72703 (501) 575-6042	Degree: Ph.D., Industrial Eng., 1985 Specialty: Reliability & Maintainability Assigned: Human Resources Laboratory: Logistics & Human Factors Div.
Prof. Anastas Lazaridis Assistant Professor Dept. of Mechanical Eng. Widener University Chester, PA 19013 (215) 499-4487	Degree: Sc.D., Thermal Fluids, 1969 Specialty: Ablation, Solar Energy Assigned: Armament Laboratory
Dr. L. James Lee Associate Professor Dept. of Chemical Eng. The Ohio State University 140 W. 19th Avenue Columbus, OH 43210 (614) 292-2408	Degree: Ph.D., Chemical Eng., 1979 Specialty: Polymer & Composite Processing Assigned: Materials Laboratory
Dr. Robert Y. Li Assistant Professor Dept. of Electrical Eng. University of Nebraska Lincoln, NE 68588 (402) 472-5892	Degree: Ph.D., Electrical Eng., 1981 Specialty: Image Processing Assigned: Avionics Laboratory
Dr. Irving Lipschitz Associate Professor Dept. of Chemistry University of Lowell 1 University Lane Lowell, MA 01854 (617) 452-5000	Degree: Ph.D., Physical Chem., 1965 Specialty: Vibrational Spectroscopy Assigned: Air Force Geophysics Lab.
Dr. Harold G. Longbotham Visiting Assistant Professor Dept. of Electrical Eng. Univ. of Texas - San Antonio San Antonio, TX 78285 (512) 691-5518	Degree: Ph.D., Electrical Eng., 1985 Specialty: Nonlinear Digital Filtering Assigned: School of Aerospace Medicine

NAME/ADDRESS	DEGREE, SPECIALTY, LABORATORY ASSIGNED
Dr. David A. Ludwig Assistant Professor Dept. of Mathematics Univ. of North Carolina at Greensboro Greensboro, NC 27412 (919) 334-5836	Degree: Ph.D., Biostatistics, 1982 Specialty: Biostatistics, Exp. Design Assigned: School of Aerospace Medicine
Dr. Douglas A. Mandra Associate Professor Dept. of Psychology Francis Marion College P O Box 7500 Florence, SC 29501 (803) 661-1378	Degree: Ph.D., Psychology, 1974 Specialty: Experimental Psychology Assigned: Human Resources Laboratory: Operations Training Division
Dr. Robert E. Masingale, Sr. Professor Dept. of Chemistry Jarvis Christian College Hawkins, TX 75765 (214) 769-2174	Degree: Ph.D., Organic Chemistry, 1968 Specialty: Organic & Analytical Chemistry Assigned: Harry G. Armstrong Aerospace Medical Research Laboratory
Dr. John P. McHugh Assistant Professor Dept. of Mechanical Eng. University of New Hampshire 133 Kingsbury Durham, NH 03824 (603) 862-1899	Degree: Ph.D., Applied Mechanics, 1986 Specialty: Fluid Mechanics Assigned: Air Force Geophysics Lab.
Dr. Michael L. McKee Associate Professor Dept. of Chemistry Auburn University Auburn, AL 36849-5312 (205) 826-4043	Degree: Ph.D., Chemical Physics, 1977 Specialty: Molecular Orbital Theory Assigned: Frank J. Seiler Research Lab.
Dr. Thomas T. Meek Associate Professor Dept. of Materials Sci. & Eng. University of Tennessee 434 Dougherty Engineering Bldg. Knoxville, TN 37966-2200 (615) 970-0940	Degree: Ph.D., Ceramic Eng., 1977 Specialty: Ceramic Processing Assigned: Materials Laboratory

NAME/ADDRESS	DEGREE, SPECIALTY, LABORATORY ASSIGNED
Dr. Tammy J. Melton Assistant Professor Dept. of Chemistry St. Norbert College DePere, WI 54115 (414) 337-3206	Degree: Ph.D., Inorganic Chem., 1986 Specialty: Inorganic Synthesis Assigned: Frank J. Seiler Research Lab.
Dr. Carolyn W. Meyers Assistant Professor Dept. of Mechanical Eng. Georgia Inst. of Technology School of Mechanical Eng. Atlanta, GA 30332 (404) 894-3264	Degree: Ph.D., Physical Metallurgy, 1984 Specialty: Microstructure Assigned: Engineering & Services Center
Dr. David W. Mikolaitis Assistant Professor Dept. of Engineering Sciences University of Florida 231 Aero Gainesville, FL 32611 (904) 392-0961	Degree: Ph.D., Theoretical & Applied Mechanics, 1981 Specialty: Applied Math Assigned: Armament Laboratory
Dr. Kwang S. Min Professor Dept. of Physics East Texas State University Commerce, TX 75428 (214) 885-5483	Degree: Ph.D., Physics, 1962 Specialty: Signal Processing Assigned: Armament Laboratory
Dr. Joseph J. Molitoris Professor Dept. of Physics Muhlenberg College Allentown, PA 18104 (215) 821-3413	Degree: Ph.D., Physics, 1985 Specialty: Nuclear Physics Assigned: Armament Laboratory
Mr. Augustus Morris Instructor Dept. of Manufacturing Eng. Central State University Wilberforce, OH 45384 (513) 376-6435	Degree: B.S., Biomedical Eng., 1981 Specialty: Biomedical Engineering Assigned: Flight Dynamics Laboratory

NAME/ADDRESS	DEGREE, SPECIALTY, LABORATORY ASSIGNED
Dr. William P. Mounfield Assistant Professor Dept. of Mechanical Eng. Louisiana State University R2513-A CEBA Bldg. Baton Rouge, LA 70803-6413 (504) 388-6488	Degree: Ph.D., Mechanical Eng., 1985 Specialty: Automatic Controls Assigned: Engineering & Services Center
Dr. Nanda L. Mukherjee Associate Professor Dept. of Chemical Eng. Tuskegee University Tuskegee, AL 36088 (205) 727-8050	Degree: Ph.D., Chemical Eng., 1967 Specialty: Kinetics Assigned: Flight Dynamics Laboratory
Dr. Richard S. Myers Professor Dept. of Physical Sciences Delta State University P O Box 3255 Cleveland, OH 38733 (601) 846-4482	Degree: Ph.D., Physical Chem., 1968 Specialty: Experimental Physical Chem. Assigned: Engineering & Services Center
Dr. Himanshoo V. Navangul Professor Dept. of Chemistry and Physical Science North Carolina Wesleyan College Wesleyan Station Rocky Mount, NC 27804 (919) 977-7171	Degree: Ph.D., Physical Chem., 1967 Specialty: Molecular Spectroscopy Assigned: Air Force Geophysics Lab.
Dr. Mark A. Norris Assistant Professor Dept. of Mechanics Virginia Polytechnic Inst. and State University 227 Norris Hall Blacksburg, VA 24061 (703) 961-4576	Degree: Ph.D., Eng. Mechanics, 1986 Specialty: Structural Dynamics & Controls Assigned: Astronautics Laboratory
Dr. Mufit H. Ozden Associate Professor Dept. of Systems Analysis Miami University 2303 Kreger Hall Oxford, OH 45056 (513) 529-5937	Degree: Ph.D. Eng. Systems, 1975 Specialty: Operations Research Assigned: Human Resources Laboratory: Logistics & Human Factors Div.

NAME/ADDRESS	DEGREE, SPECIALTY, LABORATORY ASSIGNED
Prof. Martin A. Patt Associate Professor Dept. of Electrical Eng. University of Lowell 1 University Ave. Lowell, MA 01854 (617) 452-5000	Degree: M.S., Electrical Eng., 1964 Specialty: Computer Applications Assigned: Air Force Geophysics Lab.
Dr. David G. Payne Assistant Professor Dept. of Psychology SUNY Binghamton Binghamton, NY 13901 (607) 777-4610	Degree: Ph.D., Cognitive Psy., 1984 Specialty: Human Memory Assigned: Harry G. Armstrong Aerospace Medical Research Laboratory
Dr. William Z. Plachy Professor Dept. of Chemistry & Biochem. San Francisco State University San Francisco, CA 94132 (415) 338-1436	Degree: Ph.D., Physical Chem., 1967 Specialty: Physical Chemistry Assigned: School of Aerospace Medicine
Dr. Patricia L. Plummer Professor Dept. of Physics & Chemistry Columbia Univ. of Missouri Columbia, NC 65211 (314) 882-3053	Degree: Ph.D., Chemical Physics, 1964 Specialty: Quantum Chemistry Assigned: Frank J. Seiler Research Lab.
Dr. Leonard E. Porter Professor Dept. of Physics & Astronomy University of Montana Missoula, MT 59812 (406) 243-6223	Degree: Ph.D., Nuclear Physics, 1965 Specialty: Nuclear Physics Assigned: Weapons Laboratory
Dr. Ramalingam Radhakrishnan Assistant Professor Dept. of Civil Engineering Prairie View A&M University Prairie View, TX 77084 (409) 857-2418	Degree: Ph.D, Structure Eng., 1974 Specialty: Structures Assigned: Engineering & Services Center

NAME/ADDRESS	DEGREE, SPECIALTY, LABORATORY ASSIGNED
Dr. Periasamy K. Rajan Professor Dept. of Electrical Eng. Tennessee Tech. University Box 5004 Cookeville, TN 38505 (615) 372-3308	Degree: Ph.D., Electrical Eng., 1975 Specialty: Digital Signal Processing Assigned: Avionics Laboratory
Dr. Panapakkam A. Ramamoorthy Associate Professor Dept. of Elect. & Computer Eng. University of Cincinnati M.L. #30 Cincinnati, OH 45220 (513) 475-4247	Degree: Ph.D., Digital Signal Processing, 1977 Specialty: Optical Memory Assigned: Avionics Laboratory
Dr. Dharam S. Rana Associate Professor Dept. of Management & Marketing Jackson State University 1400 J.R. Lynch Jackson, MS 39217 (601) 968-2534	Degree: Ph.D., Statistics, 1976 Specialty: Quantitative Techniques Assigned: Human Resources Laboratory: Manpower & Personnel Division
Dr. Sunita S. Rana Instructor Dept. of Computer Science Jackson State University 1400 Lynch Street Jackson, MS 39217 (601) 968-2105	Degree: Ph.D., Biology, 1969 Specialty: Computer Science Assigned: Human Resources Laboratory: Training Systems
Dr. Hal C. Reed Associate Professor Dept. of Biology Oral Roberts University 7777 S. Lewis Tulsa, OK 74171 (918) 495-6945	Degree: Ph.D., Entomology, 1982 Specialty: Insect Behavior Assigned: School of Aerospace Medicine
Dr. Michael D. Rice Associate Professor Dept. of Computer Science George Mason University 4400 University Dr. Fairfax, VA 22030 (703) 323-3884	Degree: Ph.D., Mathematics, 1973 Specialty: Computer Science/Math Assigned: Weapons Laboratory

NAME/ADDRESS	DEGREE, SPECIALTY, LABORATORY ASSIGNED
Dr. Mateen M. Rizki Assistant Professor Dept. of Computer Science Wright State University 410 Fawcett Hall Dayton, OH 45435 (513) 873-2394	Degree: Ph.D., Computer Science, 1985 Specialty: Modeling and Simulation Assigned: Avionics Laboratory
Dr. Thomas R. Rogge Professor Dept. of Eng. Science & Math Iowa State University 3015 Black Eng. Ames, IA 50010 (515) 294-2956	Degree: Ph.D., Applied Math, 1964 Specialty: Finite Element Analysis Assigned: School of Aerospace Medicine
Dr. Joe M. Ross Assistant Professor Dept. of Chemistry Central State University Wilberforce, OH 45384 (513) 376-6214	Degree: Ph.D., Molecular Bio., 1977 Specialty: Biochemistry of Macromolecules Assigned: School of Aerospace Medicine
Dr. Joseph E. Saliba Assistant Professor Dept. of Civil & Engr. Mechanics University of Dayton 300 College Park Dayton, OH 45469 (513) 229-3847	Degree: Ph.D., Solid Mechanics, 1983 Specialty: Engineering Mechanics Assigned: Harry G. Armstrong Aerospace Medical Research Laboratory
Dr. Dhiraj K. Sardar Assistant Professor Dept. of Physics University of Texas Div. of Earth & Physical Sci. San Antonio, TX 78285-0663 (512) 691-5462	Degree: Ph.D., Physics, 1980 Specialty: Materials Science & Lasers Assigned: School of Aerospace Medicine
Prof. Sonia H. Sawtelle Teaching Associate Dept. of Education Univ. of Texas - San Antonio San Antonio, TX 78285 (512) 691-4412	Degree: MS., Exercise Physiology, 1975 Specialty: Exercise Physiology Assigned: School of Aerospace Medicine

NAME/ADDRESS	DEGREE, SPECIALTY, LABORATORY ASSIGNED
Dr. Paul O. Scheie Professor Dept. of Physics Texas Lutheran College 1000 West Court Seguin, TX 78155 (512) 379-4161	Degree: Ph.D., Biophysics, 1965 Specialty: Electrophysiology Assigned: School of Aerospace Medicine
Dr. James L. Schmutz Professor Dept. of Chemistry Central Wesleyan College 1 Wesleyan Drive Central, SC 29630 (803) 639-2453	Degree: Ph.D., Chemistry, 1976 Specialty: Inorganic Polymers Assigned: Frank J. Seiler Research Lab.
Dr. Jodye I. Selco Assistant Professor Dept. of Chemistry University of Redlands P O Box 3080 Redlands, CA 92373-0999 (714) 793-2121	Degree: Ph.D., Chemical Physics, 1983 Specialty: Spectroscopy, Kinetics Assigned: Astronautics Laboratory
Dr. Shawky E. Shamma Professor Dept. of Math/Statistics University of West Florida Pensacola, FL 32514 (904) 474-2281	Degree: Ph.D., Applied Math, 1969 Specialty: Applied Mathematics Assigned: Armament Laboratory
Dr. Rameshwar P. Sharma Associate Professor Dept. of Mechanical Engineering Western Michigan University 2065 Kohrman Hall Kalamazoo, MI 49008 (616) 383-1408	Degree: Ph.D., Mechanical Eng., 1978 Specialty: Fluid Mechanics Assigned: Astronautics Laboratory
Dr. Larry R. Sherman Professor Dept. of Chemistry University of Akron Akron, OH 44325-0001 (216) 375-7333	Degree: Ph.D., Analytical Chem., 1969 Specialty: Organotin Chemistry Assigned: Occupational and Environment Health Laboratory

NAME/ADDRESS	DEGREE, SPECIALTY, LABORATORY ASSIGNED
Dr. James A. Sherwood Assistant Professor Dept. of Mechanical Eng. University of New Hampshire Kingsbury Hall Durham, NH 03824 (603) 862-2624	Degree: Ph.D., Aerospace Eng., 1987 Specialty: Solid Mechanics Assigned: Flight Dynamics Laboratory
Dr. Sanford S. Singer Professor Dept. of Chemistry University of Dayton 300 College Park Dayton, OH 45469 (513) 229-2833	Degree: Ph.D., Biological Chem., 1967 Specialty: Enzymology Assigned: Harry G. Armstrong Aerospace Medical Research Laboratory
Dr. Trilochan Singh Professor Dept. of Mechanical Eng. Wayne State University Detroit, MI 48202 (313) 577-3845	Degree: Ph.D., Mechanical Eng., 1970 Specialty: Chemical Combustion Assigned: Astronautics Laboratory
Dr. Jorge L. Sintes Chairman Dept. of Preventive Dentistry and Community Health Meharry Medical College 1005 D.B. Todd Blvd. Nashville, TN 37208 (615) 327-6185	Degree: Ph.D., Nutrition, 1978 Specialty: Dentistry Assigned: Wilford Hall Medical Center
Dr. Kenneth M. Sobel Associate Professor Dept. of Electrical Engineering The City College of New York 138th St. & Convent Ave. New York, NY 10031 (212) 690-4241	Degree: Ph.D., Electrical Eng., 1980 Specialty: Eigenstructure Assigned: Flight Dynamics Laboratory
Dr. Jonathan M. Spector Assistant Professor CSIS Jacksonville State University Pelham Road Jacksonville, AL 36265 (205) 231-5718	Degree: Ph.D., Philosophy, 1978 Specialty: Logic Assigned: Human Resources Laboratory: Training Systems Division

NAME/ADDRESS	DEGREE, SPECIALTY, LABORATORY ASSIGNED
Dr. Gary R. Stevens Assistant Professor Dept. of Statistics Oklahoma State University 301 MS Stillwater, OK 74078 (405) 624-5684	Degree: Ph.D., Statistics, 1986 Specialty: Stochastic Processes Assigned: Occupational and Environment Health Laboratory
Dr. Patrick J. Sweeney Asst. Dean of Engineering University of Dayton 300 College Park, KL201 Dayton, OH 45469 (513) 229-2736	Degree: Ph.D., Mechanical Eng., 1977 Specialty: Computer Modeling Assigned: Flight Dynamics Laboratory
Dr. Michael Sydor Professor Dept. of Physics University of Minnesota Duluth, MN 55812 (218) 726-7205	Degree: Ph.D., Physics, 1965 Specialty: Optics, Material Science Assigned: Materials Laboratory
Dr. Douglas G. Talley Assistant Professor Dept. of Mechanical Eng. University of Michigan 313 Automotive Lab Ann Arbor, MI 48109-2121 (313) 936-0429	Degree: Ph.D., Mechanical Eng., 1978 Specialty: Combustion Assigned: Aero Propulsion Laboratory
Dr. David J. Townsend Associate Professor Dept. of Psychology Montclair State College Upper Montclair, NJ 07042 (201) 893-7222	Degree: Ph.D., Cognitive Psy., 1982 Specialty: Cognitive Science Assigned: Rome Air Development Center
Dr. Donald R. Ucci Associate Professor Dept. of Elect. & Computer Eng. Illinois Inst. of Technology 3300 S. Federal Chicago, IL 60616 (312) 567-3405	Degree: Ph.D., Electrical Eng., 1986 Specialty: Adaptive Arrays Assigned: Rome Air Development Center

NAME/ADDRESS	DEGREE, SPECIALTY, LABORATORY ASSIGNED
Dr. Ahmad D. Vakili Associate Professor Dept. of AE/ME Univ. of Tennessee Space Inst. Tullahoma, TN 37388 (615) 455-0631	Degree: Ph.D., Aerospace Eng., 1978 Specialty: Unsteady Flows Assigned: Arnold Engineering Development Center
Dr. Richard S. Valpey Assistant Professor Dept. of Chemistry Wilberforce University Wilberforce, OH 45384 (513) 376-2911	Degree: Ph.D., Organic Chemistry, 1983 Specialty: Organic Synthesis Assigned: Materials Laboratory
Dr. Peter J. Walsh Professor Dept. of Physics Fairleigh Dickinson University Teaneck, NJ 07666 (201) 692-2493	Degree: Ph.D., Physics, 1960 Specialty: Superconductivity Assigned: Rome Air Development Center
Dr. Kenneth L. Walter Associate Professor Dept. of Chemical Engineering Prairie View A&M University Prairie View, TX 77446 (409) 857-2827	Degree: Ph.D., Chemical Eng., 1972 Specialty: Chemical Engineering Process Assigned: Rome Air Development Center
Dr. Gwo-Ching Wang Associate Professor Dept. of Physics Rensselaer Polytechnic Inst. Troy, NY 12180-3590 (518) 276-8387	Degree: Ph.D., Materials Science, 1978 Specialty: Surface Sciences Assigned: Rome Air Development Center
Dr. Andrew P. Whipple Associate Professor Dept. of Biology Taylor University Upland, IN 46989 (317) 998-5333	Degree: Ph.D., Biology, 1979 Specialty: Cell Biology Assigned: Harry G. Armstrong Aerospace Medical Research Laboratory

NAME/ADDRESS	DEGREE, SPECIALTY, LABORATORY ASSIGNED
Prof. Sharon T. Williams Instructor Dept. of Chemistry Southern University Baton Rouge, LA 70813-2074 (504) 771-3990	Degree: M.S., Biochemistry, 1981 Specialty: General Chemistry Assigned: School of Aerospace Medicine
Dr. Lawrence A. Witt Assistant Professor Dept. of Psychology Western Illinois University Macomb, IL 61455 (309) 298-1593	Degree: Ph.D., Psychology, 1985 Specialty: Industrial/Organ. Psychology Assigned: Human Resources Laboratory: Operations Training Division
Dr. Frank A. Witzmann Assistant Professor Dept. of Biology IUPUI - Columbus 4601 Central Avenue Columbus, IN 47203 (812) 372-8266	Degree: Ph.D., Biology, 1981 Specialty: Protein Analysis Assigned: Harry G. Armstrong Aerospace Medical Research Laboratory
Dr. William E. Wolfe Associate Professor Dept. of Civil Engineering Ohio State University 2070 Neil Avenue Columbus, OH 43210 (614) 292-0790	Degree: Ph.D., Engineering, 1979 Specialty: Geotechnical Engineering Assigned: Flight Dynamics Laboratory
Dr. John R. Wright Professor Dept. of Chem., Physical Sci. Southeast Oklahoma State Univ. Box 4181, Station A, SEOSU Durant, OK 74701 (405) 924-0121	Degree: Ph.D., Chemistry, 1971 Specialty: Biochemistry Assigned: School of Aerospace Medicine
Prof. Wafa E. Yazigi Instructor Dept. of Mathematics Columbia Basin College 2600 N. 20th Pasco, WA 99301 (509) 547-0511	Degree: M.S., Aeronautical Eng., 1986 Specialty: Solid Mechanics Assigned: Armament Laboratory

NAME/ADDRESS	DEGREE, SPECIALTY, LABORATORY ASSIGNED
Dr. Lawrence F. Young Associate Professor Dept. of QA/IS, CBA University of Cincinnati ML 30 Cincinnati, OH 45220 (513) 475-7169	Degree: D.Sc., Industrial Eng., 1978 Specialty: Industrial Engineering Assigned: Human Resources Laboratory: Logistics & Human Factors Div.
Dr. Robert K. Young Professor Dept. of Psychology University of Texas Mezes 330, Psychology Dept. Austin, TX 78713 (512) 471-9228	Degree: Ph.D., Exp. Psychology, 1954 Specialty: Experimental Psychology Assigned: Human Resources Laboratory: Manpower & Personnel Division
Dr. Juin S. Yu Professor Dept. of Mechanical Eng. West Virginia Tech. Montgomery, WV 25136 (304) 442-3248	Degree: Ph.D., Mechanical Eng., 1964 Specialty: Thermofluid Transport Assigned: Aero Propulsion Laboratory

PARTICIPANT LABORATORY ASSIGNMENT

C. PARTICIPANT LABORATORY ASSIGNMENT (Page 1)

1988 USAF/UES SUMMER FACULTY RESEARCH PROGRAM

AERO PROPULSION LABORATORY (AFWAL/APL)
(Wright-Patterson Air Force Base)

1. Bryan Becker
2. Mingking Chyu
3. Jerry Clark
4. Derek Dunn-Rankin
5. Wayne Eckerle
6. David Mikolaitis
7. Douglas Talley
8. Juin Yu

ARMAMENT LABORATORY (AD)
(Eglin Air Force Base)

1. Ibrahim Ahmad
2. Stephen Dow
3. Manuel Huerta
4. Anastas Lazaridis
5. Kwang Min
6. Joseph Molitoris
7. Shawky Shamma
8. Wafa Yazigi

HARRY G. ARMSTRONG AEROSPACE MEDICAL RESEARCH LABORATORY (AAMRL)
(Wright-Patterson AFB)

1. Praphulla Bajpai
2. Shankar Bale
3. Charles Covington
4. Barry Goettl
5. Robert Masingale
6. David Payne
7. Joseph Saliba
8. Sanford Singer
9. Andrew Whipple
10. Frank Witzmann

ARNOLD ENGINEERING DEVELOPMENT CENTER (AEDC)
(Arnold Air Force Base)

1. Eustace Dereniak
2. William Grissom
3. Darrell Hoy
4. Manjit Jawa
5. Ahmad Vakili

ASTRONAUTICS LABORATORY (AL)
Edwards Air Force Base)

1. Clarence Calder
2. Phillip Christiansen
3. Susan Collins
4. David Jensen
5. Mark Norris
6. Jodye Selco
7. Rameshwar Sharma
8. Trilochan Singh

AVIONICS LABORATORY (AFWAL/AL)
(Wright-Patterson Air Force Base)

1. Mike Burlakoff
2. Gerald Grams
3. David Hemmendinger
4. Mohammad Karim
5. Robert Li
6. Periasamy Rajan
7. Panapakkam Ramamoorthy
8. Mateen Rizki

EASTERN SPACE AND MISSILE CENTER (ESMC)
(Patrick Air Force Base)

1. Albert Heaney

C. PARTICIPANT LABORATORY ASSIGNMENT (Page 2)

ELECTRONIC SYSTEMS DIVISION (ESD)
(Hanscom Air Force Base)

1. George Bratton
2. John Dalphin

ENGINEERING AND SERVICES CENTER (ESC)
(Tyndall Air Force Base)

1. Wayne Charlie
2. David DeHeer
3. Deanna Durnford
4. Edward Greenwald
5. Neil Hutzler
6. William Mounfield
7. Richard Myers
8. Ramalingam Radhakrishnan

FLIGHT DYNAMICS LABORATORY (FDL)
(Wright-Patterson Air Force Base)

1. Larry Byrd
2. Karen Chou
3. Awatef Hamed
4. Yulian Kin
5. Augustus Morris
6. Nanda Mukherjee
7. James Sherwood
8. Kenneth Sobel
9. Patrick Sweeney
10. William Wolfe

FRANK J. SEILER RESEARCH LABORATORY (FJSRL)
(USAF Academy)

1. Dan Bruss
2. Charles Bump
3. Richard Carlin
4. Michael McKee
5. Tammy Melton
6. Patricia Plummer
7. James Schmutz

GEOPHYSICS LABORATORY (AFGL)
(Hanscom Air Force Base)

1. Lucia Babcock
2. Stephen Baker
3. Pradip Bakshi
4. Reuben Benumof
5. Donald Collins
6. Michael Frantz
7. Christopher Godfrey
8. Janet Kozyra
9. Irving Lipschitz
10. John McHugh
11. Himanshoo Navangul
12. Martin Patt

HUMAN RESOURCES LABORATORY (HRL)
(Brooks, Williams, and Wright-Patterson Air Force Bases)

1. Patricia Carlson
2. Kevin Ford
3. Hugh Garraway
4. Douglas Jackson
5. Charles Lance
6. Thomas Landers
7. Douglas Mandra
8. Mufit Ozden
9. Dharam Rana
10. Sunita Rana
11. Jonathan Spector
12. Lawrence Witt
13. Lawrence Young
14. Robert Young

C. PARTICIPANT LABORATORY ASSIGNMENT (Page 3)

MATERIALS LABORATORY (ML)
(Wright-Patterson Air Force Base)

1. Robert Arenz
2. Gene Carlisle
3. Parvis Dadras
4. Suren Dwivedi
5. Barry Fussell
6. David Grossie
7. Vijay Gupta
8. L. James Lee
9. Thomas Meek
10. Carolyn Meyers
11. Michael Sydor
12. Richard Valpey

OCCUPATIONAL AND ENVIRONMENTAL HEALTH LABORATORY (OEHL)
(Brooks Air Force Base)

1. Steven Chiesa
2. Randolph Huff
3. Larry Sherman
4. Gary Stevens

ROME AIR DEVELOPMENT CENTER (RADC)
(Griffiss Air Force Base)

1. Beryl Barber
2. Keith Christianson
3. Darin DeForest
4. Paul Dingman
5. Hugh Donaghy
6. Oleg Jakubowicz
7. Samuel Kozaitis
8. David Townsend
9. Donald Ucci
10. Peter Walsh
11. Kenneth Walter
12. Gwo-Ching Wang

SCHOOL OF AEROSPACE MEDICINE (SAM)
(Brooks Air Force Base)

1. Ronald Bulbulian
2. John Burke
3. Bennye Henderson
4. Eric Johnson
5. Daisy Kimble
6. Harold Longbotham
7. David Ludwig
8. William Plachy
9. Hal Reed
10. Thomas Rogge
11. Joe Ross
12. Dhiraj Sardar
13. Sonia Sawtelle
14. Paul Scheie
15. Sharon Williams
16. John Wright

WEAPONS LABORATORY (WL)
(Kirtland Air Force Base)

1. Lane Clark
2. David Dolson
3. William Jordan
4. Arkady Kheyfets
5. Leonard Porter
6. Michael Rice

WILFORD HALL MEDICAL CENTER (WHMC)
(Lackland Air Force Base)

1. David Cecil
2. Jorge Sintes

RESEARCH REPORTS

RESEARCH REPORTS

1988 SUMMER FACULTY RESEARCH PROGRAM

Technical Report Number	Title	Professor
Volume I		
Armament Laboratory		
1	Measuring Systems Effectiveness and Systems Availability of Hardened Targets Subject to a Variety of Weapons	Dr. Ibrahim Ahmad
2	Model Drawing Algorithms for a Matching Problem	Dr. Stephen Dow
3	Two Dimensional Simulation of Railgun Plasma Armatures	Dr. Manuel Huerta
4	Modeling Reactive Fragments	Dr. Anastas Lazaridis
5	Target-Aerosol Discrimination Techniques for Active Optical Proximity Sensors	Dr. Kwang Min
6	The Dynamics of Projectile Impact	Dr. Joseph Molitoris
7	ARIMA Modeling of Residuals in AD/KR TDOP Models	Dr. Shawky Shamma
8	Stress Analysis for a Fin Stabilized Projectile	Dr. Wafa Yazigi
Arnold Engineering Development Center		
9	Infrared Charge Transfer Device Characterization	Dr. Eustace Dereniak
10	Liquid Film Cooling In Rocket Engines	Dr. William Grissom
11	Diffuser Failure Investigation/Non-Interference Stress Measurement System Algorithms Study	Dr. Darrell Hoy
12	Solid Rocket Motor Plume Analysis Through Emission Computerized Tomography	Dr. Manjit Jawa
13	Skin Friction Measurement Using Surface Mounted Hot Films	Dr. Ahmad Vakili

Astronautics Laboratory		
14	Study of Embedded Sensors in Graphite-Epoxy Composites	Dr. Clarence Calder
15	Core Polarization in Lithium and Aluminum	Dr. Phillip Christiansen
16	The Photochemistry of μ3-(η-Diethylacetylene)-Decacarbonyltriosmium in Solid Argon	Dr. Susan Collins
17	Composite-Embedded Fiber-Optic Strain Sensors	Dr. David Jensen
18	Observer Design for the AFAL Grid Structure Using Low-frequency Accelerometer Data	Dr. Mark Norris
19	Photochemistry of Azulene Solutions and a Novel Photochemical Nitration Process	Dr. Jodye Selco
20	Injection System and Spray Characteristics	Dr. Rameshwar Sharma
21	Chemical Kinetic Mechanisms for $CH_4/NO_2/O_2$ Flames	Dr. Trilochan Singh
Eastern Space and Missile Center		
22	Generic Requirements for a CAE/CAD/CAM System	Dr. Albert Heaney
Electronics Systems Division		
23	Alaskan HF Test Data Analysis	Dr. George Bratton
24	Stage 1 Analysis of Alaskan High Frequency Radio Network	Dr. John Dalphin
Engineering and Services Center		
25	High Intensity Stress Wave Propagation in Partially Saturated Sand	Dr. Wayne Charlie
26	Individualization of Human Tissue by the Serologic Identification of Erythrocyte Antigens	Dr. David DeHeer
27	Estimation of Jet Fuel Contamination in Soils	Dr. Deanna Durnford
28	Cogeneration Assessment on Military Bases	Dr. Edward Greenwald

29	Soil Vapor Extraction of Volatile Organic Chemicals	Dr. Neil Hutzler
30	A Preliminary Investigation of Neural Networks for the Air Force Engineering and Services Center	Dr. William Mounfield
31	Rapid Measurements of Adsorption and Desorption of Volatile Organic Compounds	Dr. Richard Myers
32	Prefabricated Hypar Structural System Cost Comparison with Box and Arch Structures	Dr. Ramalingam Radhakrishnan

Volume II
Frank J. Seiler Research Laboratory

33	Thermal Decomposition Kinetic Studies of NTO by High Performance Liquid Chromatography	Dr. Dan Bruss
34	Preparation and Properties of Nitronium Tetrachloroaluminate	Dr. Charles Bump
35	Homogeneous Ziegler-Natta Catalysis in Lewis Acid Molten Salts	Dr. Richard Carlin
36	A MCSCF Study of the Rearrangement of Nitromethane to Methyl Nitrite	Dr. Michael McKee
37	The Effects of Sodium Chloride on Room Temperature Molten Salts	Dr. Tammy Melton
38	AB Initio and Chemical Dynamics Study of Energetic Materials	Dr. Patricia Plummer
39	Separators for Molten Salt Batteries	Dr. James Schmutz

Geophysics Laboratory

40	Radiative Association In Ion-Molecule Reactions: Reactions of Some Carbon Cations	Dr. Lucia Babcock
41	Upward Continuation of Gravity Data With Error Estimates	Dr. Stephen Baker
42	Impulse Approximation Formalism for Atom Molecule Collisions	Dr. Pradip Bakshi
43	Total Dose Effect on Soft Error Rate for Dynamic MOS Memory Cells	Dr. Reuben Benumof

44	Digital Photometric Calibration of and Analysis with Video Imagers in the Ultraviolet	Dr. Donald Collins
45	A Model for Intensified Frontogenesis Over a Modified Mountain Ridge	Dr. Michael Frantz
46	Gamma and X Radiation from Solar Flares	Dr. Christopher Godfrey
47	Theoretical and Observational Studies of Geomagnetic Storm-Related Ion and Electron Heating in the Subauroral Region	Dr. Janet Kozyra
48	Update of the Hitran Database	Dr. Irving Lipschitz
49	Spectral Domain Decomposition	Dr. John McHugh
50	On the Possible Inclusion of "Heavy" Molecules in the HITRAN Database	Dr. Himanshoo Navangul
51	Software Tools for Processing Large Lidar Data Streams	Dr. Martin Patt
Rome Air Development Center		
52	Noise Calculations in a RADAR Receiver	Dr. Beryl Barber
53	Stability of Au/W/GaAs and Au/Pt/Ti/GaAs Schottky Barrier Height: A Preliminary Study	Dr. Keith Christianson
54	Parallel Runtime System For Lucid	Dr. Darin DeForest
55	Pre-Sort Processor Phase Distortion Evaluation	Dr. Paul Dingman
56	A PROLOG Natural Language Front End to an ERIC Object Oriented Database	Dr. Hugh Donaghy
57	No Report Submitted at this Time	Dr. Oleg Jakubowicz
58	Design of an Optical Correlator Testbed and Optical Co-Processor	Dr. Samuel Kozaitis
59	Characteristics of Dialog in a Noisy Channel for Performing a Time-Oriented Task	Dr. David Townsend
60	The Effects of Nonlinearities of High Speed Analog-to-Digital Converters on Digital Beamforming Arrays	Dr. Donald Ucci

61	Studies in Microwave Superconductors	Dr. Peter Walsh
62	Chemical Vapor Deposition of Titanium Compounds with an Atomic Layer Epitaxy System	Dr. Kenneth Walter
63	Surface Effects on the High Temperature Superconducting YBaCuO Thin Films grown by RF Sputtering	Dr. Gwo-Ching Wang

Weapons Laboratory

64	Realization of Sublayer Relative Shielding Order in Electromagnetic Topology	Dr. Lane Clark
65	Diode Laser Probe of Vibrational Energy Transfer Kinetics in Sulfur Monoxide	Dr. David Dolson
66	Evaluating How Laser Irradiation Damages Loaded Composite Materials	Dr. William Jordan
67	Relativistic Effects in GPS Time Transfer	Dr. Arkady Kheyfets
68	Stopping Power and Penetration Physics	Dr. Leonard Porter
69	Performance Models for Parallel Algorithms	Dr. Michael Rice

Volume III
Air Force Wright Aeronautical Laboratories
Aero Propulsion Laboratory

70	Computation of the Flow Field and Heat Transfer in a Rectangular Passage with a Turbulator	Dr. Bryan Becker
71	Use of Laser Light Visualization Techniques on Studies of Film Cooling Flow And Flow Over Cavities	Dr. Mingking Chyu
72	Experimental Study of Electronic Excitation of Xenon by Electon Impact	Dr. Jerry Clark
73	Cars Thermometry in Droplet-Laden Flows	Dr. Derek Dunn-Rankin

74	Measurement of the Velocity Field and Heat Transfer Coefficients Associated with a Rectangular Wall Jet	Dr. Wayne Eckerle
75	Lifted Jet Diffusion Flames	Dr. David Mikolaitis
76	Interpretation of a Lifted Turbulent Diffusion Flame as a Problem in Stratified Combustion	Dr. Douglas Talley
77	Diffusion and Convection in the Condenser of a Gas-Loaded Heat Pipe	Dr. Juin Yu

Avionics Laboratory

78	Ada Compiler Evaluation Capability	Dr. Mike Burlakoff
79	A Study of Sky Backgrounds and Sub-Visual Cirrus at the Megalidar Site and a Proposed Turbulence Monitoring Facility for Wright-Patterson AFB	Dr. Gerald Grams
80	Formal Verification of VHDL Specifications	Dr. David Hemmendinger
81	Low Voltage Broadband Beam Steering Devices Using Liquid Crystals	Dr. Mohammad Karim
82	Model-based Target Recognition Using Laser Radar Imagery	Dr. Robert Li
83	Signal Processing for ESM Receivers	Dr. Periasamy Rajan
84	Neural Networks and their Applications in Digital Receiver Design	Dr. Panapakkam Ramamoorthy
85	Applications of Evolutionary Learning Strategies to Pattern Recognition Tasks	Dr. Mateen Rizki

Flight Dynamics Laboratory

86	Heat Flux Prediction for Nucleate Boiling in Liquid Metal Heat Pipes	Dr. Larry Byrd
87	Reliability Study of Nonlinear Structural Response under Reversible Cyclic Loading Processes	Dr. Karen Chou
88	Survey and Assessment of Validation Data Base for Shockwave Boundary Layer Interaction in Supersonic Inlets	Dr. Awatef Hamed

89	Failures of F-16 Transparencies Analysis and Failure Prevention Recommendations	Dr. Yulian Kin
90	Visual Capabilities on a Robot Aided Aircraft Refueler Prototype	Mr. Augustus Morris
91	Reaction Kinetic of Halon 1301 Suppression of Fire Explosion in an Aircraft Fuel Tank	Dr. Nanda Mukherjee
92	Development of an Aircraft Tire-Wheel Interface Model for Flange/Beadseat Contact Loads	Dr. James Sherwood
93	Robust Eigenstructure Assignment for Flight Control Design	Dr. Kenneth Sobel
94	A Computer Model for Air-to-Air Combat (Force on Force) Assessment	Dr. Patrick Sweeney
95	Damage in Graphite/Epoxy Plates Subjected to Low Velocity Impact	Dr. William Wolfe
Materials Laboratory		
96	Analysis Methods for Nonlinear Mechanical Behavior of Glassy Polymers	Dr. Robert Arenz
97	Laser Hardened Materials Via Magnetically Aligned Polypeptide-Phthalocyanines	Dr. Gene Carlisle
98	Joining of Carbon-Carbon Composite Materials	Dr. Parviz Dadras
99	Rapid Simulation for Experimental Validation of H Section Forging Using Finisher Punch	Dr. Suren Dwivedi
100	QPA Control of the End Milling Process	Dr. Barry Fussell
101	Single-Crystal Diffraction Analysis of Compounds with Potential Nonlinear Optical Properties	Dr. David Grossie
102	Effect of Various Metals on the Thermal Degradation of a Chlorotrifluorethylene Based Fluid	Dr. Vijay Gupta

103	Characterization of Heat Transfer and Reaction in the Autoclave Curing of Graphite/Epoxy Composites by Scaling Analysis	Dr. L. James Lee
104	A Study of the Melting of the Plagioclase Feldspars in a Microwave Field	Dr. Thomas Meek
105	Reaction Zone Characeristics of Titanium Aluminide Composites	Dr. Carolyn Meyers
106	Photoreflectance Measurements of Unintentional Impurities in Undoped Galium Arsinide	Dr. Michael Sydor
107	The Synthesis of 2-Formyl Pyridoimidazoles	Dr. Richard Valpey

Volume IV
Human Systems Division Laboratories
Harry G. Armstrong Aerospace Medical Research Laboratory

108	Ceramic Composites for Studying Bone Ingrowth and Remodeling	Dr. Praphulla Bajpai
109	In Vitro Cytotoxic Effects of Perfluorodecanoic Acid on Human Peripheral Blood Lymphocytes	Dr. Shankar Bale
110	Auditory Modeling	Dr. Charles Covington
111	Cognitive Demands of Tracking Strategies as Assessed by the Optimum-Maximum Procedure	Dr. Barry Goettl
112	Evaluation of an Extraction Procedure for the Analysis of Serum Steroids	Dr. Robert Masingale
113	Performance in a Visual Monitoring Task with Serial and Simultaneous Display Formats	Dr. David Payne
114	A Nonlinear Lumped Parameter Model for the Seated Humans	Dr. Joseph Saliba
115	In Vitro Modeling of Perfluoro-N-Decanoate Effects on Enzymes of Fatty Acid Metabolism	Dr. Sanford Singer
116	Perfluorodecanoic Acid Efflux from Cultured Primary Rat Hepatocytes	Dr. Andrew Whipple

117	Determination of Perfluoro-N-Decanoic Acid Toxicity in Vitro and in Vivo Via Two-Dimensional Polyacrylamide Gel Electrophoresis	Dr. Frank Witzmann
Human Resources Laboratory		
118	Hypertext and Intelligent Interfaces for Text Retrieval	Dr. Patricia Carlson
119	Linking Training Evaluation to Training Needs Assessment: Development of a Conceptual Model	Dr. J. Kevin Ford
120	A Concept for an Intelligent Tool to Facilitate the Development of Qualitative Process Models in Novice Programmers	Dr. Hugh Garraway
121	A Tool for Studying the Effect of Range Restriction on Correlation Coefficient Estimation	Dr. Douglas Jackson
122	Evaluation of a Methodology for Estimating Cross-AFS Transferability of Skills	Dr. Charles Lance
123	An Expert System Approach for Reliability Data Analysis	Dr. Thomas Landers
124	No Report Submitted at this Time	Dr. Douglas Mandra
125	Graphical Programming of Simulation Models in an Object-Oriented Environment	Dr. Mufit Ozden
126	A Study of Interaction Between Job Properties and Personal Characteristics in the New PACE System	Dr. Dharam Rana
127	An Intelligent Tutor for the IBM System/360 Assembly Language: BIGBLUE	Dr. Sunita Rana
128	Preliminary Design Considerations for an Advanced Instructional Design Advisor	Dr. Jonathan Spector
129	Effectiveness of Contract Monitors In An Air Force Human Resources Laboratory: Prediction and Measurement	Dr. Lawrence Witt

130	Computer Support of Creativity in Unified Life Cycle Engineering	Dr. Lawrence Young
131	The Relationship Between Inspection Time and Intelligence	Dr. Robert Young
Occupational and Environmental Health Laboratory		
132	Solvent Extraction of Boron From Wastewater	Dr. Steven Chiesa
133	Extention of the Detection Limits of Arsenic and Selenium in Solid Samples by ICP/AES Utilizing Preconcentration Techniques	Dr. Randolph Huff
134	Determination of Asbestos Fibers in Environmental Samples Using Scanning Electron Microscopy and Energy Dispersive X-ray Analyses (SEM-EDXA)	Dr. Larry Sherman
135	Analysis of Contaminated Ground Water Using Kriging Methods	Dr. Gary Stevens
School of Aerospace Medicine		
136	Blood Flow Distribution In The Non-Working Forearm During Exercise	Dr. Ronald Bulbulian
137	Photophysics and Photochemistry of Transition Metal Complexes of 8-Quinolinamine Schiff Bases	Dr. John Burke
138	Immunocytochemical Localization of Vasoactive Intestinal Peptide, Neuropeptide Y and Arginine Vasopressin within the Supra-chiasmatic Nuclei of the Rat	Dr. Bennye Henderson
139	Development of Improved Assays for Cholesterol and Major Lipoprotein Fractions	Dr. Eric Johnson
140	Plasma Catecholamine Assays by High Performance Liquid Chromatography	Dr. Daisy Kimble
141	Application of Nonlinear Filters to VEP Data	Dr. Harold Longbotham
142	Extensions of Several Difference Score Approaches for the Analysis of Time Ordered Repeated Measures	Dr. David Ludwig

143	Spin Label Studies of Oxygen in Biological Systems	Dr. William Plachy
144	The Stinging Wasps (Hymenopter: Vespidae) of South Texas	Dr. Hal Reed
145	Modeling of Blood Flow in the Systemic Human Arterial Tree	Dr. Thomas Rogge
146	The Separation of HDL2 and HDL3 Using the Technique of Ultra-centrifugation	Dr. Joe Ross
147	An Experimental Design to Demonstrate the Dispersion Effects of Salt Water on OPTICAL PULSES	Dr. Dhiraj Sardar
148	Literature Search on Nutrition and the Relation to Tactical Air Command Pilots, G-Tolerance and Energy Output	Dr. Sonia Sawtelle
149	A Small Inert-Gas Generator	Dr. Paul Scheie
150	High Performance Liquid Chromatography (HPLC) Determination of High Energy Phosphate Pool	Dr. Sharon Williams
151	Chemiluminescent Probes Based on Luminol and Luminol Derivatives	Dr. John Wright

Wilford Hall Medical Center

152	PC - Mainframe Interface for Data Entry	Dr. David Cecil
153	Oral Health	Dr. Jorge Sintes

1889s

1988 USAF-UES SUMMER FACULTY RESEARCH PROGRAM/

GRADUATE STUDENT SUMMER SUPPORT PROGRAM

Sponsored by the

AIR FORCE OFFICE OF SCIENTIFIC RESEARCH

Conducted by the

UNIVERSAL ENERGY SYSTEMS, INC.

FINAL REPORT

THERMAL DECOMPOSITION KINETIC STUDIES OF NTO BY HIGH PERFORMANCE LIQUID CHROMATOGRAPHY

Prepared by:	Dan R. Bruss
Academic Rank:	Assistant Professor
Department and University:	Department of Physical Sciences Albany College of Pharmacy Albany, New York
Research Location:	Frank J. Seiler Research Laboratory/ NC (AFSC) USAF Academy, CO 80840
USAF Research Colleague:	Joseph A. Menapace
Date:	15 August 1988
Contract No:	F49620-87-R-0004

THERMAL DECOMPOSITION KINETIC STUDIES OF NTO BY HIGH PERFORMANCE LIQUID CHROMATOGRAPHY

by

Dan R. Bruss

Abstract

Thermal decomposition of 3-nitro-1,2,4-triazol-5-one (NTO) was monitored over a temperature interval of 508-518 K. Rate constants were obtained for the temperatures investigated by measuring unreacted NTO as a function of time as determined by high performance liquid chromatography. The decomposition patterns are indicative of an autocatalytic mechanism. The temperature dependence of the rate constants found in the interval exhibited Arrhenius behavior, yielding an activation energy of 75.5 kCal $\pm$ 9.3 kCal. Mass spectral analysis of head space gas samples taken during decomposition demonstrate carbon dioxide as a decomposition product. Preliminary UV and IR analyses of NTO suggest a shift from the more stable keto form to the enol near a pH of 7.

I. INTRODUCTION

Compounds that exhibit improved performance as energetic materials are of considerable interest for both commercial and defense applications. An understanding of the chemistry involved in the very early stages of decomposition of these compounds may be useful, not only from a physical organic perspective, but also may prove to be a valuable tool in designing propellants and explosives in the future.

Considerable progress has been made in understanding the fundamental reaction mechanism involved in the thermal decomposition of TNT in the condensed phase.[1-3] Virtually nothing, however, is known about the initial decomposition chemistry of the nitroheterocycle 3-nitro-1,2,4-triazol-5-one (NTO), which has recently been reported as an insensitive high explosive.[4,5]

To initiate the investigation, a methodology to monitor the kinetics of NTO and related compounds needed to be established. High performance liquid chromatography affords a convenient, quantitative, non-destructive direct measurement of compound present. At the same time it provides a method to possibly detect and separate intermediates. With this in mind it was decided to explore HPLC as a kinetic tool.

The author has had previous experience in HPLC analysis, monitoring PCB levels in biological samples. In addition his current research interests include investigation of the mechanistic chemistry involved in metal mediated pinacol coupling of cycloalkanones to form diols and their subsequent acid catalyzed rearrangement to yield spiranones. Both of these experiences contributed to his assignment to the energetic materials project at the Frank J. Seiler Research Laboratory.

II. OBJECTIVES

To monitor the disappearance of NTO, a suitable separation scheme affording good resolution in a reasonable time frame, needed to be established. Once set up, measurements of loss of NTO at a given temperature could be carried out to provide a plot of weight of remaining NTO as a function of time. Replicate plots at several temperatures would then be carried out in an effort to provide a preliminary energy of activation for the thermal decomposition reaction. At the same time, detection and characterization of any stable intermediates would be pursued.

III. METHODS AND DISCUSSION

Unlike TNT, which was the predecessor in decomposition

studies by HPLC,[6] the nitrated heterocyle NTO is quite polar with unusual solubility characteristics. Initial attempts to monitor NTO utilizing a standard reverse phase column with a water/methanol gradient system proved unworkable, since NTO eluted very early regardless of the gradient. On the other hand, normal phase separation was ineffective since NTO exhibited a very long or unacceptably short retention time with a variety of solvent systems. Finally an isocratic water/1% acetic acid solvent system delivered through a bonded cyano column provided a sharp NTO peak at seven minutes which was readily detected at 254 nm.

In the process of establishing these conditions, the NTO peak changed from a sharp single peak to two sharp but poorly resolved peaks and finally back to a single peak as the concentration of acetic acid was slowly increased in increments from 0.1% to 0.5%. This suggested that perhaps a shift from the more stable keto form to the enol was in progress. Samples of NTO were then analyzed by UV and IR spectroscopy at various pH conditions. Samples analyzed in the approximate 3-6 pH range exhibited a lambda max at 317 nm while at higher pH the lambda max shifted to 343 nm. To rule out a simple solvent effect, IR spectra were taken of two samples in both of the pH ranges. The sample buffered in a low pH showed a strong absorption at 1720 cm^{-1}, while

the more basic sample exhibited a strong, broad absorption in the 3400 cm^{-1} region and a shift of the carbonyl peak to 1640 cm^{-1}, suggesting the presence of OH and C=N functionalities, respectively. Preliminary carbon NMR data gave no conclusive evidence.

With a suitable NTO assay in hand, thermal decomposition analyses were then carried out. Each run consisted of accurately weighed 100 mg samples of NTO contained in 20cm x 8mm tubes which were loosely fitted with corks. Twelve of these tubes were heated in a fluidized bath at a preset stabilized temperature. In addition, a blank was also prepared but not heated. The tubes were then removed from the bath and immediately quenched in ice water at regular 20 minute intervals. The tubes were then weighed to record weight loss.

The quenched samples were pipetted from the tubes as a DMSO solution or suspension and transferred to 2 mL volumetric flasks. The tubes were then washed with additional DMSO to assure complete transfer of NTO and precipitate, taking care to bring the volume to just 2 mL. A 50 microliter sample from each flask was then transferred to separate 5 mL vials. Each vial was tared and 2.5000 grams of water added. Analysis proceeded by injecting 20 microliters of diluted sample into the HPLC. The area of the NTO peak was then normalized to give an accurate reading of milligrams NTO remaining for each sample.

Duplicate decomposition runs were conducted at 235 ^{o}C, 240^{o}C, and 245^{o}C along with a single run at 238^{o}C. The corrected weight of NTO was then plotted as a function of time. In each case, the decomposition pattern showed an initial induction period with minor weight loss followed by rapid decomposition. Such a pattern is typical of an autocatalytic reaction mechanism. With this mechanism as a model, the data was then plotted as the log (100-X)/X as a function of time where X= the amount of NTO at a given time. The slopes of these linear plots correspond to the espective rate constants. Both types of plots are graghicallly represented for each of the temperatures investigated as illustrated by Figures 1-4.

The rate constants derived from the graphs were then used to construct an Arrhenius plot, the slope of which provides a first approximation of an activation energy. This corresponds to 75.5 +/- 9.3 kCal/mole and is summarized in Figure 5.

Since no intermediates were, as yet, discovered by the HPLC system currently employed, but a decrease in the amount of NTO along with concomitant weight loss was occurring during the course of reaction, it was felt that analysis of the head space gases of the reaction tubes be carried out by mass spectrometry. Several tubes each again containing 100 mg NTO were fitted with rubber septa and the

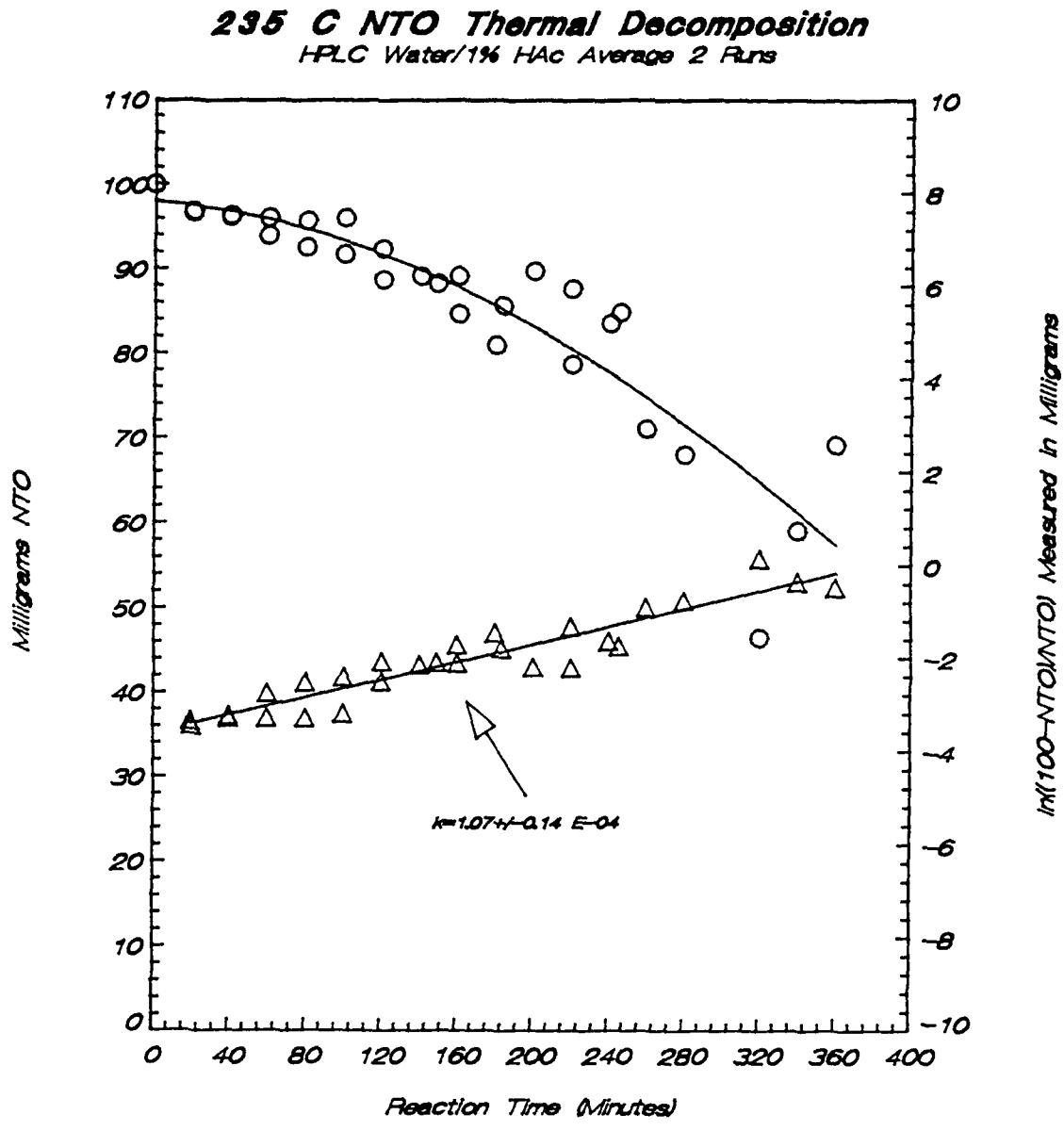
235 C NTO Thermal Decomposition
HPLC Water/1% HAc Average 2 Runs
Milligrams NTO
ln((100-NTO)/NTO) Measured in Milligrams
Reaction Time (Minutes)
k=1.07+/-0.14 E-04
110
100
90
80
70
60
50
40
30
20
10
0
10
8
6
4
2
0
-2
-4
-6
-8
-10
0
40
80
120
160
200
240
280
320
360
400

Figure 1

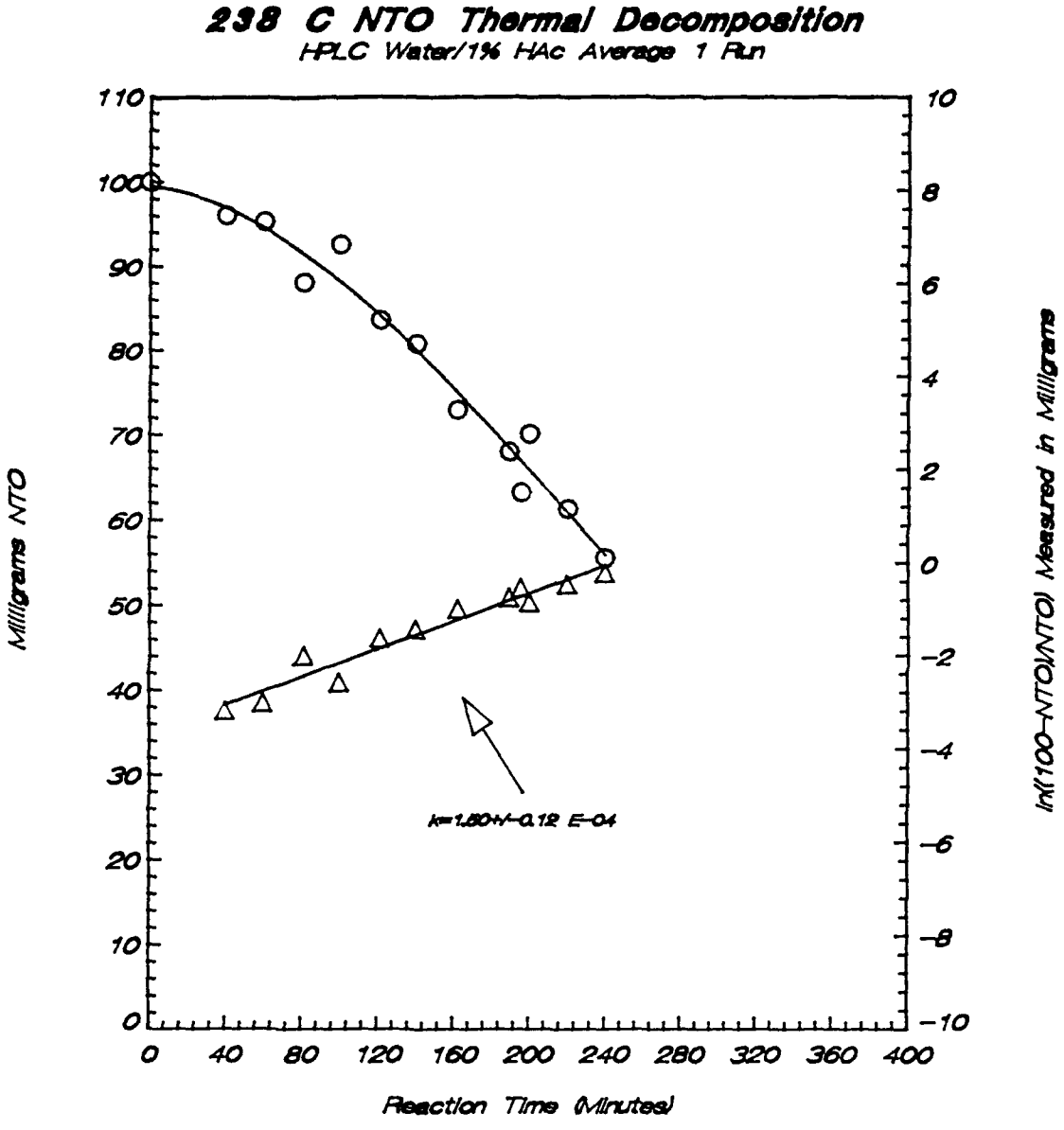
238 C NTO Thermal Decomposition
HPLC Water/1% HAc Average 1 Run
Milligrams NTO
ln(100-NTO/NTO) Measured in Milligrams
Reaction Time (Minutes)
k=1.80+/-0.12 E-04
110
100
90
80
70
60
50
40
30
20
10
0
10
8
6
4
2
0
-2
-4
-6
-8
-10
0
40
80
120
160
200
240
280
320
360
400

Figure 2

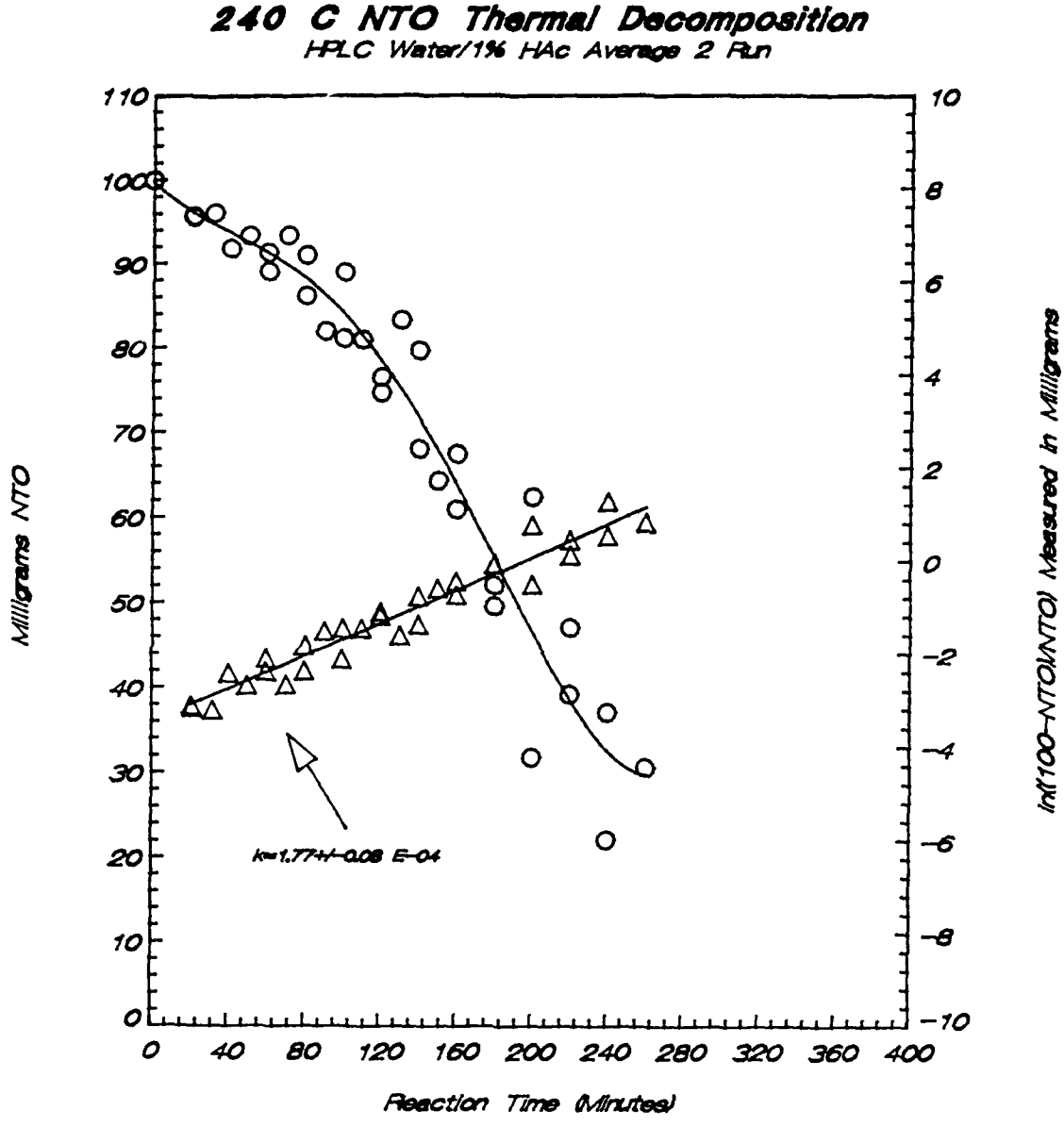
240 C NTO Thermal Decomposition
HPLC Water/1% HAc Average 2 Run
Milligrams NTO
ln(100-NTO/NTO) Measured in Milligrams
Reaction Time (Minutes)
k=1.77+/-0.08 E-04
110
100
90
80
70
60
50
40
30
20
10
0
10
8
6
4
2
0
-2
-4
-6
-8
-10
0
40
80
120
160
200
240
280
320
360
400

Figure 3

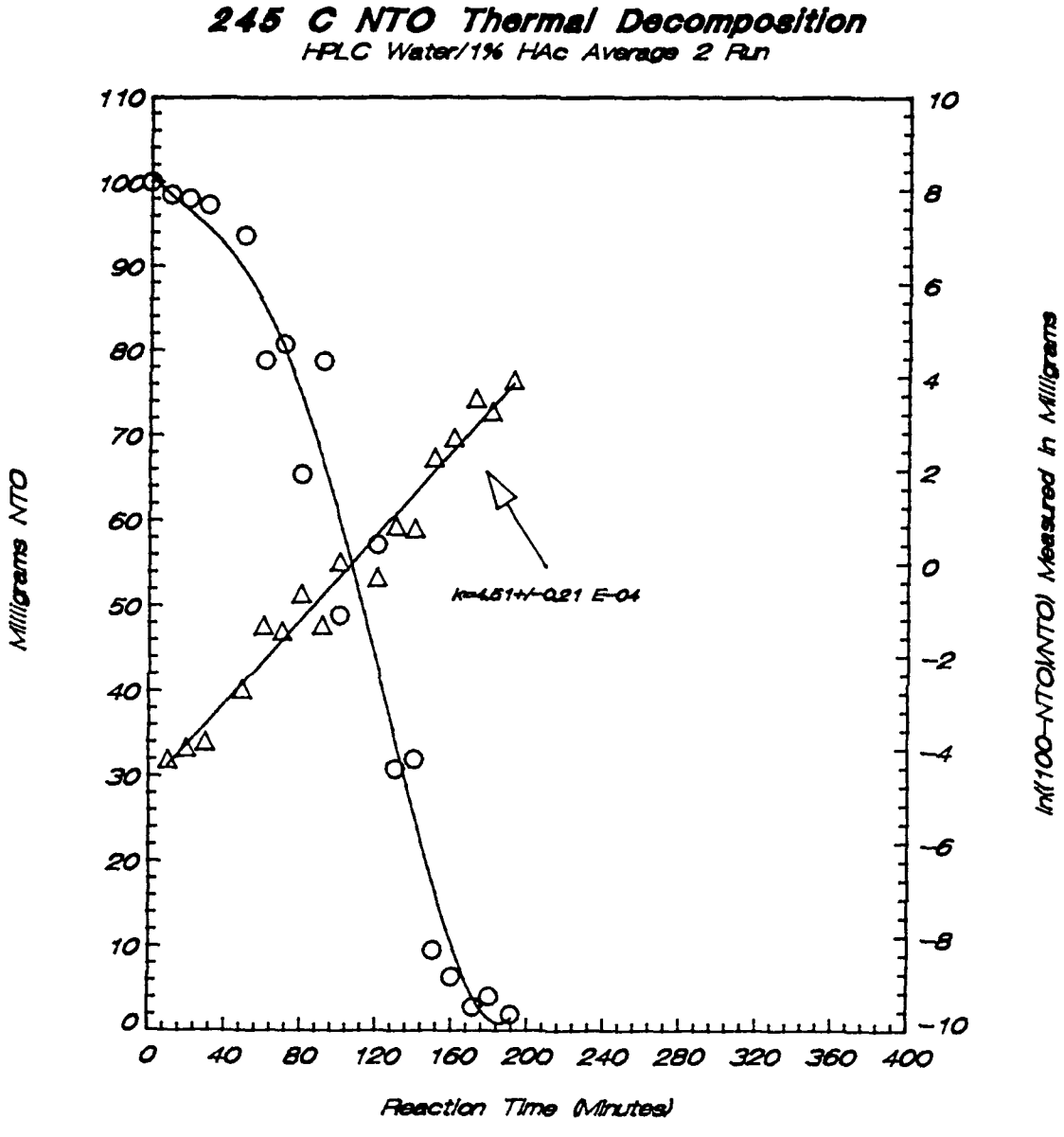
245 C NTO Thermal Decomposition
HPLC Water/1% HAc Average 2 Run
Milligrams NTO
ln((100-NTO)/NTO) Measured in Milligrams
Reaction Time (Minutes)
k=4.51+/-0.21 E-04
110
100
90
80
70
60
50
40
30
20
10
0
10
8
6
4
2
0
-2
-4
-6
-8
-10
0
40
80
120
160
200
240
280
320
360
400

Figure 4

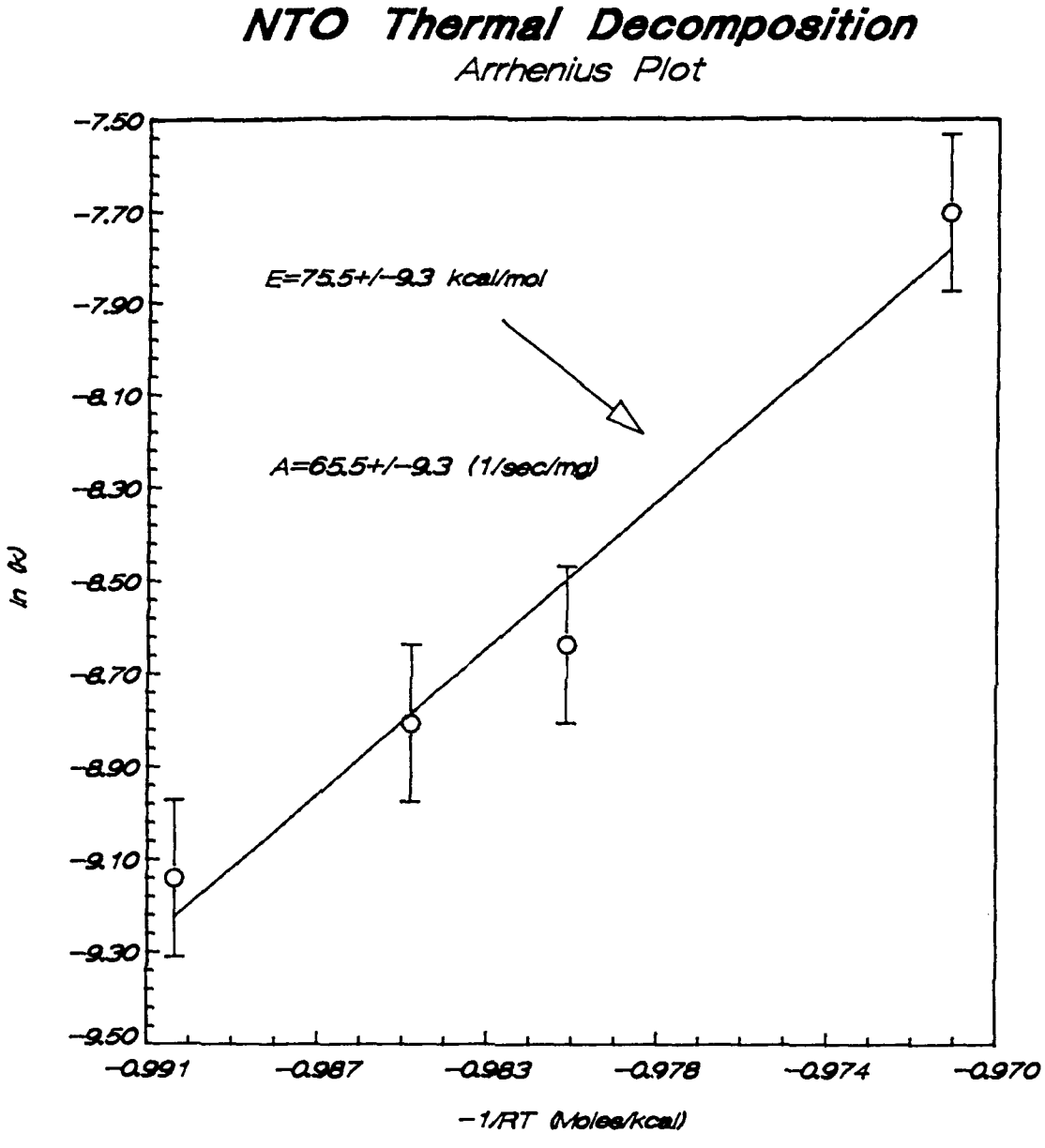
NTO Thermal Decomposition
Arrhenius Plot
E=75.5+/-9.3 kcal/mol
A=65.5+/-9.3 (1/sec/mg)
ln (k)
-7.50
-7.70
-7.90
-8.10
-8.30
-8.50
-8.70
-8.90
-9.10
-9.30
-9.50
-0.991
-0.987
-0.983
-0.978
-0.974
-0.970
-1/RT (Moles/kcal)

Figure 5

head gases evacuated by means of a vacuum pump. The tubes were then placed in the fluidized bath set at 240°C. Several microliters of gas sample were removed from the tube at regular intervals using an air tight syringe. The samples were subsequently analyzed by GC-MS. In all cases a substantial ion at mass 44 was observed after background subtraction. While it was not possible to accurately determine the rate of change in the amount of CO_2 for these samples with the system of analysis being used, the experiment clearly showed that carbon dioxide was being generated during the course of the reaction.

IV. RECOMMENDATIONS

With the kinetic data obtained from this summer's work, several avenues need to be pursued. Two further mechanistic probes can readily be followed by the methodology already established. The kinetic order of NTO can now be determined by comparing the NTO concentration profiles measured by using half or one and a half the initial amount of NTO in a given decomposition reaction. The extent of a deuterium isotope should also be investigated. Perdeuterated NTO is readily obtained by refluxing a saturated solution of NTO in D_2O, with the purified compound obtained from simple recrystallization.

Ancillary studies pertinent to elucidation of the

decomposition mechanism include: radical trapping experiments designed to characterize reactive intermediates; synthesis and decomposition studies of analogs devoid of labile hydrogens, as well as those containing labeled atoms suitable for analysis by electron spin resonance or mass spectrometry; and complimentary decomposition studies by DSC or ESR.

V. ACKNOWLEDGMENTS

The author would like to thank the Air Force Systems Command, the Air Force Office of Scientific Research and the Frank J. Seiler Research Laboratory for sponsorship of this research project. Sincere appreciation and gratitude are extended to those individuals who contributed to making this an rewarding experience for me. Special thanks are extended to Cindy Martin for patiently dealing with the HPLC, to Lloyd Pflug for his assistance with mass spectral and NMR analyses, and to Joe Menapace for his encouragement and help in every phase of the work.

VI. REFERENCES

1. J. W. Beckmann, J. S. Wilkes, R. R. Mcguire, "Kinetic Parameters Determined by the Isothermal Differential Scanning Calorimetry Technique," Thermochimica Acta, 19 111 (1977).

2. J. T. Swanson, L. P. Davis, W. R. Carper, and R. C. Dorey, "An EPR Study of the Thermal Decomposition of 2,4,6-Trinitrotoluene and Its Isotopically Substituted Analogs," Magnetic Resonance in Chemistry, 24, 762 (1986).

3. T. McKinney, L. Warren, I. Goldberg, and J. Swanson, "EPR Observation of Nitroxide Free Radicals During Thermal Decomposition of 2,4,6-Trinitrotoluene and Related Compounds," J Phys Chem, 90,1008 (1986).

4. A. Becuwe, "The Use of 5-Oxo-3-Nitro-1,2,4-Triazole as an Explosive and Explosives Containing This Substance," Demande FR 2584066 A1, 2 Jan 1987 (French patent).

5. K. Y. Lee, L. B. Chapman, M. D. Coburn, "3-Nitro-1,2,4-Triazol-5-one, a Less Sensitive Explosive," J. Energ. Mater., 5, 27 (1987).

6. M. C. Neveu, "A Kinetic Study of Thermal Decomposition of TNT by High Performance Liquid Chromatography," Final Report, Universal Energy Systems, (1987).

1988 USAF-UES SUMMER FACULTY RESEARCH PROGRAM/

GRADUATE STUDENT SUMMER SUPPORT PROGRAM

Sponsored by the

AIR FORCE OFFICE OF SCIENTIFIC RESEARCH

Conducted by the

Universal Energy Systems, Inc.

FINAL REPORT

Preparation and Properties of Nitronium Tetrachloroaluminate

Prepared by	Charles M. Bump, Ph.D.
Academic Rank	Assistant Professor
Department and	Department of Chemistry
University	Hampton University
Research Location	FJSRL/NC
	US Air Force Academy
	Colorado Springs, CO 80840
USAF Researcher	Ltc. Stephen W. Lander, Jr.
Date	August 12, 1988
Contract No.	F49620-87-R-0004

Preparation and Properties of Nitronium Tetrachloroaluminate

by

Charles M. Bump

ABSTRACT

Liquid nitryl chloride (NO_2Cl) at -80° reacts with solid aluminum chloride to produce a yellow solid. The UV-visible spectrum of this adduct is identical to that of commercial nitronium tetrafluoroborate in dry acetonitrile. Aluminum-27 magnetic resonance spectroscopy showed the presence of tetrachloroaluminate ion. The compound is tentatively labeled nitronium tetrachloroaluminate, although there is an alternate structure possible for this adduct. The adduct does not nitrate benzene or toluene in good yield using the acidic or neutral chloroaluminate melts.

ACKNOWLEDGEMENTS

I would like to thank the Air Force Systems Command and the Air Force Office of Scientific Research for the sponsorship of this research.

It is a pleasure to recognize the help of several individuals at the Frank J. Seiler Research Lab who made my work easier and more enjoyable: Ltc. Steve Lander and Dr. John Wilkes for their guidance and encouragement, Mr. J. Lloyd Pflug for running Al-27 magnetic resonance spectra, Dr. Jimmy Stewart and Mr. Greg Godek for help in using MOPAC, and Dr. John Rovang and Capt. Joe Menapace for their discussions. My summer colleagues Dr. Tammy Melton, Dr. Rich Carlin, Dr. Dan Bruss, and Dr. Mike McKee gave valuable advise on many occasions.

I INTRODUCTION

During the 1987 SFRP, I investigated nitryl chloride (NO_2Cl) as a nitrating agent for aromatic compounds in acidic chloroaluminate melts.[1] Nitryl chloride successfully nitrated a number of aromatics including acetophenone, but it also reacted with the melt. Separate reactions of nitryl chloride with the components of the melt were carried out. An adduct of nitryl chloride with aluminum chloride was discovered. That compound nitrated benzene when that adduct and neat benzene were combined in a qualitative reaction. No yield data was taken, but most of the aromatic species present at the end of the reaction was unreacted benzene. The nitration reaction may be represented as reaction (1)

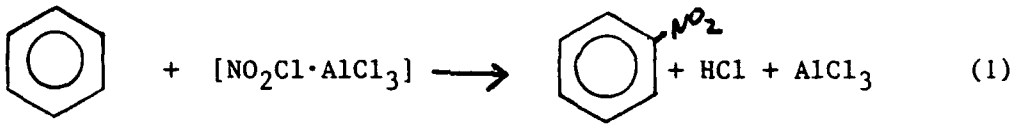

(1)

The formation of such an adduct was a surprise from the standpoint that Batey and Sisler reported that nitryl chloride did not react with Lewis acids except through vigorous oxidation-reduction paths.[2] The structure of such an adduct was unclear. Olah proposed a complex between nitryl chloride and aluminum chloride ($ClNO.O:AlCl_3$) as an intermediate in the nitration of benzene with nitryl chloride and aluminum chloride in nonaqueous solvents.[3] The other structural possibility is coordination by the chlorine of nitryl chloride. Equally unclear was the ability of this adduct to affect nitrations. Nitryl chloride reacted with the methylethylimidazolium chloride in the melt to give chlorinated nitroimidazolium compounds. The effectiveness of nitryl chloride as a nitrating agent for less activated aromatics such as acetophenone depend on the aromatic being a better substrate for the nitrating agent than is the imidazolium chloride. A means of minimizing this side reaction would make deactivated aromatics such as acetophenone, and possibly nitrobenzene, good

substrates for nitration. The reaction of nitryl chloride and methylethylimidazolium chloride is shown below.

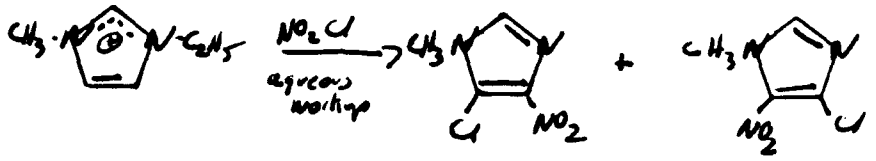

(2)

My interest in synthetic chemistry and electrochemistry as well as my participation in the 1987 SFRP led to my assignment to continue the work begun the previous summer.

II OBJECTIVES OF THE RESEARCH EFFORT

The specific objectives for the 1988 summer research period were; 1) to characterize the adduct between nitryl chloride and aluminum chloride, 2) to use that adduct to nitrate benzene in chloroaluminate melts, 3) to employ the acidic melt in catalytic amount compared to nitryl chloride dissolved in methylene chloride to nitrate benzene while minimizing the imidazolium nitration, and 4) to use MOPAC[4] semi-empirical calculations to better understand the reaction between nitryl chloride and aluminum chloride.

III SYNTHESIS AND PHYSICAL PROPERTIES OF THE ADDUCT OF NITRYL CHLORIDE AND ALUMINUM CHLORIDE

Nitryl chloride was generated following the procedure of Kaplan and Shechter.[5] Fuming nitric acid (90%, d=1.5), 8.00 g was cooled to 0° in a three-neck flask set in an ice-water bath. The flask was fitted with a solid glass stopper, an addition funnel, and a bent adapter which led to a receiving flask. A magnetic stirring bar was included to provide agitation. The apparatus was oven dried at 100° overnight and fitted with $CaCl_2$ tubes to keep the glassware free of water. Fuming sulfuric acid (30% SO_3), 9.8 g was added to the nitric acid to remove water from that source. Chlorosulfonic acid, 8.0 ml was added dropwise

via the addition funnel while the mixed acids were maintained at 0°. A receiving flask cooled to -80° in a dry ice-acetone bath held the nitryl chloride thus prepared. Pulverized anhydrous aluminum chloride, 6.6g, was added to the liquid nitryl chloride. A mild exotherm was observed. The flask was stoppered with a gas inlet adapter, the stopcock closed, and the mixture stored in a freezer for four days at -20°. At the end of the reaction period, unreacted aluminum chloride was removed by sublimation at 100° under a 1 torr vacuum. The unsublimed material was subjected to soxhlet extraction with nitromethane in order to remove any aluminum hydroxides from the adduct. The nitromethane solution thus obtained was evaporated to dryness to give 10.2 g of a yellow to yellow-brown solid.

The yellow color immediately indicates that free nitronium ion (NO_2+) is NOT present, as Olah reports that all stable nitronium salts are white.[6]

The adduct is soluble in nitromethane and acetonitrile, providing that those solvents are anhydrous. The UV-visible spectrum of the adduct in acetonitrile dried over alumina gave a λ_{max} of 232 nm. Authentic nitronium tetrafluoroborate in the same solvent gave a λ_{max} of 235 nm. In dissolving in acetonitrile, the adduct's color disappeared and no visible absorbance was recorded. In acetonitrile solution, nitronium ion is apparently present.

Aluminum-27 magnetic resonance spectroscopy in nitromethane revealed a peak near 101 ppm versus $Al(H_2O)_6^{+3}$, characteristic of the tetrachloroaluminate ion $AlCl_4^-$.[7] Aluminum chloride impurities appear at 97 ppm. From the UV-visible spectrum and the Al-27 magnetic resonance spectrum, the adduct of nitryl chloride and aluminum chloride was tentatively formulated as $NO_2^+AlCl_4^-$, nitronium tetrachloroaluminate.

An infrared spectrum of this nitronium tetrachloroaluminate gave a peak at 2431 cm^{-1}. Olah reports that a peak at 2360 cm^{-1} is characteristic of stable nitronium salts.[8] The sample did show considerable aluminum hydroxide present by a strong OH band. The slightly higher frequency (in cm^{-1}) would correspond to a more energetic

and more angular O-N-O bond than the linear one for a pure nitronium ion.

IV SEMI-EMPIRICAL CALCULATIONS OF STRUCTURES FOR NITRONIUM TETRACHLOROALUMINATE

MINDO calculations of optimized geometries in the gas phase were performed using MOPAC[4]. Geometries for a series of nitronium tetrahaloaluminates and tetrahaloborates are summarized below.

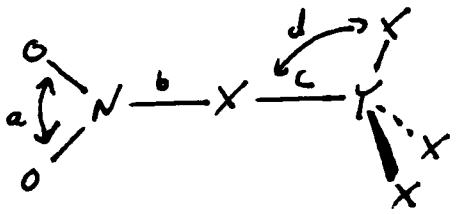

X	Y	ΔH_f	O-(a)-O	N-(b)-X	X-(c)-Y	X-(d)-X	ΔH for $NO_2^+ + YX_4^-$	structure
F	B	-239.06	175.91	2.37	1.42	107.48	-394.21	$NO_2^+BF_4^-$
Cl	B	-69.06	127.57	1.81	5.88	89.82	111.19	$NO_2Cl \cdot BCl_3$
Br	B	-13.14	126.63	1.90	6.31	89.90	122.84	$NO_2Br \cdot BBr_3$
I	B	42.12	122.68	2.10	6.03	90.79	116.49	$NO_2I \cdot BI_3$
F	Al	-292.52	133.48	1.40	1.84	99.64	92.78	$NO_2F \cdot AlF_3$
Cl	Al	-122.69	127.62	1.81	6.73	92.90	90.22	$NO_2Cl \cdot AlCl_3$
Br	Al	-39.71	125.69	1.90	7.29	91.99	108.99	$NO_2Br \cdot AlBr_3$
I	Al	-44.92	122.78	2.10	6.37	102.45	114.36	$NO_2I \cdot AlI_3$

Evidently, nitronium tetrafluoroborate is the only compound predicted to dissociate readily into nitronium ion and tetrafluoroborate ion.

Olah proposed a complex between nitryl chloride and aluminum chloride as an intermidiate in the nitration of aromatics with nitryl chloride.[3] This complex features oxygen-aluminum interaction. Such a structure would reflect a greater negative charge on oxygen than on the chlorine of nitryl chloride and hence would be more susceptible to reaction with a Lewis acid. An optimized geometry

is presented below.

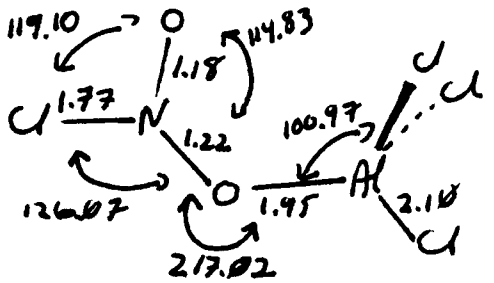

ΔH_f = -122.31

The heat of formation of this complex is, for all practical purposes, identical with the $NO_2Cl \cdot AlCl_3$ complex. Further, the two iosmers are spectroscopically indistinguishable from the UV-visible and Al-27 magnetic resonance point of view. Acetonitrile can serve as a nucleophile to release nitronium ion as illustrated in reaction (3).

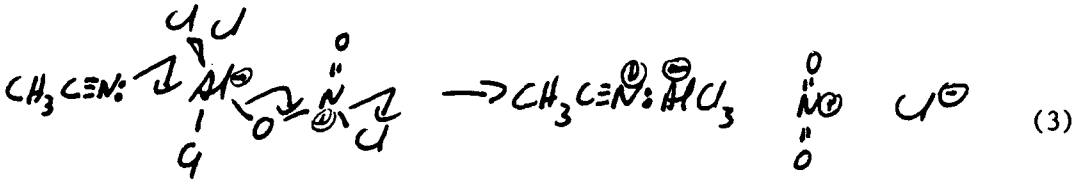

(3)

Likewise, the magnetic resonance spectrum presumed to be that of $AlCl_4^-$ is that of aluminum with four electronegative elements attached to it: four chlorines or three chlorines and one oxygen will produce that same result. Thus the two isomers are spectroscopically indistinguishable. It is even possible that the compound isolated is a mixture of both structures. Olah's complex would react in the acidic melt as shown below.

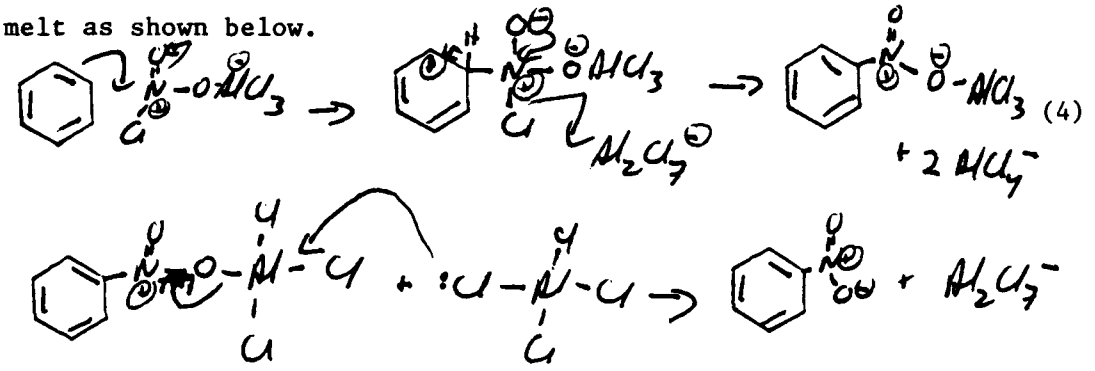

(4)

The $NO_2Cl \cdot AlCl_3$ complex would react in the acidic melt as follows.

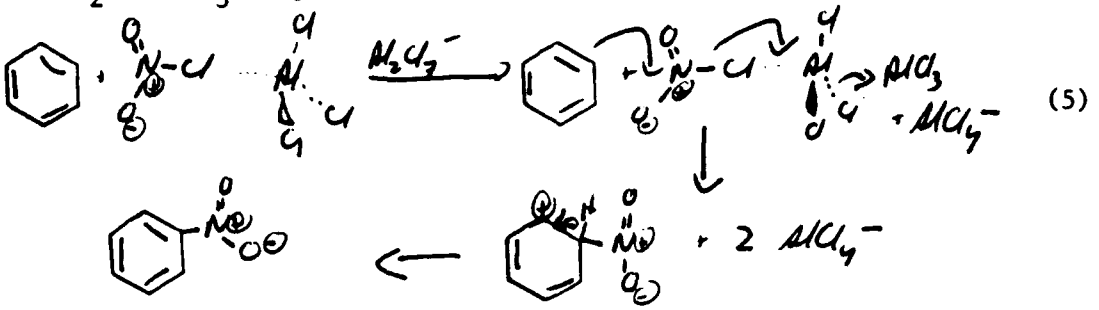

(5)

The success of the reaction depends on the NO_2Cl - $AlCl_3$ distance remaining small, held by electrostatic attraction. Otherwise, a three-body collision (benzene, NO_2Cl, $Al_2Cl_7^-$) is required to form the sigma complex from the pi complex. Heptachloroaluminate presumably cannot abstract the nitryl chloride chlorine directly, forming free nitronium ion, as it is sterically shielded from such attack.

V REACTIONS OF NITRONIUM TETRACHLOROALUMINATE WITH BENZENE AND TOLUENE

An ionic liquid solvent of 0.500 mole fraction aluminum chloride was prepared from 2.38 g of aluminum chloride and 2.62 g of methylethylimidazolium chloride. The aluminum chloride was added slowly to the imidazolium chloride in an anhydrous, anaerobic glove box. An ionic liquid of apparent mole fraction 0.667 aluminum chloride was prepared in a similar manner from 6.46 g aluminum chloride and 3.54 g methylethylimidazolium chloride. A ratio of aromatic: nitrating agent: melt was maintained at 1:1.5:1 throughout the investigation. Reactions were quenched with water and brought to pH 10 by the addition of KOH. The alkaline mixture was extracted with methylene chloride. Product identification was made on the basis of retention times of authentic compounds. Quantitative data was obtained on the basis of response factors of authentic compounds with respect to m-xylene as an internal standard.[9]

Nitronium tetrachloroaluminate in neutral (0.500 mole fraction aluminum chloride) melt failed to give any detectable nitration of benzene. A red color characteristic of a pi complex between benzene and the

nitrating agent was observed almost immediately on addition of benzene to the nitrating agent/melt solution.

The analogous reaction in acidic (0.667 mole fraction aluminum chloride) melt gave less than one percent of the theoretical yield of nitrobenzene. Toluene gave a similar yield of the o and p isomers of nitrotoluene. There was no evidence of the formation of chlorotoluenes. Again, a red pi complex was formed shortly after the aromatic was introduced to the reaction mixture.

VI REACTIONS OF NITRYL CHLORIDE WITH BENZENE IN METHYLENE CHLORIDE USING CATALYTIC AMOUNTS OF ACIDIC MELT

Nitration of benzene in methylene chloride with nitryl chloride was attempted using a ratio of aromatic: nitrating agent: catalyst of 0.6 : 1.5 : 0.1 . The solution was approximately 0.3 M in benzene. Handling of the nitryl chloride and its preparation were described in the 1987 Final Report.[1] A 0.2 M solution of 0.667 melt in methylene chloride was prepared by dissolving 1.44 g of melt (effective M.W. = 413.7) in 23.5 g (17 ml) of methylene chloride which had been dried over molecular sieve (type 4A) and alumina. The solution was prepared in an anhydrous, anaerobic glove box. The bottle containing the melt solution was sealed with a septum cap to be introduced into reactions outside the glove box via syringe. Liquid nitryl chloride, 1.5 mmole, was dissolved in 1 ml of methylene chloride. An equal volume of the methylene chloride solution of acidic melt was added after the nitryl chloride solution was capped with a septum and additional alumina added to insure the absence of water. Benzene was then added to the reaction mixture. The reactions were quenched with water after eight hours, extracted with more methylene chloride, and analyzed by gas chromatography. Results of both uncatalyzed (no acidic melt present) and catalyzed reactions are tabluated below.

CATALYTIC ACIDIC MELT AND NITRYL CHLORIDE NITRATIONS

conditions	compound	yield data			
		trial 1	trial 2	trial 3	trial 4
uncatalyzed	Bz	54 %	67 %	74 %	75 %
	ClBz	2.5%	2.7%	0.5%	0.6%
	NO_2Bz	0.4%	8.4%	(not detected)	0.1%
catalyzed	Bz	81 %	65 %	85 %	77 %
	ClBz	4 %	1.7%	6.5%	8.8%
	NO_2Bz	3 %	0.2%	1 %	0.5%

The third and fourth columns for the uncatalyzed reactions were originally to have had melt present, but water was apparently present and reacted with the melt as soon as it was introduced. The data are widely scattered, so no averages have been computed. No conclusions can be drawn from this preliminary data except that great care must be taken to remove moisture from the reaction. Not only does water react with the melt, but it also reacts with nitryl chloride.[10] The reaction is formulated as

$$H_2O + 3\ NO_2Cl \longrightarrow NOCl + 2\ HNO_3 \qquad (6)$$

VII REACTION OF NITRONIUM TETRACHLOROALUMINATE WITH AMINES

Nitronium tetrachloroaluminate was added to neutral melt (0.500 mole fraction aluminum chloride) solutions of amines in the hope of producing nitramines. Reaction conditions were 1.00 g of melt, 100 mg of amine, and 218 mg of the adduct of nitryl chloride and aluminum chloride. The reaction with diphenylamine produced no new product. The proton nmr spectrum of the material isolated was indistinguishable from the starting amine. Isolation involved allowing the melt to sit overnight to pick up atmospheric moisture, adding water and acidifying with HCl and extracting

with ether. The ether was evaporated under an air stream and taken up in chloroform. The chloroform was dried over anhydrous magnesium sulfate and analyzed. Aminodiphenylmethane did react and gave a variety of products in a gc/mass spectrum. Among the compounds isolated were 1,1-diphenylmethane, benzophenone, and the imine that results when acetophenone and starting amine condense. A possible reaction scheme is outlined below.

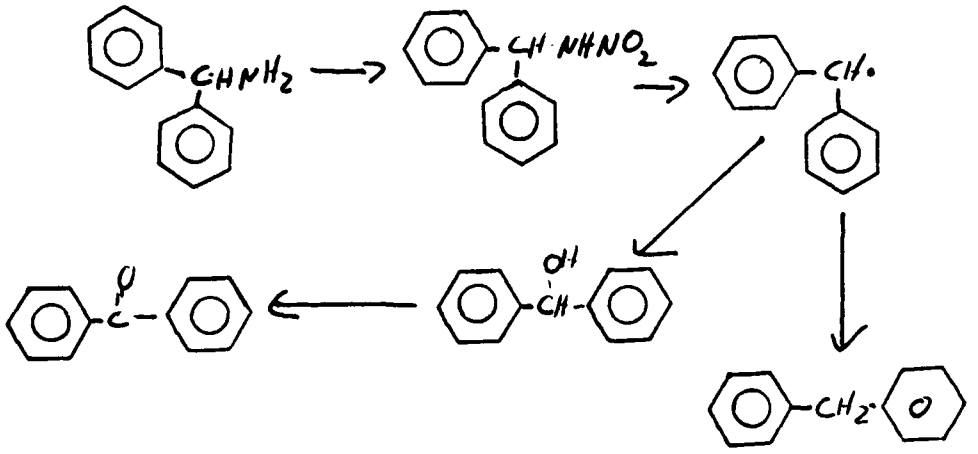

(7)

VIII CONCLUSIONS/RECOMMENDATIONS

A The identity of the adduct between nitryl chloride and aluminum chloride remains unclear. Two isomeric forms are possible: coordination through the chloride and coordination through the oxygen. Chemically, the latter makes more sense, although it would be expected to be a better nitrating agent than it has proven to be. The structure of this adduct should be clarified.

B This adduct was ineffective in nitrating benzene and toluene. Nitration of even more highly activated aromatics may prove more fruitful, ie. anisole and aniline nitrations. Such activated compounds tend to decompose when nitrated directly.

C Nitration of simple amines such as morpholine should give a better picture of the adduct's nitrating ability toward

amines. The failure of diphenylamine to react is due, no doubt,to its low basicity. Aminodiphenylmethane was apparently successfully nitrated, but it fell apart due to the radical-stabilizing aromatic rings. Morpholine should be less prone to fragment once its nitramine is formed.

REFERENCES

1. Charles M. Bump, "Reactions of Nitryl Chloride with Aromatic Substrates in Chloroaluminate Melts", Final Report, 1987 USAF-UES Summer Faculty Research Program, 27 August 1987.
2. Harry H. Batey and Harry H. Sisler, "Some Inorganic Reactions of Nitryl Chloride", J. Amer. Chem. Soc., (1952), 74, 3408.
3. George A. Olah, Industrial and Laboratory Nitrations, ACS Symposium Series #22, American Chemical Society, Washington, DC, 1976, p. 1 cited in K. Schofield, Aromatic Nitration, Cambridge University Press, New York, 1980, p. 93.
4. James J.P. Stewart, MOPAC Manual, 4th Edition, A General Molecular Orbital Package, USAF Systems Command, FJSRL-TR-87-0006, Oct. 1987, ADA 188623.
5. Ralph Kaplan and Harold Shechter, Nitryl Chloride, Inorganic Synthesis, (1953), 4, 52.
6. Stephen J. Kuhn and George A. Olah, "Aromatic Substitution. VII Friedel-Crafts Type Nitration of Aromatics", J. Amer. Chem. Soc. (1961), 83, 4564.
7. J.J. Delpuech in NMR of Newly Accessible Nuclei, Vol. 2, Chemically and Biochemically Important Elements, ed. Pierre Laszlo, Academic Press, New York, 1983, pp. 153-195.
8. Denys Cook, Stephen J. Kuhn, and George A. Olah, "Infrared Spectra of complexes of NO_2F with BF_3, PF_5, and SbF_5", J. Chem. Phys., (1960), 33, 1669.
9. Mary A. Kaiser and Frederick J. Debbrecht in Modern Practice of Gas Chromatography, ed. Robert L. Grob, Wiley Interscience, New York, 1977, pp. 199-202.
10. M.J.Collins, F.P.Gintz, D.R.Goddard, E.A.Hebdon, and G.J.Minkoff, "Nitryl Chloride. Part I Its Preparation and the Properties of its Solutions in some Organic Solvents", J. Chem. Soc., (1958), 438.

1988 USAF-UES SUMMER FACULTY RESEARCH PROGRAM

Sponsored by the

AIR FORCE OFFICE OF SCIENTIFIC RESEARCH

Conducted by the

Universal Energy Systems, Inc.

FINAL REPORT

Prepared by:	Richard T. Carlin, Ph.D.
Academic Rank:	Assistant Professor
Department and University:	Chemistry Department Polytechnic University
Research Location:	FJSRL/USAFA Colorado Springs, CO 80918
USAF Researcher:	Dr. John S. Wilkes

Date:	September 7, 1988
Contract No.:	F49620-87-R-0004

Homogeneous Ziegler-Natta Catalysis in Lewis Acid Molten Salts

by

Richard T. Carlin

Abstract

Dissolution of the Cp_2TiCl_2 catalyst and its $AlCl_{3-x}R_x$ cocatalyst in the ambient-temperature molten salt $AlCl_3$:MEIC (MEIC = 1-ethyl-3-methylimidazolium chloride) produces an active homogeneous Ziegler-Natta catalyst system. The Ti catalyst is active in acidic melts, $AlCl_3$:MEIC molar ratios > 1, but not in basic melts, $AlCl_3$:MEIC molar ratios < 1. Cp_2ZrCl_2 and Cp_2HfCl_2 with $AlCl_{3-x}R_x$ cocatalysts are not catalytically active in acidic melts. The lack of activity of Zr and Hf complexes is attributed to their inherently stronger M-ligand bonding which precludes ethylene coordination .

NMR studies of the Cp_2TiCl_2 complex in acidic melts indicate formation of a strong 1:1 complex with $AlCl_3$ while Zr and Hf form much weaker 1:1 complexes. The weaker $AlCl_3$ complexation by Zr and Hf is indicative of stronger M-Cl bonding in Zr and Hf versus Ti.

The study clearly demonstrates the usefullness of ambient-temperature molten salts as solvents to generate catalytically active transition metal complexes.

Acknowledgements

I wish to thank the Air Force Systems Command and the Air Force Office of Scientific Research for supporting this project. I am particularly indebted to the Frank J. Seiler Research Laboratories for providing the facilities which made this work possible.

I would especially like to thank Dr. John Wilkes for his helpful scientific insights during the project, Dr. John Rovange for his interest and efforts in fitting the equilibria data and in performing multi-nuclear NMR studies, and Lloyd Fluge for diligently obtaining the innumerable ^{1}H and ^{13}C spectra.

I must, also, express may appreciation to all the civilian and military personnel at FJSRL for making the project both productive and enjoyable.

Finally, I want to thank the other members of the SFRP and the GSRP for their stimulating discussions and comaraderie throughout the summer.

I. INTRODUCTION:

The nature of the active site in the homogeneous Ziegler-Natta catalyst system, Cp_2MCl_2 (M = Ti, Zr; Cp = cyclopentadienyl) catalyst + alkylaluminum cocatalyst, is still uncertain.[1-4] Recent work has lent support to the hypothesis that coordinatively-unstaturated, cationic complexes of composition Cp_2MR^+ are active sites for initial coordination of olefin.[5,6] The aluminum cocatalyst serves to alkylate the metal center and to abstract chloride from the metal coordination sphere. Insertion of the olefin into the M-R leads to polymer chain growth and to regeneration of a coordinatively-unsaturated species able to react again with an olefin. Recent work supporting this mechanism include the crystal structure of the complex $Cp_2TiCSi(CH_3)_3{=}C(CH_3)(C_6H_5)^+$ $AlCl_4^-$ formed from reaction of $(C_6H_5)CCSi(CH_3)_3$ with Cp_2TiCl_2[5] and the demonstration that the cationic complex $Cp_2Zr(CH_3)(THF)^+$ $B(C_6H_5)_4^-$ is a catalyst for ethylene polymerization without the AlR_xCl_{3-x} cocatalyst.[6]

The ambient-temperature molten salt $AlCl_3$:MEIC (MEIC = 1-ethyl-3-methylimidazolium chloride) should serve as an interesting solvent system for these homogeneous Ziegler-Natta catalyst systems. The Cp_2TiCl_2 catalyst is stable in both acidic melts, $AlCl_3$:MEIC molar ratio > 1.0, and basic melts, $AlCl_3$:MEIC molar ratio <1.0.[7] Also, alkylaluminum chlorides cocatalysts are stable in the melts, and they serve to remove protonic impurties.[8] In acidic melts, chloride abstraction from Cp_2MCl_2 is expected; however, because of the large concentration of $AlCl_4^-$ in the melts, it is unlikely true cationic species would form. Instead, species such

as $Cp_2MCl(AlCl_4)$ and $Cp_2M(AlCl_4)_2$ should be generated, and catalytic activity of these complexes in the presence of alkylaluminums may provide insight into the mechanism of Ziegler-Natta polymerization.

My research interests include the electrochemistry and reaction chemistry of inorganic complexes in the ambient-temperature chloroaluminate molten salts. I also have experience in catalytic processes and in interaction of gases with molten salts. Therefore, my project this summer became the study of ethylene polymerization (Ziegler-Natta catalysis) by the above homogeneous catalyst system in the ambient-temperature molten salt.

II. OBJECTIVES OF THE RESEARCH EFFORT:

The primary objective of the project was to demonstrate the usefullness of ambient-temperature molten salts as solvents for catalytic processes. Therefore, the homogeneous Ziegler-Natta system, Cp_2MCl_2 (M = Ti, Zr, Hf) catalyst and $AlCl_{3-x}R_x$ cocatalyst, was chosen because of the current interest in its reaction mechanism.

Initial screening for catalytic activity with various combinations of melt composition, catalyst, and cocatalyst was planned to determine the potential of obtaining useful information from reactions in the melts. Employing various spectroscopic techniques, particularly NMR, the complexation and reactivity of the Cp complexes in the melts would be explored.

III. SCREENING OF SYSTEMS FOR CATALYTIC ACTIVITY:

Ethylene polymerization does take place in the ambient-temperature ionic liquid $AlCl_3$:MEIC (MEIC = 1-ethyl-3-methylimidazolium chloride) employing Cp_2TiCl_2 as the catalyst and an $AlCl_{3-x}R_x$ (R = Me, Et) cocatalyst. Catalysis occurs in acidic melts, $AlCl_3$:MEIC molar ratio > 1, but not in basic melts, $AlCl_3$:MEIC molar ratio < 1. Bubbling ethylene at 1 atm through 6.8 g of an acidic 1.1:1.0 $AlCl_3$:MEIC melt containing 0.022 g Cp_2TiCl_2 (17 mM) and 0.118 g $Al_2Me_3Cl_3$ (330 mM in methyl) for 10 min resulted in formation of polyethylene (PE) at 25 °C. Quenching of the catalytic mixture with 150 ml methanol resulted in precipitation of the PE while the catalyt and melt components remained in solution. The PE was isolated by centrifugation giving a yield of 0.020 g or 0.023 (g PE) min^{-1} (millimole Ti)$^{-1}$ atm^{-1}. Yields of PE were in the range of 0.02 to 0.15 (g PE) min^{-1} (millimole Ti)$^{-1}$ atm^{-1} using 1.1:1.0 or 1.5:1.0 melts as solvents. (One noteworthy observation: the alkylaluminums are not pyrophoric in the melts probably a result of their complexation to chloroaluminate species; however, the dilution of the alkylaluminum is no more than in conventional organic solvents.)

These PE yields are low relative to other homogeneous systems.[9] It is, however, of the same order as that reported for the cationic complex $Cp_2ZrMe(THF)^+$.[6] The low yield may be attributed to (1) inherently lower activity of the Ti complex in the melts possibly a result of low levels of alkylated Ti species; (2) low solubility of ethylene in the melts; or (3) the presence of alkylimidazole impurities which, as nitrogen bases, block the Ti active sites. Evidence for (1) is seen in the slow reduction of Ti(IV)

to Ti(III) by alkylaluminums in the melts. By following the Ti(IV)/Ti(III) couple potentiometrically with time after addition of excess $EtAlCl_2$, the reduction process was determined to take place on a time scale of hours and days in the melt. In organic solvents, this reduction occurs on a time scale of seconds and minutes.[1,3] Competition for the alkyl groups by the high concentration of chloroaluminate species in the melts may account for this slow reduction. Evidence for (3) was seen in the low yields of PE which resulted when the polymerization was performed in acidic melts showing significant discoloration (pure melts are colorless) This discoloration of acid melts is presumed to be due to a complex resulting from coordination of alkylimidazoles, or condensed alkylimidazoles, to $AlCl_3$.

Acidic melts containing Cp_2ZrCl_2 and Cp_2HfCl_2 as catalysts and $Al_2Me_3Cl_3$ as cocatalyst showed no catalytic activity up to ca. 65 °C. This is consistent with the observation that Cp_2ZrCl_2 is not a catalyst in the presence of $AlCl_{3-x}R_x$; however, cyclopentadienyl complexes of Zr are catalytic in the presence of aluminoxanes.[1,10] Similarly, indenyl complexes of Zr and Hf are catalytic in the presence of this aluminoxanes.[11,12]

IV. NMR INVESTIGATION OF COMPLEXATION

Both ^{13}C and ^{1}H NMR of the Cp rings provide insight into the coordination of the Cp_2MCl_2 complexes in the melts Figures 1 and 2 show the variation of the ^{1}H and ^{13}C chemical shifts as a function of melt composition. Concentration of all complexes was ca. 100 mM In basic melts, the chemical shifts remain relatively constant At the $AlCl_3$:MEIC ratio of 1:1, a neutral melt, all the complexes

demonstrate a sharp downfield shift indicative of removal of electron density from the metal centers. With increasing acidity, the chemical shifts indicate a further but less dramatic deshielding.

Figure 3 shows more clearly the change in ^1H chemical shifts of the Cp rings in going from a neutral melt to an acidic melt. Concentrations of the Ti, Zr, and Hf complexes were 58, 66, and 72 mM, respectively. The Ti complex shows the sharpest downfield shift just beyond the neutral melt composition, while Zr and Hf demonstrate more gradual downfield shifts. Assuming the two complexation reactions [1] and [2] may occur, equilibrium constants, K_1 and K_2, were calculated from the ^1H NMR data using least-squares methods.

$$Cp_2MCl_2 + Al_2Cl_7^- \text{----->} Cp_2MCl(AlCl_4) + AlCl_4^- \quad [1]$$

$$Cp_2MCl(AlCl_4) + Al_2Cl_7^- \text{----->} Cp_2M(AlCl_4)_2 + AlCl_4^- \quad [2]$$

The Zr and Hf curves were fit successfully to a single equilibrium, reaction [1], assuming a constant $AlCl_4^-$ activity of 1 and using the concentrations of the other species for their activities. The Ti curve was fit using both equilibria since the initial sharp change in chemical shift is indicative of a large K_1 and the continued gradual downfield shift at increasing acidity indicates a second, weaker complex is also formed. Results are summarized in Table I.

Table I

Complexation Equilibrium Constants

$Cp_2M^{\cdot}Cl_2$	K_1	K_2
Ti	$> 10^5$	≈ 0.6
Zr	21 ± 4	---
Hf	4.1 ± 0.8	---

It is significant that Ti has the highest K_1 and is the only complex which demonstrates catalytic activity. Reaction [1] can be

viewed as breaking a M-Cl bond to form an Al-Cl bond with concurrent complexation by $AlCl_4^-$, a much weaker coordinating ligand than chloride. M-Cl bond energies for Ti, Zr, and Hf are 103, 117, 118 kcal $mole^{-1}$, respectively;[13] therefore, the K_1 values are consistent with M-Cl bond energies. For formation of a cationic complex, complete breakage of the M-Cl bond would need to occur. The high concentration of $AlCl_4^-$ in the melt (4.6 M in a neutral melt), however, would seem to preclude a true cationic complex being formed. Instead, the coordination sphere of any such cationic species would be occupied by either $AlCl_4^-$ or $Al_2Cl_7^-$. Consistent with this proposal is the fact that the anions PF_6^-, BF_4^-, and $AlCl_4^-$ coordinate strongly or react with the $Cp_2Zr(R)(THF)^+$ complex [6]

In the acidic melts used for catalysis, the Ti polymerization catalyst is, therefore, an alkylated 1:1 $AlCl_3$:Cp_2TiCl_2 complex which can be written as $Cp_2TiR(AlCl_4)$. The $AlCl_4^-$ ligand may be either mono- or bidentate.[14] Initiation of the polymerization may involve displacement of $AlCl_4^-$ by ethylene to form a complex such as $Cp_2TiR(CH_2CH_2)^+$ or addition of ethylene forming a complex such as $Cp_2TiR(CH_2CH_2)(AlCl_4)$.[14]

The Zr and Hf complexes also exist as 1:1 complexes at the $Al_2Cl_7^-$ concentrations (ca. 0.5 M) used for catalyst screening. The stronger inherent M-ligand bonding for Zr and Hf, however, may prevent complete or partial displacement of the $AlCl_4^-$ ligand by ethylene. The stronger M-Cl interaction for Zr and Hf is demonstrated by their weaker $AlCl_3$ complexation versus Ti.

In these melts, polymerization does not appear to occur by cation formation, however, cationic complexes do function as

polymerization catalyst as demonstrated by $Cp_2ZrR(THF)^+$ [6] This study demonstrates that formation of a cationic complex does not appear to be a necessary condition for polymerization.

Efforts to observe M-R species by ^{13}C and ^1H NMR were unsuccessful. However, Al-Me species were identified in melts containing 0.1 M Me_3AlCl_3. In 0.8:1.0 and 0.9:1.0 melts, where only $AlCl_4^-$ is present, the ^1H chemical shift of the methyl group appears at -0.274 and -0.251 ppm, respectively. In a 2:1 melt, where only $Al_2Cl_7^-$ is present, the ^1H resonance is shifted to 0.405 ppm. In a 1.5:1 melt, where both $AlCl_4^-$ and $Al_2Cl_7^-$ are present, the ^1H resonce appears at 0.176 ppm indicating fast exchange of the methyl group with the two Al species as expected.

IV. ELECTROCHEMICAL INVESTIGATION OF COMPLEXATION

The observable electrochemistry of the complexes is consistent with removal of electron density from the metal centers in going from a basic melt to an acidic melt. The Ti complex undergoes a reversible one-electron reduction at -0.80 V in a 0.8:1.0 basic melt and at 0.43 V in an 1.5:1.0 acidic melt (versus an Al wire in a 2:1 melt as the reference electrode).[7] The potential of the Ti reduction reportedly shifts anodically with increasing melt acidity.[7] In a basic melt, the Zr complex undergoes a reversible one-electron reduction at -1.35 V, cathodic of the Ti complex as expected.[15] No reduction of the Zr complex in an acidic melt was directly observed. However, in a slightly acidic melt there appeared to be an additional reduction process occurring near 0 V accompanying reduction of $Al_2Cl_7^-$ to Al reduction. No electrochemistry of the Hf complex was observed in either basic or acidic melts.

The complexation of Cp_2TiCl_2 in acidic melts was examined by adding the Ti complex to a slightly acidic melt. The decrease in the $Al_2Cl_7^-$ limiting current measured at a rotating glassy carbon disk (diameter = 0.5 cm; rotation rate = 1000 rpm) was used to determine the number of $Al_2Cl_7^-$ consumed by complexation of $AlCl_3$ to Cp_2TiCl_2. The experiment was complicated , however, by the fact that Cp_2TiCl_2 reduction occurs anodic of the $Al_2Cl_7^-$ reduction giving rise to two reduction waves. A plot of the $Al_2Cl_7^-$ limiting current as a function of added Cp_2TiCl_2 indicates two $Al_2Cl_7^-$ are complexed to each Cp_2TiCl_2 in contradiction to the NMR results However, this discrepancy is attributed to the Ti(IV) complex being reduced to a Ti(III) complex prior to $Al_2Cl_7^-$ reduction. This Ti(III) complex either releases a chloride to react with a second $Al_2Cl_7^-$, or it complexes a second $AlCl_3$ giving the appearance of two $Al_2Cl_7^-$ consumed per Cp_2TiCl_2 added. This difference in corrdination between Ti(IV) and Ti(III) is consistent with the previously reported shift in the Ti(IV)/Ti(III) couple with melt acidity [7]

An effort was also made to determine the complexation of Cp_2TiCl_2 in basic melts. This was done by titrating a 53 mM chloride melt with Cp_2TiCl_2. The decrese in the chloride oxidation wave with added Ti complex was monitored using a rotating glassy carbon disk (diameter = 0.5 cm; rotation rates = 1000, 2000, and 3000 rpm). The calculated equilibrium constant, K_3, for reaction [3]

$$Cp_2TiCl_2 + Cl^- \text{ <===> } Cp_2TiCl_3^- \qquad [3]$$

increased with increasing rotation rate. This is attributed to shifting of the equilibrium to the left as choride is removed by oxidation to chlorine. At faster rotation rates, less time is allowed for the

$Cp_2TiCl_3^-$ complex to release chloride. Therefore, only a minimum K_3 value of 12 l $mole^{-1}$ can be reported here. In basic melts, the high chloride concentrations ($[Cl^-]$ = 1 M in a 0.8:1.0 melt) result in a coordinatively-saturated Ti center.[14] No chloroaluminate complex is formed in basic melts accounting for the lack of Cp_2TiCl_2 catalytic activity in basic melts.

During the course of performing the chloride titration a diffusion coefficient for Cp_2TiCl_2 of $(1.48 \pm 0.01) \times 10^{-6}$ cm^2 s^{-1} was determined in a slightly basic melt at 30 °C.

VI. RECOMMENDATIONS

(1) The present work has demonstrated the catalytic activity of the Cp_2TiCl_2 complex in acidic melts; therefore, initial follow-up work should center around optimizing the catalytic activity of system. Numerous parameters including melt composition, choice and concentration of cocatalyst, and temperature need to be varied, and their effect on catalyst activity quantified.

(2) The Ziegler-Natta polymerization process results in the formation of a solid product which requires destroying the catalyst system to isolate the product. For processes giving volatile products, molten salts offer an easy method for separation of products from the catalyst medium since the ambient-temperature molten salts have little or no vapor pressure even at elevated temperatures. In essence, the molten salt containing an appropriate catalyst could serve as a supported, homogeneous catalyst system. Catalyst systems worthy of investigation include $WCl_6/RAlCl_2$ and $WOCl_4/RAlCl_2$ for olefin metathesis (olefin scrambling), and $Co_2(CO)_8$

for hydrocarbonylation of olefins (reaction of CO, H_2 and olefins to produce aldehydes).

(3) In general, the reactivity and complexation of organometallic compounds in these molten salts needs to be explored more thoroughly. The strong Lewis acidity of the melts may lead to new and interesting chemistry and to a better understanding of established chemistry.

REFERENCES

1. Sinn, H.; Kaminsky, W. "Ziegler-Natta Catalysis", In Advances in Organometallic Chemistry, Vol. 18; Stone, F. G. A.; West, R, Eds.; Academic Press: New York, 1980.

2. Keii, T. Kinetics of Ziegler-Natta Polymerization; Chapman and Hall: London, 1972.

3. Dyachkovskii, F. S. "Homogeneous Complex Catalysis of Olefin Polymerization", Coordination Polymerization; Chien, J. C. W., Ed.; Academic Press: New York, 1975.

4. Collman, J. P.; Hegedus, L. S.; Norton, J R.; Finke, R G. Principals and Applications of Organotransition Metal Chemistry; University Science Books: Mill Valley, California, 1987; p 577.

5. Eisch; J. J.; Piotrowski, A. M.; Brownstein, S. K.; Gabe, E J.;Lee, F. L. J. Amer. Chem. Soc. 1985, 107, 7219.

6. Jordon, R. F.; J. Chem. Ed., 1988, 65, 285.

7. Gale, R. J.; Job, R. Inorg. Chem. 1981, 20, 42.

8. Zawodzinski, T. A., Jr.; Carlin, R. T.; Osteryoung, R. A. Anal. Chem. 1987, 59, 2639.

9. Jeske, G.; Lauke, Harald; Mauermann, H ; Swepston, P. N; Schumann; Marks, T. J. J. Amer. Cem. Soc. 1985, 107, 8091.

10. Andresen, A.; Cordes, H. G.; Herwig, J; Kaminsky, W, Merck, A.; Mottweiler, R.; Pein, J.; Sinn, H.; Vollmer, H. Angew. Chem.

Int. Ed. Engl. 1976, 15, 630.

11. Kaminsky, W.; Kuper, K.; Brintzinger, H. H.; Wild, F. R. W. P. Angew. Chem. Int. Ed. Engl. 1985, 24, 507.

12. Ewen, J. A.; Haspeslagh, L.; Atwood, J. L.; Zhang, H. J. Amer. Chem. Soc. 1987, 109, 6544.

13. Huheey, J. E. Inorganic Chemistry: Principles of Structure and Reactivity, 3rd Ed.; Harper and Row: New York, 1983; p A-35.

14. Lauher, J. W.; Hoffmann, R. J. Amer. Chem. Soc. 1976, 98, 1729.

15. Carlin, R. T.; Osteryoung, R. A. unpublished results.

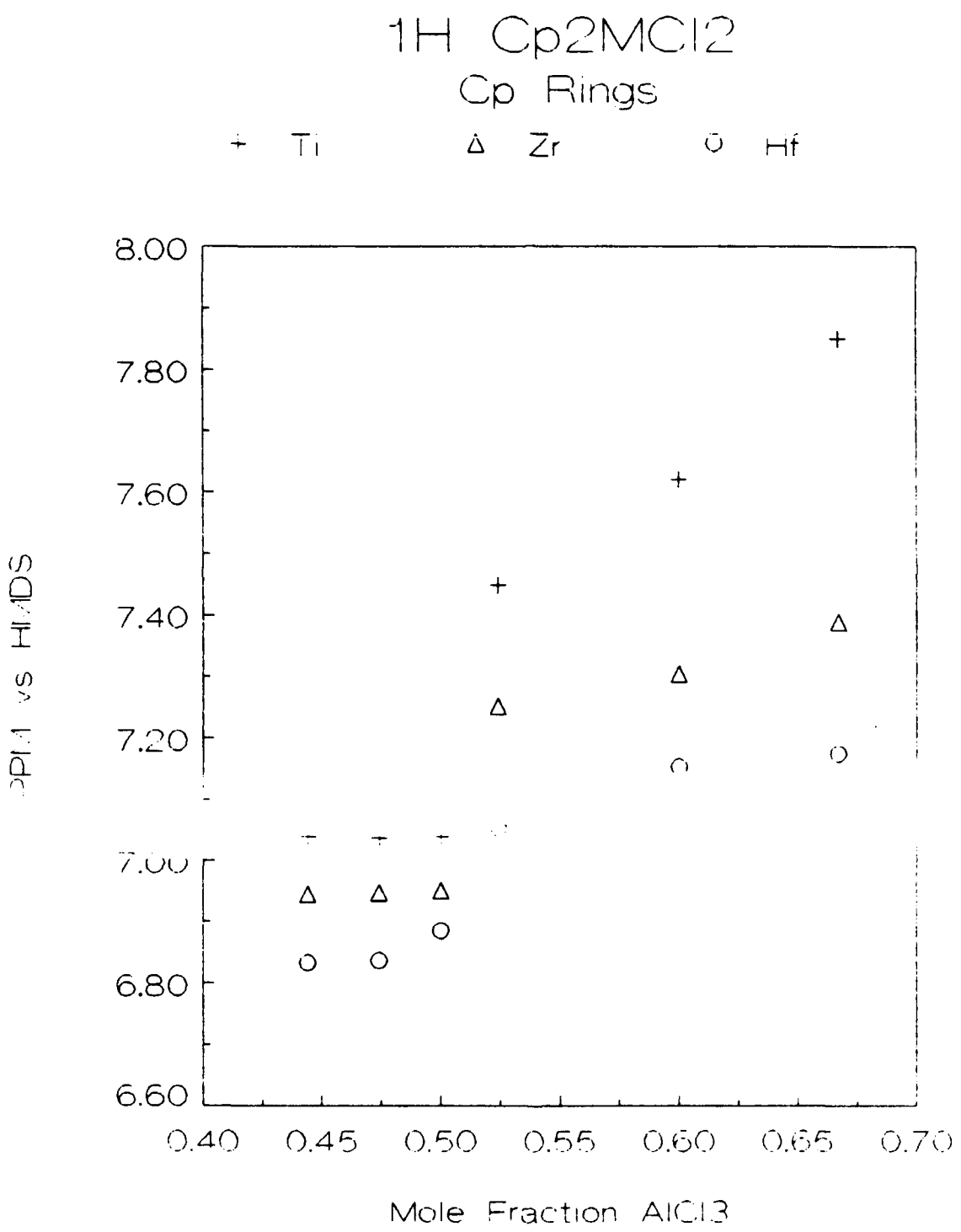

Figure 1. ^{1}H NMR of Cp rings in Cp_2MCl_2 versus melt composition. Referenced to hexamethyldisiloxane.

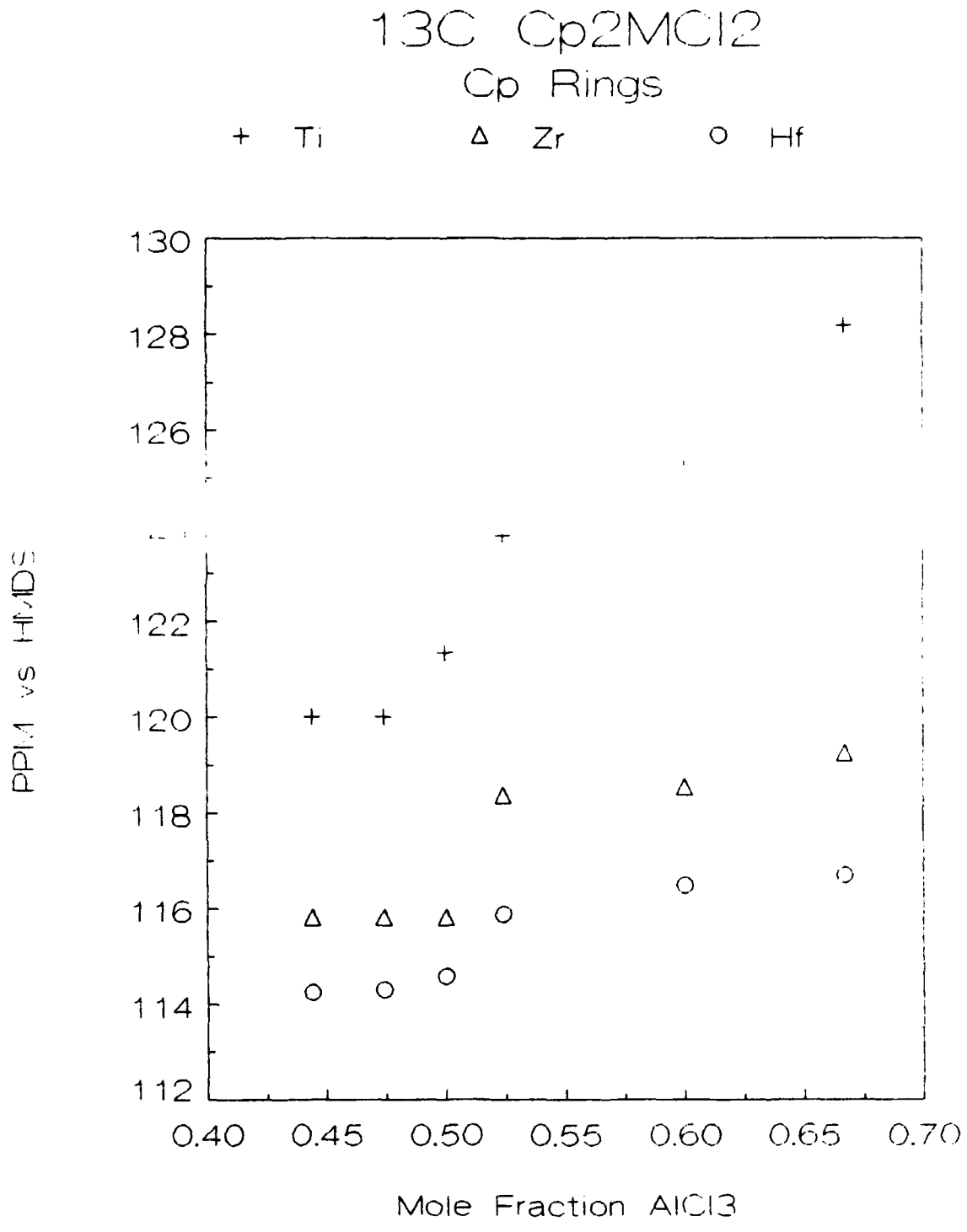

Figure 2. ^{13}C Chemical shift of the Cp rings for Cp_2MCl_2 as a function of melt acidity. Referenced to hexamethyldisiloxane.

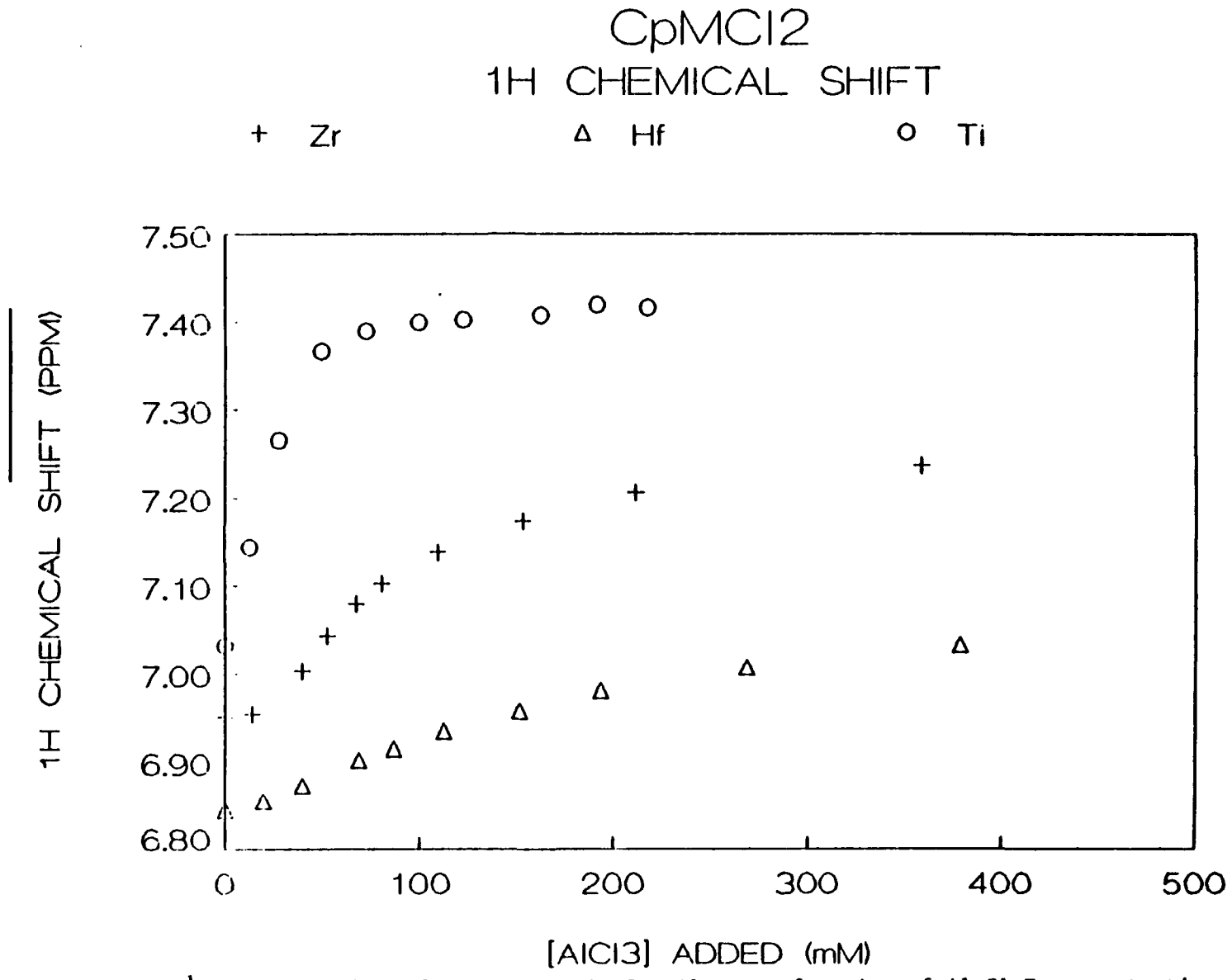

Figure 3. ^1H chemical shift for Cp rings in Cp_2MCl_2 as a function of $Al_2Cl_7^-$ concentration. Referenced to hexamethyldisiloxane.

35-19

1988 USAF-UES SUMMER FACULTY RESEARCH PROGRAM

GRADUATE STUDENT RESEARCH PROGRAM

Sponsored by the

AIR FORCE OFFICE OF SCIENTIFIC RESEARCH

Conducted by the

Universal Energy Systems, Inc.

FINAL REPORT

A MCSCF STUDY OF THE REARRANGEMENT OF NITROMETHANE TO METHYL NITRITE

Prepared by:	Michael L. McKee
Academic Rank:	Associate Professor
Department and	Department of Chemistry
University:	Auburn University
Research Location:	FJSRL/NC
	US Air Force Academy
	Colorado Springs, CO 80840
USAF Research:	Major Kenneth Deiter
Date:	27 August 1988
Contract No:	F49620-87-R-0004

A MCSCF STUDY OF THE REARRANGEMENT OF NITROMETHANE TO METHYL NITRITE

Michael L. McKee, Ph. D.

ABSTRACT

Ab initio calculations, which use the 6-31G* basis set and a multiconfigurational (MC) wavefunction, have been carried out for the unimolecular rearrangement of nitromethane to methyl nitrite. Geometry optimization of nitromethane and methyl nitrite have been carried out with a two configuration wavefunction while the unimolecular transition state was refined with a 20-configuration wavefunction which was determined by using all configurations generated by excitation from the two highest occupied orbitals into the two lowest empty orbitals (4 electron in 4 orbitals). The transition state indicates a weak interaction between a methyl radical and nitro radical. In the transition state the breaking CN bond and the forming CO bond are 3.617 and 3.700Å, respectively and there is a significant difference predicted in the NO bond lengths in the transition state (1.371/1.155Å). At the highest level of calculation (Multireference CI) the unimolecular barrier is predicted to be 57.1 kcal/mol which is 7.7 kcal/mol above the sum of CH_3 and NO_2 radical energies.

Acknowledgments

I would like to thank the Air Force Systems Command for sponsorship of this research and the Air Force Office of Scientific Research for the opportunity to carry out the research at their facilities. Financial support for the Summer Faculty Research Program Fellowship was administered through Universal Energy Systems. The hospitality shown by the members of the Frank J. Seiler Research Laboratory was greatly appreciated. In particular I would like to acknowledge helpful conversations with Major Kenneth Dieter and Dr. James Stewart.

The MCSCF program GAMESS was provided by Mark Gordon at North Dakota State University. Acknowledgment is also made to Dr. Mike Schmidt who provided assistance in running GAMESS. Calculations were carried out on the VAX cluster at the Frank J. Seiler Research Laboratory and on the CRAY2 at Kirkland Air Force Base.

I. INTRODUCTION:

It has recently been predicted[1] and verified[2,3] that the unimolecular rearrangement of nitromethane to methyl nitrite might be competitive with simple C-N bond rupture. The predictions were based on MINDO/3 calculations performed by Dewar and coworkers,[1] who found the concerted transition state to have an energy 14.6 kcal/mol lower than the energy of radicals. When a less favorable entropy for the rearrangement is taken into account, Dewar concluded that the two pathways would be competitive. Recent experimental work[3] has lead to a confirmation of these predictions. Employing infrared multiple-photon dissociation (IRMPD), Lee and coworkers[3] have been able to determine the activation barrier for the rearrangement of CH_3NO_2 to CH_3ONO. Taking into account various uncertainties, Lee determined the barrier to be between 51.5 to 57.0 kcal/mol with 55.5 kcal/mol as the most probable value. For comparison the C-N bond energy in nitromethane is determined to be 59.4 kcal/mol.

The experimental results above contrast sharply with ab initio results[4] where the unimolecular rearrangement barrier to CH_3ONO was found to be 16.1 kcal/mol higher than the C-N bond energy in CH_3NO_2 (73.5 and 57.4 kcal/mol, respectively). The calculations used the 6-31G* basis[5] to determined geometries and zero point corrections and the MP2/6-31G* electron correlation treatment[5] on 6-31G* optimized geometries to determine relative energies. It was anticipated that the method would poorly describe the unimolecular transition state since it was based on a single-determinant wavefunction while the transition state is expected to have considerable open shell character. In order to avoid an unfavorable 4-electron 2-orbital interaction the C-N bond would be expected to be nearly completely broken before the C-O bond begins to form. If the C-N bond is completely broken before the C-O bond begins to form, the pathway is best described as eq 1. If the bond rupture is not complete, eq 2 better describes the process.

$$CH_3NO_2 \rightarrow CH_3 + NO_2 \rightarrow CH_3ONO \quad (1)$$

$$CH_3NO_2 \rightarrow CH_3ONO \quad (2)$$

A careful determination of the transtion state is essential for a discrimination of the two possible pathways. The wavefunction used to determine the geometry must be able to adequately describe the $^2A''$ and $^2A_1$ states of CH_3 and NO_2, respectively and to describe the bond being broken in CH_3NO_2 and formed in CH_3ONO.

In a recent MCSCF study on the nitro-nitrite rearrangement of the isoelectronic NH_2NO_2, Saxon and Yoshimine[6] have found that the transition state is best described as an interaction of a NO_2 and a NH_2 radical. Geometries were optimized with the 4-31G basis and a CAS (Complete Active Space) MCSCF with 10 electrons in 7 orbitals. The breaking NN bond and forming NO bond in the transition state were 2.84 and 3.21Å, respectively, and the energy (MRCI/6-31G*) was 0.9 kcal/mol lower than radicals.

II. OBJECTIVES OF THE RESEARCH EFFORT:

The objective of this work was to study the rearrangement mechanism of a reaction important to the underestanding of detonation in polynitrated systems as TNT or RDX. Earlier studies[4] found that the rearrangement barrier of nitromethane to methyl nitrite was significantly higher than simple bond cleavage to NO_2 plus CH_3. Recently, the barrier to rearrangemnt has been determined to be five kcal/mol lower than the activation required for bond cleavage.[3] It is hoped that a more sophisticated treatment of the reactant and transition state may resolve the difference between the predicted and experimental activation barrier.

The calculations used in this study are based on multiconfigurational treatments[7] which allows the optimal linear combination of different configurations where the term configuration

refers to a particular occupation of molecular orbitals. In contrast to a single configurational method, the multiconfigurational method can be used to correctly describe forbidden reactions where an orbital crossing occurs as well as homolytic bond cleavages where the wavefunction must describe the radical products.

III. APPROACH

The simplest example of a nitro-nitrite rearrangement is the HNO_2 → HONO rearrangement; however, a more relevant system to the study of combustion is the nitro to nitrite rearrangement in nitromethane. It has been found[8] that an accurate description of the wavefunction of a molecule containing a nitro group requires at least two configurations. In a single configurational calculation the orbital on the left (see below) is the highest occupied orbital (HOMO) and the orbital on the right (LUMO) is unoccupied. In a two configurational calculation the orbital on the right has significant occupation.

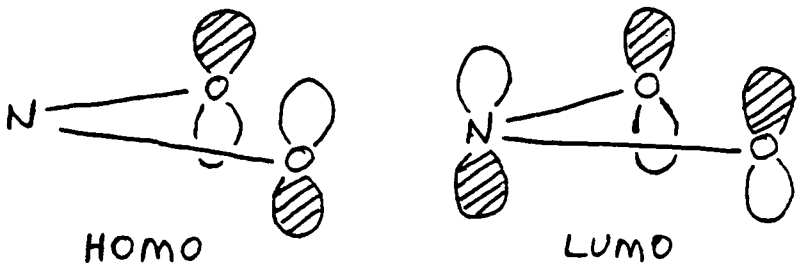

In the region of the transition state the wavefunction will be described best as two interacting radicals. The important orbitals to correlate are the bonding and antibonding combination of the CN sigma bond and the two combinations of the oxygen lone pair (see above). As the transition state is approached and the CN bond becomes long the CN bonding and antibonding orbitals can each accommodate one of the unpaired electrons of CH_3 and NO_2. The two combinations of the oxygen lone pair are required to correctly describe the nitro portion of the transition state. If all excitations are allowed from the two highest

occupied orbitals into the two lowest unoccupied orbitals, the resulting multiconfigurational wavefunction is referred to as a 4x4CAS-MCSCF (4 electrons in 4 orbitals Complete Active Space-MCSCF). For the transition state which has C_1 symmetry the 4x4CAS wavefunction consists of 20 configurations.

Exploratory calculations were carried out at the MCSCF/STO2G level in order to determine reasonable starting geometries at higher levels of theory. Geometries and energies are compared in Figure 1 and Tables I and II where the conformation choosen for geometry optimization was the lowest energy conformation at the MP2/6-31G*//6-31G* level.[4] A 2x2CAS (TCSCF) was used to determine the geometry and energy of NO_2, CH_3NO_2, and CH_3ONO, while a 4x4CAS was used for the transition state. The CN bond energy of CH_3NO_2 is overestimated by 18 kcal/mol (exptl.[9] 59.4 kcal/mol; CAS/STO2G, 78.2 kcal/mol) which indicates that the calculations at this level of theory may not be reliable. However, it is interesting that the transition state for the nitro-nitrite rearrangement is predicted to be 9.6 kcal/mol lower than the energy of NO_2 and CH_3 radicals (Table II). This result is in agreement with MINDO/3 results where a difference of 14.6 kcal/mol is obtained. The transition state is characterized by a long CO and CN bond and a significant NO bond alternation in the NO_2 fragment.

The next step was full optimization at the 4x4CAS/6-31G* level for the transition state and at the 2x2CAS/6-31G* level for NO_2, CH_3NO_2 and CH_3ONO. The results of these calculations are given in Figure 2. Total energies are given in Table I and relative energies are given in Table II. Single point calculations at the 4x4CAS/6-31G* level were not made on the optimized CH_3NO_2 and CH_3ONO geometries due to the fact that the CN or CO bond are well described as a doubly occupied orbital in the reactant or product and correlating this orbital with the antibonding orbital would have little affect on the energy.

All optimizations were straight foward except the location of the transition state. Due to the very loose nature of the transition state, a precise stationary point could not be located in 50 cycles of

optimization. The stopping criterion requires that the largest component of the gradient to be less than 5×10^{-4} hartrees/bohr (or hartrees/radian) and the root mean square (rms) gradient to be less than 1.7×10^{-4}. After about 20 cycles of optimization there was little change in geometry or energy. Since the optimization seemed to be "stalled" around the transition state, the point with the lowest rms gradient was used as the converged structure. This geometry was characterized by a rms gradient about four times larger than the normal stopping criterion.

A comparison of optimized geometries at the HF/6-31G* and MCSCF/6-31G* levels indicated that the additional configuration(s) resulted in only small geometry changes for all structures except the transition state. The largest change in the CH_3NO_2 geometry when comparing the HF/6-31G* (1 configuration) and the TCSCF/6-31G* geometries (2 configurations) is a lengthening of the NO bond length by 0.013Å. This is to be expected since the additional configuration contains two electrons in a NO antibonding orbital which is unoccupied in the SCF wavefunction. The ONO bond angle closes down by 0.9^{o} due to the bonding interaction across oxygen in the additional configuration. The coefficient of the second configuration has a value of 0.25 indicating a significant contribution. In contrast the MCSCF/6-31G* wavefuction of methyl nitrite was characterized by a smaller second coefficient (0.10) and the geometry at the HF/6-31G* and MCSCF/6-31G* levels are almost identical (Figure 2). Inclusion of an additional configuration in the optimization of the NO_2 radical had a small effect. Compared to the 6-31G* optimized geometry a 2x2CAS/6-31G* wavefunction leads to an increase of the NO bond length by only 0.004Å and no change in the ONO bond angle.

A comparison of geometric parameters calculated for the transition state at different levels of theory is given in Table III. At the 4x4CAS/STO2G and 4x4CAS/6-31G* levels the transition state is characterized by extremely long CO and CN bond distances which is in contrast to single configurational methods (MINDO/3, 6-31G*) where the transition state is much tighter. This distinction becomes important

in the context of the experimental activation barrier determined by Lee and coworkers.[3] In this work the A factor calculated by Dewar et al.[1] for the tight transition state ($10^{13.3}$) was used in fitting the data to determine an activation barrier. The transition state calculated by MCSCF methods is much looser and the associated A factor probably would be closer to the experimental A factor for simple CN bond rupture ($10^{15.6}$).[3] If the assumed A factor is too small, then the calculated activation barrier would be underestimated.

If the CN distance is decreased, or if the CO distance is decreased in the transition state, CH_3NO_2 or CH_3ONO should be formed, respectively. However, if both distances are decreased, the energy should increase. In order to see how sensitive the energy was to this geometry change, one calculation at the 4x4CAS/6-31G* level was made after moving the CH_3 group 1Å closer to the NO midpoint. This geometry led to an energy increase of 0.9 kcal/mol relative to the transition state.

IV. DISCUSSION

There are several qualitative interpretations of the rearrangement mechanism. In an approximate sense the reaction is orbitally forbidden as shown in Figure 3. The sigma CN bonding orbital correlates with a sigma CO antibonding orbital while the sigma CN antibonding orbital correlates with a sigma CO bonding orbital (Figure 3). However, since both orbitals have the same symmetry in the transition state (C_1) the crossing will be avoided. Nevertheless, the barrier would be expected to be high. As the transition state is approached the energy difference between the bonding and antibonding CN orbitals becomes smaller. At the transition state three configurations become important in the MCSCF expansion. The configuration with one electron in the sigma $_{CN}$ and sigma $_{CN}^*$ orbitals (the labels are not an accurate description in the transition state, however, they are convenient labels in the present context) makes the largest contribution to the wavefunction (61%) and suggests that the

transition state is best described as interacting radical fragments. The configuration with the sigma $_{CN}$ orbital doubly occupied and with the sigma $_{CN}^{*}$ orbital doubly occupied contribute a total of 29%.

The radicals NO_2 and CH_3 have very similar ionization potentials (9.6eV and 9.8eV, respectively[10]) which perhaps rationalizes why these three configurations contribute strongly in the transition state since the orbital energies would be quasi-degenerate.

A more intuitive interpretation can be obtained by a simple consideration of resonance structures (Figure 4). As the transition state is approached and the fragments become "radical-like", the second resonance structure of NO_2 becomes the dominant contributing resonance structure, while the third resonance structure, which indicates an alternation of single and double NO bonds opposite from that found in the transition state and product, will be unimportant. Evidence for this interpretation comes from the transition state geometry. First, there is a large alternation of NO bonds (1.371Å/1.155, CAS/6-31G*) clearly indicating a localized single and double bond. Secondly, the ONO angle is reduced from 124.9° in CH_3NO_2 to 113.0° in the transition state which is due to the increased steric repulsion of the nitrogen lone pair.

The methyl ($^2A''$ state) and the nitro radical ($^2A_1$ state) are ideally suited for combining to form a CN sigma bond in CH_3NO_2 since the unpaired electrons are directed along the bond axis. This is not the case for formation of CH_3ONO where the NO_2 radical requires promotion to a more suitable electron distribution. A promoted NO_2 radical will have more unpaired electron density on one oxygen in an orbital perpendicular to the NO_2 plane. The CH_3 radical would then approach the prepared NO_2 radical from above which is exactly what is observed in the transition state geometry.

The rearrangement barrier can be related to two factors. First, the energy required to promote the NO_2 fragment and second, the interaction energy of the two radicals. If the interaction energy is greater than the promotion energy, then the rearrangement barrier will be less than the CN bond energy. On the other hand, if the promotion

energy is greater, the barrier will be greater than the CN bond energy. The promotion energy was determined as the energy difference between optimized NO_2 and the NO_2 fragment in the transition state (Table IV). At the 3x4CAS/6-31G* level this value is 25.4 kcal/mol and increases to 46.4 kcal/mol at the PMP4/6-31G* level. For the CH_3 fragment the promotion energy is very small (Table IV). The interaction energy is the energy difference between the isolated frozen fragments, CH_3 and NO_2, and the transition state which is -17.7 kcal/mol at the 4x4CAS/6-31G* level. Thus, at the 4x4CAS/6-31G* level the activation barrier is 7.7 (25.4-17.7) kcal/mol higher than radicals.

Activation barriers calculated at the MP4/6-31G* level generally yield accurate results.[5] However, the method requires a dominant configuration which is not the case for the nitro to nitrite transition state. The PMP4/6-31G* relative energies are in good agreement with experiment (Table II) except for the activation barrier which is 51.9 kcal/mol higher than the CH_3 and NO_2 radicals!

Multireference second order CI calculations (with the 6-31G* basis) were carried out on the CAS/6-31G* geometries for fragments and transition state. Orbitals were divided into four spaces: frozen occupied (11 orbitals), active (5 doubly occupied and 2 unoccupied), external (10 orbitals), and frozen virtual (38 orbitals). The configuration list was generated by including all excitations within the active space plus single and double excitations from the active space into the external space. The virtual space of the starting wavefunction was first compacted by calculating a secord order CI with a smaller active space but including all virtual orbitals in the external space (14 frozen, 4 active, and 48 external orbitals). The CH_3 and NO_2 radicals were calculated together (C_s symmetry separated by 20.0Å) since the multireference CI is not size consistant. The CI expansion for the combined fragments contained approximately 29,300 configurations while the transition state (C_1 symmetry) contained 58,500 configurations. The relative energy for fragments and transition state at this level of theory is very simliar to the

CAS/6-31G* results (Table II). While this level of theory may correctly describe the qualitative features of the rearrangement mechanism, quantitative determination of the barrier may require more accurate computational methods (i.e. larger active space, bigger basis and more CI).

V. RECOMMENDATIONS:

On the basis of the above study the following recommendations can be made:

(1) That geometry optimizations of nitro containing compounds using a multiconfigurational wavefunction is probably unnecessary as the small changes in geometry do not justify the additional expenses.

(2) That transition states be located with an MCSCF procedure as it is shown that the geometry of the transition state depends very strongly on the level of calculation.

(3) That energies be determined with additional electron correlation, perferably multireference CI (MRCI) which will recover important dynamic electron correlation.

REFERENCE

1. Dewar, M.J.S., J.P. Ritchie, and J. Alster, "Thermolysis of Molecules Containing NO_2 Groups," J. Org. Chem. 1985, Vol. 50, pp. 1031-1036.
2. Wodtke, A.M., E.J. Hintsa, and Y.T. Lee, "The observation of CH_3O in collision free multiphoton dissocation," J. Chem. Phys., 1986, Vol. 84, pp. 1044-1045.
3. Wodtke, A.M., E.J. Hintsa, and Y.T. Lee, "Infrared Multiphoton Dissociation of Three Nitroalkanes," J. Phys. Chem., 1986, Vol. 90, pp. 3549-3558.
4. McKee, M.L., "Ab Initio Study of Rearrangements on the CH_3NO_2 Potential Energy Surface," J. Am. Chem. Soc., 1986, Vol. 108, pp. 5784-5792.
5. Hehre, W.J., L. Radom, P.v.R. Schleyer, and J.A. Pople, Ab Initio Molecular Orbital Theory, New York, Wiley, 1986.
6. Saxon, R.P. and M. Yoshimine, "Theoretical Study of Nitro-Nitrite Rearrangement of NH_2NO_2," to be published, J. Phys. Chem.
7. The GAMESS program has been used for all calculations. Dupuis, M., D. Sprangler, and J.J. Wendolski, GAMESS, QG01, Program Library of Institute for Molecular Science. The version we used had been heavily modified by M. Schmidt at North Dakota State and S.T. Elbert at Iowa State. We thank Dr. Mike Schmidt and Prof. M. Gordon for providing us with this program.
8. Marynick, D.C., A.K. Ray, J.L. Fry, and D.A. Kleier, "The Electroinc Structure of Nitromethane," J. Mol. Struct., 1984, Vol. 108, pp. 45-48.
9. Benson, S.W.; H.E. O'Neal, Kinetic Data on Gas Phase Unimolecular Reactions; Natl. Stand. Ref. Data Ser., National Bureau of Standards, Washington, DC, 1970.
10. Levin, R.D. and S.G. Lias "Ionization Potentials and Appearance Potential Measurements, 1971-1981," NSRDS-NBS 71, issued October 1982.

Table I. Total Energies (hartrees) and Zero Point Energies (kcal/mol) at Various Levels of Theory[a]

Method	CH_3NO_2	CH_3ONO	CH_3	NO_2	TS
6-31G*//6-31G*	-243.66199	-243.66864	-39.55899	-204.03149	-243.53194
MP2/6-31G*//6-31G*[b]	-244.33794	-244.33148	-39.67296	-204.55965	-244.21624
CAS/STO2G//CAS/STO2G	-233.39136	-233.38223	-37.93407	-195.33278	-233.28209
PMP4/6-31G*//CAS/6-31G*[c]	-244.36869	-244.36447	-39.69002	-204.57924	-244.18662
CAS/6-31G*//CAS/6-31G*	-243.70011	-243.70582	-39.55476	-204.05339	-243.59673[d]
MRCI/6-31G*//CAS/6-31G*			-243.65320		-243.63729
ZPE/6-31G*[e]	30.82	30.32	17.49	5.56	28.25
exptl. ZPE	30.23[f]		16.17[g]	5.40[g]	

a) Level of CAS optimization is 2x2CAS except for the transition state which was optimized at the 4x4CAS level.
b) All orbitals are correlated and spin contamination is not projected out. Reference 4.
c) The frozen core approximation is used and the energy lowering due to projecting out spin contamination at the MP3 level is used to correct the MP4 energies.
d) If the CH_3 group is move 1A closer to the NO midpoint, the energy increases 0.9 kcal/mol.
e) The calculated zero point energy is multiplied by a factor of 0.9.
f) See McKee, M.L. "Ab Initio and MNDO Study of Nitromethane and the Nitromethyl Radical," J. Am. Chem. Soc., 1985, Vol. 107, p. 1900.
g) Chase, M.W., Jr., C.A. Davies, J.R. Downey, Jr., D.J. Frurip, R.A. McDonald, and A.N. Syverud, J Phys. Chem. Ref. Data, 1985, Vol. 14, Supplement 1 "JANAF Thermochemical Tables," Third Ed.

Table II. Relative Energies (kcal/mol) of Species on the CH_3NO_2 Potential Energy Surface

Method	CH_3NO_2	CH_3ONO	$CH_3 + NO_2$	TS
MINDO/3[a]	0.0	4.1	76.7(59.5)[b]	44.9
6-31G*//6-31G*	0.0	-3.4	44.9	81.6
MP2/6-31G*//6-31G*	0.0	4.0	66.1	76.4
CAS/STO2G//CAS/STO2G	0.0	5.7	78.2	68.6
PMP4/6-31G*//CAS/6-31G*	0.0	2.6	62.4	114.3
PMP4/6-31G*//CAS/6-31G*+ZPC[c]	0.0	2.1	54.6	106.5
CAS/6-31G*//CAS/6-31G*	0.0	-3.6	57.2	64.9
CAS/6-31G*//CAS/6-31G*+ZPC[c]	0.0	-4.1	49.4	57.1
MRCI/6-31G*//CAS/6-31G*			0.0	10.0
exptl[d]	0.0	2.3	59.4[e]	55.5[e,f]

a) Reference 1.
b) The value in parentheses refers to the relative energy when the experimental heat of formation is used for NO_2 rather than the MINDO/3 calculated value.
c) A zero point correction is include. The zero point correction for the transition state is assumed to be the same as for CH_3 and NO_2.
d) See reference 4.
e) See reference 3.
f) This value may be too low due to an underestimation of the A factor for the nitro to nitrite rearrangement (see text).

Table III. Comparison of Geometric Parameters (Ångstroms, Degrees) for the Nitro to Nitrite Transition State

Parameter[a]	MINDO/3[b]	6-31G*	CAS/STO2G	CAS/6-31G*
CN	1.516	1.928	3.625	3.616
CO_1	1.584	2.010	3.538	3.700
NO_1	1.299	1.251	1.471	1.371
NO_2	1.438	1.181	1.222	1.155
ONO			110.0	113.0

a) In the transition state the CH_3 group is migrating to O_1.

b) Reference 1.

Table IV. Calculated Promotion Energy (kcal/mol) and Interaction Energy

Method	NO_2 Promotion	CH_3 Promotion	NO_2/CH_3 Interaction
CAS/6-31G*[a]	25.4	0.02	-17.7
PMP4/6-31G*	46.4	0.1	

a) The dominant configuration in the MCSCF expansion contributes only 64% to the wavefunction for the frozen NO_2 fragment. In contrast the dominant configuration contributes 96% for the optimized NO_2 radical. The second configuration for the frozen NO_2 fragment (34%) is characterized by three unpaired electrons coupled as a doublet ($^2A'$ state) where an electron from the oxygen lone pair (a" symmetry) has been promoted into a higher oxygen lone pair orbital (a" symmetry).

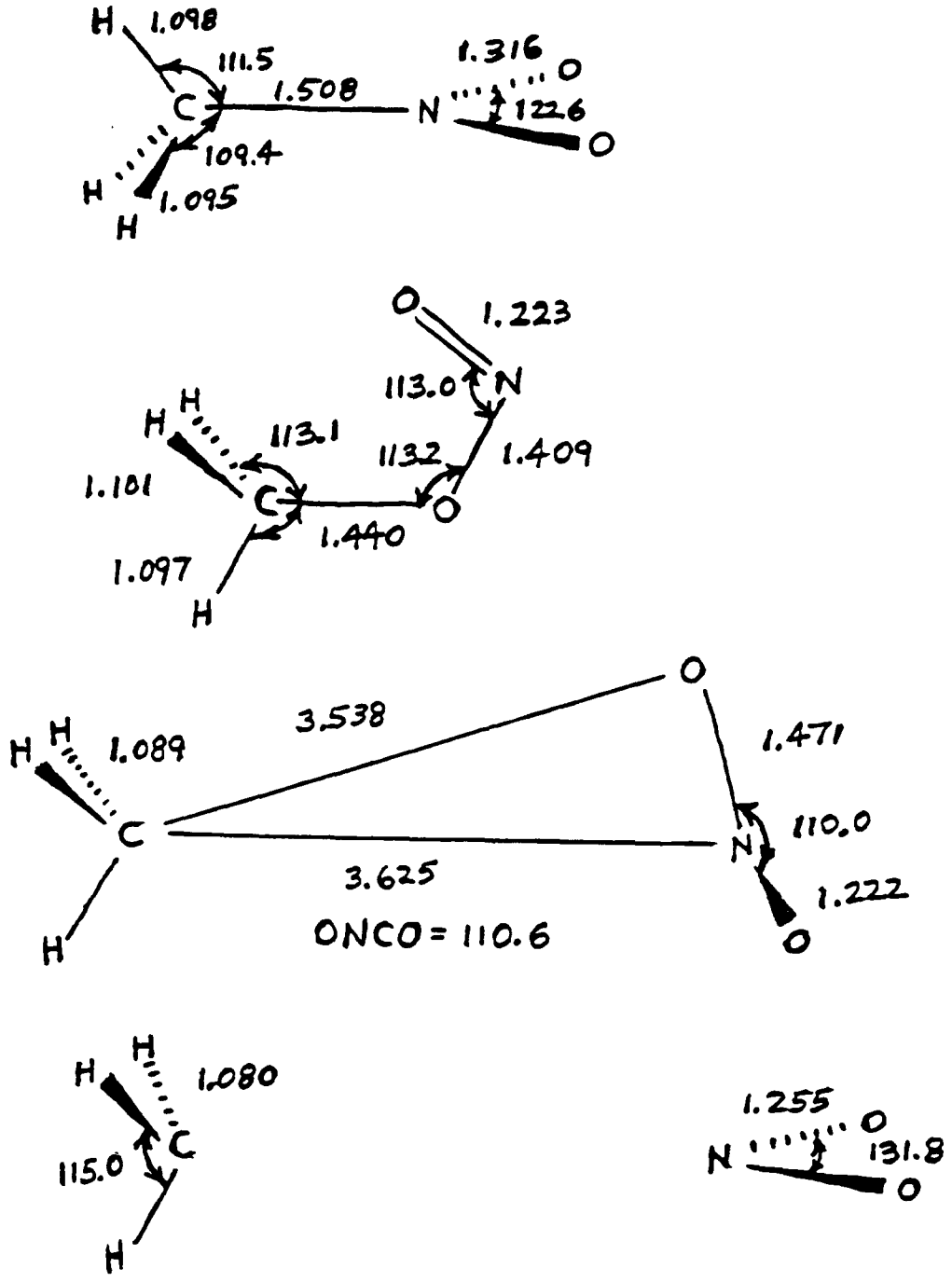

Figure 1. Geometric parameters at the CAS/STO2G level.

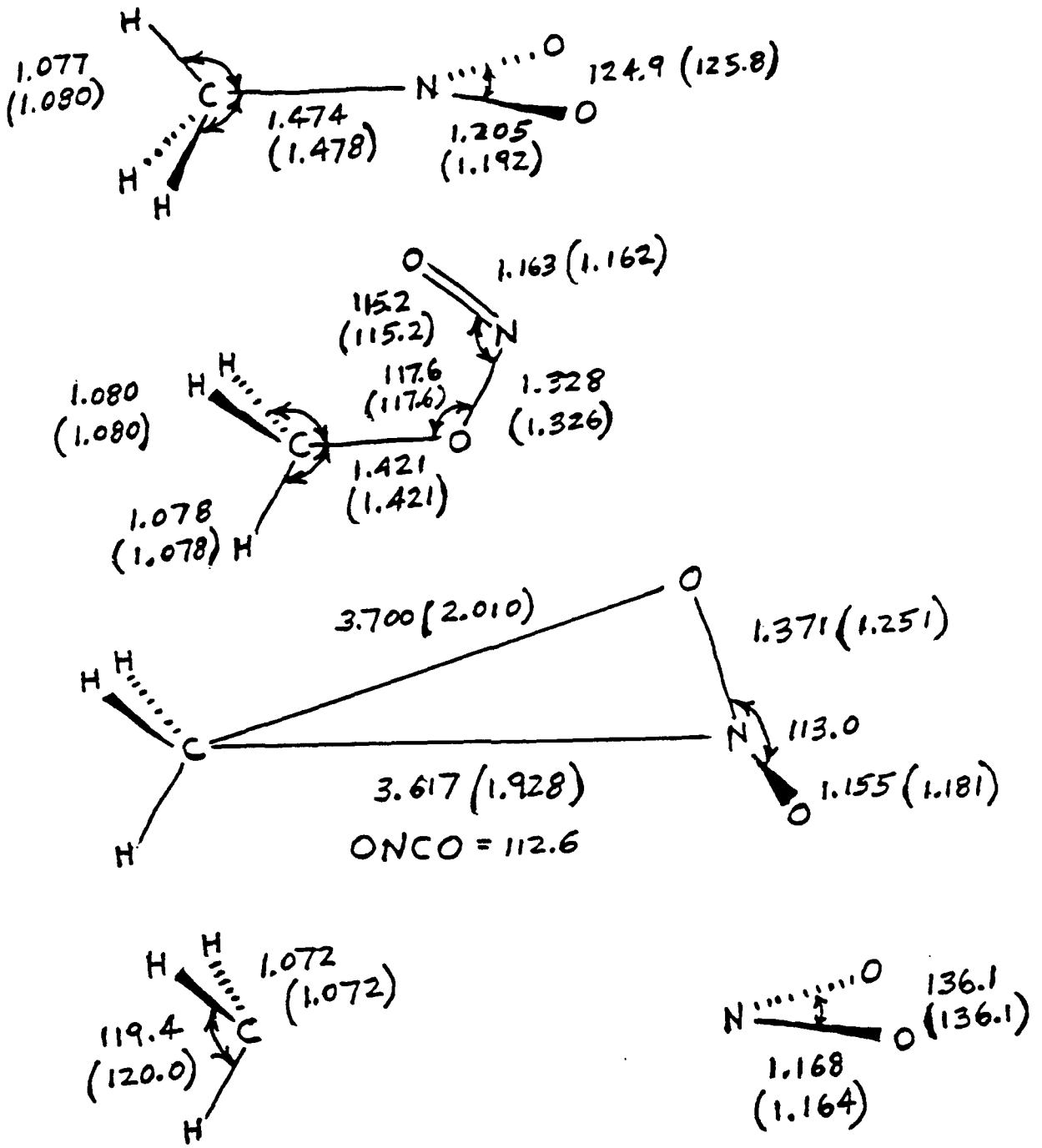

Figure 2. Geometric parameters at the CAS/6-31G* level. In parentheses are given the values at the HF/6-31G* level.

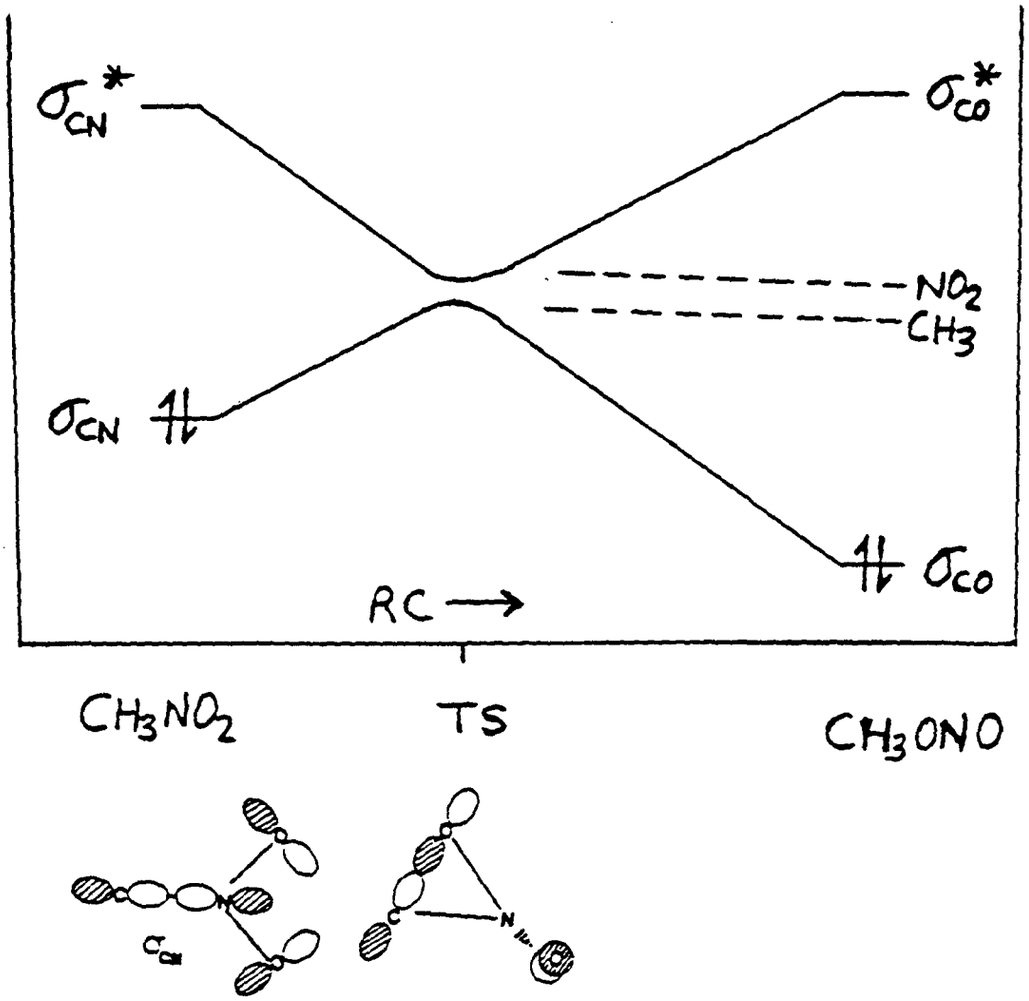

Figure 3. Correlation diagram indicating an avoided crossing of the sigma CN bonding and anitbonding orbitals. In the transition state the two orbitals will have energies similar to the orbitals containing the unpaired electrons in the CH_3 and NO_2 radicals.

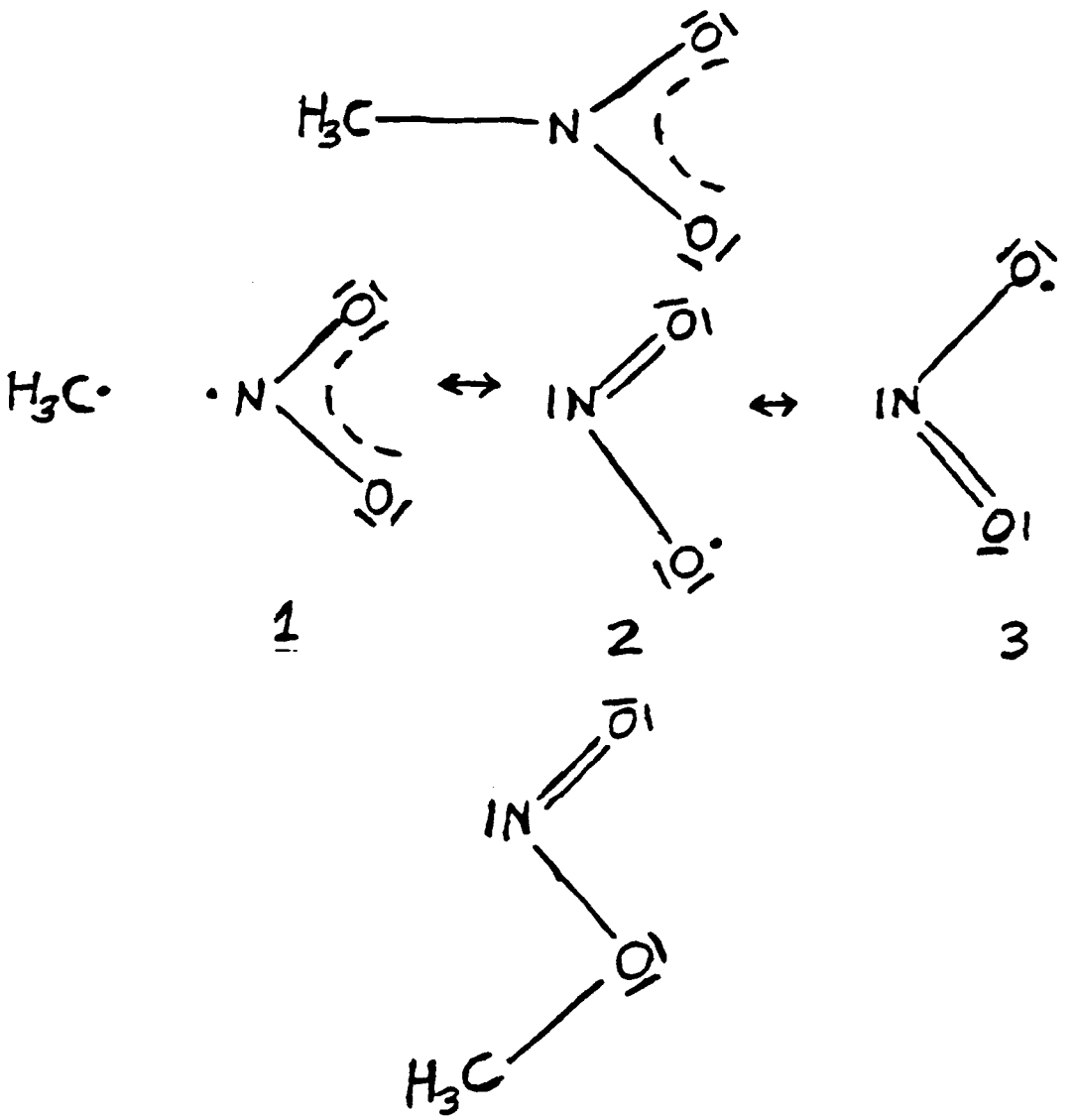

Figure 4. Resonance structures of species on the CH_3NO_2 potential energy surface. As the CN bond breaks, resonance structure 2 will become increasingly important. The CH_3 group will migrate above the NO_2 plane and form a sigma bond with the unpaired electron in an orbital perpendicular to the NO_2 plane.

1988 USAF - UES SUMMER FACULTY RESEARCH PROGRAM/

GRADUATE STUDENT RESEARCH PROGRAM

Sponsored by the

AIR FORCE OFFICE OF SCIENTIFIC RESEARCH

Conducted by the

Universal Energy Systems, Inc.

FINAL REPORT

THE EFFECTS OF SODIUM CHLORIDE ON ROOM TEMPERATURE MOLTEN SALTS

Prepared by:	Tammy J. Melton, PhD
Academic Rank:	Assistant Professor
Department and	Department of Chemistry
University	St. Norbert College
Research Location:	Frank J. Seiler Research Laboratory/NC
	United States Air Force Academy
	Colorado Springs, CO 80840-6528
USAF Researcher	Dr. John S. Wilkes
Date:	12 August 1988
Contract No:	F49620-87-R-0004

THE EFFECTS OF SODIUM CHLORIDE ON ROOM TEMPERATURE MOLTEN SALTS

by

Tammy J. Melton

ABSTRACT

The effects of adding sodium chloride to room temperature molten salts containing 1-methyl-3-ethylimidazolium chloride and aluminum chloride have been examined. Sodium chloride will dissolve in basic or neutral melts, but only in very small quantities. Sodium chloride will dissolve in larger quantitites in acidic melts. The limit of the solubility has been determined to be that quantity which will result in a neutral melt, that is, where mole fraction aluminum chloride is reduced to 0.5. Cyclic voltammetry indicates a neutral melt by showing no aluminum reduction (indicative of an acidic melt) and no chloride oxidation (indicative of a basic melt) except at extremely low concentrations. A sodium electrode was constructed which exhibited a rest potential of -2.05 V and maximum current at -0.85 V.

ACKNOWLEDGEMENTS

I would like to thank the Air Force Systems Command and the Air Force Office of Scientific Research for the sponsorship of this research. I would also like to thank Universal Energy Systems for their administrative and directional assistance in this research effort, and for the support of the graduate student who worked with me.

I am deeply indebted to my co-worker Miss Jennifer Joyce, graduate student from Texas A & M, who worked very hard to help me complete important facets of the research. Also, I am pleased to acknowledge the work of Dr. Joseph Maloy, who assisted in the electrochemistry and did extensive computer data analysis on the results.

It is a pleasure to acknowledge those individuals who have so willingly given assistance, direction, and advice to this project: Dr. John Wilkes, for his expert guidance and advice, especially in the early stages of the work, Dr. Richard Carlin for sharing his expertise in electrochemistry, Mr. Jeffrey Boon for his work in computers, Mr. Lloyd Pflug, for running ICP and NMR analyses, and Mr. Greg Godec and Mr. Fred Kibler for technical assistance and for making the starting materials. I am also grateful to Mr. Ralph Hutchinson and the Department of Chemistry at the USAF Academy for providing and assisting with AA analysis. Finally, the concern and encouragement of Dr. Charles Bump was appreciated.

I. INTRODUCTION

Mixtures of aluminum chloride and 1-methyl-3-ethylimidazolium chloride (MEICl) are ionic liquids (melts) at room temperature when the mole fraction of aluminum chloride is between approximately 0.33 and 0.666, inclusive.[1] These ionic liquids are potentially useful as electrolytes in batteries. The Lewis acid-base characteristics of these melts vary depending on the composition. Binary mixtures with mole fraction of $AlCl_3$ less than 0.5 ($N_{AlCl_3} < 0.5$) are basic due to the presence of excess Cl^-, a Lewis base.

$$\underset{\text{(excess)}}{MEI^+Cl^-} + AlCl_3 \rightleftharpoons MEI^+ + \underset{\text{(excess)}}{AlCl_4^-} + \underset{\text{(excess)}}{Cl^-} \qquad (1)$$

Acidic melts are formed when mole fractions of $AlCl_3$ are greater than 0.5. The presence of excess $AlCl_3$ drives the tetrachloroaluminate ion to heptachloroaluminate ion, a Lewis acid.

$$AlCl_4^- + AlCl_3 \rightleftharpoons Al_2Cl_7^- \qquad (2)$$

When $AlCl_3$ and MEICl are present in equimolar quantities (N=0.5) negligible concentrations of Cl^- and $Al_2Cl_7^-$ exist, and the molten salt is considered neutral.

$$MEICl + AlCl_3 \rightleftharpoons MEI^+ + AlCl_4^- \qquad (3)$$

The specific conductivity of these melts is relatively low, but reaches a maximum for the neutral melt.[2,3] This unexpectedly low conductivity has been attributed to the relatively strong association of the Cl^- to the hydrogen atoms at the 2, 4, and 5 positions of the MEI^+ (with the strongest of these at the 2 position). This interaction is believed to render Cl^- less mobile.

Melts composed of aluminum chloride and sodium chloride have been studied extensively[4] as well as melts of aluminum chloride and lithium chloride.[5] Moreover, ternary mixtures of aluminum chloride, lithium chloride, and sodium chloride have also been investigated.[6]

In this project, it was proposed to examine the effect of adding sodium chloride to the well-studied $AlCl_3$/MEICl room temperature molten salts.

My interests have been in the area of inorganic chemistry. My background is in synthesis and structural analysis by x-ray crystallography of transition metal low-to-medium valent compounds. This work and my experience in drybox/inert atmosphere technique contributed to my assignment to the Synthesis and Electrochemistry section of the Frank J. Seiler Research Laboratory.

II. OBJECTIVES OF THE RESEARCH EFFORT

Many electrode materials have been studied to characterize their redox and deposition behavior[7] for the purpose of identifying possible metals for cathode materials that could be used in batteries utilizing room temperature chloroaluminate salts. It was the goal of

the project to examine sodium as a potential material in $AlCl_3$/MEICl melts.

The initial goal was to identify the solubility of sodium chloride in $AlCl_3$/MEICl melts of varying composition. This was necessary as extremely low or extremely high solubility would preclude the use of sodium chloride or a sodium electrode.

Structural analysis was to be carried out in an effort to determine the charge-bearing species or complexation product. Since it is believed that LiCl forms $LiCl_2^-$ in these melts,[8] it was decided to examine NaCl to see whether it behaved similarly. Further, I planned to assist in the preparation of single crystals for x-ray crystallographic analysis of the $MEI^+AlBr_4^-$ to further determine the structural features of these melts.

Finally, the nature of the Na/Na^+ couple in melts of varying composition would be investigated by electrochemical techniques, specifically, cyclic voltammetry. It was desired to establish the reduction potential in the ternary melts, to quantify the conductivities, and to determine the corrosion behavior of the sodium electrode.

When it was discovered that the addition of NaCl to acidic melts resulted in the formation of neutral melts, additional goals were added. They were to determine whether additional MEICl could be added to the neutral melt and what the effect would be on the acid-base character, and to determine whether additional $AlCl_3$ could be added and what effect that would have on the acidity/basicity.

III SOLUBILITY STUDIES OF SODIUM CHLORIDE IN ROOM TEMPERATURE CHLOROALUMINATE SALTS

All procedures were carried out in an inert (helium) atmosphere drybox. Aluminum trichloride and 1-methyl-3-ethylimidazolium chloride were prepared and purified by methods established in this laboratory.[1] Ten-gram melts were prepared containing $AlCl_3$/MEICl mixtures from N_{AlCl_3} = 0.33 to N_{AlCl_3} = 0.667. (Mole fraction $AlCl_3$ is a convenient way of expressing the relative $AlCl_3$/MEICl ratios. However, it is believed that no molecular $AlCl_3$ is present in these melts.) Dried, solid NaCl was added in excess of that amount expected to dissolve and the melts were allowed to stir overnight. Any solid NaCl still remaining was considered evidence for saturation. If all the NaCl appeared to dissolve, more was added until saturation was achieved. The melts were filtered and aliquots were taken for sodium and aluminum analysis.

The aliquots were removed from drybox, hydrolyzed in deionized water, and diluted volumetrically. Analysis for aluminum was conducted by duplicate trials on an ARL 3510 ICP Spectrometer. Sodium was determined by atomic emission on a Perkin-Elmer 306 Atomic Absorption Spectrometer.

Results are summarized in the following table.

Table 1

Nominal N_{AlCl_3}	Actual N_{AlCl_3}	Actual N_{MEICl}	Actual N_{NaCl}	mg NaCl per g binary melt
0.33	0.336	0.663	0.0010	0.41
0.40	0.400	0.600	0.0008	0.34
0.45	0.441	0.559	0.0019	0.49
0.50	0.507	0.493	0.0008	0.34
0.53	0.509	0.438	0.053	22.67
0.55	0.501	0.411	0.088	41.07
0.60	0.496	0.346	0.158	79.01

Variations in the sodium content in the melts 0.33 to 0.50 are probably due to experimental errors arising from the difficulty in measuring extremely small sodium concentrations. However, clearly NaCl is much more soluble in acidic (N>0.5) melts. More importantly, it is evident that the limit to the solubility is that point where the mole fraction of aluminum chloride is driven to 0.5, neutral. The theoretical solubility of NaCl can then be expressed as S = A - M where S is moles of NaCl, A is moles of $AlCl_3$ and M is moles of MEICl. This provides a useful means of producing neutral melts.

No data was obtained for the N = 0.667 melt. NaCl appears to dissolve well in these melts, but upon approaching theoretical saturation points, these melts completely solidified.

No explanation is available to explain the behavior of dissolved NaCl in the basic melts. Since the quantities are so small, NaCl may be present as ion pairs or discrete aggregates.

IV. ANALYSIS OF $AlCl_3$/MEICl MELTS BY CYCLIC VOLTAMMETRY

Cyclic voltammetry was used to monitor the redox and acid-base nature of the acidic, basic, and neutral melts. An EG & G PAR Potentiostat Model 273 was used for all runs. All scans were performed at 100 mV/s scan rates using a 250 micron tungsten wire as a working electrode, an aluminum wire separated from the melt by a coarse glass frit as a counter electrode, and an aluminum wire in a N_{AlCl_3} = 0.60 melt as reference electrode.

The cyclic voltammogram for a binary $AlCl_3$/MEICl N = 0.52 melt is shown in Figure 1. A reduction peak at -0.5 V and stripping peak at 0.0 V are indicative of an acidic melt. The electroactive species is $Al_2Cl_7^-$. Sodium chloride was then added to the melt (in quantities less than saturation) and was allowed to dissolve. A decrease in the size of the aluminum reduction peak that has occurred because NaCl has shifted the equilibrium to the neutral side was observed.

$$Al_2Cl_7^- + Cl^- \rightleftharpoons 2\ AlCl_4^- \qquad (4)$$

Equation 4 can be likened to the autoionization of water.

Further addition of NaCl results in a neutral melt. Figure 2 shows the cyclic voltammogram of the melt over a region greater than 4V. The voltammogram was constructed in four sections, a, b, c, and d. Segments b' and c' are enhanced to 100 times the sensitivity of b and c, respectively. There is evidence for both an aluminum reduction peak at -0.5 V (indicative of an acidic melt) and a chloride oxidation peak at + 1.2 V (indicative of a basic melt).

V. SODIUM ELECTRODE IN Na^+- CONTAINING CHLOROALUMINATE SALTS

A sodium electrode was constructed by filling a 4mm glass tube with about one inch of sodium and inserting a copper or stainless steel wire into the sodium to make electrical contact. After each run, a fresh section of sodium was extruded and the surface renewed.

The resting potential of the cell with the sodium electrode was consistently approximately -2.05 V. After a few sweeps in the positive direction, a grey-black deposit was observable on the sodium surface and the rest potential became more positive (to about -1.8 V). It was observed that the current rapidly decreased with each scan, presumably as the black layer being deposited on the electrode became thicker.

A corrosion study confirmed these findings and indicated that although the rest potential was about -2.0 V, the maximum current flow was at about -0.85 V, considerably less.

An effort was made to locate the potential of the Na^+/Na reduction. The Li^+/Li reduction has been reported to occur in this system at -2.0 V.[8] It is believed that the Na^+ reduction is beyond the cathodic limit, or that it overlaps somewhat with MEI^+ reduction, but it was never conclusively observed.

VII. ADDITION OF MEICl AND $AlCl_3$ TO NEUTRAL MELTS

When NaCl was added to an acidic melt to the point of saturation, it was found that the melt displayed all the characteristics of a neutral or "buffered" melt. It was desired to determine whether any additional MEICl could be added to a melt so "buffered", and what effect the additional MEICl would have.

A small quantity of MEICl was added to a 0.52 melt which had been saturated with a known excess of NaCl and had been shown to be electrochemically neutral. The MEICl dissolved very slowly, but no chloride oxidation peak was observed in the CV. Next, a larger quantity of MEICl was added, an amount which would ordinarily create a melt of $N_{AlCl_3} = 0.495$. The melt became extremely cloudy and the chloride oxidation peak of a basic melt was easily detected. Evidently, the addition of MEICl causes precipitation of dissolved NaCl; when enough MEICl dissolves to remove the buffering NaCl, the melt becomes basic. The converse experiment was also carried out. That is, $AlCl_3$ was added to a 0.52 melt which had been saturated with

a known excess of NaCl. The $AlCl_3$ dissolved quickly, and all the excess NaCl dissolved as well, although slowly. When sufficient $AlCl_3$ was added to dissolve all the NaCl, the melt became acidic, as shown by cyclic voltammetry.

VIII. CONDUCTIVITIES OF $AlCl_3$/MEICl/NaCl MELTS

Specific conductivities of acidic melts, melts containing less-than-saturation amounts of NaCl, and melts that were saturated with NaCl were obtained. A YSI Model 31A Conductivity Bridge and a cell containing platinum-black electrodes was used for all measurements. A 0.52 melt was measured, and conductivity measurements were continued in steps as a fraction of saturation. No appreciable difference in conductivity was noted among the melt which contained no NaCl, any which were partially saturated, and that which was totally saturated.

IX. RECOMMENDATIONS

A. It is clear that a very useful way has been discovered to prepare $AlCl_3$/MEICl melts which are neutral in the Lewis sense. It should be further determined whether this function can be extended to other molten salt-alkyl halide systems, e.g. $AlCl_3$/butylpyridinium chloride.

B. The addition of sodium chloride to $AlCl_3$/MEICl melts to produce neutral melts opens an electrochemical window that is larger than 4 V. Cathode materials other than sodium should be investigated to see where they will function in this potential range.

C. A corrosion study of the sodium electrode was done. Further work is needed to determine the nature of the passivating layer on the electrode surface.

D. Sodium metal reacts extensively with acidic melts, but does not appear to react with neutral or basic melts. The sodium electrode in a Na/Na^+ couple has been examined in neutral melts. Additional work to elucidate the behavior in basic melts is recommended.

REFERENCES

1. Wilkes, J.S., Levisky, J.A., Wilson, R.A., and Hussey, C. L., "Dialkylimidazolium Chloroaluminate Melts: A New Class of Room Temperature Ionic Liquids for Electrochemistry, Spectroscopy, and Synthesis," Inorg. Chem., 21, 1263 (1982).

2. Floreani, D.A., Stech, D.J., Wilkes, J.S. Williams, J.L., Piersma, B.J., King, L.A., and Vaughn, R.L. "A New Class of Room Temperature Molten Salts for Battery Applications", Proc. 30th Power Sources Symp., The Electrochemical Society, Princeton, N.J., p. 84, June 1982.

3. Fannin, A.A., Floreani, D.A., King, L.A., Landers, J.S., Piersma, B.J., Stech, P.J., Vaugh, R.L., Wilkes, J.S., and Williams, J.L., "Properties of 1,3-Dialkylimidazolium Chloride - Aluminum Chloride Ionic Liquids." J. Phys. Chem., 88, 2614, (1984).

4. Fannin, A.A., King, L.A., Seegmiller, D.W., Øye, H.A., "Densities and Phase Equilibria of Aluminum Chloride - Sodium Chloride Melts." J. Chem. Eng. Data, 27, 114, (1982) and references therein.

5. Carpio, R.A., King, L.A., Kibler, F.C., and Fannin, A.A. "Conductivities of $AlCl_3$ - LiCl Mixtures" J. Electrochem. Soc., 126, 1650, (1979).

6. Carpio, R.A., Kibler, F.C., King, L.A., Brokner, K.T., Øye, H.A., "Density, Viscosity, and Electrical Conductivity of Acidic $AlCl_3$ - LiCl - NaCl Melts" Ber. Bunsenges. Phys. Chem., 85, 31, (1981).

7. Piersma, B.J., Wilkes, J.S., "Electrochemical Survey of Selected Cations and Electrode Materials in Dialylimidazolium Chloroaluminate Melts" Technical Report, Frank J. Seiler Research Laboratory, Project 2303, Air Force Systems Command, U.S. Air Force, September1982.

8. Lipsztajn, M. and Osteryoung, R.A. "Electrochemistry in Neutral Ambient-Temperature Ionic Liquids" Inorg. Chem., 24, 716 (1985).

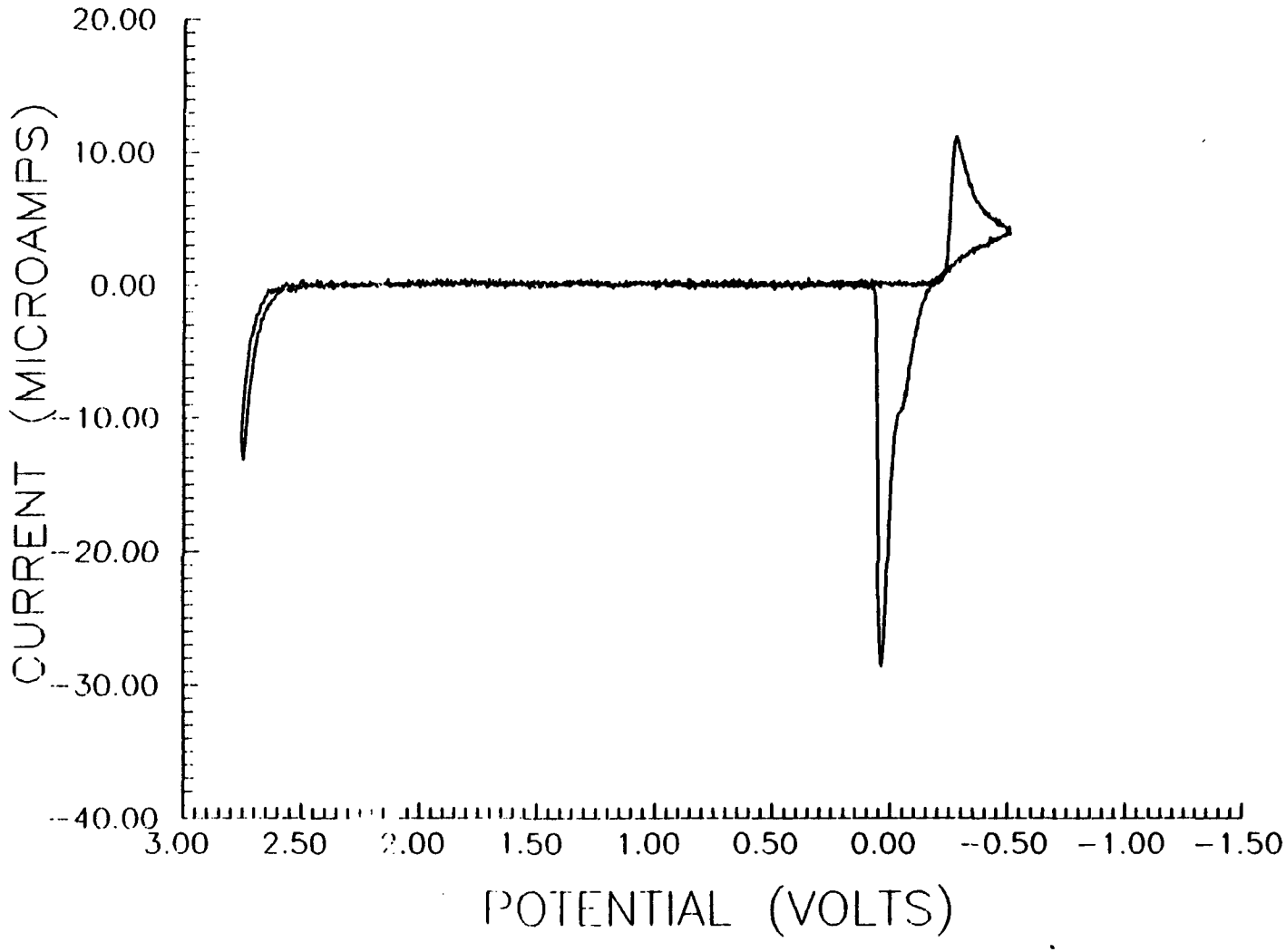

Figure 1. Cyclic voltammogram of a N=0.52 $AlCl_3$/MEICl melt.

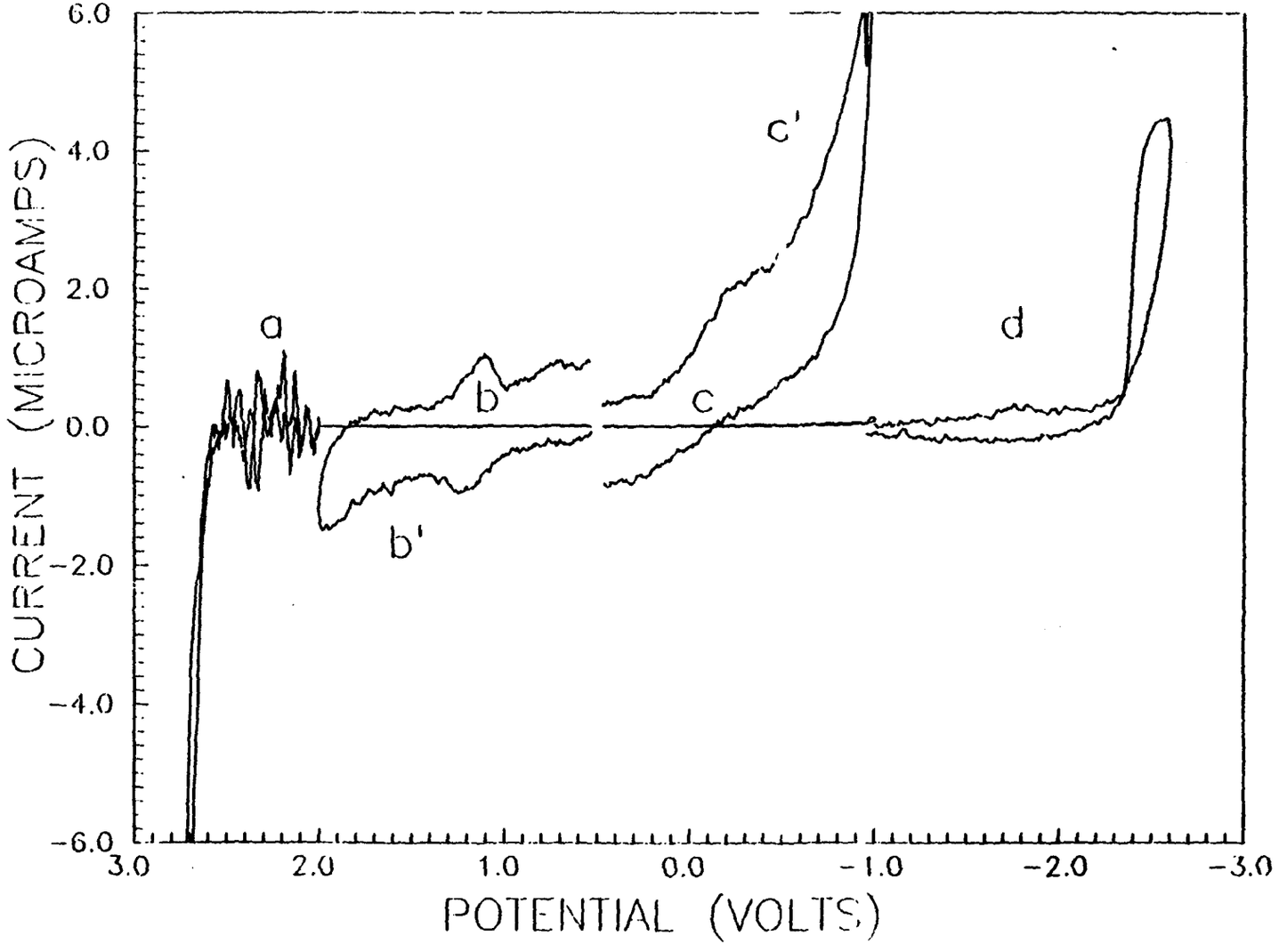

Figure 2. Cyclic voltammogram of a N=0.52 melt that has been neutralized with sodium chloride. The sections b' and c' are 100 times the intensity of sections b and c, respectively.

1988 USAF-UES SUMMER FACULTY RESEARCH PROGRAM

Sponsored by the

AIR FORCE OFFICE OF SCIENTIFIC RESEARCH

Conducted by the

Universal Energy Systems, Inc.

FINAL REPORT

AB INITIO AND CHEMICAL DYNAMICS STUDY OF ENERGETIC MATERIALS

Prepared by: Patricia L. Moore Plummer

Academic Rank: Professor

Department and Chemistry and Physics/Astronomy

University: University of Missouri-Columbia
Columbia, MO 65211

Research Location: F. J. Seiler Research Laboratory
Chemistry Division
U. S. Air Force Academy
Colorado Springs, CO

USAF Researcher: Major K. (Skip) Dieter

Date: August 28, 1988

Contract No: F49620-87-R-0004

AB INITIO AND CHEMICAL DYNAMICS STUDY OF ENERGETIC MATERIALS

by

Patricia L. Moore Plummer

ABSTRACT

Theoretical modeling of energetic materials was undertaken using the methods of ab initio quantum mechanics and molecular or chemical dynamics. This study continued the ab initio calculations of 1-nitro-propene reactions already underway at Seiler Laboratory. Both extended basis set calculations and post Hartree-Fock calculations were carried for NO_2 , HONO, OH, C_3H_5, 1-nitro-propene, 1-nitroso-propene,and related compounds. Of principal interest were reactions which involved the migration of a hydrogen from the CH_3 group to the NO_2group. Reaction energies were determined for the various levels of theory, in part to determine what level of calculations are needed for predicting experimental results.

In addition to the ab initio calculations, chemical dynamics codes were installed. Calculations were carried out on ethylene, both to test the code and to gain information on the importance of the double bond on energy transfer processes within a molecule. Preliminary work on the development of a force field for nitro-ethylene and 1-nitro-propene was initiated.

ACKNOWLEDGEMENTS

I wish to acknowledge the sponsorship of the Air Force Systems Command and the Air Force Office of Scientific Research for the Summer Faculty Research Program. I want to thank the Frank J. Seiler Research Laboratory , Chemistry Division for their hospitality during the period of this research. I want to acknowledge Dr. James J. Stewart for many interesting discussions and especially for his help in dealing with computer project numbers, obtaining information about the VAX cluster of computers and other miscellanous details required to get started in a different computing environment. Mr. Charles Bowles and Sgt. Angie Berry of the Computer Center were also very helpful. Col. Steve Lander, Director of NC, was at all times enthusiastically supportive. Major Skip Dieter,focal point officer, was equally supportive and maintained a keen interest in the research.

I. INTRODUCTION:

Understanding the detailed characteristics of energetic materials is of considerable importance to the Air Force. Such materials find applications as explosives and propellants. The properties of interest may be exhibited in only one phase , e.g. solid, or may exist in all phases but perhaps with different intensities. In support of the experimental research in thermochemical decomposition of selected energetic materials, there is a need for the development of theoretical chemical models for these materials. If the mechanism for energy transfer processes can be realistically described and the kinetics of the decomposition determined for the different phases in known, well-characterized energetic systems, new, higher energy compounds can perhaps be prepared. Such syntheses are becoming commonplace for biologically active compounds where theoretical studies have successfully predicted their desired properties.

The Chemistry Division of the Frank J. Seiler Research Laboratory is particularly concerned with reactions and properties of two nitrogen containing compounds which have shown substantial energetic properties, TNT (2,4,6 trinitrotoulene) and HMX $(CH_2NNO_2)_4$/RDX $(CH_2NNO_2)_3$. Experimental results of Shackelford and co-workers[1] have shown that for TNT, the kinetics are altered by the phase of the material. Quantum mechanical calculations at the semi-empirical level of MOPAC are unable to successfully predict the heats of reaction for all of the processes of potential importance for these compounds. Preliminary ab initio calculations indicate that large basis sets or post Hartree-Fock/multiple configurations (or both) are needed to obtain a realistic

description of the decomposition processes.

Since the quantum mechanical results primarily provide information about single molecules at 0 K, other techniques are needed to model the decomposition as a function of energy input and time. The method of molecular or chemical dynamics has the potential to follow the process from the introduction of energy to the decomposition and thus utilize and complement the information provided by the quantum mechanical results.

My research for over a decade has involved using the techniques of quantum mechanics, both semi-empirical and ab initio, and molecular dynamics to model and gain information about a variety of different systems. Specifically I have studied nucleation processes (since 1970), cluster formation and growth and defect production and migration in solids (since 1980). Thus my experience with theoretical modeling and with the techniques of quantum mechanical and molecular dynamics calculations contributed to my assignment to the Theoretical Chemical Group of the F. J. Seiler Research Laboratory.

II. OBJECTIVES OF THE RESEARCH EFFORT:

Prior to my appointment as a Summer Faculty Research Fellow, the primary theoretical studies on energetic materials had used semi-empirical quantum mechanical calculations to model the products and reactants for processes of interest. The results of these studies showed that more exact quantum mechanical calculations are required to adequately describe the potential surface (and hence the energy pathways) for the decomposition of NO and NO_2-containing compounds. Also there was a need to follow the time-evolution of the reaction process to be able to model the dynamic as well as the energetic progress of the decomposition.

Since there had not been any dynamic modelling of energetic materials at Seiler, a primary research objective during my tenure as a Summer Faculty Fellow was to add molecular dynamics to the computational techniques available to model the compounds and processes of interest. A secondary objective was to continue the ab initio studies of reactants and products of 1-nitropropene begun by Capt. Jon Swanson. With regard to the ab initio calculations, the questions of relative importance of size of basis sets and use of different post Hartree-Fock procedures were of considerable interest.

The ultimate goal of the research is to better understand and model, and eventually design, energetic materials with specified thermochemical properties. Specific objectives for the summer were 1) to acquire, implement, and test a computer code for chemical dynamics, 2) develop input for ethlene and nitroethene, as prototype molecules, and 3) develop graphical output for data display and analysis.

III. a) Molecular Dynamics Calculations

To meet the objective of acquiring the capability of conducting chemical dynamics studies on energetic materials, it was decided that the initial approach would be to examine energy transfer processes within a single molecule. Computer code for following the internal energy of a molecule as a function of time has been developed by Dr. Donald Thompson and used extensively to study benzene and HONO. This approach appeared to provide a good starting point for the dynamic modeling of energetic materials. Thus the first week of the research appointment was spent at Oklahoma State University with Professor Thompson's group. Here the basic structure of the molecular dynamics program was learned, including the specific format for input data.

Upon arrival at Seiler, the dynamics code was installed on the VAX cluster. Copies were also sent to the Gould and 'down-loaded' to the IBM-PC/Maxim-Quantum computer. The code was revised to conform to fortran77 standard and several internal inconsistencies removed. Code was added to produce output files which would subsequently permit graphical displays of the results. A literature search was made to obtain experimental data which could be used to construct and/or test potential/force fields for ethylene and nitroethylene.

The dynamics code was sucessfully compiled and executed on the VAX cluster. Compilation was not attempted on the Gould because of the instability of the hardware during the research period. Part of the code was succesfully compiled on the Maxim Quantum Board but the excessive disk requirements for the unix-compiler would have

required either reduction of the size of the 5-dimensional arrays in the subroutine DERIV or reconfiguring the disk and scratch-file space. It was decided to postpone either of these alternatives until it was determined that execution on the PC was preferable to VAX executation.

Ethylene was used both as a test molecule for the dynamics code and to examine the effect of the double bond on energy flow in the molecule. For these preliminary studies the energy flow as a function of time was followed by assuming the internal energy of the molecule could be partitioned into normal modes. The force field for ethylene was determined by describing the molecule in terms of internal coordinates and fitting the vibrational frequencies for the equillibrium structure to the experimental frequencies of Duncan et al[2]. The internal coodinates and force constants used are shown in Table 1. The bond stretches were modelled as Morse functions:

$$V_{ij}(r) = D_e\{1 - \exp[-\beta_{ij}(r_{ij} - r^o_{ij})]\}^2.$$

Bond angle bends were described in terms of harmonic potentials as were 'wag' angles:

$$V_{ijk} = k_{ijk}(\emptyset - \emptyset^o)^2.$$

Dihedral angle torsional potentials were modelled using a cosine expansion of the form[3]:

$$V_{ijkl} = 1/2 \sum_t a_t[1-\cos(n\,\partial)] \qquad t = 0,...5.$$

The calculations on ethylene involved exciting one of the CH stretches, the rest of the molecule having its equilibrium zero point energy. The flow of energy from the initially excited internal stretch was then monitored as a function of time. Levels of initial excitation from v=3 to v=8 were examined. In all cases the transfer of energy from the excited CH bond was essentially complete within 2.5 psec ($1psec=10^{-12}sec$).

This is shown in Figure 1 for initial excitation to v=5 for an ensemble of 20 trajectories. After about 3 psec all the CH bonds are seen to have approximately the same energy. The time required for the energy equillibration of the CH bonds in ethylene was nearly four times longer than in benzene[4].

To better understand the flow of energy in the molecule, plots of the energy vs time for each of the normal modes of ethylene were made for the same series of trajectories. Theses results are shown in Figures 2 - 5. The numbering of the normal modes corresponds to the atom displacements shown in Figure 6. The frequencies calculated with the force constants given in Table 1 for these normal modes are listed in Table 2.

To obtain reasonable statistics for analysis, ensembles of different sizes were examined. For the process described above ensembles of 1, 5, 10, 20 and 30 trajectories were run for times of 5, 10, 20, 25, and 30 psec. Substantial differences were seen (greater amplitude oscillations) between ensembles containing 1, 5 or 10 trajectories. No significant differences were found between ensembles containing 10, 20 or 30 trajectories. It was decided that ensembles of 20 trajectories were a good compromise between good statistics and computer time requirements.

In addition to the initial excitation of an internal coordinate such as the CH bond, the capability exists for the excitation of one or more normal modes of the molecule. [The excitation of a normal mode can be instead of or in addition to the excitation of an internal coordinate such as the CH stretch.] It is of interest to determine 1) whether excitation of a normal mode changes the decay time of an internal coordinate, 2) whether the re-distribution of the energy can be altered by the excitation of a specific normal mode and 3) whether selective excitation of one or more normal modes can produce localization of energy in, for example, a decay or decomposition channel. I will propose

to investigate these questions in detail in the research I hope to continue with the support of a Mini-grant.

III. b) ab initio Quantum Mechanical Studies

The goal of the ab initio calculations was to determine the equilibrium geometry and stability of the reactants and products for the reactions shown in Table 3. To determine the size of basis and level of theory required, the calculations were to be carried out for three split-valence basis sets[5], 3-21G*, 3-21G**, 6-31G*. Having determined the most stable structure of each of the compounds with each basis set, post Hartree-Fock calculations were planned.

The geometry optimization calculations were carried out using the GAUSSIAN86 code[6]. Initially it was planned to carry out three types of post Hartree-Fock calculations[7], MP2 and MP4 (second and fourth order Møller-Plesset perturbation theory), and MCSCF (multiple configuration self-consistent field) The MP calculations used the GAUSSIAN program while the MCSCF calculations would use the GAMESS code[8].

During my tenure at Seiler, I was able to complete the geometry optimization and obtain minimum energy structures at the 6-31G** level for all reactants and products except for the nitrosopropyl radical and the protonated nitropropene. MP2 calculations were completed at the 3-21G* and 3-21G** levels. MP4 single point calculations with single, double, triple and quadruple excitations (SDTQ) were completed at the 3-21G** level for NO_2, OH, NO_2H, the propyl radical and the nitrosopropyl radical. Calculations at the MP4(SDTQ) for the remaining compounds were in progress and had accumulated 16, 18 and 19 CPU Days when the Vax cluster suffered a power failure and went down on

28 July.

Because of the extreme length of the calculations, no MP4 calulations at the 6-31G* level were attempted. It was decided that the MCSCF calculations should follow the MP4 calculations since they would require at least as much computer time for a given basis set.

It is hoped that these calculations can be completed under the support of a Mini-grant and a grant of supercomputer time on a machine such as the CRAY2 computer at Kirkland Air Force Base.

IV. RECOMMENDATIONS:

a. Chemical dynamics modelling of energetic materials has great potential to increase the understanding of the initiation of the decomposition process. The simulations of the energy flow in these materials provide information about the mechanism for decomposition as a function of such variables as temperature and phase. Such studies can also aid in the design of new energetic materials. With the chemical dynamics code implemented on the VAX cluster, researchers at Seiler can begin to examine the temporal evolution of simple energetic materials. These simulations provide additional and complementary data to that obtained from semi-empirical and ab initio quantum mechanical calculations.

The chemical dynamics calculations require considerably less computer time for a trajectory than an ab initio calcuation for the same molecule. Ensemble averages can be built up from a series of single trajectory runs. In addition the code for the chemical dynamics is much smaller (6000 compared to 200,000 card images) than quantum

mechanical computer codes. Thus the chemical dynamics simulations can be executed on a PC provided with a large hard disk and a math co-processor.

b. Large ab initio calculations (either in terms of number of atoms or in size of basis set) should not be attempted on the Vax computers. Even if the problem of frequent system crashes caused by power failures is reduced by the use of constant power supplies, jobs which require 10's of CPU days should not be regularly attempted. For large molecular systems semi-empirical quantum mechanical calculations and chemical dynamics are much better suited to the computing environment at Seiler. Molecules up to 6 atoms can probably be successfully studied with reasonably sized basis sets using either GAUSSIAN86 or GAMESS. Larger systems require at least a large mainframe or a supercomputer for a complete ab initio investigation.

REFERENCES

1. S. A. Shackelford, J. de Physique, 48, C4-193 (1987) and references therein.

2. J.L. Duncan, D. C. McKean and P. D. Mallinson, J. Mol. Spectrosc., 45, 221 (1973).

3. B. G. Sumpter and D. L. Thompson, J. Chem. Phys., 86, 2805 (1987).

4. K. L. Bintz, D. L. Thompson, and J. W. Brady, J. Chem. Phys., 85, 1848 (1986)

5. W. J. Pientо, M. M. Frank, W. J. Hehre, D. F. DeFrees, J. A. Pople, and J. S. Binkley, J. Am. Chem. Soc., 104, 3039 (1982).

6. GAUSSIAN86, version of GAUSSIAN programs by J. S. Binkley, R. A. Whiteside, R. Krishnan, R. Seeger, D. J. Defrees, S. Topiol, L. R. Kahn, and J. A. Pople, QCPE, 13,406 (1981).

7.W. J. Hehre, L. Radom, P. v. R. Schleyer and J. A. Pople, Ab Initio Molecular Orbital Theory, J. Wiley, New York (1986).

8. GAMESS,version by M. W. Schmidt, J. A. Boatz, K. K. Baldridge, S. Koseki, M. S. Gordon, S. T. Elbert, and B. Lam, QCPE Bull., 7,115 (1987).

TABLE 1
VALUE OF THE PARAMETERS FOR THE POTENTIAL

Coordinate	Parameters		
	Morse Potential		
Bond	r_e(Å)	ß(a.u.$^{-1}$)	D_e(eV)
C - H	1.071	1.777	5.046
C = C	1.353	1.905	6.452
Angle	$Ø_e$(deg)	k(mdyn Å/rad^2)	
H-C=C	119.98	0.7555	
H-C-H	120.4	0.2725	
Motion	Equil. value	force constant	
CH_2 wag	0.0	0.1110	
HCCH torsion	0.0		
HCCH torsion	180.0		

TABLE 2
NORMAL MODE VIBRATIONAL FREQUENCIES

	Frequency (cm^{-1})	
Symmetry	Calculated	Experimental
A_u	827	826
B_{1u}	856	943
B_{2g}	995	949
B_{2u}	1060	1073
A_g	1177	1220
B_{1g}	1345	1342
B_{3u}	1439	1444
A_g	1636	1630
B_{3u}	3002	3021
A_g	3023	3026
B_{2u}	3106	3103
B_{1g}	3123	3105

TABLE 3
Summary of Nitropropene Reactions

$CH_3CH{=}CH\text{-}NO_2$ ---> $CH_3CH{=}CH\cdot + NO_2$

$CH_3CH{=}CH\text{-}NO_2H$ ---> $CH_3CH{=}CH\cdot + NO_2H$

$CH_3CH{=}CH\text{-}NO_2H$ ---> $CH_3CH{=}CH\text{-}NO + OH$

$CH_2CH{=}CH\text{-}NO_2H$ ---> $CH_2CH{=}CH\cdot + NO_2H$

$CH_2CH{=}CH\text{-}NO_2H$ ---> $CH_2CH{=}CH\text{-}NO + OH$

$CH_3CH{=}CH\text{-}NO_2$ ---> $CH_2CH{=}CH\text{-}NO_2H$

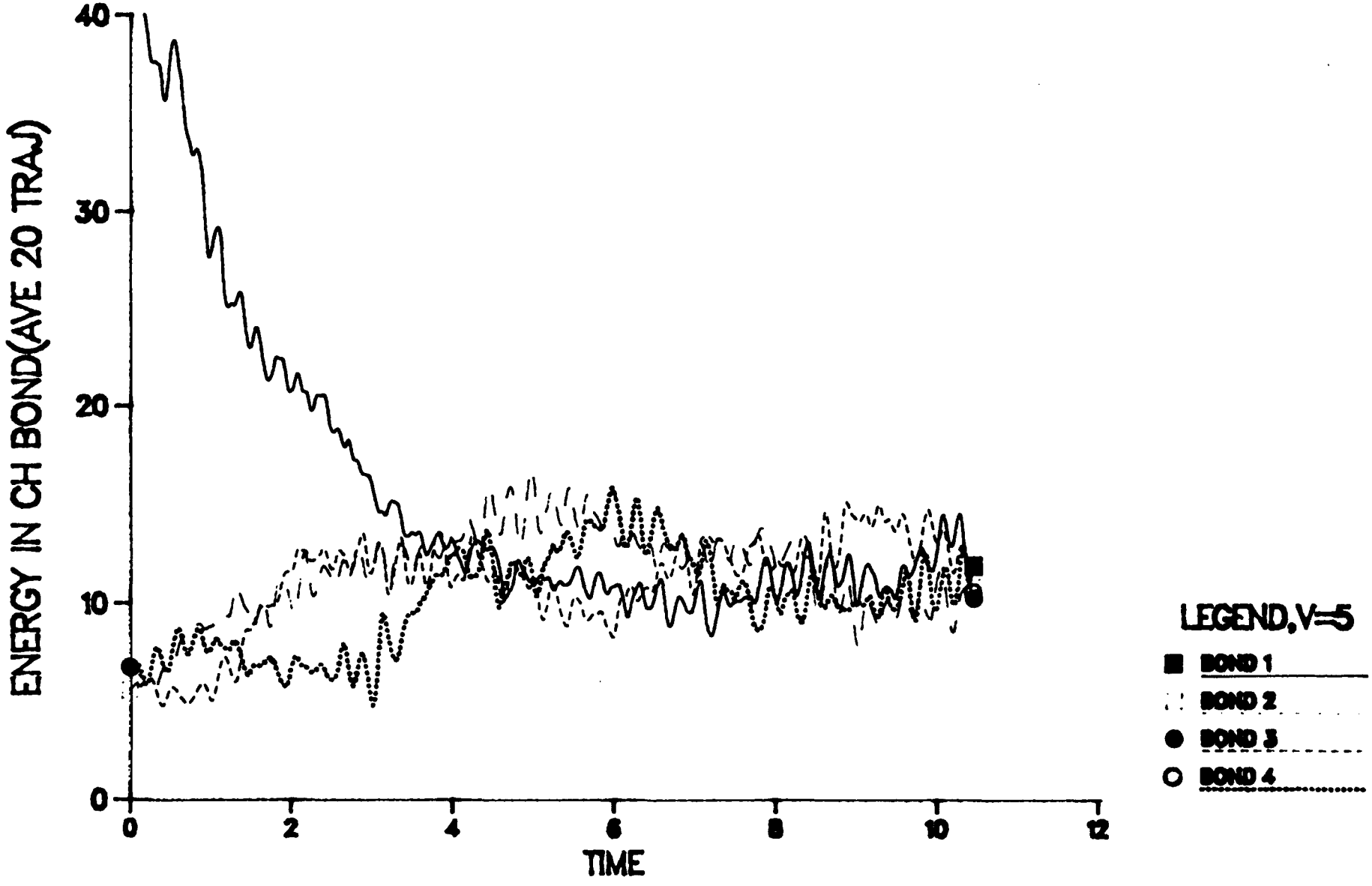
ENERGY IN CH BOND(AVE 20 TRAJ)
40
30
20
10
0
0
2
4
6
8
10
12
TIME
LEGEND,V=5
BOND 1
BOND 2
BOND 3
BOND 4

FIGURE 1

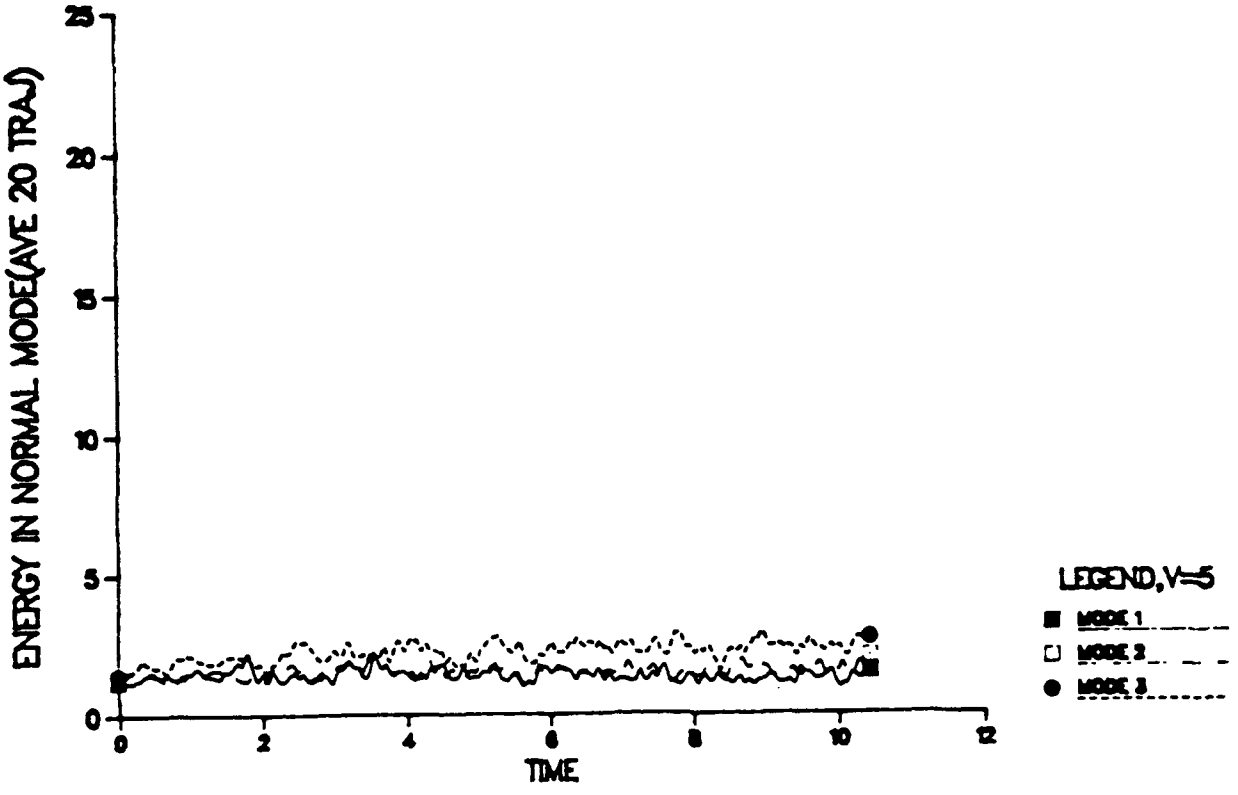

FIGURE 2

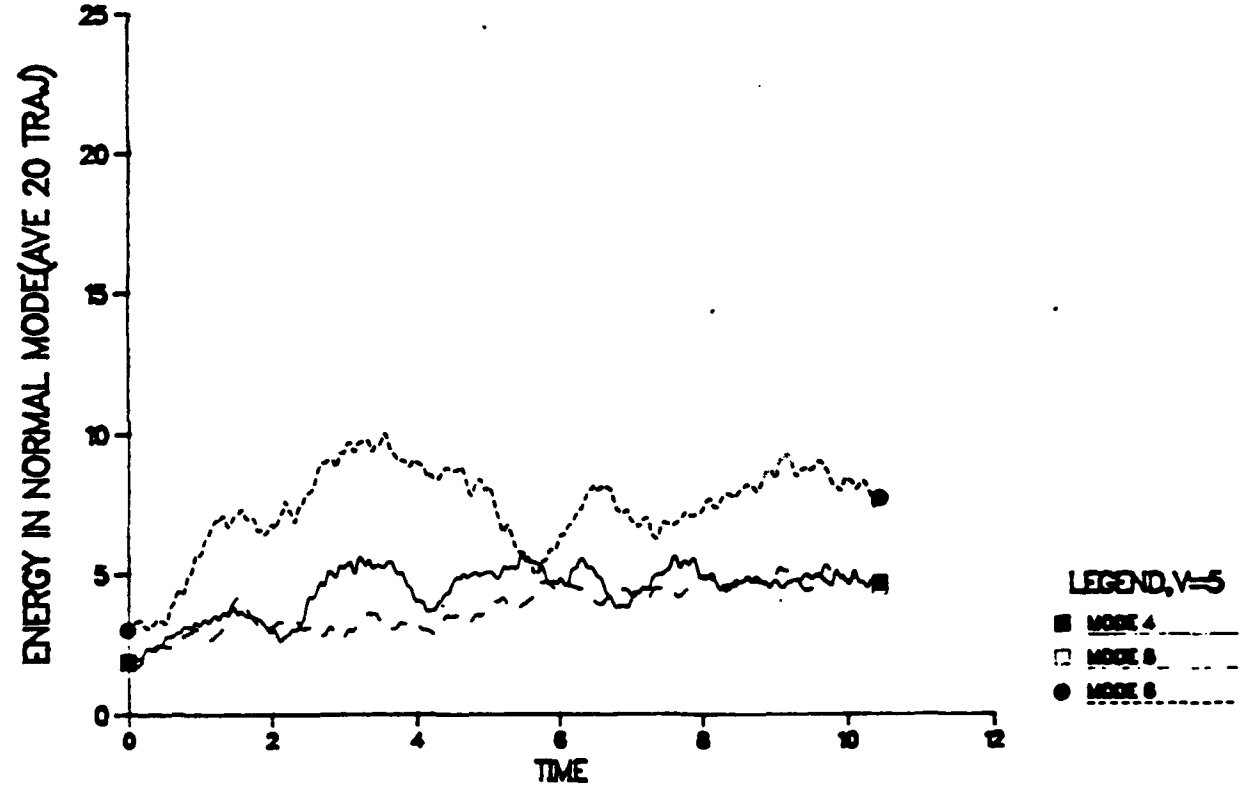

FIGURE 3

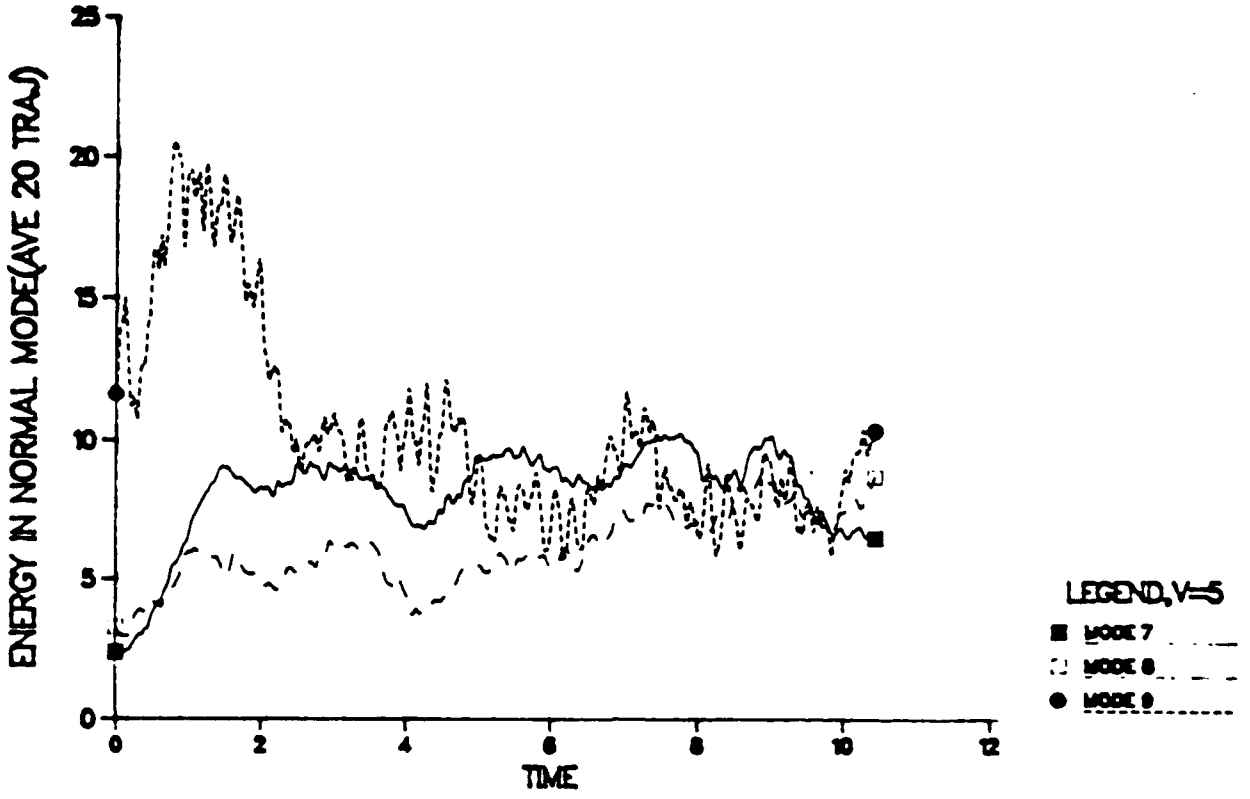

FIGURE 4

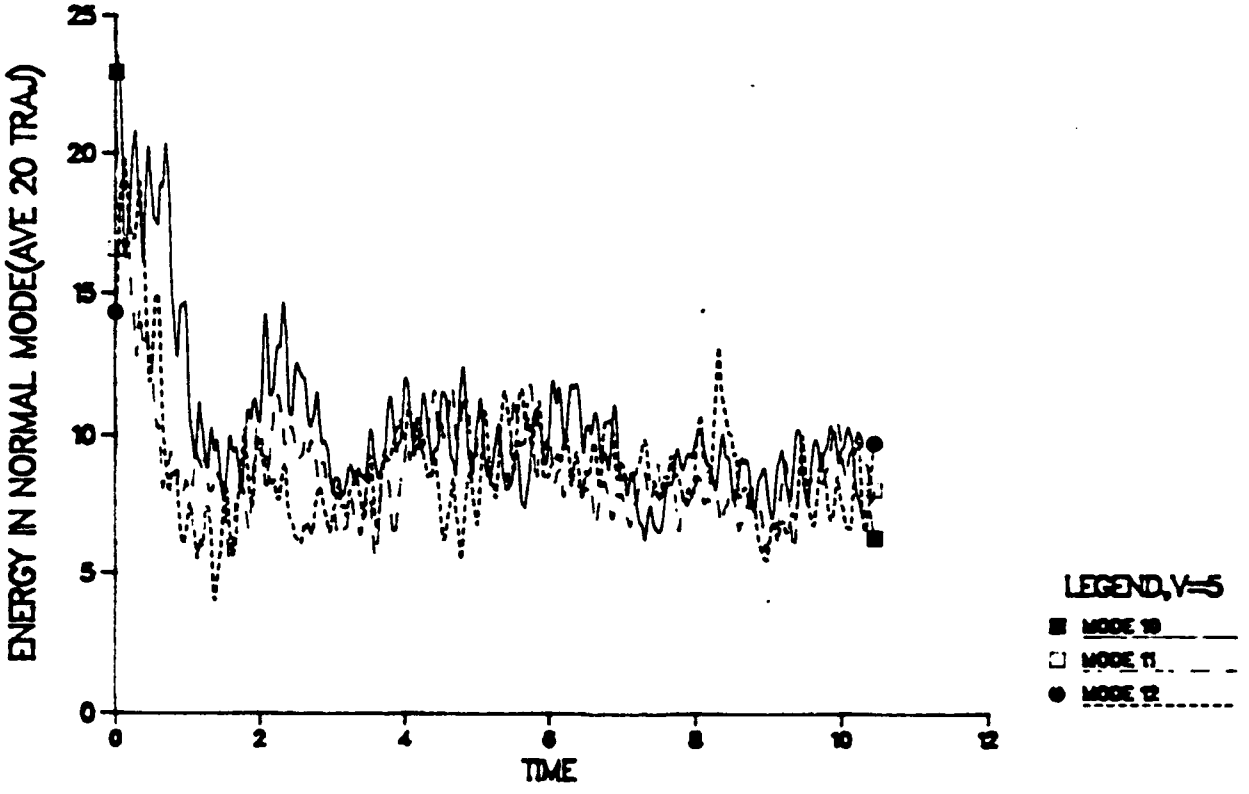

FIGURE 5

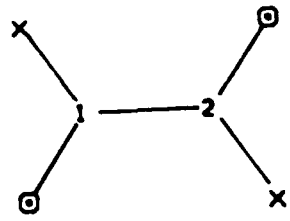

ν=1

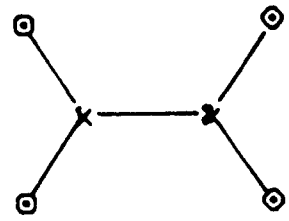

ν=2

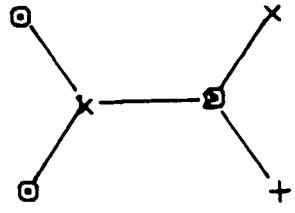

ν=3

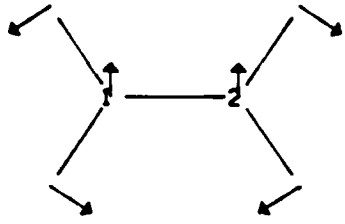

ν=4

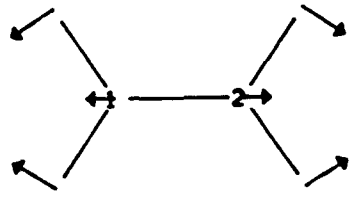

ν=5

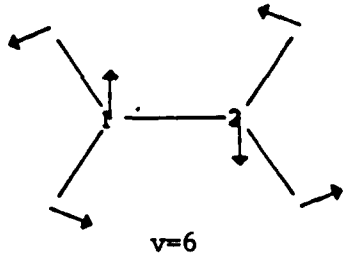

ν=6

FIGURE 6 NORMAL VIBRATIONS OF ETHYLENE

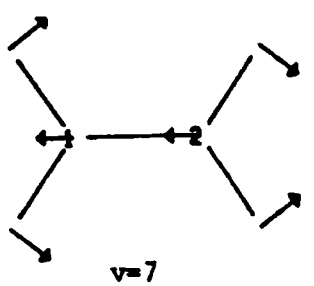

ν=7

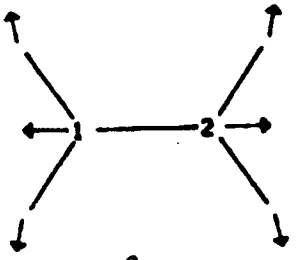

ν=8

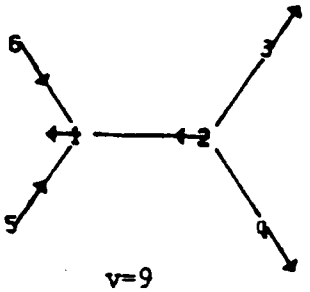

ν=9

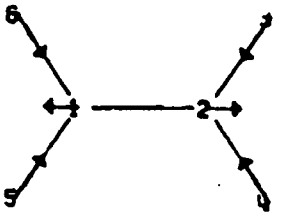

ν=10

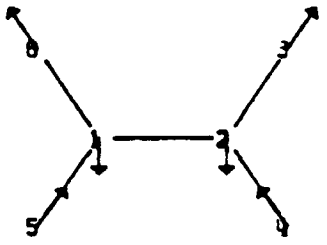

ν=11

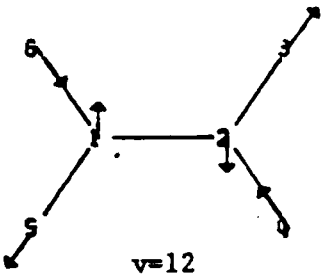

ν=12

FIG. 6 (cont) NORMAL VIBRATIONS OF ETHYLENE

1988 USAF-UES SUMMER FACULTY RESEARCH PROGRAM

GRADUATE STUDENT RESEARCH PROGRAM

Sponsored by the

AIR FORCE OFFICE OF SCIENTIFIC RESEARCH

Conducted by the

UNIVERSAL ENERGY SYSTEMS, INC.

FINAL REPORT

SEPARATORS FOR MOLTEN SALT BATTERIES

Prepared by:	James L. Schmutz, Ph.D.
Academic Rank:	Professor
Department and University:	Chemistry Department Central Wesleyan College
Research Location:	FJSRL/NC USAF Academy Colorado Springs, CO 80840
USAF Researcher:	John Wilkes, Ph.D.
Date:	27 July 88
Contract No:	F49620-87-R-0004

SEPARATORS FOR MOLTEN SALT BATTERIES

by

James L. Schmutz

ABSTRACT

Various polymeric films were made, and along with some commercially supplied membranes, were tested as possible separators for batteries with the room temperature molten salt electrolyte system: 1-methyl-3-ethylimidazolium chloride/aluminum chloride (the melt). The polymers tested were poly(1,1-dimethyl-3,5-dimethylenepiperidinium chloride) (PDDPCl); undoped and $ZnCl_2$ doped polyethylene oxide (PEO); polyphosphazenes with mixed fluorinated alkoxy side groups (FPN, supplied as Eypel-F gum by Ethyl Corp.) and polyphosphazenes with primarily trifluoroethoxy side groups (TFE). Chloride selective membranes supplied by Toyo Soda Co (Tosoh USA, Inc.) were also tested. Only the polyphosphazenes are suggested for further study.

Acknowledgements

I wish to thank the Air Force Systems Command, the Air Force Office of Scientific Research, the Frank J. Seiler Research Laboratory and Universal Energy Systems for their support of this research.

Many individuals helped make this summer an enjoyable and meaningful time. The other summer fellows and the permanent staff were all very congenial and helpful. I would especially like to thank Dr. John S. Wilkes and Dr. Chet Dymek for project guidance and Mr. Greg Godec for practical help in "learning the ropes" of molten salt research.

I. INTRODUCTION

Separators (membranes) serve two possible functions in batteries. The first is to separate reactants from one another and thus prevent their direct reaction. If direct reaction occurs the usable electrical energy is reduced or lost altogether. The second function of a separator is to act as a selective membrane allowing only the desired ions to carry the charge. Most separators are polymers.

In its work with batteries, (see for example Dymek, 1987) the Frank J. Seiler Research Laboratory at the USAF Academy is interested in separators which meet these two functions. Specifically, the batteries of interest have room temperature molten salt electrolytes (Wilkes, 1984) of 1-methyl-3-ethylimidazolium chloride/aluminum chloride mixtures (melts). Thus the separator must, first of all, be compatible with the melt. Secondly, the separators will be chloride selective membranes. If separators can be found in which chloride can be induced to be the charge carrier, an energy density advantage should result.

My area of research for the Ph.D. was phosphazene polymer chemistry. This background in polymer chemistry contributed to my assignment in the area of membranes for batteries at the Frank J. Seiler Research Laboratory.

II. OBJECTIVE OF THE EFFORT:

The objectives of this effort were to work on two broad areas. (1) The development and/or testing of anion selective separators (membranes) to encourage an anion to carry the charge in the melt rather than the imidazolium ion. (2) The development of a chlorine, oxygen and/or bromine electrode compatible with the melt. Due to the limited time and the way the work on separators developed, the second goal was dropped.

III. Poly(1,1-dimethyl-3,5-dimethylenepiperidinium chloride), PDDPCl

PDDPCl membranes showed the following characteristics which made them unsuitable for separators in the melt. Dried samples showed high electrical resistance and were very brittle, always cracking during mounting or dismounting in the cell. Partially dried PDDPCI membranes were not brittle but leathery. They also showed lower resistances. However, the presence of water in the membrane was sufficient to cause the melt to react with and eat its way slowly through the membrane.

IV. DOPED AND UNDOPED POLYETHYLENE OXIDE, PEO

Polyethylene oxide, PEO, doped with various metal chlorides (e.g., Farrington, et.al., 1986) has been shown to be a good electrolyte in aqueous systems. Thus we decided to try this polymer in the melt. Zinc chloride was chosen for our dopant because it has good conductivity and in the aqueous system chloride carries much of the charge. PEO and 24:1 PEO:$ZnCl_2$ membranes were synthesized. The PEO Film was mounted in a resistance cell and immediately developed a leak. The PEO:$ZnCl_2$ (24:1) membrane (120 microns thick) gave an initial resistance at 2450 ohms across a 6 mm diameter sample in 0.40 melt (40 mole % $AlCl_3$ and 60 mole % MEICl). The resistance rapidly dropped (10 min.) to about 400 ohms. Upon inspection, the membrane had disintegrated. After this, both PEO and PEO/$ZnCl_2$ membranes were put directly in melt and dissolved almost immediately upon agitation.

V. Polyphosphazenes, FPN and TFE

The most promising membranes proved to be polyphosphazenes. Several modifications of the polymer tested should prove to hold even greater promise. These are outlined in Section VIII on follow up recommendations.

This work was done on two types of phosphazenes. One was Eypel-F gum supplied by Ethyl Corporation. This polymer (FPN) is a phosphazene with a mixture of fluorinated alkoxide side groups. The other phosphazene (TFE) was made from FPN by reacting it with about a 15 fold excess of $NaOCH_2CF_3$ in THF. Thus, this polymer was primarily $[PN(OCH_2CF_3)_2]_n$.

TABLE
RESISTANCE OF THE TFE MEMBRANES
poly[bis(trifluoroethoxy)phosphazene]

22 MICRONS THICK		16 MICRONS THICK	
time(min)	resistance(ohms)	time(min)	resistance(ohms)
0	450,000	0	6600
3	340,000	1	4400
6	230,000	2	3800
12	90,000	3	2800
23	23,000	4	2400
128	6600	6	2100
154	6400	10	2000
228	4500	20	1900
267	4000	40	1800
1168	3850		

A test of FPN/0.33 melt compatibility showed the polymer was stable in the melt. When FPN was cast into films, they were jelly like and tore easily. Thus TFE, known to have good film strength, was synthesized as above and cast into two films of 22 and 16 microns thickness. The resistance of these films is given in the table. Values are for a 6 mm disk in 0.33 melt. These results are also shown in graphic form on the following two pages. As can be seen

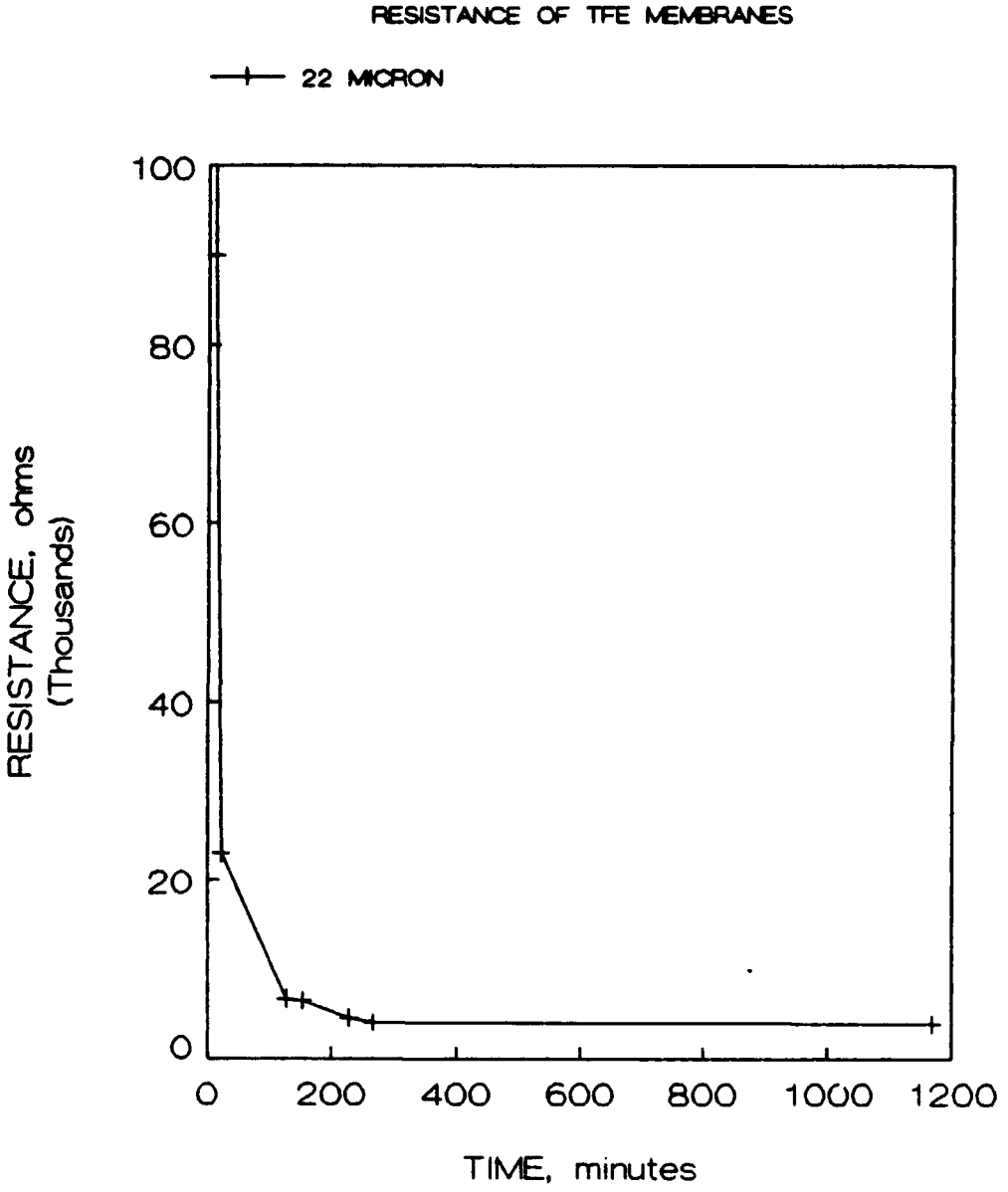
RESISTANCE OF TFE MEMBRANES
22 MICRON
RESISTANCE, ohms
(Thousands)
100
80
60
40
20
0
0
200
400
600
800
1000
1200
TIME, minutes

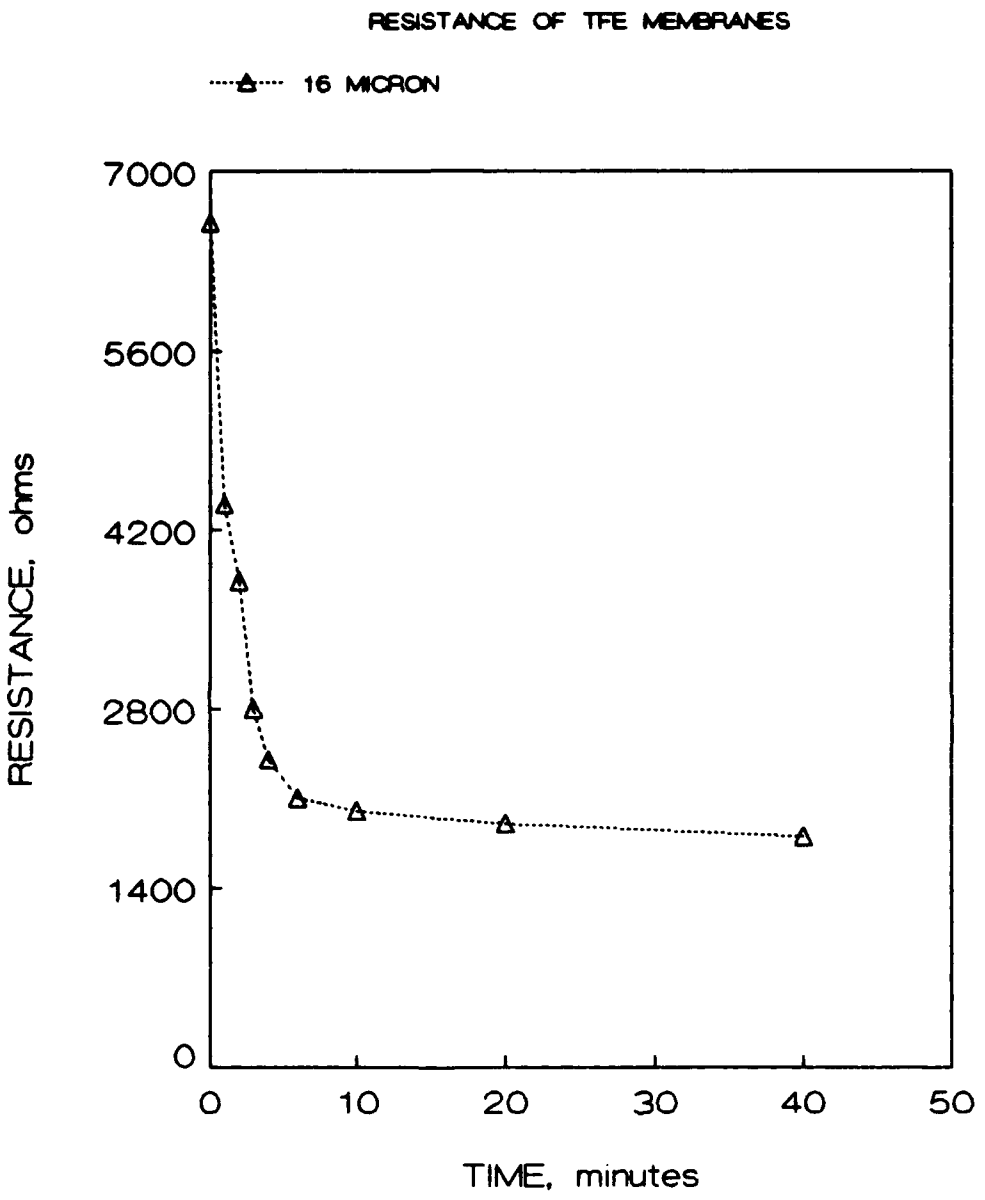
RESISTANCE OF TFE MEMBRANES
16 MICRON
7000
5600
4200
2800
1400
0
RESISTANCE, ohms
0
10
20
30
40
50
TIME, minutes

from the tables, both films resistances dropped with time. This is most likely due to melt impregnating the polymer matrix thus transforming the nonconducting polymer into an electrolyte. Further evidence for this interpretation is that the 16 micron film was clear rather than its normal opaque white when it was removed from the cell at the end of the test. This is consistent with the fact that phosphazene polymer chains are known to be very mobile in comparison to organic polymers thus allowing smaller molecules to work their way into the matrix (Allcock, 1972). Therefore, modification of the polymer to incorporate an electrolyte, as suggested in section VII, should give even better conductance.

VI. Toyo Soda Membranes

Three proprietary membranes supplied by Toyo Soda, Co. (Tosoh USA, Inc.) were tested for resistance. These were SF-34, DF-34 and SA-48. Some initial apparently low resistances with SF-34 were later found to be due to a faulty cell which did not make complete seals to the membrane. A redesigned cell showed very high resistances (all well in excess of 100,000 ohms) with all three membranes including rigorously dried samples and samples of SF-34 soaked in benzene, acetonitrile and 0.33F melt. Thus these studies were discontinued.

VII. RECOMMENDATIONS:

It is apparent from this work that, of those membranes tested, the TFE (polyphosphazene) offers the best potential for use as a separator in molten salt batteries. Yet, some other phosphazenes would be expected to perform even better. These phosphazenes could be classified into two groups. They could be either (1) phosphazenes containing a single side group or (2) a mixture of two side groups. In both cases, the side groups would be chosen for some property which would be expected to increase their usefulness as molten salt battery separators. One would expect the following phosphazenes to offer enhanced conductivity and/or chloride ion selectivity. Each of these polymers should be synthesized and then tested for high conductivity and, when high conductivity is found, transport numbers for the ions in the melt should be determined. The chart below lists the phosphazenes with their expected properties.

Polymer and Expected Properties

A $[PN(OC_6H_5)_2]_n$ - Highest chain flexibility of polyphosphazenes. (Allcock, 1972)

B $[PN(OCH_2CF_3)_2]_n$ - Excellent stability and potential for use in mixed side group polymers.

C $[PN(NRH)_2]_n$ - Good compatibility with melt.

D $[PN(NR_2)_2]_n$ - Good compatibility with melt.

E Polymers A-D with various percents of choline, $-OCH_2CH_2N(CH_3)_3^+Cl^-$, as second side group. Chloride selectivity.

F Polymers A-D with various percents of $-OCH_2CH_2OCH_2CH_2OCH_3$ doped with metal chlorides. Chloride selectivity. $[PN(OCH_2CH_2OCH_2CH_2OCH_3)_2]_n$ showed 100-1000 times the conductivity of PEO in aqueous media (Shriver and Allcock, 1986)

G Polymers C and D doped with metal chlorides. Chloride selectivity.

H Polymers A and B with "mechanically" included salts. Good conductivity.

REFERENCES

Allcock, H.R. Phosphorus Nitrogen Compounds, New York, Academic Press, 1972.

Dymek, C.J., G.F. Reynolds and J.S. Wilkes. A Rechargeable Cadium-Bromine Battery Using Room Temperature Chloroaluminate Molten Salts. J. Electrochem. Soc., 1987, Vol. 134, pp. 1658-63.

Farrington, G.C., L.L. Yound and A.R. McGhie. Ionic Conductivity of Complexes of Poly(ethylene oxide) and $MgCl_2$. J. Electrochem. Soc., 1986, Vol. 133, pp. 1380-5.

Shriver, D.F., H.R. Allcock, et.al., Complex Formation and Ionic Conductivity of Polyphosphazene Solid Electrolytes. Solid State Ionics, 1986, Vol. 18-19, pp. 258-64.

Wilkes, J.S., et.al., Properties of 1,3-Dialkylimidazolium Chloride-Aluminum Chloride Ionic Liquids. 2 papers. J. Phys. Chem, 1984, Vol. 88, pp 2609-14 and 2614-21.

1988 USAF-UES SUMMER FACULTY RESEARCH PROGRAM/
GRADUATE STUDENT SUMMER SUPPORT PROGRAM

Sponsored by the
AIR FORCE OFFICE OF SCIENTIFIC RESEARCH
Conducted by the
UNIVERSAL ENERGY SYSTEMS, INC.
FINAL REPORT

RADIATIVE ASSOCIATION IN ION-MOLECULE REACTIONS: REACTIONS OF SOME CARBON CATIONS

Prepared by:	Lucia M. Babcock
Academic Rank:	Assistant Professor of Chemistry
Department and University:	Department of Chemistry Louisiana State University, Baton Rouge, LA
Research Location:	Air Force Geophysics Laboratory/LID Hanscom AFB, MA
USAF Researcher:	John F. Paulson
Date:	1 September 1988
Contract No:	F49620-87-R-0004

RADIATIVE ASSOCIATION IN ION-MOLECULE REACTIONS: REACTIONS OF SOME CARBON CATIONS

by

Lucia M. Babcock

ABSTRACT

For some time now we have been interested in ion-molecule association reactions, particularly in the existence of a radiative stabilization channel. In previous studies, we identified the addition of halide ions to boron trihalides as a group of ion-molecule association reactions which undergo radiative as well as collisional stabilization. These systems are, to our knowledge, the first such studies reported. Association reactions of positive ions, especially those of carbon cations, are also of great interest. Since radiative stabilization has been observed in the boron halide/negative ion reactions, and since carbon cations are isoelectronic with neutral boron species, these are excellent candidates for radiative stabilization. In our work at AFGL this summer, we have looked at the reactions of CH_3^+, CD_3^+, CF_3^+, and CCl_3^+ with both SO_2 and NO as a function of temperature (over the range 210K to 470K) and pressure (over the range 0.3 to 1.0 Torr). While the CCl_3^+ ion does not react at all with either neutral, SO_2 adds to the other three carbon cations and radiative stabilization may be involved. Only charge transfer reactions are observed for NO with CH_3^+, CD_3^+, and CF_3^+.

Finally, ion velocities were measured as a function of pressure, temperature, and helium flow. While there is a monotonic dependence upon helium flow, velocities appear to be independent of pressure and only slightly dependent upon temperature.

I. INTRODUCTION:

Radiative stabilization is of central importance in interstellar chemistry[1-3] where number densities are so low that synthesis of large ions via three-body association is impossible. It is also of general interest as a subset of the broad class of chemiluminescent reactions. However, few experiments which probe the radiative association process directly have been performed. The largest single reason for the paucity of corroborating experimental evidence for such an important process is the fact that at temperatures and pressures accessible to most techniques for studying ion-molecule association reactions, collisional stabilization is the dominant reaction channel. A general mechanism for ion-molecule association reactions is given below:

$$A^+ + B \underset{k_d}{\overset{k_a}{\rightleftharpoons}} (AB^+)^* \qquad (1)$$

$$(AB^+)^* \xrightarrow{k_s(M)} AB^+ \qquad (2)$$

$$\xrightarrow{k_r} AB^+ + h\nu \,. \qquad (3)$$

The rate coefficients k_a, k_d, k_s, and k_r are those associated with formation of the excited adduct, unimolecular decomposition back to reactants, stabilization through collision with M, and radiative stabilization respectively. To date, experimental information about process (3) has been obtained from kinetic data; the photon from such a radiative association process has not yet been observed. Barlow, Dunn, and Schauer[4] reported the first low temperature, low pressure study of the addition of H_2 to CH_3^+. While studies at very low pressures and temperatures provide the best opportunity for looking at the radiative process (since low pressures minimize the $k_s(M)$ contribution and low temperatures minimize k_d), these experiments are most difficult to perform. Another approach which has been taken by Smith and Adams[5] has been examination of the related three-body process (equations (1) and (2) above) to obtain information about the average lifetime of the common intermediate $(AB^+)^*$. Theoretical

contributions in the study of radiative association have been most important also. Bass et al.[6] have used phase space theory to investigate the phenomenon and Herbst and Bates [2,3] have done extensive work using a statistical approach.

Recently we have identified some addition reactions of the boron trihalides as reactions in which radiative stabilization is occurring, and, most importantly, it occurs on a time scale which is competetive with collisional stabilization under typical flowing afterglow experimental conditions.[7-9] The radiative stabilization rate coefficients which we estimate from our kinetic data are on the order of 10^5 to 10^6 s^{-1}. While these rate coefficients are larger than the 10^3 s^{-1} associated with emission of an IR photon,[10] we have thought that a low lying electronic state many be participating in the radiative stabilization process.[8,9] It is most exciting to note that recent theoretical treatments of Herbst and Bates[2,3] have indicated that electronic states may play a much more significant role in radiative association in ion-molecule reactions than has been recognized up to now. They point out that if there are low-lying electronic states available to the system, radiative rates can be enhanced by factors of 10-100. This is certainly consistent with what we observe in the boron trihalide systems.

In our examination of the halide addition reactions of BF_3 and BCl_3,[7-9] we developed a method for determining whether radiative stabilization is playing a key role in an ion-molecule association reaction by examining the dependence of the observed two-body rate coeffficient upon the identity and the concentration of third-body as well as upon temperature. This method allows us not only to determine if radiative association is occurring, but also to estimate the rate coefficient for the process. Results of our examination of halide ion additions to SiF_4 indicate that, unlike the analogous reactions of BX_3, these reactions do not undergo radiative association to an appreciable extent at temperatures and pressures accessible to flowing afterglow and selected-ion flow tube (SIFT) studies.[11,12] Neither do halide ion addition reactions of SF_4 have a

significant radiative stabilization channel.[11] However, we have found that addition of other anions such as NO_2^- and NO_3^- to BX_3 behave similarly to the halide addition reactions; that is, they undergo radiative association.[13] Therefore there appears to be something unique to the boron systems which favors this channel. In an effort to investigate this further, we decided to look at systems isoelectronic or isovalent with the boron systems, and our work this summer at Air Force Geophysics Laboratory (AFGL) in Dr. John F. Paulson's laboratory was directed along these lines. Carbon cations are isoelectronic with neutral trigonal boron molecules, and we thought these would provide good candidates for the possibility of radiative stabilization. Furthermore, radiative association reactions of carbon cationic species have more direct implications in astrophysical studies since CH_3^+ is one of the most abundant interstellar species. Dr. Paulson's research group has a long history of contributions to the field of ion-molecule chemistry in general, and has been interested in association reactions and the temperature dependence of such processes.[14,15] The studies undertaken this summer arose out of this mutual interest and out of the complementary nature of experiments which can be performed on the AFGL variable temperature SIFT and those which can be performed on the LSU flowing afterglow.

II. OBJECTIVES OF THE RESEARCH EFFORT:

With our previous work, we have identified systems where radiative association plays a major role, and have developed a method for analyzing the data to obtain detailed information about the rate of this processs.[7-9] The halide addition reactions of BF_3 and BCl_3 are the first, to our knowledge, in which both radiative and collisional stabilization occur on similar time scales under our experimental conditions, and since radiative stabilization is such an important phemomenon, we are most interested in identifying other systems having similar behavior and in characterizing the process in general. In order to realize these goals, we have chosen to focus our studies on

the reactions of carbon cations with neutral species. Since we have determined that the boron trihalide association reactions are somewhat unique among anion addition reactions - neither SF_4 nor SiF_4 have significant radiative stabilization components in their halide ion addition reactions,[11,12] it seemed a logical step to choose systems similar to the boron systems. It is interesting that BX_3 species are isoelectronic with CX_3^+ species in view of the central role of radiative stabilization in astrophysics and the abundance of carbon cations in interstellar media. Therefore we have chosen to study the addition reactions of CX_3^+ ions.

The first neutral we chose to study was SO_2. In previous studies, we have found that NO_2^- adds to BX_3 with what appears to be a significan radiative component; SO_2 is isovalent with NO_2^-. Furthermore, as Table I indicates, energetic considerations preclude any charge transfer reactions of SO_2 with the carbon cations we selected. Thus we have a much greater chance of observing an association reaction which might not be able to compete were a rapid bimolecular reaction channel available.

Table I. Energetics (eV) for Charge Transfer Reactions[a]

$$I^+ + N \longrightarrow N^+ + I$$

N \ I^+	CH_3^+	CD_3^+	C	CCl_3^+
NO	-0.58	-0.59	+0.09	+0.48
SO_2	+2.48	+2.49	+2.61	+3.54

[a]Energetics calculated from ionization potentials from ref. 16.

The second neutral we chose to examine in reactions with our CX_3^+ ions was NO. As Table I shows, two of the charge transfer

reactions are energetically favored, one is disfavored, and the fourth is close to thermoneutral. These systems thus provide the opportunity to examine ion-molecule association reactions under a variety of energetic conditions. Some of the questions which we sought to address were: (1)will association occur where charge transfer is energetically disfavored? (2)for the systems where charge transfer can occur, will association also occur - especially under conditions of low temperature which favor association? (3) for the nearly thermoneutral system, indeed for all systems, will the availability of low-lying electronic states of the type CX_3-NO^+ enhance radiative stabilization as Herbst and Bates[2,3] have postulated?

The reactions of these two neutrals, SO_2 and NO, were examined with four carbon cations: CH_3^+, CD_3^+, CF_3^+, and CCl_3^+. Both CF_3^+ and CCl_3^+ are isoelectronic with the trigonal boron halides, BF_3 and BCl_3 respectively, which we used in our previous studies. The other two ions CH_3^+ and CD_3^+ are of prime concern in examining radiative processes which have direct bearing on interstellar reactions, and a comparison of the two permits assessment of the effect of isotopic substitution.

The eight reactions outlined above provide us with the opportunity to address several areas in our investigation of radiative stabilization in ion-molecule association reactions. As Table I shows, we can examine the effects of the presence of the low-lying electronic states which correlate to the charge transfer pairs CX_3-NO^+ and CX_3-SO_2^+ for varying energy differences. Herbst and Bates[2,3] have recently recast their theories in light of possible participation from low-lying electronic states such as the one described above, and have found that the presence of such an excited electronic state which does not correlate with the ground state reactants can enhance radiative stabilization rates by factors of 10 to 100 over radiative stabilization via emission of an IR photon. The typical rate coefficient for this latter process is on the order of 10^3 s^{-1}; it is most interesting to note that the additional factor of 10^2 brings the predicted rate coefficient to 10^4 to 10^5

s^{-1} which is exactly the order of magnitude which we observe for the boron trihalide/halide ion association reactions. The effect of substitutions (including the effect of isotopic substitution, as mentioned above) at the central carbon atom can be assessed. Finally, one of the reasons for selecting the neutral NO as a reactant was to examine potential association reactions where both reactants are not in a singlet electronic ground state; NO with its unpaired electron is a doublet.

Our research efforts at AFGL this past summer were directed toward the examination of these interesting addition reactions as a function of temperature and pressure. Through these studies, it was our hope to gain more complete understanding of both the collisional and radiative processes themselves and also to begin to characterize systems in which radiative stabilization can compete effectively with collisional stabilization in the pressure range 0.2 to 1.0 Torr. Throughout these studies involving an investigation of radiative stabilization in ion-molecule association reactions, we have had as a continuing aim the study of the temperature dependence of gas phase ion-molecule addition reactions as well. Though theory predicts the general negative temperature dependence seen in this class of reaction,[17-19] the exact temperature dependence is difficult to predict. Experimentally, the temperature dependence of collisionally stabilized ion-molecule association reactions is seen to be fairly complex and to vary from system to system.[20] It is important both for experimental and theoretical reasons, then, to learn as much as possible about the effect temperature has upon these reactions.

Finally, throughout the course of our work this summer, we have made quite a thorough study of the dependence of ion velocities upon the temperature and pressure in the flow tube and upon the rate of flow of the helium buffer gas. This is a most important quantity in studying reactions in flowing afterglow and SIFT instruments since it is the ion velocity which determines the reaction time in these continuous flow kinetic systems.

III. RESULTS:

All of our studies were carried out using the variable temperature Selected Ion Flow Tube (VT-SIFT) at AFGL. The technique and the experimental conditions employed are described briefly in Section IV. Each of the eight reactions mentioned above: CH_3^+, CD_3^+, CF_3^+, and CCl_3^+ with both SO_2 and NO, was studied over a pressure range of approximately 0.3 to 1.0 Torr and a temperature range of 190 to 500K. With the exception of systems where no reaction occurred under our experimental conditions, all of the reactions were either charge transfer or association reactions. We never observed any evidence that more than one channel was operating for a given pair of reactants. Furthermore, all of the reactions with NO were charge transfer reactions, while those involving the neutral SO_2 were association reactions. The general trend in reactivities for both sets of reactions was similar. For the association of SO_2, CH_3^+ and CD_3^+ have comparable rate coefficients, while that for CF_3^+ is much slower. Similarly, the rate coefficients for charge exchange of CH_3^+ and of CD_3^+ with NO are both essentially the collision rate, while the analogous rate coefficient for CF_3^+ with NO is several orders of magnitude smaller. It is most interesting to note that both reactions with CF_3^+ appeared to be anomalously slow and that CCl_3^+ did not react with either SO_2 or NO under the range of experimental conditions mentioned above. All reactions were carried out in helium buffer gas, and the results obtained for each of the systems studied are presented in detail below.

During the course of these kinetic studies, we also measured ion velocities over the range of temperature and pressure stated above for several different helium buffer gas flows. As a result, we have compiled a comprehensive table of the dependence of ion velocities upon these parameters. This has been a most interesting and fruitful endeavor since ion velocities, and in particular the ratio of ion velocity to bulk flow velocity, are important in obtaining rate coefficients from the data gathered in flow tube experiments. We have found that the ratio of ion velocity to bulk flow velocity, v_i/v_o, increases monotonically

with helium flow, is not dependent upon pressure, and is only slightly dependent upon temperature, increasing as the temperature is decreased. The details of our findings concerning ion velocity are presented below.

A. Reactions of Sulfur Dioxide with Carbon Cations: Association

We examined the reactions of CH_3^+, CD_3^+, CF_3^+, and CCl_3^+ with SO_2 over the temperature range 190K to 500K and pressure range 0.25 to 1.0 Torr of helium. For reactions with CH_3^+, CD_3^+, and CF_3^+, the only product observed was the association product of the general form $CX_3SO_2^+$. Over the temperature and pressure range given above, CCl_3^+ does not react at all with neutral SO_2. As shown in Figures I and II, the rate coefficients for the CH_3^+ and CD_3^+ reactions exhibit a positive dependence upon pressure (concentration of the third-body, helium) and a negative dependence upon temperature.

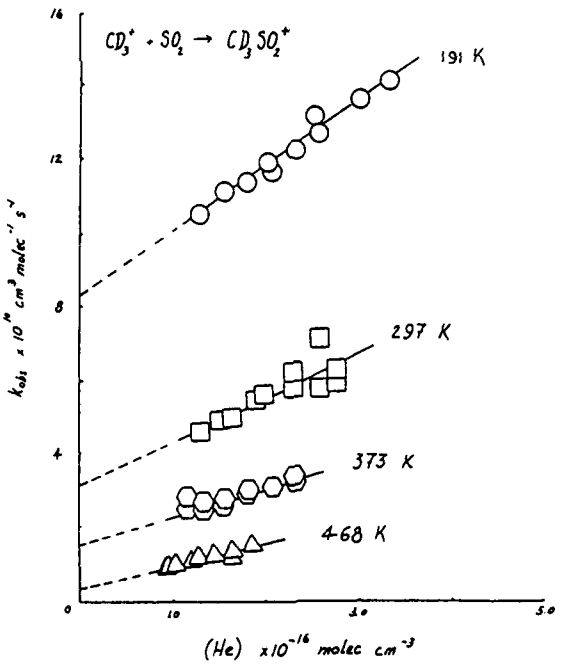

Figure I. Rate Coefficient for CD_3^+ Association with SO_2 as a Function of Temperature and Pressure

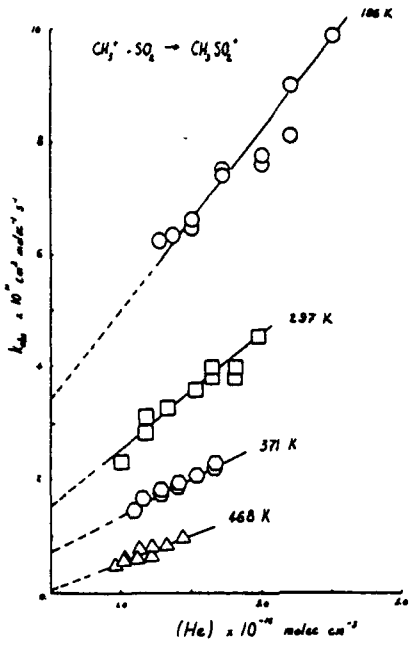

Figure II. Rate Coefficient for Association of CH_3^+ with SO_2 as a Function of Temperature and Pressure

This general type of behavior is indicative of association reactions which are occuring in a pressure and temperature regime where collisional stabilization efficiency is less than unity. That is, it takes more than a single collision with the inert buffer gas (in this case helium) to remove enough energy from the initially excited product ion to convert it into stable product. Both the pressure and temperature dependence of the reactions producing $CH_3SO_2^+$ and $CD_3SO_2^+$ are consistent with the general mechanism given previously, Equations (1) - (3), in which both radiative and collisional stabilization are occurring. The reaction of CF_3^+ with SO_2 shows somewhat different kinetic behavior. Although the only product observed is $CF_3SO_2^+$, the rate coeffieients are several orders of magnitude less than those for the other two reacting ions. Furthermore, there is significant curvature in the plots of $\log(CF_3^+)$ as a function of added neutral reactant, SO_2. This behavior could be due to production of reactant ion downstream, perhaps as the result of collisional breakup of the addition product. The curvature is reproducible, and occurs at all temperatures and pressures we

examined. It is interesting to note that if we take rate coefficients from initial slopes, we see the same general behavior as that observed in Figures I and II for the analogous CD_3^+ and CH_3^+ reactions.

The trends observed upon changing the reactant ion are interesting also. The association of CD_3^+ with SO_2 occurs almost twice as fast as that for CH_3^+ at a give temperature and pressure. The rate coefficient for formation of $CF_3SO_2^+$ is almost two orders of magnitude smaller than that for $CD_3SO_2^+$, and CCl_3^+ doesn't react at all. Under conditions where formation of the association product is most favorable, that is, at the lowest temperature and highest pressure studied, the reactions of CD_3^+, CH_3^+, and CF_3^+ reach only 60%, 40%, and 2% of their calculated collision limits respectively.

From the data presented in Figures I and II, and from the trends in initial slope for the CF_3^+ addition reactions, it appears possible that radiative stabilization plays a significant role in these systems. The non-zero intercepts in the graphs of log of reactant ion concentration as a function of added neutral reactant could be indicative of a two-body process which leads to product. However, one must be careful since extrapolation of rate coefficients for three-body processes outside of the experimental pressure range can be misleading if data correspond to rate coefficients in the fall-off regime. Further analysis of our data is required before a conclusion regarding the existence of radiative stabilization can be made. We are in the process of detailed interpretation of our results, and plan to compare them to theoretical predictions. The preliminary examination carried out thus far indicates that our mechanism in which radiative stabilization as well as collisional stabilization plays an important role is certainly a possibility.

B. Reactions of Carbon Cations with NO: Charge Exchange

The energetics for the charge exchange reactions:

$$CX_3^+ + NO \longrightarrow NO^+ + CX_3, \qquad (4)$$

where X = H, D, F, and Cl, are presented in Table I shown previously. For the methyl cation and the deuterated methyl cation, charge exchange is energetically favored. For CF_3^+ the reaction to produce NO^+ is close to thermoneutral and the analogous reaction of CCl_3^+ is energetically unfavorable. With such a range of energetic possibilities for our reactant cations, we saw the possibility for examining association in competition with a bimolecular reaction. We wanted to see whether association would begin to compete at lower temperatures (which favor the association process) where an exotherminc, bimolecular channel was available. Furthermore, even if the bimolecular channel dominated for those cases where it is energetically favored, we were curious as to whether association would be observed in cases where the thermochemistry predicted charge exchange to be unimportant. In view of this, it is most interesting to note that we did not observe association in any of the reactions of the carbon cations with NO. Both CH_3^+ and CD_3^+ yielded NO^+ in their reactions with NO, and did so at the collision rate. As one would expect, the rate coefficients for these two reactions did not depend upon either temperature or pressure. Figure III shows the rate coefficients for the reaction:

$$CH_3^+ + NO \longrightarrow NO^+ + CH_3 \qquad (5)$$

measured as a function of pressure at room temperature.

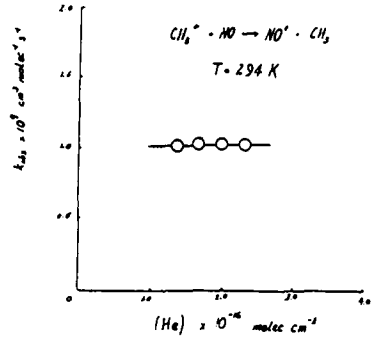

Figure III. Rate Coefficients for the Charge Exchange Reaction of CH_3^+ with NO as a Function of Pressure at 294K

C. Measurement of Ion Velocities

In flowing afterglow and SIFT techniques, experiments are carried out under continuous flow conditions. That is, the reaction time is constant, and is defined by the reaction distance (the distance from the point of mixing of the ion and neutral to the sampling orifice) and by the veloicity with which the reactants flow down the tube. Under typical experimental conditions, the flow profile in the reactor is that of laminar, parabolic flow.[12,21] The ions travelling at the point of the parabola reach the detector ahead of the bulk flow, and the ratio of the ion velocity to the bulk flow velocity is v_i/v_o, sometimes called α. While it is the ion velocity which is needed in order to obtain rate information from the data, the bulk flow velocity is more easily measured and is then adjusted by multiplication by v_i/v_o. In DRIFT experiments, because ions are moving under the influence of electric fields, measurement of ion velocities is crucial. Clearly a knowledge of the velocity ratio α is of critical importance.

The SIFT-DRIFT instrument at AFGL is equipped to measure ion times-of-flight from which ion velocities and therefore v_i/v_o values can be determined. Throughout the course of our work this past summer, we routinely measured times-of-flight for all of our kinetic experiments. As a result, we have compiled a large amount of data on the dependence of the ion velocity upon temperature, pressure, and helium flow rate. Figure IV and Table II on the following page summarize our results. Figure IVa shows the ratio of ion velocity to bulk flow velocity, v_i/v_o, plotted as a function of helium flow rate for a number of different pressures and Figure IVb shows the dependence of this ratio on the pressure in the flow tube for a given helium flow rate. Clearly there is no apparent dependence upon pressure as long as the flow rate of the buffer gas remains constant, and there is a monotonic increase in the ratio as this flow rate increases regardless of the pressure in the flow tube. This result is most interesting because it suggests that unless ion velocities are measured for each set of experimental conditions (or a

calibration curve used), it is best to operate at a given flow rate of helium and to make any adjustments in pressure by opening or closing a valve in the pumping line. The temperature dependence of v_i/v_o is given in Table II; the ratio increases as temperature decreases.

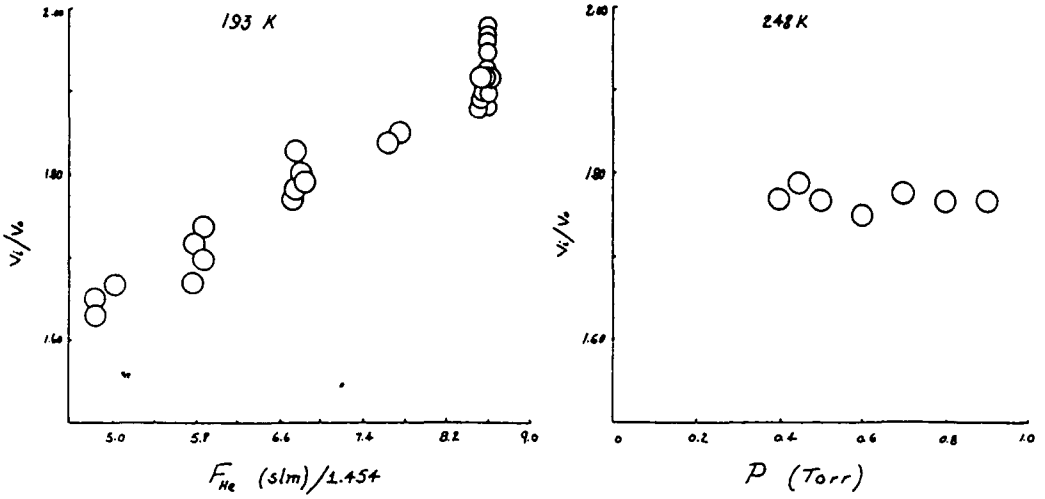

(a) (b)

Figure IV. Dependence of v_i/v_o on helium flow rate (a) and upon pressure (b)

Table II. Temperature Dependence of v_i/v_o for F_{He} = 9.7 slm

T	193	213	248	297	372	466
v_i/v_o	1.77	1.77	1.77	1.63	1.69	1.57

IV. EXPERIMENTAL TECHNIQUE:

All of the studies presented above were performed using the temperature variable selected ion flow tube (VT-SIFT) at AFGL. The SIFT technique is a method for studying gas phase ion-molecule reactions in a fast flow reactor under thermal conditions. Thermalization of the reactant ions and neutrals is brought about by collision with the large excess of inert buffer gas (helium in our case) which constantly flows through the reaction chamber; the helium makes up over 95% of the gases in the SIFT. Ions are initially produced in a high pressure ionization source and the desired reactant ion is "sifted" out of the mixture by the first quadrupole mass filter. This selection of reactant ion is a powerful technique for isolating the single reactant ion which is to be studied, and also allows for the removal of most of the neutral gas(es) used to generate the reactant ion. This is a significant advantage over the situation encountered in the conventional flowing afterglow apparatus where reactant ions are produced in the reaction tube itself, and one must deal with the complications which may occur due to production of more than one ion and/or the presence of the unreacted neutral. The ion which has been selected by the first quadrupole is injected into the flow tube; the inert helium carrier gas also enters the tube at this point. The neutral reactant gas is added downstream of the injection point, and from there to the detection chamber, the ion-molecule reactions take place. At the downstream end of the reaction chamber, a fraction of the reacting mixture is sampled through a small orifice; the rest of the gases are pumped away by a high speed Roots pump. The gases which have passed through the sampling orifice enter a second quadrupole mass filter where both the remaining reactant ion and any product ions are quantitatively analyzed. Rate information is obtained from the decay curve of the reactant ion as a function of added neutral reactant.

Temperature variation and control is achieved by circulating heated or cooled fluids through coils surrounding the reaction segment of the flow tube, or by resistance heaters. The tube is

jacketed in a vacuum chamber which is evacuated to prevent heat exchange to the atmosphere. Temperature is monitored by platinum resistance thermometers located along the reactor. Pressure in the reaction chamber is monitored using a capacitance manometer, and changes in pressure are effected by varying the helium carrier gas flow and/or by throttling the valve leading to the Roots pump.

As mentioned, ions are produced from appropriate neutrals in the high pressure ion source. For our studies, CH_3^+ was produced from CH_4, CD_3^+ from CD_4, CF_3^+ from CF_3Cl, CCl_3^+ from CCl_4. The three neutral gases (CH_4, CD_4, and CF_3Cl) were commercially obtained and used without further purification. Spectroscopic grade CCl_4 was further purified by a series of freeze/pump/thaw cycles before introduction in to ion source chamber.

V. RECOMMENDATIONS:

Radiative stabilization in ion-molecule reactions is an important and interesting area of study. Our studies of systems which can radiate on a time scale which is competitive with collisional stabilization have given us a unique opportunity to examine this phenomenon. A detailed analysis of the work we carried out this past summer at AFGL should lend us more insight into the nature of radiative stabilization. Some of the things our detailed data analysis will permit are: (1) assessment of the importance of electronic states in the radiative process, and determination of how important the proximity of a charge transfer surface is; (2) investigation of the temeprature dependence of the overall association process; (3) placement of limits on the rate coefficients for the elementary processes involved in production of stable addition product; and finally, (4) comparison of these reactions to those for the boron trihalides in order to begin to develop a general picture of the phenomenon of radiative stabilization in ion-molecule association reactions.

A series of studies involving the use of different third-bodies is a logical extension of the work we have done at AFGL this past summer. An examination of the association reactions of

CX_3^+ (X = H, D, F, CCl) with SO_2 in argon and nitrogen buffer gases will help us to determine whether or not the non-zero intercept in our data is due to radiative stabilization. Furthermore, these data will permit us to obtain values of the radiative association rate coefficients in favorable cases, and to place upper limits on them in the less favorable cases. It will be interesting to examine the CF_3^+ reaction to see whether the curvature observed in kinetic data in helium is present for other third-bodies as well. Temperature studies of the reactions in N_2 and Ar will also be of interest.

Finally, our examination of v_i/v_o as a function of T, P, and F_{He} was carried out on the AFGL SIFT using helium as the buffer gas. It will be interesting to carry out the same type of study on our flowing afterglow using He, Ar, and N_2. To my knowledge, such a comprehensive study has not been done. In contrast to the AFGL SIFT, our FA has a slightly larger inner diameter, is electropolished, does not contain DRIFT rings, and has an electron gun ion source in the tube rather than a Venturi-type injector. Our measurements will indicate whether these characteristics have a significant effect on ion velocities.

ACKNOWLEDGMENTS

I would like to thank the people at Air Force Geophysics Laboratory/LID, Hanscom AFB for their support and hospitality during my stay. In particular, John Paulson, Fred Dale, Carol Deakyne, Michael Henchman, Bob Morris and Al Viggiano deserve special thanks for their technical assistance as well as their friendship. The support of the Air Force Systems Command and the Air Force Office of Scientific Research through the Summer Faculty Research Program is gratefully acknowledged, as is the very competent administration of the program by Universal Energy Systems, Inc. Finally, a great deal of credit for the magnitude and quality of the research carried out goes to Thomas C. Pentecost, my graduate student. His long hours and enthusiasm made our accomplishments possible.

REFERENCES

1. Herbst, E., "The Formation of Complex Interstellar Molecules by Radiative Association," in Interstellar Molecules, Andrew, B.H. (ed.), D. Reidel Publishing Co., 1980, p. 317.
2. Bates, D.R. and E. Herbst, "Radiative Association," in Rate Coefficients in Astrochemistry, Millar, T.J. and D.A. Williams (eds.), Kluwer Academic Publishers, 1988, p. 17, and references therein.
3. Herbst, E. and D.R. Bates, "Radiative Association via Excited Electronic States: Model Calculations," Ap. J., Vol. 329, 1988, p. 410, and references therein.
4. Barlow, S.E., G.H. Dunn, and M. Schauer, "Radiative Association of CH_3^+ and H_2 at 13K", Phys. Rev. Lett., Vol. 52, 1984, p. 902.
5. Adams, N.G. and D. Smith, "The Rate Coefficients for Several Ternary Association Reactions at Thermal Energies," Chem. Phys. Lett., Vol. 79, 1981, p. 563.
6. Bass, L.M., P. R. Kemper, V. G. Anicich, and M. T. Bowers, "Ion-Molecule Association Reactions. A Statistical Phase Space Model," J. Am. Chem. Soc., Vol. 103, 1981, p. 5283.
7. Babcock, L.M. and G.E. Streit, "Third-Body Effects in Termolecular Reactions: Halide Ion Addition to BF_3 and BCl_3," J. Phys. Chem., Vol. 88, 1984, p. 5025.
8. Herd, C.R. and L.M. Babcock, "Radiative Stabilization in the Addition of F^- to BF_3," J. Phys. Chem., Vol. 91, 1987, p.2372.
9. Herd, C.R. and L.M. Babcock, "Radiative versus Three-Body Addition in Halide Ion Reactions with BF_3 and BCl_3 over the Temperature range 220K to 410K," J. Phys. Chem., in press.
10. Herbst, E., "An Update of and Suggested Increase in Calculated Radiative Association Rate Coefficients," Ap. J., Vol. 291, 1985, p. 226.
11. Herd, C. R., "A Study of the Temperature Dependence of Ion-Molecule Association Reactions. Halide Ion Addition to a Selected Group of Lewis Acids," Ph. D. Dissertation, Louisiana State University, 1987.

12. Babcock, L.M., W.S. Taylor, and C.R. Herd, "Ion/Molecule Association Reactions: Cl^- Addition to SiF_4 in He and N_2," Int. J. Mass Spectrom. Ion Proc., Vol. 81, 1987, p. 259.
13. Ruhr, P.S., C.R. Herd, T.C. Pentecost, and L.M. Babcock, "Gas Phase Bimolecular Reactions at Boron Centers: Nucleophilic Attack as a Probe of Reaction Surfaces," J. Am. Chem. Soc., submitted.
14. Viggiano, A.A. and J.F. Paulson, "Temperature Dependence of Associative Detachment Reactions," J. Chem. Phys., Vol. 79, 1983, p. 2241, and references therein.
15. Hierl, P.M. and J.F. Paulson, "Translational Energy Dependence of Cross Sections for Reactions of OH^- with CO_2 and SO_2," J. Chem.Phys., Vol. 80, 1984, p. 4890, and references therein.
16. Rosenstock, H.M., K. Draxl, B.W. Steiner, and J.T. Herron, "Energetics of Gaseous Ions," J. Phys. Chem. Ref. Data, Vol. 6, 1977.
17. Clary, D.C., "Rates of Chemical Reactions Dominated by Long-Range Intermolecular Forces," Mol. Phys., Vol. 53, 1984, p. 3.
18. Bates, D.R., "Ion-Molecule Association," J. Phys. B: Atom. Molec. Phys., Vol. 12, 1979, p. 4185.
19. Herbst, E., "Statistical Theory of Three-Body Ion-Molecule Reactions," J. Chem. Phys., Vol. 70, 1979, p.2201.
20. Ferguson, E.E., "Constraints on the Temperature Variation of Three-Body Ion-Neutral Association Reaction Rate Constants," Chem. Phys. Lett., Vol. 101, 1983, p. 141.
21. Ferguson, E.E., F.C. Fehsenfeld, and A.L. Schmeltekopf, "Flowing Afterglow Measurements of Ion-Neutral Reactions," Adv. Atomic Molec. Phys., Vol. 5, 1969, p. 1.

1988 USAF-UES SUMMER FACULTY RESEARCH PROGRAM/
GRADUATE STUDENT RESEARCH PROGRAM

Sponsored by the

AIR FORCE OFFICE OF SCIENTIFIC RESEARCH

Conducted by the
Universal Energy Systems, Inc.

FINAL REPORT

UPWARD CONTINUATION OF GRAVITY DATA WITH ERROR ESTIMATES

Prepared by:	Stephen D. Baker
Academic rank:	Professor
Department and University:	Physics Department, Rice University
Research Location:	Air Force Geophysics Laboratory, Earth Sciences Division, Geodesy Branch
USAF Researcher:	Christopher Jekeli
Date:	September 30, 1988
Contract No.	F49620-87-R-0004

UPWARD CONTINUATION OF GRAVITY DATA WITH ERROR ESTIMATES

ABSTRACT

An experiment performed in the past year by AFGL personnel appears to show a deviation from the Newtonian inverse square law. In this experiment, gravity measurements on the earth's surface are continued upward and are compared with gravity measurements on a TV tower. The upward continuation is not a simple exercise and has been done in several different and independent ways. It is proposed here to undertake still another approach to the upward continuation to provide a check of the earlier continuation calculations, to provide a test for the presence of discrepant data, and to obtain independent error estimates in the predicted gravity on the tower.

I. INTRODUCTION: I have taught elementary physics and have done experimental work in nuclear physics and have more recently been interested in various gravitational experiments. During the summers of 1986-87, as a NASA Summer Faculty Fellow, I considered the possibility of measurements of the Newtonian gravitational constant G in a spacecraft laboratory. As a result of the foregoing, the AFGL experiment on the variation of G with distance was of particular interest to me.

II. OBJECTIVES OF THE RESEARCH EFFORT: My primary objective for the 1988 SFRP was to become less than totally ignorant of the fields of geodesy and gravimetry and to learn about the experiments carried out by the AFGL on non-Newtonian gravity.

III. READINGS: To become familiar with the research going on in the Geodesy Branch, I have talked with the researchers there and have read from several sources and reports, among which are the references listed at the end of this report.

IV. TOWER GRAVITY EXPERIMENT: Briefly, the tower gravity experiment is a method for testing the Newtonian force law

$$F = GMm/r^2$$

at distances of separation r between about 10 and 1000 meters. The potential whose gradient gives the Newtonian force law satisfies Laplace's Equation. It turns out that a specification of the magnitude of the force per unit test mass (that is, what geodeticists call the acceleration of gravity, or gravity, for short) on the ground surrounding a tower permits one to "upward continue" to predict the value of gravity along the tower. The AFGL group finds (Eckhardt

et al., 1988, Romaides et al., 1988) that the measured gravity on the tower does not quite agree with the gravity predicted from the measurements on the ground, and they infer that there is a measurable departure from the Newtonian force law. Other workers (Stacy et al., Anders et al.) have reported deviations from the Newtonian law, although they obtain less detail on the form of the deviation from the Newtonian force law than does the AFGL group.

The upward continuation calculation is not a simple exercise. The AFGL group undertook several different approaches, two of which agree closely, and the third of which has not yet been shown to the stable. In addition, obtaining estimates of the error in the prediction of gravity on the tower has also turned out not to be simple.

V. RECOMMENDATIONS

As a result of these considerations, it would be useful to undertake still another approach to the upward continuation to accomplish two goals; first, to provide a further check of the earlier continuation calculations and, second, to provide a possible test for the presence of discrepant data and an estimate of the errors in the predicted gravity on the tower. An additional benefit from such a calculation would be to have predictions of gravity gradients which conceivably could also be measured on the tower.

In a proposal for a mini-grant through the USAF-UES SFRP, I outline a possible procedure. Briefly, after accounting for centrifugal force and the gravitational effect

of the atmosphere and tower, I propose to attempt to fit the ground data to a harmonic series

$$g_z = \sum_{m,n} A_{m,n} \exp[i(mx + ny) - (m^2 + n^2)^{1/2} z]$$

To limit the number of parameters to a manageable number, fits to the inner zone will be done after a fit to a larger outer zone has been accomplished.

ACKNOWLEDGMENTS

I am pleased to acknowledge the sponsorship of the Air Force Systems Command, Air Force Office of Scientific Research, and the Air Force Geophysics Laboratory. I very much appreciate the hospitality and interaction with all my colleagues there, especially Don Eckhardt, Tom Mooney, Chris Jekeli, and Andy Lazarewicz.

REFERENCES

General Geodesy:

"Geodesy for the Layman," Report DMA TR 80-003 (Edition 5, December 1983), available from Defense Technical Information Center

Chuji Tsuboi Gravity, Allen and Unwin 1983 ISBN-00-521-30811-9

W. A. Heiskanen and H. Moritz Physical Geodesy Freeman 1987

H. Moritz Advanced Physical Geodesy, Abacus Press 1983 ISBN-0-85626-195-5 or Herbert Wichmann Verlag ISBN-3-87907-106-3

Absolute gravimetry:

R. L. Iliff and R. W. Sands, "The AFGL Absolute Gravity Measuring System," Report AFGL-TR-83-0297 (1983)

A. R. Lazarewicz et al., "Balloon-borne, High Altitude Gravimetry: the Flight of DUCKY 1a (11 October 1983) Report AFGLL-TR-85-0342 (1985)

Gravity on a tower:

D. H. Eckhardt et al., "Tower Gravity Experiment: Evidence for Non-Newtonian Gravity," Physical Review Letters 60 (1988)2567

A. J. Romaides et al., "A Detection of Non-Newtonian Gravity," submitted to Journal of Geophysical Research, April 1988, and references cited therein

1988 USAF-UES SUMMER FACULTY RESEARCH PROGRAM/

GRADUATE STUDENT RESEARCH PROGRAM

Sponsored by the

AIR FORCE OFFICE OF SCIENTIFIC RESEARCH

Conducted by the

Universal Energy Systems, Inc.

FINAL REPORT

Impulse Approximation Formalism for Atom Molecule Collisions

Prepared by:	Pradip Bakshi, Ph.D.
Academic Rank:	Professor
Department and	Physics Department
University:	Boston College
Research Location:	AFGL/OPB Hanscom AFB Bedford, MA 01730
USAF Researcher:	Ramesh Sharma, Ph.D.
Date:	26 September 1988
Contract No.:	F49620-87-R-0004

Impulse Approximation Formalism for Atom Molecule Collisions

by

Pradip M. Bakshi

ABSTRACT

The Impulse Approximation Formalism has been developed beyond the Peaking Approximation to tackle the low projectile velocity, high internal molecular energy collisions. A new representation is given for the T-matrix for the hard core potential. This Momentum Transfer Representation converges rapidly and is found to be separable for the prior and the post forms. Explicit expressions are obtained for the differential and total cross sections in terms of vector coupling coefficients. Various theoretical extensions and experimental applications are discussed.

ACKNOWLEDGEMENTS

I wish to thank the Air Force Office of Scientific Research for sponsorship of this research. Universal Energy Systems, Inc. has been very helpful in all administrative matters of this program.

This has been a very rewarding and productive summer. I am much indebted to Dr. Ramesh Sharma at AFGL for providing a very hospitable and stimulating environment, and for his active participation in this program. I also wish to thank Joe Sindoni for his help in the substantial numerical computations of this program.

I. INTRODUCTION:

Quantum mechanical Impulse Approximation(IA) has been employed in the literature [Bogan(1974); Eckelt, Korsch and Philipp (1974); Beard and Micha (1981)] to study the collisions between fast atomic projectiles and target diatomic molecules. The central idea of IA is to treat the three body (atom-diatomic molecule) process as a pair of two-body (atom-atom) collisions with the third atom remaining a spectator. It has recently been suggested by Sharma (1988) at AFGL that IA may also be relevant for collisions of low energy particles with target molecules having large internal energy. Such an extension of the formalism may eventually prove helpful in explaining the R-branch band-heads observed in vibration-rotation band emission from high-altitude atmospheric and flow tube laboratory experiments, which are of interest at AFGL.

My past familiarity with some of this work, as well as my background in mathematical physics were relevant in my becoming involved in this Program.

II. OBJECTIVES OF THE RESEARCH EFFORT:

The preliminary objectives of this program were (1) to review the literature on IA formalism, and (2) to extend the formalism to situations involving low projectile velocity and high internal molecular energy. In IA the scattering amplitude is represented as an integral in momentum space of the product of three factors: the final state of the molecule, the off-shell two-body T-matrix and the initial

state of the molecule. In the earlier literature the evaluation of this integral was simplified by adopting the Peaking Approximation (PA) in which the T-matrix is evaluated at a fixed value of the momentum, where the product of the other two factors has its peak value. Then the T-matrix can be taken out of the integral and the remaining integration is straightforward and leads to simple molecular overlap integrals.

During the course of our work it was realized that the PA was quite inadequate for collisions involving low projectile energies. The variation of the T-matrix over the domain of integration was quite significant and had to be taken into account properly. In fact, this was the essential technical problem, which had to be solved, in order to arrive at a reasonable extension of the formalism to low energy collisions. Physically, the angular correlation between the angular momentum of the two-body process and the angular momentum of the molecule is ignored in PA. Thus (3), developing an appropriate formalism which would go beyond PA and not ignore the angular correlations, became an added objective during the course of the research effort.

The review of IA is given below in Section III. New approaches developed to go beyond PA are described in sections IV and V. A new representation was developed for the T-matrix as described in section IV. The angular momentum couplings for low projectile velocities are developed in section V. The main results, and their implications are summarized in section VI. Finally the recommendations for follow-up research are described in section VII.

III. IMPULSE APPROXIMATION FORMALISM:

The differential cross section for a rotational vibrational transition $(nj \to n'j';\ \theta;\ p_3)$ in the center of mass frame of the three atoms is given in the IA by Eckelt, Korsch and Philipp (1974),

$$\frac{d\sigma}{d\Omega}\ (nj \to n'j';\ \theta;\ p_3) = \frac{1}{2j+1}\ \frac{p_3'}{p_3} \sum_{m,m'} \left(\frac{2\pi}{\hbar}\right)^2 \mu_3 \sum_{s=1,2} I_s^{\,2}, \qquad (1)$$

where

$$I_s = \int d\vec{p}_s\ \phi_f^{*}\ (\vec{q}'_3)\ T_s\ \phi_i\ (\vec{q}_3), \qquad (2)$$

and, $\vec{p}_3$ and $\vec{p}'_3$ are the momenta of atom 3 before and after collision, θ is the angle between $\vec{p}_3$ and $\vec{p}'_3$, μ_3 is the reduced mass of the collision system, i and f denote the initial and final molecular states, s=1 and 2 describe the two possible impulse collisions where s denotes the spectator atom. The differential cross section is independent of the azimuthal angle because of the summation and averaging over the magnetic quantum numbers m' and m. The momenta p_i describe the relative momentum of atom i and the center of mass of the other two atoms, while $\vec{q}_i$ describes the relative momentum between these two atoms. The relations between the three sets of these Jacobi momenta are:

$$\vec{q}_3 = -\left(\vec{p}_1 + \frac{m_1}{m_1+m_2}\ \vec{p}_3\right) = \left(\vec{p}_2 + \frac{m_2}{m_1+m_2}\ \vec{p}_3\right)$$

$$\vec{q}_1 = \frac{m_3}{m_2+m_3}\ \vec{p}_1 + \vec{p}_3 \qquad (3)$$

$$\vec{q}_2 = -\left(\frac{m_3}{m_2+m_3}\ \vec{p}_2 + \vec{p}_3\right)$$

Similar expressions prevail for $\vec{q}'_i$ with $\vec{p}_3$ replaced by $\vec{p}'_3$. Since $\sum_i \vec{p}_i = 0$, any $\vec{q}_j$ is expressible in terms of any two $\vec{p}_i$. In view of the integration over the spectator atom momentum in Eq. (2), it will be convenient to use the forms given above in terms of $\vec{p}_1$ for s=1 and in terms of $\vec{p}_2$ for s=2.

The T-matrix for the hard core potential is given by Van Leeuwen and Reiner (1961), and Beard and Micha (1981),

$$T_s = T(\vec{q}'_s, \vec{q}_s; \varepsilon_s), \tag{4}$$

where

$$T(\vec{q}', \vec{q}; \varepsilon) = \frac{1}{4\pi} \sum_\ell (2\ell+1)\, t_\ell (q', q; \varepsilon)\, P_\ell(\cos\phi), \tag{5}$$

ϕ being the angle between $\vec{q}$ and $\vec{q}'$, and

$$t_\ell(q', q, \varepsilon) = \frac{R^2\hbar^2}{\pi m} \{ \frac{q^2-k^2}{q^2-q'^2}\, j_\ell (qR) \frac{d}{dR}\, j_\ell (q'R) \tag{6}$$

$$+ \frac{q'^2-k^2}{q'^2-q^2}\, j_\ell (q'R) \frac{d}{dR}\, j_\ell (qR)$$

$$- j_\ell (q'R)\, j_\ell (qR) \frac{d}{dR} \ell n\, h_\ell^{(1)} (kR) \}.$$

R is the hard core radius for the collision between atom 3 and atom s, $\varepsilon_s = \hbar^2k^2/2M_s$, m = reduced mass of the two body system. For s=1, m is the reduced mass for the 3-2 collision and for s=2, it is the reduced mass for the 3-1 collision. The energy ε_s in Eq. (4) represents the energy available for the collision,

$$\epsilon_s = E_T - \frac{p_s^2}{2\mu_s} , \qquad (7)$$

where μ_s is the reduced mass of system consisting of the spectator atom and the center of mass of the colliding two body system, and $E_T = E_3 + E_i = E'_3 + E_f$ is the total energy of the three body system. Eqs. (4) to (7) represent the off-shell T matrix (Beard and Micha, (1981). Half on the shell T-matrix is obtained if instead of Eq. (7) one employs as in Eckelt, Korsch and Philipp (1974),

$$\epsilon_s = \frac{\hbar^2 q_s^2}{2M_s} \text{ (Post)} \quad \text{or} \quad \epsilon_s = \frac{\hbar^2 q_s'^2}{2M_s} \text{ (Prior).} \qquad (8)$$

The different versions of the T-matrix will obviously lead to different results for the cross sections. The relative merits of the various versions will be discussed later. Explicit expressions for the various masses are:

$$\mu_s = m_s(1-\frac{m_s}{M}); \quad M_s = \frac{m_3 m_j}{m_3+m_j} , \quad (j\neq s). \qquad (9)$$

The Peaking Approximation (PA) is obtained when T_s in Eq. (2) is evaluated at the particular value of p_s, where the rest of the integrand has its peak. If the peak in the integrand is sharp, and the variation of T near the peak is relatively mild, PA will be a good approximation and the rest of the integration is relatively simple and provides as shown in Eckelt, Korsch and Philipp (1974),

$$I_s = T_s^{peak} \int \Phi_f^* (\vec{q}'_3)\, \phi_i(\vec{q}_3)\, d\vec{p}_s = T_s^{peak}\, F_{fi}\,(\Delta p \gamma_s), \qquad (10)$$

$$\gamma_s = (-1)^s\, m_s/(m_1+m_2) \qquad s = 1,2; \qquad (11)$$

$$F_{fi}(\gamma\Delta p) = \int d\vec{r}\, \Phi_f^*(\vec{r})\, e^{i\gamma\vec{\Delta}p\cdot\vec{r}}\, \Phi_i(\vec{r}). \tag{12}$$

The subsequent calculation for the differential cross section is simplified if we consider a homonuclear molecule ($m_1 = m_2$). Then we have

$$\frac{d\sigma}{d\Omega} = 4\mu^2 \left(\frac{2\pi}{\hbar}\right)^4 \frac{p'^3}{p_3} \left| T_1^{peak} \right|^2 F^2(\Delta p), \tag{13}$$

where

$$F^2(\Delta p) = \frac{1}{2j+1} \sum_{m,m'} \left| F_{fi} \right|^2 \tag{14}$$

$$= (2j'+1) \sum_{\lambda} (2\lambda+1) \left| \begin{pmatrix} j' & \lambda & j \\ o & o & o \end{pmatrix} f^{(\lambda)}_{n'j'nj}(\Delta p) \right|^2,$$

$$f^{(\lambda)}_{n'j'nj}(\Delta p) = \int_o^\infty \chi_{n'j'}(r)\, j_\lambda\left(\tfrac{1}{2} r\, \Delta p\right) \chi_{nj}(r)\, r^2 dr, \tag{15}$$

and

$$\phi_i(\vec{r}) = \chi_{nj}(r) Y_{jm}(\hat{r}); \quad \phi_f(\vec{r}) = \chi_{n'j'}(r)\, Y_{j'm'}(\hat{r}). \tag{16}$$

It should be noted that PA is also valid when T_s is almost constant over the whole range of integration of $\vec{p}_s$, irrespective of the characteristics of the rest of the integrand; PA can be valid even when $\phi_f^* \phi_i$ in Eq. (2) has no sharp peaks. In the previous calculations of Beard and Micha (1981) and Eckelt, Korsch and Phillip (1974) for hyperthermal collisions, one or the other condition for PA was satisfied, and it was by and large a reasonable approximation.

For low projectile energies, on the other hand, the variation of the T-matrix over the domain of integration is quite significant and needs to be taken into account properly. The primary difference

between the hyperthermal and the low energy collisions can be seen by expressing the two body momentum $\vec{q}_1$ in terms of the incident momentum $\vec{p}_3$ and the internal molecular momentum $\vec{q}_3$,

$$\vec{q}_1 = a\vec{p}_3 - b\vec{q}_3, \tag{17}$$

$$a = 1 - \frac{m_1}{m_1+m_2}\, b, \qquad b = \frac{m_3}{m_2+m_3}\,. \tag{18}$$

In the process of integration, $\vec{p}_3$, $\vec{p}_3'$ and $\vec{\Delta}p$ are fixed, and $\vec{q}_3$ is the variable. The significant range of $\vec{q}_3$ is determined by the momentum space product of the wave functions of the initial and the final states in Eq. (2). When p_3 is large compared to q_3, the variation in $\vec{q}_1$ is not too significant and $T(\vec{q}_1,\vec{q}_1' = \vec{q}_1 + \vec{\Delta}p)$ also remains almost invariant. For small p_3, on the other hand, $\vec{q}_1$ becomes proportional to $\vec{q}_3$ and the T-matrix undergoes significant variation over the range of integration. The PA is not a good approximation for low projectile velocities. In the next two sections, we extend the IA formalism to go beyond the PA for low energy collisions.

IV. A NEW REPRESENTATION FOR THE T-MATRIX:

The T-matrix for the hard core potential is given by Eqs. (5) to (8). For low energy collisions (p_3 small), ε_s is essentially a function of q_s^2 due to Eqs. (7) and (3), and then $T = T(\vec{q}'_s, \vec{q}_s)$, a function of only two vectors. Since $\vec{q}' = \vec{q} + \vec{\Delta}p$, such a function can be represented by a Legendre expansion in terms of the angle between the two vectors $\vec{q}$ and $\vec{\Delta}p$ as well,

$$T(\vec{q}',\vec{q}) = \sum_L P_L(\hat{q}\cdot\hat{\Delta p})\, T_L(q,\Delta p), \tag{19}$$

with

$$T_L(q,\Delta p) = \int_{-1}^{1} d\mu\; P_L(\mu)\; T\,(L+\tfrac{1}{2}), \tag{20}$$

where $\mu = \cos\theta_l$, and θ_l is the angle between $\vec{q}$ and $\vec{\Delta p}$. This representation has some interesting properties. We first note that for the prior or the post versions of ϵ, Eq. (8), this representation is exact, since no assumption is required about p_3.

We have carried out a numerical evaluation of T for the prior, the post and also the full (Eq. (8) with $p_3 = 0$) version, and then determined $T_L(q,\Delta p)$ in each case from Eq. (20). The relations

$$q' = \left[q^2 + (\Delta p)^2 + 2q(\Delta p)\cos\theta_l\right]^{1/2}, \tag{21}$$

$$\cos\phi = (q + \Delta p\cos\theta_l)/q', \tag{22}$$

and Eq. (5) define T in terms of q, Δp and $\mu = \cos\theta_l$.

The new representation, which may be called the Momentum Transfer Representation (MTR), converges rapidly. Unlike the old representation, Eq.(5), where higher and higher ℓ terms are required for increasing q, the new MTR in Eq.(19) manages to provide a fairly accurate T with just the first few terms in L.

For the "post" form ($\epsilon_s = q_s^2/2M_s$) the functions T_L have the remarkable factorization property

$$T_L\,(q,\Delta p) = j_L\,(\Delta p)\; t_L(q), \tag{23}$$

leading to

$$T(\vec{q}', \vec{q}) = \sum_L P_L(\hat{q}\cdot\Delta\hat{p})\, j_L(\Delta p)\, t_L(q). \qquad (24)$$

A similar expression can be obtained in terms of q' and Δp for the "prior" form ($\varepsilon s = q'^2_s/2M_s$). We have determined the set of functions $t_L(q)$ for L=0 to 20 and qR ranging from 0 to 100. The most significant contributions in Eq.(24) arise from L=0, 1 and 2.

It can be shown that the functions $t_L(q)$ appearing in the MTR, Eq. (24), are related to the forward scattering amplitude, obtained by setting $\phi = 0$ in Eq. (5),

$$T_f = \frac{1}{4\pi} \sum_\ell (2\ell+1)\, t_\ell. \qquad (25)$$

For the "post" form, Eq. (6) simplifies [Eckelt, Korsch and Philipp, 1974] to

$$t_\ell = \frac{\pi^2 R}{i\,\pi m} \frac{j_\ell(q'R)}{(qR)\, h^{(1)}(qR)}. \qquad (26)$$

In MTR, the forward elastic scattering amplitude ($\Delta p=0$) is represented by a single term (L=0), as all the other modified Bessel functions vanish in Eq. (24),

$$T_{f,el} = t_{L=0}(q). \qquad (27)$$

The corresponding amplitude obtained from Eqs. (25) and (26) is

$$T_{f,el} = \left(\frac{\pi}{2\pi}\right)^2 \frac{R}{im} \sum_\ell (2\ell+1) \frac{j_\ell(qR)}{(qR)\, h_\ell^{(1)}(qR)}. \qquad (28)$$

Thus we identify $t_o(q)$ in MTR with the explicit expression on the right hand side in Eq. (28). We have compared the $t_o(q)$ obtained

numerically from Eqs. (20) and (23) from our computer programs and the forward elastic amplitude given by Eq. (28); they were found to be identical, providing a confirmation of the separability, Eq. (23), in MTR. An independent asymptotic evaluation of the forward elastic scattering amplitude is available in Wu (1956); our $t_o(q)$ was found to be in complete agreement with that result as well.

Higher order $t_L(q)$ can be related to appropriate derivatives of the forward scattering amplitude. It can be shown that the $t_L(q)$ are expressible in terms of $T_{(r)}(q)$:

$$t_1 = 3\, T_{(1)} \tag{29}$$

$$t_2 = (5/2)\, t_o + (15/2)\, T_{(2)}$$

$$t_3 = (7/2) t_1 + (35/2)\, T_{(3)}$$

$$t_4 = -(63/8) t_o + (9/2) t_2 + (315/8) T_{(4)}$$

where

$$T_{(r)}(q) = \left(\frac{\partial}{\partial q'}\right)^r T_f(q',q)\Big|_{q'=q} \tag{30}$$

and $T_f(q',q)$ is given by Eqs. (25) and (26). We have verified all the relations in Eq. (29). Since the coefficients seem to increase for higher L, we have not tried to generalize Eq. (29) to the Lth order. Eqs. (20) and (23) are probably more effective for the numerical evaluation of $t_L(q)$.

We will need the MTR in the next section to obtain an expression for the IA scattering amplitude without resorting to the Peaking Approximation. The factorization property, which can be devleoped for the "prior" form as well by interhanging q' and q, will be found to be particularly useful.

V. BEYOND THE PEAKING APPROXIMATION:

As pointed out earlier, employing PA is inappropriate when the variation of T over the range of integration in Eq. (2) becomes significant. Many experimental situations fall in this category. While the IA has been around for over three decades and it is generally known that PA is an additional approximation, not inherent in the IA philosophy, the actual implementation of IA in the literature seems to rest only at the PA level. To our knowledge, what is given below is the first effort to develop the IA formalism beyond the PA.

The complete generalization of IA beyond PA to obtain explicit expressions for the differential and total cross section is a difficult endeavor. In the limited time frame of the Summer Program, it was deemed advisable to concentrate on the limiting case of low energy projectiles. As indicated in the Introduction this is also the physical domain pertinent to the observations and experiments of interest to AFGL.

For small projectile velocities, we can take from Eq. (17)

$$\vec{q}_1 = -b\vec{q}_3 , \qquad \vec{q}_1' = \vec{q}_1 + \vec{\Delta}p \tag{31}$$

to evaluate the T-matrix. The scattering amplitude I_1 is given by Eq. (2). For simplicity we consider the homonuclear case, $m_1 = m_2$, which leads to

$$\vec{q}_3' = \vec{q}_3 - \frac{1}{2}\vec{\Delta}p . \tag{32}$$

Transforming the final state to the configuration space, we have

$$I_1 = \int d\vec{r}\, \phi_f^*(\vec{r})\, e^{(i/2)\vec{\Delta}p\cdot\vec{r}}\, \psi_i(\vec{r}), \tag{33}$$

$$\psi_i(\vec{r}) = \int d\vec{q}_3\; e^{-i\vec{q}_3\cdot\vec{r}}\; \phi_i(\vec{q}_3)\, T . \tag{34}$$

Eq. (33) has the appearance of an overlap integral, Eq. (13), with $\phi_i(\vec{r})$ replaced by $\psi_i(\vec{r})$. The latter function, however, includes the effects of the variability of T over the domain of integration. The momentum space integration in Eq. (34) is carried out by separating the angular and the magnitude parts,

$$\phi_i(\vec{q}) = 4\pi i^j\, Y_{jm}(\hat{q})\, W_{nj}(q), \tag{35}$$

$$W_{nj}(q) = \int_o^\infty dr\; r^2\, \chi_{nj}(r)\, j_j(qr), \tag{36}$$

and expressing T in the MTR, Eq. (19). Choosing the z-axis along $\vec{\Delta}p$, we have

$$P_L(\hat{q}\cdot\hat{\Delta}p) = (4\pi/\hat{L})^{1/2}\, Y_{Lo}(\hat{q}), \quad \hat{L} \equiv (2L+1) \tag{37}$$

Expressing the exponential in Eq. (34) in the standard partial wave expansion, we find

$$\Psi_i(\vec{r}) = \sum_{L\lambda}\sum K(r,\Delta p)\, Y_{\lambda\hat{m}}(r)\, A(j\; L\; \lambda, m) \tag{38}$$

$$K(r,\Delta p) = \int_o^\infty dq_3\; q_3^2\; W_{nj}(q_3)\, T_L(bq_3,\Delta p)\, j_\lambda(q_3 r) \tag{39}$$

where A is the result of angular integrations and involves Clebsch-Gordan coefficients. The final integration in Eq. (33) is similarly separated into the radial and angular parts, and leads to the

separated into the radial and angular parts, and leads to the structure

$$I_1 = \sum_{L\lambda\lambda'} N(\Delta p)\, B(j\ L\ \lambda\ \lambda' j', m)\, \delta_{mm'}, \tag{40}$$

$$N(\Delta p) = \int_0^\infty dr\ r^2\, \chi_{n'j'}(r)\, j_{\lambda'}(\tfrac{1}{2}\Delta p r)\, K(r, \Delta p). \tag{41}$$

The angular part B essentially reflects the addition of three angular momenta, $\vec{j} + \vec{L} + \vec{\lambda}' = \vec{j}'$, and can be expressed in terms of the product of a Racah coefficient and four Clebsch-Gordon coefficients, only one of which depends on m. It is now possible to sum over m' and m in Eq. (1) to obtain the differential cross section,

$$\frac{d\sigma}{d\Omega} = (4\mu_3^2)\ \frac{p_3'}{p_3}\ \left(\frac{2\pi}{\hbar}\right)^4\ \sum_J\ |F_J|^2 \tag{42}$$

where F_J is the effective amplitude,

$$F_J = \sum_{L\lambda\lambda'} D(j\ L\ \lambda\ \lambda' j' J)\ N(\Delta p), \tag{43}$$

and D represents the angular momentum addition algebra through the vector coupling coefficients.

We have developed complete computer programs for the evaluation of the amplitudes F_J, the differential cross sections and the state to state ($nj \to n'j'$) total cross sections obtained by integrating over the angle θ. We are now in a position to apply this formalism to a variety of problems.

VI. DISCUSSION OF RESULTS:

A complete formalism for IA without PA has been described in the previous two sections for the low projectile velocity limit. In this section we provide some additional clarifications and comments.

1) The criterion for the smallness of p_3: The relevant parameter is the ratio $\xi = ap_3/bq_3$. When $\xi >> 1$, $\vec{q}_1$ is proportional to $\vec{q}_3$ and T becomes a function of only two vectors, $\vec{\Delta p}$ and $\vec{q}_3$. Thus an expansion in the Legendre series based on the angle between these two vectors becomes possible. It is important to have $\vec{q}_3$ as the main variable in T, otherwise the radial integrals in q_3 would not be feasible.

2) If P_3 is not so small: When ξ is not too large, the treatment in section V is no longer complete. The MTR is still exact in terms of $\vec{\Delta p}$ and $\vec{q}_1$ for the post form. The practical difficulty is that the rest of the intergrand is simple only in terms of $\vec{q}_3$. Re-expressing the wave functions in terms of $\vec{q}_1$ provides a well defined approach at the cost of more angular integrals. This should be developed further.

3) If P_3 is large: now $\xi << 1$ and T does not vary much since P_3 is fixed for the momentum space integration. Thus a PA becomes possible. This is the limit in which the work of Eckelt, Korsch and Philipp (1974) and Beard and Micha (1981) becomes a valid approximation.

4) The radial integral N has a factorization property if $T_L(q_j\Delta p)$ is factorizable. This aspect simplifies calculations for the post and prior forms of T, and entails an order of magnitude reduction in the computing time.

5) Recent experiments of Stewart, et al. (1988) with low projectile velocities show interesting "quasi-resonant" behavior with a highly favored rate for $\Delta j = -4\,\Delta n$ transitions. Their theoretical explanation in that paper and its sequel, Magill, et al. (1988), is based on classical trajectory analysis. Our formalism may prove relevant for a quantum mechanical analysis of this problem.

VII RECOMMENDATIONS:

Considerable effort has been invested in this problem during the Summer Program, and the results obtained so far already provide a significant extension of the theory of the Impulse Approximation. All earlier work has been based on the Peaking Approximation. This is probably the <u>first</u> effort to go beyond that restriction. We can thus expect this to be useful in many situations. In terms of the ξ-parameter introduced in the last section, $\xi \gg 1$ is the proper domain of application of the theory developed here. While some situations may directly fall in this category, many more are likely to have $\xi > 1$. Thus, on the <u>theoretical side</u> the next task would be to develop a more general approach:

(1) One possible avenue is to use the MTR in terms of q_1 and Δp. For post and prior forms the Legendre expansion is then exact. By expressing $\vec{q}_3$ and $\vec{q}_3{}'$ in the wave functions in terms of $\vec{q}_1$ it would be possible to do the radial integrals. The angular integrals will be more cumbersome and may lead to more Racah coefficients or even 9j symbols.

(2) Another possibility is to expand the T-matrix in the complete

set $Y_{LM}(\hat{q}_3)$ with coefficients $T_{LM}(q_3, \vec{\Delta p}, \vec{p}_3)$. The radial integrals will not pose any additional problems. Perhaps $|F_J|^2$ of Eq. (42) may be replaced by $|F_{JM}|^2$ with summation over both indices. This approach is not restricted to just the post or prior forms.

(3) Simpler approximations can also be developed.

For Applications, the results of Magill, et al. (1988) are very interesting and seem to fall in the $\xi > 1$ category in our classification.

(4) It would be worthwhile to apply the formalism as is, just to see if it captures the essence of their results. This should not take too long.

(5) Further extensions of theory should then be brought to bear on their full range of experiments.

(6) Some other papers in the literature also show the quasi-resonant phenomena; Thompson (1981). Other state selective studies such as Chawla, et al. (1988) may also be analyzed in terms of our more general IA theory.

(7) Finally, the original impetus for this work viz. the AFGL atmospheric and laboratory studies, should be analyzed in terms of our extended IA theory and its subsequent developments.

This would be a long-range, ongoing program and the next few steps can be taken through the follow-up Research Initiation Program.

REFERENCES

Beard, L.H. and D.A. Micha, J. Chem. Phys. 74, 6700, (1981).

Bogan, A., Phys. Rev. A 9, 1230, (1974).

Chawla, G., G. McBane and P. Houston, J. Chem. Phys. 88, 5481, (1988).

Eckelt, P., H.J. Korsch and V. Philipp, J. Phys. B. 7, 1649, (1974).

Magill, P., B. Stewart, N. Smith and D. Pritchard, Phys. Rev. Letters, 60, 1943, (1988).

Sharma, R.D., AFGL Report, AFGL-88-TR-0110, (1988).

Stewart B., P. Magill, T. Scott, J. Derouard and D. Pritchard, Phys. Rev. Letters, 60, 282, (1988).

Thompson, D.L., J. Chem. Phys. 75, 1829, (1981).

Van Leeuwen, J.M.J. and A.S. Reiner, Physica 27, 99, (1961).

Wu, T.T., Phys. Rev. 104, 1201, (1956).

1988 USAF-UES SUMMER FACULTY RESEARCH PROGRAM

GRADUATE STUDENT RESEARCH PROGRAM

Sponsored by the

AIR FORCE OFFICE OF SCIENTIFIC RESEARCH

Conducted by the

Universal Energy Systems, Inc.

FINAL REPORT

Total Dose Effect on Soft Error Rate For Dynamic MOS Memory Cells

Prepared by: Reuben Benumof, Ph.D.

Academic Rank: Professor

Department and University: Department of Applied Sciences, The College of Staten Island of the City University of NY

Research Location: AFGL/PHP, Hanscom AFB, Bedford MA 01731-5000

USAF Researcher: Edward G. Mullen

Date: 4 August 1988

Contract No: F49620-87-R-0004

Total Dose Effect on Soft Error Rate for Dynamic MOS Memory Cells

by

Reuben Benumof

Abstract

A simple model for the soft error rate for dynamic MOS random access memories due to normal galactic radiation was devised and then used to calculate the rate of decrease of the SEU rate with total radiation dose. The computation shows that the decrease in the soft error rate is of the order of one per cent per day if the shielding is 0.5 g/cm^2 and the spacecraft is in a geosynchronous orbit. The decrease is considerably less in a polar orbiting device.

Acknowledgement

I wish to thank the Air Force Systems Command and the Air Force Office of Scientific Research for sponsoring this research. Universal Energy Systems was concerned and helpful in all administrative aspects of this program. In particular, I wish to express my appreciation to Edward G. Mullen and A. R. Frederickson of the PHP branch of the Space Physics Division of the Air Force Geophysics Laboratory for their enlightening discussions.

1. Introduction

I have been interested in the effect of cosmic radiation on microelectronic circuits in space for a number of years. In particular, I have written several papers on models of bipolar, thin film, and metal-oxide-semiconductor field-effect transistors exposed to radiation.

The effects of cosmic radiation have been analyzed as either the result of the total absorbed dose or as the outcome of the passage of a single ion. Comparatively little work has been done on the extent to which the total dose affects single ion phenomena. Since the Space Physics Division of the Air Force Geophysics Laboratory is interested in the effects of cosmic radiation, an analysis of the effect of the total dose on single ion phenomena provides useful information.

2. Objective of the Research Effort

When a cosmic ion passes through a sensitive region of a memory cell, information may be inverted. The purpose of this research was to calculate the extent to which prolonged exposure to radiation affects the rate at which inversions or single event upsets (SEUs) occur in dynamic random access memory (DRAM) cells.

3. Effective Cross Section of a Sensitive Volume

An important consideration in the determination of the rate of occurrence of single event upsets in a DRAM cell is the effective cross section of the sensitive volume. We assume that the sensitive volume is convex and that all ion tracks intersect the surface twice, once at entrance and once at exit. No track ends in the volume.

The ionic flux producing SEUs is essentially isotropic.[1]

Consequently, the incident isotropic flux density per unit energy range of ion species i may be expressed as follows:

$$J_i(E) = \frac{n_i v_i}{4\pi} \quad , \tag{1}$$

where $J_i(E)$ is usually given in particles/cm^2 · s · sr · MEV, n_i is the number of ions per unit volume per unit energy range, and v_i is the speed of the ion in cm/s. The kinetic energy E_i of a cosmic ion and the speed v_i are related nonrelativistically as in the equation below:

$$v_i = \sqrt{\frac{2E_i}{m_i}} \quad , \tag{2}$$

where m_i is the mass of the ion.

An element of the total flux $d\Phi_i(E)$ per unit energy range incident on an element $d\underset{\sim}{S}$ of the surface of a sensitive volume may be obtained by integrating $J_i(E)$ as shown below.

$$d\Phi_i(E) = \int_0^{2\pi} \int_0^{\frac{\pi}{2}} \left(\frac{n_i v_i}{4\pi}\right)\left(-\hat{\underset{\sim}{s}}\right) \cdot \left(-d\underset{\sim}{S}\right) \sin\theta \, d\theta \, d\phi \quad , \tag{3}$$

where $-\hat{\underset{\sim}{s}}$ is an inwardly directed unit vector and $d\underset{\sim}{S}$ is outwardly directed. The origin of the spherical coordinate system is located on $d\underset{\sim}{S}$ and $\sin\theta \, d\theta \, d\phi$ is a differential solid angle in the direction of $\hat{\underset{\sim}{s}}$. All particles within the differential solid angle proceed in the direction of $-\hat{\underset{\sim}{s}}$ toward the surface element $d\underset{\sim}{S}$. Since

$$\hat{\underset{\sim}{s}} \cdot d\underset{\sim}{S} = dS \cos\theta$$

we get, after performing the integration in Eq. (3),

$$d\Phi_i(E) = \frac{n_i v_i}{4}\, dS \,. \qquad (4)$$

The total isotropic flux per unit energy range incident on the surface of sensitive volume is obtained by integrating Eq. (4). The result is

$$\Phi_i(E) = n_i v_i \left(\frac{S}{4}\right) \,. \qquad (5)$$

We note that

$$n_i v_i = 4\pi J_i(E) \,, \qquad (6)$$

and that, consequently, we may interpret $4\pi J_i(E)$ as the omnidirectional flux density per unit energy range. The quantity S/4 may be designated as the effective cross section $\bar{A}$ of the sensitive volume for the occurrence of soft errors. Thus,

$$\bar{A} = \frac{S}{4} \,. \qquad (7)$$

Equation (7) is the focal point of the above discussion.

We may now write

$$\Phi_i(E) = n_i v_i \bar{A} = 4\pi J_i(E)\, \bar{A} \,. \qquad (8)$$

The cross section $\bar{A}$ is a geometrical quantity and is the same for all species of ion. Hence, the total flux per unit energy range through the surface S due to all species of cosmic ion is

$$\Phi(E) = 4\pi \bar{A} \sum_i J_i(E) \,. \qquad (9)$$

Very often the quantity of greatest interest is the total flux through a surface S due to all species of ion having energy in excess of a minimum energy E_{min}. The total integrated flux $\Phi(>E_{min})$ is given by

$$\Phi(>E_{min}) = 4\pi \bar{A} \sum_i \int_{E_{min}}^{\infty} J_i(E)\, dE \qquad (10)$$

We shall use Eq. (10) to find the soft error rate.

3. General Formula for Soft Error Rate

A general formula for the soft error rate must take into account two conditions. The first is that a candidate ion must have enough energy to create sufficient charge in a sensitive volume to cause a single event upset. In quantitative terms, if Q_c is the critical charge to cause an SEU, then the energy E_i of the ion must be equal to or greater than a minimum energy E_{min} ; that is,

$$E_i \geq E_{min} = \frac{E_p Q_c}{q} , \tag{11}$$

where E_p is the energy required to form an electron-hole pair and q is the charge of an electron. The implied assumption in Eq. (11) is that all the electron-hole pairs formed within the sensitive volume by the cosmic ion are separated by the electric eld in the region. This assumption is reasonable and is normally made[2] when the sensitive region includes a p-n junction where the field intensity is high.

The second condition for an ion of species i to cause a soft error is concerned with the rate of deposition of energy and not merely with the amount of energy to be deposited. The rate of energy deposition L is called the stopping power or the linear energy transfer rate and is defined as follows:

$$L = - \frac{dE}{\rho dx} , \tag{12}$$

where ρ is the density of the medium and dx is an element of length. A common unit for L is MeV·cm^2/g. If we set ds equal to $\rho\, dx$, then

$$L = - \frac{dE}{ds} . \tag{13}$$

We shall call s the density path length. In terms of L and s, the energy deposited by an ion of species i along its path is sL_i. Consequently, a requirement for an ion to cause an SEU is that

$$\mathcal{A} L_i \geq \frac{E_p Q_c}{q} . \tag{14}$$

In writing Eq. (14) we assumed that L_i is constant over the entire path length s. For small sensitive volumes this is a good approximation.

Equation (14) is difficult to use because ions of species i may travel along paths having different lengths and may have different stopping powers because of their different energies. To simplify Eq. (14), we shall introduce an average density path length $\bar{\mathcal{A}}$. We define $\bar{\mathcal{A}}$ thus:

$$\bar{\mathcal{A}} = \rho \frac{V}{\bar{A}} , \tag{15}$$

where V is the volume of the sensitive region and $\bar{A}$ is given by Eq. (7). We now think of all the ions as traveling through the volume V along paths of the same average density length $\bar{\mathcal{A}}$. Substituting for s in Eq. (14) permits us to write

$$L_{min} = \frac{E_p Q_c}{q \bar{\mathcal{A}}} , \tag{16}$$

where L_{min} is the minimum stopping power that an ion may have to cause an SEU. Equation (16) states that the minimum energy $E_p Q_c/q$ must be deposited in a path of density length exactly $\bar{\mathcal{A}}$. Essentially this equation relates the minimum energy of an ion of any species to the minimum rate of energy deposition.

An ion of species i may be described by stating its energy E_i and

stopping power L_i. We note, however, that L_i is a function of E_i. The flux density of such ions may be specified per unit energy range by giving $J_i(E)$ in units of particles /cm^2·sr·s·MeV, or, alternatively, may be specified per unit stopping power range by giving $J_i(L)$ in units of particles /cm^2·sr·s·MeV·cm^2·g^{-1}. The same particle flux may be described either by $J_i(E)$ or $J_i(L)$. In fact,

$$J_i(E)\,|dE| = J_i(L)\,|dL| \,. \tag{17}$$

The absolute value signs are introduced because dL/dE may be negative. Integrating Eq. (17), we get

$$\int_{E_{min}}^{\infty} J_i(E)\,dE = \int_{L_{min}}^{L_{i\,max}} J_i(L)\,dL \,, \tag{18}$$

where $L_{i\,max}$ is the maximum possible stopping power of an ion of species i. Thus, Φ in Eq. (10) may be expressed as

$$\Phi = 4\pi \bar{A} \sum_i \int_{L_{min}}^{L_{i\,max}} J_i(L)\,dL \,. \tag{19}$$

The integrated flux Φ states the number of particles traversing the sensitive volume V per unit time. Each of these particles is capable of causing an SEU. Hence, if the volume V is sensitive only a fraction f of the time, then the soft error rate U is

$$U = 4\pi f \bar{A} \sum_i \int_{L_{min}}^{L_{i\,max}} J_i(L)\,dL \,, \tag{20}$$

where U is expressed in units of errors per unit time per information bit. Equation (20) is a simplified version of the formula for U given by Adams.[3]

4. Effect of Total Radiation Dose on Soft Error Rate

We now wish to determine the effect on the soft error rate U of

impinging ions that do not cause SEUs. Basically, we wish to find $dU/d\gamma$, where γ is the radiation dose in rads and is much larger than the energy deposited by ions causing SEUs. Since U is a function of L_{min} as shown by Eq. (20), we must first express L_{min} in terms of γ . From Eq. (16) we know that

$$L_{min} = \frac{E_p Q_c}{q \bar{A}} .$$

In a 3-transistor dynamic NMOS memory cell,[4] when the generated charge Q_c in the source depletion region of one transistor is transferred to the gate of a second transistor, the latter transistor is turned off, and the stored bit of information is destroyed. The relation between the gate voltage and Q_c is [5]

$$Q_c = C_{ox} (V_G - V_T) , \qquad (21)$$

where V_G is the gate voltage, V_T the threshold voltage, and C_{ox} the oxide capacitance. Clearly, if V_G is fixed then

$$dQ_c = - C_{ox} dV_T . \qquad (22)$$

The increment dQ_c in critical charge is positive because the threshold voltage shift due to radiation is in the negative direction.[6] Finally, we may write

$$dV_T = - K d\gamma , \qquad (23)$$

In the above equation, the constant K in V/rad is given by[7]

$$K = 3.6 (10^{-10}) X_{ox}^2 , \qquad (24)$$

where X_{ox} is the oxide thickness in angstroms. Thus,

$$dL_{min} = \frac{E_p}{q \bar{A}} dQ_c = - \frac{E_p}{q \bar{A}} (C_{ox} dV_T) = \frac{E_p C_{ox}}{q \bar{A}} K d\gamma . \qquad (25)$$

The last equality gives the relation between dL_{min} and $d\gamma$.

We now differentiate Eq. (20) and use Eq. (25). The result is

$$\frac{dU}{d\gamma} = -\left(\frac{E_p C_{ox} K}{\rho \bar{A}}\right) 4\pi \rho \bar{A} \sum_i J_i(L_{min}). \qquad (26)$$

The minus sign in Eq. (26) shows that the soft error rate decreases with increased total radiation dose. Experimentally, this was shown by R. Berger et al.[8] and A.R. Knudson et al.[9] for MOS DRAMs.

A crucial question is whether the rate of decrease is significant for radiation encountered in satellite orbits. We use the data provided by Pickel and Blandford[4,10] for a 3-transistor dynamic NMOS RAM cell. The data are listed below.

Dimensions of sensitive region:

$23.5\,\mu m \times 31.5\,\mu m \times 8.5\,\mu m$

Volume of sensitive region:

$V = 6.292 \times 10^{-9}\ cm^3$

Effective cross section of sensitive region:

$\bar{A} = \frac{S}{4} = 6.04 \times 10^{-6}\ cm^2$

Density of silicon: $\rho = 2.3\ g/cm^3$

Average density length:

$\bar{\lambda} = \rho \frac{V}{\bar{A}} = 2.4 \times 10^{-3}\ g/cm^2$

Formation energy of an electron-hole pair in Si:

$E_p = 3.6 \times 10^{-6}$ MeV/e-h pair

Experimentally determined critical charge Q_c:[10]

$Q_c = 0.6 \times 10^{-12}$ C

Electron charge q: $q = 1.6 \times 10^{-19}$ C

Minimum stopping power from Eq. (16):

$L_{min} = 5.6 \times 10^3\ MeV \cdot cm^2 \cdot g^{-1}$

Gate voltage V_G: $V_G = 5$ V

Threshold voltage V_T: $V_T = 2$ V

From Eq. (21): $C_{ox} = 0.2 \times 10^{-12}$ F

From Eq. (24) with $x_{ox} = 700$ Å :

$K = 1.8 \times 10^{-4}$ V/rad

Fraction f of time that bit is stored: $f = \frac{1}{2}$

From E.L. Petersen et al.:[11]

$$4\pi \sum_i J_i(L_{min}) = \frac{5.8(10^6)}{L_{min}^3} = 3.3 \times 10^{-3} / cm^2 \cdot day \cdot Mev \cdot cm^2 \cdot g^{-1}$$

Using the above data and substituting in Eq. (26), we obtain

$$\frac{dU}{d\gamma} = -3.4 \times 10^{-9} \text{ errors/day} \cdot \text{bit} \cdot \text{rad} .$$

A 4K RAM contains 4096 cells, and the memory on which the above data is based contains 24 such RAMs. Consequently, $dU/d\gamma$ for this memory is -3.3×10^{-4} errors/day rad. In a spacecraft in a geosynchronous orbit the daily increment in γ beneath 0.5 g/cm^2 of shielding is of the order of 300 rads.[12] Since the observed error rate U for this memory was approximately 1/day,[4] the decrease in error rate would be approximately one per cent per day in a geosynchronous orbit. Polar orbiting satellites experience radiation dose rates that are considerably less than that in a geosynchronous orbit, and consequently, the decrease in error rate is much smaller.

5. Discussion and Summary

Information is stored in a MOS DRAM cell in the form of the charge on a MOS capacitor. The occurrence of a SEU in such a cell depends on whether the charge induced by a cosmic ion causes the MOS capacitor to discharge. If the MOS storage capacitor is the gate oxide capacitance of a transistor, the system is simple to model on a first order basis, as

was done above. The crucial parameter in the model is the critical charge Q_c for upset.

For comparison, we briefly consider a CMOS static RAM (SRAM) cell. A CMOS SRAM cell consists of two cross-coupled inverters, each consisting of a p-channel MOSFET connected drain to drain to an n-channel MOSFET. In state 1 of this flip-flop, p-channel MOSFET P_1 of the first inverter and n-channel MOSFET N_2 of the second inverter are on. The other two transistors, N_1 and P_2, are off. As a result of a cosmic ion strike in the drain region of P_2, N_1 is turned on with N_2 still on.[13] Only one of these two transistors can remain on. If N_1 remains on, the flip-flop has undergone a transition to state 2, with the result that information is lost. If N_2 remains on, the flip-flop remains in state 1, and information is conserved. We now recall that exposure to radiation causes the threshold voltage of both N_1 and N_2 to shift in the negative direction. This means that more charge is needed to turn N_2 off as shown by Eq. (22), whereas less charge must be supplied to the gate of N_1 to turn N_1 on. Whether the SEU rate increases or decreases is difficult to determine analytically. The critical charge Q_c for upset depends upon various circuit parameters and is best determined by experiment as was done by Pickel and Blandford[10] for the DRAM considered above. Campbell and Stapor[14] found experimentally that the SEU rate in an SRAM increases with total dose in contrast to the decrease of SEU rate with total dose in a DRAM.

In summary, the decrease of the soft error rate in a DRAM in a geosynchronous orbit is of the order of one per cent per day if the shielding is 0.5 g/cm^2. In a polar orbit, the decrease would be considerably less.

7. Recommendations

a. The rate of single event upsets is an important consideration in the design of electronic circuits in space. As indicated in the foregoing analysis, to minimize the SEU rate the effective cross section of a memory cell must be made as small as possible and the critical charge must be made as large as possible.

b. Research is needed to extend the results of the above analysis to static MOS random access memory cells for which experiments indicate that the SEU rate increases as the exposure to cosmic radiation increases.

References

[1] D.F. Smart and M.A. Shea, Galactic Cosmic Radiation and Solar Energetic Particles in Handbook of Geophysics and the Space Environment edited by A.S. Jursa (Nat. Tech. Inf. Service, Springfield, VA, 1985).

[2] J.C. Pickel, IEEE Trans. Nucl. Sci. NS-29, 6, 2049 (1982).

[3] J.H. Adams, Cosmic Ray Effects on Microelectronics, Part IV, NRL Memorandum report 5901 (Naval Res. Lab., Wash., D.C., 1986), p. 7.

[4] J.C. Pickel and J.T. Blandford, IEEE Trans. Nucl. Sci. NS-25, 6, 1166 (1978).

[5] R.S. Muller and T.I.Kamins, Device Electronics for Integrated Circuits, 2nd Ed. (John Wiley, New York, 1986) p. 398.

[6] J.R. Srour et al., Radiation Effects on and Dose Enhancement of Electronic Materials (Noyes Publications, Park Ridge, N.J., 1984), p. 63.

[7] J.M. McGarrity, IEEE Trans. Nucl. Sci. NS-27, 6, 1739 (1980).

[8] R. Berger et al., IEEE Trans. Nucl. Sci. NS-30, 6, 4256 (1983).

[9] A.R. Knudson et al., IEEE Trans. Nucl. Sci. NS-30, 6, 4506 (1983).

[10] J.C. Pickel and J.T. Blandford, IEEE Trans. Nucl. Sci. NS-27, 2, 1006 (1980).

[11] E.L. Petersen et al., IEEE Trans. Nucl. Sci. NS-30, 6, 4533 (1983).

[12] A.L. Vampola, Radiation Effects on Space Systems and Their Modeling in Space Systems and Their Interactions with Earth's Space Environment edited by H.B. Garrett and C.P. Pike (Amer. Inst. of Aeronautics and Astronautics, New York, 1980).

[13] L.L. Sivo et al., IEEE Trans. Nucl. Sci. NS-26, 6, 5042 (1979)

[14] A.R. Campbell and W.J. Stapor, IEEE Trans. Nucl. Sci. NS-31, 6, 1175 (1984).

1988 USAF-UES SUMMER FACULTY RESEARCH PROGRAM

GRADUATE STUDENT RESEARCH PROGRAM

Sponsored by the

AIR FORCE OFFICE OF SCIENTIFIC RESEARCH

Conducted by the

Universal Energy Systems, Inc.

FINAL REPORT

DIGITAL PHOTOMETRIC CALIBRATION OF AND ANALYSIS WITH VIDEO IMAGERS IN THE ULTRAVIOLET

Prepared by:	Donald F. Collins, PhD
Academic Rank:	Faculty are unranked
Department and University:	Physics Department Warren Wilson College
Research Location:	AFGL/LIU Hanscom AFB, MA 01731-3000
USAF Researcher:	Dr. Chris Stergis

Date:	5 August 1988
Contract No:	F49620-87-R-0004

DIGITAL PHOTOMETRIC CALIBRATION OF AND ANALYSIS WITH VIDEO IMAGERS IN THE ULTRAVIOLET

by

Donald F. Collins

ABSTRACT

Algorithms and computer programs were developed for the following tasks: a) analyze close-up images of plumes from rocket engine test firings to determine the plume axis and the plume profile near the edge of the nozzle; b) to calibrate imaging photometers with point-like images; c) to measure the total signal in faint star images with poor signal/noise. The focal length of a supplementary telescope lens was determined which would enhance the images of a large format telescope with respect to field of view and speed. Tutorial instruction was given to AFGL personnel on the use of commercial software packages (ASYST and MATLAB) which the author has used extensively in his analysis.

Acknowledgements

I wish to thank the Air Force Systems Command and the Air Force Office of Scientific Research for sponsorship of this research. I am grateful to Universal Energy Systems, Inc. for the administrative and directional aspects of this program and to the Air Force Geophysics Laboratory for providing the facilities and a stimulating environment for conducting this research.

Special recognition should be made to Mr. Victor Baisley of AFGL for his assistance in obtaining calibration data and field data and Mr. Joe Larrabee of AFGL for the operation of the UV calibration facility, and to Dr. Tony Dentamaro for running the LOWTRAN 6 code for atmospheric transmission. Above all I wish to thank Dr. Chris Stergis of AFGL for his support, encouragement, and direction for this summer experience.

DIGITAL PHOTOMETRIC CALIBRATION OF AND ANALYSIS WITH VIDEO IMAGERS IN THE ULTRAVIOLET

I. INTRODUCTION:

Having developed image processing procedures during a 1986-87 research initiation program, I was selected to continue this work during the summer of 1988 at AFGL to develop calibration analysis programs and field analysis programs for video imagers sensitive to the ultraviolet.

II. OBJECTIVES OF THE RESEARCH EFFORT:

The research goals and objectives for the summer of 1988 are:

A. Calibrate several UV Imagers. This includes spectral sensitivity, resolution vs. intensifier gain, and geometric properties.

B. Develop a universal standard procedure for the analysis of optical calibration data.

C. Develop automatic algorithms for the analysis of rocket plume images acquired with the imagers.

D. Instruct AFGL personnel in the use of ASYST and MATLAB (data analysis packages Dr. Collins uses at Warren Wilson College and since acquired by the AFGL). These packages and the instruction have proved to be extremely beneficial to the AFGL - especially for the UV calibration facility.

E. Develop and learn utility programs for various sophisticated image processing functions.

F. In addition to the work of direct interest to the AFGL with rocket plumes, Dr. Collins will work with ionospheric and auroral data, develop additional applications for image processing for physics and

Warren Wilson College, and will plan future research for Warren Wilson College by submitting an RIP proposal or an AFOSR proposal or both.

G. Upon arrival at AFGL image photometry was developed to locate the plume axis of rocket test firings in order to study the brightness profiles near the edge of the plumes. These images were photographed close to the rocket engine at Arnold Engineering and Development Center (AEDC).

H. A modification of an existing telescope was calculated in order to improve the match in field of view of the instrument with the size of the detector.

Careful evaluation of the objectives A - F above indicated that item C would not be very beneficial. Item A was largely omitted because only one UV imager was available, only for a small fraction of the 10 week residence. The calibration procedure had already been developed by the author in 1986, a procedure which has since been implemented by AFGL personnel on other imagers. Items G and H were added to the plan.

III. ANALYSIS OF CALIBRATION DATA

A major improvement for analyzing the calibration images was developed. The imager is placed in a calibration chamber which consists of collimated monochromatic light. The telescope focuses the collimated light as a spot on the photocathode. When the images are digitized, 32 frames are averaged to minimize the noise. The total signal in Analog Digital Units (ADU) is calculated by adding the net signal ADU's over a frame (64 x 64 pixels) surrounding the point-like image. The new procedure subtracts a background frame (recorded in the absence of light) from the raw digitized image to obtain the net signal. This method eliminates fixed-pattern noise in the CCD camera from the image.

The old method determined the background by averaging around the perimeter of the 64 x 64 frame and determining a threshold of pixel values to contribute to the sum which could omit a sizeable fraction of the signal (about 5%).

The uncertainty in the total signal by means of adding all net ADU's in the frame is determined by the noise in the video electronics. The standard deviation in the signal is calculated from

$$\delta(\text{signal}) = \sigma\sqrt{(N)} \qquad (1)$$

where σ is the standard deviation of the net ADU values obtained from the perimeter of the 64 x 64 frame, and N is the total pixels in the frame (64 x 64 = 4096). This uncertainty is about 35 ADU when averaging 32 frames and is less than 1% of the total signal for moderate signals.

IV. STELLAR PHOTOMETRY

When conducting rocket plume photometry during a launch, a measurement of the transmission of the atmosphere at the wavelengths of interest is needed to calculate the absolute plume radiance at the source. Because the UV intensities of many stars are known from spacecraft measurements,[1] it was proposed to photograph at least one star with various filter configurations near launch time to measure the atmospheric transmission at various wavelengths. Images of several bright stars were photographed on 25 July 1988 from the rooftop of AFGL. This was a night of high humidity, thin clouds, and a bright moon, but several stars were successfully photographed through a single filter (30% transmission at 2970 A x 500 A bandwidth). Both α-Lyr (Vega) and α-Aql (Altair) were analyzed by procedures similar to the analysis of the signal in the calibration runs: the total signal in ADU is obtained by summing all the net pixel values in the image. However, for faint point-

[1] Code, A. D. and M. R. Meade, Astrophysical Journal Supplement Series 39, pp.195-289 (Feb. 1979)

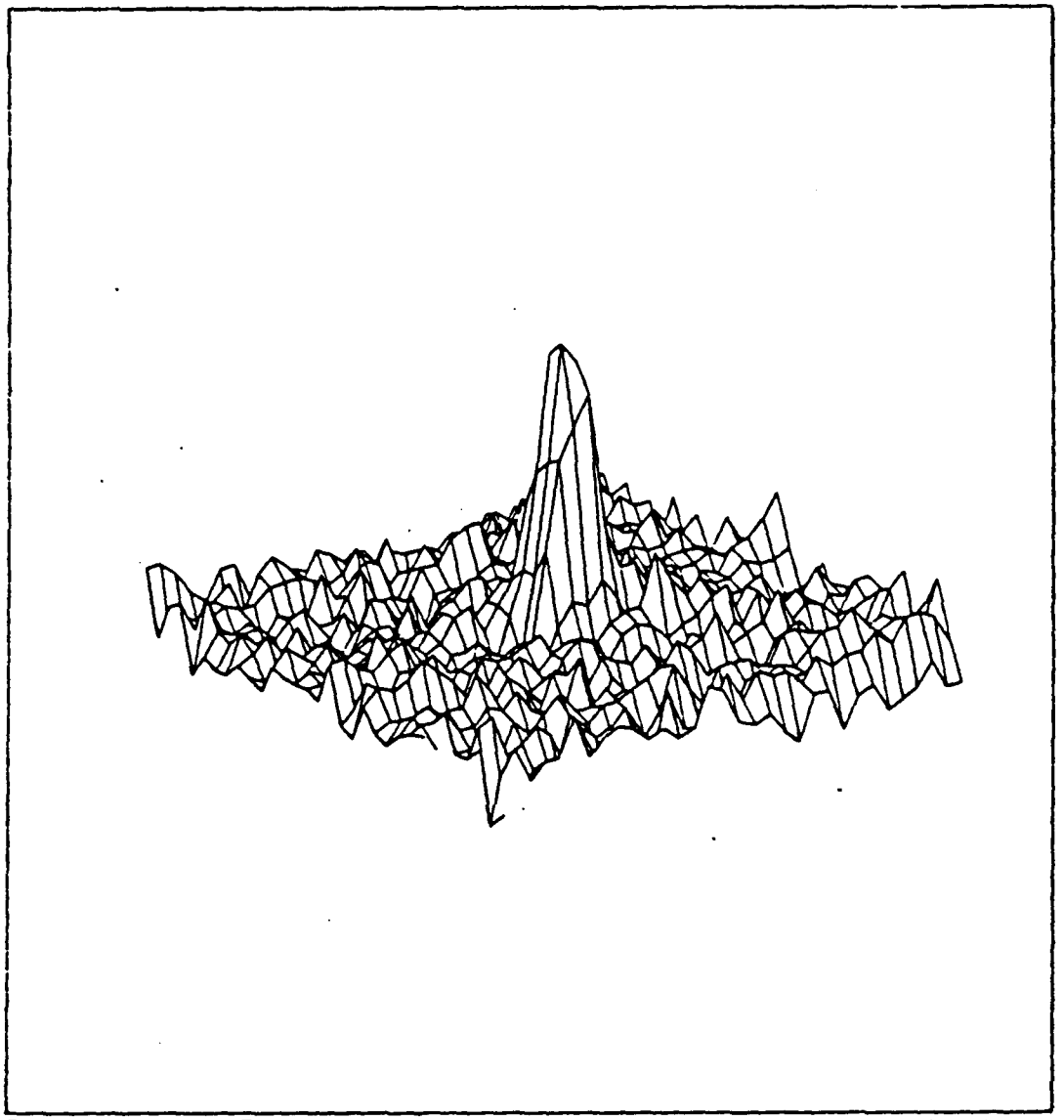

Figure 1. A 3-dim display of the star α-Lyr (Vega) at 2970 A showing the large noise in the background.

like images, the noise or fluctuations in the background part of the image can dominate the signal (see Figure 1).

The successful solution to this problem consists of making the summing box sufficiently small that the noise is minimized. First the background frame is subtracted from the stellar frame. Second the width of the image spot is estimated by calculating the full-width at half maximum (FWHM). The FWHM is estimated by counting all pixels with

values greater than the mid-range of pixel values in the frame. The square root of this count is approximately the diameter of the spot (FWHM). The integration size is chosen to be 2.2 times the FWHM which includes about 97% of the area of the image spot. The calculated results for the atmospheric transmission measured for both α-Lyr and α-Aql are shown in Table I. The estimated atmospheric transmission[2] under the conditions of viewing at 2970 A x 500 A bandwidth, zenith, and "excellent" visibility is 0.038. The factor of four discrepancy may be accounted for light leakage through the rejection regions of the single 2970 A filter used for the star test. Further calibration of the filters in question are needed to resolve this discrepancy.

Table I. Atmospheric transmission as measured by stellar photometry in the UV.

Star	UV flux Measured *detector* outside atmosphere (Code and Meade) (Photon/ms)	Atm signal (Photon/ms)	trans
α-Lyr	3.48x104	4.7x103	.14
α-Aql	1.19x104	1.7x103	.14

[2] Kneizys, F. X., E. P. Shettle, W. O. Gallery, H. H. Chetwynd, Jr, L. W. Abreu, J. E. A. Selby, S. A. Clough, and R. W. Fein, "Atmospheric Transmittance/Radiance: Computer Code LOWTRAN 6", AFGL-TR-83-0187, 1 Aug. 1983.

V. TELESCOPE ENHANCEMENT

The UV imagers consist of a UV transmitting Cassegrain telescope, filter wheel, an image intensifier consisting of a photo cathode, micro-channel-plate electron multiplier, and phosphor readout. The phosphor is imaged onto the CCD sensor of a video camera by an f/0.95 copy lens. The copy lens also reduces the image from the 25 mm diameter intensifier output to the 8.8 mm x 6.6 mm CCD sensor. The CCD camera produces a standard TV video (RS-170) which is recorded on video tape to be later digitized by a video processing unit (FG-100/AT) in an MS-DOS desk-top computer.

When designing a telescope for photometry of near point-like sources (flames, stars, distant plumes) the only geometrical parameters are the focal-length and diameter (as well as the related f/no: focal-length/diameter). The performance trade-offs are spatial resolution (enhanced by a long focal-length) and image brightness (enhanced by a small f/no or short focal-length.

One of the imaging units is currently being fitted with an 18 inch diameter Cassegrain telescope with 131 inch effective focal-length (f/no = f/7.3). With this long focal length, the field of view subtended by the 1 inch diameter intensifier is 0.44 degree (less than the diameter of the moon or sun when viewed from earth) which makes tracking of a moving rocket difficult. In addition, the 1 inch diameter detector is a poor match for the large format telescope (the image size is about 3.5 times the size of the photocathode).

A converging lens of appropriate focal length placed on the output aperture of the telescope improves the optical coupling efficiency as well as increases the speed (smaller f/no.) as shown in Figure 2. Using the thin lens equation,

$$\frac{1}{i'} = \frac{1}{f} - \frac{1}{i} \qquad (2)$$

where f is the focal length of the converging lens, i is the original image distance from the lens and is negative in eq.

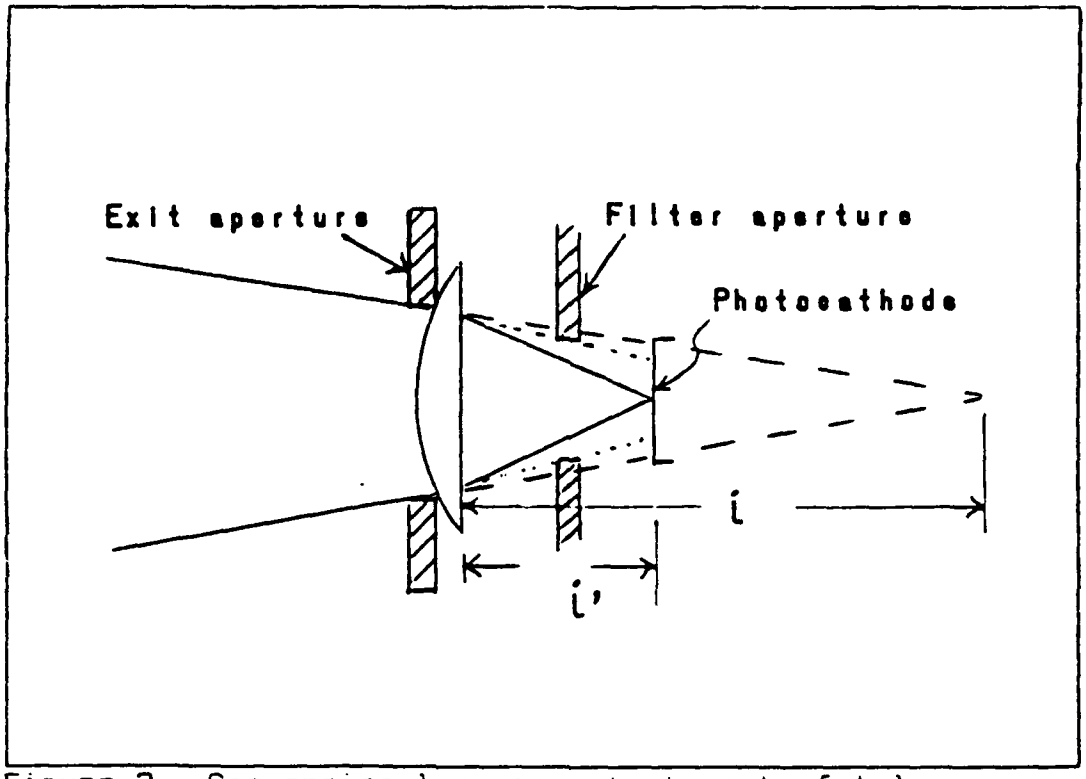

Figure 2. Converging lens on output port of telescope to increase field of view and telescope speed.

(2), corresponding to a virtual "object" and i' is the new image position. From geometry the parameters of interest are calculated and shown in Table II for the various focal-length quartz lenses available. As can be seen from Table II the presence of the converging lens decreases the f/no by a factor of about 7 thus increasing the brightness by about

Table II. Comparison of various focal-length converging lenses at output of 18 inch telescope.

Focal length	f/no	Image location wheel (cm)	Field of view (deg)	Vignetting by filter (in)
No lens	f/7.3	18.0	.437	---
200 mm	f/0.95	9.5	.83	.25
500 mm	f/1.3	13.2	.58	.2
1000 mm	f/1.5	15.25	.514	.16

50 $(1/(f/no)^2)$. One will also expect numerous aberrations and coma from such a small f/no using a simple lens. With a plano-convex lens, the convex side should be away from the image to minimize spherical aberration. Another important factor is the vignetting by the filter aperture in the much larger angle of the convergence cone (see Figure 2). The vignetting in Table II is the radial reduction in the edge of the image caused by the shadow of the filter aperture.

VI. CLOSE-UP BRIGHTNESS PROFILES

A. Description of the problem

An AFGL UV imager had photographed the plume produced by the test firing of a solid fuel propulsion unit at Arnold Engineering and Development Center (AEDC). A preliminary scan of the brightness of the plumes immediately aft of the nozzle showed that the intensity of the plume radiation extended radially beyond the edge of the nozzle opening.[3] This was not expected. The images have since been analyzed more carefully to determine the center of the nozzle. The nozzle is not visible in the UV images, and only one edge of the flame was visible due to a limited field of view. The center of the flame was determined from the maximum brightness; the nozzle edge was determined by the field of view. The radiation profile relative to the nozzle immediately below the nozzle opening was then determined.

B. Location of the nozzle center

It is assumed that the image is brightest along the rocket axis aft of the exit nozzle. Therefore the center of the plume should be located where the average maximum from every line in the digital image is located. Because of the noise in the images, one finds considerable fluctuation in

[3] C. Stergis, V. Baisley, J. Lowrance, and G. Lemunyan, "Ultraviolet Radiations from Super Bates Motors (U)", Paper 1105, Proc. JANNAF Plume Technology Meeting, April, 1988.

the horizontal position of each lines' maximum value. To locate the plume axis, each image line is read and the maximum brightness value in each line is located. The pixel corresponding to that maximum value is replaced by a white dot. Figure 3 shows a digital image processed with this technique. The center of the plume is then taken to be the average horizontal position of the white dots in the figure. The average position was located using the a screen cursor and human judgement, and the uncertainty was located by repeating the process and noting the fluctuations in the estimated position. Some of the images did not permit this technique because the peak brightness of the image was outside the field of view.

C. Photometry curves

The first 10 lines at the top of the flame were averaged and plotted in Figure 4 for each of the 4 test firings. If one examines the brightness curves in Figure 4, one observes that the brightness is relatively constant near the center of the plume; then there is a knee, or abrupt change in slope near the lateral edge of the nozzle. Beyond the knee towards the outside of the plume, the intensity drops to zero at varying rates. The intensity for largest aluminum composition in the fuel drops to zero the slowest. The edge of the flame is more poorly defined for the test with the largest aluminum loading. The curves in Figure 4 are aligned horizontally so that the knees are all in the same horizontal positions.

D. Results

From Figure 4, three positions are located for each curve: 1) the position of the center of the plume from the procedure outlined in section VI.B; 2) the knee or change in slope; and 3) the limit of detectability of the flame - where the flame disappears into the background noise. The various distances are shown in Table III. By comparing the tail length between the background level and the knee one

sees that the greater the composition of aluminum in the fuel, the greater the diffusion of radiation beyond the geometric limits defined by the nozzle. The anomaly found for the 5 % aluminum loading in Table III can be attributed by the noisy data for those images. The raw images were barely detectable due to the filters on the detector, hence the large uncertainty in the edge-knee distance.

It should also be emphasized that these measurements make use of the assumption discussed in section VI.B that the intensity of the plume is a maximum along the axis of the rocket engine. If the field of view were adjusted wider to show both sides of the plume, these measurements could be made with more confidence. In any case, the presence of aluminum in the fuel mixture changes the pattern in the photometry of the plume near the nozzle opening.

Table III. Comparison of brightness profile for various aluminum loadings.

Aluminum composition	Edge-knee distance	Edge-center distance
20 %	(14.7 ± .5)cm	(45.9 ± 2)cm
15 %	(12.2 ± .5)cm	
5 %	(19 ± 4)cm	
0.5 %	(7.4 ± .5)cm	(24 ± 2)cm

E. Visualization Enhancements

The radial sections plotted in Figure 4 show the brightness only in the image next to the nozzle opening. The images shown in Figure 3 contain more information (i.e the whole image) but one cannot examine the gradients in the images very well. 3-D plots of the images for 20 % aluminum and 0.5 % aluminum are shown in Figure 5 and in Figure 6. These 3-D plots show the gradients in the images very well. In addition they show the curvature in the intensity vs

position better than the false color images. The primary purpose of these 3-D plots is to enhance the morphology and gradients of the images.

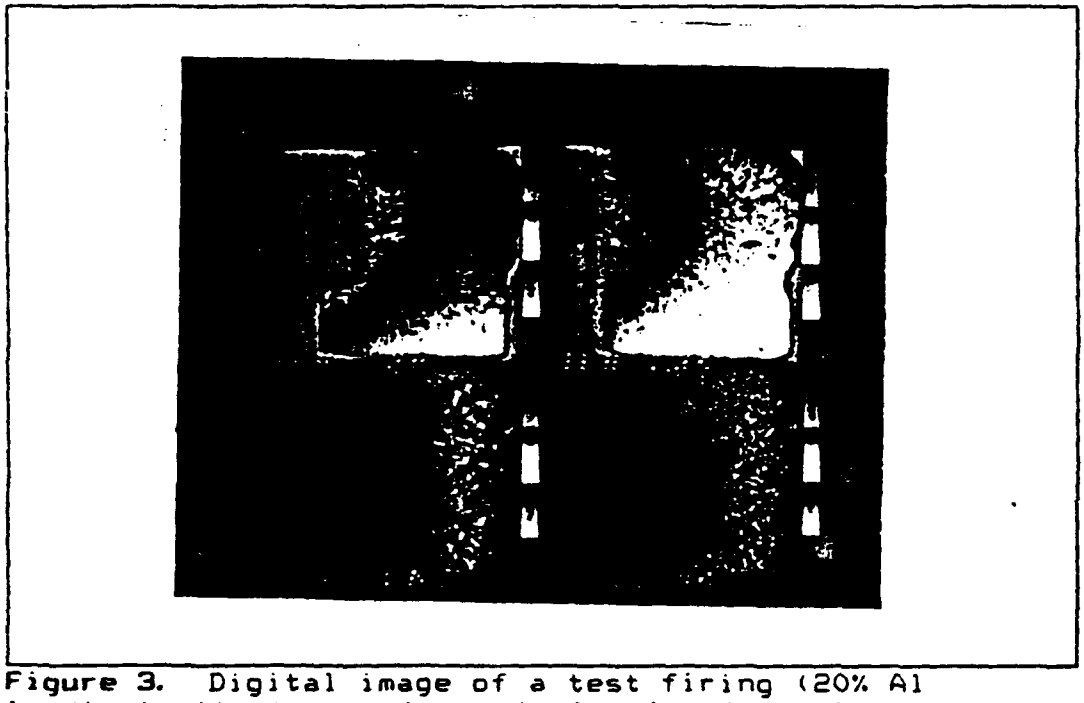

Figure 3. Digital image of a test firing (20% Al loading) with the maximum pixel value in each row indicated. Left: 300 nm; right: 320 nm

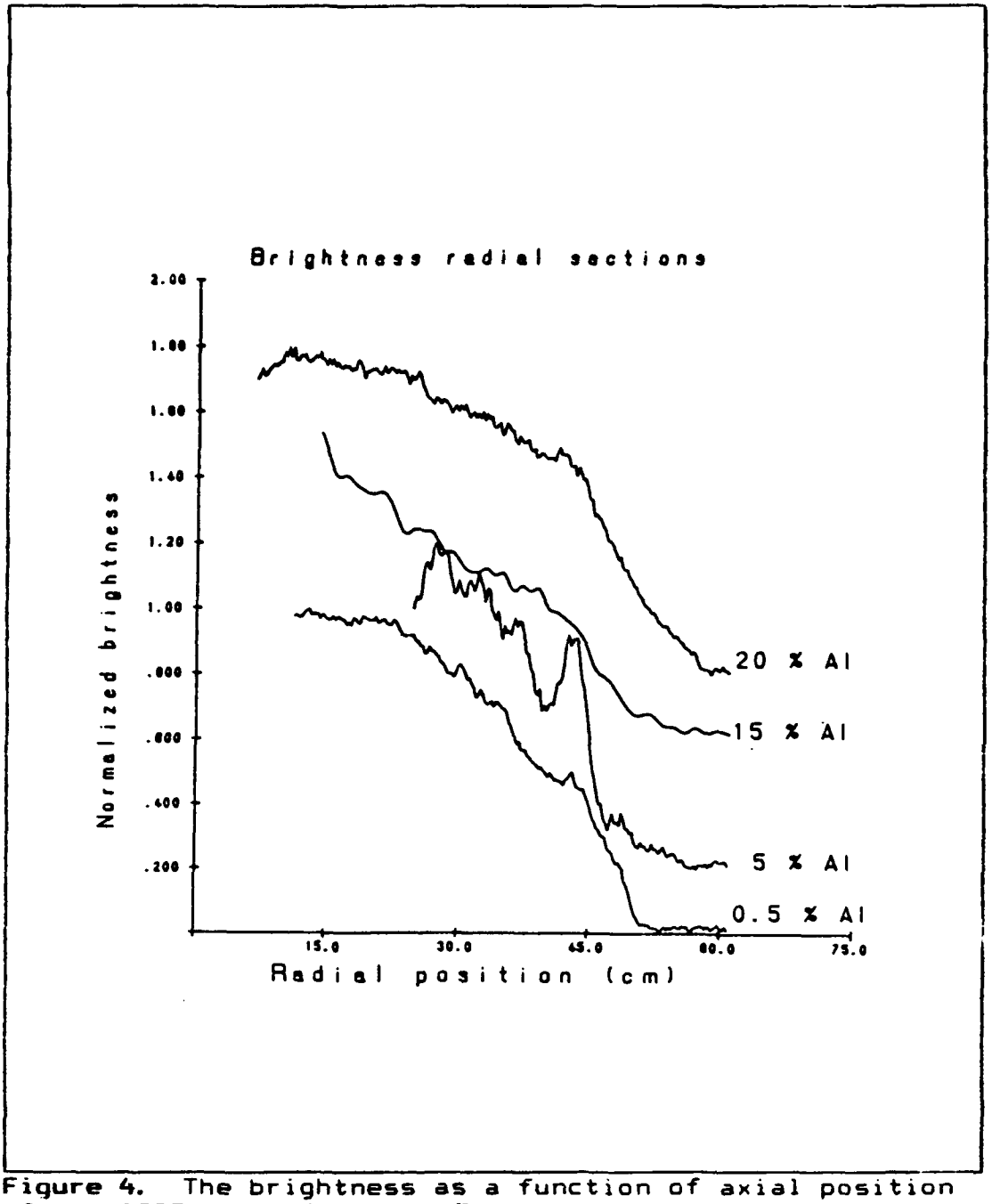

Figure 4. The brightness as a function of axial position of the AEDC plume images. The curves have been displaced vertically for visibility.

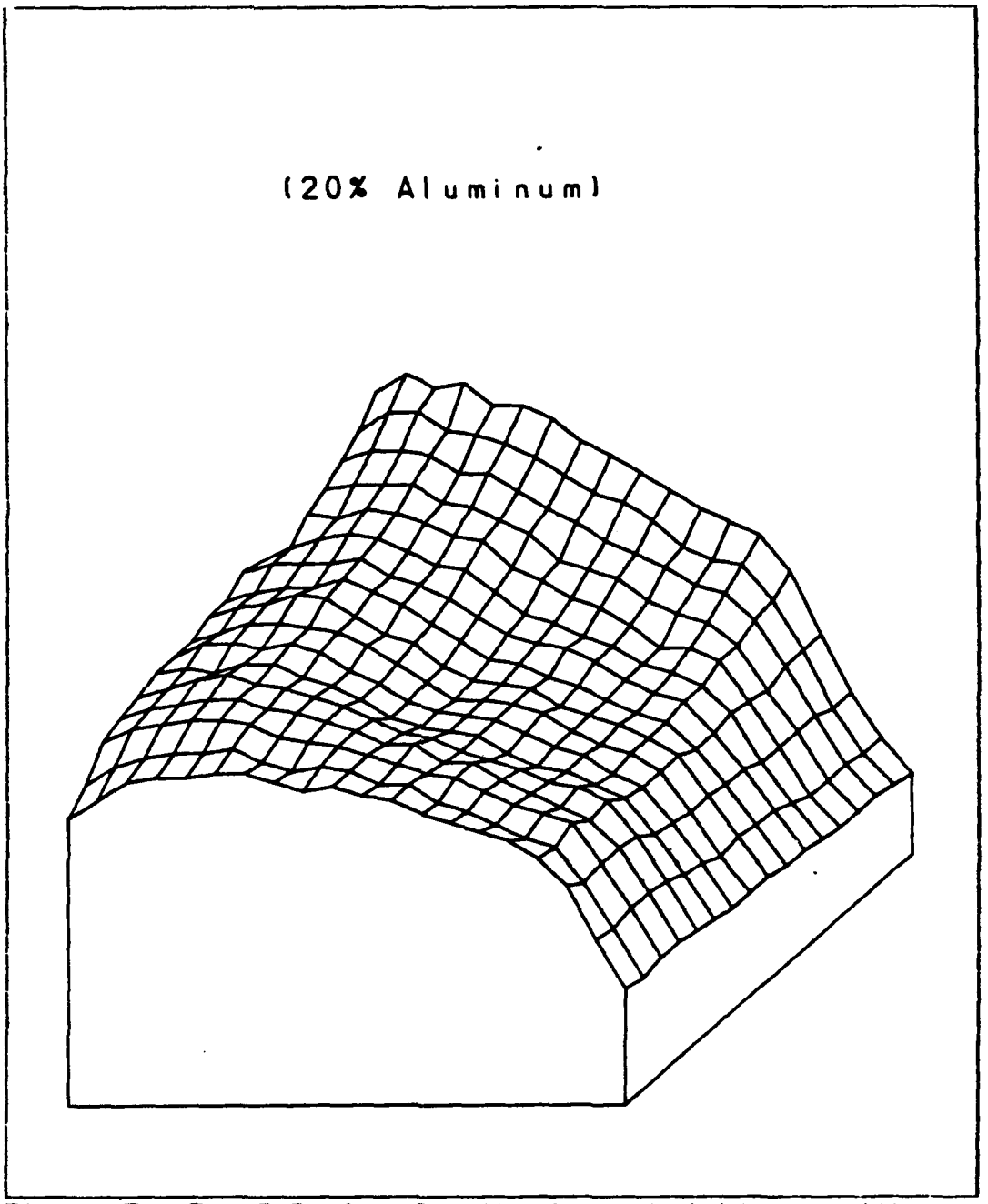

Figure 5. The 3-D plot for the image brightness with 20% aluminum loading. This plot is obtained from the digital image of ?. The nozzle opening in both Figure 5 and this figure is facing the observer

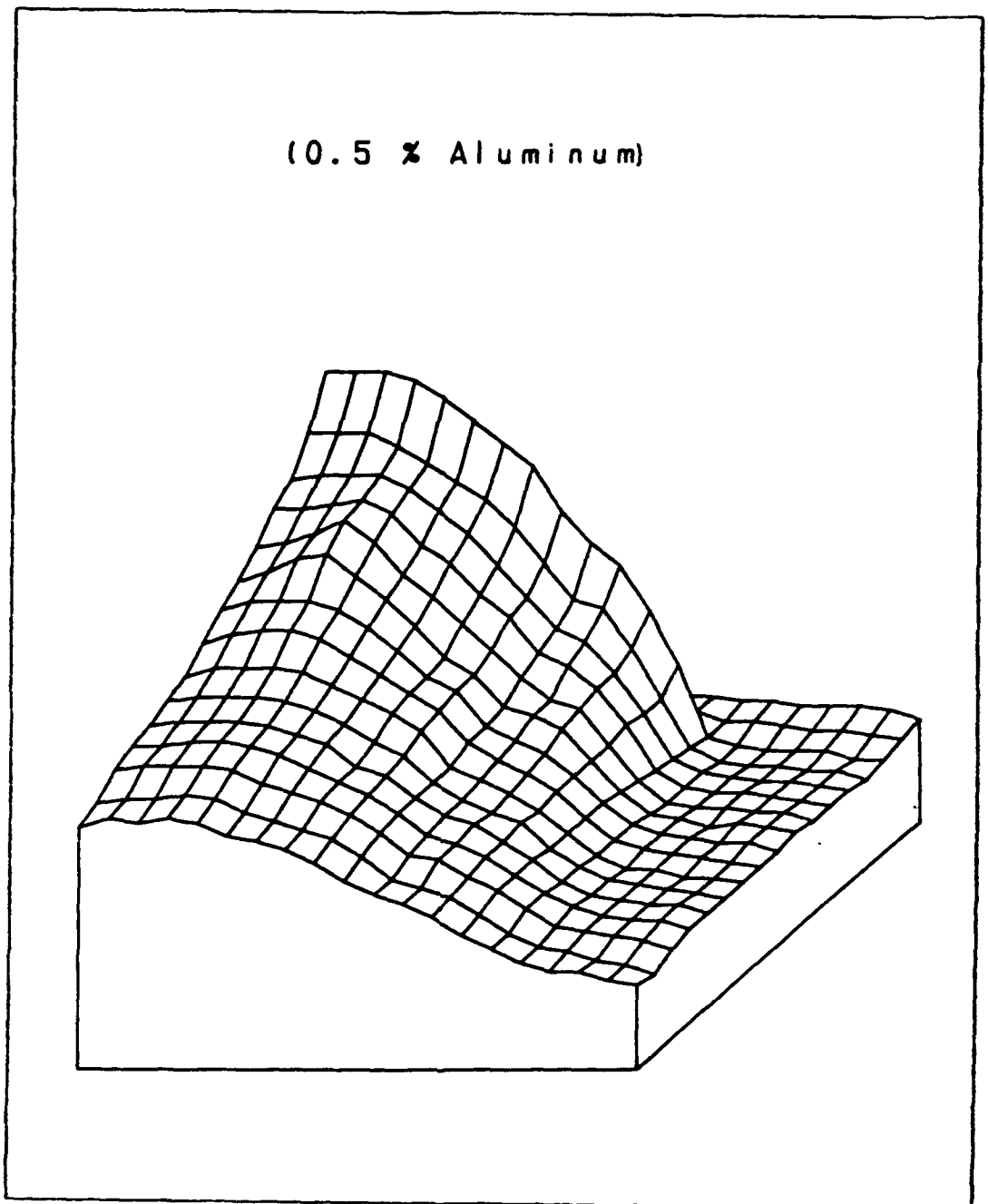

Figure 6. 3-D plot of the image from 0.5 % aluminum loading in the fuel

VII. RECOMMENDATIONS

A. 12-Bit Images

The 8-bit digitizer, the video recording system, and the Moire interference between the CCD pixel grid and the digitizing grid result in a rather limited dynamic range (≈100). By developing a system in which every pixel of a CCD detector is digitized at 12-bit precision, bypassing RS 170 video, the dynamic range should be improved by a factor of ≈10 at the expense of speed of acquisition (several seconds per frame as opposed to 1/30 sec per frame.

B. Commercial Image Packages

The success of ASYST for analyzing and plotting typical laboratory data indicates that an analogous package for images as large as 512 × 512 pixels should also prove beneficial for the AFGL, especially since the death of Dr. Norman Rosenberg who had devoted his full professional effort to developing and maintaining image processing software, and the extensive use of image processing work by the AFGL in reducing UV auroral images from the Polar BEAR satellite and future missions.

C. Computer Interface to UV Calibration Facility

The availability of laboratory desk-top computers and data acquisition programs (ASYST) enable complete computer control and data acquisition in the UV Calibration Facility. This project, in the initial planning stages at AFGL, will allow a much greater throughput of instrumental calibration.

D. Software for Faint Star Images

The procedure for measuring the stellar flux in the UV for calibrating the atmospheric transmission requires additional work. To minimize the noise, the software must permit the averaging of up to 32 frames. Currently, the procedures developed for the faint images can only access a single digitized frame.

BIBLIOGRAPHY

Code, A. D. and M. R. Meade, Astrophysical Journal Supplement Series 39, pp.195-289 (Feb. 1979)

Kneizys, F. X., E. P. Shettle, W. O. Gallery, H. H. Chetwynd, Jr, L. W. Abreu, J. E. A. Selby, S. A. Clough, and R. W. Fein, "Atmospheric Transmittance/Radiance: Computer Code LOWTRAN 6", AFGL-TR-83-0187, 1 Aug. 1983.

Stergis, C., V. Baisley, J. Lowrance, and G. Lemmyan, "Ultraviolet Radiations from Super Bates Motors (U)", Paper 1105, Proc. JANNAF [illegible] Meeting, April, 1988.

1988 USAF-UES SUMMER FACULTY RESEARCH PROGRAM/
GRADUATE STUDENT RESEARCH PROGRAM

Sponsored by the
AIR FORCE OFFICE OF SCIENTIFIC RESEARCH
Conducted by the
Universal Energy Systems, Inc.

FINAL REPORT

A MODEL FOR INTENSIFIED FRONTOGENESIS OVER A MODIFIED MOUNTAIN RIDGE

Prepared by:	Michael E. Frantz
Academic Rank:	Assistant Professor
Department and	Mathematics Department
University:	University of La Verne
Research Location:	AFGL/LYP Hanscom AFB Lincoln, MA 01731-5000
USAF Researcher:	Samuel Yee

Date:	September 17, 1988
Contract No:	F49620-87-R-0004

A MODEL FOR INTENSIFIED FRONTOGENESIS OVER A MODIFIED MOUNTAIN RIDGE

by

Michael E. Frantz

ABSTRACT

A thorough review of meteorology fundamentals was conducted, followed by an analysis of current models in use for representation of frontogenesis. The intensification of frontal strength due to a particular type of mountain/plateau combination profile such as found at the eastern edge of the Rockies is considered, via the development of a model using the geostrophic momentum equations. The atmosphere is assumed to be a stratified, adiabatic, rotating fluid with the Boussinesq and hydrostatic approximations made. Scaling arguments justify use of the geostrophic momentum approximation, and diagnostic and prognostic equations for both the geostrophic and ageostrophic velocity fields are derived. Boundary conditions are established for the numerical solution of these equations. Numerical simulations are proposed for the cases of front only, mountain only, and front and mountain combined.

ACKNOWLEDGEMENTS

I wish to thank the Air Force Systems Command and the Air Force Office of Scientific Research for sponsorship of this research. I would also like to thank the Air Force Geophysics Laboratory for my selection and sponsorship.

I would also further like to acknowledge the assistance and guidance provided by Sam Yee in the initial stages of the research period, including his encouragement toward mesoscale dynamics. In addition, Don Chisholm helped provide an effective working environment as well as administrative assistance. Dr. Keith Seitter was instrumental in the selection of a specific area of interest, as well as in providing valuable resources and references, including guidance from Dr. Kerry Emanuel and Dr. Stephen Garner. Finally, Dr. John McHugh and Vincent Falcone provided sources of stimulation as well as a balanced perspective on all aspects of the work.

I. INTRODUCTION:

Frontogenesis has long been a subject of interest to dynamic meteorologists, due to the great importance of fronts in determining accurate development of both synoptic and mesoscale weather systems. As such, fronts have probably been one of the most studied phenomena in meteorology, and many key concepts concerning fronotogenetic mechanisms have been elucidated through observation, numerical simulation, and more recently through analytic breakthroughs in the mathematical modeling of fronts.

In spite of these efforts, there still remain a great number of questions which have no answers or only partial answers, including mechanisms for rapid frontogenesis, multiple front formation, frontal rainband formation, and the complicated balance between frontogenesis and frontolysis which maintains sharp temperature gradients over extreme distances and for extended time periods. Interaction of frontal regions with topography and with other large scale atmospheric phenomena is not well understood and is an area open to current research. Some atmospheric non-precipitating cold fronts retain properties characteristic of a density current, and it is not known whether these undergo a transformation from a conventional-type sloping front or might be created from a precise set of atmospheric conditions. The full effect of the influences of latent heat condensation, surface friction, and turbulent mixing on the frontogenetic/frontolytic process is not known.

My own research interests lie in theoretical and mathematical modeling, and partial differential equations, particularly in the areas of atmospheric science and biomathematics. Modeling of frontal dynamics includes strong components of all my interests, and thus contributed to my assignment to the Atmospheric Prediction Branch of the USAF Geophysics Laboratory at Hanscom AFB, where ongoing efforts are being made to improve numerical weather prediction techniques.

II. OBJECTIVES OF THE RESEARCH EFFORT:

There were essentially three components to my summer research period. Due to my limited knowledge (as a mathematician) of atmospheric processes and

dynamics, the first objective was to obtain a satisfactory working knowledge of the fundamental physical and dynamic concepts of atmospheric science, with emphasis on the modeling assumptions and derivations in the prediction equations, as well as modifications usefully applied in frontal situations.

Dynamic modeling of fronts requires a thorough understanding of frontal physics and the various parameters which come into play in the model formulation. Special assumptions and approximations abound in the attempt to reduce the analytically intractable primitive equations to a mathematically simpler and yet physically meaningful model set. Therefore, a second objective was to obtain a solid background in the techniques peculiar to atmospheric frontal modeling, with special emphasis on coordinate systems, coordinate transformations, and physical and dynamical assumptions relevant to frontal situations.

After obtaining the proper background for working with fronts, the third objective was then to formulate a model for some aspect of surface frontogenesis not well understood, and develop information from analytic solutions. The aspect selected was rapid frontal intensification via topography. However, the limitations introduced by physically modeling a mountain ridge in a geostrophic coordinate system amenable to analytic solutions of the equations, together with accurate non-linear representations of the lower boundary, combined to require a change to a model no longer conducive to analytic solution. It then became a further objective (unfulfilled during this summer tenure) to establish the validity of the model and measure the effect of orography on the frontogenetic process through numerical simulation.

III. ATMOSPHERIC SCIENCE/FRONTAL DYNAMICS REVIEW:

The first objective of obtaining a working knowledge of meteorological physics, dynamics and equations was met by working through various texts, sourcebooks and review papers on dynamic meteorology. These included works by and in Atkinson (1981), Holton (1979), Hess (1959), Haltiner and Williams (1980), Ray (1986), Bolin (1959), and Pedlosky (1987).

The second objective, that of obtaining a working knowledge of the particular techniques, assumptions, approximations and models applicable specifically to frontal dynamics, was initially met by performing an extensive computer literature search keyed to frontogenesis. This identified approximately 150 recent papers and dissertations, of which about 50 proved to be both directly applicable and accessible. A general summary of the various coordinate systems and models which have been used in the recent past is provided by McWilliams and Gent (1980).

Some of the first modern fundamental results on frontogenesis were obtained through numerical simulation by Williams (1967), using the quasi-geostrophic model equations in which all terms of order Rossby number or smaller are neglected. This is an approximation which is valid as long as the frontal zone is not too small; however, in the latter stages of frontogenesis, the Rossby number becomes too large for this to remain a valid model. Specifically, quasi-geostrophic theory does <u>not</u> predict the formation of discontinuities in finite time, nor the characteristic tilting slope, but rather a vertical boundary. Hoskins (1982) in a recent review has explained the role of the ageostrophic flow field in contributing to the frontogenetic effects, a role which by definition is omitted from quasi-geostrophic theory.

Hoskins and Bretherton (1972), hereafter referred to as HB, were able to make considerable progress in eliciting realistic frontal characteristics through analytic solutions of what Hoskins later termed the semi-geostrophic equations in Hoskins (1975). This model has two major components. One is the transformation to geostrophic coordinates, $X = x + v_g/f$, $Y = y - u_g/f$, where (u_g, v_g) is the geostrophic velocity field and f a constant Coriolis parameter. The other is the use of the geostrophic momentum approximation, in which the full momentum terms are replaced by the geostrophic momentum, but the advecting velocities used in that calculation are full velocities, not just geostrophic ones. When used jointly, these two modifications give a convenient interpretation to geostrophic coordinates, being the positions which parcels would be at if they had been carried along by the geostrophic winds alone. This follows from $dX/dt = u_g$, $dY/dt = v_g$, easily derived from the above remarks.

The formation of fronts with extremely strong temperature gradients has been documented by Shapiro et. al. (1985), in particular, in the form of a density current or hydraulic head. It is not known what seems to cause certain fronts to (albeit rarely) attain an intensity at least an order of magnitude greater than usual. Garner (1986) has discussed the possible effect of orography on rapid frontogenesis, and the current study builds on work of Bannon (1983, 1984) in examining the possibility of frontal intensification through topography of a particular type. The geostrophic momentum approximation will be made, to retain the physical aspects crucial for frontogenesis, but the geostrophic coordinate system will be abandoned, due to the problems associated with specifying a topographic profile in geostrophic coordinates. Since the new spatial coordinates are time-varying in that system, the mountain profile is not fixed; thus a solution can only be obtained for a fixed time for a particular profile. It is not possible to document the time-dependent passage of a front over a fixed mountain ridge in geostrophic coordinates. Thus, the analytic results obtained through that transformation must be replaced by numerical simulations.

IV. MODEL OF INTENSIFIED FRONTOGENESIS OVER A MODIFIED RIDGE:

The third objective of the research period was to develop a model for frontogenesis occurring over a modified mountain ridge, utilizing model equations with more accuracy than quasi-geostrophic theory, but without the disadvantage of a time-dependent topographic profile associated with the geostrophic coordinate system. The assumption of cross-front geostrophic balance is made. A general description and detailed development of the model follows.

The atmosphere is assumed to be adiabatic, inviscid, and in rotating Cartesian coordinates, with constant Coriolis parameter f. The Boussinesq and hydrostatic approximations are made, and a uniform buoyancy frequency $N_o = \left(\frac{g}{\theta_o}\frac{\partial \theta}{\partial z}\right)^{1/2} > 0$ assumed in the basic state (θ a constant reference potential temperature). The domain is bounded above by a horizontal rigid-lid tropopause at z = H, and bounded below by the mountain topography, z = h(x), a modified Gaussian-type curve to be specified later, and of infinite extent in the y (meridional) direction. The

mountain profile will be modified for this model in order to provide a slope which it is believed will be more conducive to the intensification of horizontal temperature gradients. It will consist essentially of a high plateau, followed by a normal mountain ridge profile, then dropping rapidly to a much lower plateau on the lee side (see Fig. 1). The descent will be of magnitude approximately triple the magnitude of tha ascent. This asymmetry is expected to contribute to a net strengthening of the front after passing over the ridge. The basic solution will be considered to be independent of y. These assumptions are made from the perspective not only of mathematical simplicity, but also in an attempt to isolate any frontogenetic intensification in the topography alone.

The overall imposed synoptic flow consists of two components: a constant zonal wind with magnitude U_o, and a horizontal deformation field with streamfunction αxy, for $\alpha > 0$, giving net zonal and meridional velocities of $U_o - \alpha x$ and αy, respectively. Initially, a fairly diffuse frontal zone will lie upstream from the ridge, and parallel to it. The deformation field will act to intensify the front, while the zonal wind drives it across the ridge and down onto the lower plateau.

A diagram describing the basic model is given below:

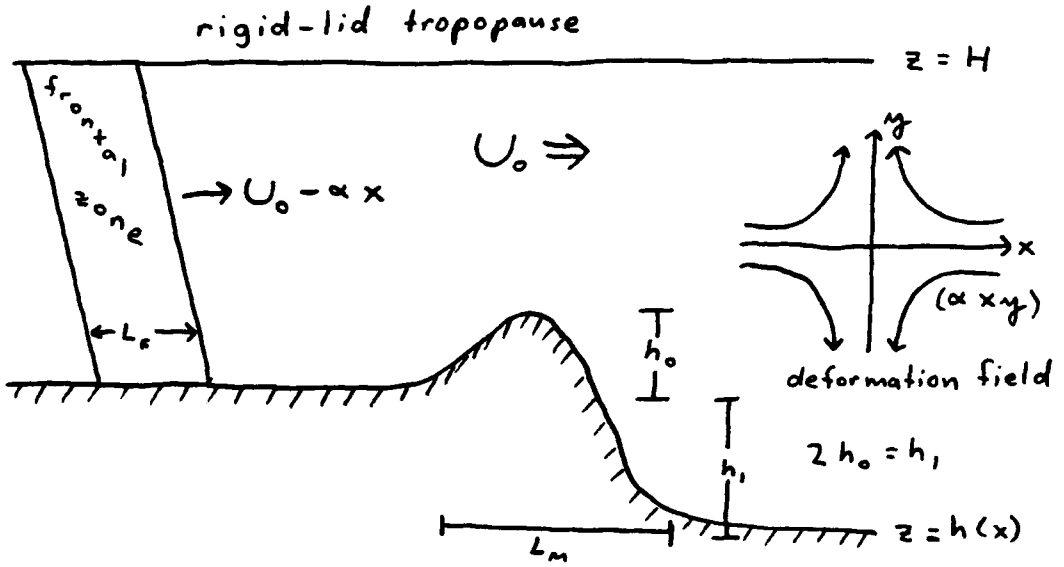

Fig. 1 The basic model for intensified frontogenesis

The basic equations governing the model consist of:

$$du/dt = fv - \phi_x \tag{1a}$$

$$dv/dt = -fu - \phi_y \tag{1b}$$

$$\partial\phi/\partial z = \frac{g}{\theta_o}\theta \tag{1c}$$

$$\partial u/\partial x + \partial v/\partial y + \partial w/\partial z = 0 \tag{1d}$$

$$d\theta/dt = 0 \tag{1e}$$

where $d/dt = \partial/\partial t + u(\partial/\partial x) + v(\partial/\partial y) + w(\partial/\partial z)$

Boundary conditions: $w = 0$ on $z = H$ (1f)

$w = dh/dt \ (=) \ u(\partial h/\partial x)$ *on* $z = h(x)$ (1g)

Note that ϕ is geopotential, θ is potential temperature, g gravity, and u, v and w the zonal, meridional and vertical velocity components.

The assumptions of no meridional variation in topography and the initial frontal zone parallel to the ridge provide for a solution in the following simple form, where primed quantities denote perturbations in the flow field due to frontal and mountain effects, and subscripts refer to ageostrophic components:

$$u = U_o - \alpha x + u_a'(x,z,t) \tag{2a}$$

$$v = \alpha y + v'(x,z,t) \tag{2b}$$

$$w = w'(x,z,t) \tag{2c}$$

$$\theta = \theta_o + (\partial\theta/\partial z)z = \theta_o + (\theta_o N_o^2)z/g + \theta'(x,z,t) \tag{2d}$$

The geopotential must be derived from the knowledge that the basic state solves (1), where the basic state is given by:

$$u = U_o - \alpha x \tag{3a}$$

$$v = \alpha y \tag{3b}$$

$$w = 0 \tag{3c}$$

From (1a) and (3),

$$\phi_x = fv - du/dt = f(\alpha y) - \partial u/\partial t - u(\partial u/\partial x) - v(\partial u/\partial y) - w(\partial u/\partial z)$$
$$= f\alpha y - 0 - (U_o - \alpha x)(-\alpha) - 0 - 0 = f\alpha y + U_o\alpha - \alpha^2 x$$

Hence, $\phi = f\alpha xy + U_o\alpha x - \alpha^2 x^2/2 + G(y,z)$ (4)

From (1b), (3) and (4),

$$\phi_y = -fu - dv/dt$$
$$= -f(U_o - \alpha x) - \partial v/\partial t - u(\partial v/\partial x) - v(\partial v/\partial y) - w(\partial v/\partial z)$$
$$= -fU_o + f\alpha x - 0 - 0 - (\alpha y)\alpha - 0 = f\alpha x - fU_o - \alpha^2 y = f\alpha x + \partial G/\partial y$$

Hence, $G(y,z) = -fU_o y - \alpha^2 y^2/2 + G'(z)$, and

$$\phi = f\alpha xy + U_o\alpha x - \alpha^2 x^2/2 - fU_o y - \alpha^2 y^2/2 + G'(z) \quad (5)$$

Finally, from (1c) and (5),

$\phi_z = \frac{g}{\theta_o}\theta = \frac{g}{\theta_o}(\theta_o + (\theta_o N_o^2 z/g) = g + N_o^2 z = \partial G'/\partial z$, so
$G(z) = gz + N_o^2 z^2/2$, and we must have:
$\phi = f\alpha xy + U_o(\alpha x - fy) - \alpha^2(x^2 + y^2)/2 + gz + N_o^2 z^2/2$

Hence, the perturbed solution takes the form of:

$$\phi = f\alpha xy + U_o(\alpha x - fy) - \alpha^2(x^2 + y^2)/2 + gz + N_o^2 z^2/2 + \phi'(x,z,t) \quad (2e)$$

We now derive the basic equations for the perturbed quantities by substituting (2) into (1):

From (1a), $dU_o/dt - \alpha(dx/dt) + du_a'/dt = f(\alpha y + v') - (f\alpha y + U_o\alpha - \alpha^2 x + \phi_x')$

or $du_a'/dt = \alpha u + f\alpha y + fv' - f\alpha y - U_o\alpha + \alpha^2 x - \phi_x'$
$= \alpha(U_o - \alpha x) + \alpha u_a' + fv' - \alpha(U_o - \alpha x) - \phi_x' = fv' + \alpha u_a' - \phi_x'$

From (1b), $\alpha(dy/dt) + dv'/dt = -f(U_o - \alpha x + u_a') - (f\alpha x - fU_o - \alpha^2 y + \phi_y')$

or $dv'/dt = -\alpha v - fU_o + f\alpha x - fu_a' - f\alpha x + fU_o + \alpha^2 y - \phi_y'$
$= -\alpha(\alpha y + v') - fu_a' + \alpha^2 y - 0 = -fu_a' - \alpha v'$

From (1c), $g + N_o^2 z + \phi_z' = \frac{g}{\theta_o}(\theta_o + \theta_o N_o^2 z/g + \theta') = g + N_o^2 z + \frac{g\theta'}{\theta_o}$,

or $\partial\phi'/\partial z = \frac{g}{\theta_o}\theta'$

From (1d),

$$0 = \partial u/\partial x + \partial v/\partial y + \partial w/\partial z = -\alpha + \partial u_a'/\partial x + \alpha + \partial v'/\partial y + \partial w'/\partial z,$$

or $\partial u_a'/\partial x + \partial w'/\partial z = 0$, since $v' = v'(x,z,t)$.

From (1e), $0 = d\theta/dt = d\theta'/dt + (\theta_o N_o^2/g)(dz/dt) = d\theta'/dt + \theta_o N_o^2 w'/g$,

or $d\theta'/dt = -\theta_o N_o^2 w'/g$

These five equations, with the boundary conditions given below, then constitute the full set of equations for the perturbed quantities:

$$du_a'/dt = fv' + \alpha u_a' - \phi_x' \tag{6a}$$

$$dv'/dt = -fu_a' - \alpha v' \tag{6b}$$

$$\partial \phi/\partial z = \frac{g}{\theta_o}\theta' \tag{6c}$$

$$\partial u_a'/\partial x + \partial w'/\partial z = 0 \tag{6d}$$

$$d\theta'/dt = -\theta_o N_o^2 w'/g \tag{6e}$$

Boundary conditions: $w' = 0$ at $z = H$ (6f)

$$w' = dh/dt \text{ at } z = h(x)\ , \tag{6g}$$

where it may be noted that in terms of the perturbed quantities,

$$d/dt = \partial/\partial t + (U_o - \alpha x + u_a')(\partial/\partial x) + w'(\partial/\partial z)$$
$$= \partial/\partial t + (U_o - \alpha x)(\partial/\partial x) + [u_a'(\partial/\partial x) + w'(\partial/\partial z)],$$

noting the purely ageostrophic advection on the right-hand side.

We now make scaling arguments in order to justify the cross-front geostrophic balance approximation and to determine pertinent dimensionless parameters. One equation (6a) will be transformed to dimensionless form in detail and the other transformed equations merely listed for reference. The basic length scaling is somewhat complicated by having different frontal and mountain scales, L_f and L_m, so a general scale L will be utilized which can then take on either value in further analysis. Letting U be the characteristic horizontal velocity scale, L the characteristic length scale, and D the characteristic depth scale, the time scale then becomes L/U, and we have: $x = Lx^*$, $z = Dz^*$, $t = (L/U)t^*$. The thermal wind equation, $\partial v/\partial z = \frac{g}{f\theta_o}(\partial\theta/\partial x)$, indicates a general scale for v of

$\frac{g}{f\theta_0}\frac{\Delta\theta}{L}D$, where $\Delta\theta/L$ represents the characteristic temperature gradient. Hence, $v = V_T Dv^*$, where we have put $V_T = \frac{g\Delta\theta}{f\theta_0 L}$. Geostrophic balance in the form of $\phi_x \sim fv'$ implies a scale of $fV_T DL$ for ϕ, i.e., $\phi = fV_T DL\phi^*$. Scales for u_a' and w' are obtained by first noting that the continuity equation (6d) implies the existence of an ageostrophic streamfunction, say $\bar{\Phi}$ with characteristic amplitude $\bar{\Phi}_0$. Then clearly u_a' and w' must have scales $\bar{\Phi}_0/D$ and $\bar{\Phi}_0/L$ respectively, since $u_a' = \bar{\Phi}_z$ and $w' = -\bar{\Phi}_x$. A scale for $\bar{\Phi}$ is suggested by equation (6e) when the dominant thermal advection of the left-hand side, $u(\partial\theta/\partial x)$, is considered balanced by the cooling due to the geostrophic vertical wind, hence, integrating with respect to x, we obtain the scale for $\bar{\Phi}$, $\bar{\Phi}_0 = \frac{U\Delta\theta g}{N_0^2\theta_0}$, which may also be written as

$$\bar{\Phi}_0 = \frac{fULV_T}{N_0^2}, \tag{7}$$

utilizing the thermal scaling for v. Hence, we have: $u_a' = \frac{\bar{\Phi}_0}{D}u_a^*$ and $w' = \frac{\bar{\Phi}_0}{L}w^*$. It should also be noted that the depth scale D is defined as the deformation depth scale based on the length scale L,

$$D = \frac{fL}{N_0}, \tag{8}$$

as discussed in Pedlosky (1987).

Details are now given for the most important equation in terms of approximations, (6a). Application of the above scaling factors to this equation yields:

$$\frac{\bar{\Phi}_0 U}{LD}\frac{\partial u_a^*}{\partial t^*} + \frac{\bar{\Phi}_0}{LD}\left[U_0 - \alpha L x^* + \frac{\bar{\Phi}_0}{D}u_a^*\right]\frac{\partial u_a^*}{\partial x^*} + \frac{\bar{\Phi}_0^2}{LD^2}w^*\frac{\partial u_a^*}{\partial z^*}$$
$$-\alpha\frac{\bar{\Phi}_0}{D}u_a^* - fV_T Dv^* = -\frac{fV_T LD}{L}\frac{\partial\phi^*}{\partial x^*} \tag{9}$$

Making use of (7) and (8), multiplying (9) through by and dropping *'s yields:

$$\frac{U^2}{f^2L^2}\frac{\partial u_a}{\partial t} + \frac{U_0 U}{f^2L^2}\frac{\partial u_a}{\partial x} - \frac{\alpha U}{Lf^2}x\frac{\partial u_a}{\partial x} + \frac{U\bar{\Phi}_0}{f^2L^2D}u_a\frac{\partial u_a}{\partial x} + \frac{\bar{\Phi}_0 U}{f^2L^2D}w\frac{\partial u_a}{\partial z} - \frac{\alpha U}{f^2L}u_a - \frac{V_T UD^2}{fL\bar{\Phi}_0}v^*$$
$$= -\frac{V_T D^2 U}{fL\bar{\Phi}_0}\frac{\partial\phi}{\partial x}$$

and then:

$$R_0^2\frac{\partial u_a}{\partial t} + \hat{u}R_0^2\frac{\partial u_a}{\partial x} - \hat{\alpha}R_0^2 x\frac{\partial u_a}{\partial x} + R_0^2\frac{V_T}{N_0}u_a\frac{\partial u_a}{\partial x} + R_0^2\frac{V_T}{N_0}w\frac{\partial u_a}{\partial z} - R_0^2\hat{\alpha}u_a$$
$$-v = -\partial\phi/\partial x,$$

or $R_0^2\left[du_a/dt - \hat{\alpha}u_a\right] - v = -\phi_x$

where $d/dt = \partial/\partial t + (\hat{u} - \hat{\alpha}x)\partial/\partial x + (Ri)^{-1/2}(u_a\partial/\partial x + w\partial/\partial z)$ (10)

and $\hat{u} = U_a/U$, $\hat{\alpha} = \alpha(L/V)$, $Ri = N_o^2/V_o^2$ = Richardson number, $R_o = V/fL$ = Rossby number. In similar fashion, it may be demonstrated that the set (6) is nondimensionalized into the complete set below:

$$R_o^2 (du_a'/dt - \hat{\alpha} u_a) - v = - \phi_x \qquad (11a)$$

$$dv/dt = -\hat{\alpha} v - u_a \qquad (11b)$$

$$\partial \phi / \partial z = \theta \qquad (11c)$$

$$\partial u_a / \partial x + \partial w/\partial z = 0 \qquad (11d)$$

$$d\theta/dt + w = 0 \qquad (11e)$$

with boundary conditions:

$$w = 0 \text{ at } z = \hat{H} \qquad (11f)$$

$$w = (Ri)^{1/2} (Ri_M)^{-1/2} \hat{\ell}\, db/dt \quad \text{at } z = \hat{\ell} (Ri_M)^{-1/2} b(x/\hat{\ell}), \qquad (11g)$$

where the following dimensionless parameters have been used:

$R_o = U/(fL)$ = Rossby number

$Ri = (N_o/V_T)^2 = \left(\frac{N_o f L \Theta_o}{g \Delta\Theta}\right)^2$ = Richardson number

$Ri = \left(\frac{N_o f L_M \Theta_o}{g \Delta\Theta_M}\right)^2 = \left(\frac{f L_M}{N_o \hat{h}}\right)^2$ = mountain Richardson number

since $\Delta\Theta_M = \frac{\partial \theta}{\partial z} \hat{h} = \frac{\Theta_o}{g} N_o^2 \hat{h}$

$\hat{u} = U_a/U$

$\hat{\alpha} = (L/U)\alpha$

$\hat{\ell} = L_M/L$

$\hat{H} = N_o H/(fL)$

and d/dt is as defined in (10). b represents the nondimensional topographic profile, ranging from 0 to 1, and $\hat{h} = h_o + h_1$ = maximum mountain height.

There are two points which should be made concerning these nondimensionalized equations. The first is that $Ri^{-1/2}$ is clearly an indicator of the strength of the ageostrophic flow. The second is that

the criterion in HB for cross-front geostrophic balance will be satisfied if $R_o << 1$ and $\hat{u}$, $\hat{\alpha}$ and $Ri^{-1/2}$ are $\leq O(1)$.

We now consider the methods used to actually solve the system (11) by looking at the prognostic and diagnostic equations involved. The assumption that the long-front wind is in balance with the cross-front pressure gradient is now made, i.e., $v' = v_g$, and henceforth all primes will be dropped.

The potential vorticity q, defined by $q = [\nabla \times (u,v,w) + f\vec{k}] \cdot \nabla \theta$, can be expanded into the form :

$$q = -\partial v_g/\partial z \cdot \frac{\partial \theta}{\partial x} + \left(f + \partial v_g/\partial x\right) \partial \theta/\partial z \qquad (12)$$

by making use of $v = v_g$ and the independence of y. Conservation of potential vorticity is then:

$$dq/dt = 0 \qquad (13)$$

Also, following HB, if we define the absolute momentum as $M = v_g + fx$, a brief calculation using (6b) gives:

$$dM/dt = dv_g/dt + fu = -\alpha v_g - fu_a + f(u_a + u_g) = fu_g - \alpha v_g ,$$

that is, , $dM/dt = fu_g - \alpha v_g$. (14)

Equations (13), (14) and (6e) form the set of prognostic equations used to advance the solution in time.

We may obtain a diagnostic equation for the geostrophic streamfunction, $\psi = \phi/f$, by utilizing the relations:

$\psi_x = v_g$, $\psi_y = -u_g$ (streamfunction) (15a)

$\partial v_g/\partial z = \frac{g}{f\theta_o} \partial\theta/\partial x$ (thermal wind) (15c)

$\partial\phi/\partial z = \frac{g}{\theta_o} \theta$ (hydrostatic) (15c)

with equation (12), to give:

$$q = -\psi_{xz}^2 \frac{f\theta_o}{g} + (f + \psi_{xx}) \frac{\theta_o}{g} \phi_{zz} = -\psi_{xz}^2 \frac{f\theta_o}{g} + (f + \psi_{xx}) \frac{\theta_o}{g} f \psi_{zz}$$

That is, $q = \frac{f\theta_o}{g} [(f + \psi_{xx}) \psi_{zz} - \psi_{xz}^2]$ (16)

This is a nonlinear elliptic equation (for $q > 0$) of the Monge-Ampere type discussed briefly in HB. It is noted there that Heinz (1962) has shown

that singularities in the second derivatives of ψ are possible only on boundaries, provided that ψ_x and ψ_z remain bounded and q has continuous spatial derivatives up to the second order. This implies that if v_g and θ remain bounded, then discontinuities in v_g or θ can only occur on boundaries or at a discontinuity in potential vorticity q or its first or second derivatives. This is in complete agreement with observations that very, very strong fronts occur only near the earth's surface or near the tropopause, which can be considered a discontinuity in potential vorticity, since it separates the troposphere and stratosphere which are very different in their potential vorticities. Given q, we may diagnose the geostrophic streamfunction from (16).

Next we concentrate on obtaining ageostrophic velocities. Using the nondivergence of the geostrophic velocity field and the continuity equation (6d), an ageostrophic streamfunction may be postulated with

$$u_a = \Phi_z \ , \quad w_a = -\Phi_x \tag{17}$$

Differentiating (6b) with respect to z, differentiating (6e) with respect to x, and algebraically manipulating the two resulting equations using (17) and the thermal wind and hydrostatic equations, after extensive calculation, a Sawyer-Eliassen type equation may be obtained for the ageostrophic streamfunction:

$$N^2\Phi_{xx} - 2f(\partial v_g/\partial z)\Phi_{xz} + f(f + \partial v_g/\partial x)\Phi_{zz} = 2f(\partial v_g/\partial z)(\partial u_g/\partial x) \tag{18}$$

Equations (16) and (18) then provide the diagnostics for ψ and Φ to complete the solution. The general procedure is now described.

An initial geostrophic streamfunction will be specified, which must contain a uniform thermal straification, the zonal wind, horizontal deformation field, initial diffuse frontal structure, and an initial temperature perturbation for the mountain. Thus, the initial geostrophic streamfunction will take the form of:
$\psi(x,y,z) = \frac{g}{f} z + N_0^2 z^2/(2f) + \alpha U_0 x/f - U_0 y + \alpha xy + \psi_F(x,z) + \psi_M(x,z)$,
where ψ_F and ψ_M represent the frontal and mountain components, which have not been completely determined by this study. However, ψ_F should be chosen so as to provide a frontal temperature distribution of the type

$\theta_s(x,z) = \delta\theta \tan^{-1}(\beta_1 x + \beta_2 z)$, where $\delta\theta$ is the temperature differential across the front, in keeping with previous models of Hoskins (1971).

Given the initial values of ψ, it will then be possible to compute initial values for M, then θ, then q, since u_g and v_g will be known. The initial ageostrophic streamfunction may be diagnosed via (18) from the initial geostrophic streamfunction. Equations (13), (14) and (6e) can then be used to step q, M and θ forward in time. The new potential vorticity may then be used to compute a new geostrophic streamfunction via (16), which can than be used to diagnose a new ageostrophic streamfunction, yielding the full new velocity field, and the whole procedure then iterated.

In order to solve the diagnostic equations (16) or (18), either the values of the streamfunctions or their normal derivatives must be known at the boundaries. Since the geostrophic momentum equations are a balanced set, there will be no gravity waves. Also, the f-plane approximation filters out Rossby waves. Hence, there can be no upstream wave propagation, and therefore no upstream influence at the upstream lateral boundary, x_L.

The rigid-lid condition on top implies that $w_a = 0$ there, so Φ = constant at z = H. For the bottom boundary condition on Φ, put $\vec{s} = \vec{i} + \frac{\partial u}{\partial x}\vec{k}$, then $\vec{s}$ is a vector tangent to the mountain profile. Since w = dh/dt on the bottom surface, we have:

$$-\Phi_x = \partial h/\partial t + u(\partial h/\partial x) + v(\partial h/\partial y) + w(\partial h/\partial z)$$
$$= (u_g + u_a)(\partial h/\partial x) = (u_g + \Phi_z)(\partial h/\partial x),$$

hence, $$-u_g(\partial h/\partial x) = \Phi_x + \Phi_z(\partial h/\partial x) = \vec{s} \cdot \nabla \Phi \qquad (19)$$

and (19) can then be integrated along h(x) to specify $\Phi(x,z)$ there.

No upstream influence implies $u_a = \Phi_z = 0$, so Φ = constant on x_L. At the downstream boundary x_R, we put $w_a = -\frac{\partial \Phi}{\partial x} = 0$, which implies that the vertical ageostrophic flow is localized in the mountain region, but still permits a net ageostrophic zonal flow, which is needed for mass conservation, as the geostrophic flow up the mountain produces a source of ageostrophic flow which must be accounted for.

There is no simple way to specify conditions for the geostrophic streamfunction on the upper and lower boundaries, so normal derivatives will be used instead. For the upper boundary, we know that

$$d\theta/dt + \theta_o N_o^2 w/g = 0 \qquad (20)$$

and $$\partial \psi/\partial z = \partial(\phi/f)/\partial z = \phi_z/f = g\theta/(f\theta_o) \qquad (21)$$

But θ is known at the upper boundary for all time, so $(\partial \psi/\partial z)(\partial \psi/\partial n)$ is specified also, by (21).

Let $\vec{n} = -(\partial h/\partial x)\,\vec{i} + \vec{k}$ be a normal to the boundary $z = h(x)$. Then

$$\vec{n}\cdot\nabla\psi = [-(dh/dx)\,\vec{i} + \vec{k}]\cdot(\psi_x \vec{i} + \psi_z \vec{k})$$
$$= -(dh/dx)(\partial \psi/\partial x) + \partial \psi/\partial z \quad \text{at } z = h(x) \qquad (22)$$

But (20) and (14) provide values of $\theta = \frac{f\theta_o}{g}(\partial \psi/\partial z)$ and $v_g = \partial \psi/\partial x$ at all times on the boundary, so (22) may be evaluated on $z = h(x)$.

On the lateral upstream boundary x_L, no upstream influence means $\partial \theta/\partial t = 0$ there, so $\theta = \frac{f\theta_o}{g}(\partial \psi/\partial z)$ can be specified at x_L and integrated with respect to z to give $\psi(z)$, independent of time. Conservation of absolute momentum gives values of $v_g = \partial \psi/\partial x$ at all times, allowing specification of $\partial \psi/\partial n$ at the lower boundary x_R.

In order to simplify application of the bottom boundary conditions, a terrain-following vertical coordinate is proposed:
$\zeta = H[z - h(x)]/[H - h(x)]$,
giving $\zeta = H$ on the top and $\zeta = 0$ on the bottom. Since the tangential boundary derivative is simply $\partial/\partial x$ in ζ, we can then integrate (19) on $z = h(x)$ to give: $\tilde{\Phi}(x) = \int_{x_L}^{x_R} -u_g(\partial h/\partial x)\,dx$ on $\zeta = 0$.
Also, specification of $\partial \psi/\partial \zeta$ at $\zeta = 0$, H is as follows:
$\partial \psi/\partial \zeta = (\partial \psi/\partial z)/(\partial \zeta/\partial z) = \frac{H - h(x)}{H}\frac{g}{f\theta_o}\theta = \frac{g}{f\theta_o}\theta(x,\zeta)\left[1 - h(x)/H\right]$
One last point pertains to the measurement of the strength of the frontal region. Now $d\theta/dt = 0$ implies $\partial/\partial x[d\theta/dt] = 0$, and

$$\partial/\partial x[d\theta/dt] = \frac{\partial^2\theta}{\partial x\partial t} + \frac{\partial u}{\partial x}\frac{\partial \theta}{\partial x} + u\frac{\partial^2\theta}{\partial x^2} + \frac{\partial v}{\partial x}\frac{\partial \theta}{\partial y} + v\frac{\partial^2\theta}{\partial x\partial y} + \frac{\partial w}{\partial x}\frac{\partial \theta}{\partial z} + w\frac{\partial^2\theta}{\partial x\partial z} \qquad (23)$$

Also, $$d/dt(\partial\theta/\partial x) = \frac{\partial^2\theta}{\partial t\partial x} + u\frac{\partial^2\theta}{\partial x^2} + v\frac{\partial^2\theta}{\partial x\partial y} + w\frac{\partial^2\theta}{\partial x\partial z} \qquad (24)$$

Combining (23) and (24), we obtain:

$d/dt(\partial\theta/\partial x) = -(\partial u/\partial x)(\partial\theta/\partial x) - (\partial u/\partial x)(\partial\theta/\partial y) - (\partial u/\partial x)(\partial\theta/\partial z)$, a Miller-type (1948) equation for the strength of the frontal horizontal temperature gradient. The first term is due to the deformation field, the second term is absent in this present setting, and the third term is due to differential vertical motion.

IV. RECOMMENDATIONS:

As is always the case with a mathematical model, the full validity of the model cannot be established until solutions for the equations are given and examined for realistic features. Due to the retention of ageostrophic advection and complicated bottom topography, it does not seem possible to provide such solutions other than through numerical simulation.

Several tasks remain before the model can be implemented on a computer. The exact forms for the frontal and mountain components of the initial geostrophic streamfunction, ψ_F and ψ_M, must be determined with a view toward realistic simulation. Neither is the exact functional form for the bottom topography specified here. Optimal methods for the forward time-stepping and solution of the diagnostic equations, particularly in the nonlinear case, should be investigated.

The logical extension to this study would be to complete the above mentioned tasks, then run numerical simulations of the model to establish its validity. Tests should be done in at least six basic modes: with no front and no topography, with no front and plateau features only, with no front and full topography, with the front and no topography, with the front and plateaus only, and with the front and full topography. With this data it should be possible to ascertain the contributions of both the plateau differential and its combination with a mountain ridge on the process of intensifying a front.

It would also remain for future work to investigate the effects of finite mountain ridges and isolated mountains in the frontogenetic process. This would, however, complicate the model considerably by introducing dependence of the solution in the meridional direction.

REFERENCES

Atkinson, B.W. (ed.), Dynamical Meteorology, An Introductory Selection, New York, Methuen and Co., 1981.

Bannon, Peter R., Quasi-Geostrophic Frontogenesis Over Topography, J. Atmos. Sci., Vol. 40: 2266-2277, 1983.

_____, A Semi-Geostrophic Model of Frontogenesis Over Topography, Beitr. Phys. Atmosph., Vol. 57, No. 3, pp. 393-408, 1984.

Bolin, Bert (ed.), The Atmosphere and the Sea in Motion, New York, The Rockefeller Press, 1959.

Garner, Stephen T., An Orographic Mechanism for Rapid Frontogenesis, Ph.D. thesis, M.I.T., 1986.

Haltiner, George J.; Williams, R.T., Numerical Prediction and Dynamical Meteorology, New York, John Wiley and Sons, 1980.

Heinz, E., Interior Estimates for Solutions of Elliptic Monge-Ampere Equations, Proc. Symp. Pure Mathematics, Vol. IV., Partial Differential Equations, Providence, R.I., Amer. Math. Soc., pp. 149-155.

Hess, Seymour L., Introduction to Theoretical Meteorology, New York, Henry Holt and Co., 1959.

Hobbs, Peter V., Atmospheric Science, An Introductory Survey, New York, Academic Press, 1977.

Holton, James R., An Introduction to Dynamic Meteorology, 2nd ed., New York, Academic Press, 1979.

Hoskins, B.J., Atmospheric Frontogenesis Models: Some Solutions, Quart. J. R. Met. Soc., Vol. 97, pp. 139-153, 1971.

Hoskins, Brian J.; Bretherton, Francis P., Atmospheric Frontogenesis Models: Mathematical Formulation and Solution, J. Atmos. Sci., Vol. 29, pp. 11-37, 1972.

Hoskins, B.J., The Mathematical Theory of Frontogenesis, Ann. Rev. Fluid Mech., 14:131-151, 1982.

McWilliams, James C.; Gent, Peter R., Intermediate Models of Planetary Circulations in the Atmosphere and Ocean, J. Atmos. Sci., Vol. 37, No. 8, pp. 1657-1678.

Miller, James E., On the Concept of Frontogenesis, J. of Met., Vol. 5, pp. 169-171.

Pedlosky, Joseph, Geophysical Fluid Dynamics, 2nd ed., New York, Springer-Verlag, 1987.

Ray, Peter S. (ed.), Mesoscale Meteorology and Forecasting, Boston, American Meteorological Society, 1986.

Shapiro, M.A. (et. al.), The Frontal Hydraulic Head: A Micro-α Scale (~1 km) Triggering Mechanism for Mesoconvective Weather Systems, Mon. Wea. Rev., Vol. 113, pp. 1166-1183, 1985.

Williams, R.T., Atmospheric Frontogenesis: A Numerical Experiment, J. Atmos. Sci., Vol. 24, pp. 627-641, 1967.

1988 USAF-UES SUMMER FACULTY RESEARCH PROGRAM

GRADUATE STUDENT RESEARCH PROGRAM

Sponsored by the

AIR FORCE OFFICE OF SCIENTIFIC RESEARCH

Conducted by the

Universal Energy Systems, Inc.

FINAL REPORT

Prepared by:	Christopher Godfrey
Academic Rank:	Associate Professor
Department and	Mathematics and Physics
College:	Missouri Western State College
Research Location:	USAF AFGL Hanscom AFB Lexington, MA
USAF Colleague:	Edward W. Cliver
Date:	29 August 1988
Contract No.:	F49620-87-R-0004

Gamma and X Radiation from Solar Flares

by

Christopher Godfrey

ABSTRACT

Solar flares are known to produce a variety of types of electromagnetic and charged particle radiation including radio, microwave, visible, x-ray, and gamma ray radiation, and energetic protons. The sites in the solar atmosphere where the x-rays and gamma rays are produced varies in a number of solar flare models. In this study the onset time of the E > 300 KeV x-ray emission was compared with the time of onset of 4-7 MeV gamma ray excess. The results indicate that the > 300 KeV x-rays and 4-7 MeV gamma rays are produced simultaneously in some flares, but that the onsets are separated by as much as 30 seconds or more in others.

This implies that either the x-rays and gamma rays are not generally produced by the same energetic particles, or they are not produced at the same site, or both. In many gamma ray flares, the particles which generate the x and gamma rays cannot be accelerated by a single shock wave moving continuously upward through the solar atmosphere.

Acknowledgements

I would like to thank the staff of the Air Force Geophysics Laboratory and the Air Force Office of Scientific Research for sponsoring this research project. In addition, I thank Universal Energy Systems, Inc. for their efficient and helpful manner in which they have administered the program.

The experience gained during my visit to AFGL was rewarding in many ways, but it was the warmth and professional dedication of the people who I met and worked with that I will remember most clearly. In particular I would like to mention Edward W. Cliver, my AF colleague for the program, David J. Forrest of the SMM group and the University of New Hampshire, and S. Kahler and D. Webb of the solar physics group at AFGL, for their invaluable assistance.

I. INTRODUCTION:

Solar flares are sources of copious amounts of electromagnetic radiation ranging from kilometric wavelengths to gamma rays, and energetic particles with energies up to several GeV. Flares extend up to 100,000 km in diameter and exhibit characteristic rise times of 1 to 1000 seconds, and decay times of hours. The total energy released during a solar flare may range from 10^{21} to 10^{25} J. In most flare models, the flare energy is released in the low solar corona. Energetic electrons and protons stream upward through the corona and downward into the photosphere, along with shock waves which heat the atmosphere. Gamma rays are produced primarily via electron bremsstrahlung in the flare plasma, neutron capture on protons, nuclear de-excitation radiation resulting from the interaction of flare-accelerated protons and nuclei with the solar atmosphere. The upward moving shocks generate radio and microwave bursts in the corona, and soft x-rays in shock heated plasma. Accelerated electrons produce non-thermal hard x-rays via electron-ion bremsstrahlung. The radio bursts are classified into five types. Type II bursts, for example, are believed to be the result of gyro-synchrotron radiation emitted by electrons in the corona which are

accelerated by the passing magnetohydrodynamic (MHD) shock wave. Type II MHD shocks may accelerate and eject electrons and ions into interplanetary space (Cliver, et.al. (1988)).

II. OBJECTIVES OF THE RESEARCH EFFORT:

The central theoretical problem of solar flares is the particle acceleration, storage, and release mechanism (Forman, Ramaty, and Zweibel (1986), and Brown, Smith, and Spicer (1981)). Various models have invoked stochastic Fermi acceleration and scattering from magnetic field irregularities in and behind turbulent MHD shocks (e.g. Ellison and Ramaty (1985)). But flare observations are varied and complex, and no complete theory of solar flares exists.

This report describes an investigation into the relationship between observed onset time of hard x-ray (E > 300 KeV) emission and gamma ray (4-8 MeV) emission in ten gamma ray flares observed in 1981 and 1982 from the SMM (Solar Maximum Mission) spacecraft. The 4-8 MeV gamma rays are produced by prompt nuclear de-excitation, and thus originate at or near the acceleration/energy release site, whereas the >300 KeV x-rays may be produced at the flare particle acceleration site or possibly higher in the atmosphere in the type II MHD shock wave.

If the particles originating in the impulsive phase acceleration are re-accelerated in Type II shocks (the gradual phase) into interplanetary space, then the relative timing of the x- and gamma ray emission must be consistent with this fact.

The data were acquired from the SMM data archives at the University of New Hampshire, and were analyzed at the Air Force Geophysics Laboratory, Hanscom AFB, MA. The flares used in the analysis each exhibited large Type II radio bursts which occured high in the solar corona ($r > 200000$ Km) and relatively strong >300 KeV x-ray emission (Cliver, et.al. (1988)), and were chosen solely on this basis. Ten such flares were isolated and chosen for analysis. Of these ten, four were deleted from further analysis because part or all of the impulsive phase of the flare was obscured by Earth shadowing or SAA (South-Atlantic Anomoly) passage. The x-ray and gamma ray emission of the remaining six flares listed in Table 1 were analyzed as described below.

II. METHOD OF ANALYSIS:

Four thousand seconds of gamma ray and x-ray data were obtained in 1.024 second time bins for each flare, centered around the reported time of onset of the >300 KeV x-ray emission. Each data set was examined visually, and 200 seconds of data was extracted from each, beginning 50 seconds before the onset of the impulsive x-ray flare. Because the number of gamma ray counts per one second bin is small, the statistical (Poisson) errors cause the data to appear very noisy. To improve the efficiency of data fitting algorithims, the gamma and x-ray data were smoothed using a Blackman moving window low pass filter (Yule, 1967). The raw counting rates for each of the six flares are shown in the upper half of Figures 1-6. The lower half of each Figure shows the smoothed data.

The onset time of impulsive phase emission was determined as follows. The rise time of each significant (>2.5 sigma) peak in the counting rate was fitted with a straight line. The immediate background (50 seconds prior to the >300 KeV onset) was also fitted with a straight line. The time of intersection of the two fits is designated as the "onset time". The onset times of peaks in the gamma ray and x-rays counting rates which visually match are compared.

IV. RESULTS:

Of the six flares that remained in the data set, the 13 May 1981 flare did not fit the parameters of an impulsive event. The x-ray counting rate increases gradually and an onset time cannot be uniquely assigned. Thus the 13 may 1981 flare was thrown out. Data from the remaining five events were smoothed and fitted as discussed above. The Universal Time calculated for the onset of x-ray emission from each of the five flares, and the time difference in the x-ray and gamma ray emission onsets, are listed in Table 1.

In four of the five cases, the impulsive gamma ray emission begins after the x-ray emission, contrary to what might be expected if the x-rays are produced by the same particle population as the gamma rays, but at a higher altitude well above the particle acceleration region.

The later gamma ray emission is consistent with the suggestion that Type II shocks, while they are relatively low in the corona, might play an important role in the acceleration of the gamma ray producing ions generated in impulsive flares. The energetic protons must be stored in low-lying coronal magnetic loops, while the Type II shock propagates upward eventually to produce the Type II radio burst.

V. RECOMMENDATIONS:

Questions that should be addressed in order to clarify the relationship between coronal shocks and impulsive gamma and x-radiation include the rate of shock formation, the requirements for energetic particle storage, and particle acceleration. The problem is that gamma ray rates obtained with the current generation of detectors are to low to clearly define the impulsive phase of any but the largest of flares.

References

Brown, J.C., Smith, D.F., and Spicer, D.S., Solar Flare Observations and Their Interpretations. The Sun as a Star, 1981, NASA SP-450, pp. 181-227.

Cliver, E.W., et. al., Astrophysical Journal, 1988, in press.

Ellison, D.C., and Ramaty, R., Shock Acceleration of Electrons and Ions in Solar Flare. Astrophysical Journal, 1985, Vol. 298, pp.400-408.

Forman, M.A., Ramaty, R., and Zweibel, E.G., The Acceleration and Propagation of Solar Flare Energetic Particles, Physics of the Sun, Vol. II, 1986, pp. 249-289.

Ramaty, R., Nuclear Processses in Solar Flares. Physics of the Sun, Vol. II, 1986, pp. 291-323.

Yule, H.P., Mathematical Smoothing of Gamma Ray Spectra. Nuclear Instruments and Methods, 1967, Vol. 54, pp. 61-65.

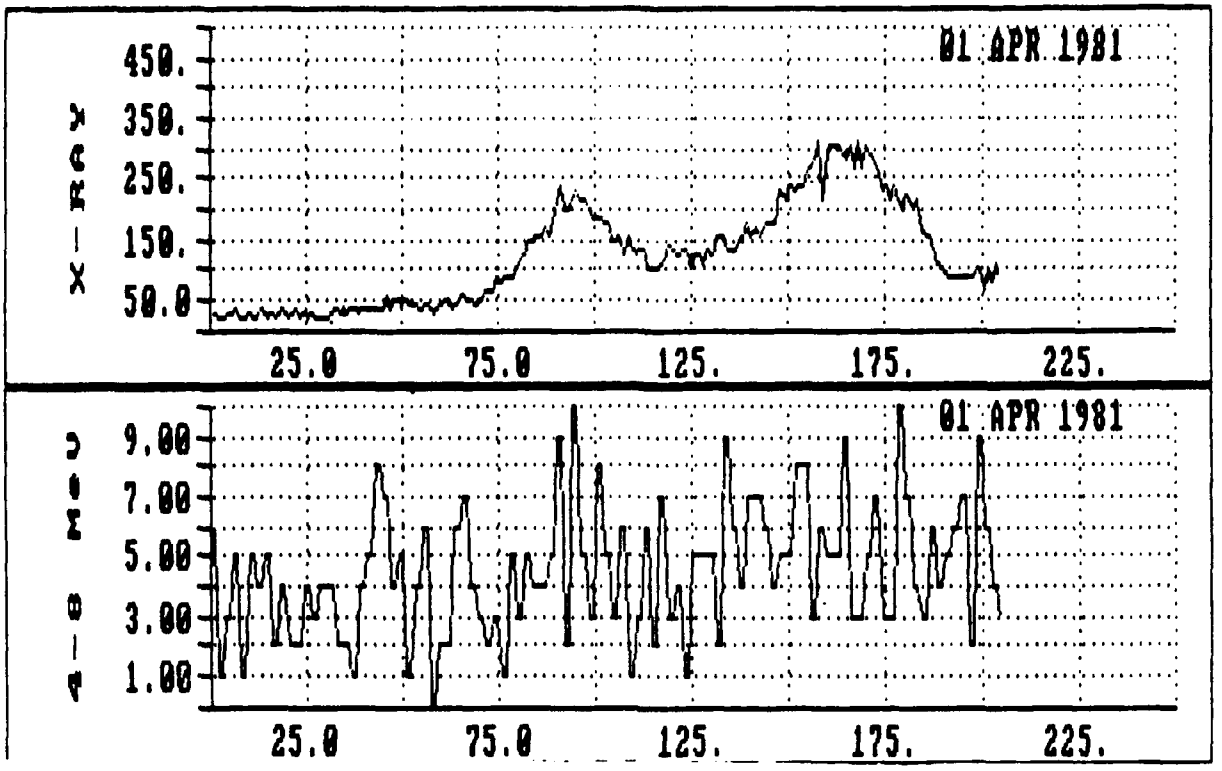

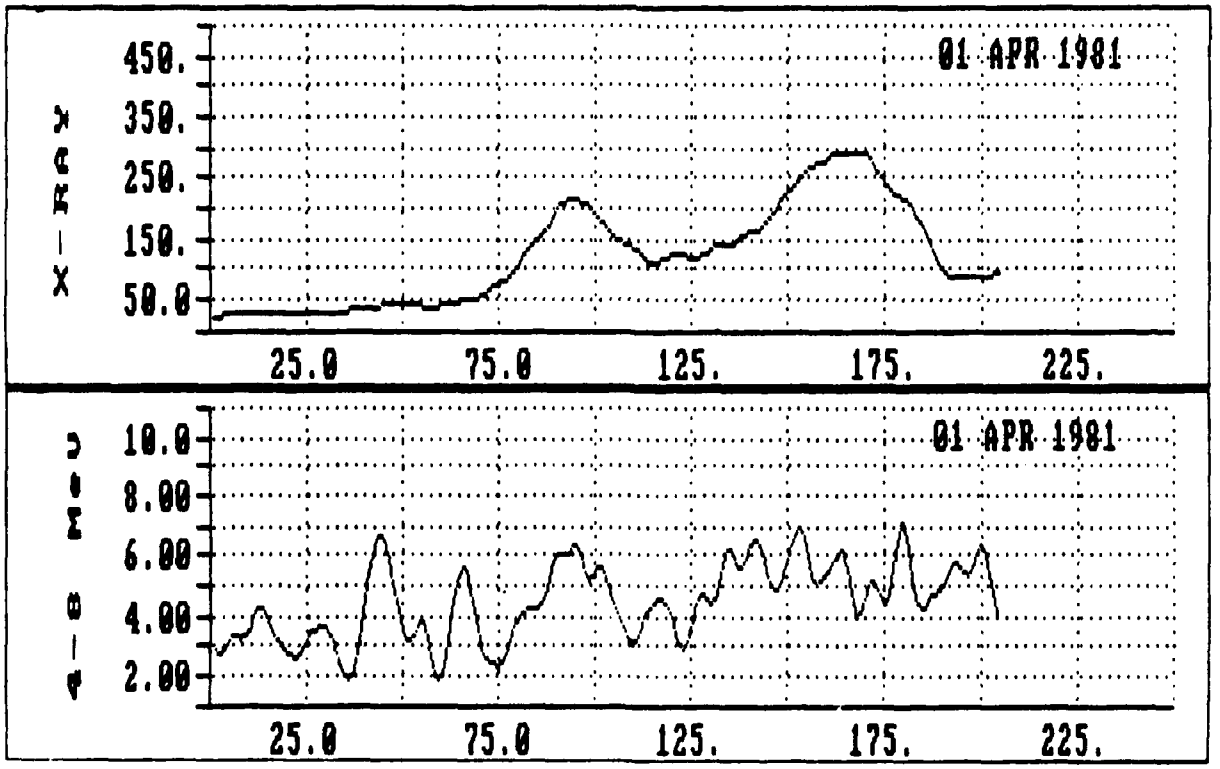

Figure 1. 01 April 1981 event.

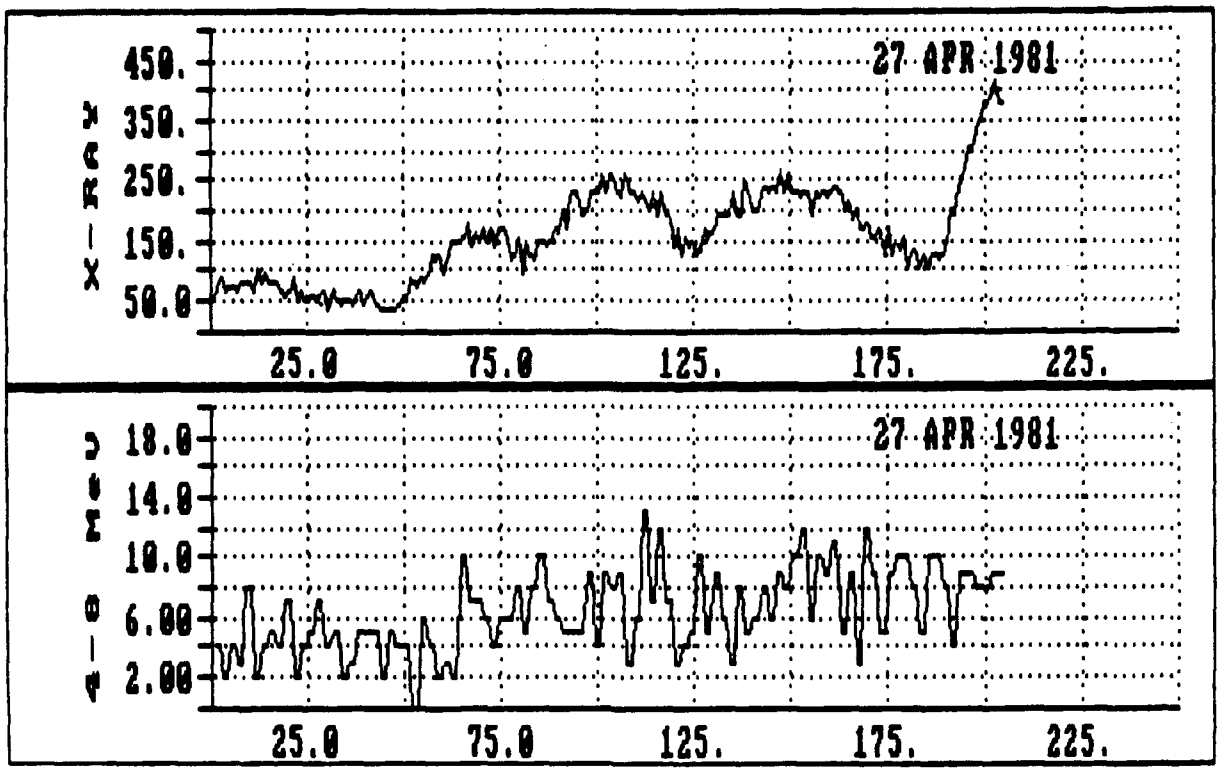

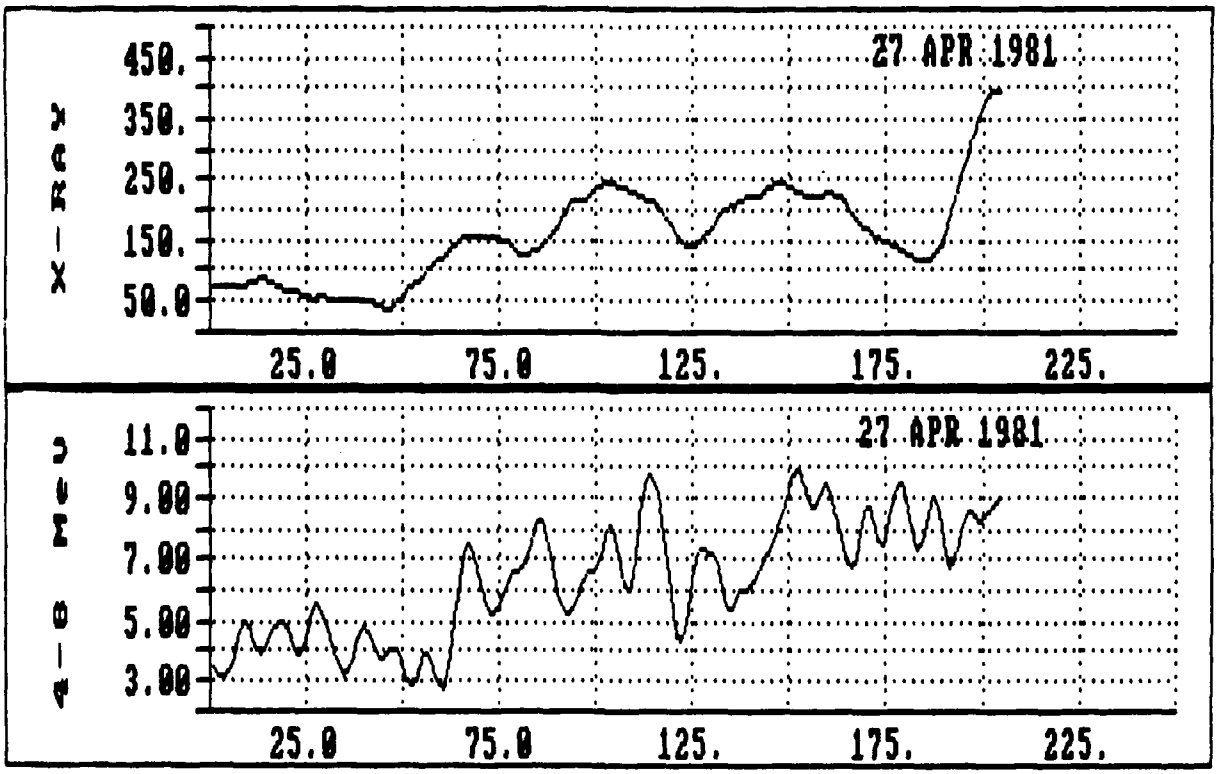

Figure 2. 27 April 1981 event.

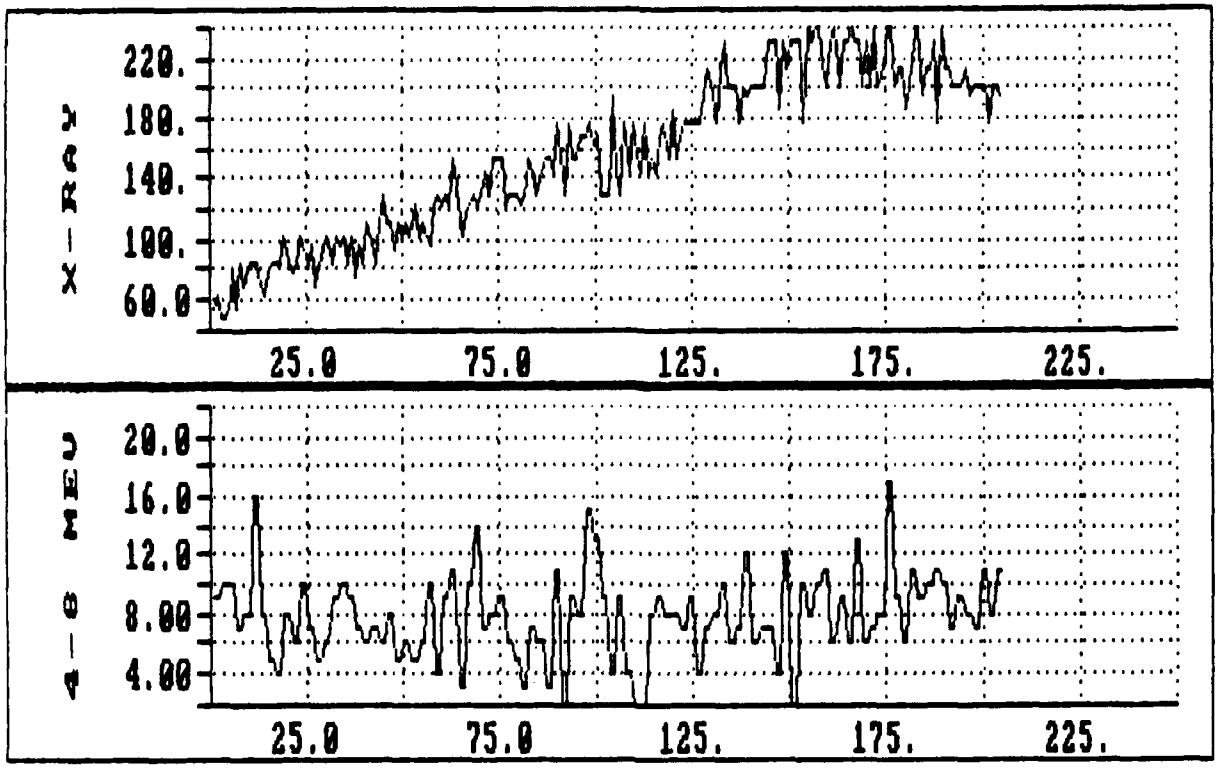

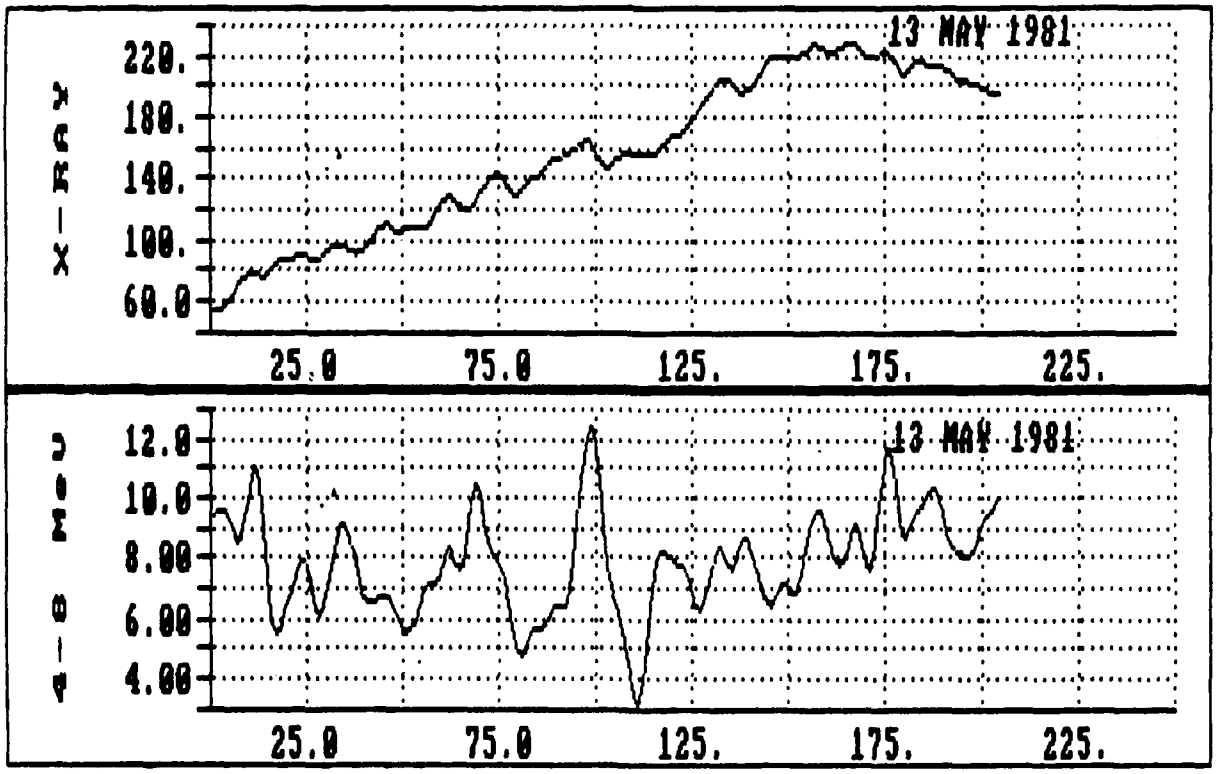

Figure 3. 13 May 1981 event.

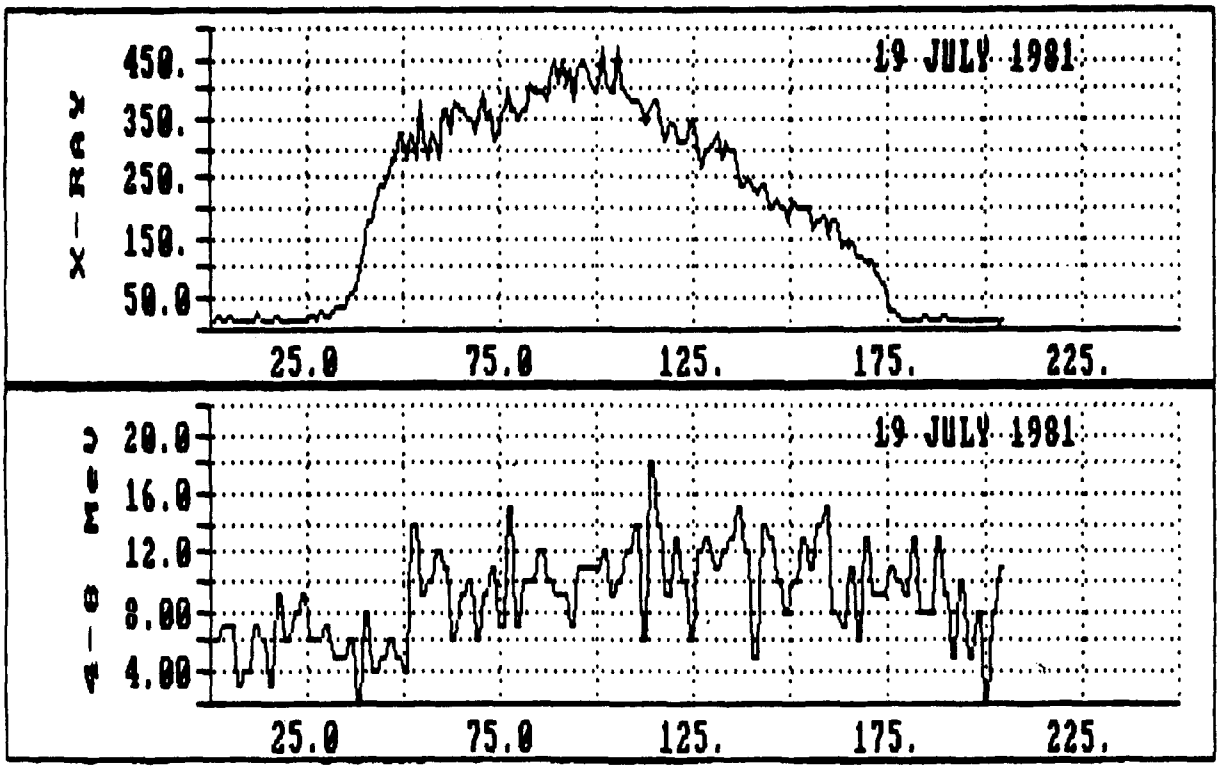

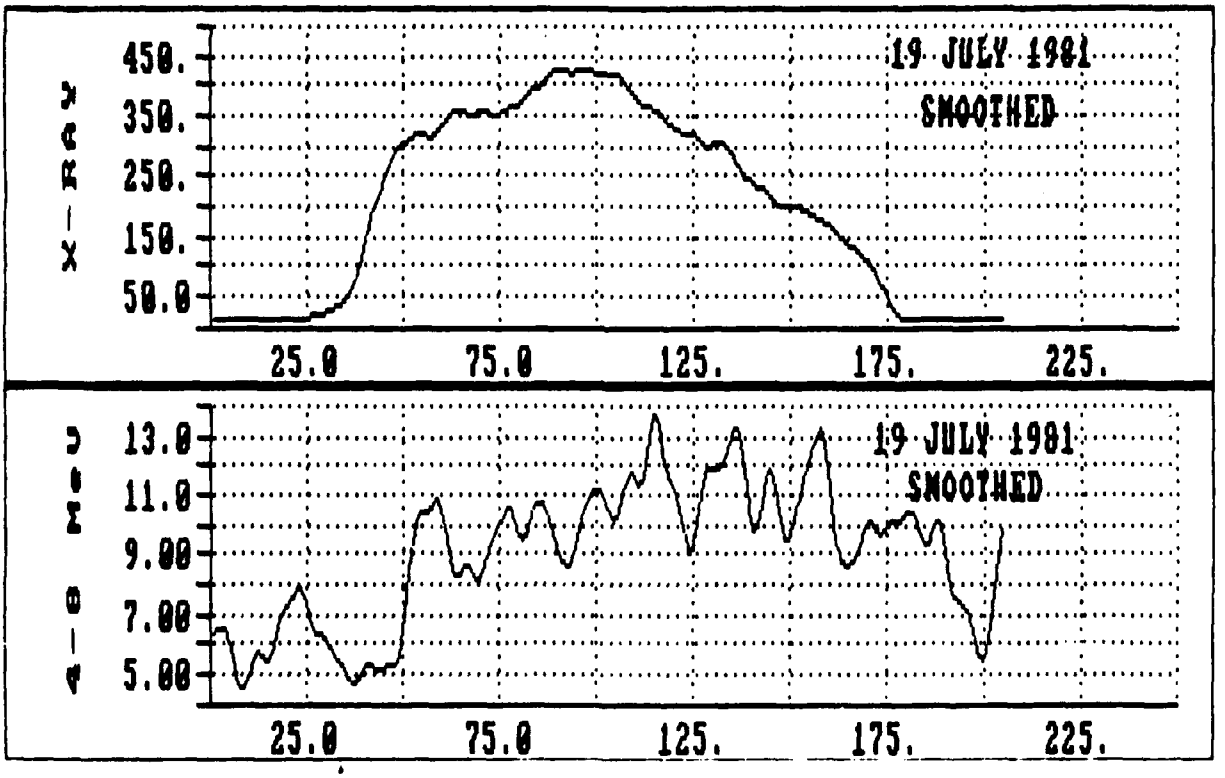

Figure 4. 19 July 1981 event.

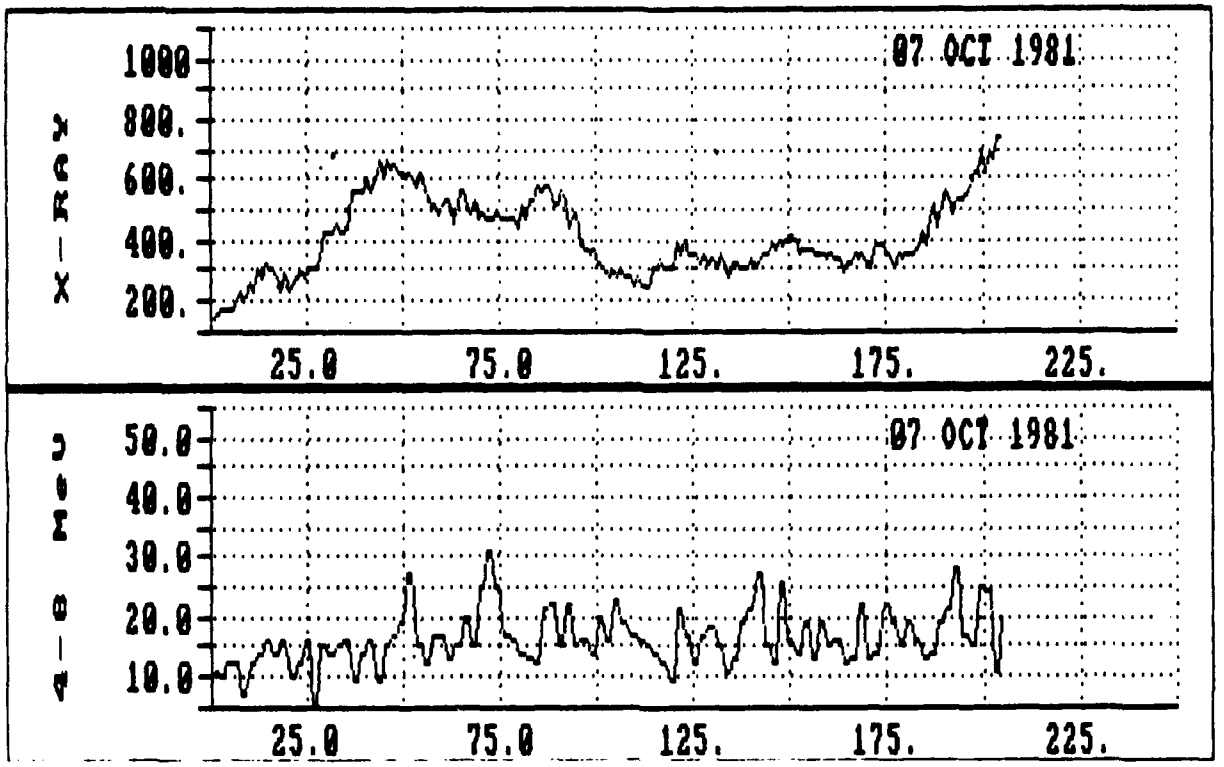

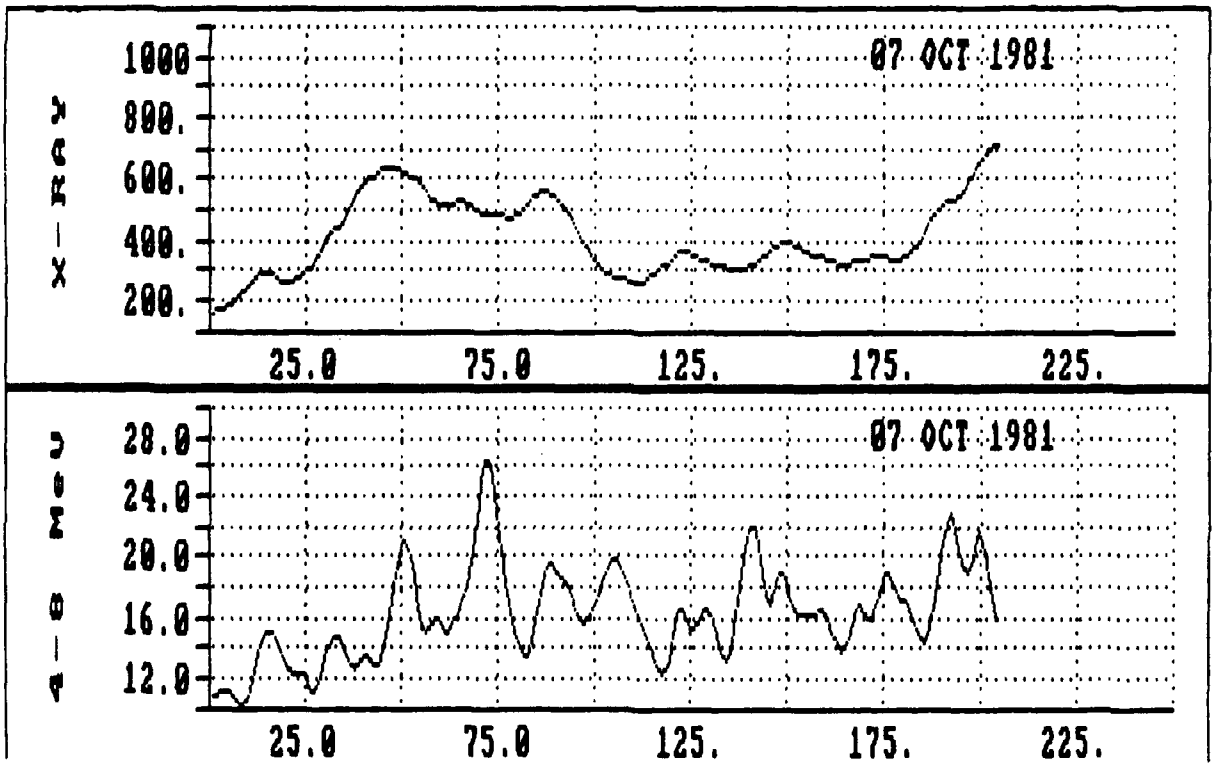

Figure 5. 07 October 1981 event.

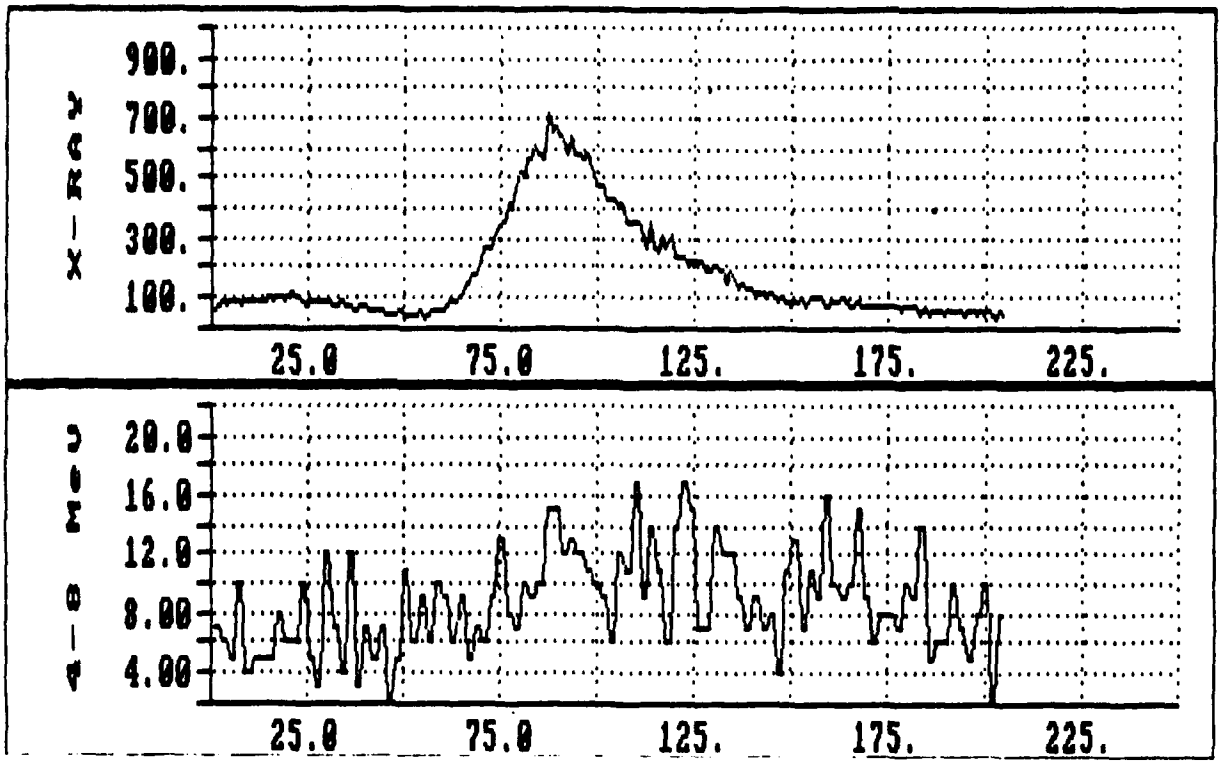

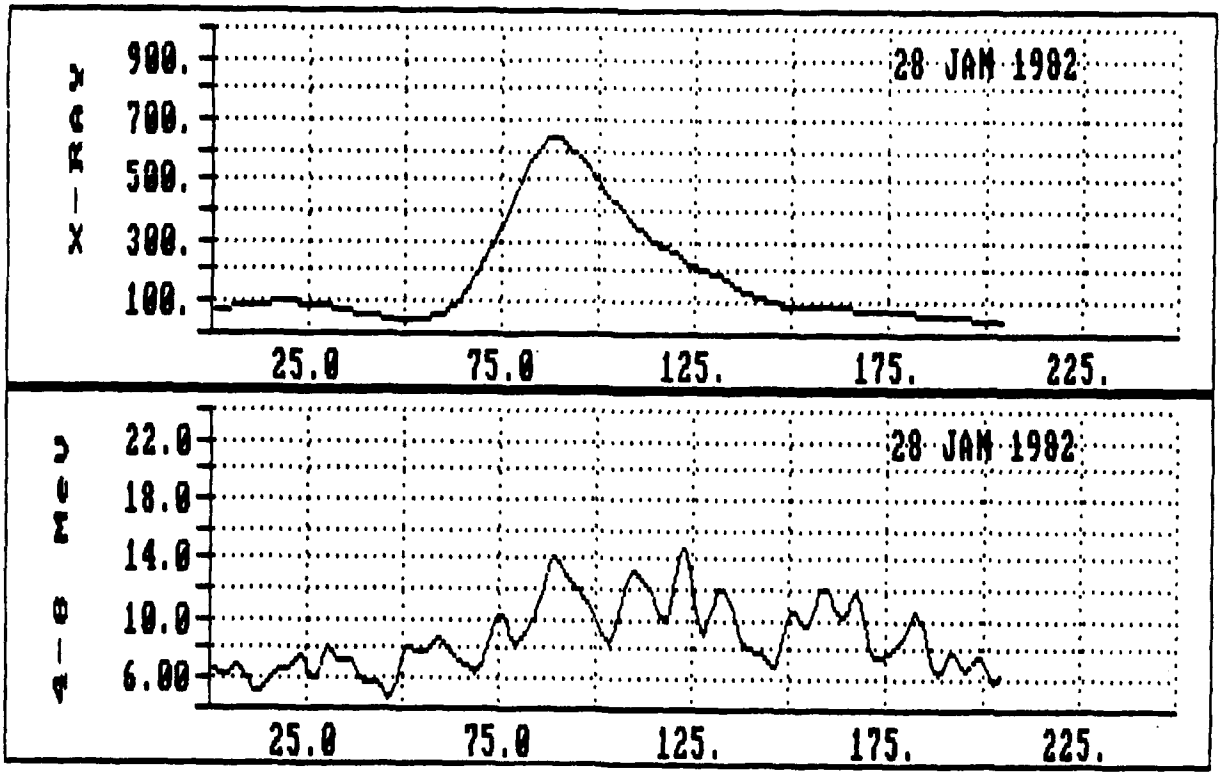

Figure 6. 28 January 1982 event.

Table 1.

DATE AND UT	CALCULATED X-RAY ONSET	X-RAY - GAMMA RAY ONSET
01 APRIL 1981 01:33:21	01:33:36.5	30.1 SECONDS
27 APRIL 1981 08:03:28	08:03:28.0	-12.5 SECONDS
13 MAY 1981 04:13:41	-----	--------
19 JULY 1981 05:58:44	05:58:23.4	-20.2 SECONDS
07 OCTOBER 1981 22:56:15	22:55:27.5	-5.1 SECONDS
28 JANUARY 1982 07:21:24	07:21:36.5	-2.5 SECONDS

1986 USAF-UES SUMMER FACULTY RESEARCH PROGRAM/
GRADUATE STUDENT RESEARCH PROGRAM

Sponsored by the
AIR FORCE OFFICE OF SCIENTIFIC RESEARCH
Conducted by the
Universal Energy Systems, Inc.

FINAL REPORT

Theoretical and Observational Studies of Geomagnetic Storm-Related Ion and Electron Heating in the Subauroral Region

Prepared by :	Janet U. Kozyra
Academic Rank:	Assistant Research Scientist
Department and	Atmospheric, Oceanic and Space Science Department
University:	University of Michigan
Research Location:	Air Force Geophysics Laboratory,
	Hanscom AFG, MA 01731
USAF Researcher:	Dr. Herbert Carlson
Date:	September 23, 1988
Contract No:	F49620-87-R-0004

Theoretical and Observational Studies of Geomagnetic Storm-Related Ion and Electron Heating in the Subauroral Region

by

Janet U. Kozyra

ABSTRACT

Recent theoretical work indicates that energetic oxygen ions (1 - 200 kev), a component of the earth's ring current, and suprathermal oxygen ions (< 1kev), that accumulate in the outer plasmasphere during geomagnetic activity, may be responsible for elevated electron and ion temperatures, respectively, associated with the subauroral region as a result of Coulomb interactions with the thermal plasma. Stable auroral red arcs are a visible consequence of elevated subauroral electron temperatures. SAR arc observations extend over several solar cycles and contain information on seasonal, solar cycle and magnetic activity variations in the subauroral electron temperature peak and its energy source. Such variations in SAR arc intensity and occurrence frequency may be due to differences in the high altitude heat source or to seasonal and solar cycle changes in the atmosphere and ionosphere. Past studies of SAR arcs have not addressed the question of their solar cycle or seasonal variability and detailed modelling has been done only for solar maximum observations. The ETS/GTMS campaign, which was carried out during the 19-24 September 1984 magnetic storm, however, has now provided a complete set of data detailing atmospheric and ionospheric conditions during the same time period that three solar minimum SAR arcs were observed by the MASP chain of photometers. A parametric study was carried out, using a truncated version of an ionosphere model described in Young et al (1980) and typical ionospheric and neutral atmospheric density profiles for each season and for various stages in the solar cycle given by the IRI and MSIS-86 models, respectively. Electron temperature profiles and resulting 6300Å emission intensity were obtained for different seasonal and solar cycle conditions holding upper boundary heat flux constant. The solar minimum SAR arc observations during the 19-24 September 1984 storm will be interpreted in light of the results of the parametric study and compared to models and observations of solar maximum SAR arcs which have appeared in the literature as work on this topic progresses. This study will provide an insight into causes of solar cycle variations in the intensity of SAR arcs and associated elevated electron temperatures. In addition to this work, a statistical study of the relationship between suprathermal oxygen ions, measured by the DMSP satellite and elevated ion temperatures, observed by the RIMS instrument on DE-1 was initiated. A number of individual storms will be examined in detail using the combined DMSP and DE-1 data sets.

I. INTRODUCTION

The subauroral region of the ionosphere is marked by elevated electron temperatures with associated enhanced 6300Å emissions (SAR arcs), steep plasma density gradients and low electron densities (associated with the main electron density trough), enhanced electron density irregularities, and occasionally, penetration of the convection electric field. At high altitudes, the subauroral ionosphere is overlain by the plasmapause and outer plasmasphere where a warm zone is observed in the ion and electron temperatures. The ion and electron temperatures in the outer plasmasphere and the electron temperatures in the subauroral ionosphere increase with increasing magnetic activity. All of these characteristic structures make the subauroral ionosphere a highly variable environment.

The Air Force Geophysics Laboratory at Hansom Air Force Base is concerned with the effects of the high altitude environment on radio and radar signals and on spacecraft communications, performance, and lifetime. In order to obtain the capability to predict the high altitude environment under different seasonal and solar cycle conditions as well as for different levels of magnetic activity, models of the thermosphere-ionosphere system are being assembled and tested against comprehensive measurements of ionospheric and thermospheric parameters. One such effort, made to better understand the response of the thermosphere - ionosphere system to geomagnetic storm conditions, was the ETS/GTMS (Equinox Transition Study/Global Thermospheric Mapping Study) campaign. This campaign involved coordinating the observational efforts of six incoherent scatter radars, 6 polar orbiting satellites, 4 Fabry-Perot interferometers and other supporting instrumentation to obtain a comprehensive set of diagnostics of thermospheric and ionospheric responses to the 19-24 September 1984 magnetic storm.

The Air Force Geophysics Laboratory, Space Physics Division also houses the DMSP data base. The DMSP satellites make extensive observations of ion and electron precipitation. These observations are important diagnostics of regions where energetic magnetospheric populations are undergoing diffusion into the loss cone due to collisions or wave-particle interactions. Such precipitation can cause interesting ionospheric effects.

My research interests lie in understanding the energy source of the ion and electron heating in the subauroral region. Recent theoretical work, by myself and coworkers, indicates that energetic oxygen ions (1 - 200 kev), a component of the earth's ring current, and suprathermal oxygen ions (< 1kev), that accumulate in the outer plasmasphere during geomagnetic activity, are a significant energy source (possibly the dominant energy source) for elevated electron and ion temperatures, respectively, associated with the subauroral region (Kozyra et al., 1987; Chandler et al., 1988). Energy transfer from the energetic

populations to the thermal plasma proceeds as a result of Coulomb interactions in the outer plasmasphere. An understanding of the energy source and its variation with magnetic activity, solar cycle and season as well, as an understanding of the corresponding variation in ionospheric signatures resulting from this high altitude heat source, is paramount to accurate modelling of the subauroral ionosphere and outer plasmasphere, and possible development of forecasting capabilities.

II. OBJECTIVES OF THE RESEARCH EFFORT

The objectives are twofold and involve investigations into the variation of electron and ion temperatures in the subauroral ionosphere and the outer plasmasphere. These studies are discussed below.

(i) Studies of the Subauroral Electron Temperature (Te) Enhancement

Though the subauroral electron temperature peak was first discovered by Brace et al. (1967) and attributed to heat conduction from the magnetosphere in the vicinity of the plasmapause, statistical studies of the variation of the intensity and position of the Te peak with magnetic activity have only recently been performed (Kozyra et al., 1986; Buchner et al.,1983; Brace et al., 1988) over limited time intervals. These studies, however, do not contain information on the seasonal and solar cycle variations in the observations. Stable auroral red (SAR) arcs are the optical manifestation of the subauroral Te peak. In the region of the subauroral Te peak, significant populations of thermal electrons with energies in excess of 1.96 eV exist in the high energy tail of the Maxwellian distribution. These electrons are capable of exciting atomic oxygen to the ^1D state during a collision. The ^1D state relaxes in 110 seconds with the emission of a photon at 6300Å. The ^1D state can also be quenched via collisions with molecular nitrogen. Significant 6300Å emission only results at altitudes high enough so that collisions with molecular nitrogen are infrequent. The amount of 6300Å emission which results from this process is dependent on the neutral atmospheric densities of O and N_2, the N_e density at the F2 peak, the height of the F2 peak, and the electron temperature.

SAR arc observations extend over several solar cycles and contain information on seasonal, solar cycle and magnetic activity variations in the subauroral electron temperature peak and its energy source. SAR arcs occur most frequently during the equinoxes, are rarely observed in June or July (Hoch, 1973), and there is a 2-3 year phase lag between the maximum in the solar cycle and the maximum in SAR arc occurrence frequency (Slater and Smith, 1981). Initial results of a study of the variation of SAR arc intensity with solar cycle, currently underway in collaboration with D. W. Slater at Battelle Observatory in

Washington, indicate that SAR arcs are weaker during solar minimum than during solar maximum for the same intensity of ring current as indicated by the D_{st} index. Such variations in SAR arc intensity and occurrence frequency may be due to differences in the high altitude heat source or to seasonal and solar cycle changes in the atmosphere and ionosphere resulting in lower electron temperatures for a given heat flux. Past studies of SAR arcs have not addressed the question of their solar cycle or seasonal variability and detailed modelling has been done only for solar maximum observations.

The ETS/GTMS campaign, which was carried out during the 19-24 September 1984 magnetic storm, however, has now provided a complete set of data detailing atmospheric and ionospheric conditions during the same time period that three solar minimum SAR arcs were observed by the MASP chain of photometers. DE-1 satellite observations of energetic and thermal ion populations were available making it possible to characterize the high altitude heat source. A parametric study was carried out, using a truncated version of an ionosphere model described in Young et al (1980) and typical ionospheric and neutral atmospheric density profiles for each season and for various stages in the solar cycle given by the IRI and MSIS models, respectively. Electron temperature profiles and resulting 6300Å emission intensity were obtained for a variety of model conditions. This study is intended to explore the effect that typical seasonal, solar cycle and magnetic storm-time variations in the neutral atmosphere and ionosphere have on the intensity of SAR arcs by holding the heat flow constant at the upper boundary and allowing only atmospheric and ionospheric parameters to vary. The solar minimum SAR arc observations during the 19-24 September 1984 storm will be interpreted in light of the results of the parametric study, as work continues, and compared to models and observations of solar maximum SAR arcs, which have appeared in the literature, to provide an insight into causes of solar cycle variations in the intensity of SAR arcs.

(ii) Studies of elevated ion temperatures in the outer plasmasphere and ionospheric effects

There has been a wealth of observational evidence for ion heating in the outer plasmasphere in the last two decades. Bezrukikh and Gringauz (1976) presented observations of ion temperatures from Prognoz and suggested that the plasmasphere should be considered as consisting of both "cold" (Ti< 8000K) and "warm" (Ti ~10,000 to 200,000K, L>3) zones. Observations from ATS-6, GEOS, ISEE and SCATHA as well as DE-1 all confirm these observations of a warm outer zone and a cold inner zone.

Theoretical modelling, using observed energetic and thermal ion populations, indicates that suprathermal oxygen ions that accumulate in the outer plasmasphere are responsible for heating the thermal ions in this warm outer zone via Coulomb collisions (Chandler et al.,

1988). The behavior of this suprathermal oxygen ion population in the outer plasmasphere with magnetic activity has not yet been established. However, recently there have been observations of an ion population precipitating into the F region during geomagnetic storms with similar energy and composition characteristics which likely originates from this source population in the outer plasmasphere. Newell and Meng (1986) report on observations by the DMSP satellite of up to 1 KeV ion precipitation within the plasmasphere as a common feature during and after prolonged magnetic substorm activity. They infer that injections occur from postmidnight to ~ 8:30 MLT and the ions subsequently co-rotate and precipitate with a lifetime of approximately 1 day. There is indirect evidence that these ions are predominantly O^+. Though Newell and Ming site magnetospheric injection processes as a potential source, these observations are remarkably similar to those of Bosqued (1985), Jorjio (1985), and Menietti et al. (1986) who propose an ionospheric source.

The source of these suprathermal oxygen ions as well as the location and strength of this population during different levels of magnetic activity are still very much open to question. Although plasmaspheric ion temperatures in general increase during magnetic storms, the statistical behavior of these temperatures is not clearly correlated with magnetic storm activity as indicated by the D_{st} or K_p indices (R. H. Comfort, private communication) but must have a more complicated dependence. The statistical behavior of the ion temperatures and of the precipitating ion populations on the same L shells during the same time interval should give clues to the source of the ions and to the relationship of this ion population to elevated ion temperatures. There exists a period of overlap between DE-1 observations of thermal ion temperatures in the outer plasmasphere and DMSP observations of precipitating low energy ions. In cooperation with Dr. R. H. Comfort, at the University of Alabama, we plan to compare the statistical behavior of the ion temperatures in the outer plasmasphere as they respond to changing geomagnetic storm conditions with that of suprathermal ion populations observed by DMSP. In addition, we plan to look in detail at the relationships between precipitating suprathermal ions seen by DMSP, thermal plasma boundaries, suprathermal oxygen ions and thermal ion temperatures in the outer plasmasphere observed by the instruments on DE-1 for a number of individual geomagnetic storms.

III. SOLAR CYCLE AND SEASONAL VARIATIONS IN SAR ARCS

(i) Theoretical Ionosphere Model

The model used in this study is based on a plasmasphere model developed by D.G. Torr and co-workers. The details of the model have been referenced in previous works (cf. Young et al., 1980). The model in its original form solves the continuity, momentum,

energy and heat flow equations for a plasma consisting of O^+, H^+, and electrons along an entire plasmaspheric flux tube. The model was modified by M.O. Chandler to accept an upper boundary flux condition at some specified altitude, thus allowing one hemisphere to be modelled with properly specified upper boundary conditions.

For the present study nightside ionospheric and neutral density profiles are specified and the model is employed to solve the energy equation only and obtain ion and electron temperature profiles. At the upper boundary (~3000 km altitude), a magnetospheric heat flux in the ions and electrons is specified. At the lower boundary (200 km altitude), the electron and ion temperatures are set equal to the neutral temperature. In the subauroral ionosphere where field-aligned currents are not generally present and quasi-steady state conditions prevail, the electron energy equation reduces to a particularly simply form (Schunk and Nagy, 1978):

$$\sin^2 I \frac{\partial}{\partial z} (K^e \partial Te/\partial z) + \Sigma Q_e - \Sigma L_e = 0 \qquad (1)$$

where I is the geomagnetic dip angle, z is the vertical coordinate, Te is the electron temperature and K^e is the electron thermal conductivity in the limit of zero current. Above ~300 km, K^e reduces to the fully ionized conductivity given by Spitzer (1956).

$$K^e = 7.7 \times 10^5 \, Te^{5/2} \text{ eV s}^{-1} \text{ cm}^{-1} \text{ deg}^{-1} \qquad (2)$$

The first term on the right in equation (1) is the divergence of the electron heat flow vector, The second and third terms are the sum of the heating and cooling terms, respectively. At low altitudes, thermal conductivity in the electrons is negligible. The electron temperature is established by a competition between local heating and cooling rates. The magnetospheric heat flow is very important in determining the topside electron temperatures. Large magnetospheric heat fluxes can occur in the subauroral region during magnetic storms. Model studies indicate that electron heat fluxes of the order of 7×10^9 - 1×10^{11} eV cm^{-2} s^{-1} are required to produce the range of SAR arc intensities observed by ground-based photometers (Rees and Roble, 1975). For the present study no local heat sources are considered. Heat conduction from the magnetosphere is the only energy source in the electron gas. This is reasonable for the near-midnight subauroral ionosphere.

The relative importance of various electron cooling rates for high electron temperatures typical of SAR arcs were examined by Rees and Roble (1975). The authors found the dominant electron cooling under these conditions to be due to excitation of the vibrational levels of N_2 below ~450 km and to excitation of $O(^1 D)$ above this altitude.

(ii) 6300Å Emission Model

Electron impact excitation of $O(^1D)$ is calculated in the ionosphere model using the cross-sections of Henry et al. (1969). The radiative lifetime of $O(^1D)$ is 110 seconds, therefore collisional deactivation must be taken into consideration. The most important species for collisional quenching is N_2. The volume emission rates were calculated using the relation

$$\varepsilon_{6300} = \frac{A_\lambda}{A_D} \cdot \frac{P(O^1D)}{[1 + S_D n(N_2)/A_D]} \qquad (3)$$

where A_λ and A_D are the Einstein transition probabilities for emission at 6300Å and at (6300Å + 6364Å), respectively. The values of these probabilities are given by Kernahan and Pang (1975) as $A_\lambda = 5.15 \times 10^{-3}\ s^{-1}$ and $A_D = 6.81 \times 10^{-3}\ s^{-1}$. S_D is the rate coefficient for collisional quenching by N_2 given as $2.3 \times 10^{-11}\ cm^3\ s^{-1}$ (Link et al., 1981). $P(O^1D)$ is the production rate of $O(^1D)$ atoms by electron impact.

(iii) Model Inputs

The purpose of the parametric study is to represent as accurately as possible characteristic solar cycle and seasonal variations in the atmospheric and ionospheric conditions in the subauroral region in order to establish solar cycle and seasonal trends in SAR arc emission due to these characteristic variations. The magnetospheric heat flow is held constant in these calculations. To represent the neutral atmosphere, the MSIS86 empirical model (Hedin, 1987) was selected with the following parameters chosen as representative of a magnetic storm characterized by a minimum D_{st} index of -80 γ during solar maximum and minimum conditions.

	F10.7	F10.7A	Ap	Local Solar Time	Sunspot No.
Solar Maximum	186	175	30	23 hours	145
Solar Minimum	84	74	30	23 hours	20

The International Reference Ionosphere (IRI) model was chosen to represent general solar cycle and seasonal trends in the ionospheric densities. Seasonal variations were represented by ionospheric profiles in March, June, September and December at the location of Millstone Hill (42.6°N, 71.5°W). The IRI model does not represent magnetic storm variations in the height (HMF2) and magnitude (NMF2) of the F2 peak or the characteristics of the main electron density trough which encroaches into the subauroral region during magnetic storm conditions. SAR arcs are located on or within the equatorward wall of the main electron density trough (cf. Rees and Roble, 1975);

therefore, solar cycle, seasonal and geomagnetic storm variations in the trough depth are very important to properly represent the ionosphere in the vicinity of the SAR arc. Characteristic changes in NMF2 and HMF2 ionosphere due to increased magnetic activity are imposed on the baseline IRI model for the purposes of this study.

Proper representation of the variations in the characteristics of the main electron density trough are very important to the present study. The trough is a persistent large-scale feature of the nightside subauroral region. The occurrence frequency of the trough as determined using ISIS-1 and INJUN-5 satellite data, in the time interval November 1968 - November 1970, on the nightside, is ~96% (Best and Wagner, 1983). The electron density trough is typically 10^{o} latitude wide with a decrease in electron density of about one order of magnitude at 400 km (Kohnlein and Raitt, 1977). During magnetic disturbances the trough becomes shallower. Observations of 1000 troughs by ARIEL-III indicates that trough occurrence frequency increases with increasing geomagnetic activity (Tulunay and Sayers, 1971). Examination of troughs observed by IK-10 and IK-18 satellites indicates that the frequency of nighttime troughs increases from 78% for K_p =1 to 95% for K_p=4. Therefore, we might expect significantly depressed densities in the vicinity of the SAR arc routinely. In fact, a study of the relative positions of the trough minimum and subauroral Te peak using IK-18 data indicates that the Te peak often coincides with the trough minimum at altitudes between 400 and 750 km at local times between 23 hours and 3 hours. At other local times the trough minimum occurs within 0.3^{o} - 1.5^{o} invariant latitude poleward of the Te peak (Best and Wagner, 1983).

Wagner et al. (1981) found, using measurements from a network of ionosonde stations during the magnetic storm of January 22 - February 4, 1974 at 5 hours local time, that initially during storm main phase, the trough becomes shallower, densities dropping by a factor of 2.5 from the equatorward wall to the trough minimum. As storm recovery proceeds, the densities drop by a factor of 6 in the trough.

Profiles from Millstone Hill Observatory for summer and winter, solar maximum and solar minimum conditions were compiled (M. Bdonsanto, private communication). In general the observed NMF2 during magnetically active conditions appeared to be a factor of 1.5 less and HMF2 50 km higher than in the IRI model. This is consistent with the results of Lockwood (1980), who deduced that HMF2 inside the trough is greater than its value outside by between 30 and 80 km. It appears the IRI profiles more closely represent magnetically quiet conditions at the location of Millstone Hill.

In light of the observational evidence, the IRI model profiles were scaled by a factor of 0.66 and HMF2 increased by 50 km to represent magnetically active periods. To examine

the sensitivity of the model results to these parameter, NMF2 was scaled by factors of 5.0, 2.0, 0.5, 0.2, 0.1 and 0.05 and HMF2 shifted up and down by 50 km from the IRI model value. Such variations in HMF2 are reasonable. During magnetically active times, heating of the thermosphere over the polar and auroral regions contributes a strong component to the equatorward wind (cf. Miller et al., 1986) which blows ionization up the field line to higher altitudes and increases the height of the F2 peak. Another consequence of neutral heating over the polar and auroral regions is an increase of the scale heights in the neutral atmosphere. Increased scale heights bring more N_2 to high altitudes in the vicinity of the F2 peak and decreases the O/N_2 ratio at high altitudes. This has significant effects both on the electron temperature and on the amount of 6300Å emission produced from a given magnetospheric heat flux. Elevated neutral temperatures have been observed all the way down to subauroral latitudes as a result of heating in the high latitude regions. Variations on the exospheric temperatures predicted by MSIS86 of $\pm$ 100°K and +400°K are thought to bracket reasonably well normal storm time variations.

(iv) Results of the Parametric Study

(a) Baseline Study

First a baseline set of models was run using the *IRI* and *MSIS86 models to represent* solar cycle and seasonal variations in the subauroral ionosphere and atmosphere, respectively, at an L shell of 3 during a magnetic storm with a main phase decrease in the surface magnetic field of approximately -80γ. Such a storm in solar maximum has statistically been shown to produce electron temperatures at 400 km of about 3200°K (Kozyra et al., 1986) and 6300Å emission of some 100's of Rayleighs to nearly a kR depending on the neutral atmosphere and ionospheric conditions. The magnetospheric electron heat flux associated with such a storm is ~2.5 x 10^{10} ev/cm^2/s (Rees and Roble, 1975). This heat flux was held constant for all model runs. Figure 1(a) shows the results of this baseline study. Interestingly enough, maximum emissions are observed during solar minimum conditions for a fixed heat flux. The corresponding model seasonal and solar cycle variations in NMF2 (Figure 1b) and HMF2 (Figure 1c) are also presented. Solar minimum values of NMF2 are lower than those in solar maximum. This trend is largely responsible for the enhanced 6300Å column emission during solar minimum. Lower electron densities (Ne) result in the magnetospheric heat flux being distributed among fewer particles. At the same time lower ion densities result in less cooling to the ions in solar minimum. The combination of these effects causes high electron temperatures and correspondingly, more 6300Å emission. Figure 2 (b-d) displays model atmospheric and ionospheric conditions during winter and summer for the baseline study. Volume emission rates are given in Figure 2(a). Volume emission rates peak at lower altitudes in solar minimum than solar

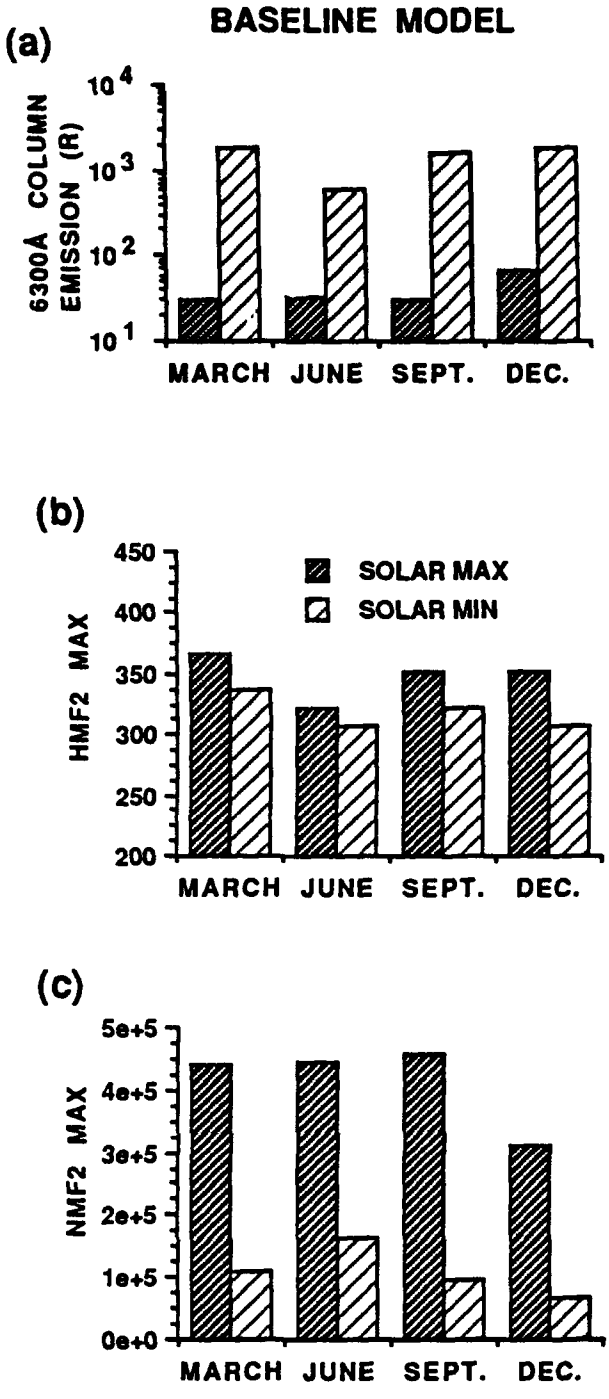

Figure 1: Results of the baseline study. Solar cycle and seasonal changes in the neutral atmosphere and ionosphere were represented by the MSIS-86 model and the IRI model, respectively, with inputs appropriate to the season and part of the solar cycle. Presented above are (a) 6300Å column emission intensity and the corresponding variation in (b) NMF2 and (c) HMF2.

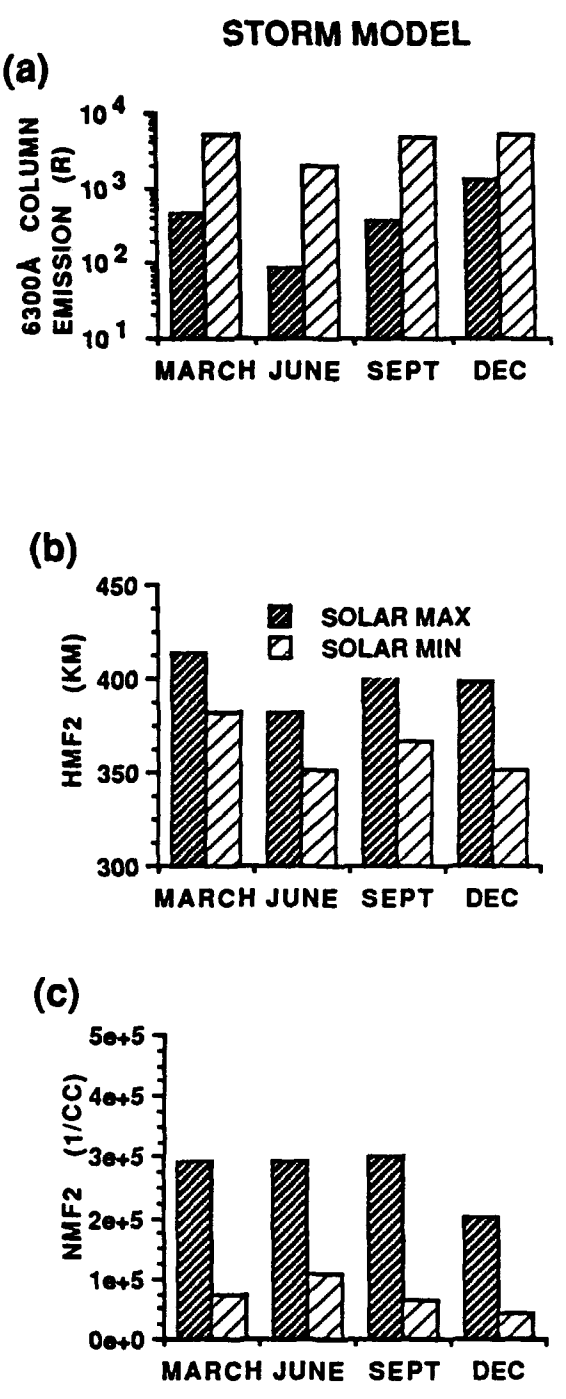

Figure 4: Characteristic magnetic storm-time variations in NMF2 and HMF2 were superimposed on the baseline model to better represent conditions in the subauroral ionosphere in the vicinity of SAR arcs. Presented here are (a) the 6300Å column emission intensity and the corresponding seasonal and solar cycle variations in (b) HMF2 and (c) NMF2.

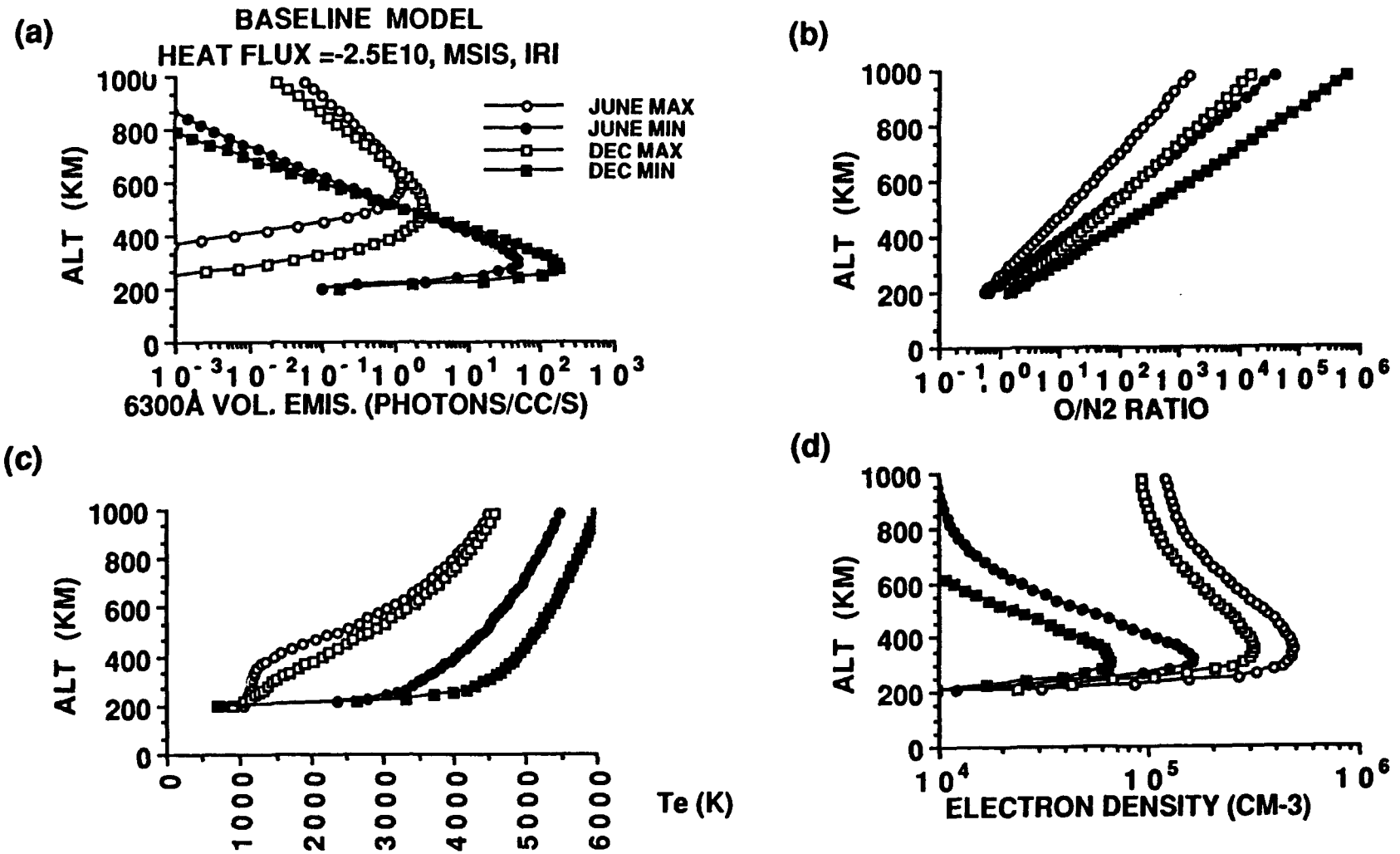

Figure 2: Altitude profiles of (a) 6300Å volume emission rate, (b) O/N_2 ratio from the MSIS-86 model atmosphere, (c) calculated electron temperatures and (d) IRI model electron density for conditions representative of June and December in solar maximum and solar minimum. These profiles correspond to the models presented in Figure 1.

maximum and are greater in December than in June. Electron temperatures (Fig. 2c) in general are inversely related to electron densities - the highest temperatures are established for the lowest electron densities. Higher O/N_2 ratios (Fig. 2b) are more favorable for the production of 6300Å emission because the production of $O(^1D)$ is proportional to the O density and the collisional quenching to the N_2 density.

(b) Sensitivity Study

The following reasonable variations on the standard December solar minimum model were considered to examine the sensitivity of the calculated 6300Å emission to model assumptions: (1) ± 100°K, +400°K in the neutral exospheric temperature, (2) ± 50 km in HMF2, and (3) NMF2 scaled by 5.0, 2.0, 0.2, 0.1, and 0.05. Figure 3 gives the results of this sensitivity study. By far, the largest variation in 6300Å emission intensity results from an increase in the height of the F2 layer by 50 km. When the F2 peak is shifted upward with respect to the neutral atmosphere, electron-neutral cooling resulting from the vibrational excitation of N_2 is decreased due to a decrease in the N_2 density in the vicinity of the Ne peak. As a result of diminished cooling rates, higher electron temperatures are established. At the increased altitude of the F2 peak, the O/N_2 ration is greater resulting in more 6300Å emission for a given electron temperature.

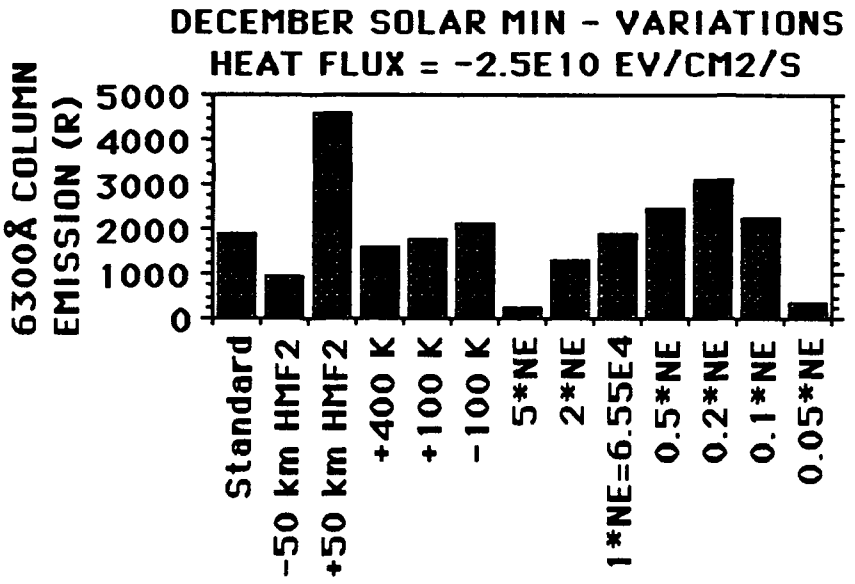

Figure 3: Variations in the 6300Å column emission intensity resulting from reasonable modifications in model inputs for the December solar minimum baseline model. The neutral exospheric temperature calculated by the MSIS-86 model was changed by ± 100°K, and +400°K, HMF2 was changed by ±50 km, and NMF2 was scaled by factors of 5.0, 2.0, 0.5, 0.2, 0.1, and 0.05.

Increasing the neutral temperature results in larger neutral scale heights and thus an increase in neutral density , an increase in the relative amount of heavy ions and a decrease in the O/N_2 ratio at the altitude of the electron density peak. The reverse occurs as a result of a decrease in the neutral exospheric temperature. Increased neutral densities at the altitudes of the F2 peak results in increased electron-neutral cooling and thus reduced electron temperatures . In addition to the increased electron-neutral cooling, a more unfavorable ratio of O/N_2 contributes to a decrease in the 6300Å emission (see Fig.3). The reverse situation for lower neutral exospheric temperatures results in increased 6300Å emissions.

Finally, changes in the electron density significantly effect the 6300Å column emission resulting from a given magnetospheric heat flux as demonstrated in Figure 3. But whether the result is an increase or decrease in the 6300Å column emission depends on the value of the electron density. Initially a decrease in the density produces an increase in the 6300Å emission rate but as the electron density is decreased further, eventually the 6300Å emission begins also to decrease. In all cases as the electron density is decreased the electron temperature increases for a fixed magnetospheric heat flux. This is because the heat flux is distributed among fewer electrons. Electrons with energies in excess of 1.96 ev are responsible for exciting oxygen atoms to the ^1D state. Initially an increase in the electron temperature results in a larger population of electrons with energies in excess of 1.96 ev. But as the density is decreased further, smaller and smaller populations of >1.96 ev electrons exist, even in the presence of higher electron temperatures and the 6300Å emission begins to decrease.

(c) Storm Study

Since detectable SAR arcs occur only during magnetically active times, modifications to the ionosphere and atmosphere were made which are characteristic of observed variations during magnetic storms. These adopted magnetic storm variations are in agreement with Millstone Hill observations during active times. For all seasons, NMF2 was multiplied by 0.66 and HMF2 was increased by 50 km. Model results are presented in Figure 4. Two trends are immediately obvious. First, there is a very pronounced seasonal variation in the 6300Å emission intensity in solar maximum and a less pronounced variation in solar minimum. In both cases, weaker emissions occur in June for the same magnetospheric heat flux. This is in agreement with the SAR occurrence frequency which reaches a minimum in June and July (Hoch, 1973). Second, significantly more 6300Å emission results in solar minimum than in solar maximum for the same magnetospheric heat flux. Initial results of a statistical study of solar cycle changes in SAR arc intensity indicate that weaker SAR arcs occur during solar minimum than during solar maximum for the same level of magnetic activity indicated by the D_{st} index (Slater, private communication). The

D_{st} index is a measure of the strength of the ring current since it represents the depression in the surface magnetic field resulting from the magnetic field generated by the ring current. Strong theoretical and observational evidence indicates that the ring current is the source of the electron heating in the subauroral region (cf. Hoch, 1973; Rees and Roble, 1975; Kozyra et al., 1987). This initial result indicates that the magnetospheric heat flux is less in solar minimum than in solar maximum for the same ring current intensity. If the result holds true under more detailed modelling, this is an important clue to the nature of the energy transfer mechanism.Seasonal and solar cycle trends in the depth of the main electron density trough and/or in the height of the F2 peak in the trough region are not well established and systematic variations in these quantities may change the result reported above. More modelling is definitely warranted, looking in detail at selected well-measured storms in solar maximum and solar minimum.

(v) Model of the September 19-24, 1984 Magnetic Storm

The magnetospheric storm period of September 19-24, 1984 was chosen for detailed modelling. SAR arcs were observed on the 19th, 20th and 24th by the MASP chain of photometers (D. Slater, private communication). Elevated electron temperatures associated with the SAR arc of September 20 are clearly visible in Millstone Hill observations from 00:23:17 UT to 2:02:17 UT . Also available are electron densities for this time interval and neutral exospheric temperatures. Efforts are underway to obtain these observations for use in a detailed model of the emissions during this time interval. Models will be constructed at intervals during the storm period - for both SAR arc and non-SAR arc conditions. Results of these models will be compared to models of SAR arcs observed during solar maximum magnetic storms (Rees and Roble, 1975; Kozyra et al., 1982; Slater et al., 1987; Kozyra et al., 1987).

Observations of electron density and temperature were on hand, however, at an L shell of ~3 (directly overhead at Millstone Hill) for several intervals on September 23, 1984. During this time, weather conditions prevented ground-based detection of SAR arc emissions, if any existed. Modelling of this time period serves as an initial test of the ability of the ionosphere model to represent conditions which were observed during this solar minimum storm period. Figure 5(a) presents electron densities observed by Millstone Hill (B. Oliver, private communication). Also plotted are model O^+ and H^+ profiles constructed to be consistent with observations. Figure 5(b) is an MSIS86 neutral atmosphere model consistent with observed magnetic storm and solar conditions during this time interval, with an exospheric temperature of 1000^o K. The model electron temperature profile which results from a magnetospheric heat flux of 3.5×10^{10} ev/cm^2/s is compared to measured electron temperatures in Figure 5(c) showing very good agreement.

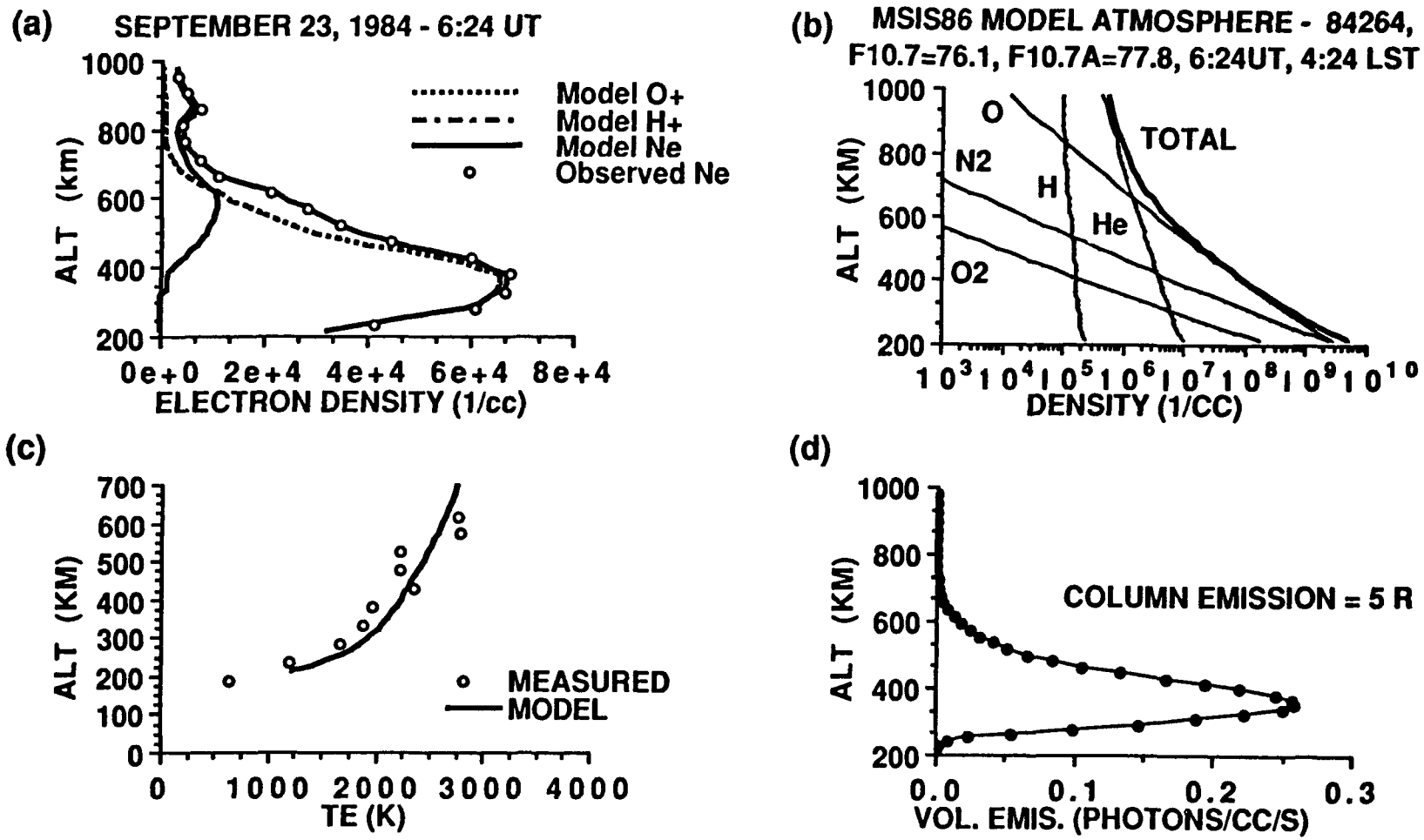

Figure 5: Model results for conditions on September 23, 1984 at 6:24 UT. Presented here are (a) model and observed electron densities and model O^+ and H^+ profiles, (b) MSIS-86 neutral atmosphere representative of conditions at this time, (c) observed and calculated electron temperatures, and (d) calculated 6300Å volume emission rates.

The model 6300Å volume emission rate profile is given in Figure 5(d) and corresponds to a column integrated 6300Å emission intensity of only 5 rayleighs. A number of other intervals will be modelled during the storm to gain information on the storm-time variations in the electron temperature and 6300Å emission intensity in the subauroral region.

V. RECOMMENDATIONS

The results of the SAR arc studies indicate that seasonal variations in SAR arc intensities can be attributed to seasonal variations in the neutral atmosphere and ionosphere but solar cycle variations cannot be explained by normal solar cycle changes in these quantities. A word of caution should be injected here. In view of the uncertainties in our observational knowledge of the solar cycle, seasonal, and magnetic storm-time variations in relevant model inputs, a detailed theoretical and observational study of a number of solar minimum SAR arcs is indicated. Comparison of solar minimum SAR arcs with examples of solar maximum SAR arcs in the literature, interpreted in light of the parametric study presented in this report, would help to verify the above somewhat tentative conclusions which imply that the magnetospheric heat flux is decreased during solar minimum when compared to solar maximum for the same ring current intensity. Kozyra et al. (1987) find that Coulomb collisions between thermal electrons and the oxygen ion component of the ring current, heat the electron gas sufficiently to support the elevated electron temperatures observed in the F region ionosphere during several SAR arcs in solar maximum. The oxygen ion component of the ring current, however, has been observed to decrease with the sunspot number (Young et al., 1982). A ring current which produces a given depression in the surface magnetic field indicated by the D_{st} index would contain a significantly lower percentage of oxygen during solar minimum than during solar maximum. Thus solar cycle changes in the energy source could modulate the SAR arc intensity in the manner indicated by observations. Since the Coulomb collision rate is also directly proportional to the thermal electron density in the plasmasphere, systematic solar cycle variations in the plasmaspheric densities could also be responsible for modulating the magnetospheric heat flow resulting from a given ring current population. However, plasmaspheric densities inferred from whistler observations indicate no significant solar cycle variation in the outer plasmasphere (Park et al., 1978).

The next step to a better understanding the energetics of the plasmapause region is a parametric study of the magnetospheric heat source. A reasonable ring current distribution could be adopted for the study assuming different percentages of heavy ions as the solar cycle progresses. These variations in composition would be based on the observational work of Young et al. (1982) and others. The ultimate aim of this recommended work and the aim of the study detailed in this report is to attempt to parametrize the magnetospheric

heat source in the subauroral ionosphere. This would allow more accurate modelling of the spacecraft environment in the subauroral region for different solar cycle and seasonal conditions.

The heat flux in the ions is also important to the energetics of the outer plasmasphere and magnetically connected subauroral ionosphere. Studies of the relationship between elevated ion temperatures in the outer plasmasphere and topside ionosphere and suprathermal oxygen ion populations that accumulate in the outer plasmasphere indicate that these suprathermal oxygen ions may be the energy source for the thermal protons via Coulomb collisions (Kozyra et al., 1987; Chandler et al., 1988). This being the case, statistical studies should indicate a relationship between (<100 ev) ions precipitating into the ionosphere from the source populations in the outer plasmasphere and elevated ion temperatures on the same field lines. A comparison between observations of low energy ion precipitation in the subauroral region by the DMSP satellite and observations by the retarding ion mass spectrometer on the DE-1 satellite of elevated ion temperatures could form the basis for the statistical study outlined above. In addition, a close comparison of DMSP observations of precipitating ions, DE-1/RIMS observations of thermal ion temperatures and observations of the suprathermal oxygen ion population in the outer plasmasphere by the energetic ion composition spectrometer (EICS) on DE-1 during selected individual magnetic storms would contribute immeasurably to our understanding of the energetics of the subauroral region. These statistical and observational studies may help to determine under what conditions ion temperatures will be elevated in the outer plasmasphere, leading ultimately to more accurate modelling of the plasma environment in the subauroral region.

ACKNOWLEDGEMENTS

I wish to thank the Air Force Systems Command, the Air Force Office of Scientific Research and the Air Force Geophysics Laboratory at Hanscom Air Force Base for sponsorship of this research. I would like to express appreciation to Drs. Nelson Maynard, Gary Mullen, Kenneth Vickery and Dolph Jursa for help and hospitality in dealing with administrative problems and assistance in setting up an enjoyable and efficient working environment in the PHG, PHP and LI branches. I would like to especially acknowledge the efforts of Drs. Herbert Carlson and Cesar Valladeres whose assistance was invaluable in designing and carrying out the SAR arc study described in this report. In addition, I would like to express my appreciation to Dr. Henry Wadzinski for the use of his IRI model and associated programs and to Dr. Jurgen Buchau for interesting and helpful discussions on the characteristics of the subauroral ionosphere. Discussions with Drs. Susan Gussenhoven and William Swider were instrumental in understanding and

interpreting DMSP ion precipitation and in designing future studies to examine multi-satellite observations in the subauroral region. A great advantage in spending the last ten weeks at AFGL was the opportunity to discuss scientific topics of mutual interest with highly respected scientists in the space physics and aeronomy communities. Such discussions are an invaluable source of insight and inspiration. In this regard, I would like to express appreciation to Drs. William Burke, Elaina Villalon, Gary Erickson, Greg Ginet, Paul Rothwell, Howard Singer, David Anderson and Frank Marcos for interesting and stimulating scientific discussions.

REFERENCES

Best, A., C.-U. Wagner, Variations of electron density and electron temperature in the main trough of the ionosphere. Morphology and characteristic parameters of the trough in "Physical Processes in the Main Ionospheric Trough Region, Proceedings of the Symposium organized by KAPG projects 5 and 6, Praha, 28-31 March 1983.

Bezrukikh, V. V. and K.I. Gringauz, J. Atmos Terr. Phys., 38, 1085, 1976.

Bosqued, J. M., Ion precipitation into the ionosphere during geomagnetic storms, Adv. Space Res., 5, 179, 1985.

Brace, L. H., B. M. Reddy, and H. G. Mayr, Global behavior of the ionosphere at 1000-kilometer altitude, J. Geophys Res., 72, 265, 1967.

Brace, L. H., C. R. Chappell, M.O. Chandler, R. H. Comfot, J. L. Horwitz, W. R. Hoegy, F region electron temperature signatures of the plasmapause based on Dynamics Explorer 1 and 2 measurements, J. Geophys. Res., 93, 1896, 1988.

Buchner, J., H.-R. Lehmann, and J. Rendtel, Properties of the subauroral electron temperature peak observed by Langmuir-probe measurements on board intercosmos-18, Gerlands Beitr. Geophys., 92, 368, 1983.

Chandler, M.O., J. U. Kozyra, J. L. Horwitz, R. H. Comfort, W. K. Peterson, and L. H. Brace, Modelling of the thermal plasma in the outer plasmasphere: a magnetospheric heat source, AGU Monograph on Magnetosphere and Ionosphere Plasma Models, eds., T. E. Moore, J. H. Waite, Jr., and T. Moorhead, 1988.

Hedin, A. E., MSIS-86 thermospheric model, J. Geophys. Res., 92, 4649, 1987.

Henry, R. J. W., P. G. Burke, and A. L. Sinfailam, Scattering of electrons by C, N, O, N^+, O^+, and O^{++}, Phys. Rev., 178, 218, 1969.

Hoch, R. J., Stable auroral red arcs, Rev. Geophys. Space Phys., 11, 935, 1973.

Jorjio, N. V., R. A Kovrazhkin, M. M. Mogilevsky, J. M. Bosqued, H. Reme, J. A. Sauvaud, C. Beghin, and J. L. Rauch, Adv. Space Res., 5, 141, 1985.

Kernahan, J. H., and P. H. L. Pang, Experimental determination of absolute A coefficients for "forbidden" atomic oxygen lines, Can. J. Phys., 53,455, 1975.

Kohnlein, W., and W. J. Raitt, Position of the mid-latitude trough in the topside ionosphere as deduced from ESRO 4 observations, Planet. Space Sci., 25, 600, 1977.

Kozyra, J. U., T. E. Cravens, A. F. Nagy, M.O. Chandler, L. H. Brace, N. C. Maynard, D. W. Slater, B. A. Emery and S. D. Shawhan, Characteristics of a stable auroral red arc event, Geophys. Res. Lett., 9, 973, 1982

Kozyra, J. U., L. H. Brace, T. E. Cravens, and A. F. Nagy, A statistical study of the subauroral electron temperature enhancement using Dynamics Explorer 2 Langmuir probe observations, J. Geophys. Res., 91, 11270, 1986.

Kozyra, J. U., E. G. Shelley, R. H. Comfort, L. H. Brace, T. E. Cravens, and A. F. Nagy, The role of ring current O^+ in the formation of stable auroral red arcs, J. Geophys. Res., 92, 7487, 1987.

Link, R. J., J. C. McConnell, and G. G. Shepherd, A self-consistent evaluation of the rate constants for the production of the O I 6300 Å airglow, Planet. Space Sci., 29, 589, 1981.

Lockwood, M., The bottomside mid-latitude ionospheric trough, J. Atmos. Terr. Phys., 42, 605, 1980.

Menietti, J. D., J. D. Winningham, J. L. Burch, W. K. Peterson, J. H. Waite, Jr., and D. R. Weimer, Enhanced ion outflows measured by the DE 1 high altitude dayside plasmasphere during the recovery phase, J. Geophys. Res., 90, 1653, 1985.

Miller, K. L., D. G. Torr, and P. G. Richards, Meridional winds in the thermosphere derived from measurement of the F_2 layer height, J. Geophys. Res., 91, 4531, 1986.

Newell, P. T., and C.-I. Meng, Substorm introduction of $\leq$ 1kev magnetospheric ions into the inner plasmasphere, J Geophy. Res., 91, 11133, 1986.

Park, C. G., D. L. Carpenter, and D. B. Wiggin, Electron density in the plasmasphere: whistler data on solar cycle, annual and diurnal variations, J. Geophys. Res., 83, 3137, 1978.

Rees, M. H., and R. G. Roble, Observations and theory of the formation of stable auroral red arcs, Rev. Geophys., 13, 201, 1975.

Schunk, R. W. and A. F. Nagy, Electron temperatures in the F region of the ionosphere: theory and observations, Rev. of Geophys. Space Phys., 16, 355, 1978.

Spitzer, L., Physics of Fully Ionized Gases, Interscience, New York, 1956.

Slater, D. W., and L. L. Smith, Modulation of stable auroral red (SAR) arc occurrence rates, J. Geophys. Res., 86, 3669, 1981.

Slater, D. W., C. Gurgiolo, J. U. Kozyra, E. W. Kleckner, and J. D. Winningham, A possible energy source to power stable auroral red arcs: precipitating electrons, J. Geophys. Res., 92, 4543, 1987.

Tulunay, Y.K. and Sayers, Characteristics of the mid-latitude trough as determined by the electron density experiment on ARIEL-3, JATP, 33, 1737, 1971

Wagner,C.-U., A. Best and H.-R. Lehmann, Response of the electron density in the ionosphere and protonosphere to an ionospheric storm, Gerlands Beitr. Geophysik, 90, 273, 1981

Young, D. T., H. Balsiger, and J. Geiss, Correlations of magnetospheric ion composition with geomagnetic and solar activity, J. Geophys. Res., 87, 9077, 1982.

Young, E. R., D. G. Torr, P. Richards, and A. F. Nagy, A computer simulation of the midlatitude plasmasphere and ionosphere, Planet. Space Sci., 28, 881, 1980.

1988 USAF-UES FACULTY RESEARCH PROGRAM

Sponsored by the

AIR FORCE OFFICE OF SCIENTIFIC RESEARCH

Conducted by the

Universal Energy Systems, Inc.

FINAL REPORT

Prepared by:	Irving Lipschitz, Ph.D.
Academic Rank:	Associate Professor
Department and	Chemistry Department
University:	University of Lowell
Research Location:	AFGL/OPI Hanscom AFB Bedford, MA
USAF Reseacher:	Laurence S. Rothman

Date:	29 July 88
Contract No.:	F49620-87-R-0004

UPDATE OF THE HITRAN DATABASE

by

Irving Lipschitz

ABSTRACT

Six gases were evaluated for the HITRAN database. Two, hydrogen sulfide (H_2S) and formic acid (HCOOH), were not included in previous editions of the database. For H_2S, the ν_1, ν_2, $2\nu_2$ and ν_3 bands, detailed line position, transition intensities, lower state energies, pressure broadening, molecule and isotope indices and upper and lower state vibration and rotation quantum numbers were reported. For formic acid, only lower state energies and line measurements for the ν_6 band were cited. Four gases, methyl chloride, hydrogen peroxide, hydrogen cyanide and formaldehyde are already on the database. We wanted to replace the estimated values used for certain parameters with the latest experimental data. Except for hydrogen peroxide, however, there was precious little suitable information to add to or update the previous values of the database. For these four molecules, the database appears to be correct.

ACKNOWLEDGEMENTS

I wish to thank the Air Force Systems Command and the Air Force Office of Scientific Research for sponsorship of this research. Universal Energy Systems must be mentioned for their concern and help to me in all administrative and directional aspects of this program.

It was enjoyable working with Dr. Laurance S. Rothman, my focal point and Dr. Himanshoo V. Navangul, my office mate. Thanks to the library staff, Mr. Jim Agnew, Connie Wiley and Ann King, for their assistance.

It was a pleasure to work with Jim Chetwynd, Sue LaGasse, Gail Anderson and Frank Kneizys.

I. INTRODUCTION

The high-resolution transmission molecular absorption database (HITRAN) (1) is a compilation of spectroscopic parameters from which a wide variety of computer simulation codes are able to calculate, and predict the transmission and emission of radiation in the atmosphere.

This database is a prominent and long-running effort established by the Air Force at the Air Force Geophysics Laboratory (AFGL) in the late 1960's in response to the requirement of a detailed knowledge of infrared transmission properties of the atmosphere. With the advent of sensitive detectors, rapid computers, and higher-resolution spectrometers, a large database representing the discreet molecular transitions that affect radiative propagation throughout the electromagnetic spectrum became a necessity. Initially, HITRAN had three major components of the atmosphere, H_2O, CO_2, and O_3. Subsequently, it was expanded to 28 molecules. The purpose of this research was to determine what new molecules to add, to update parameters for the molecules already included in the database, and to modify the organization of the database in order to make it easier to use.

My research interests are in the area of normal coordinate analysis of polymers and their precursors. This is used to develop a force field that predicts the fundamental vibrations in a polymer. Since the Air Force was interested in enlarging the HITRAN database with "larger molecules" this would mesh with my background. I also have background with computers and have reasonable understanding of the nature of databases.

II. OBJECTIVES

The purpose of this reseach was to evaluate six gases in order to update the HITRAN database (1). We were looking for intense bands in which the line positions, transition intensities, lower state energies, pressure broadening of line width, molecule and isotope indices, and upper and lower state vibration and rotation quantum numbers were reported. The gases were methyl chloride, hydrogen peroxide, hydrogen cyanide, formaldehyde, hydrogen sulfide, and formic acid.

A second objective was to suggest ways of making the menu screens easier to use on the HITRAN database and changing its format. Currently, there are several hundred thousand lines in the database. But, as new molecules, especially larger ones, with greater number of lines, are added, the database is expected to grow to several million lines. Thus, the present sequential method of listing lines, which was previously considered efficient now is laborious, taking immense computer time to generate a listing as well as using enormous amounts of memory.

The last objective was to ascertain what aspects of the research needs to be continued in order to make the available data appropriate for inclusion into the HITRAN database.

CH_3Cl Methyl Chloride

Methyl chloride, H_3C-Cl, is considered the principal carrier of chlorine in the atmosphere and is intimately involved in the ozone depletion cycle. It is produced from the biomass and has been seen in volcanic emissions. There are two species of methyl chloride; one with chlorine 35 isotope and the other with chlorine 37 isotope in the ratio of 3 to 1, respectively.

A symmetric top of C_{3v} symmetry group molecule, methyl chloride has only six vibrational modes; three A and three doubly degenerate E modes. The three A_2 modes are translational modes, thus, instead of the calculated 3n-6 = 9 vibrational modes there are only six active vibrations Mode 4 of E symmetry the medium strength C-H stretch at 3042 cm^{-1}; mode 1 of A symmetry is a strong C-H stretch at 2966 cm^{-1}; mode 5 of E symmetry the medium strength H-C-H bend at 1455 cm^{-1}; mode 2 of A symmetry is a medium strength H-C-H bend at 1355 cm^{-1}; mode 6 the relatively weak H-C-Cl bend at 1015 cm^{-1}, and mode 3 of A symmetry the strong C-Cl stretch at 732 cm^{-1}. The first three modes ν_1, ν_2, and ν_3 are parallel bands and the last three are perpendicular bands.

If the transition moment of the vibrational transition is parallel to the top axis (ll band) we have for the rotational quantum numbers

$\Delta K = 0$, $\Delta J = 0, \pm 1$, if $K \neq 0$,

$\Delta K = 0$, $\Delta J = \pm 1$, if $K = 0$.

If the transition moment is perpendicular to the top axis (l band), we have:

$\Delta K = \pm 1$, $\Delta J = 0, \pm 1$.

Consequently, a multitude of sub-bands occur, which are designated $^{\Delta K}\Delta J_K$. Those with $\Delta K = 0$ are designated Q (parallel bands), the ΔJ value is represented by the usual P,Q,R designation. The rotational levels with K = 3q ($\neq 0$) have double the statistical weight of the levels K = 3q ±1; that is, we have an alternation 2,1,1,2,1,1,2,···. For a degenerate vibrational level, a similar alternation results for both +l and −l sublevels, but for the +l sublevels the rotational levels with K = 3q + 1, and for the −l sublevels the rotational levels with K = 3q − 1 have the higher statistical weight (since they are the A levels).

HIGH INTENSITY BANDS

Besides the fundamental bands, several overtones and combination bands exhibit strong absorptions in the infrared and near-infrared regions of the spectrum. They are as follows: $\upsilon_2 + \upsilon_5$ between 2650 and 2950 cm^{-1}; $\upsilon_3 + \upsilon_5$ between 2036 and 2093 cm^{-1}; $\upsilon_2 + \upsilon_3$ between 2062 and 2099 cm^{-1}; $\upsilon_3 + \upsilon_4$ and $\upsilon_3 + 3\upsilon_6$ between 3690 and 3870 cm^{-1}; $\upsilon_2 + \upsilon_4$ and $\upsilon_2 + 3\upsilon_6$ between 4310 and 4450 cm^{-1}; $\upsilon_3 + 2\upsilon_5$ between 3588 and 3613 cm^{-1}; $\upsilon_6 + 2\upsilon_5$ between 3840 and 3944 cm^{-1}; $2\upsilon_2 + \upsilon_5$ between 4073 and 4249 cm^{-1}, and $\upsilon_2 + 2\upsilon_5$ between 4226 and 4252 cm^{-1} (2,3,4,5).

Recent measurements of the ground state rotational states have extended the J and K values, but more importantly, the energy of the states are now known to the sixth or seventh decimal place (6). Upper state rotational levels for υ_3 and υ_6 have been measured nearly equally well.

The ν_5 and ν_2 bands are reported as their line positions, but in the experimental section of the paper it is stated that line intensity, quantum numbers, and line width were obtained (7,8).

Fermi resonance and coriolis effects are rampant among the bands because of the severe overlapping and density of states of the fundamental bands and many of the overtone and combination bands. Experimental band centers for most of the bands are displaced 50 to 60 cm^{-1} from the theoretical center. However, for many of the systems, the scheme describing their interaction with one another has been worked out and a complete set of ground state as well as upper state constants has been given.

Band strengths are reported for ν_3, ν_6, ν_2, ν_5, $2\nu_5$, ν_1, $\nu_4(3\nu_6)$, $\nu_2(\nu_5)$, $\nu_1(2\nu_5)$ plus $\nu_4(3\nu_6)$ (9).

The HITRAN database (1): The 1986 edition reports three transitions each for both the 215 and 217 isotopic species with a total of 6687 lines. They are ground to ν_1; ground to ν_4, and ground to $3\nu_6$ (10). The ATMOS supplemental list gives ν_3 with 725 lines for the 215 molecule and 500 lines for the 217 molecule and ν_2 with 513 lines for the 215 molecule (11). These are reported with intensities and pressure broadened halfwidth.

H_2O_2 HYDROGEN PEROXIDE

Hydrogen peroxide, H-O-O-H, is perhaps the most complex four atom molecule we will encounter. It has two basic conformations; the cis, in which both hydrogens are on the same side of the O-O bond and the trans, in which the

hydrogens are on opposite sides of the O-O bond. The planar cis and trans conformations of hydrogen peroxide were shown to be unstable. As a result, two isomeric gauche conformations of hydrogen peroxide exist, with a dihedral angle at the equilibrium position of about 111^{0}. Between the cis- and trans-conformations, there are barriers V_c and V_t on the potential energy curve for internal rotation. These two barriers are not equal, with $V_c > V_t$, 2460 and 386 cm^{-1}, respectively. There are tunneling transitions between the two conformations through the trans-barrier, V_t. The tunneling effect produces a doubling of the H_2O_2 lines, similar to the inversion doubling in the NH_3 spectrum. That is, every rotational level splits into four levels characterized by two quantum numbers n and τ, where n is the principal quantum number which orders the energy of the torsional levels of a given symmetry, and τ defines the symmetry of these levels. Since the cis barrier is high, the splitting between levels 1,2 and 3,4 is so small that it cannot be detected; while the splitting generated by the trans barrier is fairly high - about 11.3 cm^{-1} for the n = 0 level.

Hydrogen peroxide in its gauche conformation is an asymmetric rotor belonging to the symmetry group C_2, yielding four A and two B modes. They are as follows: mode 5 of symmetry B is the asymmetric O-H stretch at 3608 cm^{-1}; mode 1 of symmetry A is the symmetric O-H stretch at 3599 cm^{-1}; mode 2 of symmetry A is the O-O-H torsion(1380 cm^{-1} not observed) but calculated to be strong; mode 6 of symmetry B is the O-O-H torsion at 1266 cm^{-1}; mode 3 of symmetry type A is the O-O stretch at 880 cm^{-1}, and mode 4 of symmetry type A is the H-O O-H twisting at 314cm^{-1}.

Recent work on the ν_5 band in the region 3400 to 3900 cm^{-1} yielded 14,000 lines (12). The $\nu_2 + \nu_6$ combination bending mode in the region 2400 to 3000 cm^{-1} yielded nearly 11,000 lines. There was overlapping and blended lines in this region (12).

Lines have been reported up to 428 cm^{-1} in the microwave region (13). For the ν_6 asymmetric deformation band in the region 1100 to 1350 cm^{-1} 708 transitions have been assigned yielding both upper and lower state constants and local quantum numbers (13,14). Even at Doppler-limited rresolution, many lines are still blended and there are numerous weaker lines, some of which may originate from transitions between torsionally excited states (n ≥ 1)(13).

Line and band intensities (15,16) and air broadened line widths (17) have been reported for the $\nu_6(b)$ band around 1266 cm^{-1}.

The HITRAN database (1) reports 883 microwave transions from 0 to 100 cm^{-1} and 2389 transitions for ν_6 in the ranse 1186 to 1350 cm^{-1}.

HCN HYDROGEN CYANIDE

Hydrosen cyanide, H-C-N, is a linear molecule belonsins to the $C_{\infty v}$ symmetry sroup. It has two A modes and one desenerate E mode. Mode 1 of symmetry A is the C-H stretch at 3446.2 cm^{-1}; mode 2 of symmetry A is the C-N stretch at 2124.7 cm^{-1}, and mode 3 of symmetry E is the H-C-N bend at 726.7 cm^{-1}.

Measurements of the hydosen cyanide ν_3 band broadened by nitrosen (18) and spectral parameters of hydrosen cyanide at room temperature (19) were used to update the 1986 version of the HITRAN database (1). No new work has been published since then.

The HITRAN database (1) lists 772 lines for the 124, 125, and 134 isotopic species. Of these, there are a total of 115 lines in the microwave resion 2 to 132 cm^{-1}. The remainder of the lines are for the 124 molecule. They are sround to ν_3: sround to $2\nu_2$; sround to ν_2^1; ν_2^1 to $2\nu_2^2$, and ν_2^1 to $2\nu_2$.

H_2CO FORMALDEHYDE

Formaldehyde is a planar molecule of C_{2v} symmetry sroup with three A_1, two B_1, and one B_2 modes. Mode 4 of symmetry B_1 is the asymmetric C-H stretch at 2843.4 cm^{-1}; mode 1 of A_1 symmetry is the symmetric C-H stretch at 2766.4 cm^{-1}; mode 2 of A_1 symmetry is the C=O stretch at 1746.07 cm^{-1}; mode 3 of A_1 symmetry is the H-C-H bend at 1500.6 cm^{-1}; mode 5 of B_1 is the O-C-H bend or the "CH_2 rock" at 1247.4 cm^{-1}, and mode 6 of symmetry B_2 is the C=O out-of-plane vibration or "CH_2 was" at 1169.5 cm^{-1}.

Absolute line strensths for 28 transitions and pressure broadenins coefficients due to collision with foreisn sases, air, H_2, O_2 and N2 in the ν_4 and ν_6 bands were determined (20). A brief report on pressure line shifts in the millimeter wavelensth resion has been reported (21). The ATMOS supplemental list contains some questionable lines of the ν_2 fundamental band (11,22).

Infrared absorption intensities of the ν_1 and ν_5, ν_2, ν_3, ν_4 and ν_6 bands have been reported (23).

The HITRAN database (1) lists 2702 lines for the 126, 128, and 136 isotopic species. Of these, there are a total of 1541 lines in the microwave region 0 to 100 cm^{-1} for these molecules. The rest of the lines are for the 126 molecule. They are ground to $\nu_2 + \nu_6$; ground to $\nu_2 + \nu_4$; ground to ν_5; ground to ν_1; ground to $\nu_3 + \nu_6$; ground to $\nu_3 + \nu_4$, and ground to $2\nu_6$.

H_2S HYDROGEN SULFIDE

Hydrogen sulfide is a nonlinear molecule of symmetry group C_{2v} with two A_1 and one B_1 modes, just like water. Mode 3 of symmetry B_1 is the asymmetric S-H stretch at 2625 cm^{-1}; mode 1 of symmetry A_1 is the S-H symmetric stretch at 2614.56 cm^{-1}, and mode 2 of A_1 symmetry is the H-S-H bend at 1182.68 cm^{-1}.

The pure rotation spectrum of hydrogen sulfide has been recorded between 50 and 320 cm^{-1}. A listing of the calculated and observed line positions, experimental error, rotational quantum numbers, lower state energy, and intensity of the line at 296 K are given (24). Spectra of hydrogen sulfide have been recorded between 2150 and 2950 cm^{-1}. A listing of the line positions, upper and lower state quantum numbers, isotopic species, lower state energy, and intensity of the line at 296 K (25) for the $2\nu_2$, ν_1, and ν_3 bands of the 121, 131, and 141 isotopic species observed in natural abundance (26). Microwave measurements of the self-broadening parameters of four pure

rotational transitions of hydrogen sulfide have been carried out in the millimeter and submillimeter wavelength region. In addition, Anderson theory calculations have been carried out for these transitions (27).

The HITRAN database (1) has no listing for hydrogen sulfide.

HCOOH FORMIC ACID

Formic acid monomer is a planar molecule of C_s symmetry with seven A' and two A" modes. All the modes are strong absorbers of radiation. Mode 1 of A' symmetry is the O-H stretch at 3570 cm^{-1}; mode 2 of A' symmetry is the C-H stretch at 2942 cm^{-1}; mode 3 of A' symmetry is the C=O stretch at 1770 cm^{-1}; mode 4 of A' symmetry is the O-C-H bend at 1387 cm^{-1}; mode 5 of A' symmetry is the interaction of the C-O-H bend and the C-O stretch at 1229 cm^{-1}; mode 6 of A' symmetry is the interaction of the C-O stretch with the C-O-H bend at 1105 cm^{-1}; mode 8 of A" symmetry is the out-of-plane C-H vibration at 1033 cm^{-1}; mode 7 of A' symmetry is the O-C-O deformation at 625 cm^{-1}, and mode 9 of A" symmetry is the out-of-plane O-H vibration (torsion) at 638 cm^{-1}.

The investigation of the infrared spectrum of formic acid is complicated by the fact that at room temperature the vapor consists mainly of double molecules (dimers) and only a small fraction of single molecules.

High-resolution spectroscopy of the ν_3 band vibration rotation band yielded ground and upper state constants and some assignments of lines. However, no other parameters

were reported (28). Absolute energies for rotational sublevels and unambiguous assignments for microwave transitions in both ν_7 and ν_9 bands were reported (29). Several papers (30,31,32,33,34,35) report rotational spectra of formic acid and its isotopic species.

The HITRAN database (1) has no listing for formic acid. ATMOS supplemental list (11) reports tentative identification of the 1105 cm^{-1} ν_6 band Q branch (36).

IV. RECOMMENDATIONS

a. Hydrogen sulfide: should be included in the database, as there is sufficient data for several bands.

b. Formic acid: research efforts should continue in order to find enough appropriate information for it to be included in the database.

c. Methyl chloride: ν_3 and several combination and overtone bands should be added.

d. Hydrogen peroxide: more lines should be added for the ν_6 band.

e. Hydrogen cyanide: no new work has been found.

f. Formaldehyde: intensity measurements have been made and should be added to the database.

g. We should undertake a library study to ascertain if the spectra of dimers of HCN with formaldehyde or formic acid and HCl with formaldehyde or formic acid should be included in the database since they may act as a reservoir for these molecules in the atmosphere.

h. The database should be separated into the original main atmospheric molecules of water, carbon dioxide and ozone and a program written that allows inclusion of the lines of specific other molecules into the computer generation of the atmosphere as desired by the user.

REFERENCES

1. L. S. Rothman, R. R. Gamache, A. Goldman, L. R. Brown, R. A. Toth, H. M. Pickett, R. L. Poynter, J.-M. Flaud, C. Camy-Peyret, A. Barbe, N. Husson, C. P. Rinsland, and M. A. H. Smith, "The HITRAN database: 1986 edition," Appl. Opt. 26, 4058 (1987).

2. N. Bensari-Zizi and C. Alamichel, "Study of the $\nu_2 + \nu_3$ band of CH_3Cl in Coriolis resonance with $\nu_3 + \nu_5$," Mol. Physics 46, No.1 171 (1982).

3. N. Bensari-Zizi and C. Alamichel, "Study of the infrared bands in resonance $2\nu_2$, $\nu_2 + \nu_5$, $2\nu_5^0$, $2\nu_5^{\pm}$, $2\nu_3 + \nu_5$ and $4\nu_3$ of Methyl Chloride," Can. J. Phys. 60, 825 (1982).

4. N. Bensari-Zizi, C. Alamichel, "Study of the anharmonic resonance between ν_2 and $\nu_4^{\pm 1}$ and $\nu_2 + 3\,\nu_6^{\pm 1}$, and between $\nu_3 + \nu_4^{\pm 1}$ and $\nu_3 + 3\,\nu_6^{\pm 1}$ infrared bands of $CH_3{}^{35}Cl$," J. Physique 42, 827 (1981).

5. N. Bensari-Zizi, C. Alamichel, and G. Guelachvili, "Rovibrational analysis of the $\nu_3 + 2\nu_5^0$, $\nu_6{}_{35} + 2\nu_5^0$, $2\nu_2 + \nu_5$ and $\nu_2 + 2\nu_5^0$ infrared bands of $CH_3{}^{35}Cl$," Spectrochim. Acta, 37A, No. 9 773 (1981).

6. G. Wlodarczak, D. Boucher, R. Bocquet, and J. Demaison, "The Microwave and Submillimeter-Wave Spectrum of Methyl Chloride," J. Mol. Spectroc. 116, 251 (1986).

7. M. Morillon-Chapey, G. Guelachvilli, and P. Jensen, "Analysis of the high resolution spectrum of the ν_2 and

ν_5 absorption bands of methyl chloride," Can. J. Phys. 62, 247 (1984).

8. N. F. Henfrey and B. A. Thrush, "The analysis of high-resolution spectra of the ν_2 and ν_5 bands of $CH_3{}^{35}Cl$ and $CH_3{}^{37}Cl$," J. Mol. Struc. 146, 71 (1986).

9. J. W. Elkins, R. H. Kasann, and R. L. Sams, "Infrared Band Strensths for Methyl Chloride in the Resions of Atmospheric Interest," J. Mol. Spec. 105, 480 (1984).

10. M. Dans-Nhu, M. Morillon-Chapey, G. Graner, and G. Guelachvili, "Intensities of the ν_1 Bands of $^{12}CH_3{}^{35}Cl$ and $^{12}CH_3{}^{37}Cl$ near 3μm,"J. Quant. Spectrosc. Radiat. Transfer 26, No. 6, 515 (1981).

11. L. Brown, C.B. Farmer, C. P. Rinsland, and R. A. Toth, "Molecular line parameters for the atmospheric trace molecule spectroscopy experiment," Applied Optics 26, No 23, 5154 (1987).

12. J. J. Hillman, D. E. Jenninss, W. B. Olson, and A. Goldman, "High-Resolution Infrared Spectrum of Hydrosen Peroxide: The ν_6 Fundamental Band," J. Mol. Spectrosc. 117, 46 (1986).

13. W.B. Olson, R. H. Hunt, B. W. Youns, A. G. Maki, and J. W. Brault, "Rotational Constants of the Lowest Torsional Component (0G) of the Ground State and Lowest Torsional Component (1G) of the First Excited Torsional State of Hydrosen Peroxide,"J. Mol. Spec. 127, 12 (1988).

14. P. Helminser, J. K. Messer, W. C. Bowman, and F. De-

Lucia, "Prediction and Assignment of the FIR Spectrum of Hydorgen Peroxide," J. Quant. Spectrosc. Radiant. Transfer 32, 4, 325 (1984).

15. D. Goorvitch, F. P. J. Valero, F. S. Bonomo, and P. M. Silvassio, "Band Model Analysis of the H_2O_2 ν_6(b) Band," J. Quant. Spectrosc. Radiat. Transfer 27, No. 6, 575 (1982).

16. F. P. Valero, D. Goorvitch, F. S. Bonomo, and R. W. Boese, "Intensity of the hydrogen peroxide ν_6(b) band around 1266 cm^{-1}," Appl. Opt. 20, No. 23, 4097 (1981).

17. V. M. Devi, C.P. Rinsland, M. A. H. Smith, D. C. Benner, and B. Fridovich, "Tunable Diode Laser Measurements of Air-Broadened Linewidths in the ν_6 Band of H_2O_2," Appl. Opt. 25, 1844 (1986).

18. M. A. H. Smith, G. A. Harvey, G. L. Pellett, A. Goldman, and D. J. Richardson, "Measurements of the HCN ν_3 Band Broadened by N_2," J. Mol. Spectrosc. 105, 105 (1984).

19. P. L. Varghese and R. K. Hanson, "Tunable Diode Laser Measurements of Spectral Parameters of HCN at Room Temperature," J. Quant. Spectrosc. Radiat. Transfer 31, 545 (1984).

20. S. Nadler, S. J. Daunt, and D. C. Reuter,"Tunable diode laser measurements of formaldehyde foreign-gas broadening parameters and line strengths in the 9-11 μm region," Appl. Opt. 26, No. 9, 1641 (1987).

21. Y. L Alekhin, G. M. Al'tshuller N. F. Zobov, E. N.

Karyakin, M. I. Kirillov, and A. F. Krupnov, "Study of the H_2CO pressure lineshift using a millimeter-wave Rad Spectrometer with a Solid-state Reference-frequency Synthesizer," Izvertiya Uchebnykh Zavedenii, Radiofizika, 28, No. 11, 1382 (1985) 965 in Eng. Trans.

22. G. Brechignac, J.W.C. Johns, A.R.W. McKellar, and M. Wong, "The ν_2 Fundamental band of H_2CO," J. Mol. Spec., 96, 353 (1982).

23. T. Nakanaga, S. Kondo, and S. Saeki, "Infrared band intensities of formaldehyde and formaldehyde-d_2," J. Chem. Phys. 76 (8), 3860 (1982).

24. J.-M Flaud, C. Camy-Peyret, and J. W. C. Johns, "The far-infrared spectrum of hydrogen sulfide. The (000) rotational constants of $H_2{}^{32}S$, $H_2{}^{33}S$, and $H_2{}^{34}S$," Can. J. Phys. 61, 1462 (1983).

25. L. L. Strow, "Line Strength Measurements using Diode Lasers: The ν_2 Band of H_2S," J. Quant. Spectrosc. Radiat. Transfer 29,No. 5, 395 (1983).

26. L. Lechuga-Fossat, J.-M. Flaud, C. Camy-Peyret and J. W. C. Johns, "The spectrum of natural hydrogen sulfide between 2150 and 2950 cm^{-1}," Can. J. Phys. 62, 1889 (1984).

27. P. Helminger and F. C. De Lucia, "Pressure Broadening of Hydrogen Sulfide," J. Quant. Spectrosc. Radiat. Transfer, 17, 751 (1977).

28. H. Kuze, T. Amano, and T. Shimizu, "High-resolution laser spectroscopy of the ν_3 vibration-rotation band of

HCOOH," J. Chem. Physics, 77, No. 2, 714 (1982).

29. J-C. Deroche, J. Kauppinen, and E. Kyro, "ν_7 and ν_9 of Formic Acid Near 16 um," J. Mol. Spec. 78, 379 (1979).

30. R. W. Davis, A. G. Robiette, and M. C. L. Gerry, "Microwave Spectra and Centrifugal Distortion Constants of Formic Acid Containing ^{13}C and ^{18}O: Refinement of the Harmonic Force Field and the Molecular Structure," J. Mol. Spect. 81, 93 (1980).

31. E. Willemot, D. Dangoisse, and J. Bellet, "Microwave Spectrum of the Vibrational Excited States ν_6 and ν_8 of Formic Acid," J. Mol. Spect. 77, 161 (1979).

32. J. Bellet, C. Samson, G. Steenbeckeliers, and R. Wertheimer, "Study of the rotational spectra of the formic acid molecule. A. Study of the $H^{12}C^{16}O^{16}OH$ molecule in its ground state," J. Mol. Struc. 9, 49 (1971).

33. B. M. Landsberg, D. Crocker, and R. J. Butcher, "Offset-Locked CO_2 Waveguide Laser Study of Formic Acid: Reassessment of Far-Infrared Laser Assignments," J. Mol. Spec. 92, 67, (1982).

34. E. Willemot, D. Dangoisse, and J. Bellet, "Microwave Spectrum of Formic Acid and Its Isotopic Species in D, ^{13}C and ^{18}O. Study of Coriolis Resonances between ν_7 and ν_9 Vibrational Excited States," J. Mol. Spec. 73, 96 (1978).

35. H-T Man and R. J. Butcher, "Laser-Radiofrequency Double-Resonance Spectroscopy of Formic Acid:

Assignment and Analysis of the ν_6 and ν_8 Bands," J. Mol. Spec. 107, 284 (1984).

36. A. Goldman, F. H. Murcray, D. G. Murcray, and C. P. Rinsland, "A search for formic acid in the upper troposphere: A tentative identification of the 1105 cm^{-1} ν_6 band Q branch in high-resolution balloon-borne solar absorption spectra," Geophy. Res. Letters, 11, No. 4, 307 (1984).

1988 USAF-UES SUMMER FACULTY RESEARCH PROGRAM

Sponsored by the

AIR FORCE OFFICE OF SCIENTIFIC RESEARCH

Conducted by the

Universal Energy Systems, Inc.

FINAL REPORT

Prepared by:	John P. McHugh, Ph.D.
Academic Rank:	Assistant Professor
Department and	Department of Mechanical Engineering
University:	University of New Hampshire
Research Location:	AFGL/LYP Hanscom AFB Bedford, MA 01731-5000
USAF Researcher:	Samuel Y.K. Yee
Date:	19 Aug 88
Contract No:	F49620-87-R-0004

Spectral Domain Decomposition

by

John P. McHugh

ABSTRACT

Spectral Domain decomposition was investigated for application to partial differential. A method of elimination is proposed which allows decomposition to any number of sub-domains without any special requirements on the interfacial conditions. This method allows solution on a parallel processor, where each processor operates on one domain, separate from the others. The method is applied to the one-dimensional heat equation using the Chebychev collation discretization. Accuracy of the method is discussed briefly.

Acknowledgements

I wish to thank the Air Force Systems Command and the Air Force Office of Scientific Research for sponsorship of this research. Universal Energy Systems must be mentioned for their concern and help to me in all administrative and directional aspects of this program.

I would like to thank all the members of the Atmospheric Prediction Branch at the Geophysics Lab for their help with various aspects of the research, including their willingness to discuss at length numerous topics concerning weather prediction. I must also include many people from other branches who are too numerous to list. I would like to especially thank Sam Yee, first for suggesting the research problem, and then for his continued interest and encouragement.

1. Introduction

2. Objectives

3. An Application

4. A Spectral Method

5. Decomposition Into Two Domains

6. More Than Two Domains

7. Truncation Error

8. Recommendations

9. References

1. Introduction

The numerical solution of partial differential equations has become a popular tool for research in all areas of physics, including weather prediction. There are many methods of approach to numerically solving a given set of equations. Each approach has its advantages and disadvantages, and there is no perfect all-around method that can always be used with guaranteed success. The state of computational mechanics is such that more research is necessary and there is much improvement that will be gained.

The methods of solution can usually be categorized into finite element, finite difference, boundary element, and spectral methods. The methods appear similar during the problem formulation, but usually result in a linear matrix equation which depends strongly on the choice of method. Spectral methods, which are the focus of this report, have the advantage of accuracy over the other methods. The disadvantage of spectral methods is that they require large amounts of computer time. Despite the computer requirement, spectral methods have become the method of choice for meteorological and many other problems.

A promising method of reducing the required computer time for a spectral method is to use domain decomposition. Domain decomposition involves decomposing the physical domain into sections. Solution for each section is then found with appropriate interfacial conditions. A substantial degree of the accuracy of a spectral method is retained, and a large improvement is found in a much simpler matrix structure. Further improvements can also be obtained by solving on a parallel computer, for which domain decomposition appears to be particularly well-suited.

Previous work by Gottlieb and Hirsh (1988) indicates that the interfacial conditions effect the applicability of domain decomposition to a particular problem. The method demonstrated in this report will show that any interfacial conditions can be used along with domain decomposition. Furthermore, and of equal importance, the resulting decomposed system still retains a high degree of parallelism, making solution on a parallel processor a good possibility.

This report contains work performed while the author was in summer residence at the AF Geophysics Lab at Hanscom Field. This is a final report of that effort.

2. Objectives

The objectives of this research during the ten-week period were to investigate the applicability of spectral domain decomposition to partial differential equations. This work was intended to be the start of extended research along these lines, not a terminal project, and provide a route for future research.

The work has produced a novel solution method, outlined below, and many paths for future research. It has, therefore, exceeded the original objectives.

3. An Application

The eventual application of the methods described here is the solution of complicated, nonlinear, partial differential equations. However, the complexity of implementation of this method (and any other method) to the "real" equations makes a clear understanding of the method

difficult at this early stage of development. Hence, a relatively simple linear equation has been considered, which is

$$\frac{\partial u}{\partial t} = \frac{\partial^2 u}{\partial x^2} , \qquad (1)$$

where $u = u(x,t)$, and $u = b_1$, b_2 on the boundaries. This equation extends the work of Gottlieb (1988) to include the time dependence. This equation is simply the one dimensional heat equation.

4. A Spectral Method

Spectral methods have many different forms and have been reviewed by Gottlieb and Orszag (1977), Gottlieb, et al. (1982), and more recently by Canuto, et al., (1988). The variation chosen for this paper is the Chebychev collocation method, which is a pseudospectral method.

All spectral methods include an approximation to the dependent variable, in this case $u(x,t)$, by the finite series expansion,

$$u \sim \sum_{n=0}^{N} c_n \phi_n , \qquad (2)$$

where $c_n = c_n(t)$ and $\phi_n = \phi_n(x)$. In general, the ϕ_n's are chosen to belong to some series of base functions, such as Chebychev, Legendre, trigonometric, etc. Hence the name "Chebychev" collocation method. For this discussion,

$$\phi_n(x) = \cos(n \cos^{-1} x), \qquad (3)$$

which is the standard form for the Chebychev function (see Johnson and Johnson, Chap 11). The coefficients, $c_n(t)$, are determined in the numerical solution by some time-stepping method, as will be explained.

The solution to (1) begins by inserting (2) into (1) to obtain

$$\left(\frac{\partial}{\partial t} - \frac{\partial^2}{\partial x^2}\right) \sum_{n=0}^{N} c_n \phi_n = R \tag{4}$$

where R is the residual. Since u(x,t) is only approximated by the expansion (2), then the differential equation is not exactly satisfied, leaving the residual R. If we choose the c_n's so that the weighted residual (global error) is zero for some set of weighting functions, $\psi_j(x)$, then

$$\int_x R\psi_j(x)\, dx = \int_x \left(\frac{\partial}{\partial t} - \frac{\partial^2}{\partial x^2}\right)\left[\sum_{n=0}^{N} c_n \phi_n\right]\psi_j\, dx = 0 \tag{5}$$

There are various choices for $\psi_j(x)$, such as the popular Galerkin method where

$$\psi_j = \phi_j.$$

A more appropriate choice for the eventual application to domain decomposition, however, is the collocation method, where

$$\psi_j = \delta(x-x_j), \tag{6}$$

and δ is the Dirac delta function.

Using (6), (5) becomes

$$\left[\left(\frac{\partial}{\partial t} - \frac{\partial^2}{\partial x^2}\right) \sum_{n=0}^{N} c_n \phi_n = 0\right]_{x=x_j} \tag{7}$$

The above expression gives one equation in terms of the coefficients, c_n, at every collocation point, x_j. When the number of equations is chosen to be equal to the number of unknowns by making N equal to the number of x_j's, a square matrix results.

The time-dependence must be dealt with. Many schemes are available. A simple backward difference has been chosen for ease of study. Hence,

$$\frac{\partial u}{\partial t} = \frac{u^i - u^{i-1}}{\Delta t} \quad ,$$

which results in

$$\left[\sum_{n=0}^{N} (\phi_n - \Delta t \phi_n'') \, c_n^i = u^{i-1} \right]_{x = x_j} \quad . \tag{8}$$

This matrix equation must be solved for the c_n's subject to the boundary conditions.

5. Decomposition Into Two Domains

The simplest version of domain decomposition is to let the domain be split in half, which is now considered. The problem then becomes

$$\begin{aligned} Lu^l = 0 \quad , \quad Lu^r = 0 \ , \\ L = \frac{\partial}{\partial t} - \frac{\partial^2}{\partial x^2} \ . \end{aligned} \tag{9a}$$

where the superscripts l and r mean left and right. The solution, u^l is valid in the left half of the domain, while u^r is valid in the right. The solutions u^l and u^r must be matched at the interface. Canuto, et al., (1988) has shown that the interfacial conditions

$$\begin{aligned} u^l &= u^r, \\ u_x^{\,l} &= u_x^{\,r}, \end{aligned} \tag{9b}$$

where these values are taken at the interface and the variable subscript means differentiation, make the decomposed system equivalent to the original system. Hence, (9) is taken to be the governing system.

Expand u^l and u^r as before using

$$\begin{aligned} u^l &= \sum c_n^l \, \phi_n(x), \\ u^r &= \sum c_n^r \, \phi_n(x), \end{aligned}$$

so that the same ϕ_n is used for both domains; only the coefficients, c_n, are different between two domains. This makes the extension to more domains much easier.

There are two approaches that can be followed at this stage. The equations can be arranged in a one large matrix, which would have a block diagonal form. Various solution techniques can then be applied, including attempts at parallel processing. The main advantage of domain decomposition when one large matrix is used then becomes the advantage of having a block diagonal matrix. When the domain is segmented in many smaller domains, the matrix becomes a narrow band along the diagonal, the remaining elements being zero. This is a significant advantage in computer requirements, however, greater improvements can be obtained with the second alternative.

The second alternative is to form a matrix for each domain, with the interfacial conditions linking their solutions. This approach has direct parallel processing attributes, and has been pursued for this study. The difficulty with this approach is satisfying the interfacial conditions without ruining the innate parallelism of the approach.

Using the second alternative, each of the resulting matrices is full. Each row of the matrix for a given domain is equation (9a) evaluated at a point x_j in the domain. The only exceptions are when x_j is a boundary point or the interfacial point. For the boundary point in the left domain (9a) is replaced by the boundary condition

$$\sum c_n^1 \phi_n = b_1 \ .$$

The right side of the left domain is the interfacial point, and (9a) could be replaced by either of the two conditions given by (9b).

The key element to the method proposed is how to meet the interfacial conditions. It will be shown that the conditions can be met using standard Gaussian elimination without jeopardizing the inherent parallelism of the decomposed system.

The first of (9b) is, from the left domain's point of view,

$$\sum c_n^l \phi_n = w \ ,$$

where w is the unknown interfacial value fo u. If this is inserted into the left domain matrix, the result is

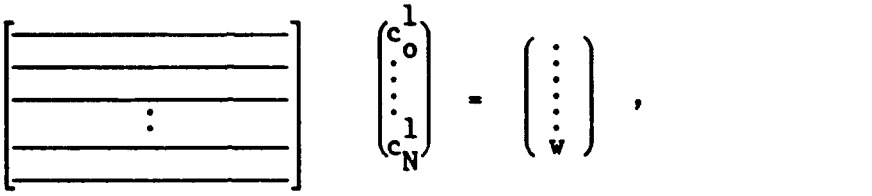

where w is unkr and the matrix is full. Similarly for the right domain:

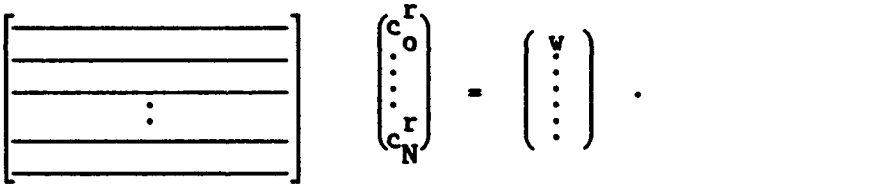

Using Gaussian elimination (after some strategic pivoting), these can be reduced to upper triangles:

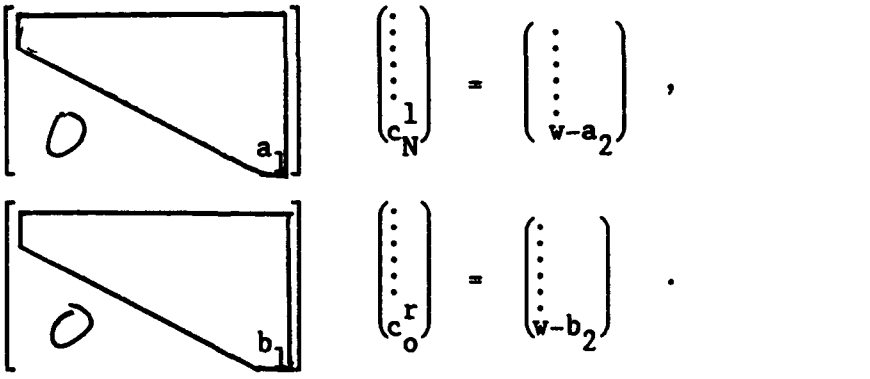

where a_1, a_2, b_1, and b_2 are constants resulting from the elimination process. Note that the reduction of each matrix is independent of the other matrix. Now the last equation in each row is

$$\left.\begin{aligned} a_1\, c_N^{\,l} &= w - a_2 \ , \\ b_1\, c_o^{\,r} &= w - b_2 \ . \end{aligned}\right\} \qquad (10)$$

There are three unknowns here, $c_N^{\,l}$, $c_o^{\,r}$, and w, so more equations are needed.

Replace the last equation in the original matrices by the second of (9b), and perform the same procedure. This gives

$$\left.\begin{aligned} c_1\, c_n^{\,l} &= w' - c_2 , \\ d_1\, c_o^{\,r} &= w' - d_2 , \end{aligned}\right\} \qquad (11)$$

where w′ is the unknown derivative at the interface. Equations (10) and (11) can now be solved exactly for the four variables $c_1^{\,n}$, $c_o^{\,r}$, w, and w′. Then either w or w′ may be used to return to the reduced matrices and perform backsubstitution to get the remaining values of $c_n^{\,r}$ and $c_n^{\,l}$.

Several things must be pointed out. First, two complete reductions are not necessary; merely include the third condition as an extra row in the elimination. Second, the elimination of a matrix is completely independent of the other matrix, hence perfect for a parallel processor. The back substitution step is also completely independent. Only the step where w and w′ are calculated uses information from both domains. Hence this approach should lend itself nicely to parallel computing. Third, for many domains, the interior domains have the same original matrix, making reduction to upper triangles much easier. These advantages must be sorted out with further research.

6. More Than Two Domains

Consider three domains. The extension from three domains to many domains is trivial. Using the same interfacial conditions as before results in three matrices which contain the quantities w_1 and w_1', which are the values of u and u_x at the left interface, and w_2 and w_2', which are the values for the right interface. These matrices can be reduced to upper triangles:

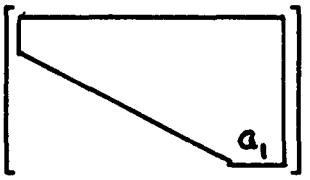

$$\begin{pmatrix} \vdots \\ c_N^1 \end{pmatrix} = \begin{pmatrix} \vdots \\ w_1 - a_2 \end{pmatrix} \quad \text{or use } w' \tag{12}$$

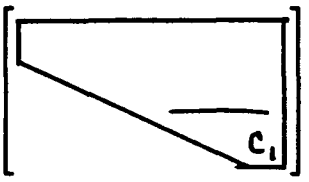

$$\begin{pmatrix} \vdots \\ c_o^m \\ c_N^m \end{pmatrix} = \begin{pmatrix} \vdots \\ w_1 - b_2 \\ w_2 - c_2 \end{pmatrix} \quad \text{or use } w' \tag{13}$$

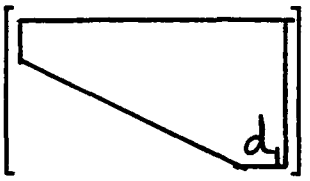

$$\begin{pmatrix} \vdots \\ c_o^r \end{pmatrix} = \begin{pmatrix} \vdots \\ w_2 - d_2 \end{pmatrix} \quad \text{or use } w', \tag{14}$$

where the superscript, m, signifies the middle domain. Taking the last of (12) and (14) and the last two equations in (13) gives eight equations in the eight unknowns, w_1, w_2, w_1', w_2', c_N^1, c_o^m, c_N^m, c_o^r. These can be obtained analytically. The remaining solution can then be obtained by backsubstitution using the above values, as for the two domain case.

7. Truncation Error

Spectral methods are known to be exponentially accurate, which means the error decays exponential with the addition of collocation points. The finite difference method, for example, offers only an

algebraic decay with an increasing number of points, hence the spectral method offers superior accuracy. The decomposition into finite domains, when a spectral method is used, will certainly have a negative influence on the accuracy, although this has yet to be determined. In the extreme case of domain decomposition, where the smallest domain consists of only two points, the discretization would then appear to be equivalent to finite difference with a fancy interpolation function. At the other extreme of decomposition, only one domain, the accuracy is again spectral, or exponential. To compare the spectral method, finite difference method, and spectral domain decomposition method for accuracy, the total number of points must be kept constant. Any method improves its accuracy with increasing data points, but that is cheating a comparison between methods. So an increasing level of decomposition for this comparison keeps a constant number of total points in the domain, with a decreasing number of points in each sub-domain. Now consider an intermediate step between the two extremes. The accuracy is somewhere between exponential and algebraic. In fact, an increasing amount of domain decomposition results in a decreasing level of accuracy. Decomposition, however, is accompanied by a much faster method of solution. Therefore, spectral domain decomposition should offer an infinite set of choices, the trade-off being between accuracy and speed. Further study is needed to determine quantitatively the accuracy of relative levels of decomposition.

8. Recommendations

The method outlined in the previous sections has been implemented in a two-domain case, and demonstrated to work. However, several characteristics of the method have yet to be fully evaluated. These include the truncation error, convergence rate, and stability. With these in hand, a detailed comparison with other methods (non-decomposition methods) can be made.

There are other alternatives to the Gaussian elimination procedure outlined in this report, with seemingly infinite variations on the central theme, which may prove to be useful for this type of analysis.

Other parameters which could significantly effect the performance of a decomposition technique, but were not considered in this study, include

1. Decomposition with multiple space variables,
2. Different interfacial conditions,
3. Matching the method to a certain parallel architecture, and
4. Considering basis functions other than Chebychev functions.

Gottlieb (1988) discusses a method which requires the inversion of matrices, which is not typically a fast method, but is highly parallel, and could be competitive with the elimination method.

A relaxation method, such as successive over-relaxation, which is completely iterative, must be considered as a candidate for the solution technique. Any iterative technique can easily be implemented to a parallel computer.

There are many other techniques. These items will be considered in forthcoming research as time and resources allow.

In conclusion, there are many opportunities for improvement using domain decomposition and parallel computing. Much research is needed to understand the attributes of the various options; however, it is clear, even at the infant stage of this method, that great improvements in computing speed are available using domain decomposition.

9. References

1. Gottleib, D. and S. Orszag, "Numerical Analysis of Spectral Methods: Theory and Applications," SIAM, 1977.

2. Canuto, C., M. Hussaini, A. Quarteroni, T. Zang, "Spectral Methods in Fluid Dynamics," Springer-Verlag, 1988.

3. Gottleib, D., M. Hussaini, S. Orszag, "Theory and Applications of Spectral Methods," in Spectral Methods for Partial Differential Equations, pp 1-54, SIAM, 1982.

4. Gottleib, D., and R.S. Hirsh, "Parallel Pseudospectral Domain Decomposition Techniques," ICASE report #88-15, 1988.

5. Johnson, D. and J. Johnson, "Mathematical Methods in Engineering and Physics: Special Functions and Boundary-Value Problems," Ronald Press, 1965.

1988 USAF-UES SUMMER FACULTY RESEARCH PROGRAM

SPONSORED BY THE

AIR FORCE OFFICE OF SCIENTIFIC RESEARCH

CONDUCTED BY THE

UNIVERSAL ENERGY SYSTEMS, INC.

FINAL REPORT

Prepared by: Himanshoo V. Navangul, PhD

Academic Rank: Chairman and Professor

Department: Chemistry and Physical Science

College: North Carolina Wesleyan College, Rocky Mt.

Research Location: Air Force Geophysics Laboratory
Optical Physics/ Infrared Branch
Hanscom AFB, MA 01731-5000

USAF Researcher: Dr. Laurence S. Rothman

Date: July 28, 1988

Contract No: F49620-87-0004

On The Possible Inclusion Of " Heavy " Molecules In The HITRAN Database

by

Himanshoo V. Navangul, PhD

ABSTRACT

Since the early 60's work has been done at the Hanscom AFB on the compilation of various spectroscopic parameters of molecules present in the Earth's atmosphere.

Earlier, the emphasis was placed on simple molecules with relatively high atmospheric concentration. These were generally of small size such as water, carbon dioxide, ozone, methane and so on, and were also highly infrared active. Now efforts are being made to add more data on some of these molecules as well as on others that are relatively large in size and have small atmospheric concentration. These include: Ethane, Ethene(Ethylene), Ethyne(Acetylene), Propane, and others.

A thorough literature search had to be carried out to locate information relevant to the spectroscopic parameters of these molecules and then a critical examination was conducted to see which of the molecular data could be included in the future versions of the HITRAN.

ACKNOWLEDGEMENT

I would like to thank Dr. Laurence S. Rothman and the USAF-UES for giving me the opportunity to work in the Summer Faculty Research Program.

I would also like to thank Professor Irving Lipschitz for providing exciting discussions not only on the topics researched in optical physics but also in other equally interesting areas.

Lastly, I would like to thank Jim Chetwynd of AFGL, a native Bostonian, for being helpful, hospitable, and thus instrumental in making my stay at Hanscom an enjoyable one.

I. INTRODUCTION:

The Air Force Geophysics Laboratory has served as one of the focal points for research in atmospheric physics and related areas for well over forty years. Dr. Larry Rothman of AFGL and his group have been working on the compilation of spectroscopic parameters of various atmospheric gases for nearly two decades. Their work deals with the infrared activity of these gases in terms of the highly resolved vibrational and rotational structure of their molecules.

Most of this information is now available as a database known as HITRAN (an acronym for High Resolution Transmission) and is in line with the interests shared by the U.S. Air Force, DOD, DOT, and NASA.

This database also serves the scientific community worldwide and acts as a conduit for exchanging information on most areas of vibrational and rotational spectroscopy.

The HITRAN database is frequently revised for the following reasons:

* Certain molecules have more applications and higher priority; any changes in their status must be registered
* With improved technology, instruments now available are able to improve resolution of bands further. Some of these also work in regions once thought inaccessible and hence of little interest. In addition, these instruments also

detect the most minute traces of matter that could not be detected earlier.

* Data taken can also vary depending upon their mode of collection; e.g.,those taken from ground looking up vs. from sky looking down, horizontal cross-sections vs. vertical cross-sections, and so on.

The last version of HITRAN, published in 1986 (Applied Optics/ Vol.26(19), 4058(1986)), reported parameters for twenty eight molecules detected in the Earth's atmosphere.

Not equal emphasis, however, was placed on each of these twenty eight molecules for a variety of reasons stemming from a lack of interest on the Air Force side, paucity of data(lack of IR activity), and very low atmospheric concentration to the complex nature of some these molecules. As a result, initially, complete data were gathered only on a few small molecules with high atmospheric concentration and strong infrared activity. These included water, ozone, nitrous oxide, carbon dioxide, carbon monoxide, methane, and oxygen. Now that the situation is changing, it seems appropriate to pay attention to the remaining molecules and some additional entrants newly detected in the atmospheres of Earth and/or other celestial bodies.

II. OBJECTIVES OF THE RESEARCH EFFORT:

During the ten-week project, attention was paid to a variety of molecular systems called as the " Heavy Molecules; " although somewhat of a misnomer, heavy means molecules with four or more atoms and comprise the following: Acetylene(Ethyne), Ethylene (Ethene), Ethane, Propane, Methyl Chloride, Formic Acid, Formaldehyde, and others. I had the opportunity to study the first four. The blank spaces that one observes in the summary tables following the introduction section will be filled when appropriate data are available and/or when decisions are made about their suitability with respect to HITRAN.

In the following pages an attempt will be made first to give a brief theoretical background on the type of spectroscopic parameters being studied and then to introduce summaries of various data available on each of these molecules in a format suitable to HITRAN.

Theoretical Background:

When a molecule is exposed to any electromagnetic radiation, depending upon the nature of that radiation(its frequency, wavelength and energy), the molecule may undergo a change in its translational, electronic, vibrational, rotational, or combinations of them by absorbing that radiation.

The current study is restricted to changes in the vibrational and rotational structure brought about by radiation of energy as

low as few cm^{-1} to high values of few thousands of cm^{-1}. This spectral span extends from the millimeter region in microwaves to the near infrared and corresponds to molecular changes any where from pure rotational to rovibrational to pure vibrational motion.

For a molecule with N number of atoms, the number of fundamental modes of vibration is equal to 3N - 6(3N-5, if linear), while the degrees of freedom related to rotations are left fixed at three(the remaining three are for translation). The vibrational modes and their interactions can be further described in terms of various stretches, bends as well as overtones, Fermi resonance, Coriolis interactions, and other complex phenomena.

A molecule may absorb the e.m. radiation only if certain criteria are met. If the incident radiation has intensity I_o, it can be absorbed by the molecule if the rotational and/ or vibrational energy levels are appropriately spaced, with the result that the transmitted light has a diminished value, I(v), dictated by the Beer-Lambert law as follows:

$$I(\nu) = I_o \exp(-k(\nu)x)$$

$x = nl$; n is the uniform concentration and l is the path length the radiation travels, and

$k(\nu) = S\, f(\nu - \nu_o)$; where S is called the line intensity, $f(\nu - \nu_o)$ is the shape function, and $k(\nu)$ is the absorption coefficient.

The band intensity, $S = \int_{-\infty}^{\infty} k(\nu)\, d\nu$

For a transition from state i to state f , the spectral line intensity, S_{if} , can be written in its expanded form as follows:*

$$S \quad (T) = (8\pi^3/3hc)\, \nu_{if}\, [1 - \exp(-c_2 \nu_{if}/T)]\{ g_i I_a /Q(t) \}$$
$$\times \quad [\exp(-c_2 E_i /T)\, R_{if} \times 10^{-36}$$

This expression describes some of the spectroscopic parameters entered in the HITRAN database. Their significance is as follows:

$R = |\langle i / M / f \rangle|^2$, temp. independent effective electric dipole moment between the two states, i and f, squared

ν = the resonant frequency of the line

g = the nuclear spin degeneracy of the lower level

I = natural isotopic abundance

c = second radiation constant(= hc/k)

Q = total internal partition function

E = energy of the lower state of the transition

T = temperature in K, assumed to be 296 K, unless stated otherwise

γ = the self-broadened half-width of a band at 296 K

γ_a = the air-broadened half-width

n = coefficient of temperature dependence

γ_p = effect of pressure on a given transition

* Similar expression can be written for intensity corresponding to weaker quadrupole transitions.

In addition, information may also be furnished on the following properties:

v = upper state global quanta index

v = lower state global quanta index

Q' = upper state local quanta

Q" = lower state local quanta

Finally, various indices expressing accuracy and errors in the calculation of the values mentioned above are also included in the output.

Next, you will find the summaries of the information currrently available, its source, and other pertinent data on the four molecules, **Ethane, Ethylene, Ethyne, and Propane.** Some of this information is already included in the 1986 version of HITRAN.

1. THE ETHANE MOLECULE, C_2H_6

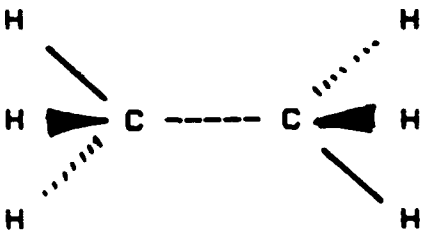

8 ATOMS

NO. VIBRATIONS = 3N - 6 = 18

6 NON-DEGENERATE and 6 DBLY-DEGEN.

(A-TYPE) (E-TYPE)

INFRARED ACTIVE FUNDAMENTAL MODES:
ν_5 (A_2''), ν_6 (A_2''), ν_7 (E'), ν_8 (E') and ν_9 (E')

2954.3, 1379.0, 2994.3, 1486.0, 820.8 in cm^{-1}

RAMAN ACTIVE FUNDAMENTAL MODES:
ν_1 (A_1'), ν_2 (A_1'), ν_3 (A_1'), ν_4 (A_1'), ν_8 (E'), ν_{11} (E"), ν_{12} (E")

2899.2, (1375), 993.0, (275), 1491 (1qd), 2963 (1qd), 1460, (1155)

SYMMETRY GROUPS POSSIBLE: D_3h (Eclipsed) or D_3d (Staggered)

ROTATIONAL BARRIER: 2750 cal/mole (1024 CM^{-1})

2. THE ETHENE MOLECULE(ETHYLENE), C_2H_4

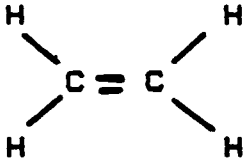

N = 6

3N -6 = 12 FUNDAMENTAL VIBRATIONS

INFRARED ACTIVE FUNDAMENTAL MODES:

ν_7 (B_{1u}), ν_9 (b_{2u}), ν_{11} (b_{3u}), ν_{12} (b_{3u})

949.2, 3105.5, 2989.5, 1443.5 in cm^{-1}

RAMAN ACTIVE FUNDAMENTAL MODES:

ν_1 (a_g), ν_2 (a_g), ν_3 (a_g), ν_4 (a_u), ν_5 (b_{1g}), ν_6 (b_{1g}), ν_7 (b_{1u}), ν_8 (b_{2g}), ν_9 (b_{2u})

SYMMETRY GROUP: D_{2h} (V_h)

3. THE ETHYNE(ACETYLENE) MOLECULE, HCCH, A LINEAR MOLECULE

H - C ≡ C - H N = 4; 3N -5 = 7 FUNDAMENTAL VIBRATIONS

SYMMETRY GROUP: D h

INFRARED ACTIVE FUNDAMENTALS:

ν_5( ) and ν_9( ) show up strongly in the IR region

729.1 and 3287 cm^{-1}

RAMAN ACTIVE BANDS:

Two strong and two weak bands show as follows:

1973.8, 3373.7 and 589, 646 respectively

4. THE PROPANE MOLECULE, $CH_3CH_2CH_3$

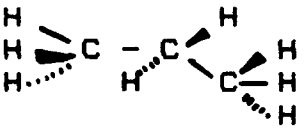

N = 11, 3N - 6 = 27 FUNDAMENTAL MODES

BECAUSE OF ITS COMPLEXITY AND THE RECOMMENDATION, NOT TO CONSIDER INCLUSION OF THIS MOLECULE, THE VIBRATIONS WILL NOT BE DISCUSSED HERE.

Molecule # 1: Ethane $CH_3 - CH_3$

Ethane is one of the twenty eight molecules reported in the 1986 version of HITRAN. However, the following criticism seems worth mentioning:

* While data are available on ν_7 and ν_9 , only ν_9 data appear ; (the region studied comprises 720 to 933 cm)
* Values of all the upper state indices could not be found in its designated location(it is fair to assume that such data must also be missing in the original file
* No justification appears for using the assumed values of some of the parameters.

It is hoped that data from the following summaries will improve the file on ethane.

Record #	Molecule	Structure	Isotopes
1	Ethane		1221,1231,1331

# Fund. Vibrations	Reported Work
18	ν_9 , ν_7 , ν_5 , $\nu_6 + \nu_{11}$

Frequency	Strength	HW-Air	HW-Self	HW-T dep	Shift	Energy/cm^{-1}
y	y	y	n	n	n	y

Source:

Rinsland et al, Applied Optics, submitted in 1986

Vibrataion:	ν in cm^{-1} lower	ν in cm^{-1} upper	Use:
ν_7 (near 3000 cm^{-1})	0	3000	y

Location: File Name:

NASA, Langley, Va

Status: Completion Date: / /

Record #	Molecule	Structure	Isotope(s)
2	Ethane		1221,1231,1331

Frequency	Strength	HW-Air	HW-Self	HW-T dep	Shift	Energy/cm^{-1}
y	y	n	n	n	n	y

Source:
M.Dang-Nhu and A. Goldman, J.Quant.Spec.Radiat.Transfer,38(2),159 (1987)

Vibrataion:	ν in cm^{-1} lower	ν in cm^{-1} upper	Use:
ν_7 (3000cm^{-1})	0	3000	yes

Location: File Name:
Universite de Paris-Sud and
University of Denver
Status: Completion Date: / /

Record #	Molecule	Structure	Isotope(s)
3	Ethane		1221,1231,1331

Frequency	Strength	HW-Air	HW-Self	HW-T dep	Shift	Energy/cm^{-1}
y	n	y	y	n	y	n

Source:
W.E.Blass et al, J.Quant.Spec.Radiat.Transfer,38(3),183,1987
Contains data foreign-gas broadening near 12 μm using TDL

Vibrataion:	ν in cm^{-1} lower	ν in cm^{-1} upper	Use: yes
ν_9 (12 μM)			

Location: File Name:
UT Knoxville and Goddard Space
Flight Center,MD

Status: **Completion Date:** / /

Record #	Molecule	Structure	Isotope(s)
4	Ethane		1221, 1231, 1331

Frequency	Strength	HW-Air	HW-Self	HW-T dep	Shift	Energy/cm^{-1}
y	n	n	n	n	n	y

Source:
C.Rinsland et al,Applied Optics, 25(24),4522(1986)

Vibrataion: ν in cm^{-1} lower: 2970; ν in cm^{-1} upper: 2990; **Use:** yes

ν_7 (3.3 μM)

Location: NASA, Langley Res. Ctr.,Va **File Name:**

Status: **Completion Date:** / /

Molecule #2. Ethene(Ethylene): $CH_2 = CH_2$

Ethene is not included in the 1986 version of HITRAN. The information given below suggests the addition of it to the database.

Record #	Molecule	Structure	Isotope(s)
1	Ethene(Ethylene)		1221,1222,2222

# Fund. Vibrations	Reported Work
12	ν_1 ,ν_5 ,ν_7 ,ν_9 ,ν_{11} ,ν_{12} & combinations/ overtones

Frequency	Strength	HW-Air	HW-self	HW-T dep	Shift	Energy/cm^{-1}
y	y	n	n	n	n	n

Source:

M.Dang-Nhu, A.S.Pine et al Canadian J. Physics, 61,514,1983

Vibrataion:	ν in cm lower	ν in cm upper	Use:
ν_{11} , $\nu_{12}+\nu_2$, $2\nu_{10}+\nu_{12}$, ν_9 , $\nu_3+\nu_8+\nu_{10}$	2920	3240	may be

Location: Universite de Paris-Sud, and Insitut de Physique,

File Name: NSF Belgique

Status:

Completion Date: / /

Record #	Molecule	Structure	Isotope(s)
2	Ethene(Ethylene)	same as in the record # 1	

Frequency	Strength	HW-Air	HW-Self	HW-T dep	Shift	Energy/cm
y	n	n	n	n	n	n

Source:
F.Hegelund and J.L.Duncan, J.Chem.Soc.,Farady Trans.2,78,549,1982
This work deals primarily with stretching fundamentals of isotope 1222

Vibrataion:	ν in cm^{-1} lower	ν in cm^{-1} upper	Use:
ν_1 , ν_5 , ν_9 and ν_{11}	600	3100	may be

Location:

File Name:

University of Aberdeen, Scotland and Aarhus University, Denmark

Status:

Completion Date: / /

Record #	Molecule	Structure	Isotope(s)
3	Ethene(Ethylene)	same as in the report #1	

Frequency	Strength	HW-Air	HW-Self	HW-T dep	Shift	Energy/cm^{-1}
y	y	n	n	n	n	n

Source:
M.Buback and F.W.Ness, Berichte der Buensen-Geselschaft,1976
Molar intensities are also studied.

Vibrataion:	ν in cm lower	ν in cm upper	Use:
Assignment of ethylene absorption to various bands	5910	6200	may be

Location: **File Name:**
Institut der Phys.Chemie
Universitaet Karlsruhe,Deutschland

Status: **Completion Date:** / /

Record #	Molecule	Structure	Isotope(s)
4	Ethene(Ethylene)	Same as in the report #1	

Frequency	Strength	HW-Air	HW-Self	HW-T dep	Shift	Energy/cm^{-1}
y	n	n	n	n	n	n

Source:
FW.Ness and M.Buback, Berichte der Buensen-Gesselschaft,1976 pp1690
This work is similar to the one described in report #3

Vibrataion:	ν in cm^{-1} lower	ν in cm^{-1} upper	Use:
$3\nu_9$, $3\nu_{11}$, $2\nu_1+\nu_{11}$, $2\nu_1+\nu_9$	8200	9500	may be

Location: **File Name:**
Institut fuer Phys.Chemie
Universitaet der Karsruhe,Deutschland

Status: **Completion Date:** / /

Molecule No. 3 Ethyne(Acetylene) CH ≡ CH

Acetylene is also included and adequately covered in the 1986 version of HITRAN. The strongest recommendation would be to look at the the most recent data listed here and see if any improvement is necessary.

Record #	Molecule	Structure	Isotope(s)
1	Ethyne		1221,1222,2222

# Fund. Vibrations	Reported Work
6	ν_3, ν_4, ν_5 plus combination bands

Frequency	Strength	HW-Air	HW-Self	HW-T dep	Shift	Energy/cm^{-1}
y	y	y	y	y	n	n

Source:

A personal communication from Curt Rinsland dated 21 March, 1988

Vibrataion:	ν in cm^{-1} lower	ν in cm^{-1} upper	Use:
$(\nu_4 + \nu_5)^0$	1192	1470	

Location: NASA, Langley, Va

File Name:

Status:

Completion Date: / /

Record #	Molecule	Structure	Isotope(s)
2	Ethyne		1221,1222,2222

# Fund. Vibrations	Reported Work
6	same as reported in # 1 above

Frequency	Strength	HW-Air	HW-Self	HW-T dep	Shift	Energy/cm^{-1}
y	n	n	n	n	n	n

Source:
Curtis Rinsland et al, Applied Optics 24(14)2044(1985)
This work identifies acetylene lines in solar spectra

Vibrataion:	ν in cm^{-1} lower	ν in cm^{-1} upper	Use:
$(\nu_2 + \nu_4 + \nu_5)$	ca 3200	ca 3310	may be

Location: NASA, Langley,Va

File Name:

Status:

Completion Date: / /

Record #	Molecule	Structure	Isotope(s)
3	Ethyne		1221,1222,2222

# Fund. Vibrations	Reported Work
6	same as reported in # 1 above

Frequency	Strength	HW-Air	HW-Self	HW-T dep	Shift	Energy/cm^{-1}
y	n	y	y	n	n	n

Source:
W.E.Blass and V.W.L.Chin, J.Spect.Radiat.Transfer,38,185(1987)
This work identifies hydrogen and nitrogen broadening at 14 uM.

Vibrataion:	ν in cm^{-1} lower	ν in cm^{-1} upper	Use:
ν	14 uM		yes

Location: File Name:
UT Knoxville, TN

Status: Completion Date: / /

Record #	Molecule	Structure	Isotope(s)
4	Ethyne		1221,1222,2222

# Fund. Vibrations	Reported Work
6	same as reported in # 1 above

Frequency	Strength	HW-Air	HW-Self	HW-T dep	Shift	Energy/cm^{-1}
y	n	y	n	n	n	n

Source:
Curtis Rinsland et al, J. Mol.Spectroscopy, 114,49(1985)
This work also deals with nitrogen and hydrogen gas broadening

Vibrataion:	ν in cm^{-1} lower	ν in cm^{-1} upper	Use:
$(\nu_4+\nu_5)^0$	1250	1380	yes

Location: File Name:
NASA, Langley,Va and William and Mary College

Status: Completion Date: / /

Record #	Molecule	Structure	Isotope(s)
5	Ethyne		1221,1222,2222

# Fund. Vibrations	Reported Work
6	same as reported in # 1 above

Frequency	Strength	HW-Air	HW-Self	HW-T dep	Shift	Energy/cm^{-1}
y	n	y	n	n	n	n

Source:
P. Varanasi et al, J.Mol.Spectroscopy,107,241(1984)

Vibrataion:	ν in cm^{-1} lower	ν in cm^{-1} upper	Use:
ν_3, ν_4, $\nu_4+\nu_5$ bands	near 7.4 μM		may be

Location:
SUNY, Stoney Brook

File Name:

Status:

Completion Date: / /

Record #	Molecule	Structure	Isotope(s)
6+ 7	Ethyne		1221,1222,2222

# Fund. Vibrations	Reported Work
6	same as reported in # 1 above

Frequency	Strength	HW-Air	HW-Self	HW-T dep	Shift	Energy/cm^{-1}
y	y	y	y	y	n	n

Source:
P.Varanasi et al, J.Quant.Spec.Radiat.Transfer,30(6),497(1983) and ibid, pp 505(1983)

Vibrataion:	ν in cm^{-1} lower	ν in cm^{-1} upper	Use:
various bands in the regions 7.53μM and 13.μM regions are studied			

Location:
SUNY, Stony Brook

File Name:

Status:

Completion Date: / /

Record #	Molecule	Structure	Isotope(s)
8	Ethyne		1221,1222,2222

# Fund. Vibrations	Reported Work
6	same as reported in # 1 above

Frequency	Strength	HW-Air	HW-Self	HW-T dep	Shift	Energy/cm^{-1}
y	y	n	n	n	n	y

Source:

Curtis Rinsland et al, Applied Optics 24(14)2044(1985)
This work identifies acetylene lines in carbon stars

Vibrataion:	ν in cm^{-1} lower	ν in cm^{-1} upper	Use:
3 μM region			yes

Location: NASA, Langley,Va

File Name:

Status:

Completion Date: / /

Molecule No.4 Propane, $CH_3-CH_2-CH_3$

The molecule propane suffers from problems such as extremely low concentration, too many possible fundamental vibrations and hence more complex, and hence absence of data. Therefore, it is not suitable for inclusion.

Record #	Molecule	Structure	Isotope(s)
1	Propane	too many to list	

# Fund. Vibrations	Reported Work
27	On many fund. vibrations

Frequency	Strength	HW-Air	HW-Self	HW-T dep	Shift	Energy/cm^{-1}
y	y	n	n	n	n	n

Source:
P.Varanasi et al, J.Quant.Spectr.Radiat.Transfer,31,203(1983)

Vibrataion:	ν in cm^{-1} lower	ν in cm^{-1} upper	Use:
Several of the 27 bands	680	1580	yes

Location:
SUNY, Stony Brook

File Name:

Status:

Completion Date: / /

Record #	Molecule	Structure	Isotope(s)
2	Propane		too many possible

# Fund. Vibrations	Reported Work
27	same as reported in # 1 above

Frequency	Strength	HW-Air	HW-Self	HW-T dep	Shift	Energy/cm^{-1}
y	y	n	n	n	n	n

Source:
D.E.Jennings et al, Nature,292,683(1981)
This work identifies propane in Titan's atmosphere

Vibrataion:	ν in cm^{-1} lower	ν in cm^{-1} upper	Use:
Many of the possible 27	ca 200	ca 1450	may be

Location:
Goddard FSC, Md

File Name:

Status:

Completion Date / /

RECOMMENDATIONS:

Based on the examination of the various data on each of these four molecules(as summarized previously), it is strongly felt the next vital step would be to take the following course of action:

* Each of these four molecules distinctively identifies one or more publications that contain potentially useful data for HITRAN and, therefore, warrant further critical examination. Such an examination should be carried out and the authors contacted to see if any of these data are available on tape that could be read directly into the HITRAN database.

* Information on a good number of spectrometric parameters (too many to list here) is simply not available for many molecules. Attempts should be made to contact the individuals who have done pioneering work in each of these fields to see if they can furnish the missing data.

* The current project should be continued either on a R.I.P. grant or at AFGL in subsequent years until all the new data have been entered in HITRAN.

* Use of the same faculty people is encouraged since they have done the initial work and hence may prove to be more efficient.

1988 USAF-UES SUMMER FACULTY RESEARCH PROGRAM/

GRADUATE STUDENT SUMMER SUPPORT PROGRAM

Sponsored by the

AIR FORCE OFFICE OF SCIENTIFIC RESEARCH

Conducted by the

Universal Energy Systems, Inc.

FINAL REPORT

SOFTWARE TOOLS FOR PROCESSING LARGE LIDAR DATA STREAMS

Prepared by :	Martin A. Patt
Academic Rank:	Associate Professor
Department and University	Dept. of Electrical Engineering University of Lowell
Research Location:	Geophysics Laboratory, Optical Physics Division
USAF Researcher:	Dr. Donald Bedo
Date:	29 July 1988
Contract No:	F49620-87-R-0004

Software Tools For Processing Large LIDAR Data Streams

by

Martin A. Patt

ABSTRACT

A careful study was performed to ascertain what kind of software tools would aid in the development of new LIDAR data analysis programs. A "toolbox" of software utilities was developed and documented.

ACKNOWLEDGMENTS

I would like to thank the Air Force Systems Command and the Air Force Office of Scientific Research for sponsorship of my research. In order to be meaningful, scientific research must be conducted in an intellectually stimulating environment. The Geophysics Laboratory provided this environment. The genuine support and encouragement by the scientists and engineers of the Optical Physics Division at AFGL is hereby acknowledged with gratitude.

- M.A.P.

I. INTRODUCTION

One of the nagging problems faced by scientists, engineers, and other occasional computer programmers is the large number of logical errors which find their way into new computer programs. This is especially true when creating software to analyze large data files such as those expected to be collected during a series of experiments which are expected to be performed in the atmosphere this coming September. It was felt that AFGL could benefit from the availability of a set of tailor-made software tools. Programming aids of this sort are quite helpful in that they speed the development of new computer software while, at the same time, improving readability, reliability, and "revisability" (the three R's ?).

II. OBJECTIVES OF THE RESEARCH EFFORT

The objective of the summer research effort was to create and document a "toolbox" consisting of software utilities and other intelligent programming aids which could prove useful in the development of new LIDAR-analysis software at AFGL.

III. THE RESEARCH EFFORT

The research effort consisted of developing the following software tools:

rewind_data
rewind_block_to_first_frame
rewind_frame
total_frames_in_block
frames_remaining_in_block
time_block
test_block

skip_frame
more_data
next_block
read_block_header
find_block_read_header
test_frame
find_frame_in_block
get_frame
add_frames
subtract_frames
multiply_frames
divide_frames
add_constant_to_frame
multiply_frame_by_constant

Although users will still need to write computer programs to analyze the LIDAR data, they are relieved of the burden of building file-maneuvering software into their programs. It is precisely that kind of pointer-manipulation software that is so prone to the introduction of logical errors. Thus, users of the software tools will find their programs more clear, more concise, and less error prone than would have been the case otherwise.

IV. RESULTS AND CONCLUSIONS

The objectives of the summer research effort were met and exceeded. The proposed software tools were developed, tested, and documented.

V. RECOMMENDATIONS

It is respectfully suggested that a companion box of "power tools" be developed to supplement the software "toolbox" developed during this summer effort.

The power tools would be made up of routines which process the experimental data to obtain information about aerosol concentrations in the atmosphere. It is important to try to keep the power tools fairly general so that they can be used not only with this summer's data, but also with data which will be obtained from future experiments, the precise details of which are not currently known.

REFERENCES

Journal Publications

1. M. A. Patt, "THE INS AND OUTS OF PROGRAM-WRITING PROGRAMS", (Interface - The Computer Education Quarterly, Summer 1987)vol.9, no.2.

Internal Publications

2. M. A. Patt, "LIDAR FRAME TOOLBOX & APPLICATIONS" Air Force Geophysics Laboratory, Summer 1988

3. M. A. Patt, "QUICK_AND_CLEAN USER'S MANUAL" Air Force Geophysics Laboratory, Summer 1987

Technical Manuals

4. M. Patt and R. Dirkman, "PROGRAM DEVELOPMENT ON THE VAX", University of Lowell, 1988.

1988 USAF-UES SUMMER FACULTY RESEARCH PROGRAM

Sponsored by the

AIR FORCE OFFICE OF SCIENTIFIC RESEARCH

Conducted by

Universal Energy Systems, Inc.

FINAL REPORT

Prepared by:	Beryl L. Barber and Daryl W. Sprehn
Academic Rank:	Assistant Professor and Graduate Student
Department:	Electronic Engineering Technology
University:	Oregon Institute of Technology
Research Location:	AFRADC/OCTP
	Griffiss AFB NY 13440-5700
USAF Researcher:	Frank E. Welker
Date:	26 August 1988
Contract No:	F49620-85-C-0013

Noise Calculations in a RADAR Receiver

by

Beryl L. Barber

and

Daryl W. Sprehn

ABSTRACT

The availability of low noise receiver preamps has created the need for a new look at the effective noise of radar receivers. The high cost of low noise amplifiers may not be justified without first considering the effects of other system noise sources more carefully.

The theory and approach for looking at the transmitter and antenna effects on receiver noise are presented. The overall effects of temperature, loss, and VSWR are considered.

ACKNOWLEDGEMENTS

The authors wish to thank Air Force Systems Command and the Air Force Office of Scientific Research for sponsorship of this research. Universal Energy Systems must be mentioned for their concern and help in all administrative and directional aspects of this program.

The group under the direction of Mr. Frank Welker has been exceptionally helpful in this project which we have undertaken. Mr. Tom McEwen has been very helpful with the entire program. He has patiently listened to various theories and has given us very useful information in return. Jim Van Damme has assisted in various ways towards generating successful data.

NOISE CALCULATIONS IN A RADAR RECEIVER

An approach to the calculation of the
true overall system noise figure

I. INTRODUCTION

Electrical noise can be defined as any electrical energy which is undesired. This may be man-made or due to natural phenomena. It may be coherent or incoherent and FM and/or AM in character. It should be noted that AM always generates FM. Noise can also be classed as correlated or uncorrelated.

For the purposes of this report, only noise affecting the receiver will be considered.

Noise figure is very complex and is dependent on the temperature of each item in the system, the loss in each item, and the VSWR presented to the remainder of the system. This report covers a technique for calculating the overall system noise contribution.

Because counteracting the effects of undesireable noise increases the cost of a detection system, interest has been generated in finding ways to decrease the total noise.

II. OBJECTIVES OF RESEARCH EFFORT

A study made of the various noise contributing elements of a system, and not limited only to radar, will provide a technique for evaluating the various specifications of a system and give an understanding of the specifications for the individual components in that system. Each component has critical factors which must be closly evaluated while others may be of little importance. Decisions regarding the selection of critical and non-critical factors should be easily made. This should not only improve the operation of any system but should enhance the cost effectiveness of component procurement. It will also allow a trade-off of final system performance versus cost.

III. NOISE

Twenty years ago our radars and communication systems were rather simple devices, not only from a circuit standpoint but also from the standpoint of sensitivity. When radar receiver noise figures were in the range of 10dB to 13dB noise temperatures and VSWR's were generally ignored.

Currently it is no longer necessary to build parametric amplifiers to obtain RF noise figures of 1.5dB to 2dB as this is presently available using transistor amplifiers. The ready availability of low noise RF amplifiers has made it necessary to look again at the entire system. Testing of low noise figures is also much more complicated.

Let us now look at the RF section of a modern radar and examine the various components. Looking at figure 1, the noise figure of the system may be calculated as follows:

$$NF = Rd(Te1/To) + Lin(Te2/To) + Ltr(Te3/To) + Famp(Te4/To) \qquad \text{Equation 1}$$

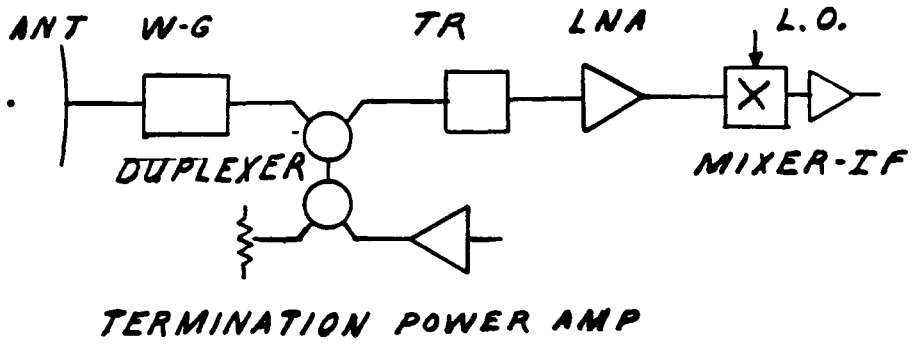

Figure 1

where Rd is the radiation or thermal temperature of the antenna, Lin is the loss in the input waveguide and duplexor, Ltr is the loss in the TR device, and Famp is the noise figure of the receiver looking into the low noise amplifier.

The ambient thermal noise may be expressed as N=KTB where N is in Watt-seconds per Hertz, K=1.38E-23 (Boltzmann's Constant), T is the thermal temperature in Kelvins, and B is the bandwidth in Hertz. At room temperature, 293.2K, this translates to -174dBm per Hertz or -114dBm/MHz.

We can also look at the noise power developed in a resistor. If we have an energy conversion source, (temperature to electrical power), and a load which is matched, the resultant rms voltage will be E/2. Using this in the noise equation we have

$(E/2)^2/R = KTB$ Equation 2

or sometimes written as $E^2/R = 4KTB$ where $Erms = \sqrt{E^2}$, where equation 2 is the noise power in a resistor R. Note that this is the noise power produced due only to the temperature of the resister.

In order to conform to Nyquist's noise criterion, it may not be appropriate to consider voltage at all, but rather to consider the power equation $P = E^2/R$, due to the complex nature of the noise spectrum. Let us only consider power and understand that any lossy device has noise energy dependent on the device temperature.

For further studies into the fundementals of noise see the references at the end of this report.

Let us now look at the noise involved in a transmitter-receiver system. The first noise taken into consideration is the effective noise of the antenna. This may include sky temperature, radiation resistance of the antenna, and possibly externally generated noise. Low noise systems are affected by the thermal temperature and solar absorbtion of the antenna. Next, any losses in the antenna feed must be multiplied by Te/To, the temperature of the device divided by 293.2 kelvins. As we will see, the VSWR of the antenna will be a significant factor.

The duplexor is used to selectively couple either the transmitter or receiver to the antenna. It has a small loss in each pass, a VSWR, and a thermal temperature associated with each junction or circuit. As the termination must be very well matched to the circulator to obtain good isolation, we will disregard this internal match; but the termination itself is a thermal noise generator which, at high power levels, may contribute considerable noise power. The transmitter port will

be by design a very low VSWR when on, however; when the system is in the receive mode the transmitter VSWR may be very high.

The transmitter is operated only a small percentage of the total time. During the off time the output port will have a thermal noise output. This noise varies from device to device but will usually vary from 5000 kelvins for a Klystron to 15000 kelvins for a helical TWT and with solid-state transmitters the thermal noise output is as low as 400-500 kelvins. The noise power from the transmitter and termination will pass through the duplexor, with a small attenuation, and be reflected off the antenna, (antenna feed VSWR), and then passes back through the receive port of the duplexor to the T/R device and LNA.

Each device in the system has an insertion loss, VSWR, and noise temperature which affect the overall noise of the system.

Looking at figure 1 we can trace out the noise path for each component and evaluate the critical items. Setting typical values for each component the overall system noise consideration may be as follows: (for the present we will disregard the antenna except for the feed VSWR)

The output window of a twystron, in an operating mode and beam off condition, will appear as a noise source of approximately 6000 kelvins. This "signal" will pass through the duplexor and waveguide with .8dB loss, resulting in 5000 kelvins at the antenna. If the antenna has a VSWR of 2, then 500 kelvins will be reflected back into the receiver path of the duplexer with a reduction of 50 kelvins in the waveguide. If the termination has a noise temperature of 600 kelvins then it will result in a contribution of an additional 50 kelvins. The waveguide will contribute in two ways; one in loss and the other in temperature. This contributes an additional 50 kelvins. The total is now 550 kelvins input to the receiver path of the duplexor. The loss due to the duplexor in receiver path will almost equal the noise contribution. The T/R will also contribute slightly more than it attenuates. We have disregarded VSWR's in this path which may contribute or reduce noise.

Using a LNA with a measured noise temperature of 170 kelvins now results in an effective noise temprature of 720 kelvins or over 6dB.

An easier method of performing receiver path calculations as shown in figure 2 is to multiply path losses by the normalized thermal temperature of the device. Normalized temperatures have been created by dividing by the constant for room temperature, 293.2 kelvins.

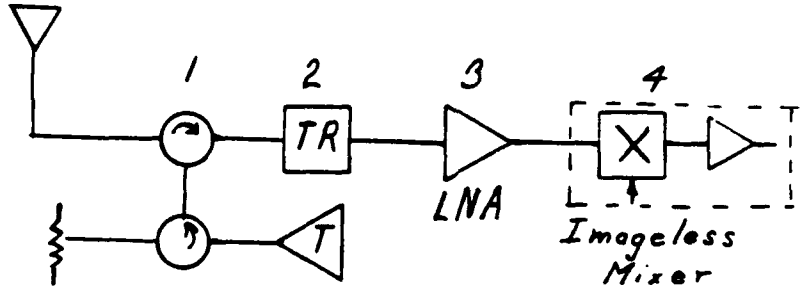

$$F = \frac{T_1}{T_o} Loss\,1 + \frac{T_2}{T_o} Loss\,2 + 10 Log_{10}\left[NF_3 + \frac{NF_4 - 1}{G_3}\right]$$

T is in Kelvins
T_o = 290 Kelvins
Loss is in db
NF is a ratio defined as noise factor
F is in db defined as noise figure

Figure 2

The calculations of figure 2 are in error because they disregard the thermal noise contributions of the transmitter, and the impedence match of the antenna. Figure 3, shown on the next page, is accurate for any receiver system by assigning the correct component characteristics to the model. Figures 2 and 3 show two different methods for calculating system noise.

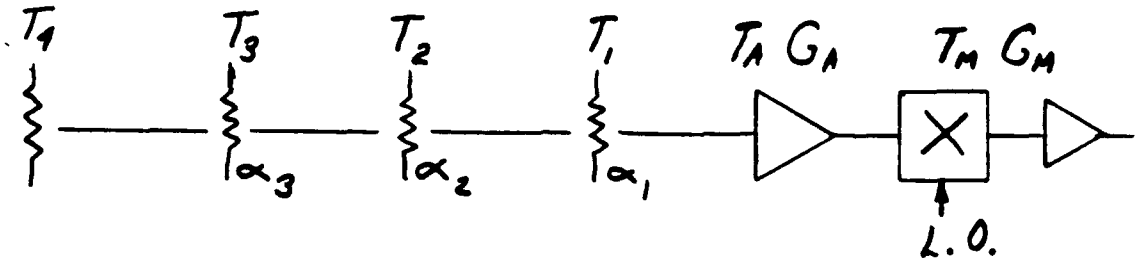

$$T_{system} = T_4(1-[\alpha_1+\alpha_2+\alpha_3]) + T_3(1-[\alpha_1+\alpha_2]) + T_2(1-\alpha_1) + T_1 + T_A + \frac{T_M}{G_A}$$

T is in Kelvins

α is the Loss Ratio

G is the Gain Ratio

$$\alpha = \frac{P_{IN} - P_{OUT}}{P_{IN}}$$

$$G = \frac{P_{OUT}}{P_{IN}}$$

figure 3

In the case of phased arrays a considerable improvement is seen in the "transmitter off" thermal noise. There is a higher VSWR looking into the antenna however, and the resulting noise contribution remains approximately the same as with a tube transmitter. It should be noted that in a phased array the noise increases in the receiver as the angle is varied on either side of the "forward look". This is due to the VSWR which is dependent upon the "look angle".

It is shown that it is not always the pre-amplifier which is the main noise contributor in the system. It can be seen that under bad match conditions of the antenna, the loss in the duplexor may be beneficial. This should be used as a "trade-off" with the loss in the effective transmitter output power. In the receive system the LNA is usually the most costly component, with the cost going up exponentially as the noise figure goes down. Often it will be found that the system input noise can be reduced less costly than can the reduction of LNA noise.

All of our previous discussions were based on a single channel noise path. Since we usually use a superhetrodyne receiver, the above discussion is valid for an imageless mixer. If a conventional two channel mixer is used without filtering 3dB of noise must be added to the overall calculations. If a filter is used, all the noise generated in the image channel, after the filter, must be added. This is a big selling point for the imageless or image-rejection mixer. If a filter is used then it should be placed between the LNA and the mixer. Though not derived in this paper, best dynamic range is achieved when the

gain of the LNA is low but consistant with the noise figure. Usually a gain of 15dB to 17dB is adaquate. Rarely is more than 20dB of gain needed or desired

A narrowband tunable LNA is often a specified component. This amplifier has gain in the signal channel but almost no gain in the image channel. The technique is very effective in image rejection.

All ancillary devices in the system should be inserted into the calculations in their appropriate positions. These include such things as noise measuring equipment, arc detectors, power monitoring and VSWR measuring equipment. If phase shifters are used, these should be looked at over the full phase and frequency ranges.

SUMMARY OF NOISE CONSIDERATION

We have shown that each item in the RF portion contributes to the noise figure of a system. Each component must be considered to compute the true noise input. As the ambient noise in the system is -114dBm/MHz, any excess noise decreases this sensitivity decibel for decibel and all of the components must be taken into account. Loss, VSWR, and temperature all contribute to the sensitivity of a system. By varying these three characteristics the least costly technique can be found to obtain the required performance. Using this technique, the performance of a system can be predicted.

RECOMMENDATIONS

This theory would yeild itself to computer programs which allow variations in parameters. The actual noise calculations are quite straightforward but successive parameter variation would become quite tedious.

REFERENCES

1. Freeman, J. J., Principles of Noise, New York, John Wiley and Sons Inc, 1958.
2. Goldman, Stanford, Frequency Analysis Modulation and Noise, York, PA., McGraw-Hill Book Company, Inc., 1948.
3. Schwartz, Mischa, Information Transmission, Modulation, and Noise, New York, McGraw-Hill Book Company, Inc., 1980.

1988 USAF-UES SUMMER FACULTY RESEARCH PROGRAM/

GRADUATE STUDENT RESEARCH PROGRAM

Sponsored by the

AIR FORCE OFFICE OF SCIENTIFIC RESEARCH

Conducted by the

Universal Energy Systems, Inc.

FINAL REPORT

STABILITY OF Au/W/GaAs AND Au/Pt/Ti/GaAs SCHOTTKY BARRIER HEIGHT: A PRELIMINARY STUDY

Prepared by:	Keith A. Christianson
Academic Rank:	Assistant Professor
Department:	Electrical Engineering Department
University:	University of Maine
Research Location:	RADC/RBRP Griffiths AFB Rome, NY 13440
USAF Researcher:	A.L. Tamburrino
Date:	September 14, 1988
Contract no:	F49620-87-R-0004

STABILITY OF Au/W/GaAs AND Au/Pt/Ti/GaAs SCHOTTKY BARRIER HEIGHT: A PRELIMINARY STUDY

by

Keith A. Christianson

ABSTRACT

The stability of the barrier height of Au/W/GaAs and Au/Pt/Ti/GaAs Schottky barriers under long term biasing conditions has been examined. Both types were found to exhibit decreases in barrier height under long term reverse bias conditions, with the changes seen for the Au/W/GaAs diodes (≈30-50 meV) much greater than those for the Au/Pt/Ti/GaAs diodes (≈5 meV). The changes in barrier height were seen to have a characteristic logarithmic dependence on time. Recovery of the barrier height was seen to occur over a period of days in a zero bias condition, or in an accelerated manner under forward biasing for both sets of samples. A preliminary Auger study has correlated the presence of oxide at the interface with the barrier height shift observed, and this oxide is presumably involved in the formation/destruction of deep traps/interface states which are responsible for the change in barrier height.

ACKNOWLEDGEMENTS

I wish to thank the Air Force Systems Command and the Air Force Office of Scientific Research for sponsoring this research. Also, special thanks to Universal Energy Systems for their management of the summer faculty program.

At Rome Air Development I would especially like to thank A. L. Tamburrino, whose help made this an enjoyable and productive stay. Special thanks also to D. Burns, S. Drager, C. Lane, L. Laziki, M. Levi, M. Pronobis, F. Robenski, L. Walsh, and M. Walter.

I. INTRODUCTION:

Metal/semiconductor contacts are a fundamental part of all semiconductor devices and integrated circuits. Two main types can be distinguished: the ohmic (low resistance) and the Schottky (rectifying) type contacts. Despite the widespread usage of these contacts some fundamental properties still are not well understood, particularly those involving Schottky contacts on compound semiconductors.

For example, there is the question of barrier height. It is not understood why the barrier height of a metal on GaAs is relatively insensitive to the work function of the metal. For example, a wide variety of metals give a barrier height of ≈0.75 eV above the valance band for n-type GaAs, and ≈0.5 eV above the valance band edge for p-type GaAs.[1] A number of theories have been proposed to explain the pinning of the Fermi level, including the unified defect model by Spicer[2,3] and the effective work function model by Woodall.[4] There is no general agreement at this point on the responsible mechanism.

In addition to not understanding what causes the barrier height to be fixed at a relatively constant level, a new series of experiments have changed the barrier height, temporarily, after photochemical and/or chemical treatments.[5,6] Also, a recent study by Miret et. al.[7] has shown that the barrier height of a number of metal Schottky barrier systems on GaAs temporarily changes after long term reverse bias conditions. In this study (Ag, Au, Cr, Pd, Al)/GaAs Schottky barriers were fabricated under both freshly cleaved UHV (ultra high vacuum) and chemically cleaned HV (high vacuum) conditions. In general the air exposed diodes showed greater shifts in barrier height than the UHV cleaved diodes, with the largest variation in barrier height being an 85 meV decrease for air exposed Ag/GaAs diodes. The diodes were found to return to their original barrier height within a few days after the reverse bias aging voltage was removed. Speculation that the formation of deep traps and/or interface states was involved, but no work in this area has been reported.

With the exception of Al, the metals examined in Miret study are not typical of current GaAs processing techniques. Most commercial practice uses

some sort of refractory metal/alloy, followed by a diffusion barrier with Au on top to lower the resistivity. Typical combinations are Au/Ti-W/GaAs, Au/Pt/Ti/GaAs, and more recently Au/W-Si/GaAs.[8] The use of these refractory metals is particularly important for self-aligned-gate (SAG) structures, where the post implant annealing of the drain and source regions may exceed 800°C.

The microelectronics reliability division at Rome Air Development (RADC/RBR) is the primary microelectronics reliability center for the DoD. Of the various branches of RBR, the reliability physics group (RBRP) is responsible for most the research efforts within the division. RBRP has interest in current reliability problems, as well as looking ahead to see what might limit the reliability of upcoming technologies. Thus a study which examines the electrical characteristics of GaAs Schottky barriers with biasing conditions is of interest to RBRP. Note that a changing of the characteristics of the Schottky barrier will also influence the properties of more complicated devices based upon it, e.g, the MESFET.

My research interests are in the various properties and application of compound semiconductors. I have experience in crystal growth, device fabrication, and various characterization techniques. My knowledge of these areas, including deep level characteristics, contributed to my assignment at the Reliability Physics Group of the Microelectronics Reliability Division of Rome Air Development Center.

II. OBJECTIVES OF THE RESEARCH EFFORTS

The barrier metals on GaAs, with the exception of Al, which have been examined for long term reverse bias stability are not characteristic of current commercial processes. Thus, the primary objective was to characterize one or more typically commercially used gate metal structures for long term bias stability. In order to do this a measurement system was needed which would hold the sample at a given bias for a given length of time, check the barrier height, and repeat the process indefinitely as required.

If a change in the barrier height was noted it was desired to look for recovery of the barrier height change, at room temperature and/or under accelerating biasing conditions. Also since surface analytical capabilities are available in RBR, a further objective was to try to relate any barrier height change seen to the presence of oxide, etc. at the Schottky barrier/GaAs interface. The objective was to see if this phenomena, if observed, was related more to the barrier metal itself or to the interfacial conditions.

III. EXPERIMENTAL PROCEDURE

A) Measurement of Barrier Height

The IV properties of the Schottky barriers were obtained in an automated fashion using an HP 4062A semiconductor parameter analyzer. The barrier height of the Schottky diodes was then determined from the IV properties by substitution into the thermionic emission equation:

$$I = SA^{**}T^{2}\left(e^{-\phi_{bo}/V_T}\right)\left(e^{\frac{V-IR}{nV_T}} - 1\right) \qquad (1)$$

where I is current, S is area, A** is the modified Richardson constant (taken to be 8.67), T is the temperature, ϕ_{bo} is the zero bias barrier height, V_T is the thermal voltage, V is the sample voltage, R is the sum of contact and bulk resistances and n is the ideality factor. A plot of log I vs $V_{forward}$ should be a straight line, with the slope yielding the ideality factor

$$n = \frac{1}{kT}\,\frac{\delta V}{\delta \ln I} \qquad (2)$$

The slope was obtained by a least squares fit over the linear portion of the forward bias curve. An estimated current was then obtained at V = 0.25 V (to allow neglection of the -1 term) followed by extrapolation to zero bias to get ϕ_{bo}. Note that in general the barrier height is a function of bias

$$\phi_b(V_j) = \Phi_{bo} + K_1 V_j + \ldots \qquad (3)$$

and typically only the linear term is kept, so that

$$K_1 = 1 - 1/n \qquad (4)$$

where n is the ideality factor.

As can be seen in equation 1 there is a strong temperature dependence in the thermionic process. To forestall problems, the sample temperature was monitored and recorded at each measurement step, and the updated value used in the calculation. Also, since the case temperature is not an accurate measure of the junction temperature, the ideality factor was watched for drifting after bias aging as per Miret.[7] In all cases the estimated temperature rise was less than 5K.

B) Samples

Samples from the two vendors were obtained, along with documentation. Note that the use of vendor's samples required disassembly to confirm (and in one case dispute) the manufacturer's claim as to what they are.

The samples from Vendor A were GaAs power MESFETs, designed for two watts output at 7.5 GHz. They have 24 gate fingers, each 200 μm wide by 1 μm length, for a total gate width of 4.8 mm. Figure 1 shows a part of one of these MESFET's. Note the transistor had been flip chip mounted, and dismantling tore the source metalization (heavily textured area) away from the device itself. As confirmed by EDAX and SAM the metalization system for the Schottky was Au/W/GaAs.

The samples from the Vendor B were also GaAs power MESFETs designed for a 2 watt output at 4 GHz. The structure has six gate fingers, each 1 μm length, with a total gate width of 1.7 mm, as is seen in Figure 2. The Schottky metalization was confirmed to be Au/Pt/Ti/GaAs by SAM. Note that EDAX was not useful in this case since the poly glass encapsulation had to be sputtered away.

The use of MESFETs instead of simple Schottky barrier complicated the investigation. With the MESFET the gate-source, gate-drain, and gate-source and drain connected together configurations can all be examined. Also, a shift

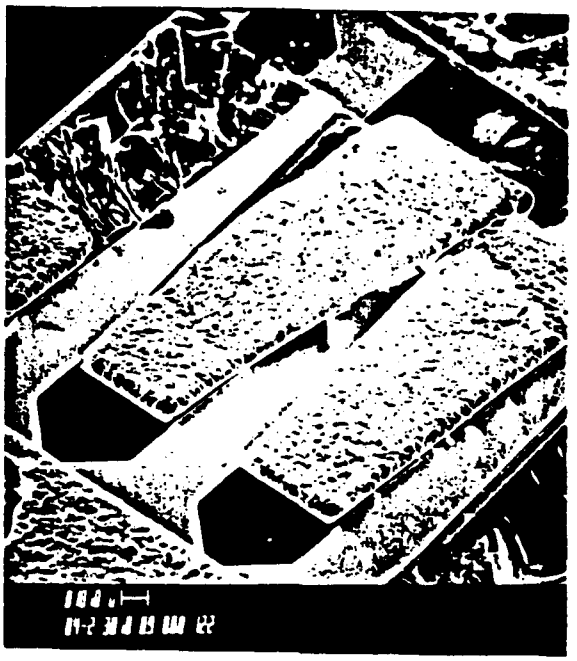

Figure 1. Portion of a 2 watt, 7.5 GHz GaAs MESFET. The heavily textured area is the source, which was torn away when the device was un-flip chipped. Gate metalization is Au/W/GaAs.

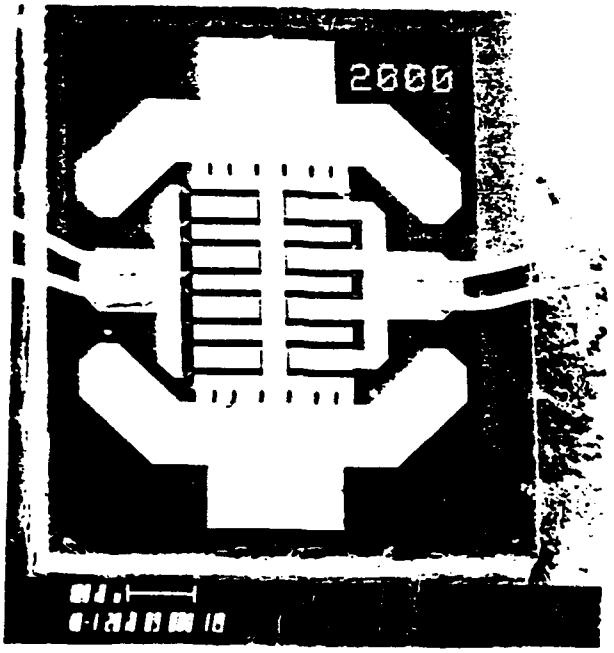

Figure 2. 2 watt, 4 GHz GaAs MESFET. Gate metalization is Au/Pt/Ti/GaAs.

in the barrier height should be reflected in a change in the gate-source voltage necessary to close off the channel. The link is tenuous, however, since it depends on how the built-in voltage is changed by barrier height changes, which goes back to the original Schottky controversy.

IV. BARRIER HEIGHT STABILITY OF Au/W/GaAs

The first set of samples examined had a tungsten Schottky barrier. Upon probing typical depletion mode MESFET like characteristics were obtained (Figure 3). Note that these samples are high pinchoff voltage MESFETs, as defined by M. Shur,[9] with the pinchoff voltage being near -5V. The individual junctions present in the MESFETs were then probed. Typical results in the forward and reverse bias directions are shown in Figures 4 and 5 respectively, for the gate-source diode configuration. Only a small variation in IV characteristics was seen between sample to sample, or for that matter between the different diode configurations on a given transistor. Notice the soft breakdown characteristics in the reverse direction, commencing shortly after the pinchoff voltage is reached. More will be said about this region later.

Upon plotting the forward I-V characteristics as log I vs. V, the characteristics shown in Figure 6 were obtained. Note that the plot is linear over at least four orders of magnitude, thus justifying the use of the barrier height extrapolation technique used. Also, no bending over of the curve at higher biases such as documented by Newman[10] was observed. For this reason the series internal resistances were neglected, and the ideality factor was attributed to changes in barrier height with voltage.

Two types of aging experiments were performed. The first was an isochronal type. The diode was biased at given voltage for a set length of time, then a shift in the barrier height was looked for. The process was continued at increasing voltage until sharp breakdown was starting to occur. For those samples with no previous aging history no change in barrier height was seen for either forward bias or zero bias conditions.

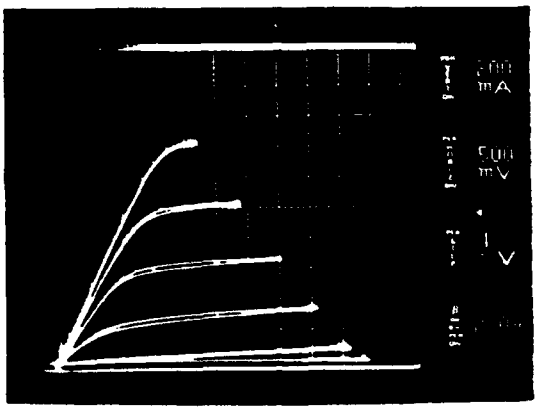

Figure 3. Typical Au/W/GaAs MESFET 3 terminal characteristics.

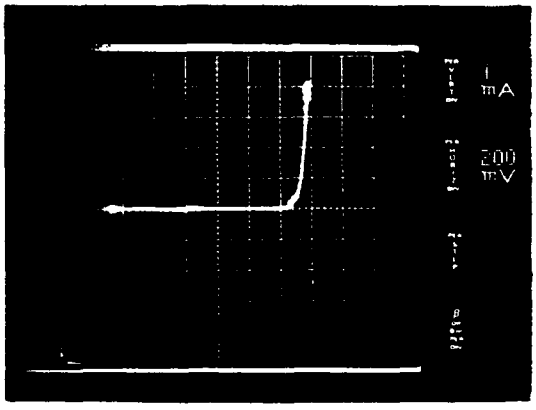

Figure 4. Typical gate-source forward IV characteristics for Au/W/GaAs Schottky barriers.

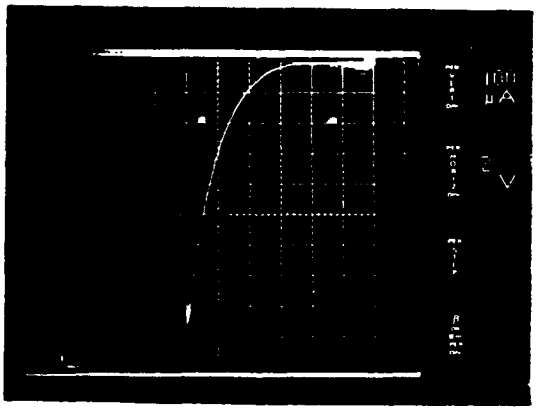

Figure 5. Typical gate-source reverse bias IV characteristics for Au/W/GaAs Schottky barriers.

When aged in the reverse bias direction decreases in barrier height were seen, with the greatest decrease occurring in the gate-source configuration as Figure 7 shows. The degradation did not occur immediately upon entering the reverse bias regime, but instead had a threshold approximately where the soft region in the reverse characteristics began. It was not possible to compare results with the Stanford group in this regard,[7] since they did not publish details of the reverse bias breakdown of their diodes. As we see in Figure 7 once the aging voltage leaves this soft breakage regime the amount of barrier height change slows down, and for some samples aged in the hard reverse breakdown region recovery of the barrier height was taking place instantaneously.

By picking a voltage in this soft breakdown region isovoltage aging experiments were performed. Figure 8 shows a typical result plotted on a linear time scale, but perhaps more is revealed when $\Delta\phi$ is plotted versus log time, as is shown in Figure 9. The same logarithmic dependence noted by the Stanford group is seen.[7]

The barrier height change observed was reversible, either by letting the sample sit at zero bias for several days, (Figure 10a) or in an accelerated manner by applying a positive bias (Figure 10b). There did not seem to be a threshold voltage for recovery (Figure 11), and in general greater current resulted in a faster recovery rate.

V. BARRIER HEIGHT STABILITY OF Au/Pt/Ti/GaAs.

The same testing procedure was followed for the samples with the Ti barrier metals, i.e., measurement of junction characteristics followed by isovoltage aging and then isochronal aging. The vendor indicated these these are again high pinchoff voltage MESFETs, but I was unable to confirm the three terminal properties due to the lack of a suitable test fixture to prevent oscillation. The measured diode properties in the gate-source, gate-drain, and gate-source, drain configurations looked roughly similar to each other and from sample to sample. Figure 12 shows typical forward bias response, while

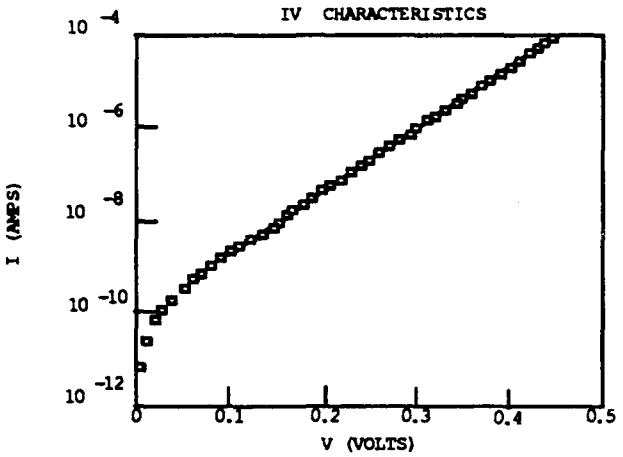

Figure 6. Log I versus V for gate-source configuration of a typical Au/W/GaAs Schottky barrier.

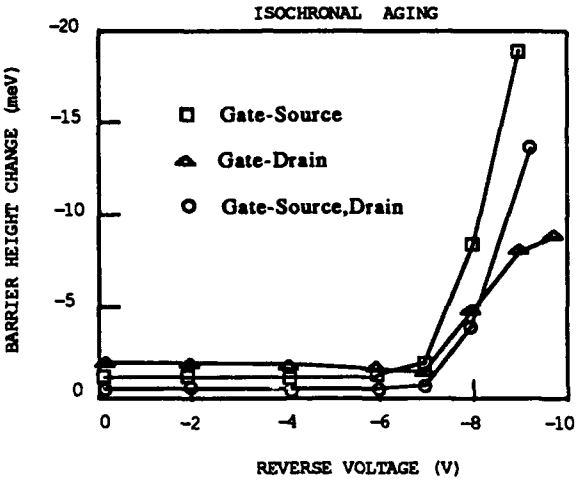

Figure 7. Change in barrier height versus aging voltage for various configurations of a Au/W/GaAs Schottky barrier. Aging increments were 50 minutes.

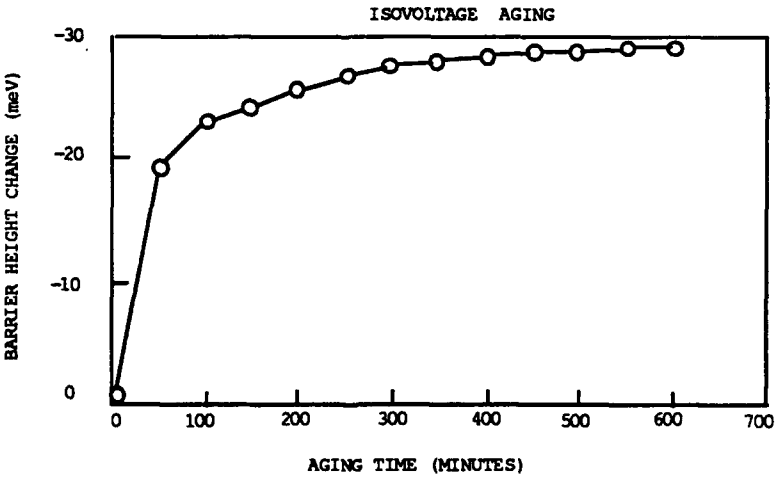

Figure 8. Change in barrier height versus aging time for gate-source configuration of a Au/W/GaAs Schottky barrier. Aging voltage was -9V.

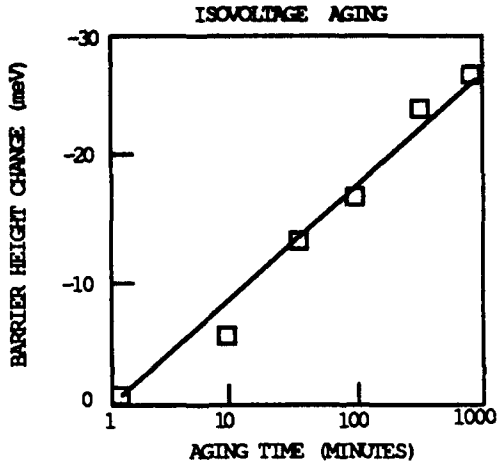

Figure 9. Change in barrier height versus log aging time for gate-source configuration of a Au/W/GaAs Schottky barrier. Aging voltage was -9V.

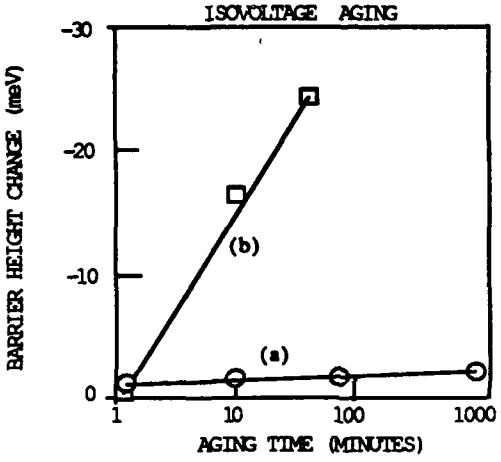

Figure 10. Recovery of barrier height change at room temperature, (a) no accelerating voltage applied, (b) with 0.5 volts forward bias for Au/W./GaAs Schottky barrier.

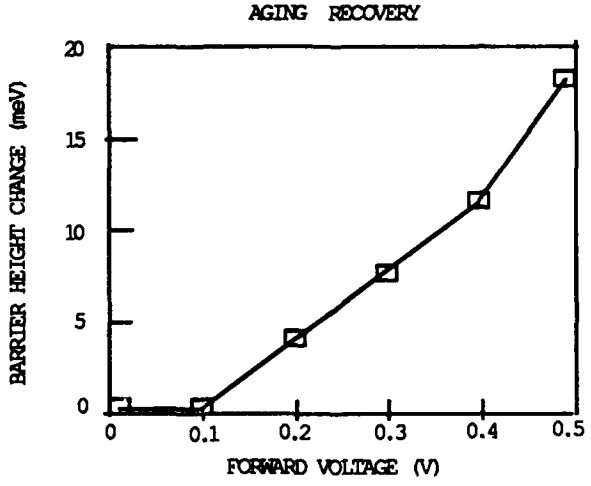

Figure 11. Dependence of recovery of $\Delta\phi$ on forward biasing voltage for Au/W/GaAs Schottky barriers. Aging increments were each 50 minutes.

Figure 13 shows typical reverse bias response. The most immediate difference between the two types of MESFETs is the relative lack of "soft" breakdown in the reverse bias characteristics. Another difference can be more readily seen in log I vs V plots (Figure 14), where a large nonlinear region at low bias exists. Newman et al. have seen such a response in highly stepped structures, which this device certainly qualifies as (see Figure 15).[10]

Isochronal aging has revealed decreases in barrier height in gate-source, gate-drain, and gate-source, drain configurations. The decreases seen are very small compared to the W gated devices, but once again a threshold is observed in all configurations, as Figure 16 illustrates. The most prominent aging was seen to occur in the gate-drain configuration for this particular Schottky device. If we ignore the early portion of the curve which is at the limit of the instrumentation resolution (2 meV) the barrier height changes once again in the "soft" portion of the curve.

Isovoltage aging revealed the characteristic logarithmic dependence again, in both reverse aging and forward recovery, as Figures 17 and 18 illustrate.

VI. INTERFACIAL STUDIES

Because of the large variation between the aging response of the Au/W/GaAs and Au/Pt/Ti/GaAs barriers the following question arose: Is the variation seen due to the nature of the metal, or more to the nature of the interfacial region between the metal and the GaAs? In an attempt to find any gross differences between the two types of devices depth sputtering using Scanning Auger Microscopy (SAM) was performed.

Figure 19 shows the results for a Au/W/GaAs Schottky barrier after 5 minutes sputtering time. Note that peaks for Au, Ga, As and W are seen. In addition a very prominent peak for O is seen. In contrast, a depth profile for the Au/Pt/Ti/GaAs Schottky barriers (Figure 20) shows a SiN cap, followed by the Au/Pt/Ti/GaAs structure. Note that for this device the oxygen line remains in the background for the entire structure. Although O can be a contaminent

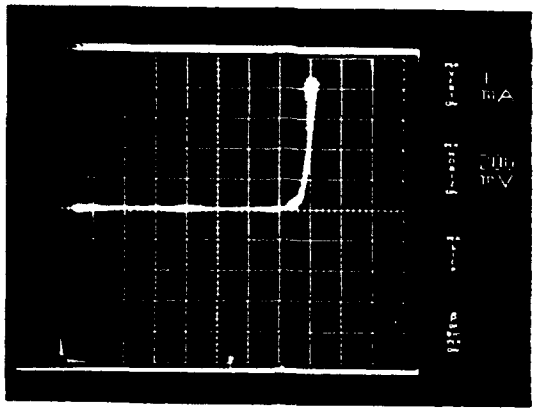

Figure 12. Typical gate-drain forward bias characteristics for Au/Pt/Ti/GaAs Schottky barriers.

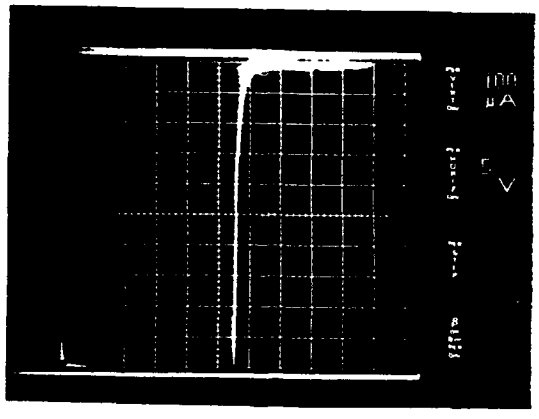

Figure 13. Typical gate-drain reverse bias characteristics for Au/Pt/Ti/GaAs Schottky barriers.

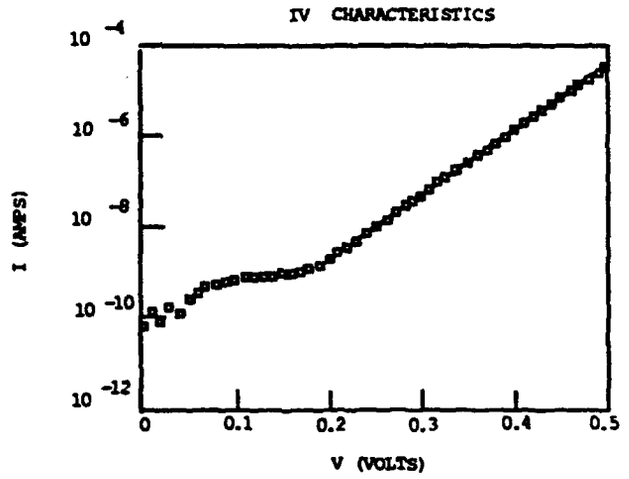

Figure 14. Log I versus V for gate-source configuration of a typical Au/W/GaAs Schottky barrier.

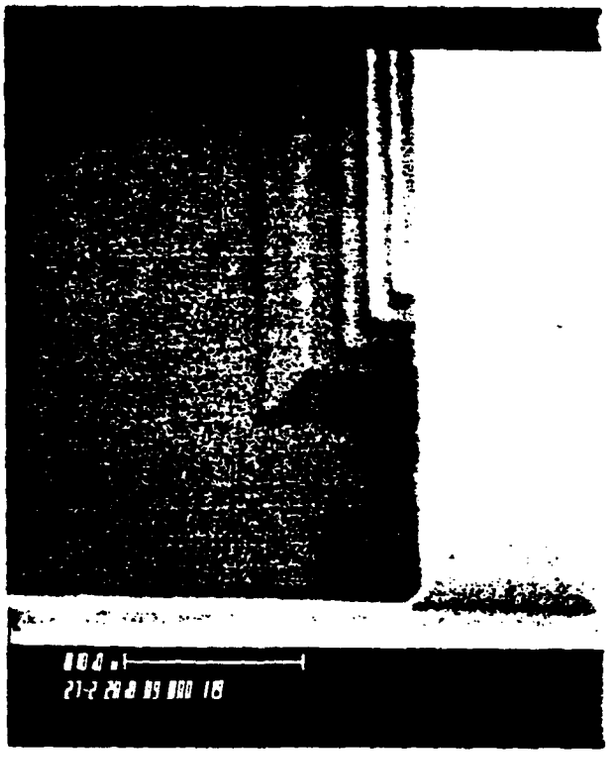

Figure 15. SEM photo of Au/Pt/Ti/GaAs structure, showing the highly stepped nature.

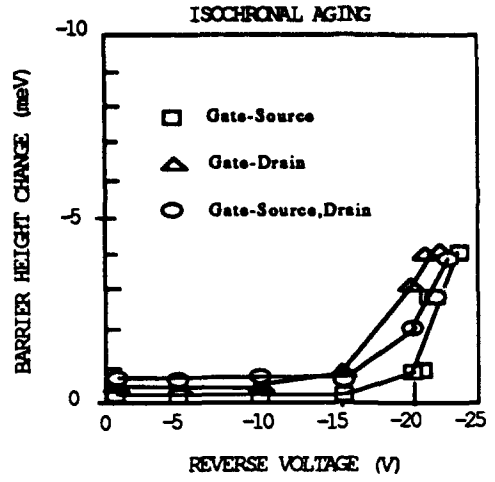

Figure 16. Barrier height change versus aging voltage for various configurations of a typical Au/PT/Ti/GaAs Schottky barrier. Aging increments were each 50 minutes.

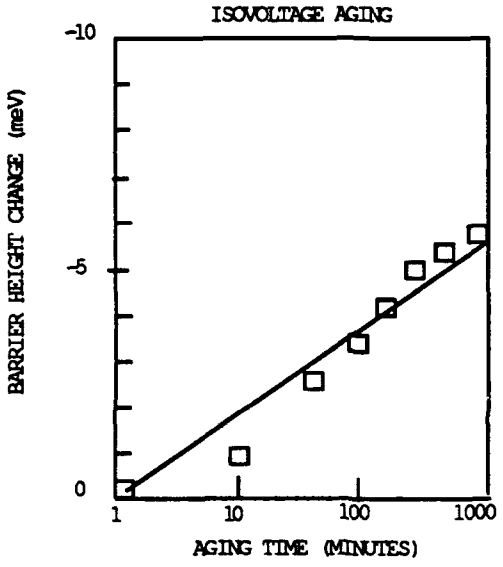

Figure 17. Barrier height change versus log time for reverse bias aging of gate-drain barrier of a typical Au/Pt/Ti/GaAs Schottky barrier. Aging voltage was -22V.

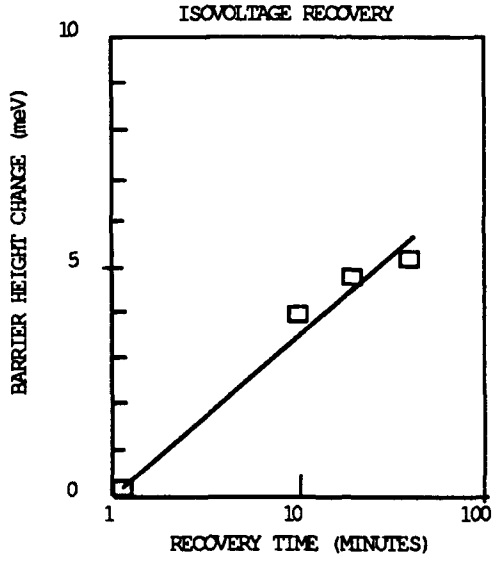

Figure 18. Barrier height change versus log time for forward bias recovery (v=0.55V) of gate drain barrier of a typical Au/Pt/Ti/GaAs Schottky barrier.

in any UHV environment, the fact that O clearly shows in the Au/W/GaAs barriers and not in the Au/Pt/Ti/GaAs barriers when the same measurement procedure was used indicates that oxide at the interface may be affecting the electrical properties.

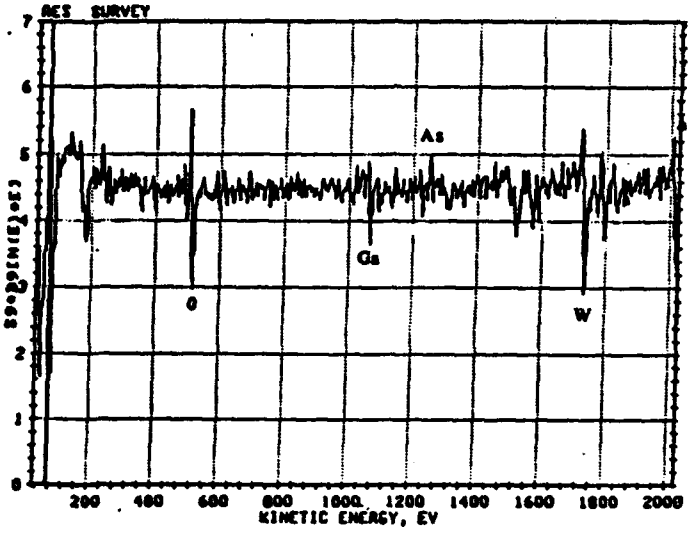

Figure 19. AES survey after five minutes sputtering time for a Au/W/GaAs Schottky barrier.

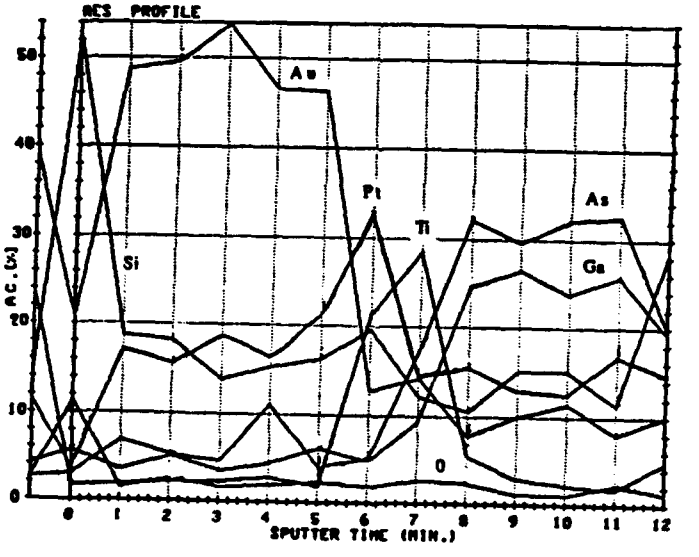

Figure 20. AES depth profile for a Au/Pt/Ti/GaAs Schottky barrier.

VII. CONCLUSIONS AND RECOMMENDATIONS

1) Samples of Au/W/GaAs and Au/Pt/Ti/GaAs Schottky barriers present in MESFETs have been evaluated for Schottky barrier height stability under long term biasing conditions. The barrier height of both types of devices was found to be stable under zero and forward biasing conditions. In contrast, both types of samples exhibited decreases in barrier height after long term reverse bias. The changes were found to be recoverable after sitting at zero bias for a few days, or in an accelerated manner by application of forward bias. The changes in barrier height for the Au/W/GaAs diodes were much larger (30-50 meV) than for the Au/Pt/Ti/GaAs barriers (5 meV).

2) A preliminary Auger study has indicated the presence of oxide at the W/GaAs interface which is not observable at the Ti/GaAs interface. Due to the limited number of samples characterized by AES it is recommended that this procedure be repeated for more samples.

3) The long time constant of the change in barrier height and the fact that it is recoverable would tend to indicate some sort of a reversible defect reaction producing deep traps/interface states is occurring, rather than a change in occupation of existing traps. Various methods of characterization of deep traps are possible, and the follow on proposal will suggest various techniques to see if the change in barrier height is related to the concentration/occupation of the deep traps/interface states. Also, as a follow on question: Is the recovery of the barrier height a recombination enhanced defect reaction?

4) Variations in aging response between the gate-source, gate-drain and gate-source, drain configurations of the MESFETs were seen. It should be possible to model the electric field present in these various configurations to help explain the aging variations.

5) What is the nature of the link between barrier height and pinch-off voltage? A very preliminary study has shown a correlation, but more detailed experiments between the two and three terminal characteristics need to be done.

6) The characterization of a third set of samples, perhaps Ti-W or W-Si, would lend much additional information to the subject.

REFERENCES

1) J.R. Waldrop, Appl. Phys. Lett. 44, 1002 (1984).

2) W.E. Spicer, I. Lindau, P. Skeath, and C.Y. Su, J. Vac. Sci. Technol. 17, 1019 (1980).

3) W.E. Spicer, P.W. Chye, P.R. Skeath, C.Y. Su, and I. Lindau, J. Vac. Sci. Technol. 16, 1422 (1979).

4) J.M. Woodall and J.L. Freeout, J. Vac. Sci. Technol. 19, 794 (1981).

5) S.D. Offsey, J.M. Woodall, A.C. Warren, P.D. Kirchner, T.I. Chappell, and G.D. Petit, Appl. Phys. Lett. 48, 475 (1986).

6) M.S. Carpenter, M.R. Mellach, and T.E. Dungan, Appl. Phys. Lett. 53, 66 (1988).

7) A. Miret, N. Newman, E.R. Weber, Z. Liliental-Weber, J. Washburn, and W.E. Spicer, J. Appl. Phys. 63, 2006 (1988).

8) Gallium Arsenide: Materials, Devices and Circuits, edited by M.J. Howes and D.V. Morgan, John Wiley and Sons, 1985, Chapter 6.

9) GaAs Devices and Circuits, M. Shur, Plenum Press, 1987, page 322.

10) N. Newman, M. Van Schilfgaarde, T. Kendelwicz, M.D. Williams, and W.E. Spicer, Phys. Rev. B 33, 1146 (1986).

1988 USAF-UES SUMMER FACULTY RESEARCH PROGRAM
GRADUATE STUDENT RESEARCH PROGRAM

Sponsored by the
AIR FORCE OFFICE OF SCIENTIFIC RESEARCH
Conducted by the
Universal Energy System, Inc.
FINAL REPORT

Parallel Runtime System For Lucid

Prepared by:	Darin DeForest
Academic Rank:	Research Associate
Department and University:	Computer Science Arizona State University
Research Location:	RADC/COTC Bldg. 3 Griffiss AFB, NY 13441
USAF Researcher:	Chris Flynn
Date:	8 July 88
Contract No:	F49520-87-R-0004

Parallel Runtime System For Lucid

by

Darin DeForest

ABSTRACT

As parallel computers are becoming more commercially available, programmers are being forced in reorganizing their programming skills as well as developing new strategies to utilize the parallel properties. Unfortunately different parallel computer systems are not identical thus each computer system requires the use of a slightly different strategy. These subtle differences preclude porting a program from one computer system to another, an unacceptable condition since the lifetime of computer systems is approximately 5-10 years while the lifetime of software is 15-20 years. In this paper we outline a portable, parallel runtime system for a high level programming language Lucid. A Lucid program is devoid of instructions specifying sequencing, concurrency, and communication. The runtime system is designed to be generic as possible through the use of abstraction. The instantiation of the runtime system to a specific parallel architecture is done only once when the runtime system is installed by the system administrator. The runtime system manipulates the execution of code blocks which resemble light-weight tasks, independent threads of control sharing a common memory space. The code blocks were generated before execution by a Lucid compiler which have of used specific architectural properties during the generation of code blocks. The exact execution of a code block depends not only on the dynamic execution of the Lucid program, but also uses the load information from each processor.

ACKNOWLEDGMENTS

I wish to thank the Air Force Systems Command and the Air Force Office of Scientific Research for sponsorship of this research. Universal Energy Systems provided help in understanding and performing administrative duties.

Thanks must also be extended to Rome Air Development Center for their support in providing unlimited access to the necessary computer equipment to make this research feasible. Lt. Alan Williams provided much needed insight into the mysterious of the local computer operations. Lt. Doug Atkinson who provided accommodations and moral support for the duration of my tenure. Chris Flynn provided me with assistance and encouragement. The concern and encouragement of Lt. Gale Paeper and Ray Luizzi was greatly appreciated.

I. INTRODUCTION

The major focus within computer science is increasing the performance of computing elements. There are two approaches to this problem. In the first approach, computing elements are made faster through the use of newer, faster materials and improvements in the manufacturing processes which makes computing elements more complex while decreasing their area size. Further improvements in these areas are increasingly becoming more difficult since the technology is approaching the theoretical limits.

The second approach in increasing performance focuses on how the computing elements can operate concurrently with each other. Ideally, by utilizing n computing elements, the total execution time of any program can be decreased by n. This goal is not practical for a large number of problems since concurrently executing computing elements may need to communicate results with each other or to work closely together in synchrony. This communication reduces the total system performance. Previous and current research has focused on many different configurations and communication topologies of computing elements. With these new parallel systems, a new problem appears, namely how does a programmer effectively specify computations for the parallel computer system?

Currently, three approaches have been fo"~ved in solving this dilemma. In the first approach, a traditional, sequential programming language is used to encode the computation. The burden is placed on a parallelizing compiler to identify computations that can occur concurrently. This approach has several drawbacks. The sequential programming language is inherently sequential. The compiler can not detect and transform all the "parallel" sequential instructions into suitable parallel code. The programmer may need to add compiler directives that informs the compiler to relax several sequential assumptions built into the language.

The second approach is the development and use of a parallel language which expresses parallelism explicitly. This forces a more difficult burden on the programmer. With a single computation element, the programmer only needs to think about only one execution state. When the programmer uses n computation elements, then the programmer needs to remember n execution states. The execution state is critical when designing and implementing any interaction between the computing elements. Moreover, the execution speeds of the computation elements may vary ever so slightly between successive executions thus providing an opportunity for subtle errors to occur.

The third approach is the most ambitious of the three approaches but would yield the most benefit. The programmer uses either a functional or a logic specifications to describe what the computation is to do. The specifications are devoid of information specifying how the computation occurs. The specifications can be transformed through a series of well-defined transformations into an reasonable efficient parallel program (Boyle 1987). Programs are portable between various computer systems since they are divorced from the low-level architectural configuration of the computation elements.

In earlier work, I developed the operational semantics for a sequential Virtual Machine (VM) as well as a compiler that automatically translates Lucid programs into the sequential VM instructions. The compiler performed traditional optimizations such as constant propagation, folding, and data flow analysis on the intermediate Lucid representation. Lucid is a very high level, functional language which has no instructions specifying sequencing, concurrency, or communication. The VM instructions were defined to be suitable for a variety of computation elements. The MC68000 and the VAX instruction sets were used to ensure the robustness of the instructions.

In another project I participated in, a parallel architecture, similar in many respects to the Manchester dataflow machine, for Lucid was emulated. The architecture uses Lucid as machine instructions. Performance is achieved through fine grain parallelism. Recently, the emulator has been parallelized to execute on the Jet Propulsion Laboratory's Mark III hypercube.

II. OBJECTIVES

The research problem addressed in this research project was the design and implementation of a prototype parallel runtime system for Lucid for the Encore Multimax. The Encore Multimax is classified as a multiprocessor computer system which supports shared memory and semaphores.

The parallel runtime system should include in its design:

1) The ability to reschedule tasks from highly utilized processors to less utilized processors, a process called load-balancing.
2) The execution of tasks with varying degrees of parallelism from fine-grain parallelism to coarse-grain parallelism.
3) A methodology for verifying the runtime system behavior through the ability to take snapshots of the computation.

4) Portablity to a wide-range of parallel message passing and shared memory parallel computer systems.
5) Built-in instrumentation to measure performance and utilization.
6) Ability to permit small-scale reconfiguration, such as the number of processors, for any particular architecture.

In the remaining sections, the focus will be on explaining the design of the runtime system along and on the load-balancing policies.

III. RUN TIME SYSTEM

The approach that is used to parallelize Lucid programs, is similar to a partitioning scheme developed by Bic (1987). The Lucid program is first translated as a group of sequential VM instructions. Each VM instruction describes an operation on a hypothetical stack machine. One or more sequential VM instructions are partitioned into a code block. A code block defines a set of variables along with a set of instructions. Each of the variables are accessed one or more times within the instruction block. Each instruction in the code block has the property that it can be eagerly evaluated after all the variables have been initialized. When a code block is first invoked, all the variables are initialized by generating demands. Each demand may cause the creation of another code block. Executing a code block will eventually produce an result which is sent as a reply to the creator of the code block.

An instantiated instance of a code block is called a task. A task is composed of a data segment and a code segment as shown in Figure 1. The code segment is created only once when the program is loaded. The code segment is write protected since it can be shared between several tasks. A data segment is created for each task. Only one task can access the data segment. The data segment contains the following information:

PC	–	program counter, specifies the address of the currently executing instruction in the code segment
SP	–	a stack pointer, points to the top of stack with in the data segment.
Tag	–	specifies the execution environment of the instantiated task.
Var[0...N]	–	Variable values used within the code segment.
Stack[0...M]	–	Stores temporary values computed within the code segment.

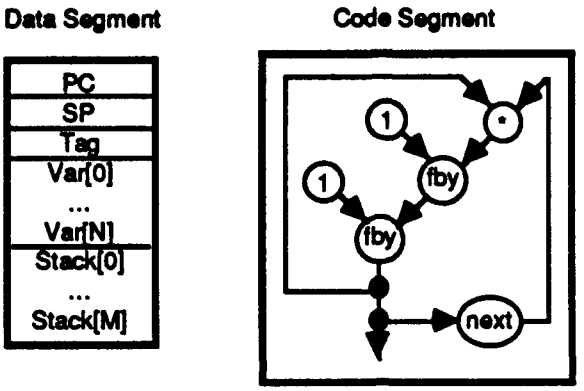

Figure 1. Task Representation

The abstract machine model for executing task is shown in Figure 2. The model is composed of three components:

TaskStore	–	Manages task creation, destruction, and execution.
VarStore	–	Saves the results computed by tasks.
Queue	–	Buffers communication between the TaskStore and VarStore.

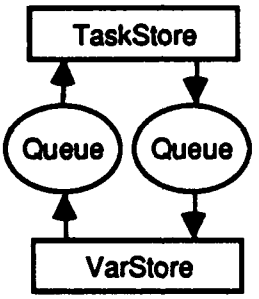

Figure 2. Abstract Machine Model

The TaskStore maintains three lists internally: a ready list, tasks that are ready to execute; a suspended list, tasks awaiting the arrival of values; and an eval list, the currently executing task on the processor. Figure 3 shows a state transition diagram of tasks between the three lists. A task is created on the ready list at the request of another processor. The currently executing task is moved from the eval list to the suspended list when the task requests variable values from other tasks. When all of the requested variable results are received by the suspended task, the task is moved from the suspended list to the ready list. The currently executing task is destroyed when the task completes execution by producing a result.

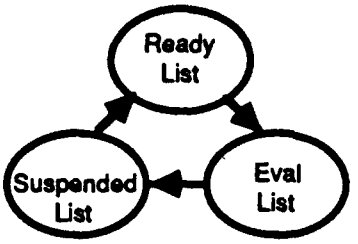

Figure 3. Task Life Cycle

The VarStore saves the results computed by tasks. Before a task is invoked, the VarStore is first consulted to check whether the task's value has been previously computed. If the value has been previously computed then value is returned, otherwise the VarStore records that the value is currently being computed so that later request do not repeat the computation. When the task terminates, the value is placed into the VarStore and all tasks requiring the value are sent the value.

The Queue buffers communication between the TaskStore and the VarStore. Buffering permits asynchronous operation between these two elements. The Queue internally maintains three separate queues for three different types of messages, i.e. results, demands, and system messages. This internal division permits fast checks to the status of the queue, i.e. is a particular queue empty or full. The queue status is used for dynamic rescheduling where only some messages can be processed migrate to another processor.

To parallelize the abstract machine model, the TaskStore, VarStore, and Queue modules are duplicated and connected as shown in Figure 4. The salient features of this configuration are the connections to the queues. A queue may have one or more producers but is restricted to one consumer. Informally, the queue is said to operate on behalf of the consumer. Each producer has the ability to decides which destination queue a demand message can be sent to. All other message types have a predetermined destination.

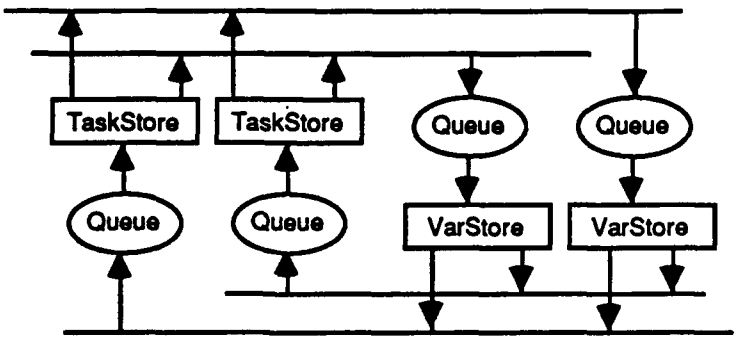

Figure 4. Parallel Configuration

The runtime system was implemented in C using the Encore Multimax and the UMAX operating system. The mapping of the runtime system onto the Encore Multimax is complicated. All memory used by the runtime system in shared. However only a portion of the memory, that devoted to the queues, can be accessed by more than one process. Queue memory is protected by making the queues into monitors. The rest of memory is partitioned among the TaskStores and VarStores, a TaskStore/VarStore has exclusive access to a memory block. Access to the TaskStore/VarStore memory is restricted by mutual consent of all modules, however a runaway TaskStore/VarStore could potentially corrupt the entire runtime system.

IV. DYNAMIC SCHEDULING

The mapping of a program onto the runtime system can occur in either of three ways:

Static	–	the execution of code blocks on TaskStore are determined before the program is executed.
Dynamic/Static	–	the scheduling of code blocks depend on which code blocks are created during execution.
Dynamic	–	Processor state information is used in determining the scheduling of demands.

Static scheduling is not considered as a viable choice since a single module failure within the runtime system is catastrophic. Another drawback of static scheduling is that for non-trivial programs, the optimal partitioning cannot be decided without knowing the precise execution behavior of the program.

Dynamic/Static scheduling affects the transmission of demand messages from VarStores to TaskStores. Selecting the message's destination is performed by applying a hash function to the demand message tag. Remember that the tag defines the contextual environment of the computation. No parameters of the hash function reflect the current load information of any processor. The distribution of tasks are dynamic since the generation of demand messages reflects the dynamic execution history of the program.

Dynamic scheduling is identical to dynamic/static scheduling. If the hash function is excellent, then the resulting distribution will be completely uniform. Given any hash function, a program can be created that will defeat the hash function, i.e. the hash function will not yield an uniform distribution. To smooth out the distribution, two new policies are employed, "Pass The Buck" policy and "Leach" policy. These policies can be understood

with the aid of Figure 5. In the Figure, a Writer represents a VarStore while a Reader represents a TaskStore.

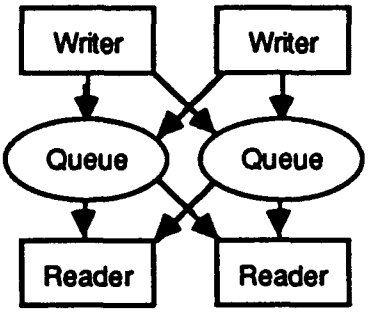

Figure 5. Readers and Writers Problem

With the "Pass the Buck" policy, writers are attempting to place a message into a reader's queue. Before the message is placed into the queue, the writer checks to make sure if the queue has a empty slot for the message. If there is not an empty slot, and the writer continues placing the message into the queue, then the writer must wait until the reader removes a message so that the necessary empty slot is created to place the message in. This situation is not desirable since the writer may have other work to perform and other readers may be idle. The situation is rectified by allowing the writer to check other readers to see if they have an empty slot on their queue. In examining the other reader's queue, the writer must assume that potentially all the other active writers are attempting the same action, thus there must be enough empty slots for every writer.

The "Leach" policy is carried out by the readers. When a reader becomes idle, because of the lack of messages on it's queue, the reader starts examining other readers queues to find demand messages. When the reader finds a demand message, it removes the demand and begins to process the demand. Before the reader can remove the demand, the reader must assume that all of the other readers are also searching for work. For the reader to remove the demand, there must be enough demands for all potential readers except when the queue belongs to the reader. In this case, the reader always has the right to remove any message.

In the preceding policies, a necessary condition for inserting/removing demand messages was the requirement that the writer/reader assumed that all other writers/readers also were performing the same task. This assumption arises from the separability of the testing of queue from the inserting/removing of the queue. These are separate actions to increase performance. The testing operation can be performed by one or more writers/readers while the inserting/removing operation can only be performed by only one writer/reader. If the

two operations were combined together then the operations may cause a loss of efficiency since the operation time for a Queue has become longer and only one reader/writer may call the function at any given time.

Another question may arise as to the efficiency of the above policies. The work performed does result in a loss of efficiency. In the "Pass the Buck" policy, the writer would have been blocked. By utilizing the "Pass the Buck", the writer at best can deliver the demand message to another queue and at worst no queue can found and the writer will remain blocked. In the "Leach" policy, the reader is idle. By leaching work from another queue, the reader is using what was idle time to perform useful work. If no work exists, then the leaching reader remains idle.

Both dynamic-static and dynamic scheduling scheduling policies were implemented in the runtime system. Slight speed and utilization improvement was obtained by the dynamic scheduling policies over the dynamic-static scheduling policies. More noticeable effects arose from the perspective of preventing deadlock of the runtime system. With dynamic-static scheduling, whenever one of the runtime systems resource, e.g. TaskStore or VarStore, became depleted, the execution of the program would not terminate since demands scheduled for the resource could not be rescheduled or fulfilled by the depleted resource. With the dynamic scheduling policies, whenever a resource became depleted, eventually one or more of the other resources would reach an idle state and would invoke the rescheduling policies which would execute steals demands scheduled for the depleted resource. Deadlock with the dynamic scheduling algorithms in effect could only arise if all of the resources became depleted, a more tolerable situation since there are always physical limitations to a computer system.

V. RECOMMENDATIONS

The runtime system which was initially designed for a functional language. The runtime system is also suitable for imperative languages such as C or Pascal. A code block would correspond to a function/procedure invocation. A major problem encountered in the implementation of the runtime system is lack of adequate operating system and language support for supporting parallelism. Most current research effort is focused on shared memory and message passing on computer systems. What has been neglected is the operating system support for calling functions such as input, output, and file operations in parallel.

Programming languages and their environments for developing parallel programs is not as advanced as for sequential programs. More operating system support for the Encore Multimax is required; system and library functions should be automatically protected from multiple entry from concurrent invocation by tasks. The software environment should permit debugging multiple executing threads of a program.

The runtime system as it is currently developed for the Encore Multimax only provides minimal support for executing Lucid programs. Further work needs to be done in two areas. The first area would focus on the runtime system while the second area would focus on the compilation of Lucid onto the runtime system. These two activities should be pursued concurrently since results obtained in one area provides the opportunity for new insight and strategies for the other area. The following lists outlines the objectives of each activity in order of importance.

Runtime System

1) Add eager evaluation mode to the runtime system.
2) Extend the runtime system to handle Lucid's higher order functions and nested space operations.
3) Develop a benchmark suite and a unit of measurement for comparing performance.
4) Port the runtime system to a variety of parallel architectures to obtain comparison performance data.
5) Add instrumentation for monitoring Lucid program execution.
6) Extend the runtime system to include a graphical interface to trace and debug executing Lucid programs.
7) Refine the runtime system to increase performance, i.e. compile the VM instructions straight into machine code instead of simulating the VM instructions.

Compiler System

Extend the Lucid compiler system to perform the following activities:

1) automatic task partitioning,
2) generate code for higher order functions,
3) strictness analysis of equations, and
4) type inferencing of functions and variables.

REFERENCES

Bic, L. Process-Oriented Model for Efficient Execution of Dataflow Programs. Proc. IEEE 7th International Conference on Distributed Computing Systems, Berlin, West Germany, September 1987, pp. 332-336.

Boyle, J.M., et. al. Deriving Sequential and Parallel Programs from Pure LISP Specifications by Program Transformation, Program Specification and Transformation, L.G.L.T. Merrtens (Editor), Elsevier Science Publishers, North Holland, 1987, pp. 1-19.

1988 USAF-UES Summer Research Faculty Program

Sponsored by the

Air Force Office of Scientific Research

Conducted by

Universal Energy Systems, Inc.

Final Report

Prepared by:	Paul T. Dingman, MSEE
Academic Rank:	Assistant Professor
Department and University:	Department of Electronics Engineering Oregon Institute of Technology
Research Location:	Griffiss AFB Rome NY 13441
USAF Research Colleague:	Lt Mark Wilbanks
Effort Focal Point:	Mr Albert A. Jamberdino
Date:	2 SEP 88
Contract Number:	F49620-85-C-0013

Pre-sort Processor Phase Distortion Evaluation

by

Paul T. Dingman

ABSTRACT

The Pre-Sort Processor demonstrates signal excision in the frequency plane by means of an optical technique. The process interfaces with analog systems using a Bragg Cell transmitter and a photo cell receiver. A spatially disbursed frequency band is broken into two hundred sub bands that are individually removable by bragg cell difractors. The theory behind the Pre-Sort Processor did not indicate that phase shift would be frequency dependent or increase around the edges of an excised notch.

This researcher has observed that excision does not introduce either of these types of phase distortion. However, during the process of examining the phase shift introduced by optical excision, the researcher became convinced that acousto-optic devices may introduce phase perturbations that could destroy the information content needed for many applications.

Acknowledgments

I thank the Air Force Office of Scientific Research, the Air Force Systems Command and Universal Energy Systems for their assistance with the administrative duties associated with this project.

The experience was made stimulating and rewarding through the efforts of the many informative and supportive individuals that I met during this SFRP. My effort focal point Albert Jamberdino provided me with the support necessary to create an enjoyable working environment. The dedication of research collaborators Lt. Mark Wilbanks and Capt. Edward Raudenbush was truly indispensable.

The Photonics directorate personal were also of great assistance to me in this project. I wish to thank Dr. Donald Hansen, Andy Pirich and James Rosetti for their gifts of time, space and equipment. I also thank Sgt. Finneman for providing three phase power and an endless series of optical and electrical components at times of critical need.

I. Introduction:

The Pre-Sort Processor, built for the Intelligence Recognizance Directorate of the Rome Air Development Center, is a device that provides an alternative to electronic filtering for the removal of unwanted RF signals. This alternative is referred to as optical excision.

It was assumed that optical excision would have advantages over electronic filtering for many applications. Optical excision should not introduce phase shift in non-filtered portions of the passband as is often the case for electronic filtering. Integrated optics may in the future make it possible to produce presort processors that will be smaller and/or lighter than competing electronic filtration devices.

In my research effort for the Intelligence Recognizance Directorate of Rome Air Development Center, I set out to prove that optical excision does not introduce phase distortion for frequencies close to the excised notches in the passband.

II. OBJECTIVES OF THE RESEARCH EFFORT:

Microwave signals that are of interest for intelligence reconnaissance are inherently broadband. In order to capture, transmit or record these signals their dynamic range must be effectively manipulated to conform to the medium of choice. Attenuating strong signals that are not of interest for intelligence gathering, can effectively increase dynamic range by allowing the level of the remaining pass band to be raised.

My assignment as a participant in the 1988 Summer Faculty Research Program (SFRP) was to pursue two goals. The first goal was two provide meaningful data relating to phase shift caused by optical excision. It was hoped that the process of optical excision would produce only small amounts of phase shift in non excised channels. The second goal was is to make information pertaining to any undesirable aspects of optical excision available to those who would further the study of optical excision.

After collecting the necessary phase measuring equipment and conducting initial phase shift measurements an additional problem became apparent. The phase shift produced by this acousto optic system will not be constant, because the delay produced by this type of system is long when compared to the periods of the signals being processed. For constant phase in processed signals, acoustic delay would need to remain constant to within fractional percentages of their predicted values. Since these delays exist as acoustic phenomenon in crystals, temperature change can be expected to affect phase shift.

III. At the beginning of this SFRP appointment, the Pre-Sort Processor was an experimental proof of concept provided by Harris Corp. that met the intended minimum performance specifications. Its passband stretched from 250 MHz to 450 MHz. Within this 200 MHz range were two hundred equally spaced switch selectable notches. The notch depth was 30 dB and the passband ripple was 6 dB. The rest of the original specifications and performance test results can be found in the pre-sort processor final report produced by Harris Corp and retained by RADC.

In order to examine the effects of excision upon phase response it was necessary to collect instrumentation for the expansion of the pre-sort processor set-up. An HP141T spectrum analyzer provided the graphic representation of frequency response. An HP8620C sweep frequency generator worked well for provided an input signal and had the necessary interface connectors for coordination with the other Hewlet Packard instruments. Phase measurement was performed with an HP8410B Hewlet Packard network analyzer an HP8411A interface kit and an HP8414A polar display.

The first effect noted in phase measurement was that any attempt to compare a swept frequency processed by the PSP to the original PSP would result in hundreds of phase reversals on the polar display. This effect was caused by the acoustic delay in the of 1.3 microseconds in he bragg cell. This delay corresponds to 325 periods of a 250 MHz wave or 586 periods of a 450 MHz wave. Therefore, sweeping the frequency over the pass band will result in 261 phase reversals. The cure for this problem was to insert an equivalent amount of delay in the path between the signal

generator and the reference input to the network analyzer.

The network analyzer was used to determine the unknown delay in the bragg cell by making use of a relation discovered during this SFRP. In the equation below delta T is the bragg cell delay, phi is the phase angle in radians, and delta F is the frequency difference that caused the phase reversal.

$$(\text{delta T}) = \frac{\text{PHI}*2*\text{PIE}}{(\text{delta F})}$$

Before a PSP output signal was compared to the original signal using the polar display of the network analyzer, the anticipated result was a dot representing the phase and amplitude relationships between the two signals. However, as can be seen in figure 1, the result was very different. It indicated that the processor would turn a single frequency constant amplitude sine wave into a signal of varying phase and as well as amplitude. It was encouraging to note that the excision of adjacent frequency bands did not appear to effect the phase in any way. However, the stochastic variation in phase reproduction raised serious questions about the utility of the PSP for intelligence applications. Although the exact nature of these applications is classified, it is commonly known that phase carries much of the intelligence information that would need to be analyzed.

After noting the phase perturbation, it became necessary to pursue its source. The most logical source for phase change seemed to be the signal bragg cell. Since the acoustic delay of

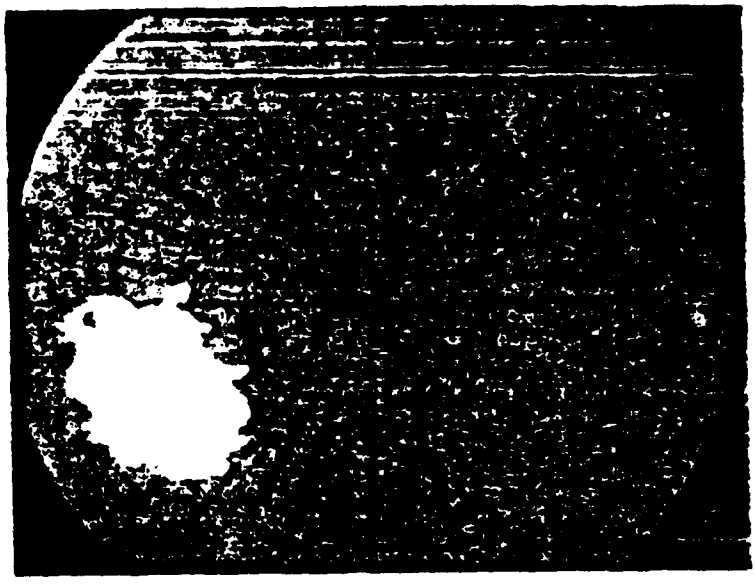

FIGURE 1: Phase Perturbations Present In PSP Output

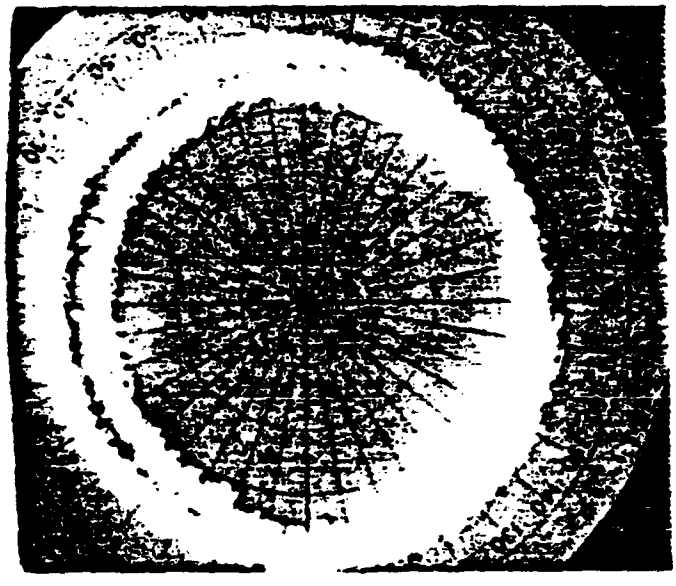

FIGURE 2: Phase Shift Caused By Cooling

the bragg cell was equivalent to several hundred periods of an incoming signal, small variations in this delay could be expected to produce large variations in phase. One might also expect stochastic variations in transmission time through materials whose velocity of propagation changed with temperature.

The question of velocity changing with temperature was answered by cooling the bragg cell at a rate of nine degrees centigrade per minute. The results of this cooling upon phase can be seen in figure two. The shutter of the camera was left open for sixty seconds producing 1.92 phase reversals for a 350 MHz signal. This corresponds to a rate of 1.34 radians per degree centigrade of phase shift relative to temperature change.

During the second half of the SFRP, the researcher's time was split between experiment expansion and experiment repair. It was determined that the experiment needed to be expanded upon to further support earlier observations. Unfortunately, the original collection of components that comprised the proof of concept began to need attention. This made the expansion of the experiment considerably more difficult by requiring that previous work be duplicated for consistency and assurance of proper function.

For the period following the anticipated repair of the PSP, two methods of data gathering were proposed. Both of these methods are based upon a supposition expressed by Harris Corp. They felt that phase could be expected to drift during periods of time long enough to be seen by a human operator. The original purpose of

this research was not to determine phase stability over time but to determine the effects of optical excision upon the phase of non excised signals. However, phase stability had been shown to interfere with excision. It was therefore necessary to develop methods for phase measuring and recording during short periods of time. Two such methods were developed. Neither could be implemented due to the inoperative state of the experimental equipment. This researcher hopes that these two methods will be used by RADC staff following equipment repair.

For the first method, the digital circuit of figure three was constructed and tested. The circuit allows an excision channel to be turned on and off at any desired frequency below 40 kHz. When this circuit is used, it will allow phase measurements to be made without concern for temperature induced short term drift. The procedure will be used to measure the phase of a non excised frequency channel while turning the excision of a neighboring channel on and off with a square wave signal source. This will allow the operator to differentiate between thermally introduced phase shift and the phase shift produced by excision. Measurements made in July 1988 did not allow this differentiation.

For the second method, a storage oscilloscope and a ramp generator will be used. The frequency source should be swept linearly over a five megahertz range. This will allow the system phase response to be observed over a five excision channel range. The center channel will be excised. The frequency will be swept through this range quickly so that effects of thermal phase drift

Added to Channel 274 On Interface Board

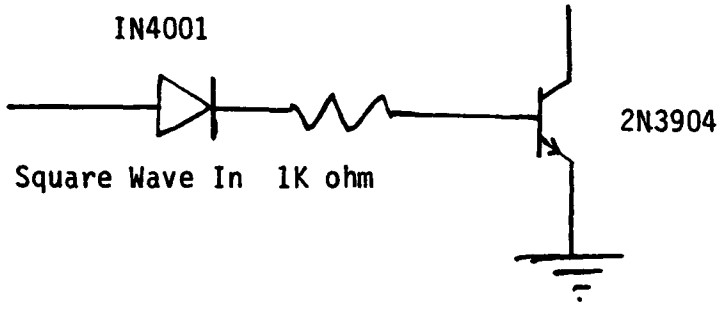

FIGURE 3: Circuit For Excision By External Square Wave

may be minimized. The resulting phase plot should appear as a square wave across the screen of an HP8412 rectangular phase display. Although the vertical position will drift, the magnitude of the square wave will indicate any phase shift produced by excision.

IV. Recommendations:

The Pre-Sort Processor has proven that optical excision can provide an alternative to filtering for broad band signals. The difficulties in maintaining phase fidelity may be curable in the future with advanced technology. This technical cure will be brought about by better signal bragg cell and/or housing designs. It is important to note that the proposed substitution of magneto-optic excisors, although costly, will have no effect upon the phase problem, because the phase problem occurs in the signal bragg cell. However, even if the phase fidelity problem is not solved, there are many application for which this short-coming will have less significance.

Research should be continued with the Pre-Sort Processor, either in its present form or with the proposed magneto-optic substitution. Since this summer's research was halted by equipment failure before completion we cannot say that the phase will remain sufficiently constant over millisecond or microsecond time scales. As a result of our observations, we are certain that optical excision does not effect the phase of adjacent signal bands. However, it would be of value to obtain more data by using the two methods proposed earlier in this paper.

Computer modeling of an alternative all electronic systems must be performed for the purpose of comparison. Since the PSP is an electronic filter that employs an optical technique, the Air Force should make certain that the added expense created by the optical approach can be justified. If an electronic filter can

be designed and analyzed by computer with specifications superior to those expected by any device using optical excision that exceeds the best limits of PSP technology, then it must be built and allowed to compete with future pre-sort processor designs.

REFERENCES

Harris Corp. Government Information Systems Division, Pre-SOrt Processor Final Report F30602-86-C-0081. RADC Internal. 1988.

Goutzoulis, A.P. Abramovitz, I.J., Digital Electronics Meets its Match. IEEE Spectrum, August 1988.

Mietzka, A. Study and Investigation of Input Electronics for Wideband Recorders, Tech. Report No. RADC-TR-67-529, December 1967.

Vanderlugi, A., Short Term Research Objectives. Photonics Center Seminar, July 1988.

Turpin, T. 'Spectrum Analysis Using Optical Processing' Proceedings of the IEEE, Vol 69, No.1, p.79, 1981. (See Appendix H)

Rhodes, W. 'Acousto-Optic Signal Processing: Convolution and Correlation' Proceedings of the IEEE, Vol 69, No.1, p.65, 1981. (See Appendix I)

1988 USAF-UES SUMMER FACULTY RESEARCH PROGRAM

GRADUATE STUDENT RESEARCH PROGRAM

Sponsored by the

AIR FORCE OFFICE OF SCIENTIFIC RESEARCH

Conducted by the

Universal Energy Systems, Inc.

FINAL REPORT

A PROLOG Natural Language Front End to an ERIC Object Oriented Data Base

Prepared by:	H.Kevin Donaghy, Ph.D.
Academic Rank:	Assistant Professor
Department and	Computer Science Department
University:	Rochester Institute of Technology
Research Location:	RADC/COES Griffiss AFB, NY 13441-5700
USAF Researcher:	Sharon Walter

Date:	25 Sep 88
Contract No:	F49620-87-R-0004

A PROLOG Natural Language Front End to an ERIC Object Oriented Data Base

by

H. Kevin Donaghy

ABSTRACT

CHARISMA, a natural language front end to a PROLOG relational data base, was modified to serve as a front end to an ERIC object oriented database. CHARISMA was translated from Quintus to Symbolics PROLOG. CHARISMA was then altered so that its outputs were logical forms corresponding to natural language query types. Since Symbolics PROLOG supports calls to LISP, and since ERIC code can be embedded in LISP functions, it was then possible to extend CHARISMA so that it directly queried the ERIC data base.

ACKNOWLEDGEMENTS

I gratefully acknowledge the Air Force Systems Command and the Air Force Office of Scientific Research for sponsorship of this project. And I wish to thank Universal Energy Systems for its courtesy, patience and assistance.

Special thanks are due Sharon Walter and Douglas White for their gracious hospitality and unflagging support during my stay at Griffiss. I am in debt to Michael McHale and John Crowter for their many helpful suggestions and ideas. Lieutenant Mark Mayberry and Captain Mark Fausett will be remembered for their invaluable technical assistance. Finally, Jean Carletta, my student assistant, contributed substantially and enthusiastically to whatever success this project may enjoy.

I. INTRODUCTION

As an in-house project, the staff at RADC (COES) designed a map display data base of a sizable portion of Europe. The data base was written in ERIC, a LISP based object oriented language also developed at RADC. As an ancillary project, Mr. Michael McHale (COES) rewrote a segment of the data base (approximately 10%) in Quintus PROLOG, and used Fernando Pereira's CHAT80, a public domain natural language tool, to develop a front end to the revised data base. The result, called CHARISMA, enabled a user to enter natural language queries at the keyboard, e.g. "Where is Apolda?", "What is the distance from Merseburg to Seesen?", "Where are the airports?", and to receive natural language responses.

II. OBJECTIVES OF THE RESEARCH EFFORT

During my ten week tenure at Rome, my objective was to refine CHARISMA so that it would query the original ERIC data base. Since the database as well as the ERIC compiler resides on Symbolics machines, CHARISMA was first translated into Symbolics PROLOG. CHARISMA was then modified so that its outputs were logical forms corresponding to natural language query types. Since Symbolics PROLOG supports calls to LISP and since ERIC code can be embedded in LISP functions, it was then possible to extend the program so that it directly queried the ERIC data base. In the revised CHARISMA, data retrieval is accomplished via a set of such functions which together serve as a LISP interface to the data base. A PROLOG procedure, eric_query/1, whose inputs are the logical forms generated by CHARISMA, calls the appropriate LISP functions. Answers to natural language queries input to CHARISMA are then retrieved and displayed in textual form on the user's monitor. At present, approximately fifteen query types have been implemented. The program has been designed in such a way that additional types can easily be added. A sample session follows. To keep output within manageable bounds, only a small segment of the data base is queried. Comments are parenthesized.

III. SAMPLE SESSION

```
| ?- hi.

Next question:

Where is merseburg.

32uqb0595                    (location of Merseburg)

Next question:

What is seesen.

town

Next question:

Show me seesen.

32unc8149                    (location of Seesen)

Next question:

Seesen.

32unc8149

Next question:

Please show me seesen.

32unc8149

Next question:

What is the population of apolda.

type 2                       (between 25 and 100 thousand people)

Next question:

What is apolda's population.

type 2

Next question:
```

How large is apolda.

type 2

Next question:

What roads go thru apolda.

87.

Next question:

How far is apolda from merseburg.

25 kilometers

Next question:

What is the distance from merseburg to apolda.

25 kilometers

Next question:

Is apolda mountainous.

no.

Next question:

What are the mountainous roads. (actual output is in column form)

4 6 27 81 82 185 241 242 243 244 248 498 a395

Next question:

What are the airports. (actual output is in column form)

allstedt aschersleben ballenstedt cochstedt erfurt_north hassleben

kothen nordhausen schlotheim

Next question: Airstrips. (what and where are the airstrips)

allstedt 32upb1481

aschersleben 32upb1679

ballenstedt	32upb4265
cochstedt	32upb4354
erfurt_north	32upb7196
hassleben	32upb2507
kothen	32upb2707
nordhausen	32upb5533
schlotheim	32upc5535

Next question:

Where is each airstrip. (same output as previous query)

Next question:

In which block is goslar.

32unc9050

Next question:

Which block is goslar in.

32unc9050

IV. HOW IT WORKS: AN EXAMPLE

Consider the following query.

(1) What is the population of Apolda?

Given (1) as input, the program (or more precisely CHAT80) generates the PROLOG logical form

(2) answer([_01]) :- _02^(((((true,true), true), population(_03,02), true,true), true), ((true,true), true), true, _01=_02, true,true))

The program then calls

(3) eric_query(X,Answer)

where the variable X has been instantiated to (2) and Answer is as yet uninstantiated. (3) matches the head of the eric_query clause (4), and in so doing instantiates Object to 'apolda'.

```
(4) eric_query((answer([X]) :- Type^(((((true,true), true), population(Object, Type),
      true,true), true), ((true,true), true), true, X=Type,true,true)), Answer) :-
        class_name(Object,Class),
        Answer is db_query(quote(Class), quote([type]),
          quote([[string_eq, name,Object]])).
```

'Class_name(Object,Class)' now invokes the LISP function

(5) (classes-of obj)

whose purpose is to retrieve the class name (town) of an ERIC object (apolda). This is accomplished via the embedded ERIC command

(6) (ask obj recall your common-name)

Finally, Answer is instantiated to 'type 2', the value retrieved by the LISP function 'db_query', in the last line of (4).

A comment on db_query is in order. Class objects in an ERIC data base are defined by a class object name and a set of attribute types. For example, 'town' is the name of a class object whose attribute types are name (the name of an actual town or city), type (a small integer indicating the population size of the town), and roads (a list of roadways intersecting the town). ERIC class objects are analogous to relations in a relational database, relations whose tuples describe class instances. 'Db_query' exploits this analogy and is modeled on the relational algebra command 'PROJECT <table name> OVER <attributes> WHERE <restrictions> GIVING <result table>.' In the example query, the class object 'town' is in effect being projected over attribute 'type' where attribute 'name' equals 'apolda'. As do all LISP functions in the program, 'db_query' retrieves information from the data base by invoking ERIC commands.

V. RECOMMENDATIONS

a. As mentioned, this revision of CHARISMA is capable of processing approximately fifteen natural language query types. However, since the CHAT80 parser upon which CHARISMA is based generates logical forms for a far greater number of query types, performance could be greatly enhanced without substantial modifications to the design of the program. To take full advantage of the parser, additional clauses should be added to eric_query/2. CHARISMA's limited vocabulary should also be extended.

b. At present, a user may query, but may not alter the ERIC data base. Since the purpose of the map display system is to serve as a "backdrop for simulations and a testbed for ... work in spatial reasoning", this seems an undesirable limitation. The natural language interface should be extended to allow users to define new class objects, create new instances of existing class objects, modify attribute values of objects, and so on. (To preserve the integrity of the data-base, users should not be allowed to effect permanent changes, of course.) The framework for this extension to the natural language front end is already in place, since the CHAT80 parser processes commands and statements as well as questions.

c. Finally, the procedure eric_query should be modified in such a way as to take full advantage of the capabilities of the color map display system by highlighting appropriate areas of the map in response to queries. This would be especially helpful for queries such as "Show me the air-ports", "Where is Apolda?", "What are the mountainous roads?", etc.

---

[1]Design and Implementation of the Map Display System Revised Edition, pg 1

REFERENCES

Booch, G., "Object Oriented Development," IEEE Trans. Software Engineering, Feb. 1986.

Hilton, M. L., Design and Implenentation of the Map Display System, Rome Air Development Center, May 1988.

Hilton, M. L., The New ERIC Manual, Rome Air Development Center, May 1988.

Maier, D., et al., "Development of an Object Oriented DBMS," Proc. ACM OOPSLA Conf., ACM, New York, N.Y., 1986.

McHale, M, L., M. Huntley, CHARISMA, Rome Air Development Center, 1988.

Pereira, F., S. Sheiber, PROLOG and Natural-Language Analysis, Center for the Study of Language and Information, 1987.

Stefik, M., D. G. Bobrow, "Object Oriented Programming: Themes and Variations," AI Magazine, Vol. 6, No. 4, pp.40-62.

DR. OLEG JAKUBOWICZ

FINAL REPORT NUMBER 57

NO REPORT SUBMITTED

1988 USAF-UES FACULTY RESEARCH PROGRAM/

GRADUATE STUDENT RESEARCH PROGRAM

Sponsored by the

AIR FORCE OFFICE OF SCIENTIFIC RESEARCH

Conducted by the

Universal Energy Systems, Inc.

FINAL REPORT

DESIGN OF AN OPTICAL CORRELATOR TESTBED AND OPTICAL CO-PROCESSOR

Prepared by:	Samuel P. Kozaitis
Academic Rank:	Assistant Professor
Department and	Department of Electrical and Computer Engineering
University:	Florida Institute of Technology
Research Location:	Rome Air Development Center/OP
	Griffiss AFB, NY, 13441
USAF Researcher:	Andrew R. Pirich
Date:	28 Aug 88
Contract No:	F49620-87-R-0004

DESIGN OF AN OPTICAL CORRELATOR TESTBED AND OPTICAL CO-PROCESSOR

by

Samuel P. Kozaitis

ABSTRACT

An analysis and evaluation of devices and techniques for analog optical pattern recognition is presented. A software package for producing a variety of filters, and a liquid crystal television operating as a spatial light modulator are analyzed. A highly flexible correlator testbed for the testing and evaluation of a variety of devices is given. The testbed consists of three parts. The first is an input system which is capable of enhancing an input image to the correlator. The next part is a computer-driven portion which is capable of producing a variety of filters. The third section is used for the evaluation of detectors.

A digital optical co-processor is designed based on an optical programmable logic array. the system performs edge detection on an image by storing reference patterns of an algorithm of interest.

Acknowledgements

I wish to thank the Air Force Systems Command and the Air Force Office of Scientific Research for sponsorship of this research. In addition, Universal Energy Systems did an excellent job in all administrative and directional aspects of this program.

I would like to thank Andrew R. Pirrich for taking an interest in this program and Dick Michalik for allowing me to work witin his group. The help of Lt. Michael Ward was invaluable in getting settled. The help of James Battliato in bringing to my attention the characteristics of the video input signal to the LCTV was extremely helpful. Joe Osman was also a great deal of help on this and the digital optical computing effort. I would like to thank Don Hanson as well as the entire Photoics center staff for their support and assistance.

1.0 Introduction

Real-time pattern recognition requires on the order of 10^{12} operations/sec which is well beyond the capability of modern electronic computers. The Photonics center at the Rome Air Development Center at Griffiss AFB is investigating the role of optics in constructing a real-time optical correlator for pattern recognition. A real-time optical correlator currently does not exist. Through a hybrid approach, the use of analog optics and digital electronics, the prospect for a real-time pattern recognition system appers excellent. The goal of this work is to design a highly flexible analog optical correlator which can be used to: test and evaluate current approaches for optical pattern recognition and, serve as a research testbed so advances in optical pattern recognition can be achieved. In addition, the prospect of of incorporating digital otpical components for high-speed digital computing is also being investigated.

My research intersests are in the area of analog and digital optical computing. My work in the area of analog optical pattern recognition allows advances to the present technology to be made. A research testbed is to be facricated which will allow a variety of devices and approaches to be evaluated. My work in digital optical computing demonstrates the present state of development of this technology.

2.0 Objectives

Currently, an optical real-time pattern recognition system does not exsist. Much work has been done in this area, there have been two major problems. One is that experiments by other researchers in the field have looked at a much simpler problem than that exisits in the real-world. The second problem is that a detailed analysis of the real-world problem has not been reported.

My assingment as a participant in the 1988 Summer Faculty Research Program (SFRP) was to design a testbed to test, evaluate and advance the technology in the area of analog optical pattern recognition. I also assisted in the development of a digital optical co-processor. It was determined that the pattern recognition system (correlator) would be a hybrid system, using both analog optics and digital electronics. An analysis and evaluation of the current state of technology was performed and available devices such as a liquid crystal spatial light modulator and a software package for analysis of correlations were characterized. The detailed plan of work for the tasks involved in using the testbed to develop a real-time pattern recognition is presented.

3.0 Design of correlator testbed

This present section describes the design of a testbed for evaluating devices and methods for use in optical pattern recognition. Once a list of specific components ordered are obtained, then the final more detailed design can be presented.

The testbed is a flexible correlator used to evaluate a correlation system under a variety of conditions, The testbed will be primarily composed of three modular sections which can be removed, replaced, or function independently of each other. The first section produces an input image for the system. Input devices such as SLMs will be tested and evaluated along with image enhancement functions. Image enhancement will be used in conjunction with different filters and imagery.

The second section of the system will control and display the types of filters to be used. Computer generated holograms will be primarily used to evaluate filters and methods for pattern recognition.

The third section may be used for detector evaluation. It also has the ability to to test algorithms for pattern recognition and target detection. The resulting system is a highly flexible correlator that may be used to test, evelauate, and develop correlator systems for optical pattern recognition.

3.1 Image input system

The task of the image input system is to display an input scene so that it may be processed by the testbed. A diagram of the three sections that make up the testbed is shown in Fig. 8. The image input system consists of the following devices: camera, frame grabber, still video recorder, and signal processing computer. The signal processing computer performs image enhacement operations on the image from the camera. This

is done to extract information from the input image to aid in pattern recognition.

The size of the target in the input scene is usually not scaled to the filter in the Fourier plane. To alleviate this scaling problem, a box is drawn around the target, and this box is displayed so that the box height or width exactly fits the SLM. This ensures that an image of the proper size is always displayed and corresponds to the filter being used. This box is drawn with a simple region growing algorithm. The aspect ratio of the box is calculated, the box height divided by the box width, and sent to the filter selection computer which selects filters.

3.2 Filter selection section

The filter selection section consists of a still video recorder and a computer which both act as a database. The aspect ratio from the input system is sent to the database computer. Here, filters correponding to a particular aspect ratio may be displayed. Each filter has an aspect ratio and can be considered to be in a class of targets. When the aspect ratio from the input system is received, a set of filters is displayed. The filters are displayed sequentially and the output plane is examined. A variety of filters may be implemented such as phase-only and amplitude-only filters. Furthermore, different transforms may be used as an approximation to the Fourier transform. These include, for example the Sine, Cos and Hartley transforms. These filters primarily depend on the optical implementation and not on the supporting electronics. The database can be generated from models of targets. Differemt views of the models may also be stored. The automation of the recording of filters for the database would reduce errors.

3.3 Detector section

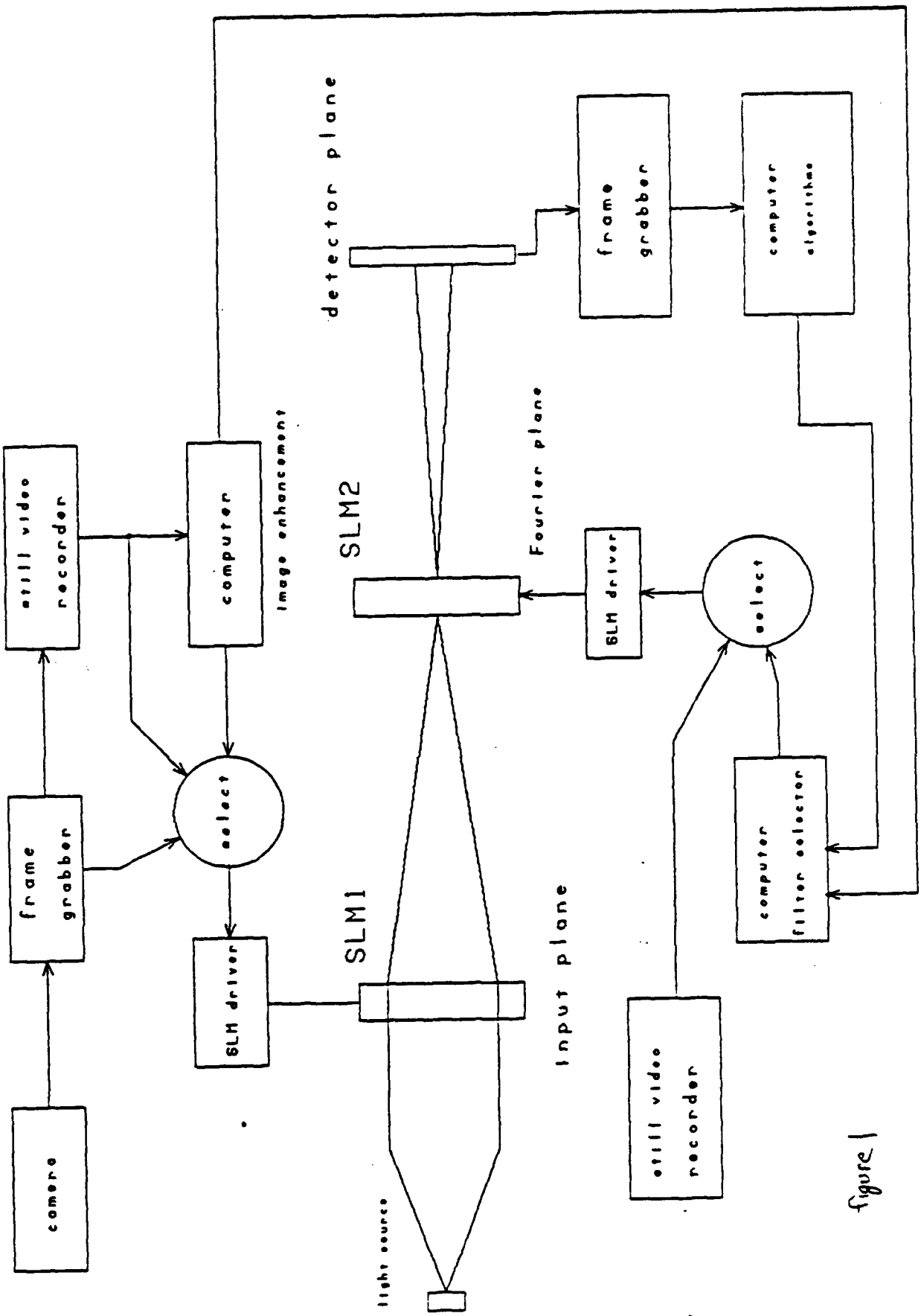
detector plane
frame grabber
computer algorithms
still video recorder
computer
image enhancement
SLM2
Fourier plane
SLM driver
select
frame grabber
select
SLM1
SLM driver
computer filter selector
camera
still video recorder
Input plane
light source

figure 1

The detector section consists of a detector array, frame grabber and computer. Different detectors may be tested and evaluated. Some of the detecors under consideration are high dynamic range and high resolution components. The parameters to be determined are given in the recommendation section. In addition, the response of different filters may be examined in detail. The system also has the ability to implement pattern recogfnition algorithms

4.0 Digital optical computing

The design of an optical co-processor is given in this section. Because a fast optical memory element does not exist, the role of optics in digital computing is limited. Optics is used here where it works best, where it has advantages over electronics. A programmable logic array (PLA) requires a large fan-in and fan-out. In electronics, large fan-in and fan-outs produce capacitive loading. This does not occur in optics. Within this section, an optical co-processor is described. This device can perform a limited amount of combinational functions. It is used to help speed up an electronic computer. A simple function, but one that illustrates the advantages of this approach is described in the next section. The following sections discuss the implementation of this function.

4.1 Co-processor function

The goal of this effort is to construct a optical co-processor which demonstrates the advantages of the optical PLA (OPLA) architecture. A PLA implements a function in a simple two-level AND-OR circuit. To fully take advantage of this type of realization, the function to be implemented is one commonly is performed in many steps. The function is the logarithmic Sobel operator which is primarily used in image processing for edge detection,

$$\begin{aligned} & | \log(A+2B+C) - \log(G+2H+I) | > \text{threshold} \\ \text{OR} \quad & | \log(A+2D+G) - \log(C+2F+I) | > \text{threshold} \end{aligned} \qquad (1)$$

The variables, A,B,C,D,E,F,G,H,I are the values of pixels in a 3 x 3 window of an image as shown in figure 9. The threshold is a number

usually close to the average of the maximum and minimum possible values of the function. The result of the function is either yes=1 or no=0. This value is the new value of variable E. The window is scanned over the entire image so that the result is a binary image which consists of only edges.

The significance of implementing the Sobel operator is that electronically, it is usually implemented in about ten steps. Here, optically, it is implemented in just one. The advantage offered by the optical implementation is that processing steps can be eliminated and combined into one step. To implement the Sobel operator, a camera and frame grabber must be connected to a computer. An image is then stored in the computer memory. The data corresponding to the 3x3 window can be sent to the co-processor and the result is returned to the computer. In this fashion, edge detection can be performed on an image with an optical co-processor speeding up the computation. A schematic of the system is shown in Fig. 10.

To implement the function described above, it must first be minimized. The system is to operate on binary images to reduce the complexity. The variables in the 3 x 3 window will therefore be binary and a truth table of the function can be easily generated. The logarithms were dropped from equation 11 since the results will be the same when working with binary values. An eight variable truth table was generated with a single output E, 32 reference patterns were found. After logical minimization, the truth table was reduced to 16 reference patterns.

4.2 Mask

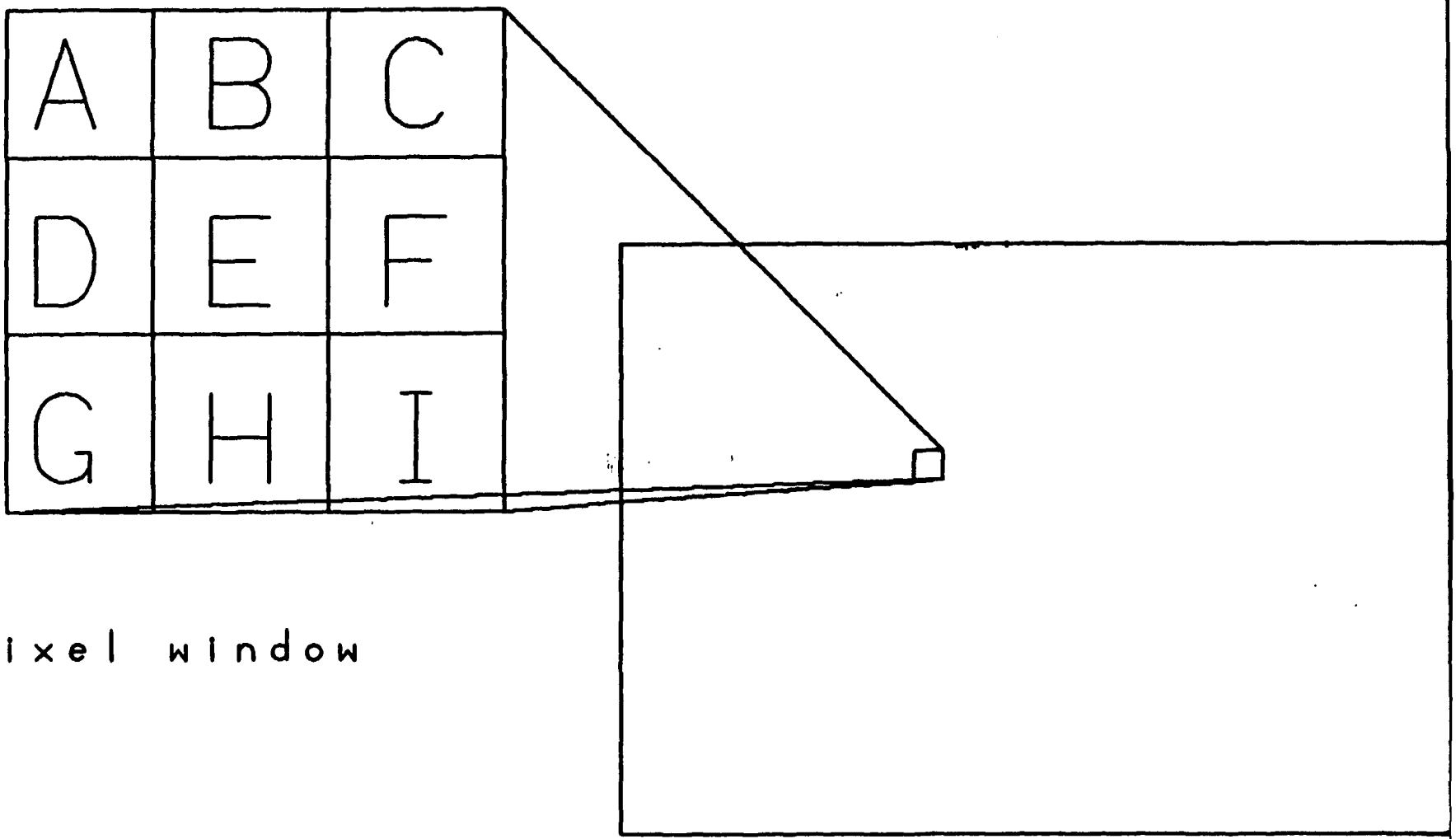

figure 7

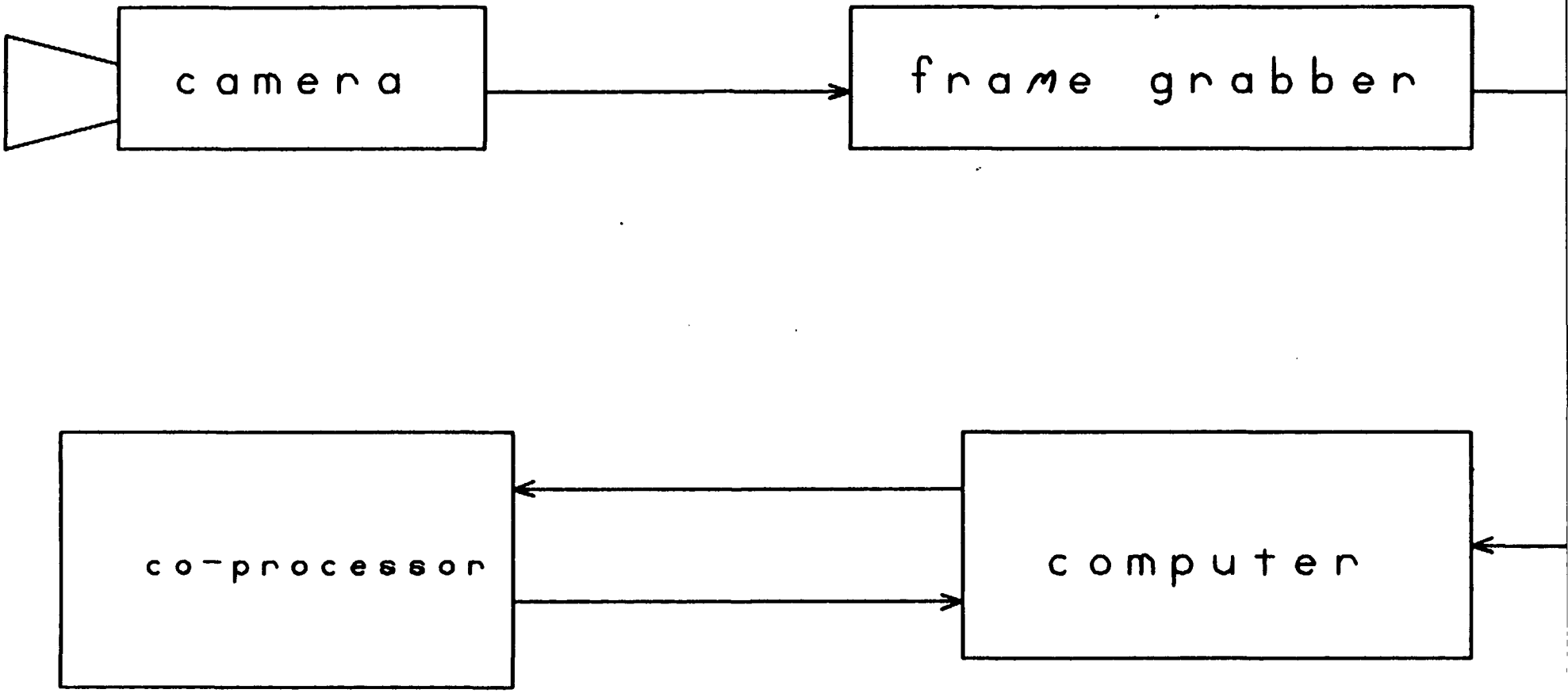

figure 3

To implement the minimized function, a 16 x 16 mask is needed. To relax the requirements of the system, the image will be scanned twice. The first scan will produce horizontal edges and the second scan will produce vertical edges. Eight patterns are needed for each type of edge. The form of the patterns are the same, this means that the same mask is used for both scans, for both the horizontal and vertical edges. The only difference is the way the variables are introduced to the mask. In the first pass, the variables are: A,B,C,G,H,I. Keeping the same mask for the next pass, the variables are entered as A,D,G,C,F,I. Using this approach, only eight patterns are needed. The mask needs only to be a 12 x 8 mask. In both cases the result is the variable E. The reference patterns for the threshold = 2.5 are shown below.

$\bar{A}B\bar{C}HI+\bar{A}B\bar{C}GH+\bar{A}\bar{B}GHI+BC\bar{G}\bar{H}\bar{I}+\bar{B}\bar{C}GHI+AB\bar{G}\bar{H}\bar{I}+ABC\bar{G}\bar{H}+ABC\bar{G}\bar{H}$ hor. edge

$\bar{A}D\bar{G}FI+\bar{A}D\bar{G}CF+\bar{A}\bar{D}CFI+DG\bar{C}\bar{F}\bar{I}+\bar{D}\bar{G}CFI+AB\bar{C}\bar{F}\bar{I}+ADG\bar{C}\bar{F}+ADG\bar{C}\bar{F}$ ver. edge (2)

4.3 Interconnections

The interconnections between the mask is the critical portion of this project. A schematic diagram of the system is shown in figure 12. The interconnections can be made with fiber tree couplers. These have been ordered but were not available during this summer. Alternatively, lenses can be used. The light from the input fibers in Fig. 12 can be imaged on to the mask. This approach would lend itself well to large masks where a large number of fibers would be impractical. The imaging is a simple problem for small a system, but a lens analysis or design package must be used for larger systems.

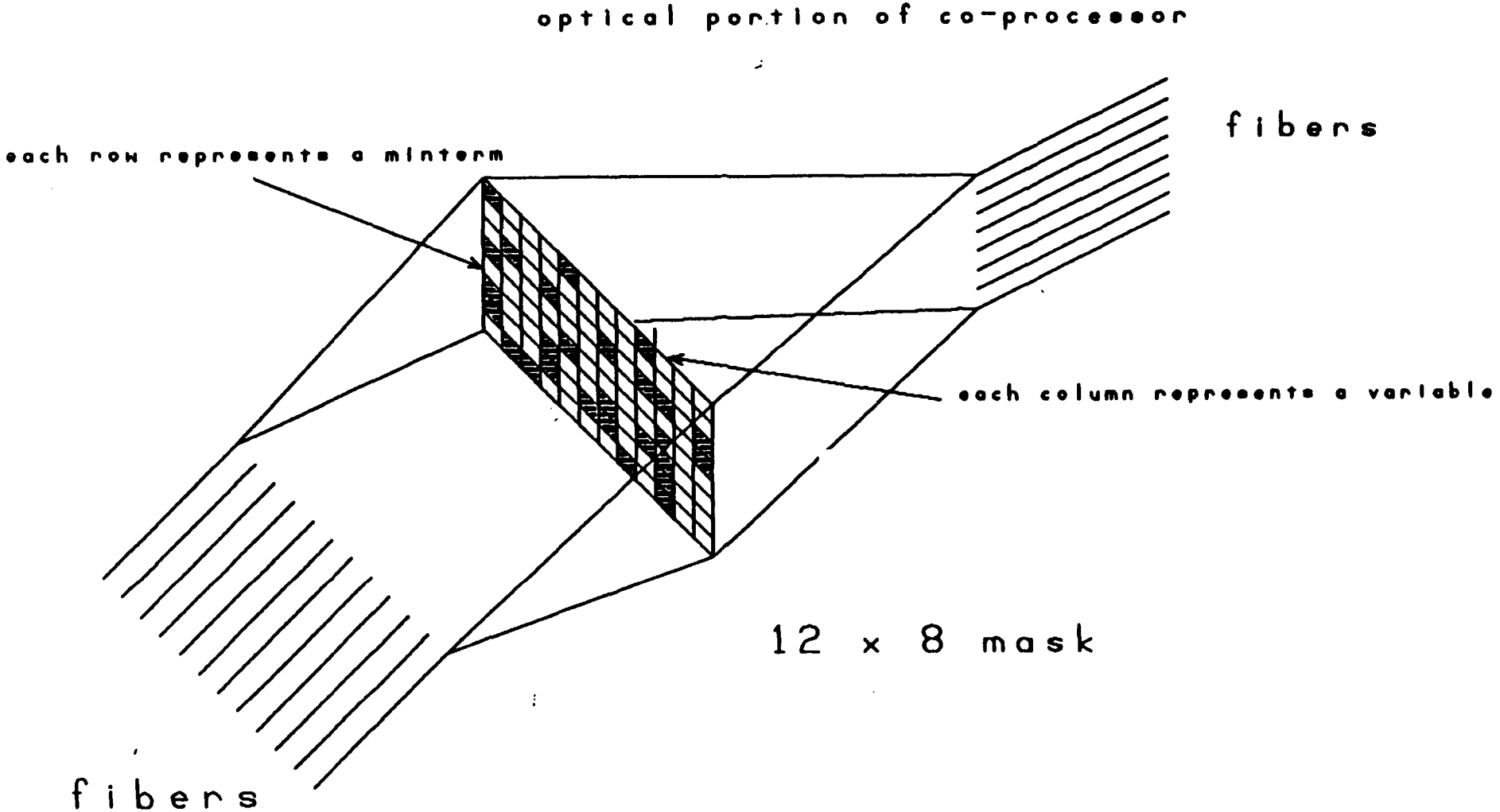
optical portion of co-processor
each row represents a minterm
fibers
each column represents a variable
12 x 8 mask
fibers

figure 4

6.0 Recommendations

An outline of the tasks for the test and evaluation of current devices and approaches is shown below. The outline describes a procedure which will have evaluate the major trends and generate more research in optical pattern recognition. The time schedule is also given which shows that these tasks can be completed in about a year. Follow-on support for the Summer Faculty Research Program should include one of the following sections. The digital optical computing effort should complete the optical co-processor.

Outline for analog signal processing

1.0 Design testbed, which consists of a correlator for the test, evaluation, and research of devices and methods for optical pattern recognition.
- 1.1 Evaluation of current technology and methods
- 1.2 Design a flexible, modular, testbed which can be rearranged to test different devices

2.0 Based upon the design and options provided during the Summer Faculty Research Program, construct a testbed consisting of the following:
- 2.1 imagery input system
- 2.2 spatial light modulator (SLM) drivers
- 2.3 supporting software for driving SLMs and displaying imagery to testbed
- 2.4 optical components
- 2.5 detectors

3.0 Perform non-real time correlation using a variety of SLMs and filters
- 3.1 characterize SLMs (LCTV, MOSLM, LCLV), determine the following:
  - 3.1.1 number and size of pixels
  - 3.1.2 uniformity and spacing of pixels
  - 3.1.3 resolution; spatial frequencies which can be resolved
  - 3.1.4 frame rate; time to display an image
  - 3.1.5 temporal response; time image remains on display
  - 3.1.6 gray level operation; determine if and how many gray levels be used
  - 3.1.7 scattering effects; determine how light is scattered from an individual pixel
  - 3.1.8 optical flatness; may induce phase errors
  - 3.1.9 absorption; measure wavelength dependence

3.1.10 measure amount of optical rotation due to SLM; can determine contrast ratio and modulation depth
3.1.12 modulation transfer function

3.2 Characterize and evaluate detectors (Dalsa high dynamic range, 2-D CCD, High resolution 2-D CCD, other high resolution, large dynamic range detectors as they become available, determine:
3.2.1 size and number of pixels
3.2.2 frame rate
3.2.3 dynamic range; range of light levels whixh can be detected
3.2.4 quantum efficiency; ratio of absorbed optical power to incident power
3.2.5 resolution
3.2.6 sensitivity; minimum optical power to produce a meaningful result
3.2.7 responsivity; output photocurrent per unit of incident optical power, response due to wavelength (spectral response)
3.2.8 dark response; photocurrent without optical signal applied
3.2.9 saturation exposure; maximum optical power which can be detected
3.2.10 signal to noise ratio

3.3 test and evaluate SLMs for use as:
3.3.1 amplitude filters; contains only amplitude information
3.3.2 matched filters; contains both amplitude and phase information
3.3.3 phase only filters; contains only phase information
3.3.4 determine the following characteristics for all filters
3.3.4.1 signal to noise ratio (SNR)
3.3.4.2 sensitivity to distortion; effects when the input image is scaled or rotated
3.3.4.3 broadness of correlation peak
3.3.4.4 performance in a noisy or cluttered environment

3.4 perform image enhancement
3.4.1 digitally, algorithm enhancement
3.4.2 optical, spatial frequency manipulation
3.4.3 identify differences between photographic, IR, and SAR imagery
3.4.4 identify parameters to help distinguish objects

3.5 test and evaluate other transforms as approximation to Fourier transform(identify modifications to testbed, perform theoretical and experimental evaluation
3.5.1 sin = Im {FT}
3.5.2 cos = Re {FT}
3.5.3 Hartley = sin-cos transforms
3.5.4 Walsh = square wave series expansion

4.0 Perform real-time correlation using above components
4.1 detail capabilties and limitations
4.2 performance with real-world imagery
4.3 performance with scaling and rotation

Tentative Schedule

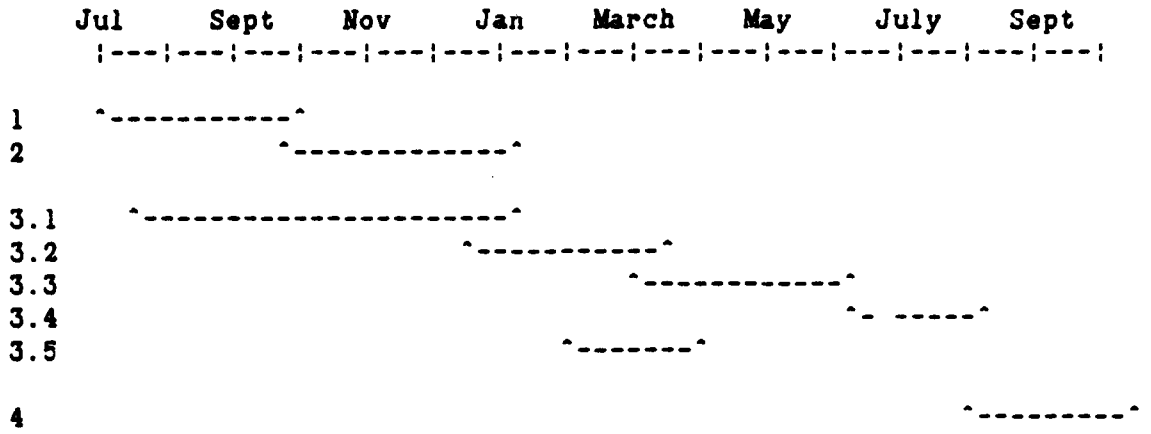

1988 USAF-UES SUMMER FACULTY RESEARCH PROGRAM/
GRADUATE STUDENT SUMMER SUPPORT PROGRAM

Sponsored by the
AIR FORCE OFFICE OF SCIENTIFIC RESEARCH
Conducted by the
Universal Energy Systems, Inc.
FINAL REPORT

CHARACTERISTICS OF DIALOG IN A NOISY CHANNEL FOR PERFORMING A TIME-ORIENTED TASK

Prepared by:	David J. Townsend
Academic Rank:	Professor
Department and University:	Department of Psychology Montclair State College
Research Location:	RADC/IRAA Griffiss AFB Rome, N.Y. 13441-5700
USAF Researcher:	Capt. David Stockton
Date:	September 7, 1988
Contract No.:	F49620-87-R-0004

CHARACTERISTICS OF DIALOG IN A NOISY CHANNEL FOR PERFORMING A TIME-ORIENTED TASK

by

David J. Townsend

ABSTRACT

This paper is a preliminary report of on-going research on the system that controls the presentation of primary and secondary information in human dialog. In this research we examine dialog between people who are using recording equipment for transcribing speech signals. Experienced transcribers spoke commands for operating the recording equipment, which a second subject heard and executed. By varying the level of noise in the channel of communication from the transcriber to the second subject, we observe how humans modify messages depending on how likely misperceptions are. By varying the time constraints for transcription, we observe the properties of speech when dialog participants are under pressure to communicate quickly. The results will be used to develop a system of speech synthesis that varies the timing and form of utterances depending on the costs, risks, and payoffs of communication.

Acknowledgments

I am grateful to the Air Force Systems Command and the Air Force Office of Scientific Research for sponsoring this fellowship. Universal Energy Systems deserves credit for its capable administration of the program.

I wish to acknowledge the help which Mr. John Ritz and Mr. Richard Vonusa personally provided to me to make my visit productive. I thank the entire staff of the Speech Processing Group at RADC/IRAA for providing a congenial and supportive atmosphere during my summer residence. Mr. Jim Cupples deserves special acknowledgment for his support of the Verbal Dialog Project. Captain David Stockton deserves credit for developing the overall structure of the Verbal Dialog Project and the experiment reported here, for recognizing the usefulness of information theory, and for connecting dozens of electronic devices. This paper constitutes a preliminary report of research that is in progress.

I. INTRODUCTION:

The possibility of controlling machines through vocal commands is a goal that has been both persistent and elusive. If voice control were effective, however, it could be used in many applications. For example, in one Air Force task transcribers convert speech signals into text on a computer keyboard. They use an Audio Signal Management System (ASMS) to record speech signals, play back sections of speech, "call" a specified section on the recorded signal, "loop" or successively play back a short segment of speech, etc. The ASMS now requires the transcriber to enter commands on keyboard. Since the transcriber's hands already are entering text onto a keyboard, we could increase efficiency by enabling the transcriber to give ASMS commands in a non-manual way. The goal of the Verbal Dialog Project at Rome Air Development Center is to develop and evaluate methods of controlling devices through speech (Stockton & Cupples, 1986).

Developing an efficient speech interface requires a method of dealing with automatic recognition errors. Recognition errors are inevitable for several reasons: the technology of automatic recognition devices is not adequately developed (see Waterworth, 1984 for a review), natural human speech recognition contains errors even in normal communication situations (see Clark, 1985 for a review), the speech signal is transitory, and the environments in which devices are used are often noisy. The Verbal Dialog Project seeks to repair automatic recognition errors by providing intelligent feedback to operators with an automatic speech synthesis device. But since operators may be extremely busy, we have the problem of determining when and how a synthesizer should

provide vocal feedback to the operator. My role in this project was to develop techniques to determine the properties of natural vocal commands and vocal feedback in the context of using ASMS.

My training has been in experimental psychology and linguistics. My previous research has examined the implications of theories in artificial intelligence, cognitive psychology, and linguistics for how people understand spoken and written discourse.

II. OBJECTIVES:

The objectives were to develop techniques to assess the efficiency of voice control in general, to examine the feasibility of improving transcription efficiency by using vocal commands to manipulate audio signals, and to gather information about the properties of human dialog when there are limitations on time and the communication channel.

III. APPROACH:

The relative efficiency of voice control will depend on what other tasks operators must perform in conjunction with the control task. From one point of view, voice control of the ASMS should be relatively expensive: giving vocal commands will cost a certain amount of processing resources that could otherwise be devoted to transcribing. Previous research has established that time-sharing two tasks generally is harder when the tasks involve a single modality, such as executing spoken commands and listening to speech, than when the tasks involve different modalities, such as executing manual commands and listening to speech (Wickens, 1984). This research leads to the quandary that

voice control is inappropriate when there is simultaneous speech perception, yet manual control is inappropriate when there is simultaneous manual transcription. Nevertheless, other evidence suggests that voice control will be useful for the transcription task. There are conditions in which highly skilled transcribers have time-shared two verbal tasks successfully (e.g., Shaffer, 1975). And there are two advantages that speech possesses over other forms of control: speech is natural, making it more resistant to failure in stressful situations, and it is flexible, allowing one to encode a wide range of messages in a variety of ways. The flexibility of speech means that the operator can easily reduce the costs of uttering a vocal command by expressing the command in a shorter utterance, but doing so carries an increased risk that the utterance will not be accurately recognized.

The complexity of time-sharing illustrates the need for techniques that compare the efficiency of different methods of control. One goal of this research is to develop such techniques. At the same time, we are examining ways in which humans balance the costs, risks, and payoffs of speaking in particular ways at particular times.

In our experimental research, one subject, the "operator," listened to connected speech and to sequences of random digits on two channels simultaneously. The task was to transcribe both signals. The operator had the option of manipulating recordings of these signals with the ASMS by speaking to a second subject, the "machine," who made the appropriate keyboard responses to carry out the operator's commands. The machine was allowed to talk freely with the operator. The machine simulates what ultimately will be an automatic speech recognition-synthesis system.

We are examining how time pressure and noisy listening conditions influence the dialog between the operator and the machine. We manipulated time pressure by varying allowed lag time -- how far behind real-time the operator was allowed to play back the recorded speech signals. In some conditions there was noise that the machine heard while listening to the operator, and in others the machine heard no noise. The purpose of adding noise in the machine's ears was to induce errors in perceiving the operator's commands, mimicking the general fact that speech recognition devices make errors.

If dialog participants consider only the cognitive costs of producing utterances, but not the risks of communication failure, we expect more efficient communications between the operator and the machine when time constraints are more severe. If an operator is allowed to lag behind real time by different amounts during playback, but produces equally accurate transcriptions of two equally difficult speech signals, communication time should be shorter when the allowed lag time is shorter: in order to maintain the same transcription rate as in the longer allowed lag time, the operator must spend less time in communication. For example, instead of (1a) the operator might speak (1b), relying on the machine to infer the secondary information that executing a loop on channel two requires that channel two is playing, and that playing channel two requires that channel one is not playing.

(1a) Stop playing channel one, play channel two, and loop 15 seconds.

(1b) Loop 15 on two.

For (1a) and (1b), the machine's keyboard responses and the ASMS's response time are both constant, but the interface between the operator and ASMS will be more efficient for (1b) because of the shorter communication time between operator and machine.

Time constraints may influence the form of the machine's utterances as well. For example, knowing that the allowed lag time is short, the machine might change a query such as (2a) into the shorter (2b), spoken with rising intonation.

(2a) Did you say that you want your loop on channel two to be 13 seconds long?

(2b) Thirteen?

With (2a) the machine sends secondary information acknowledging receipt of information about the desired playing channel, and primary information requesting confirmation of a belief about the desired loop length. With (2b) the machine sends only the primary information: he implies that he received the information about the playing channel, and requests confirmation of a supposed loop length. The machine requests confirmation with cues such as "did" in (2a), but with intonational cues in (2b). A shorter communication like (2b) should be more efficient than a longer one like (2a).

We measure communication efficiency using the concepts of information theory (e.g., Miller, 1951). The amount of information in an utterance depends on the number of messages that are possible at the time of the utterance: the greater the number of possible messages, the more informative is an utterance that allows the receiver to select one of those messages. For example, an utterance

that indicates simply that some information is coming shortly allows the receiver to select one of two possible messages -- information is coming or it is not -- and carries one bit of information, whereas an utterance that indicates one of ten possible messages carries 3.3 bits of information. Increasing the probability of any particular message, however, decreases the informativeness of utterances that convey that message.

Our definition of a message includes the speech act (e.g., Searle, 1969) that the operator performs along with the commands that his utterance implies. The informativeness of utterances like (1) is the sum of the informativeness values of utterances about two types of messages: (a) the speech acts that the operator could perform, such as commanding, requesting information, asserting information, etc., and (b) the state of the ASMS after each command that is presupposed by the utterance has been executed. Since the (b) versions of (1) and (2) allow the machine to select the same messages as the (a) versions in less time, the (b) versions are more efficient.

Speaking more efficiently, however, entails the risk that the intended message will not be received. The cost of repairing such a communication failure may be greater than the original cost of making a longer, more stable utterance. The risk of communication failure may lead dialog participants to lengthen utterances in order to avoid the costs of repairing communication failures. The risks of communication failures may be greater for a command such as loop, which begins repeating a segment of the recorded signal at the time it is executed, than for a command such as call, which jumps to a specified location on the recorded signal regardless of when it is executed. If the machine

requires a great deal of time to recognize a loop command, the loop when executed may not include the portion of the speech signal that the operator wishes to hear.

Hypotheses. Our experiment examines hypotheses like the following:

(H1) Operators issue fewer ASMS commands in noisy conditions -- especially commands such as loop whose effectiveness depends on when they are executed.

(H2) Transcription accuracy improves when operators use the ASMS.

(H3) The duration of operators' utterances increases in noisy conditions.

(H4) The duration of operators' utterances decreases when allowed lag time is short. Note that this hypothesis assumes no risk of a communication failure; if the risk of a communication failure is high, operators may lengthen utterances.

(H5) Operators effectively shorten utterances by relying on pitch to encode messages.

(H6) The pitch variation in operators' utterances increases when allowed lag time is short.

Method

We tested two pairs of subjects for three full days. The first day was devoted to acquainting the subjects with the equipment and the tasks, the second day to setting parameters of the primary transcription task, and the third day to formal testing. The two operator subjects were experienced Air Force transcribers, and the two machine subjects were staff members from RADC. Each operator worked with only one machine.

Pilot Testing. On the first day the subjects worked independently on their respective tasks for a total of three hours: the operators practiced transcribing narratives and digits on two channels, and the machines practiced entering the ASMS commands. For three more hours, the operators and machines practiced together.

The first day ended with a 10 minute session in which the operator transcribed signals on two channels by speaking ASMS commands to the machine with and without noise in the machine's ears. Operators were told that their main task was to transcribe continuous narratives verbatim, but that they should transcribe the digits and letters from a second channel as well. The operators adjusted the continuous speech, the digits, their own voice, the machine's voice, and the playback channel to either or both ears to the volume levels they preferred. The subjects were allowed a 50 second lag behind real time. In follow-up interviews the operators indicated that the task of transcribing continuous speech was much harder than their usual task, which involves transcribing sporadic speech that is highly constrained in content and wording. They indicated that only 10-50% of a typical primary signal contains speech.

On the second day each operator-machine pair participated in three 20 minute sessions to determine the appropriate rate of the speech signal in the primary channel. In the first session, the primary channel was 50% speech and 50% silence: we randomly presented bursts of speech lasting one to nine seconds followed by silence of one to nine seconds. In the second session, the primary channel was approximately 25% speech and 75% silence: we randomly presented bursts of speech containing one, two, or three sentences, followed randomly by 24, 48, or 72 seconds of silence. The operators

reported that both of these primary tasks were very difficult. In the third session, the primary channel was approximately 15% speech and 85% silence. We randomly presented clusters of two or three sentences, with either three or six seconds between sentences within a cluster, and with either 90 or 120 seconds between clusters. The operators reported that this format was similar in content and difficulty to their normal primary transcription task.

Procedure. The third day was devoted to careful testing with the task of transcribing a primary signal like that just described and a secondary signal that consisted of digits and letters. Each pair of subjects participated in four 20 minute sessions. The machine's listening channel was either clear or noisy, and the operator was allowed either 180 or 80 seconds lag behind real time. The combinations of these conditions were presented to both pairs of subjects in the following order: clear/180 seconds lag time, noisy/180 seconds lag time, noisy/80 seconds lag time, and clear/80 seconds lag time. Particular combinations of conditions were presented with exactly the same primary and secondary signals to both pairs of subjects. The four sessions contained different randomly arranged combinations of length of sentence clusters (two or three sentences), between-sentence silence (three or six seconds), and between-cluster silence (90 or 120 seconds). The primary materials were narrative and dialog selections from a recording of a Sherlock Holmes story titled "The Final Episode." Each session was followed by a 10-30 minute joint interview with the operator and the machine.

We recorded on different channels of tape what the operator heard, what the operator said, what the machine said, the noise in the machine's ears, the primary data and the

secondary data. The ASMS provided a printout of what commands were executed, the time at which they were executed, and what the operator transcribed from the primary and the secondary channels. We also recorded the post-session interviews.

Secondary Signal. The secondary signal consisted of letters and random digits. In each session we varied factorially the length of the sequences of digits (three or six triplets of digits), the rate at which the digits were spoken (180 or 230 wpm), the warning (present or absent), and the time between bursts (21, 42, or 64 seconds). A synthesizer spoke the digits with a single letter following each triplet in alphabetical order. The warning was a synthesized utterance of the word "digits" spoken with rising pitch and lasting 0.6 seconds. The 24 combinations of variables were arranged into a single pseudo-random order with the following constraints. Each block of 12 sequences contained six of each length, six of each rate, six of each warning condition, and four of each inter-burst interval. No more than three in a row for any particular condition was allowed. This pseudo-random order constituted the order of presentation of digits in the first session for each of the subjects. The remaining sessions were obtained iteratively by moving the first condition of each block in the preceding session to the end of the same block.

Equipment. The machine operated the ASMS on a PDP 11/70 through a VT102 terminal in a Tracoustics RE241001 acoustical enclosure. The operator transcribed on a WYSE terminal. The primary signal was played on a Sony cassette CSF100, and the secondary signal on DEC-talk and a Texas Instruments 320K computer. A Hewlett-Packard 8904A multi-function synthesizer, a General Radio 1390B random noise

generator, and a General Radio 1396B tone-burst generator produced noise for the machine's ears. Both subjects heard audio signals and spoke through Bilsom Viking 2318 combination headphone and microphone sets. The operator adjusted the volume of all audio signals on separate channels of a Shure SR110 mixer, and the machine adjusted the volume of the noise and the operator's voice together on one channel of a Sansui A-500 amplifier. The subjects' dialog was recorded on a Teac 40-4, the signals that the operator heard on a Sony TC755, and the post-session interviews on a Sony TC755. The ASMS screen and the subjects' dialog were recorded with a Panasonic video cassette recorder.

IV. RESULTS:

We collected approximately 160 minutes of ASMS audit trail and 440 minutes of recordings of interviews, dialog between operator and machine, primary signals, and secondary signals. Although we plan to place all the data on a detailed second by second time-line, our analysis will focus on those aspects of the data that are most relevant for testing hypotheses like those described earlier. This section describes the kinds of analyses that we can perform on the data in order to test hypotheses about verbal dialog.

To test the hypothesis that operators issue fewer commands under noisy conditions, we will count the number of times that each ASMS command was given in each of the four conditions. We will determine whether these frequencies are significantly greater for loop than for other commands by applying appropriate non-parametric statistical tests.

To test the hypothesis that transcription accuracy improves when operators use ASMS, we will determine the correlation between frequency of commands and transcription accuracy across the eight conditions. We will score transcription accuracy in terms of how many words, digits, and letters the operator copied from the primary and secondary channels.

The third and fourth hypotheses were that the duration of operators' utterances increases in noisy conditions, and decreases in short allowed lag time. These two hypotheses predict independent effects of noise and allowed lag time conditions, as well as an interaction: utterance duration and length should be greatest in the noisy, longer allowed lag time condition, and smallest in the quiet, shorter allowed lag time condition. To test these hypotheses, we will calculate the duration of operators' utterances with a Kay Elemetrics 6087 Visi-pitch, and count the number of words in each of the operators' utterances. We will perform 2 x 2 (noise conditions x allowed lag time) within subject analysis of variance on the duration and length scores. We will test differences between specific cells with appropriate post hoc statistical tests.

To test the hypothesis that pitch successfully encodes information in place of words, we will compare the speed and accuracy of the machine's keyboard response to operator's commands that differ in pitch variation. We will calculate machine response times from video-taped ASMS times that are displayed at the onset of the operator's utterance of a command and at the final keystroke that the machine makes to activate the command. We will also score the accuracy of the commands that the machine executes. We can test the statistical significance of any differences in machine response time and accuracy by first dividing in half the

distribution of operators' utterances along the dimensions of duration, length, and pitch range, and then performing a 2 x 2 x 2 (characteristics of utterances x noise x allowed lag time) analysis of variance on speed and accuracy scores.

To test the hypothesis that pitch variation increases in shorter allowed lag time, we will calculate pitch ranges from the Visi-pitch record for each utterance, and perform 2 x 2 analysis of variance on these scores.

We also plan to analyze the data in more qualitative ways by examining the pitch contours and syntax of utterances. We will focus especially on how these aspects of utterances depend on the pressures to shorten utterances because of time constraint and to lengthen utterances because of the risk of communication failure.

V. RECOMMENDATIONS:

We have progressed toward our objectives: we collected data on the properties of human dialog and began to develop some general analytic tools to evaluate costs and risks of making information explicit in utterances. Further work will focus on (a) analyzing the data, (b) developing measures of the informativeness of primary and secondary portions of speech, and (c) developing measures of the costs, risks, and payoffs of formulating utterances in particular ways and executing them at particular times. Additional experimentation should focus on (a) isolating time constraints from practice as factors that influence the presentation of primary and secondary information, (b) examining the timing of utterances to levels of accuracy that are greater than the current nearest second level, and (c) examining the properties of speech that repairs communication errors.

REFERENCES

Clark, H. H. (1985). Language use and language users. In G. Lindzey & E. Aronson (Eds.), Handbook of social psychology, Vol. II. (p. 179-231). New York: Random House.

Miller, G. A. (1951). Language and communication. New York: McGraw-Hill.

Searle, J. R. (1969). Speech acts. Cambridge: Cambridge University Press.

Shaffer, L. H. (1975). Multiple attention in continuous verbal tasks. In S. Dornic (Ed.), Attention and performance V. New York: Academic Press.

Stockton, D. B. & Cupples, E. J. (1986). Goal-directed man-machine dialog for audio information processing. Proceedings of Speech Tech '86. Pp. 250-254. New York, N.Y.

Waterworth, J. A. (1984). Interaction with machines by voice: A telecommunications perspective. Behavior and Information Technology, 3, 163-177.

Wickens, C. (1984). Engineering psychology and human performance. Columbus, Ohio: Merrill Publishing Company.

1988 USAF-UES SUMMER FACULTY RESEARCH PROGRAM

GRADUATE STUDENT RESEARCH PROGRAM

Sponsored by the

AIR FORCE OFFICE OF SCIENTIFIC RESEARCH

Conducted by the

Universal Energy Systems, Inc.

FINAL REPORT

The Effects of Nonlinearities of High Speed Analog-to-Digital Converters on Digital Beamforming Arrays

Prepared by:	Donald R. Ucci, Ph.D. / Robert G. Petroit
Academic Rank:	Associate Professor / Graduate Research Assistant
Department and University:	Electrical and Computer Engineering Department The Illinois Institute of Technology
Research Location:	RADC/EEA Hanscom AFB Bedford, MA 01731
USAF Researcher:	Dr. Hans Steyskal

Date:	12 AUG 88
Contract No:	F49620-87-R-004 / F49620-88-C-0053

Dr. Donald Ucci &
Mr. Robert Petroit

ABSTRACT

The Effects of Nonlinearities of High Speed Analog-to-Digital Converters on Digital Beamforming Arrays

Investigation of degradations to digital beamforming arrays caused by nonlinear characteristics of Analog-to-Digital Converters (ADCs) was performed. The study revealed that degradation to the array beam pattern is minimal when only the desired signal is present. However, severe pattern distortion occurred when the signalling environment contained both desired signal and jammer.

These results strongly suggest further investigation into the degradations caused by several jammers and means to counter their effects. Several approaches are proposed to perform these tasks.

ACKNOWLEDGMENTS

We express our thanks to the Air Force Systems Command and the Air Force Office of Scientific Research for their sponsorship of this research. In addition, we are grateful to the Universal Energy Systems for their efforts and help in our endeavors.

We also wish to thank the staff and researchers of the Rome Air Development Center, especially our close contacts at RADC/EEA at Hanscom Air Force Base. In particular, we thank Dr. Hans Steyskal and Dr. Robert Shore for the aid and continued guidance, comments and criticisms which made our work worthwhile. Thanks also goes to Mr. Daniel Jacavanco, The Branch Chief of the Antenna Division for providing working facilities and computer access. Capt. Michelle Champion and Lt. Joseph Fortney have our special thanks for providing us with information and help in operating the personal computers which allowed us to perform many of our tasks at RADC. Finally, our gratitude is extended to Mr. John Antonucci for use of his personal computer upon which this report was typed.

The time we spent at the laboratory was most worthwhile and rewarding because of both the challenging work and amicable atmosphere. These two aspects make RADC a desirable place to be.

I. INTRODUCTION:

A recent trend in adaptive antenna signal processing [Barton (1980), Curtis (1980), Mathews (1986), Wardrop (1984)], is to employ digital techniques for forming antenna beams. Additionally, there is a desire to perform the digital tasks at an Intermediate Frequency (IF) rather than at Base Band (BB) [Steyskal (1987)]. These digital beamformers use high-speed Analog-to-Digital Converters (ADCs). It has been observed by many researchers [Doernberg (1988), Kumamoto (1986), Peetz (1986)] when ADCs are operated near their upper limit in speed of conversion and dynamic range, that harmonics of the input signal frequencies and their cross products are produced.

The Antenna Systems Branch of the Antennas and Components Division of the Rome Air Development Center (RADC) at Hanscom Air Force Base is concerned with the effects of these harmonics upon an adaptive digital beamforming processor. Specifically, the modulating effects of the harmonics and intermodulation distortion degrade the beam pattern producing a loss in the array output signal. Our work at the laboratories has been focused upon an effort to quantify the degradation in digital beamformers and to possibly examine solutions to overcome these degradations in future research through the Mini-Grant Program (Research Initiation Program - RIP).

Our research interests have been in the area of adaptive array signal processing and digital systems. Dr. Ucci has worked in both the areas of performance degradation in adaptive arrays and digital signal processing. This work is closely akin to the

problem of performance loss because of the nonlinearities in the signal processing path for the problem described in this research report. Mr. Petroit has been working on adaptive array problems for one year. His familiarity with this type of system is an invaluable asset in performing necessary tasks associated with this research. In part, these relationships were responsible for our assignment with the Adaptive Antennas Group of the Antenna Systems Branch of RADC.

II. OBJECTIVES OF THE RESEARCH EFFORT:

High speed ADCs are necessary for performing digital beamforming at IF. Until now, no effort had been made to analyze the nonlinearities in the ADC as to their effects on beamformer output. It is well known that any nonlinearities in the signal processing channel will tend to degrade overall performance. Close scrutiny of the output power spectral density curves of actual high speed ADCs proposed for use in this type of channel revealed that several spectral components arose which had levels substantially above the quantization noise floor. These components caused concern as to the effect on the digital beamformer.

Our overall goal as Summer Research Program participants was to determine these effects. Specific objectives were to determine pattern variations caused by the presence of harmonics as compared to a quiescent pattern assuming an ideal ADC, and the associated increase in degradation because of intermodulation distortion when interference is present. Additionally, it was initially discussed that if the degradations were substantial our efforts would continue through the Mini-Grant program in order to

further evaluate these effects and investigate possible solutions. Results indicate that there are indeed severe degradations which warrant further investigation.

The overall goal stated above is completely congruous to our preliminary goals of a relevant literature search, ADC model development and incorporation of the model into the digital beamforming system. The results we have obtained meet the set of goals we established prior to and during our visit with RADC.

III. ACCOMPLISHMENTS:

An extensive literature search on digital and related adaptive array research, as well as on high speed ADCs, was conducted. This search revealed several sound techniques for analyzing beamformers employing digital methods for processing, and appropriate models for the ADCs.

Using data provided to us by RADC we developed two related models for the converters. Incorporating these models into an appropriate array structure we developed relationships for the array output signals and beam patterns for the digital beamformer. The system was then simulated by digital computer.

IV. PROBLEM FORMULATION:

Consider an array which forms its weights digitally at IF. Assume the ADCs have a K^{th} order nonlinear characteristic modeled by

$$y(t) = \sum_{k=0}^{K} a_k \, x^k(t), \qquad (1)$$

where the set $\{a_k\}$ is the set of coefficients of the power law relationship, $x(t)$ is an arbitrary input to the ADC and $y(t)$ is its corresponding output. For $x(t)$ a single tone sinusoid the

representation of the nonlinearity can be made as

$$y(t) = \sum_{k=0}^{K} A_k \, x(kt), \qquad (2)$$

where the set $\{A_k\}$ is a set of coefficients of a harmonic law model and are related to the set $\{a_k\}$, and $x(kt)$ is the k^{th} harmonic of $x(t)$ with maximum index K. Thus, if $x(t) = s_d(t) = \cos(\omega_d t + \phi_d)$ then $x(kt) = s_d(kt) = \cos[k(\omega_d t + \phi_d)]$ where the subscript d indicates the desired signal, and ω_d and ϕ_d are respectively the fundamental radian frequency and arbitrary initial phase of the desired signal, $s_d(t)$.

Using the FFT power spectral density plots shown in Fig. 1 we determine the amplitude coefficients, A_k for a given K. Expanding Eq. (1) and collecting like terms we evaluate the a_k. If we choose to employ a different order approximation we recompute the appropriate a_k. Figure 2 and Table 1 show the FFT spectral plots and values, respectively, for these models for K=17. Both show excellent agreement with each other and with the original plots of Fig. 1.

Consider a system with M array elements using element 1 as the reference as shown in Fig. 3 and assume half-wavelength spacing of the array elements at the desired signal frequency, f_d. Then, with $w_m = b_m \exp[j(m-1)\pi \cdot \sin\theta]$ as the quiescent weights (where b_m denotes the amplitude weighting), and with $y_m(t)$ the output of the m^{th} ADC, the output of the m^{th} weight is given as $z_m(t) = w_m \, y_m(t)$. Assume the desired signal arrives at an angle θ_d. The time delay encountered by the desired signal at each element is Δ_{dm} such that the spatial phase

delay at the m^{th} element at frequency ω_d is ϕ_{dm}, and is given by

$$\phi_{dm} = \omega_d \Delta_{dm} = (m-1)\pi \cdot \sin\theta_d. \tag{3}$$

The output of the m^{th} weight can be shown to be

$$z_m(t) = \sum_{k=0}^{K} A_k\, b_m \exp\{jk[\omega_d(t-\Delta_{dm})+\phi_d+(m-1)\pi\cdot\sin\theta]\}. \tag{4}$$

and the array output is given by

$$z(t) = \sum_{m=1}^{M} z_m(t). \tag{5}$$

We use the beam pattern power gains formed for the ideal and nonideal cases as a performance measure; that is respectively,

$$P_1 = 20\log_{10}|z(\theta;t_\ell)|, \tag{6}$$

$$P_2 = 20\log_{10}|z_g(\theta;t_\ell)|. \tag{7}$$

V. DISCUSSION:

A. Desired Signal Only Case

Consider a simple situation. For the case M=K=2 and $b_m=1$, $\forall_m$ with $\phi_d=0$ it can be shown that the beam pattern, $|z|^2$, is given by

$$\begin{aligned}|z|^2 = {} & 4A_0^2 + A_1^2|1+\exp(-j\Delta_\psi)|^2 + A_2^2|1+\exp(-j2\Delta_\psi)|^2 \\ & + A_0A_1\{\exp(j\omega_d t)[1+\exp(-j\Delta_\psi)]+\exp(-j\omega_d t)[1+\exp(j\Delta_\psi)]\} \\ & + A_0A_2\{\exp(j2\omega_d t)[1+\exp(-j2\Delta_\psi)]+\exp(-2j\omega_d t)[1+\exp(j2\Delta_\psi)]\} \\ & + A_1A_2\{\exp(j\omega_d t)[1+\exp(j\Delta_\psi)][1+\exp(-j2\Delta_\psi)] \\ & \qquad +\exp(-j\omega_d t)[1+\exp(-j\Delta_\psi)][1+\exp(j2\Delta_\psi)]\}.\end{aligned} \tag{8}$$

where $\Delta_\psi=\psi-\psi_d$, with $\psi_d = \pi\sin\theta_d$ and $\psi = \pi\sin\theta$. Thus, the harmonics will cause the beam pattern to modulate at multiple frequencies of the fundamental. The only desired term is the second term. The first and third terms represent the spatial distortion while the other terms are the temporal variations.

B. Interference Case

Investigation of a more general case of signalling environment in which interference (or jammers) are present is now described. We define the Jammer-to-Signal ratio, (J/S), to be the ratio of the jammer to signal power. The input to the array is $x(t) = s_D(t) + s_I(t)$ where $s_D(t)$is the desired signal and $s_I(t)$ is the interference. Specifically, we have that the desired signal is $s_D(t) = \alpha\, s_d(t) = \alpha \cos(\omega_d t+\phi_d)$ where α is the amplitude of the desired signal and ϕ_d is its phase. Similarly, $s_I(t) = B^T \cdot s_i(t) = \sum_{j=1}^{J} \beta_j \cos(\omega_j t+\phi_j)$. Here we have that β_j is the amplitude of the j^{th} interferer with frequency ω_j and phase ϕ_j, $j=1,2,\ldots,J$. B is a Jx1 vector of interference amplitudes and $s_i(t)$ is a Jx1 vector of elementary interference signals, $s_j(t)$, and T denotes transpose. Let $\omega_j = \delta_j \omega_d$, $j=1,2,\ldots,J$, so that δ_j is a measure of the j^{th} interference bandwidth with respect to the desired signal frequency. Then $s_I(t) = \sum_{j=1}^{J} \beta_j \cos(\delta_j \omega_d t+\phi_j)$.

Consider now the input at the m^{th} element of the array, $x_m(t)$,

$$x_m(t) = \alpha\, s_d[t-(m-1)\Delta_d+\phi_d/\omega_d]+\sum_{j=1}^{J}\beta_j s_j[t-(m-1)\Delta_j+\phi_j/\omega_j], \qquad (9)$$

where $\Delta_d=(\lambda_d/2)\sin\theta_d/\nu$ and $\Delta_j=(\delta_j\lambda_d/2)\sin\theta_j/\nu$ and ν is the velocity of propagation. The output of the m^{th} ADC is then

$$y_m(t) = \sum_{k=0}^{K} a_k\, [x_m(t)]^k. \qquad (10)$$

Thus, at each ADC, output self and cross harmonics of signal and interference will be present. When weighted by w_m and summed

over the M elements these distortion terms will corrupt the final output. Again, the harshness of the effects depends upon the severity of the nonlinearity. The above equations are now ready to be simulated on computer. However, before we proceed to the results let us examine a simple case of a signal plus single interference source.

Let $\psi_{mp} = \omega_p t - (m-1)\psi_p + \Omega_p$ where p represents desired signal, d, or interference, i, $\psi_p = \pi \sin\theta_p$ and Ω_p is an arbitrary initial angle. Assume that only harmonics up to the third order are present. Then the harmonic representation at the output of the ADC can be shown to be given by

$$\begin{aligned} y_m(t) = {} & [a_0 + a_2(\alpha+\beta)/2] + [a_1\alpha + a_3\{3\alpha^3/4 + 3\alpha\beta^2/2\}] \cos\psi_{md} \\ & + [a_1\beta + a_3\{3\beta^3/4 + 3\alpha^2\beta/2\} \cos\psi_{mi} \\ & + a_2\alpha^2 \cos 2\psi_{md} + a_2\beta^2 \cos 2\psi_{mi} \\ & + a_2\alpha\beta [\cos(\psi_{md} + \psi_{mi}) + \cos(\psi_{md} - \psi_{mi})]. \\ & + (a_3/4)\alpha^3 \cos 3\psi_{md} + (a_3/4)\beta^3 \cos 3\psi_{mi} \\ & + (3a_3)/4\alpha\beta^2 [\cos(\psi_{md} + 2\psi_{mi}) + \cos(\psi_{md} - 2\psi_{mi})] \\ & + (3a_3)/4\alpha^2\beta [\cos(2\psi_{md} + \psi_{mi}) + \cos(2\psi_{md} - \psi_{mi})]. \end{aligned} \quad (11)$$

From the above expression it is apparent that there will be new harmonic terms created and that their associated coefficients will be different from those of the signal only present case. Additionally, the more (noncoherent) jammers in the array Field of View (FOV) the more spectral components will be present in the ADC output.

VI. RESULTS:

We now describe the results of our computer simulations. For the simulations we used a 12-bit ADC and concentrated on

20 dB sidelobe Dolph-Chebyshev weighting for the quiescent pattern although a provision has been made for uniform weighting. We plotted the beam patterns for various scenarios. All figures show the quiescent pattern for the signal only for comparison. These are plots of z_g and are shown in dashed lines. Each plot originally consisted of eight separate figures with various instants of time as a parameter and with the look angle θ as the variable as shown in Eqs. (6) and (7). Examination of the plots revealed that when interference was present a variation with time was discernible. However, these variations reveal the same general trend in performance degradation for any given instant of time. Thus, we confine the discussion to the case of t_ℓ=0. In the interference case note that we use a single jammer and assume a maximum of a fourth order nonlinearity. This seemed reasonable until further investigation can be performed since, as shown in Fig. 1, the harmonics up to the fourth order are the largest.

Figure 4 illustrates the array performance for the desired signal only for all 17 harmonics present in the ADC model. The parameters are M=MM= 10 elements, td=θ_d=0° and phid=ϕ_d=0°; n represents the time parameter, t_ℓ. As can been seen from the curve there is little or no degradation in the beam pattern for signal only present. Thus, in the unrealistic case of single excitation and with no thermal noise present we conclude that the array performance does not severely degrade.

In the more realistic case of signal plus jammer present there is appreciable variation in the beam pattern because of the harmonics for most sets of parameters. The interference results are shown in Fig. 5 to Fig. 12. In all these figures we

assume that θ_d=0°, ti=θ_i= 15° and δ=D=1.5. In Figs. 5 to 8 we use a 10 element array. We examine the beam pattern for the ideal (K=1) and non-ideal (K=4) ADC while holding the J/S Ratio (JSR) fixed for each consecutive pair of figures. We repeat this process for a 21 element array in Figs. 9 to 12. Figures 5 and 6 illustrate the array response for J/S = 10 dB. Figures 7 and 8 do the same for J/S = 20 dB. Comparing the figures it is apparent that severe degradation in the array output pattern is experienced and, as is expected, worsens as the J/S ratio increases.

Figures 9 and 10 repeat the process for a 21 element array with a J/S of 10 dB while Figs. 11 and 12 show similar results for a 20 dB J/S ratio. The harmonics do not appreciably degrade the performance in the 10 dB J/S case but produce substantial degradation for a 20 dB J/S ratio as shown in Fig. 12. In fact, Fig. 12 shows 4 significant lobes at values of $\theta \approx -60°$, 0° (signal direction), 25° (proportional to the interference direction), and 55°.

VII. RECOMMENDATIONS:

This study revealed that the nonlinearities in a high-speed ADC can cause substantial degradation in a digital beamforming array depending upon the severity of the nonlinearity when interference is present. Necessary research to be performed in the future, as a continuation of this work under the auspices of a Mini-Grant, is as follows.

A high priority topic is investigation of an adaptive system's performance in the presence of the ADC nonlinearity. Although time did not permit us to evaluate this case the

adaptive array problem formulation as well as its translation into computer code, has been done for the Sampled Matrix Inversion (SMI) algorithm. It is only necessary for this code to be properly incorporated into the existing computer program and then have the simulation performed. Additionally, other algorithms such as the LMS, RLS, and Minmax algorithms need to be evaluated.

The determination of the highest order nonlinearity which effects a substantial degradation in array performance must be determined. This can be done by an incremental method which examines the next highest order nonlinearity and compares the performance degradation with the previous one. When no appreciable variation is found the order is determined.

In conjunction with the above, the effect of multiple jammers as opposed to a single jammer needs to be studied. This is a straight forward extension of the analysis and simulation reported here. Expansion of the power law model for a composite signal needs to be performed to develop a harmonic model consisting of self and intermodulation products of the signal and multiple jamming frequencies. Additionally, thermal noise should be added to the environment and a spectral analysis performed for this case. The signal x noise and noise x noise terms can become significant in contributing to array degradation when a high enough order nonlinearity is assumed.

Finally, a more difficult task needs to be examined. The research performed and reported above was based on a particular ADC functioning at a prescribed sampling frequency and a specific input signal frequency. This resulted in a unique model

for the ADC under consideration. In general, it is highly probable that for another physical device (even the same model from the same manufacturer) and different signal parameters, an entirely different model will be needed. That is to say that the power law model will be used but its coefficients, $\{A_k\}$, and thus $\{a_k\}$, will be different. A stochastic model should be used in this case since each ADC's characteristic depends upon its internal structure which is in turn dependent on its elements such as comparators. These comparators are, in part, responsible for the nonlinear effects because of their switching characteristics. These characteristics are random in nature as they are created at production time. Thus, a probabilistic description is necessary to characterize them. A possible probability density function for their time to switch is a uniform density since prior to manufacture the comparators are all equally likely to switch at some particular voltage over a specified range. In order to determine this both theoretical and experimental development is necessary. Once the random behavior is determined a statistical analysis for average array degradation can be performed.

REFERENCES

Barton, P., "Digital Beamforming for Radar," IEE Proc., vol. 127, Pt. F., No. 4, August 1980, pp. 266-277.

Curtis, T.E., and Ward, R.J., "Digital Beamforming for Sonar Systems," IEE Proc., vol. 127, Pt. F., No. 4, August 1980, pp. 257-265.

Doernberg, J., Lee, H.S. and Hodges, D.A., "Full speed testing of A/D Converters," IEEE J. on Solid State Circuits, vol. SC-19, No. 6, December 1984, pp. 820-827.

Kumamoto, T., Nakaya, M., Honda, H., Asai, S., Akasaka, Y., and Yasutaka, H., "An 8-Bit High-Speed CMOS A/D Converter," IEEE J. on Solid State Circuits, vol. SC-21, No. 6, December 1986, pp. 976-981.

Mathews, B.D., "Nonlinearities in Digital Manifold Arrays," IEEE Trans. on Antennas and Propagation, vol. AP-34, No. 11, November 1986, pp. 1346-1355.

Peetz, B., Hamilton, B.D., and Kang, J., "An 8-Bit 250 Megasample per Second Analog-to-Digital Converter without a Sample and Hold," IEEE J. on Solid State Circuits, vol. SC-21, No. 6, December 1986, pp. 997-1002.

Steyskal, H., "Digital Beamforming Antennas, An Introduction," Microwave Journal, January 1987, pp. 107-124.

Wardrop, B., "Digital Beamforming in Radar Systems: A Review," Military Microwave Conference Proc., U.K., 1984, pp. 319-323.

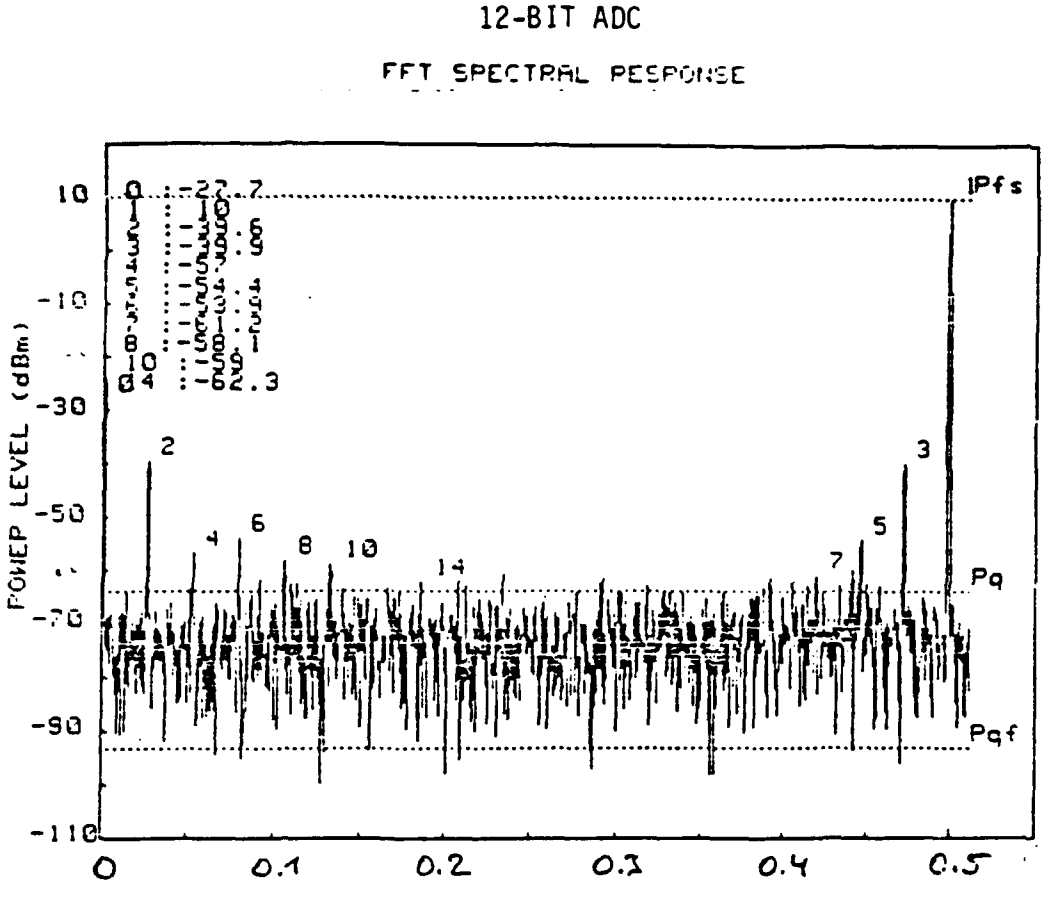

Fig. 1 12-BIT ADC FFT spectral response

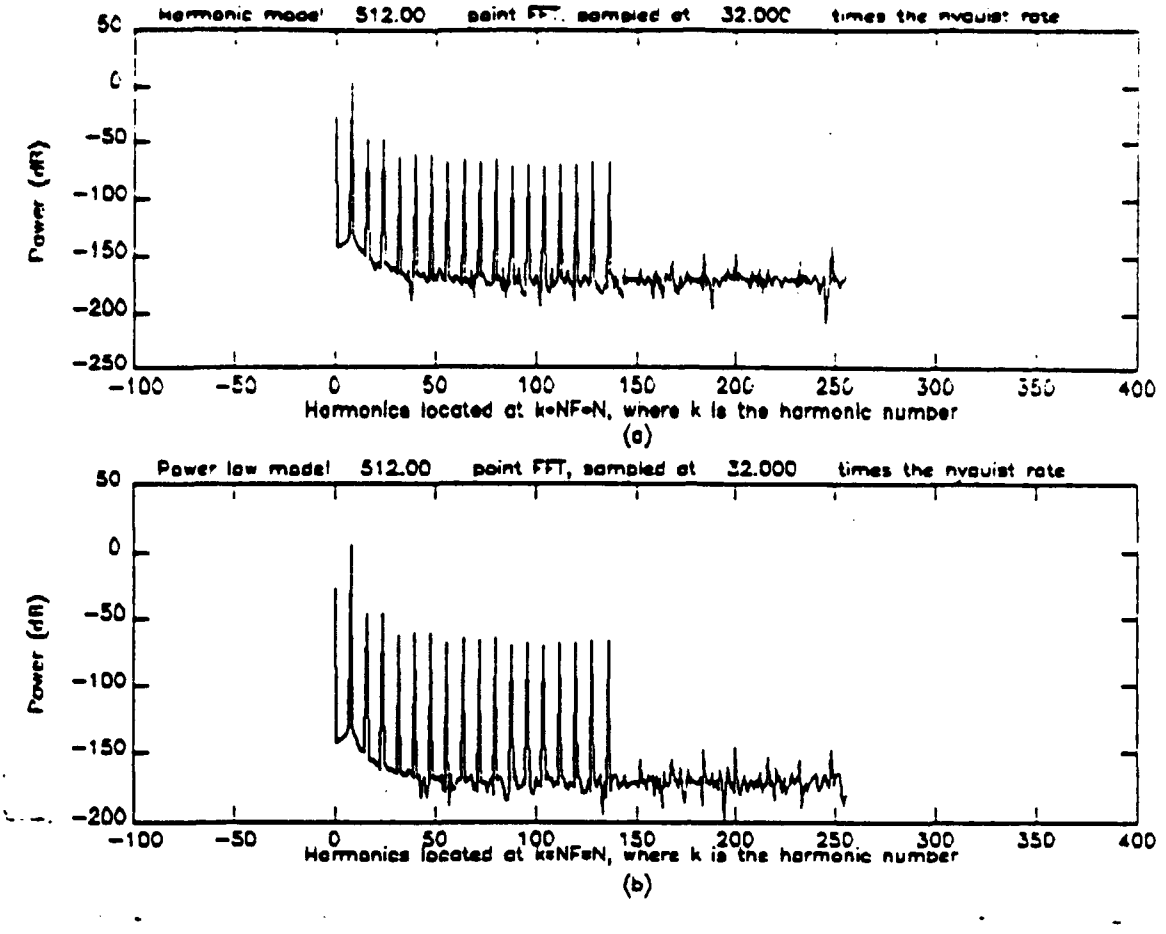

Fig. 2 FFT spectral response of ADC models

Harmonic Number	Harmonic Model	Power Law Model
k = 0.00000E+00	-27.698	-27.700
k = 1.0000	3.9794	3.9794
k = 2.0000	-45.708	-45.621
k = 3.0000	-45.827	-45.921
k = 4.0000	-62.694	-63.021
k = 5.0000	-60.484	-60.422
k = 6.0000	-60.273	-59.920
k = 7.0000	-69.142	-67.221
k = 8.0000	-64.118	-64.120
k = 9.0000	-67.335	-67.221
k = 10.000	-65.012	-65.020
k = 11.000	-70.056	-70.021
k = 12.000	-69.027	-69.021
k = 13.000	-70.020	-70.021
k = 14.000	-68.321	-68.321
k = 15.000	-69.020	-69.020
k = 16.000	-66.521	-66.521
k = 17.000	-67.222	-67.221

512.00 point FFT, sampled at 32.000 times the nyquist rate

Table 1

Spectral components of ADC models

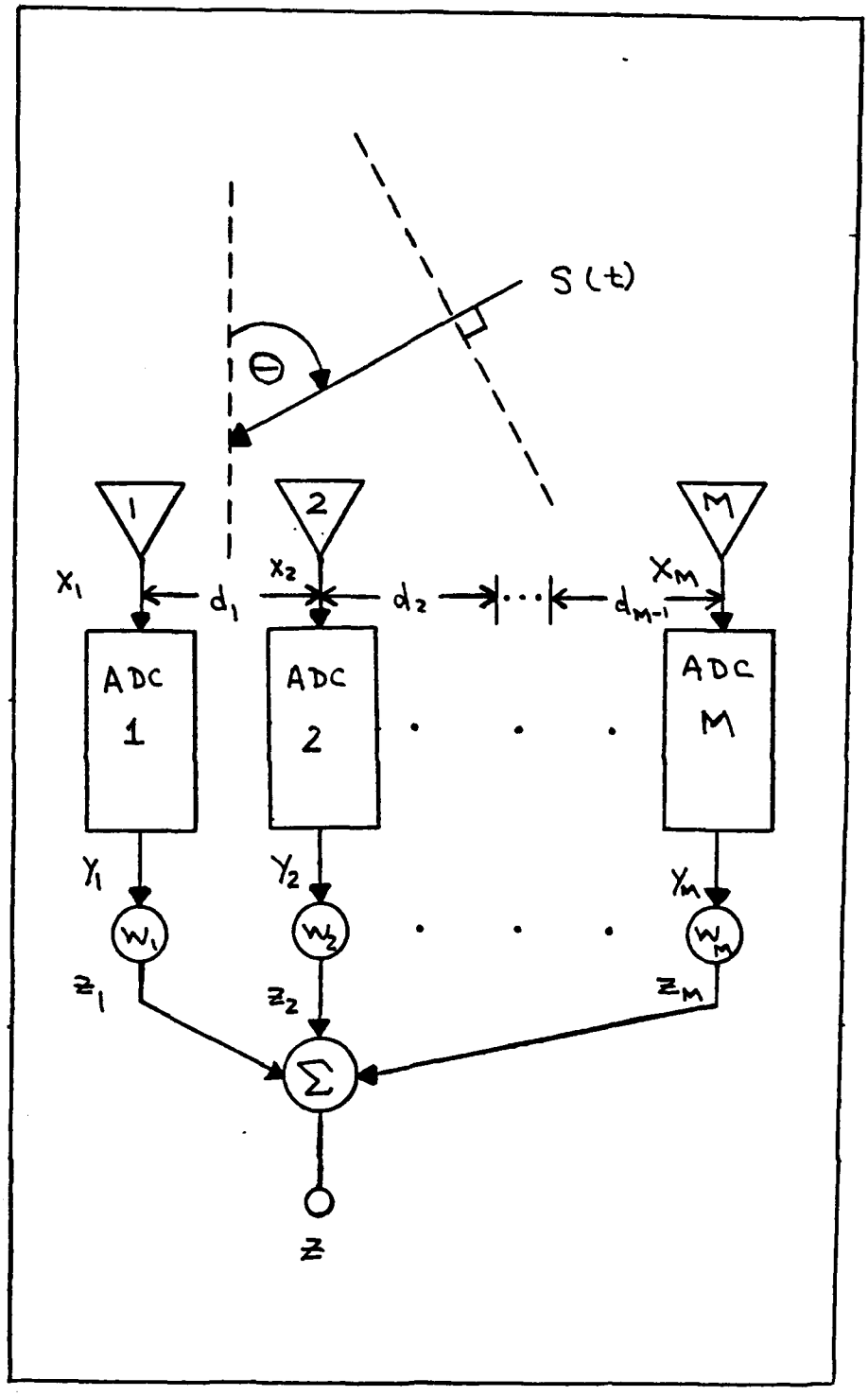

Fig. 3 Array Structure

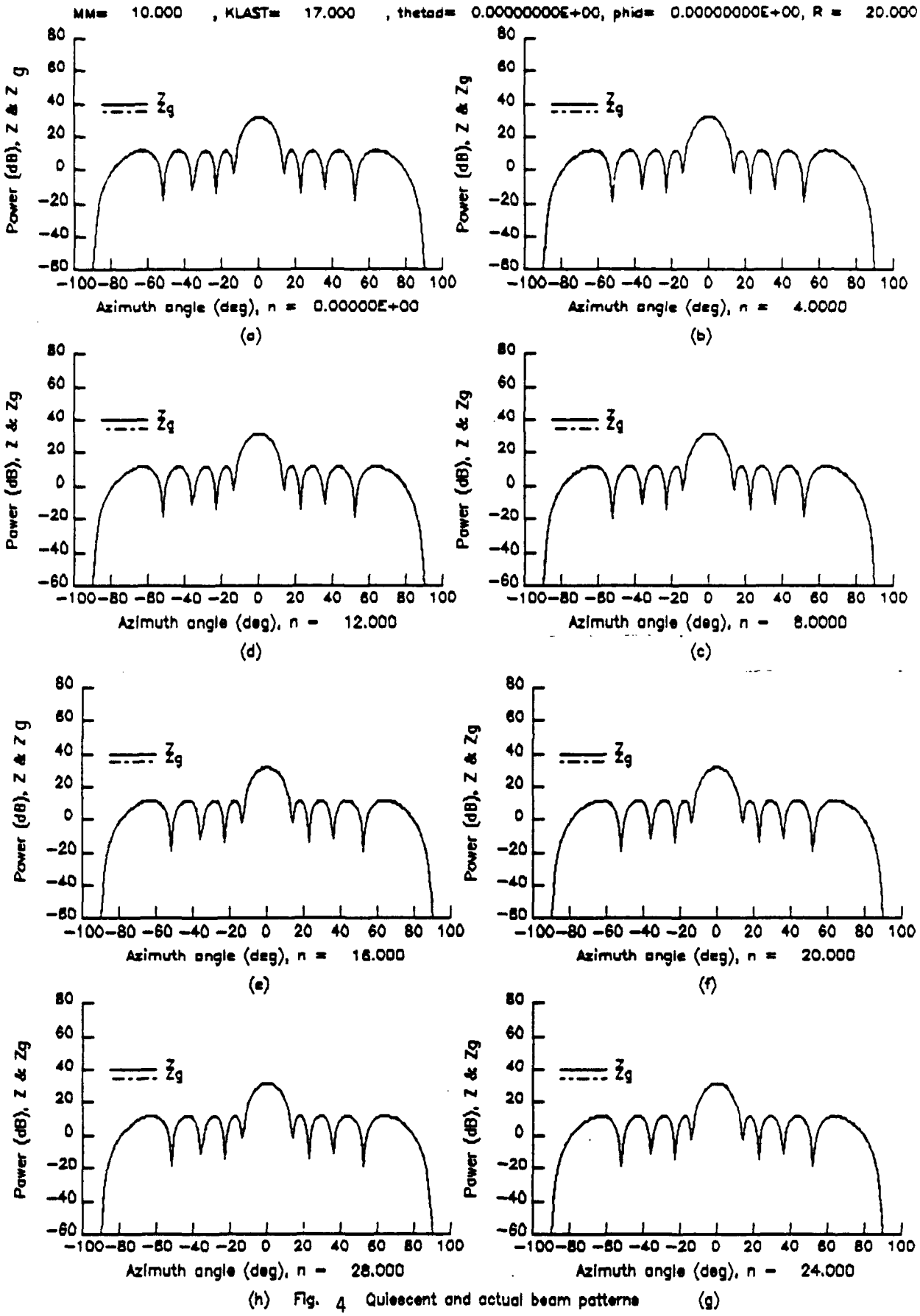

Fig. 4 Quiescent and actual beam patterns

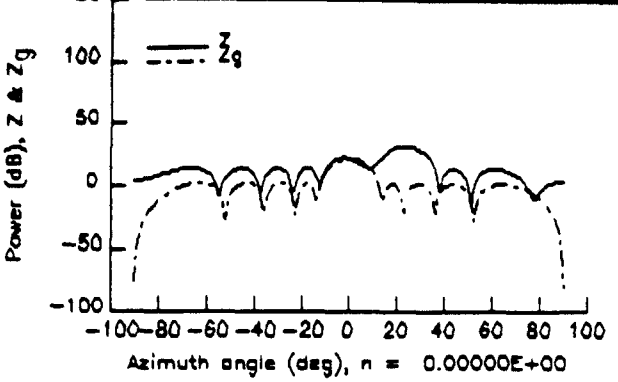

Fig. 5 Beam pattern - case I

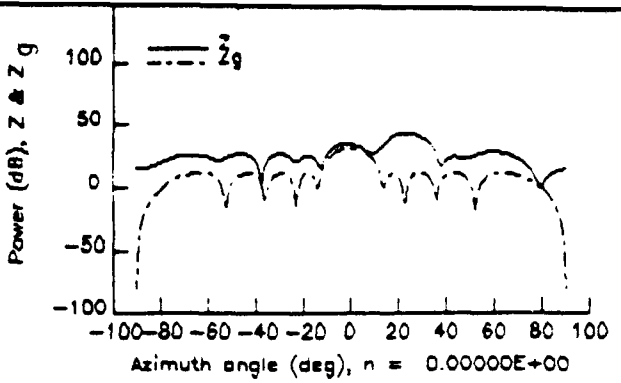

Fig. 6 Beam pattern - case II

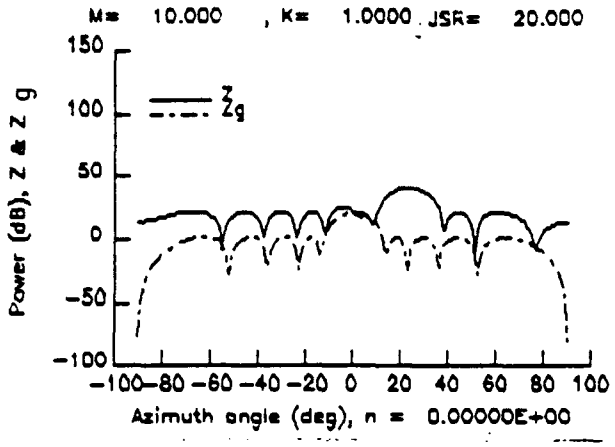

Fig. 7 Beam pattern - case III

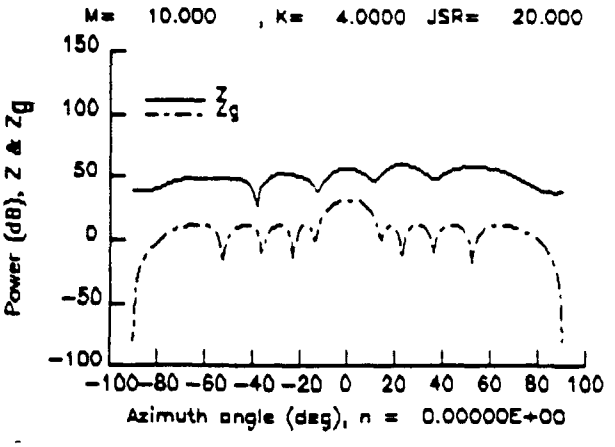

Fig. 8 Beam pattern - case IV

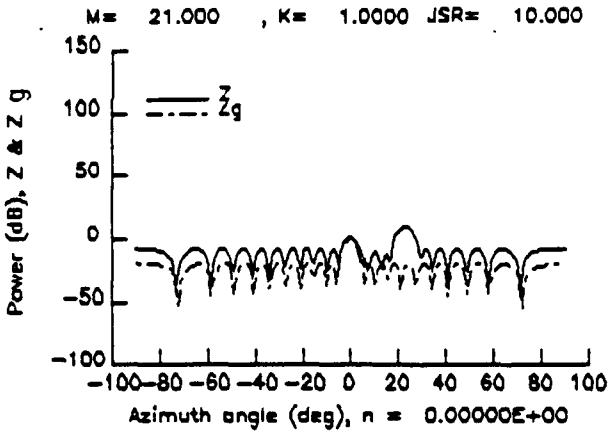

Fig. 9 Beam pattern - case V

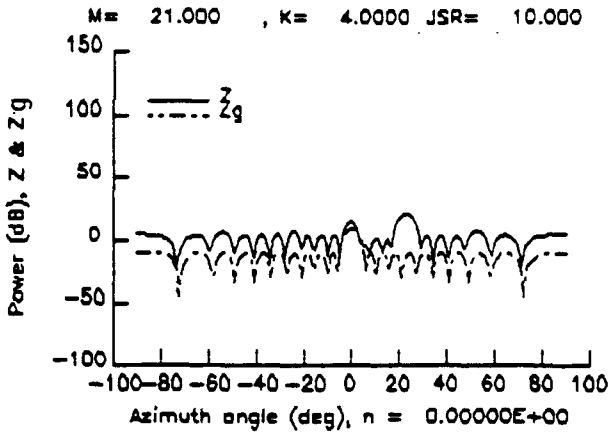

Fig. 10 Beam pattern - case VI

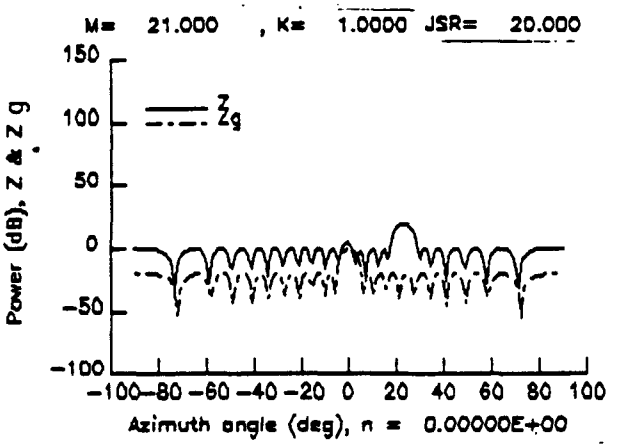

Fig. 11 Beam pattern - case VII

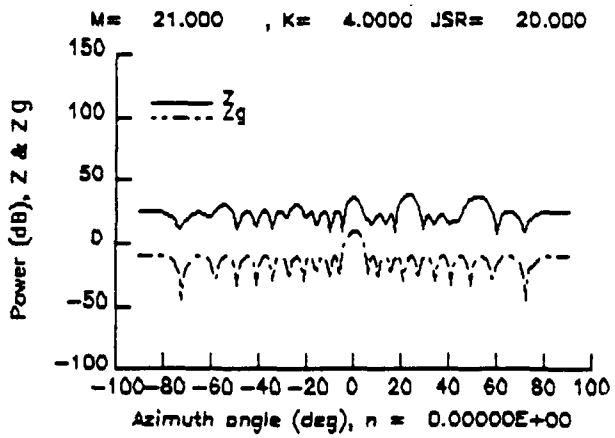

Fig. 12 Beam pattern - case VIII

1988 USAF-UES SUMMER FACULTY RESEARCH PROGRAM

GRADUATE STUDENT RESEARCH PROGRAM

Sponsored by the

AIR FORCE OFFICE OF SCIENTIFIC RESEARCH

Conducted by the

Universal Energy Systems, Inc

FINAL REPORT

STUDIES IN MICROWAVE SUPERCONDUCTORS

Prepared by:	Peter J. Walsh, Ph. D.
Academic Rank:	Professor
Department:	Physics
University:	Fairleigh Dickinson University
Research Location:	Hanscom AFB/EEAC
	Bedford, MA 01730
Date:	01 Aug 88
Contract No:	F49620-87-R-0004
USAF Researchers:	Drs. Paul Carr & John Derov

STUDIES IN MICROWAVE SUPERCONDUCTORS

P. J. Walsh

SUMMARY

This report covers work which was carried out at Hanscomb Air Force Base, EEAC/Antennas and Components Section during the summer of 1988 as a Air Force Summer Research Fellow. There are two self-contained sections. The first section reviews the theory and experimental studies of the microwave surface impedance of the new classes of high temperature superconductors while the second section† presents a theoretical review of microwave surface impedance applicable both to superconductors and metals. A paper has beeen prepared with John Derov and other scientists at HAFB for submission to Applied Physics Letters.

† not included. Full version at HAFB

MICROWAVE SUPERCONDUCTORS

Analysis was carried out of microwave measurements made at HAFB on a pressed, polycrystalline Y-Ba-Cu-O (YBCO) superconductor. Fig. 1 gives a schematic of the YBCO crystal. Conduction occurs in the lowermost and topmost regions incicated while the Y-containing region act as an insulating region. Fig. 2 illustrates the geometry of a microwave field at a conducting surface and defines out time dependences, fields and their directions and presents tne fundamental equations whose solutions are required to obtain the complex surface impedance Z. The electric field is E, Magnetic field H and the radian frequency and permeability of free space in their common greek symbols and MKS units will be used througnout. The theoretical determination of the impedance requires a specific model for the current density J.

The experimental absolute surface resistance R measured at 16.5 GHz in a TE011 mode cylindrical brass cavity wity a YBCO pressed disc as one end wall is given in Fig. 3 over tne temperature range from 6 to near 90 K [1]. The experimental limits on the data are indicated and the solid curve presents the results of a local-limit, "dirty" superconductor, Mattis-Bardeen analysis which will be described below.

The analysis is outlined in Fig. 4. In sigle phase superconductors a common empirical finding is that the superconductor surface resistance Rsfr is due a sum of a residual surface resistance Ro, which is substantially temperature independent,

and the superconducting surface resistance Rs(T) which has a strong, unmistakeable temperature dependence. A component of the residual mechanism apparently remains in series with the superconductor at any given frequency. The experimental data on our sample clearly show the common residual resistance and a middle temperature residual which, however, disappears at around 52 K. Apparently the middle temperature residual is a low temperature superconducting phase contained in our mixed-phase material which seems identical to the " 60 K bulk" oxygen-defficient superconductor of YBCO [2].

We carried out our analysis by extending the residual resistance empirical finding to include a middle-temperature superconcucting residual and then applying the superconductor scaled resistance relation given in Fig. 4. Rn is the non-superconducting material resistance which is identified just above the transition temperature marked by the sharp drop in surface resistance. The values of the two Rn and of Ro are given in Fig. 3. The sigma ratios are given by Mattis-Bardeen [3] while m is the dirty parameter introduced most recently by Sridhar [4]. This analysis produces the theoretical curve of Fig. 3.

An implication of this analysis is that the surface reactance of a superconductor is the sum of its residual components. Experiments testing this relation would be most welcome.

The measured non-conducting surface resistance of YBCO above the 88 K transition can be used to estimate the conductivity of YBCO in the <u>non-superconductor</u>, metallic state near 90 K. This conductivity is presented in Fig. 5 and is 3 10^4 mho/m which

might be compared with 6 10^7 mho/m for Cu at 300 K. Our value of YBCO conductivity agrees with that in Ref. 2 and with others in the literature for polycrystalline YBCO. The dc conductivity of single crystal YBCO has been measured recently [5] and is 2.5 10 ^5 mho/m parallel to the conducting plane of YBCO and about 2.5 10^3 mho/m perpendicular to the plane.

It appears the a RULE OF THUMB may be that the conductivity of polycrystalline YBCO is the gerometrical average - the square root of - the product of parallel and perpendicular conductivities.

Fig. 6 summarizes estimates ofsome useful parameters of YBCO. In sequence down the table in that figure the quantities are conductivity, carrier density, electron effective mass, mean free path, electron velocity at the Fermi energy, London penetration depth and Pippard coherence length [4] [6] [7]. These quantities are defined more precisely in Van Duzer and Turner [8].

Fig. 7 illustrates a typical calculation of the mean free path using the density estimate of Sridhar et al, Bardeen's effective mass estimate and the conductivities of Oda et al. The mean free path parallel to the conducting planes is very small while the value perpendicular is so small that the normal carriers must undergo tunnelling with very low probabilities through the insulating layers. A smaller density would raise the mean free path estimates but the Sridhar's density used in the calculation is already very small.

We can see from Figs. 6 and 7 that in YBCO, and most likely

the other high temperature superconductors, the following condition holds

coherence length $\leq$ mean free path $\ll$ London penetration depth.

Fig. 9 begins simple considerations leading to the surface impedance by obtaining the conventional local model for current density. In our frequency regime the radian frequency is much less than the collision frequency for a metallic carrier while the collision frequency is exactly zero for a superconducting carrier pair. The local model current density is given in Fig.9 for a "low frequency" metal with a real conductivity and for an ideal superconductor in which there are no normal elec trons to absorb energy an so has a purely imaginary conductivity. In the more general case the conductivity is complex.

When a conductor is taken well into the superconducting state so that all the normal electrons become paired, the ratio of metal real conductivity to imaginary conductivity of the ideal superconductor is just the ratio of radian frequency to metal collision frequency. This ratio is commonly very high.

The electric within a wave which penetrates a metal or a superconductor is considered in Fig. 10. Since the conductivity is comples the propagation constant k is also complex. The usual result for metal skin depth follows. In a superconductor the London penetration depth is equivalent to the skin depth although a variety of effects may increase the real depth of penetration to a much larger effective penetration depth. While the electric field penetrating a metal has a wave component the field penetrating the superconductor is purely damped.

The microwave impedance is finally obtained in Fig. 11. The derivative of field needed in Fig. 2 is simply requires multiplying the field by the complex propagation constant of the previous slide. It is very convenient to scale results to the non-superconducting state existing above the superconducting transition temperature. The general relation between superconducting surface impedance and resistance involves the ratio of the real and imaginary components of the complex superconducting conductivity to the normal-state, real metal conductivity. A consequence of the relation given is that the superconducting reactance must be greater than the superconducting resistance. When the mean free path is large compared to the coherence length and penetration depth, the relation between current density and electric field is not local and the theory is modified so that the negative one half root for the impedance ratio in Fig. 11 is replaced by a negative one third root.

Versions of the Mattis-Bardeen theory can be used to calculate the conductivity ratios needed. The imaginary superconductivity is inversely proportional to the square of the London penetration depth, or the pair density, as indicated in Fig. 12. The density of states in a superconductor is quite different than in a normal material and Mattis-Bardeen theory tells us how to get the proper pair density along with coherence factors and calculate an ideal super-conductivity. A variety of dirty theories take this ideal conductivity, note that the penetration depth appears as an inverse square and replace London's penetration value by an empirical effective penetration

depth. The result is to introduce an adjustable parameter, which we have labelled m, which reduces only the imaginary ideal conductivity in the superconductor. This is the basis of our original calculation.

The two appendices illustrate the convolutions of the full and local limit (equivalent to the anomalous limit) Mattis-Bardeen theory. An indicator that the local limit is applicable is that the ratio given in Appendix II is small as it appears to be. This condition is equivalent to the requirement that the coherence length be approximately equal or smaller than the mean free path (See Fig. 6). Appendices and remaining Figs. not included.

Fig. 14 presents the real and imaginary super-conductivity ratios calculated by the local limit Mattis-Bardeen theory and used in the analysis for Fig. 3. In the normal metal the real ratio is, of course, unity. Fig. 15 compares the clean M-B local limit theory (m=1) with the dirty theory with ms as given in Fig. 3. Since our conditions seem to satisfy the local limit conditions it does not appear that the full M-B theory will be able to reproduce the experimental results. A question which arises at this juncture is whether there is a relation between the residual resistance Ro and the dirty multipliers m.

Finally Fig. 16 summarizes thoes conditions which are neccessary for good microwave superconductors. Obviously the nature of the residual resistances and the dirty multipliers must be clarified and low Ro with m near unity is desired. The superconductor starts its resistance drop from the normal state resistance and so low normal state resistanc e is required

pointing to single crystal or large crystal poly material oriented properly. High transition temperatures since this give more temperature range for the resistance to decrease if liquid nitrogen is used. This points to the new Bismuth and Thallium based materials. However, if YBCO were clean with very low residual resistance, it would prove extremely useful.

1. Peter J. Walsh, John S. Derov, W. D. Cowan, C. Vi\on Benken and A. Drehman, "Measurement and analysis of the surface resistance in a mixed phase Y-Ba-C-O superconductor," to be submitted Appl. Phys. Letters.

2. R. J. Cava et al, Phys. Rev. B 36, 5719 1987.

3. D. C. Mattis and J. Bardeen, Phys. Rev. 111, 412, 1958.

4. S. Sridhar, C. A. Shifman and H. Hamden, Phys. Rev. B 36, 2301, 1987.

5. M. Oda, Y. Hidaka, M. Suzuki and T. Murakami, Phys. Rev. B 38, 252, 1988.

6. J. Bardeen, D. M. Ginsberg and M. B. Salamon, "Novel Superconductivity," eds. S. T. Wolf and V. Z. Kresin, Plenum Press, N. Y. 333-339, 1987.

7. M. Dreselhaus, Private communication.

8. T. Van Duzer and C. W. Turner, "Principles Of Superconductive Devices and Circuits," Elsevier, N. Y, see front and back fly leaves, 1981.

$YBa_2Cu_3O_7$

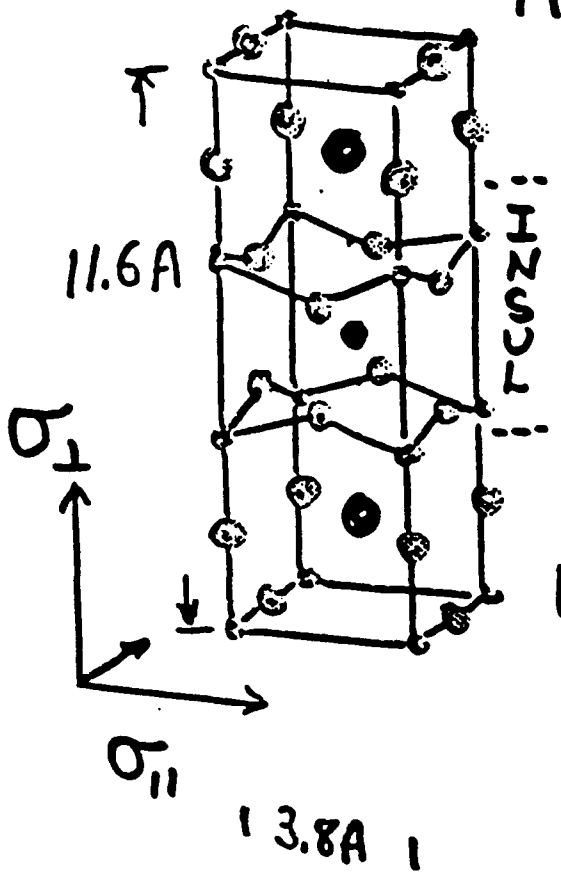
METALLIC
Oxygen
Barium
Copper
Yttrium
11.6A
INSUL
METALLIC
← O varies here
$\sigma_\perp$
$\sigma_{||}$
3.8A

SURFACE IMPEDANCE

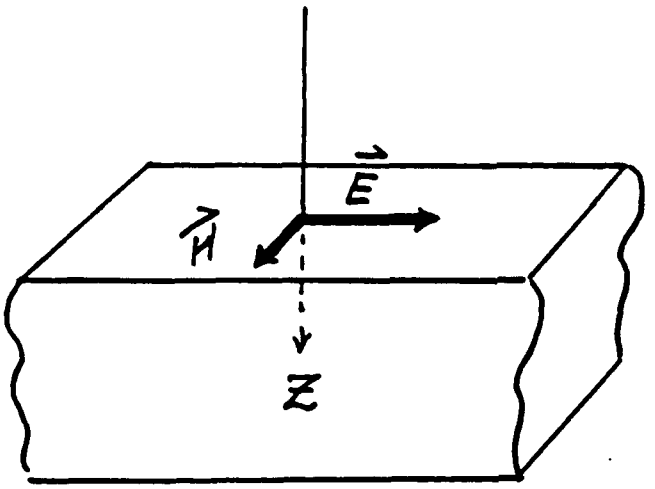

$e^{i\omega t}$ TIME DEPENDENCE

$$\frac{d^2 E_x(z)}{dz^2} \equiv i\omega\mu J$$

MAXWELL

$$\tilde{Z} = \frac{E(0)}{H(0)} = -i\frac{\omega\mu E(0)}{E'(0)}$$

COMPLEX

$m_1 = 0.045$, $m_2 = 0.1$

—— calc, $R_0 = 0.033$, $R_{1n} = 1.5$, $R_{2n} = 0.07\ (\Omega)$

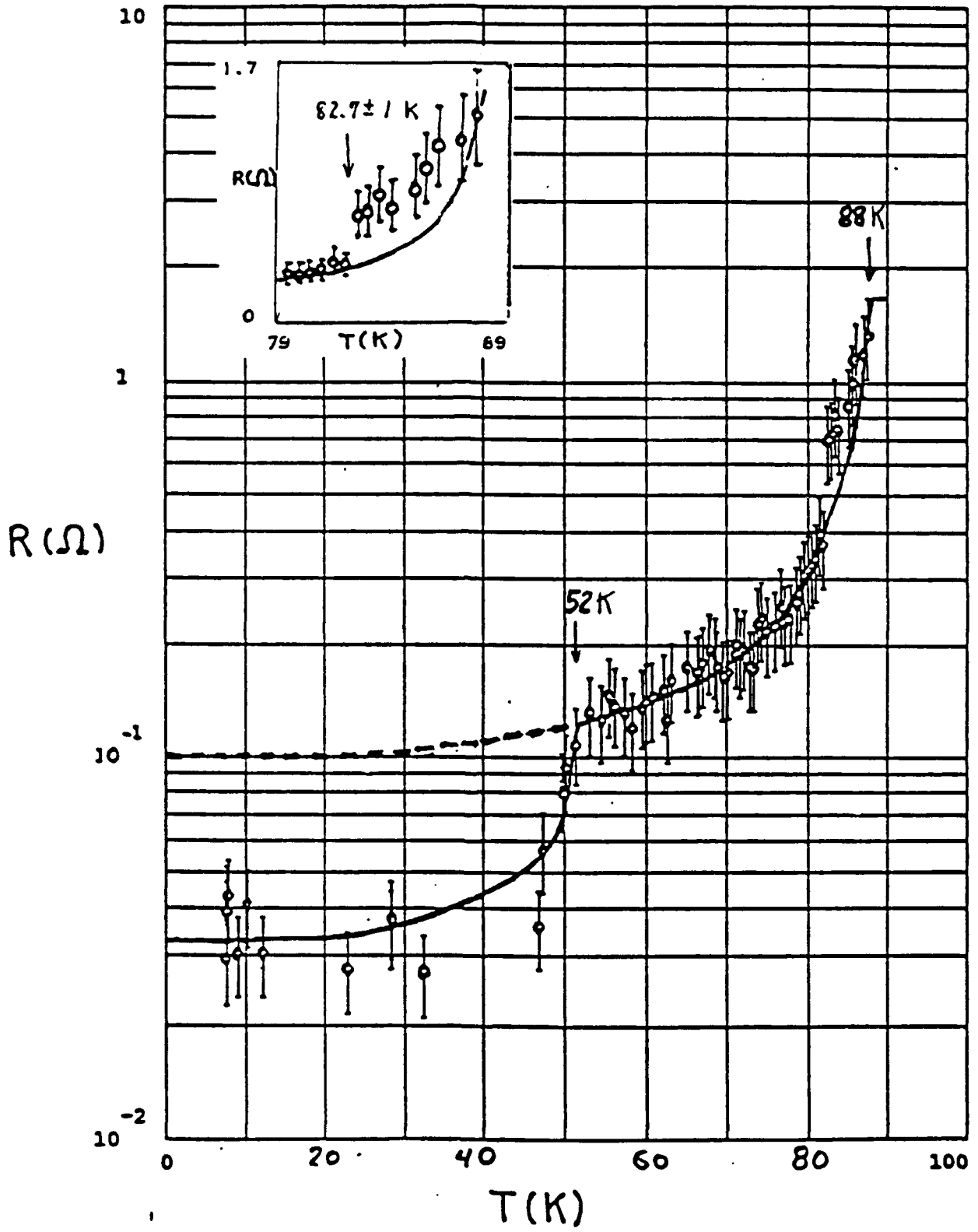

ANALYSIS of RESISTANCE

1. ONE PHASE MATERIAL

$$R_{SRF} = R_o + R_s(T)$$ EMPIRICAL

2. YBCO MIXED PHASES

$$R = R_o + R_{s1}(T) + R_{s2}(T)$$

$$\Rightarrow \quad X = X_o + X_{s1}(T) + X_{s2}(T) \; ?$$

$$\frac{R_s}{R_n} = Re\left[\frac{2i}{\frac{\sigma_1}{\sigma_n} - im\frac{\sigma_2}{\sigma_n}}\right]^{1/2}$$

σ_1/σ_n & σ_2/σ_n : M-B extreme coherent

$m = \left(\frac{\lambda_L}{\lambda_{eff}}\right)^2$: Sridhar "dirty" parameter

YBCO

at $90\,^{\circ}K$; $R_n = 1.5\Omega$

16.5 GHz ; POLYCRYSTALLINE

$$\sigma_{YBCO} = \frac{\omega \mu}{2 R_n^2} = 3 \times 10^4 \frac{mho}{m}$$

vs $\sigma_{Cu} = 6 \times 10^7 \frac{mho}{m}$ (at 300 K)

SINGLE CRYSTAL YBCO

(M. Oda, Y. Hidaka, M. Suzuki & T. Murakami P.R.B 38, 252, 1988)

$\sigma_{YBCO,\,11} = 2.5 \times 10^5$ mho/m in plane

$\sigma_{YBCO,\,\perp} \simeq 2.5 \times 10^3$ mho/m c axis

$\sigma_{11} / \sigma_{\perp} \simeq 100$:

RULE OF THUMB

$$\sigma_{POLY} \simeq \sqrt{\sigma_{11}\,\sigma_{\perp}}$$

YBCO

		HAFB	OHSM
σ ($\frac{mho}{m}$)	$5 \cdot 10^5$	$3 \cdot 10^4$	$2.5 \cdot 10^5$ ∥ $2.5 \cdot 10^3$ ⊥
n ('/cc)	$9 \cdot 10^{21}$		$1 \cdot 10^{21}$
m_{eff}/m	9		
ℓ (Å)	15	(uncertain 30-60)	5
v_0 (m/s)	$8 \cdot 10^4$	—	$4 \cdot 10^4$
λ_L (Å)	1700	8000 ∥ 900 ⊥	5000
ξ_0 (Å)	12	30 ∥ 5 ⊥	6
	BARDEEN (87)	DRESS'H'S (88)	SRIDHAR

CARRIER DENSITY

METALS
LOW T SC : $n \sim 3\text{-}8 \times 10^{28}\ /m^3$
$3\text{-}8 \times 10^{22}\ /cc$

Using $\sigma = \frac{ne^2}{m\nu} \quad \frac{ne^2 l}{m v_0}$

Electron Gas : $v_0 = \hbar (3\pi^2 n)^{1/3}\ m/s$

$m = 9\, m_e$: Bardeen

If $n = 1 \times 10^{27}/m^3 = 1 \times 10^{21}/cc$ SRIDHAR GUESS

$v_0 \sim 3.7 \times 10^4 / m/s$

$l_{\parallel} = 4.5 \text{Å}$

$l_{\perp} = 0.045 \text{Å}$!!

$\lambda_L \sim 5000 \text{Å}$

CONDUCTORS

ONE CARRIER:

$$m\frac{d\vec{v}}{dt} + \nu\vec{v} = -e\vec{E}$$

$$\vec{v} = \frac{-e\vec{E}}{m}\left(\frac{1}{i\omega+\nu}\right)$$

ν: collision frequency

$$\vec{J} = ne\vec{v} = \tilde{\sigma}\vec{E}$$

NORMAL METAL : $\omega \ll \nu$

SC: FREE FALL : $\nu \equiv 0$

COMPLEX CONDUCTIVITY
- LOCAL MODEL -

MANY CARRIERS: $J\left(\frac{AMP}{m^2}\right) = \frac{ne^2}{m}\frac{1}{(i\omega+\nu)}E$

LOW ω

NORMAL: $J_n = \frac{ne^2}{m\nu}E = \sigma_1 E$

"IDEAL"

SUPERCON: $J_s = -\frac{i n^* e^{*2}}{m^* \omega}E = -i\sigma_2 E$

GENERAL $\tilde{\sigma} = \sigma_1 - i\sigma_2$

Commonly: $\frac{n^* e^{*2}}{m^*} \equiv \frac{1}{\Lambda} \equiv \frac{\mu}{\lambda_L^2} = \omega\sigma_2$

IF

$\frac{ne^2}{m} = \frac{n^* e^{*2}}{m^*}$: $\frac{\sigma_{1n}}{\sigma_{2s}} = \frac{\omega}{\nu}$

FIELD PENETRATION

$$E = E(0) \exp i(\omega t - \tilde{k} z)$$

$$-\tilde{k}^2 = i \omega \mu \tilde{\sigma}$$

NORMAL : $\tilde{k} = \frac{1-i}{\delta}$; $\delta = \sqrt{\frac{2}{\omega \mu \sigma}}$ SKIN DEPTH

$$E_n = E(0) \exp i(\omega t - \frac{z}{\delta}) \exp(-\frac{z}{\delta})$$

SUPERCON: $\tilde{k} = \frac{i}{\lambda_L}$; λ_L LONDON DEPTH

$$E_s = E(0) \exp i\omega t \exp(-\frac{z}{\lambda_L})$$

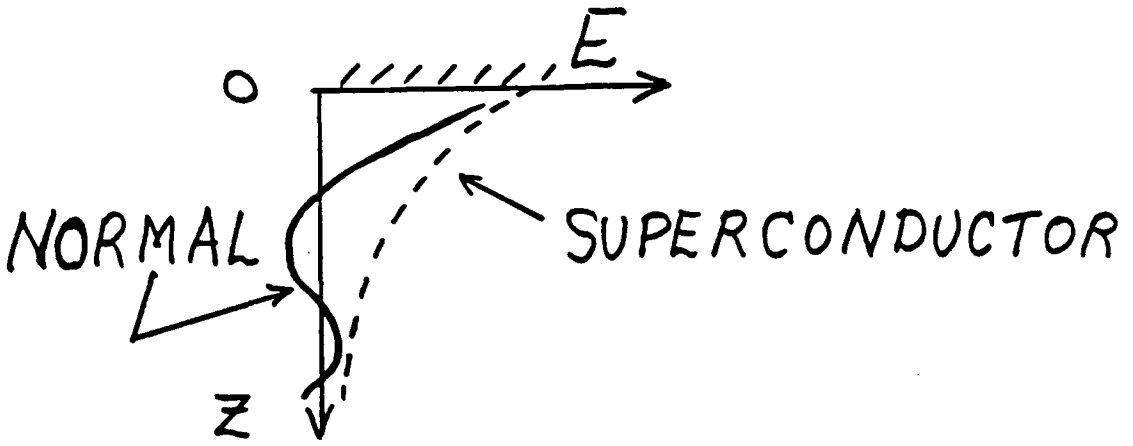

IMPEDANCE

$$E' = -ic\tilde{k}E$$

so $$\tilde{Z} = \left(\frac{i\omega\mu}{\tilde{\sigma}}\right)^{1/2}$$ IMPEDANCE

NORMAL CONDUCTOR

$$Z_n = R_n + iX_n \; ; \; R_n = X_n = \sqrt{\frac{\omega\mu}{2\sigma}}$$

SUPERCON - IDEAL

$$Z_s = iX_s \; ; \; X_s = L_s\omega = \mu\lambda_L\omega$$

GENERAL: SCALE TO NORMAL STATE

$$\frac{\tilde{Z}_s}{\tilde{Z}_n} = \left(\frac{\sigma_1}{\sigma_n} - i\frac{\sigma_2}{\sigma_n}\right)^{-1/2}$$

$$\frac{R_s}{R_n} = \left(\frac{2i}{\frac{\sigma_1}{\sigma_n} - i\frac{\sigma_2}{\sigma_n}}\right)^{1/2} \; ; \; X_s > R_s$$

"DIRTY" APPROXIMATION

$$\sigma_2 = \frac{1}{\lambda_L^2}\frac{\mu}{\omega} \quad : \text{IDEAL SC}$$

IF $\lambda_{eff} > \lambda_L$ due to

- Impurities
- Imperfections
- Flux Pinning
- ⋮

M-B TELLS HOW TO GET THIS ↓

Calculate σ_2 as "ideal", coherent then replace λ_L by λ_{eff} so

$$\sigma_2 \Rightarrow \left(\frac{\lambda_L}{\lambda_{eff}}\right)^2 \sigma_2(\text{coherent}) :$$

Gittleman & Rosenblook
Van Duzer & Turner
Tinkham
⋮

M-B LOCAL LIMIT σ_s/σ_n

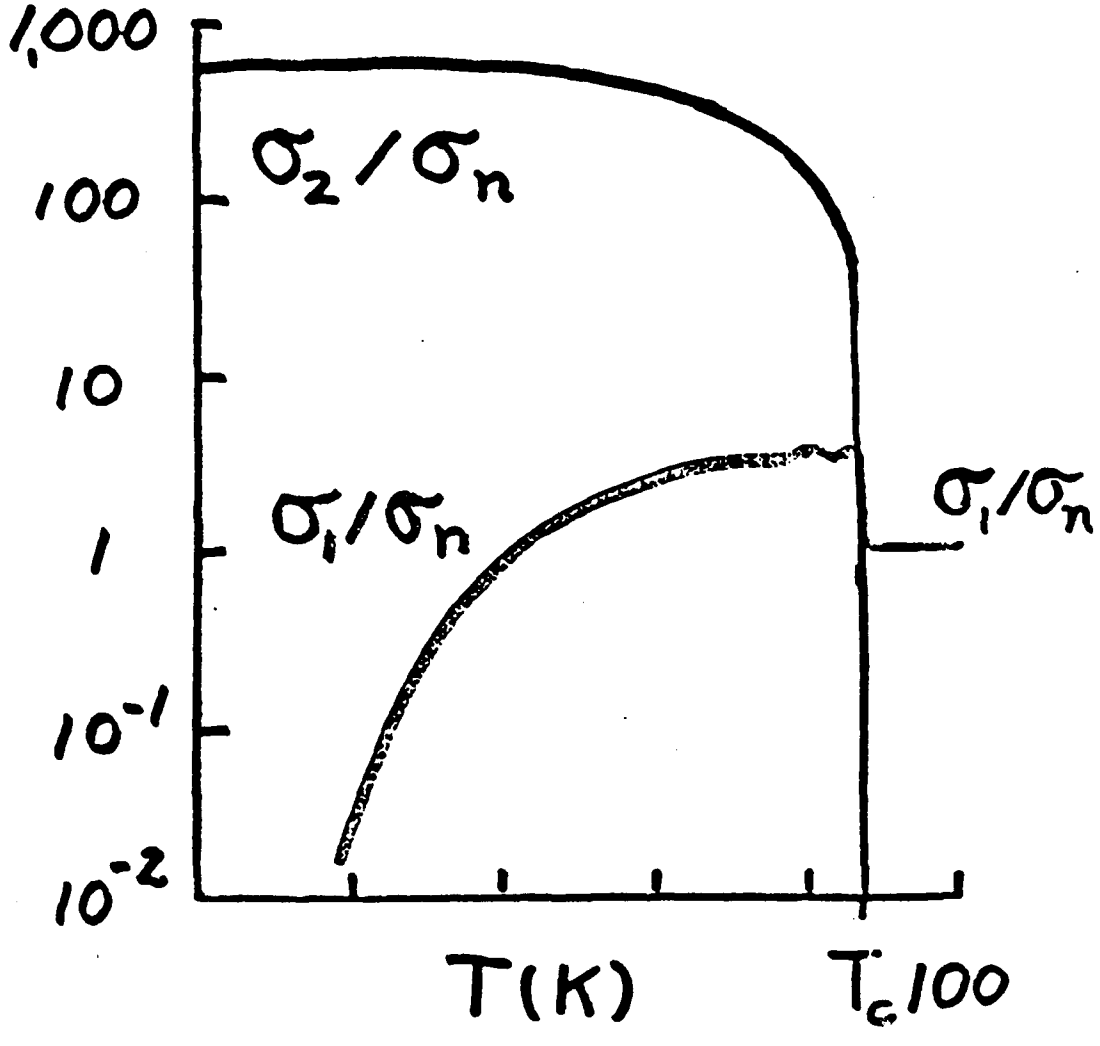

$m_1 = 0.045$, $m_2 = 0.1$

—— Calc, $R_0 = 0.033$, $R_{1n} = 1.5$, $R_{2n} = 0.07(\Omega)$

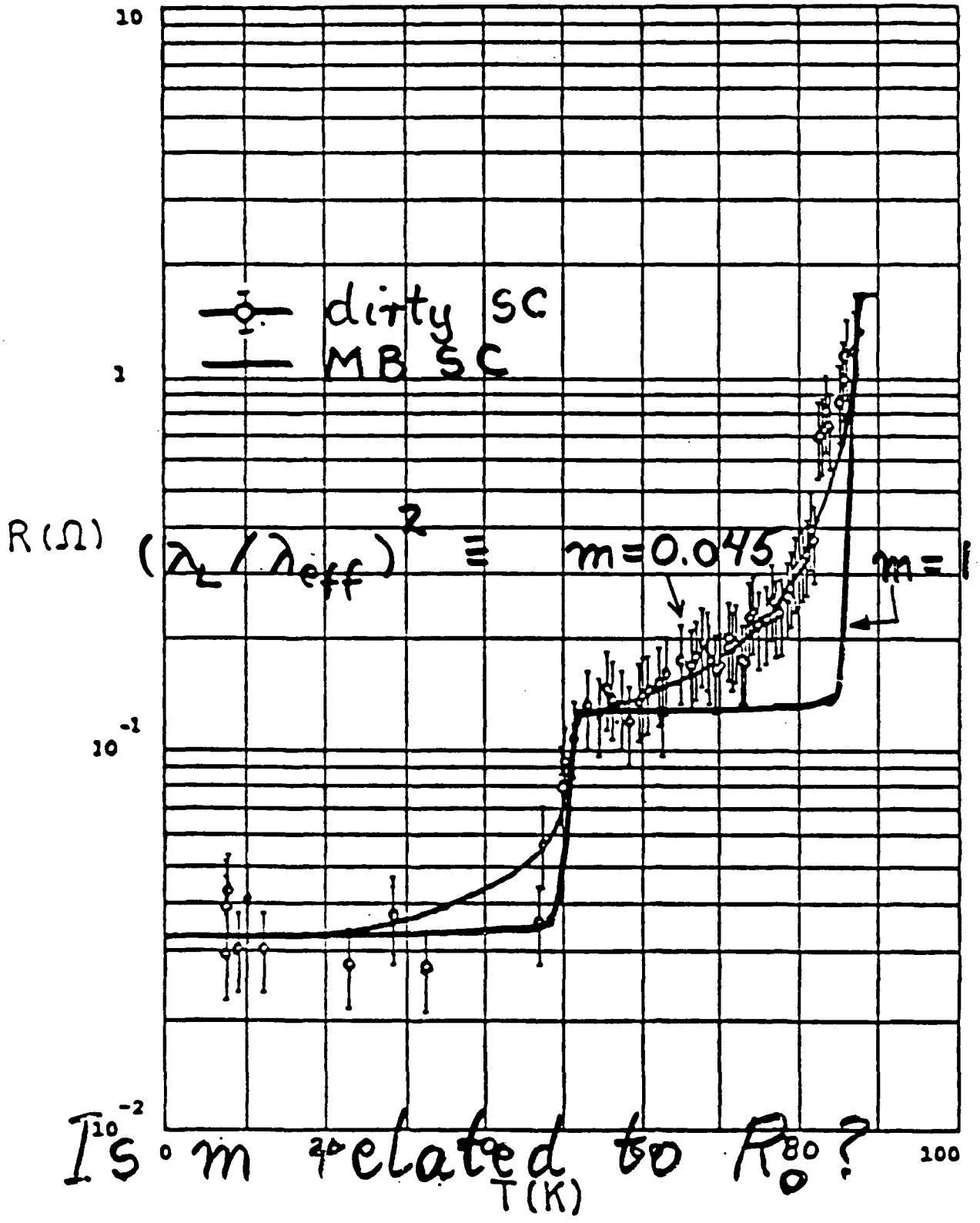

Is m related to R_0^{80}?

GOOD MW SUPERCONS

- Low Residual Resistance
- Clean : $m \Rightarrow l$
- Low Normal Resistance
  - Single Crystal
  - Epitaxial
  - Proper Growth Direction
- High T_c

1988 USAF-UES SUMMER FACULTY RESEARCH PROGRAM/

GRADUATE STUDENT RESEARCH PROGRAM

Sponsored by the

AIR FORCE OFFICE OF SCIENTIFIC RESEARCH

Conducted by the

Universal Energy Systems, Inc.

FINAL REPORT

CHEMICAL VAPOR DEPOSITION OF TITANIUM COMPOUNDS WITH AN ATOMIC LAYER EPITAXY SYSTEM

Prepared by:	Kenneth L. Walter, Ph.D.
Academic Rank:	Associate Professor
Department and University:	Chemical Engineering Department Prairie View A&M University
Research Location:	RADC/ESM Solid State Sciences Directorate Electromagnetic Materials Technology Division Hanscom AFB Bedford, MA 01731
USAF Researcher:	David W. Weyburne
Date:	29 September 1988
Contract No:	F49620-87-R-0004

Chemical Vapor Deposition of Titanium Compounds with an Atomic Layer Epitaxy System

by

Kenneth L. Walter

ABSTRACT

Equipment was designed, constructed and partially assembled for the purpose of depositing thin films of compounds containing titanium (primarily titanium nitride and titanium boride) on various substrates.

One technique to be used is atomic layer epitaxy (ALE), wherein single monolayers of atoms are deposited one at a time by chemical vapor deposition. This technique has recently been reported in the literature as applied to gallium arsenide, but has not yet been reported for titanium compounds. If successful, this work could produce precisely controlled films with electronic, mechanical and corrosion applications. This work is currently being continued by researchers at Hanscom AFB, Massachusetts.

ACKNOWLEDGMENTS

I wish to thank the Air Force Systems Command, the Air Force Office of Scientific Research and Rome Air Development Center for their sponsorship of this research. I also wish to thank Universal Energy Systems, Rodney Darrah and his staff for their excellent job of organizing and administering the USAF Summer Faculty Research program.

I am particularly grateful to Dr. David W. Weyburne, my technical focal point, for his guidance, technical expertise and hospitality. Captains Daniel K. Johnstone and Steven Bachowski deserve special thanks for their valued laboratory assistance and discussions. Dr. Brian S. Ahern, in addition to design assistance, helped provide insight into new research. Messrs. Meckie T. Harris, Robert M. Hilton, Alok Tripathi and Michael J. Suscavage, were very helpful in assembling and testing components, as was Ms. Michelle A. Neal with office needs. Both the Solid State Sciences and Air Force Geophysical Laboratory shops provided excellent custom fabrication services.

Finally, I wish to thank Dr. Alton F. Armington, Acting ESM Division Chief, and Dr. Harold Roth, ES Director, as well as many others not specifically mentioned at Hanscom AFB, and also Mr. John Ritz, my effort focal point for RADC at Griffis AFB in New York.

I. INTRODUCTION:

Many private and public organizations in this and other nations recognize the importance of materials to the discovery of new physical phenomena and the application of these discoveries to new technologies. The US Air Force Office of Scientific Research has delegated a large share of its efforts in electromagnetic and optical materials to the Solid State Science Directorate of the Rome Air Development Center at Hanscom Air Force Base. The Electronic Materials Branch of the Electromagnetic Materials Division has specialized in the preparation of high purity bulk crystals, fibers and epitaxial thin films useful for electronic and electro-optic applications. This branch has special expertise in depositing thin films of indium phosphide and is developing advanced capability for gallium arsenide films. There is currently ongoing work with bulk titanium diboride, and thin films of this material were also desired.

My career has been devoted until recently to Chemical Engineering research and development on industrial processes for producing a variety of chemicals and primary metals. Since joining Prairie View A&M University four years ago, I have turned to materials research, especially thin films.

During the summer of 1987, I worked at AT&T Bell Laboratories in Murray Hill, New Jersey. My work consisted of two parts - (1) assisting with the design if a new hot wall reactor for depositing epitaxial thin films on multiple silicon wafers and (2) carrying on experimental work on an existing lab-scale system for depositing thin films of titanium diboride using plasma-enhanced chemical vapor deposition. This latter experience meshed with the RADC/ESM needs.

II. OBJECTIVES OF THE RESEARCH EFFORT:

During my pre-summer visit to Hanscom AFB, we jointly decided that my ten-week work would consist of designing and building a lab-scale system to deposit thin films of titanium nitride, titanium diboride and possibly other materials on various substrates. Later, properties of these films would be analyzed for electronic, mechanical and corrosion-resisting applications.

About four weeks into the project, we decided to change the emphasis from a chemical vapor deposition (CVD) system to a slightly different atomic layer epitaxy (ALE) system. In conventional CVD, reactive gas mixtures are continuously flowing over the substrate and reacting to deposit films. In ALE

however, reactive gases and inert gases are alternately pulsed into the system with the objective of depositing only one monolayer of film at a time. For example, in depositing titanium nitride, TiN, a gas mixture of TiO_4 in excess H_2 is first spurted into the system to deposit a layer of Ti. Next, a second or a few seconds later comes a spurt of only H_2 to flush the substrate. Finally NH_3 in H_2 spurts in to deposit a layer of N, followed by another H_2 flush spurt. This sequence is repeated for an hour or a few hours to achieve films of significant thickness. Of course, system cleanliness and high gas purities are essential to obtaining low-defect films.

Very accurately-controlled film thicknesses are potentially achievable by this ALE technique, which are important in applications involving superlattices and junctions among others. It was decided to concentrate on titanium nitride films at first, since this system's crystal structure and stoichiometry are better defined than those of titanium diboride.

III. LITERATURE REVIEW:

Holleck (5,6) offers review papers on selecting materials useful for hard, wear resistant coatings. He emphasizes that substrate and coating must have

similar thermal expansion coefficients, and lists titanium nitrides, borides and carbides as candidate materials. Knotek (10) et al. investigate sputtered films of titanium nitrides, carbides and mixtures for hardness. Tsakalos (24) shows that superlattices with wavelengths of the order of about one nanometer show improved elastic moduli, which show maxima at certain wavelengths. Takahashi and Kamiya (21) used CVD to deposit Ti-V-B films.

Helmersson et al. (4) show a hardness maximum in the TiN/VN strained-layer superlattice system at a wavelength of about 6 mm. They also show a maximum in hardness when the ratio of TiN layer thickness to total layer thickness is about 0.35. They used a sputtering technique to grow the films at about 750°C.

Kim and Chun (9) used CVD to deposit TiN onto TiC at about 900-1150°C and Itoh (7) deposited alternating TiN and TiB_2 layers at the same temperatures. High-hardness, adherent coatings were achieved. Moore et al. (13) produced four sequential layers on a WC cutting tool using CVD, including TiN and TiC. Kim et al. (8) discuss CVD of TiC alone.

Kurtz and Gordon (11) discuss the use of TiN in electronic and several other applications, and deposit films from 400-700°C, with 600°C being the lower limit

for best results. They also test metal-organic gas sources.

Titanium boride films are complicated by the fact that the boron component can be lost by reaction with residual water vapor and subsequent volatilization, as shown by Feldman et al. (3). The result is often uncertain stoichiometry. Lynch et al. (12) showed this was a problem even in bulk single crystals.

Work on the TiB_2 system dates back to least as far as 1949, when Ehrlich (2) prepared several titanium compounds by sintering. Shappiro et al. discuss some of the electronic applications for TiB_2. Caputo et al. (1) and Motojima et al. (14) discuss erosion resistance and hardness of CVD coatings of TiB_2. Pierson et al. (17,18) used CVD to produce TiB_2 coatings on graphite from 600-925^{o}C. Takahashi and Itoh (20) used an ultrasonic field during CVD to decrease the grain size of the deposit. Williams (26) uses a plasma to lower the CVD deposition temperature of TiB_2 films.

Ozeki et al. (16) and Tischler and Bedair (22,23) give explanations of why monolayers can be deposited by ALE in the GaAs system and the InAs and In-Ga-As systems. Nelson (15) describes ALE applied tp ZnS and ZnSe.

Wang et al. (25) show how TiO_2 smoke particles allow visualization of flow patterns, and assist in spatial design of CVD reactors.

IV. DESIGN OF THE HARDWARE:

Figure 1 shows the atomic layer epitaxy (ALE) gas supply and exhaust system schematic diagram. The film is deposited on a substrate (not shown), which rests on top of a 1-1/2 inch diameter graphite susceptor. The susceptor is heated by a radio-frequency (RF) induction coil also inside the 4 inch inside diameter, 18 inch long quartz tube. A 10 kw Lepel RF Generator easily allows temperatures up to 1100°C to be achieved, although TiN deposition will occur at lower temperatures. The susceptor rests inside a 2 inch diameter boron nitride insulating cup. A stainless steel, closed-end shaft supports the boron nitride cup, and contains a chromel-alumel thermocouple. In operation, actual substrate surface temperatures will be measured by an optical pyrometer, and referenced to this thermocouple for temperature control purpose.

The shaft can be rotated, as shown in Figure 2, by a D.C. Bodine Motor with speed control. The shaft is supported by a thrust bearing with a rotating bearing surface. Thermocouple leads, which rotate,

also pass into a rotary connector, from which stationary leads exit. The support for this assembly (not shown) rests on a 10-1/2 inch diameter aluminum baseplate. This plate also supports the stainless steel bottom plate on which rests the gasketed quartz tube. This bottom plate has holes with matching fittings for the two water-cooled RF electrode tubes, the rotating shaft, vacuum port and two additional thermocouple ports.

The stainless plate on top of the quartz tube also has a gasket seal. It contains holes to match fittings for supplying the reactive gases to the substrate through only one such tube, but there are provisions to have separate tubes for each gas.

Returning Figure 1, one can see a needle valve beneath the quartz tube. This controls the total pressure inside the tube by throttling the gas flows removed by the vacuum pump. System pressure is indicated on a vacuum gage.

The Tylan Tymer 16 (shown inside dashed lines in Figure 1) controls the flow sequencing of feed gases according to a programmed schedule. The shortest cycle period possible is one second. A fixed quantity of ammonia can be trapped between the two air-to-open valves by the the Tymer 16. When released, the NH_3, is

carried into the system by hydrogen flowing at about 40 standard cubic centimeters per minute (SCCM). An additional 3000 SCCM H_2 flow is provided all the time by a mass flow controller.

Titanium tetrachloride liquid must be vaporized in a hydrogen stream. Since such a bubbler cannot be cycled as frequently as one second, a so-called vent-and-run line is set up. In this way the $TiCl_4$ is always vaporizing at the same rate, but the flow is diverted from vacuum exhaust to the reactor only as needed, according to the ALE plan.

The Englehard Hydrogen Purifyer provides a pure supply by diffusing it through high temperature solid tubes. A nitrogen supply can be used to flush all hydrogen from the entire system before opening it to the atmosphere.

V. RESULTS:

The system was partially assembled and leak tested. Since the shop was still fabricating some components, no runs have yet been made.

VI. RECOMMENDATIONS:

At this time another member of the RADC/ESM staff has completed system assembly, and is leak testing the

new parts. It is planned that the system be operated to achieve atomic layer epitaxy with TiN. Until the runs are made, specific recommendations cannot be made.

We do believe that a new O-ring seal design for the rotating shaft will be required.

I am applying for a follow-on mini-grant to set up a similar system on Prairie View A&M's campus. We would expect to attain ALE capability with several titanium compounds, and then do exploration in ternary systems. We do not expect to be able to use toxic compounds such as arsine or phosphine on our campus.

We have also submitted other proposals in the same general area to NASA (with expected Jan. 1, 1989 starting date) and to Battelle Northwest.

REFERENCES

1. Caputo, A.J., W.J. Lackey, I.G. Wright and P. Angelini, "Chemical Vapor Deposition of Erosion-Resistant TiB2 Coatings," J. Electrochemical Society:Solid State Science and Technology 132(9),pp. 2274-80, 1985.

2. Ehrlich, Paul, "Uber die binaren Systeme des Titans mit den Elementen Stickstoff, Kohlenstoff, Bor und Beryllium," Zeit. fur Anorg. Chemie 259, pp. 1-41, 1949.

3. Feldman, Charles, Frank G. Satkiewicz and Gerard Jones, "Preparation and Electrical Properties of Stoichiometric TiB2 Thin Films," J. Less Common Metals 79, pp. 221-235, 1981.

4. Helmersson, U., S. Todorova , S.A. Barnett and J.-E. Sundgren, "Growth of single-crystal TiN/VN strained-layer superlattices with extremely high mechanical hardness," J. Appl. Phys. 62, pp. 481-484, 1987.

5. Holleck, H., "Material selection for ha oatings", Vac. Sci. Technol. A4, pp. 2661-2669, 19oo.

6. Holleck, H., Ch. Kuhl, and H. Schulz, "Summary Abstract: Wear resistant carbide-boride composite coatings," J. Vac. Sci. Technol. A3, pp. 2345-2347, 1985.

7. Itoh, Hideaki, "Effect of TiB2 Interlayer on the CVD of an Amorphous Titanium Nitride Film," J. Crystal Growth 57, pp. 456-458, 1982.

8. Kim, D.G., J.S. Yoo and J.S. Chun, "Effect of deposition variables on the chemical vapor deposition of TiC using propane," J. Vac. Sci. Technol. A4, pp. 219-221, 1986.

9. Kim, Moo Sung and John S. Chun, "Effects of the Experimental Conditions of Chemical Vapor Deposition of a TiC/TiN Double Layer Coating," Thin Solid Films 107, pp. 129-139, 1983.

10. Knotek, O., M. Bohmer and T. Leyendecker, "On structure and properties of sputtered Ti and Al based hard compound films," J. Vac. Sci. Technol. A4, pp. 2695-2700, 1986.

11. Kurtz, S.R., and R.G. Gordon, "Chemical Vapor Deposition of Titanium Nitride at Low Temperatures," Thin Solid Films 140, pp. 277-291, 1986.

12. Lynch, C.T., S.A. Mersol and F.W. Vahldiek, "The Microstructure of Single-Crystal Titanium Diboride," J. Less Common Metals 10, pp. 206-219, 1966.

13. Moore, R.L. and L. Salvati, Jr., "Surface analysis of diffusion zones in multiple chemical vapor deposition coatings," J. Vac. Sci. Technol. A3, pp. 2425-2431, 1985.

14. Motojima, Seiji, Masahiko Yamada and Kohzo Sugiyama, "Low-Temperature Deposition of TiB2 on Copper and Some Properties Data," J. Nuclear Materials 105, pp. 335-337, 1982.

15. Nelson, Jeffrey G., "Epitaxial growth of ZnS and ZnSe on the low index faces of GaAs using atomic layer epitaxy," J. Vac. Sci. Technol. A5(4), pp. 2140-2141, 1987.

16. Ozeki, M., Mochizuki, N., Ohtsuka, N., Kodam, K., "Kinetic processes in atomic-layer epitaxy of GaAs and AlAs using a pulsed vapor-phase method," J. Vac. Sci. Technol. B, Vol. 5, No. 4, pp. 1184-1185, 1987.

17. Pierson, H. O., and Mullendore, A.W., "The Chemical Vapor Deposition of TiB_2 From Diborane," Thin Solid Films 72, pp. 511-516, 1980.

18. Pierson, H.O., E. Randich and D.M. Mattox, "The Chemical Vapor Deposition of TiB2 on Graphite," J. Less Common Metals 67, pp. 381-388, 1979.

19. Shappirio, J.R., J.J. Finnegan and R.A. Lux, "Diboride diffusion barriers in silicon and GaAs technology," J. Vac. Sci. Technol. B4, pp. 1409-1411, 1980.

20. Takahashi, Takehiko, and Hideaki Itoh, "Ultrasonic Chemical Vapor Deposition of TiB2 Thick Films," J. Crystal Growth 49, pp. 445-450, 1980.

21. Takahashi, Takehiko, and Hideo Kamiya, "Chemical vapor deposition of the system Ti-Zr-B," High Temp.-High Press. 9, pp. 437-443, 1977.

22. Tischler, M.A. and S.M. Bedair, "Self-limiting mechanism in the atomic layer epitaxy of GaAs," Appl. Phys. Lett. 48, pp. 1681-1683, 1986.

23. Tischler, M.A. and S.M. Bedair, "Improved uniformity of epitaxial indium-based compounds by atomic layer epitaxy," Appl. Phys. Lett. 49, pp. 274-276, 1986.

24. Tsakalakos, T., "Mechanical properties and diffusion of

metallic superlattices," J. Vac. Sci. Technol.B4, pp. 1447-1456, 1986.

25. Wang, C.A., S.H. Groves and S.C. Palmateer, "Flow Visualization Studies for Optimization of OMVPE Reactor Design," J. Crystal Growth 77, pp. 136-143, 1986.

7-13-88
Rev. 7-25-88
7-26-88

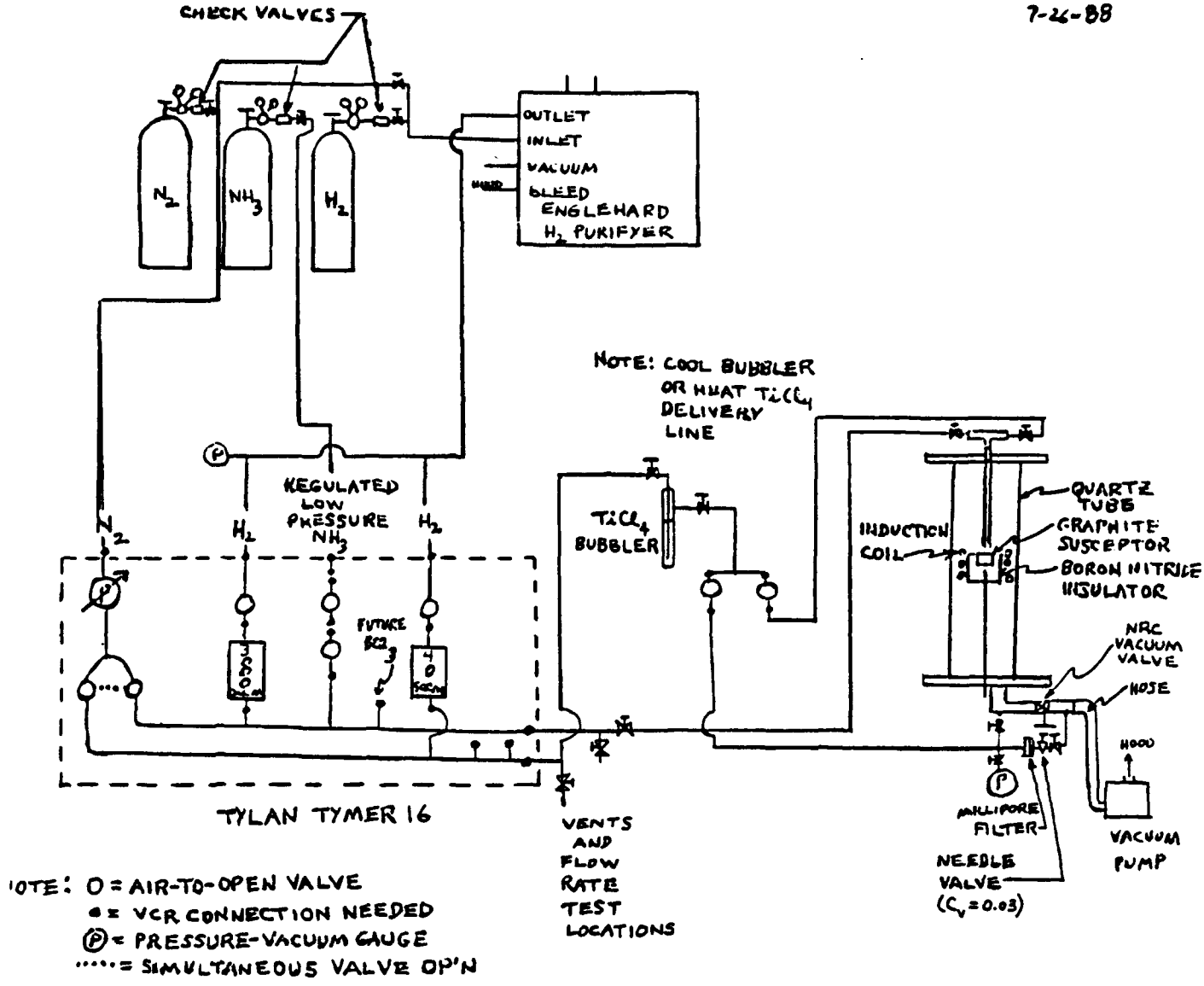

NOTE: O = AIR-TO-OPEN VALVE
● = VCR CONNECTION NEEDED
Ⓟ = PRESSURE-VACUUM GAUGE
····· = SIMULTANEOUS VALVE OP'N

FIG. 1. TiN ALE GAS SUPPLY AND EXHAUST SYSTEM SCHEMATIC

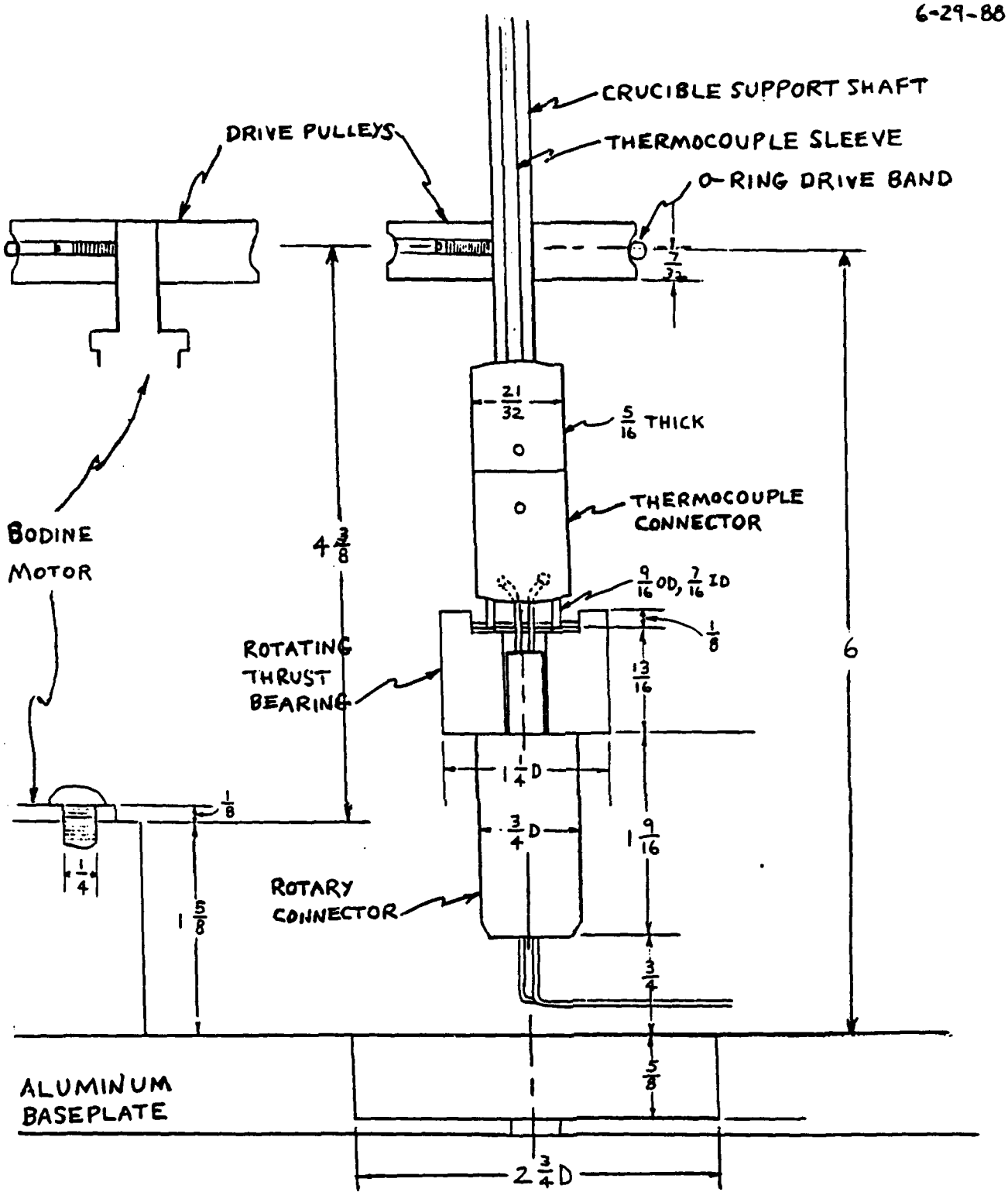

FIG. 2.

ROTARY DRIVE-THERMOCOUPLE ASSEMBLY (W/O SUPPORTS)

1988 USAF–UES SUMMER FACULTY RESEARCH PROGRAM

Sponsored by the

AIR FORCE OFFICE OF SCIENTIFIC RESEARCH

Conducted by the

Universal Energy Systems, Inc.

FINAL REPORT

Prepared by:	*Gwo–Ching Wang, Ph.D.*
Academic Rank:	*Associate Professor*
Department and	*Physics Department*
University:	*Rensselaer Polytechnic Institute*
Research Location:	*Solid State Sciences Division*
	Rome Air Development Center
	Hanscom, MA 01731
USAF Researcher:	*Alvin J. Drehman*
Date:	*September 12, 1988*
Contract No:	*F49620–87–R–0004*

Surface Effects on the High Temperature Superconducting YBaCuO Thin Films grown by RF Sputtering

by

Gwo–Ching Wang

ABSTRACT

The surface morphology and near surface chemical composition of high temperature superconducting YBaCuO thin films grown on $SrTiO_3(001)$ substrates by RF sputtering technique are studied by Scanning Electron Microscopy (SEM), Scanning Tunneling Microscopy (STM) and the depth profile of Auger Electron Spectroscopy (AES). A new surface effect on superconducting was found that is the chemical compositions at and near the surface of thin films are different from the bulk composition determined by Energy Dispersive X–Ray Analysis (EDX). At about 500Å deep into the film the Auger peak to peak heights of elements in YBaCuO gradually approach th ık to peak heights obtained from the elements at the surface of a fractured bulk material. This off–stoichiometry transition layer near the surface implies that there is a minimum thickness of thin film, i.e., about twice of 500Å, that will exhibit superconductivity. It also decreases the critical temperature and broadens the superconducting transition width of YBaCuO thin films and this effect is very drastic on films that have submicron size grains.

Acknowledgements

I would like to thank the Air Force Systems command and the Air Force Office of Scientific Research for Sponsorship of this summer research, Universal Energy System and Dr. Agnes S. Bain (on site program coordinator for UES) for their help to me in housing, administrative and directional aspects of this program.

The time spent in the past summer was rewarding and the research program on high temperature superconducting films was challenging. Dr. Alvin Drehman provided me with many valuable samples of high temperature superconducting thin films and taught me the techniques of RF sputtering and the electrical characterization of the samples. The skill that Maurice Dumais has in producing SEM micrographs and interpreting them belongs only to a true professional. The identification of X–Ray diffraction peaks by Jane Horrigan is amazingly powerfull. The friendly atmosphere created for me by Joseph Hutta, John Fitzgerald and Bill Ewing is very much appreciated. The discussions held in the high temperature superconductivity group biweekly meeting were stimulating and beneficial to me. Special thanks go to Mike Suscarage, Drs. Nicholas Yannoin and Harold Roth.

I. *Introduction*

Since the announcement of superconductivity in Y–Ba–Cu oxides above 92K, enormous worldwide activity in preparation and characterization of the new oxide superconductors has happened.[1] An unprecedented effort by many research groups was to explore the physical mechanisms underlying the superconductivity phenomenon and its technological applications. The preparation of bulk superconducting oxide samples using conventional ceramic techniques has been well established and reproduced by many groups. However, the preparation of thin films of the superconducting materials for device and circuit applications is a much more difficult job due to substrate effects and the relatively large surface to volume ratio, i.e., surface effects. There are many techniques to synthesize the Y–Ba–Cu–O material in the thin film form. These include Molecular Beam Epitaxy, electron beam co–evaporation, pulsed laser evaporation, and sputtering. Among these different techniques, the single target RF glow discharge sputtering is especially challenging because of some of its unique effects; substrate heating, resputtering and stoichiometric deposition. Nevertheless, high quality thin films were fabricated successfully by single target RF sputtering. In this report, we studied the surface morphology and near surface chemical composition of the RF sputtered Y–Ba–Cu–O thin films on $SiTiO_3(001)$ substrates by Scanning Electron Microscopy (SEM), Scanning Tunneling Microscopy (STM) and Auger Electron Spectroscopy (AES) Depth Profile. For a comparison, similar studies on the bulk Y Ba_2 Cu_3 O_7 were also performed where the bulk composition was determined by the Energy Dispersive X–Ray Analysis (EDX) instead of AES.

II. *Objectives of the Research Effort*

The research objectives are:

1. To grow high temperature (>92K) superconducting (HTSC) thin films (1 to 2 μm thick) on different insulating substrates.
2. To characterize the electrical, chemical and geometrical properties of the

HTSC thin films as well as the surface morphology and near surface composition of the films.

The approaches to achieve these objectives are:

1. An existing RF sputtering machine will be used to sputter different bulk concentration targets to grow Y Ba_2 Cu_3 O_7 thin films on MgO and $SrTiO_3$ substrates. The optimum sputtering conditions will be determined experimentally by varying:
   a) target chemical compositions,
   b) bias voltages on both the target and the substrate,
   c) distance between the target and the substrate.
2. a) The electrical property of HTSC thin films will be characterized by the four–point probe analysis. The resistivity vs temperature curve can be measured and the onset of superconducting temperature as well as the transition region can be determined.
   b) The surface morphology of HTSC thin films will be examined by the Scanning Electron Microscope and the Scanning Tunneling Microscope. The crystalline quality of HTSC thin films will be measured by the X–ray diffraction technique.
   c) The near surface chemical composition of HTSC thin films will be measured by Auger Electron Spectroscopy depth profiling. The bulk chemical composition of HTSC thin films will be determined by Energy Dispersive X–ray analysis.

III. Sample Preparation

Single–target RF sputtering using a nominal YBaCu composition of 1:3:4 was carried out in a stainless steel chamber that was turbo–pumped to a base pressure of $3*10^{-6}$ torr. Sputtering was done in an Ar + (16–20)% O_2 atmosphere onto a substrate platform. The

target to substrate platform distance was about 3 cm, the sputtering power was 160 watts, the bias voltage was –30 volts D.C. Targets were fabricated by mixing reacted powders of $Y_1\ Ba_2\ Cu_3\ O_x$ and $BaCuO_2$ and pressing the mixture in a 5000 psi press into discs of 12.5 cm diameter and <1 cm thick. These discs were sintered in air for 16 hours at 930°C.

Films $\gtrsim$ 1μm thick were grown on $SrTiO_3$ (001) substrates. The surface of $SrTiO_3$ has been x–ray examined to be the (001) orientation and was degreased by methanol before it was inserted into the growth chamber. Annealing of the films was carried out by heating the films up to 850°C in a quartz tube furnace with a continuous flow of oxygen. Films were held at 850°C for 30 min. and cooled slowly down to 400°C at a cooling rate of ~ 1.5°C/min.

IV. Characterization Results and Discussions

A. Resistance vs Temperature and X–Ray Diffraction

An important method for studying the quality of films is to measure the resistance versus temperature curve R(T). These measurements were done by the four point probe technique in a liquid nitrogen cooled cell. The resultant R(T) curves of the 0.9μm film / $SrTiO_3$ (001), 2.4 μm film / $SrTiO_3$ and the bulk compound are shown as curves A, B and C in Fig. 1 respectively. The R(T) curve reveals the onset temperature T_c of superconducting and the width of the transition, ΔT_c, or the tail in the resistive transition. The T_c and ΔT_c are sensitive to the material parameters and the fabrication processes. All the bulk materials show reproducible T_c (~ 92K) and a narrow transition width ΔT_c (~ 4K). These bulk materials were examined by X–Ray diffraction and appeared to have identical structure: Orthorhombic $YBa_2Cu_3O_7$. However, the films show different T_c and ΔT_c depending on different growth conditions. It is commonly thought that a board transition is often related to the existence of phases other than the 1–2–3 phase and a tail in the transition may be the result of off–stoichrometry, incorrect annealing and substrate

interaction during the high temperature annealing procedure. As we will discuss later, a surface effect associated with an off–stoichiometry region near the surface region of a finite size grain may contribute to the lower T_c and wider ΔT_c and sets a lower critical thickness of a superconducting thin film.

B. Surface Morphology

Scanning Electron Micrographs of annealed films magnified at 500 times are shown in Fig. 2a (0.9 μm thick) and Fig. 2c (2.5 μm thick). They appear smooth compared with the SEM micrograph of a fractured bulk material shown in Fig. 2e which is rough and porous. Much higher magnification (10,000 X) micrographs show that there are submicron small islands on the 0.9 μm thick film (Fig. 2b) and islands of a couple microns in the 2.5 μm thick film (Fig. 2d) in contrast to much larger, > 5 μm, grains of rectangular plate like structures in the bulk material (Fig. 2f). For magnification higher than 10,000 times, SEM micrographs showed poor contrast, so we examined the surfaces using a Scanning Tunneling Microscope. Fig. 3a shows the image of the film surface over an area of 3000Å x 3000Å taken in a normal atmosphere at room temperature. Over one hundred scans were performed on each sample. Most of them show terraces varying from a few hundred Å to submicrons and separated by steps of various heights (less than 1000Å). The terraces also appeared to be rectangular in shape. Similar results were found on fractured bulk materials where one of the rectangular shape grain is shown in Fig. 3b. These STM and SEM images show that the microstructures of the superconducting phase of the annealed thin film and the bulk material are similar except for the sizes of the grains. It will be shown later that the surface effect on the superconductivity is closely related to the grain size.

C. Chemical Composition Determination

Energy Dispersive X–Ray Analysis was used to determine the bulk chemical compositions of Y, Ba and Cu in the annealed thin films and in bulk materials. Table 1 lists the ratios of Ba/Y and Cu/Y for both the thin film and the bulk material. If we just take the ball park figure, the bulk composition is about 1–2–3. However, in the thin film, there is a deficiency of Ba if we compare its Ba/Y ratio (1.51) with that of the bulk ratio (2.28). Also, the Cu/Y ratio of the film (3.50) is slightly less than Cu/Y ratio of the bulk (3.84).

For the surface and near surface chemical composition studies, we have used inert gas ion sputtering to obtain the Auger depth profiles. The AES peak to peak heights of four elements vs sputtering time are shown in Fig. 4 and Fig. 5 for the annealed thin film and the bulk material respectively. The results in common are:

1. There are heavy carbon and chlorine contaminations at the surfaces and less contaminations below the surfaces of both thin film and fractured bulk material (not shown in Figs. 4 and 5). The heavy contaminations are removed after 1 minute sputtering. The sputtering rate is approximately 10Å/min.
2. At about 1000Å deep below the surface, the Ba/Y, Cu/Y and O/Y ratios are stabilized and their ratios are listed in Table 1. The Ba/Y ratio of the film (1.5) is lower than that of the bulk (1.9). Also, Cu/Y ratio of the film (1.2) is slightly less than Cu/Y ratio of the bulk (1.3). These AES results are consistent with that of the EDX.

However, one striking difference between the film and the bulk material was found at the near surface region of the film, i.e., at about 10Å deep into the film, the Ba/Y ratio is less than the Cu/Y ratio. At about 300Å deep, the Ba/Y ratio is about equal to the Cu/Y ratio.

After 300Å, the Ba/Y ratio is higher than the Cu/Y ratio and both ratios stabilized at about 500Å (See Fig. 4). The off–stoichiometry at the surface, the switching of the magnitude of compositional ratios and/or the gradually approaching of asymptotic compositional ratios have been found on many thin films we tested. These imply that there is a composition transition region near the surface of the film. This is in contrast to the depth profile obtained at the near surface region of the fractured bulk material (Fig. 5) where there is no thick compositional transition layers. All the compositions approach asymptotic values almost within 50Å deep into the material. The findings on the thin film implies that there is a critical thickness for a thin film to be superconducting. This critical thickness probably has to be at least twice thicker than the thickness of the compositional transition layers, i.e., roughly 1000Å. Any 1–2–3 film with a thickness less than 1000Å will contain a large portion of off–stoichiometry material near the surface region which may not be superconducting. In addition to the off–stoichiometry detected by AES depth profiles near the surface region, we also observed from SEM that if the average islands in the thin film is in the submicrons range (See Fig. 2b) then the R(T) curve has a lower onset critical temperature T_c and a very board ΔT_c (see curve A in Fig. 1) in contrast to a high T_c and a narrow ΔT_c (see curve B in Fig. 1) associated with islands of a couple microns (see Fig. 2d). If the grain size of the film can reach several microns in size as in the bulk, then a 92K T_c and a sharp ΔT_c is expected. The surface effects on a thin film supports why the T_c and critical current density J_c of films are thickness dependent and the drastic decrease of T_c and J_c happens at a film thickness less than 2000Å as observed by H. Akoh et al.[2] Why is there a off–stoichiometry near the surface region of the film? It is known that after annealing, a variety of compounds in precipitate form are often present at or near the surface, e.g. copper oxides, barium copper oxides and yttrium oxides.[3] Also, water corrosion results in the fine $Ba(OH)_2$ and $BaCO_3$ microcrystals on the surface[4]. These oxides and corrosion products may contribute to the off–stoichiometry which is observed in the AES depth profile. It is also known that an enrichment of a chemical element near the surface implies that the heat of segregation,

defined as the change in enthaply that occurs when a solute atom is exchanged between a bulk and surface site is negative. There exists a graphical prediction of segregation proposed by Hamilton[5] based on extensive works of Miedema and co–workers[6] on the heats of solution of binary alloys, and works well for both substitutional and interstitial alloys. However, the Y Ba Cu O is a complex multicomponent, multiphase system and we did not attempt to apply Miedema and co–workers' theory to this system. In practice, we always observe that Ba and Cu are enriched but Y is deficient near the surface region compared to the bulk equilibrium compositions.

Another interesting thing we found when we tried to convert the Auger peak to peak height of a certain element to the atomic concentration at 1000Å deep below the surface using the sensitivity factors (Y = 0.108; Ba = 0.12; Cu = 0.2) provided by Perkin Elmer company is that the atomic concentration of the bulk material is 1:1.8:0.7. In order to obtain the 1:2:3 ratio which is indicated by the result of EDX analysis, the sensitivity factor of Cu has to be reduced from 0.2 to about 0.05, a factor of 4 smaller than the sensitivity factor associated with a pure Cu sample. This implies that the Auger yield and sputtering yield of Cu in a pure Cu sample is quite different from that of Cu compounds. A literature search on chemical composition determination of superconducting materials using AES reveals that a couple results[7],[8] gave the Cu concentration ranging from 10% to 20% which is low compared with the 50% bulk value. We therefore suggest an empirical conversion factor of 4 (or reducing the sensitivity factor of Cu by 4) may be useful in calculating quantitative atomic concentration of Cu in a Y Ba Cu O compou

V. *Recommendations*

In the sample preparation, I suggest that the substrate orientation and perfection be characterized before a thin film is deposited. It is known that the substrate orientation and the defects on a surface would affect the nucleation and growth of the thin film. It is evident that carbon and chlorine were detected in AES profiles of every sample we tested, therefore

pressure in the growth chamber needs to be pumped to as low as possible in order to cut down the chemical reactions and contaminations due to the residual gases (mostly water and hydrocarbons) during the growth of thin films.

The off–stoichiometry found at the surface and near the surface region forms a nonsuperconducting layer and affects drastically the superconducting properties of thin films which have submicron size grains, e.g., decreases the onset of superconducting temperature and widens the transition region. This effect has set a lower limit on the minimum thickness required for a superconducting thin film. Right now, our findings indicate a critical thickness of about 1000Å. This critical thickness may be reduced by using fast quenching to the temperature of compound formation and minimizing the off–stoichiometry which result from elements segregation in films. A follow up proposal will be submitted in the near future to investigate the surface effects of superconducting thin films

1. grown under different kinetic reaction conditions,
2. grown on different substrates (e.g. MgO and $SrTiO_3$, Si and etc.),
3. as well as epitaxial thin films grown by the multitarget RF sputtering technique and characterized by X–Ray Pole Figure Analysis.

References

1. M.K. Wu, J.K. Ashburn, C.J. Torng, P.H. Hor, K.L. Meng, L. Gao, Z.J. Huang, Y.Q. Wang and C.W. Chu, Phys. Rev. Lett. 58, 908 (1987).
2. H. Akoh, F. Shinoki, M. Takahashi, and S. Takada, Appl. Phys. Lett. 52, 1732 (1988).
3. R.B. Laibowitz, AIP Conf. Proc. 165, 2 (1988).
4. I. Kirchner, T. Trager, J. Matrai, T. Porjesz and J. Gyorgy, Physica C 153–155, 1419 (1988).
5. J.C. Hamilton Phys, Rev. Lett. 42, 989 (1979).
6. A.R. Miedema, Z. Metallkd. 69, 455 (1978); A.R. Miedema, Philips Tech. Rev. 30, 217 (1976); R. Boom, F.R. deBoer, and A.R. Miedema, J. Less–Common Met. 46, 271 (1976).
7. L. Cota, L. Morales de la Garza, G. Hirata, L. Martinez, E. Orozco, E. Carrillo, A. Mendoza, J.L. Albarran, J. Fuentes–Maya, J.L. Boldu, J.G. Perez–Ramirez, R. Perez, J. Reyes Gasga, M. Avalos and M. Jose–Yacaman, J. Mater. Res. 3, 417 (1988).
8. D. Pavuna, W. Baer, H. Berger, H.J. Mathieu, A. Vogel, M. Schmidt, V. Gasparov, M. Affronte, F. Vasey, F.K. Reinhart, Physica C 153–155, 1449 (1988).

Table I

		FILM(0.9μm)	BULK
EDX	Y/Y	1.00	1.00
	Ba/Y	1.51	2.28
	Cu/Y	3.50	3.84
		FILM(0.9μm)	BULK
AES	Y/Y	1.0	1.0
	Ba/Y	1.5	1.9
	Cu/Y	1.2	1.3
	O/Y	5.5	5.0

Figure Captions

Fig. 1 Temperature dependence of the resistivity for (A) RF sputtered Y Ba Cu O 0.9μm thick film on $SrTiO_3$ (001) (B) 2.5 μm thick film on $SrTiO_3$ (C) bulk Y Ba Cu O compound.

Fig. 2 Scanning electron micrographs of (a) and (b) a 0.9μm thick Y Ba Cu O thin film on a $SrTiO_3$ (001) substrate, of (c) and (d) 2.5μm thick film on $SrTiO_3$, of (e), (f) fractured bulk Y Ba Cu O compound.

Fig. 3 Topographic STM image of a (a) 4000Å x 4000Å area of Y Ba Cu O thin film (b) 3000Å x 3000Å area of fractured bulk Y Ba Cu O compound.

Fig. 4 Auger depth profile of 0.9μm thick Y Ba Cu O thin film. The sputtering rate is about 10Å/min .

Fig. 5 Auger depth profile of fractured Y Ba Cu O compound. The sputtering rate is about 10Å/min.

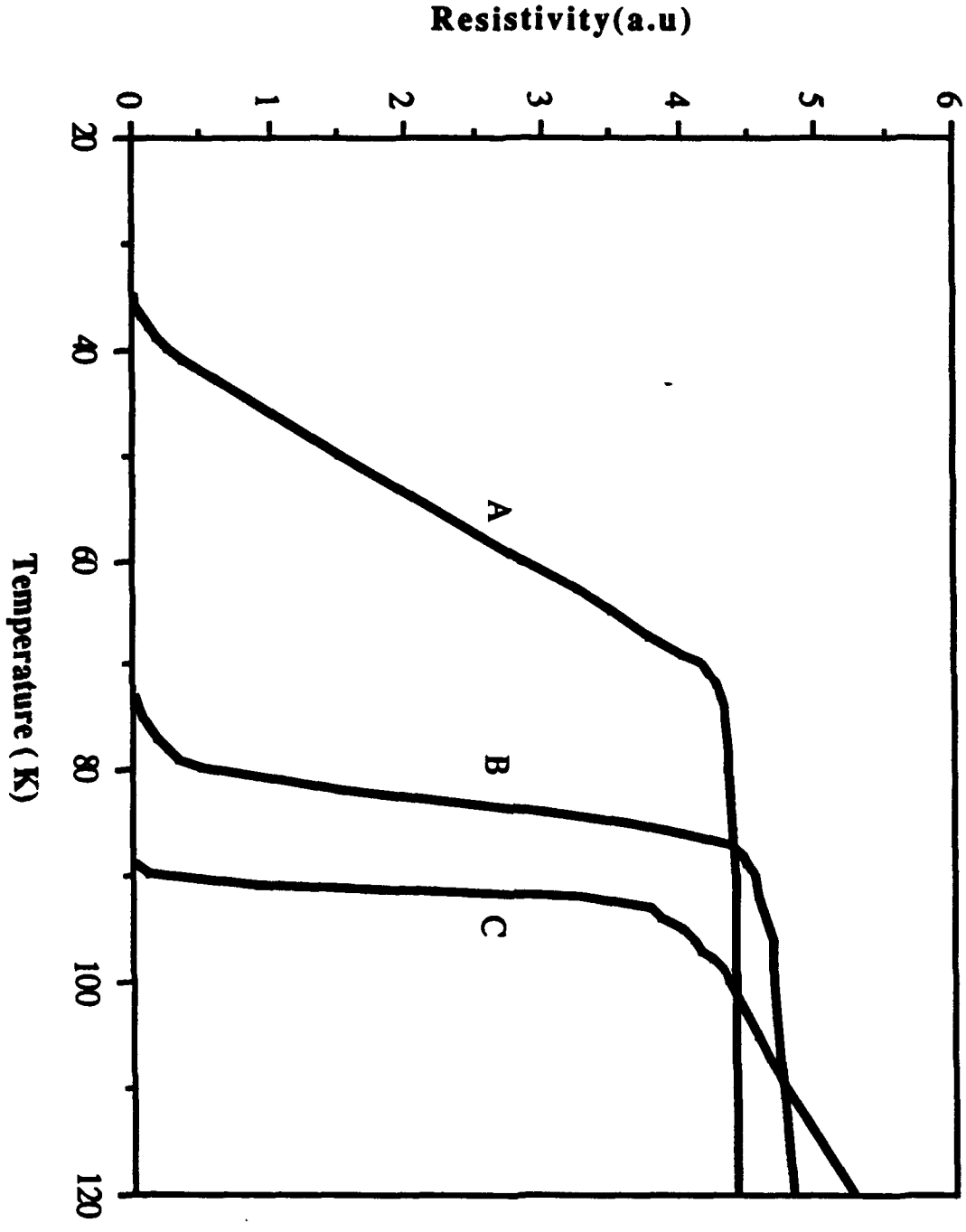

Fig.1

a)

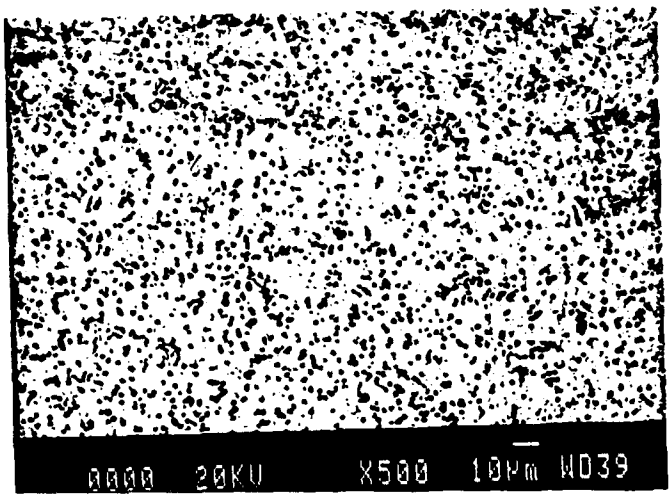
0000 20KV X500 10μm WD39

b)

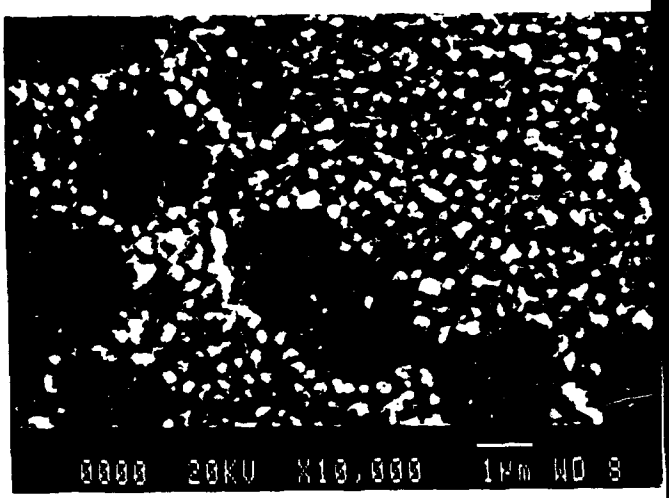
0000 20KV X10,000 1μm WD 8

c)

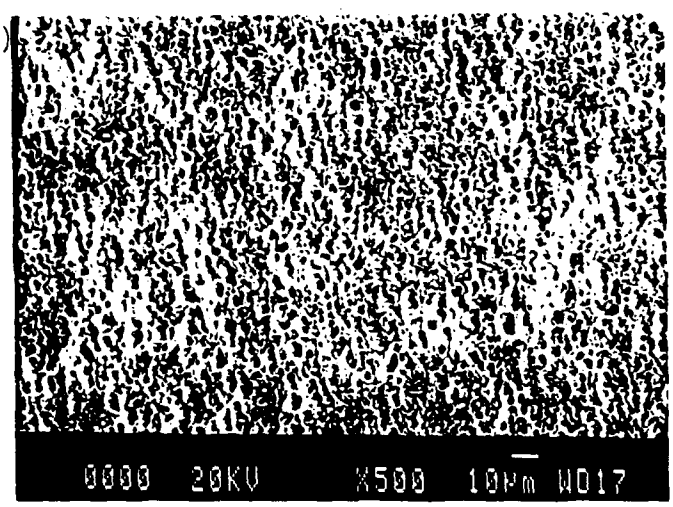
0000 20KV X500 10μm WD17

d)

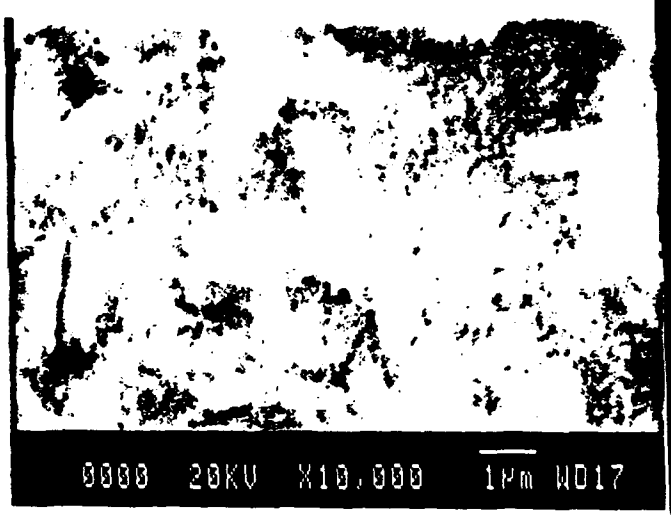
0000 20KV X10,000 1μm WD17

e)

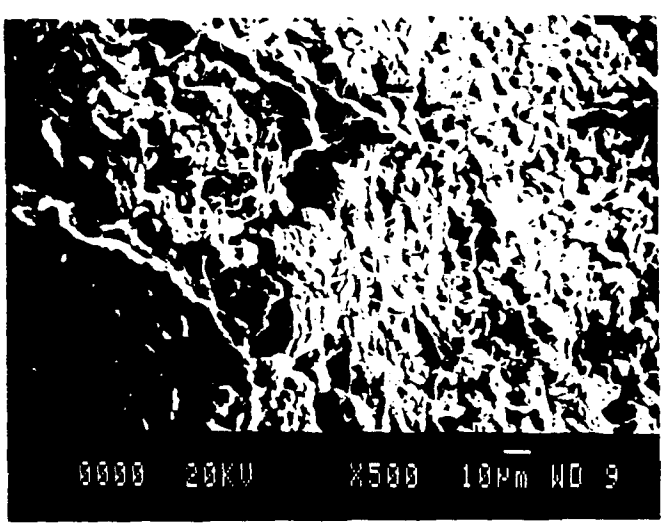
0000 20KV X500 10μm WD 9

f)

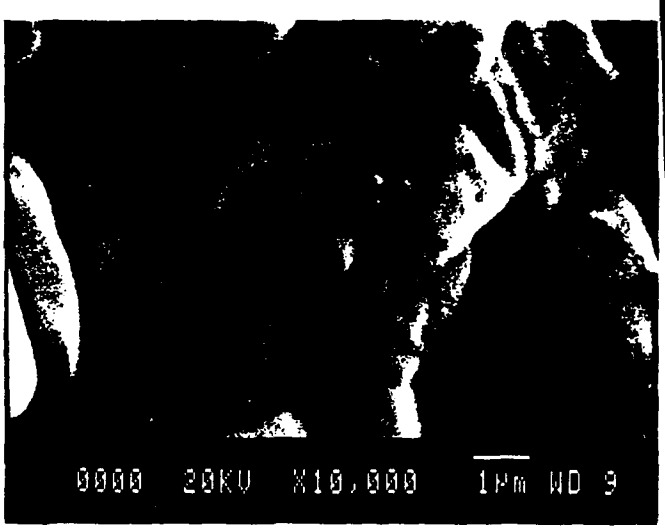
0000 20KV X10,000 1μm WD 9

 Fig.2

a)

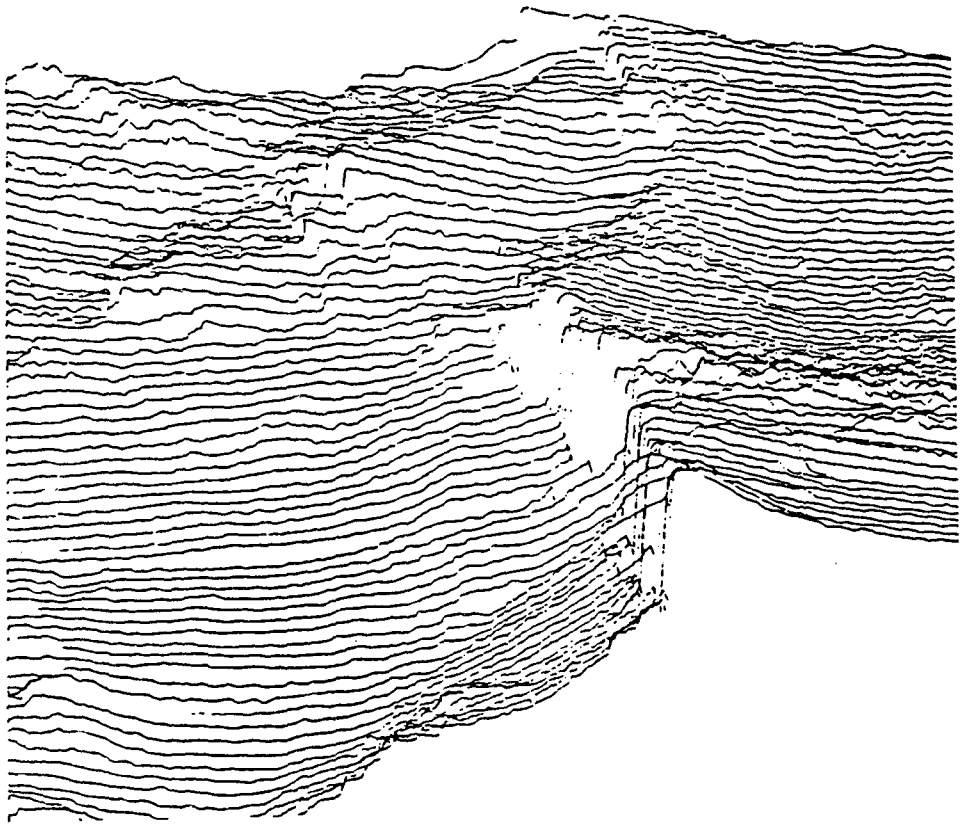

b)

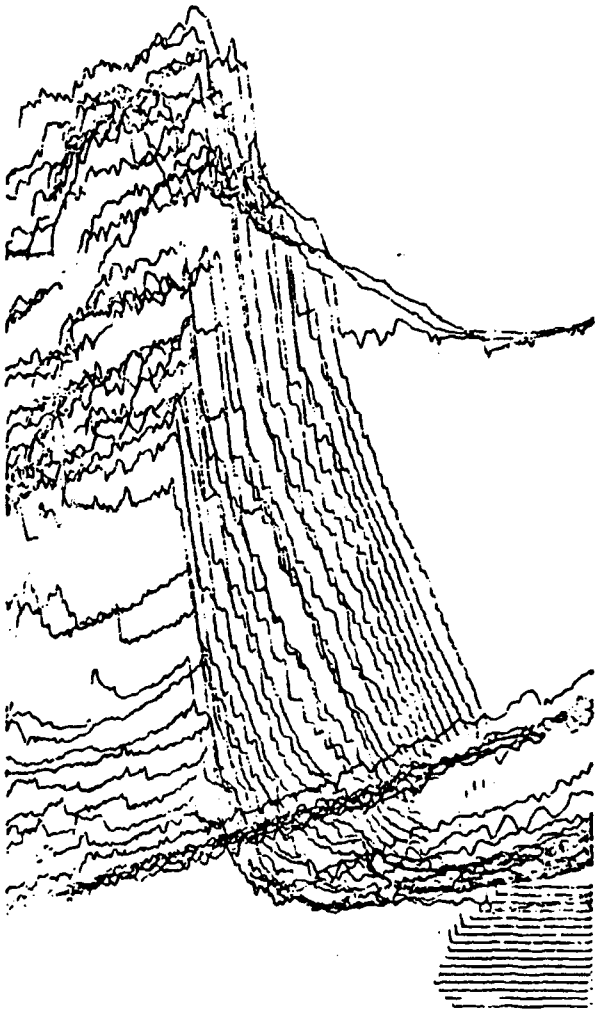

Fig.3

63-18

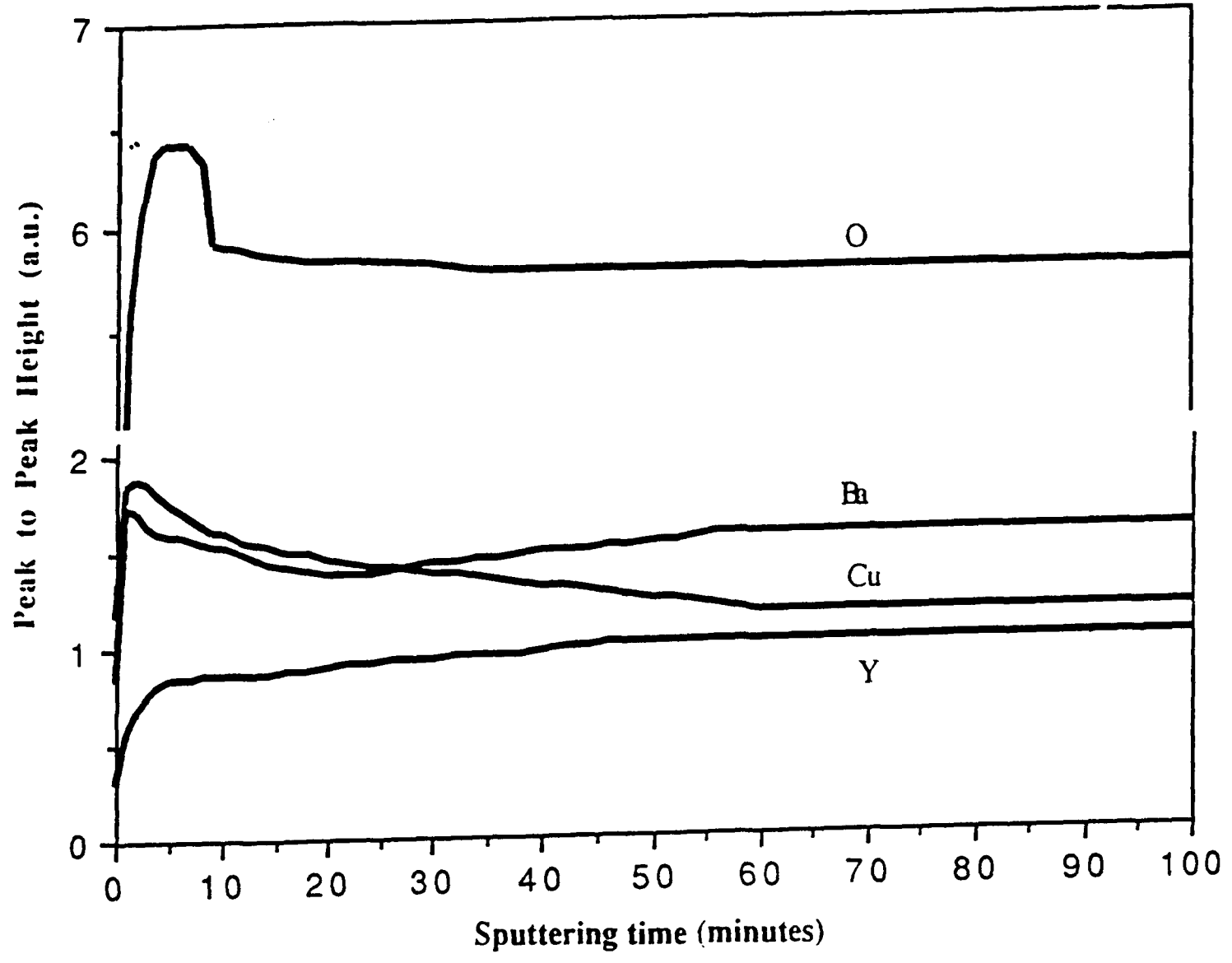
Peak to Peak Height (a.u.)
7
6
2
1
0
O
Ba
Cu
Y
0
10
20
30
40
50
60
70
80
90
100
Sputtering time (minutes)

Fig.4

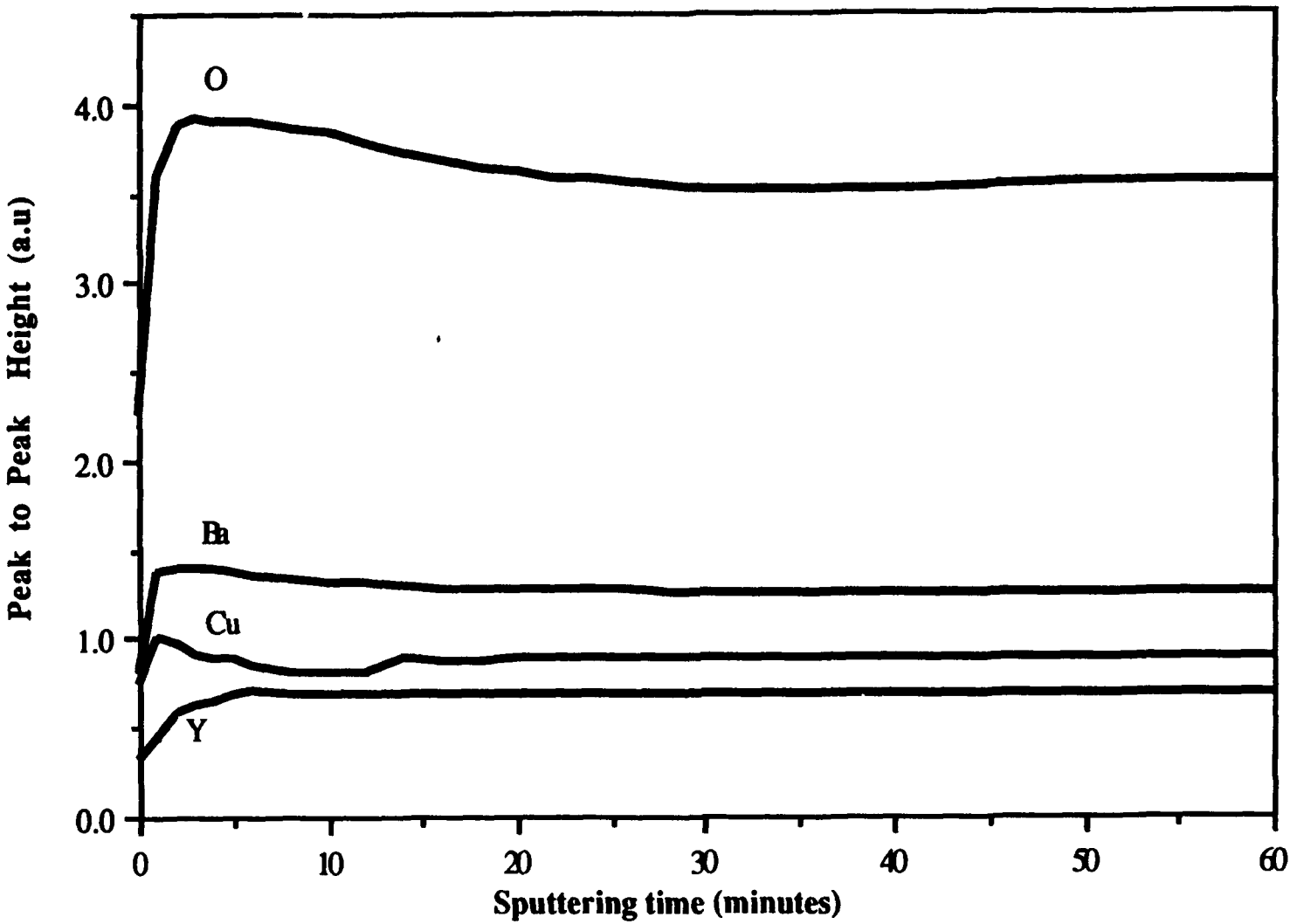
O
Ba
Cu
Y
Peak to Peak Height (a.u)
0.0
1.0
2.0
3.0
4.0
0
10
20
30
40
50
60
Sputtering time (minutes)

Fig.5

1988 USAF-UES SUMMER FACULTY RESEARCH PROGRAM

Sponsored by the

AIR FORCE OFFICE OF SCIENTIFIC RESEARCH

Conducted by the

Universal Energy Systems, Inc.

FINAL REPORT

Prepared by:	Dr. Lane H. Clark
Academic Rank:	Assistant Professor
Department and University:	Department of Mathematics and Statistics University of New Mexico
Research Location:	Air Force Weapons Laboratory/NTATT Kirtland Air Force Base Albuquerque, New Mexico 87117
USAF Researcher:	Dr. Carl E. Baum

Date:	30 September, 1988
Contract No:	F49620-87-R-0004

Realization of Sublayer Relative Shielding Order in Electromagnetic Topology

by

Lane H. Clark

Abstract

A fundamental problem in qualitative electromagnetic topology is the construction of the interaction sequence diagram given a preassigned shielding between all pairs of primary sublayers. Idealizing this into one of relative shielding order makes this problem amenable to graph theoretic treatment. A constructive characterization of the relative shielding order matrix for primary sublayers of an electromagnetic topology defined to the level of layers and sublayers is given. In addition, all possible sublayer topologies with relative shielding order at most 5 are explicitly given.

Acknowledgements

I wish to thank the Air Force Office of Scientific Research for sponsorship of this research and Universal Energy Systems for their administration of this program. I also wish to thank Dr. Carl E. Baum for suggesting the research area and for his support and encouragement.

I. Introduction

Electromagnetic (EM) topology is a mathematical abstraction of the electromagnetic design of systems and is primarily concerned with the electromagnetic interaction process [1,2,3,5]. Given system requirements, one can hopefully find an appropriate electromagnetic topology and assign design specifications to the parts of the system. For an electromagnetic topology defined to the level of layers and sublayers we abstract this by introducing a relative shielding order (the number of subshields crossed in passing between two sublayers) applied to selected sublayers–the primary sublayers–and ask whether an electromagnetic topology exists with these specifications.

In [2] it was shown that for the special case that the relative shielding order between all pairs of primary sublayers was constant R the results were quite simple. In particular, R could only be even and the case $R = 2$ was of practical significance. In this paper we characterize the relative shielding order matrix for the primary sublayers of an EM topology when the primary sublayers are extremal (leaves of the dual graph), when the primary sublayers include the extremal sublayers together with specified internal sublayers, when all sublayers are primary and when the primary sublayers are arbitrary.

Corresponding to the EM topology is the interaction sequence diagram. This diagram is essentially the dual graph of the electromagnetic topology and, as such, may be analyzed from the graph-theoretic vantage. For an EM topology defined to the level of layers and sublayers, the dual graph is particularly nice since it is a tree and our relative shielding order matrix is the distance-matrix applied to selected vertices–the primary vertices–of this tree. We then characterize the relative shielding order matrix for the primary sublayers of an EM topology by solving the analogous problem for the dual graph. Our characterization gives a recursive procedure for constructing the interaction sequence diagram and, hence, an EM topology.

Having determined necessary and sufficient conditions for the realization of EM topologies subject to various constraints on the primary sublayers, illustrative examples are given. In particular, if the maximum relative shielding order R_{max} among the primary sublayers is given, all possible trees and associated EM topologies, including differences introduced by inversion, are exhibited. This is treated for R_{max} at most 5 for which the trees and dual EM topologies are not overly complicated.

For electromagnetics, see [2,5] for a discussion of EM topology defined to the level of layers and sublayers, the relative shielding order matrix for primary sublayers and inversion of the interaction sequence diagram at a vertex and see [3] for a discussion of EM topology defined to the level of elementary volumes, which is beyond the scope of this paper.

For graph theory see [4] for a discussion of trees and distance matrices.

II. Objectives

In [2] it was shown that for the special case that the relative shielding order between all pairs of primary sublayers was constant R the results were quite simple. In particular, R could only be even and the case $R = 2$ was of practical significance. In this paper we characterize the relative shielding order matrix for the primary sublayers of an EM topology when the primary sublayers are extremal (leaves of the dual graph), when the primary sublayers include the extremal sublayers together with specified internal sublayers, when all sublayers are primary and when the primary sublayers are arbitrary.

III. Realization of Specified Sublayer Relative Shielding Order Matrices

Recall that an electromagnetic topology is given by partitioning Euclidean space into a set $\{V_\lambda\}$ of nested volumes called layers where each V_λ is composed of one or more subvolumes $\{V_{\lambda,\ell}\}$ called sublayers and by separating layers V_λ and $V_{\lambda+1}$ by disjoint closed surfaces $S_{\lambda;\lambda+1}$ called shields where each $S_{\lambda;\lambda+1}$ is composed of one or more closed surfaces $\{S_{\lambda,\ell;\lambda+1,\ell'}\}$ called subshields [1,2,3,5]. We construct the interaction sequence diagram from the EM topology by placing a vertex in each sublayer and joining two sublayers with an edge provided they share a common subshield. (See Figure 1.) Note that the above construction is equivalent to the usual formulation of the interaction sequence diagram as we identify each edge with the appropriate subshield in place of subdividing each edge and then identifying the new vertex with the appropriate subshield.

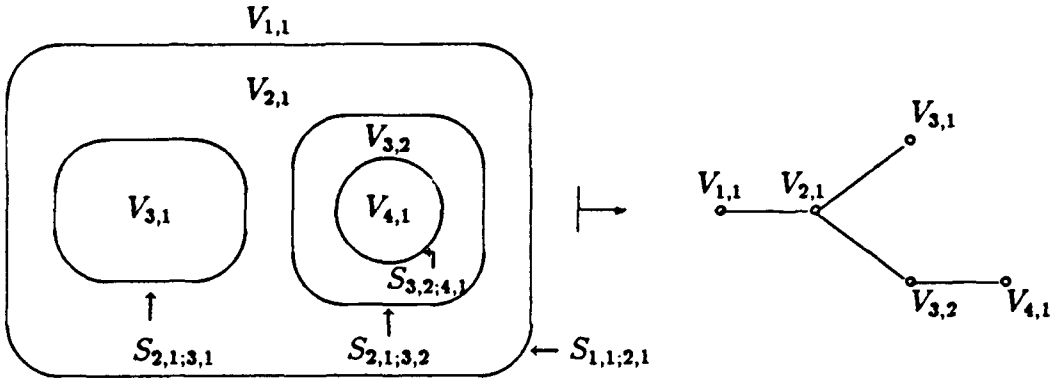

Figure 1.

For example, sublayers $V_{1,1}$, $V_{3,1}$ and $V_{4,1}$ are said to be extremal in the EM topology since they are leaves (endvertices) in the interaction sequence diagram.

Recall that the distance $d_T(v, w)$ between vertices v and w of the interaction sequence diagram T is the number of edges traversed in traveling from one vertex to the other. We assume that the weights of all subshields have been normalized to 1 so that the relative shield-

ing order between sublayers in the EM topology is the distance between the corresponding vertices in the interaction sequence diagram.

We designate certain sublayers of the EM topology as primary sublayers $\Delta^{(1)}$ and the corresponding vertices of the interaction sequence diagram as primary vertices and note that the relative shielding order matrix among primary sublayers is the distance-matrix among the corresponding vertices of the interaction sequence diagram. (See Table 1 where we refer to Figure 1.)

	$V_{1,1}$	$V_{3,1}$	$V_{4,2}$	
$V_{1,1}$	0	2	3	For primary sublayers
$V_{3,1}$	2	0	3	$\Delta^{(1)} = \{V_{1,1}, V_{3,1}, V_{4,2}\}$;
$V_{4,2}$	3	3	0	the extremal sublayers.

and

	$V_{1,1}$	$V_{2,1}$	$V_{3,1}$	$V_{3,2}$	$V_{4,1}$	
$V_{1,1}$	0	1	2	2	3	
$V_{2,1}$	1	0	1	1	2	For primary sublayers
$V_{3,1}$	2	1	0	2	3	$\Delta^{(1)} = \{V_{1,1}, V_{2,1}, V_{3,1}, V_{3,2}, V_{4,1}\}$;
$V_{3,2}$	2	1	2	0	1	all sublayers.
$V_{4,1}$	3	2	3	1	0	

Table 1.

Relative Shielding Order Among Primary Sublayers.

Let $\Upsilon_{m\times m}$ denote the set of $m \times m$ symmetric matrices whose entries are nonnegative integers and which are zero precisely on the main diagonal. For $D \in \Upsilon_{m\times m}$ and distinct $1 \leq i_1, \ldots, i_s \leq m$, we call the $s \times s$ matrix $D_{i_1,\ldots,i_s}$ obtained from the $i_1^{\text{st}}, \ldots, i_s^{\text{th}}$ rows and columns of D a *principal* $s \times s$ submatrix of D. For example, if D is given below

$$D = \begin{bmatrix} 0 & 1 & 2 & 2 & 3 \\ 1 & 0 & 1 & 1 & 2 \\ 2 & 1 & 0 & 2 & 3 \\ 2 & 1 & 2 & 0 & 1 \\ 3 & 2 & 3 & 1 & 0 \end{bmatrix}$$

then

$$D_{1,2,4} = \begin{bmatrix} 0 & 1 & 2 \\ 1 & 0 & 1 \\ 2 & 1 & 0 \end{bmatrix}$$

is a principal 3×3 submatrix of D obtained from the first, second and fourth rows and columns of D.

A. Primary Sublayers are Extremal Sublayers

In this section we characterize the symmetric matrices that are relative shielding order matrices of an EM topology where the primary sublayers are extremal by characterizing the symmetric matrices that are distance-matrices for the leaves of a tree.

For $D = (d_{i,j}) \in \Upsilon_{m \times m}$, we say D is *leaf-realizable* iff there exists a tree T with precisely m leaves labelled $\{1, \ldots, m\}$ satisfying $d_T(i,j) = d_{i,j}$ for $1 \leq i, j \leq m$.

Theorem 1. Let $D = (d_{i,j}) \in \Upsilon_{3 \times 3}$. The following are equivalent.

(a) D is leaf-realizable.

(b) $b_p \in Z_p^+ = \{1, 2, 3, \ldots\}$ for $p \in \{1, 2, 3\}$ where

$$b_p = \begin{cases} (d_{i,j} + d_{i,k} - d_{j,k})/2 & \text{for } p = i \\ (d_{p,i} + d_{p,q} - d_{q,i})/2 & \text{for } \{p, q\} = \{j, k\}. \end{cases}$$

Remark. Condition (b) expresses that the branches a_1, a_2, a_3 of the tree have positive integral length.

Corollary 1.1. If $D \in \Upsilon_{3\times 3}$ is leaf-realizable by a tree T then T is unique.

Theorem 2. Let $D = (d_{i,j}) \in \Upsilon_{4\times 4}$. The following are equivalent.

(a) D is leaf-realizable.

(b) For some $\{i, j, k, \ell\} = \{1, 2, 3, 4\}$ we have

(i) $d_{i,k} + d_{j,\ell} = d_{i,\ell} + d_{j,k}$,

(ii) $b_p \in \mathbf{Z}^+$ for $p \in \{1, 2, 3, 4\}$ where

$$b_p = \begin{cases} (d_{p,j} + d_{p,k} - d_{j,k})/2 & \text{for } p \in \{i, \ell\} \\ (d_{p,i} + d_{p,\ell} - d_{i,\ell})/2 & \text{for } p \in \{j, k\}, \end{cases}$$

(iii) $d_{i,\ell} - b_i - b_\ell \in N = \{0, 1, 2, \ldots\}$.

Remark. Condition b(i) expresses the consistency of the system, condition b(ii) expresses that the branches a_i, a_j, a_k, a_ℓ have positive integral length and condition b(iii) expresses that e has nonnegative integral length.

Corollary 2.1. If $D \in \Upsilon_{4\times 4}$ is leaf-realizable by a tree T then T is unique.

Denote the tree whose leaves are precisely $i_1, \ldots, i_s$ by $T\{i_1, \ldots, i_s\}$. For a tree T containing leaves $i_1, \ldots, i_s$, let $T_{i_1,\ldots,i_s}$ denote the subtree of T whose leaves are precisely $i_1, \ldots, i_s$.

We give now the main result of this section.

Theorem 3. $D = (d_{i,j}) \in \Upsilon_{m\times m}$ is leaf-realizable iff all principal 4×4 submatrices of D are leaf-realizable.

Corollary 3.1. $D = (d_{i,j}) \in \Upsilon_{m\times m}$ is leaf-realizable iff for all $1 \le i_1 < i_2 < i_3 < i_4 \le m$ some $\{i,j,k,\ell\} = \{i_1, i_2, i_3, i_4\}$ satisfies

(i) $d_{i,k} + d_{j,\ell} = d_{i,\ell} + d_{j,k}$,

(ii) $b_p \in \mathbf{Z}^+$ for $p \in \{1,2,3,4\}$ where

$$b_p = \begin{cases} (d_{p,j} + d_{p,k} - d_{j,k})/2 & \text{for } p \in \{i,\ell\} \\ (d_{p,i} + d_{p,\ell} - d_{i,\ell})/2 & \text{for } p \in \{j,k\}, \end{cases}$$

(iii) $d_{i,\ell} - b_i - b_\ell \in \mathbf{N}$

Remark. See the remark following Theorem 2 for a discussion of conditions (i), (ii), (iii).

Corollary 3.2. If $D \in \Upsilon_{m\times m}$ is leaf-realizable by a tree T then T is unique.

Remark. The proof of Theorem 3 is constructive and gives an algorithm for finding the tree T that leaf-realizes $D \in \Upsilon_{m\times m}$.

Leaf-Realizable Algorithm

1. Set $T_4 = T\{1,2,3,4\}$.
2. For $\ell \le m$, choose $1 \le i,j,k \le \ell - 1$ with $d_{T\{i,j,k,\ell\}}(x,\ell)$ as small as possible where x is the vertex of degree at least 3 closest to ℓ in $T\{i,j,k,\ell\}$.
3. Set $T_\ell = T_{\ell-1} \cup T\{i,j,k,\ell\}$.
4. Stop.

B. Primary Sublayers Include Extremal Sublayers and Specified Internal Sublayers

In this section we characterize the symmetric matrices that are relative shielding order matrices of an EM topology where the primary sublayers include the extremal sublayers by characterizing the symmetric matrices that are distance-matrices for at least the leaves of a tree.

For $D = (d_{i,j}) \in \Upsilon_{4\times 4}$ and $L \subseteq \{1,2,3,4\}$, we say D is *L-realizable* iff there exists a tree T with labelled vertices 1, 2, 3, 4 so that $L \subseteq V_1(T) \subseteq \{1,2,3,4\}$ and satisfying $d_T(i,j) = d_{i,j}$ for $i,j \in \{1,2,3,4\}$. Here $V_1(T)$ denotes the leaves of T.

Theorem 4. Let $D = (d_{i,j}) \in \Upsilon_{4\times 4}$ and $L \subseteq \{1,2,3,4\}$. The following are equivalent.

(a) D is L-realizable.

(b) For some $\{i,j,k,\ell\} = \{1,2,3,4\}$ we have

(i) $d_{i,k} + d_{j,\ell} = d_{i,\ell} + d_{j,k}$,

(ii) $b_p \in \mathbf{N}$ for $p \in \{1,2,3,4\} - L$ and $b_p \in \mathbf{Z}^+$ for $p \in L$ where

$$b_p = \begin{cases} (d_{p,j} + d_{p,k} - d_{j,k})/2 & \text{for } p \in \{i,\ell\} \\ (d_{p,i} + d_{p,\ell} - d_{i,\ell})/2 & \text{for } p \in \{j,k\}, \end{cases}$$

(iii) $d_{i,\ell} - b_i - b_\ell \in \mathbf{N}$.

Remark. Condition b(i) expresses the consistency of the system, condition b(ii) expresses that the branches a_i, a_j, a_k, a_ℓ have nonnegative integral lengths and condition b(iii) expresses that e has nonnegative integral length.

Corollary 4.1. If $D \in \Upsilon_{4\times 4}$ is L-realizable by a tree T then T is unique.

For $D = (d_{i,j}) \in \Upsilon_{(m+r)\times(m+r)}$, we say D is (m,r)-*realizable* iff there exists a tree T with precisely m leaves labelled $\{1,\ldots,m\}$ and (at least) r internal vertices labelled $\{m+1,\ldots,m+r\}$ satisfying $d_T(i,j) = d_{i,j}$ for $1 \le i,j \le m+r$ and we say D is r-*linear* iff for all $m+1 \le k \le m+r$ and for all $1 \le i \le m$ there exists $1 \le j \le m$ satisfying $d_{i,j} = d_{i,k} + d_{k,j}$. In words, D is r-linear iff for each internal vertex $m+1 \le k \le m+r$ and each leaf $1 \le i \le m$ there exists another leaf $1 \le j \le m$ with vertex k on the (i,j)-path in the tree.

For $D \in \Upsilon_{(m+r)\times(m+r)}$ and $E = D_{i_1,\ldots,i_s}$ where $1 \le i_1 < \cdots < i_s \le m+r$, let $L(E) = \{i_1,\ldots,i_s\} \cap \{1,\ldots,m\}$.

We give now the main result of this section.

Theorem 5. $D = (d_{i,j}) \in \Upsilon_{(m+r)\times(m+r)}$ is (m,r)-realizable iff D is r-linear and all principal 4×4 submatrices E of D are $L(E)$-realizable.

Corollary 5.1. $D = (d_{i,j}) \in \Upsilon_{(m+r)\times(m+r)}$ is (m,r)-realizable iff for all $1 \le i_1 < i_2 < i_3 < i_4 \le m+r$ some $\{i,j,k,\ell\} = \{i_1,i_2,i_3,i_4\}$ satisfies

(i) $d_{i,k} + d_{j,\ell} = d_{i,\ell} + d_{j,k}$,

(ii) $b_p \in \mathbf{N}$ for $p \in \{i_1,i_2,i_3,i_4\} - \{1,\ldots,m\}$ and $b_p \in \mathbf{Z}^+$ for $p \in \{i_1,i_2,i_3,i_4\} \cap \{1,\ldots,m\}$ where

$$b_p = \begin{cases} (d_{p,j} + d_{p,k} - d_{j,k})/2 & \text{for } p \in \{i,\ell\} \\ (d_{p,i} + d_{p,\ell} - d_{i,\ell})/2 & \text{for } p \in \{j,k\}, \end{cases}$$

(iii) $d_{i,\ell} - b_i - b_\ell \in \mathbf{N}$.

Remark. See the remark following Theorem 4 for a discussion of conditions (i), (ii), (iii).

Remark. The proof of Theorem 5 is constructive and gives an algorithm for finding the tree T that (m,r)-realizes $D \in \Upsilon_{(m+r)\times(m+r)}$.

(m, r)-Realizable Algorithm

1. Set $T_m = T\{1, \ldots, m\}$.
2. For $\ell \leq m + r$, choose $1 \leq i, j \leq m$ with $d_{i,j} = d_{i,\ell} + d_{\ell,j}$.
3. Set $T_\ell = T_{\ell-1}$ where the appropriate vertex has been labelled ℓ.
4. Stop.

C. All Sublayers are Primary Sublayers

In this section we characterize the symmetric matrices that are relative shielding order matrices of an EM topology where all sublayers are primary sublayers by characterizing the symmetric matrices that are distance-matrices for a tree.

For $D = (d_{i,j}) \in \Upsilon_{n \times n}$ and $1 \leq i \leq n$, let $d(i) = |\{1 \leq j \leq n : d_{i,j} = 1\}|$ and let $L(D) = \{1 \leq i \leq n : d(i) = 1\}$.

For $D = (d_{i,j}) \in \Upsilon_{n \times n}$, we say D is *tree-realizable* iff there exists a tree T with precisely n vertices labelled $\{1, \ldots, n\}$ satisfying $d_T(i, j) = d_{i,j}$ for $1 \leq i, j \leq n$ and we say D is *linear* iff $|L(D)| \geq 2$ and for all $k \notin L(D)$ and for all $i \in L(D)$ there exists $j \in L(D)$ satisfying $d_{i,j} = d_{i,k} + d_{k,j}$.

For $D \in \Upsilon_{n \times n}$ and $E = D_{i_1, \ldots, i_s}$ where $1 \leq i_1 < \cdots < i_s \leq n$, let $L(E) = \{i_1, \ldots, i_s\} \cap L(D)$.

We give now the main result of this section.

Theorem 6. $D = (d_{i,j}) \in \Upsilon_{n \times n}$ is tree-realizable iff D is linear and all principal 4×4 submatrices E of D are $L(E)$-realizable.

Corollary 6.1. $D = (d_{i,j}) \in \Upsilon_{n\times n}$ is tree-realizable iff for all $1 \leq i_1 < i_2 < i_3 < i_4 \leq n$ some $\{i, j, k, \ell\} = \{i_1, i_2, i_3, i_4\}$ satisfies

(i) $d_{i,k} + d_{j,\ell} = d_{i,\ell} + d_{j,k}$,

(ii) $b_p \in \mathbf{N}$ for $p \in \{i_1, i_2, i_3, i_4\} - L(D)$ and $b_p \in \mathbf{Z}^+$ for $p \in \{i_1, i_2, i_3, i_4\} \cap L(D)$ where

$$b_p = \begin{cases} (d_{p,j} + d_{p,k} - d_{j,k})/2 & \text{for } p \in \{i, \ell\} \\ (d_{p,i} + d_{p,\ell} - d_{i,\ell})/2 & \text{for } p \in \{j, k\}, \end{cases}$$

(iii) $d_{i,\ell} - b_i - b_\ell \in \mathbf{N}$.

Remark. See the remark following Theorem 4 for a discussion of conditions (i), (ii), (iii).

Remark. The proof of Theorem 6 is constructive and gives an algorithm for finding the tree T that tree-realizes $D \in \Upsilon_{n\times n}$.

Tree-Realizable Algorithm

1. Set $T_3 = T\{i_1, i_2, i_3\}$ a path of length 2.
2. For $\ell \leq n$, choose $i_k \in \{i_1, \ldots, i_{\ell-1}\}$, $i_\ell \in \{1, \ldots, n\} - \{i_i, \ldots, i_{\ell-1}\}$ with $d_{i_k,i_\ell} = 1$.
3. Set $T_\ell = T_{\ell-1}$ plus the edge $i_k i_\ell$.
4. Stop.

D. Primary Sublayers are Arbitrary Sublayers

In this section we characterize the symmetric matrices that are relative shielding order matrices of an EM topology where the primary sublayers are arbitrary by characterizing the symmetric matrices that are distance-matrices of a set of vertices for a tree.

For $D = (d_{i,j}) \in \Upsilon_{p \times p}$, we say D is *realizable* iff there exists a tree T containing p vertices labelled $\{1, \ldots, p\}$ satisfying $d_T(i,j) = d_{i,j}$ for $1 \leq i, j \leq p$.

Remark. With no loss of generality, we may assume that all leaves of T are labelled vertices in that we may rid the EM topology of excess secondary sublayers.

We give now the main result of this section.

Theorem 7. $D = (d_{i,j}) \in \Upsilon_{p \times p}$ is realizable iff all principal 4×4 submatrices of D are realizable.

Remark. The proof of Theorem 7 is constructive and gives an algorithm for finding the tree T that realizes $D \in \Upsilon_{p \times p}$.

Realizable Algorithm

1. Set $T_m = T\{i_1, \ldots, i_m\}$ the tree of leaves of D.
2. For $\ell \leq p$, choose $i, j \in \{i_1, \ldots, i_m\}$ with $d_{i,j} = d_{i,i_\ell} + d_{j,i_\ell}$.
3. Set $T_\ell = T_{\ell-1}$ where the appropriate vertex has been labelled i_ℓ.
4. Stop.

IV. Construction of All Sublayer Electromagnetic Topologies with $R_{\max}$ at Most 5

In this section we exhibit all EM topologies with the properties that the primary sublayers include all the extremal sublayers, possibly some of the internal sublayers and that the relative shielding order matrix among primary sublayers has largest entry $R_{\max}$ of at most 5 by examining all trees of diameter (length of longest path) at most 5 and constructing the EM topology by inversion at a vertex in the tree. Note that only inversion at a leaf of the tree, which is always a primary sublayer, results in a connected system. Observe that a system is connected iff there exists one subshield which contains all other subshields and all but one sublayer. In our diagrams it will not be necessary to distinguish primary and secondary sublayers.

In what follows we construct the electromagnetic topology by inversion of the tree at the darkened vertex designated by an arrow and note that inversion at any of the other darkened vertices yields a similar topology. We leave the trivial cases $R_{\max} = 0, 1$ to the interested reader.

V. Summary

We have characterized the relative shielding order matrix among primary sublayers for an electromagnetic topology defined to the level of layers and sublayers. Moreover, our characterization gives a recursive procedure for constructing the interaction sequence diagram and, hence, an EM topology. For small relative shielding order the EM topologies and dual graphs are not overly complicated and are exhibited.

In the results of the present paper we have found that there are cases of specified relative shielding order matrices which are not realizable. An important related problem is to determine when such a matrix can be appropriately repaired so as to become a realizable relative shielding order matrix. By this we mean that certain matrix elements may be increased (more shielding) and so achieve at least the desired shielding performance. Ideally this would be done in some optimal manner involving minimum repair. We have some results concerning this to report in a future paper.

Since electromagnetic systems can acquire considerable complexity, also of interest is a similar analysis of the realizability and repairability of the relative shielding order matrix for an EM topology defined to the level of elementary volumes. This will produce a dual graph which is not a tree and complicate matters considerably.

References

1. C. E. Baum, Electromagnetic Topology: A Formal Approach to the Analysis and Design of Complex Electronic Systems, *Proc. EMC Symposium*, Zurich, pp. 209-214 (1981).

2. C. E. Baum, Sublayer Sets and Relative Shielding Order in Electromagnetic Topology, *Electromagnetics* vol. 2, no. 4 (1982).

3. C. E. Baum, On the Use of Electromagnetic Topology for the Decomposition of Scattering Matrices for Complex Physical Structures, Interaction Note 454, July 1985, Air Force Weapons Laboratory, Kirtland Air Force Base, New Mexico (1985).

4. R. J. Gould, *Graph Theory*, Benjamin Cummings (1988).

5. K.S.H. Lee (ed.), *EMP Interaction: Principles, Techniques and Reference Data*, Hemisphere Publishing (1986).

1988 USAF-UES SUMMER FACULTY RESEARCH PROGRAM

GRADUATE STUDENT RESEARCH PROGRAM

Sponsored by the

AIR FORCE OFFICE OF SCIENTIFIC RESEARCH

Conducted by the

Universal Energy Systems,. Inc.

FINAL REPORT

Diode Laser Probe of Vibrational Energy Transfer Kinetics in Sulfur Monoxide

Prepared by:	David A. Dolson, Ph.D.
Academic Rank:	Assistant Professor
Department and	Chemistry Department
University:	Wright State University
Research Location:	AFWL/ARBI Kirtland AFB Albuquerque, NM 87117
USAF Researcher:	Dr. Ernest A. Dorko

Date:	September 20, 1988
Contract No:	F49620-87-R-0004

Diode Laser Probe of Vibrational Energy Transfer Kinetics in Sulfur Monoxide

by

David A. Dolson

ABSTRACT

A new experimental apparatus has been assembled for the purpose of measuring the rates of collisional energy loss from low vibrational levels of sulfur monoxide (SO). The design calls for excimer laser photolysis of sulfur dioxide at 193 nm to prepare the SO radicals. High resolution diode laser absorption spectrometry will be used to obtain time-dependent concentrations of SO in specific energy levels. Preliminary results have suggested directions for improving the signal levels and reducing electrical interference.

Acknowledgements

I wish to thank the Air Force System Command, the Air Force Office of Scientific Research, and the Air Force Weapons Laboratory for sponsorship of this research. Mr. Rodney Darrah and the staff at Universal Energy Systems are to be commended for their efficient adminstration of the Summer Faculty Research Program.

I am pleased that Mr. John McCord was able to accompany me via the Graduate Student Research Program. He quickly learned to operate the equipment, and his assistance was invaluable. I thank Dr. Ernest Dorko, Dr. Mike McAuliffe, and Capt. Glenn Perram for their assistance at various stages of the project and for the many stimulating discussions that we had over the course of the work. We would not have progressed far without the help of Mr. Len Hanko, Capt. Brian McFeeters and SSgt. Matt Pederson in acquiring several items of laboratory equipment and assisting with assembling the apparatus. Finally I would like to express my appreciation to Czeslaw Deminet for his skillful glassblowing.

I. INTRODUCTION:

The molecular radical, sulfur monoxide (SO), is currently being investigated by the Advanced Radiation Branch of the Air Force Weapons Laboratory (AFWL) as a gas phase chemical laser candidate. This assessment requires a knowledge of the energy removal rates for the lower energy levels involved in the laser transitions. Rapid energy removal rates from the lower levels is favorable for maintaining the population inversion while slow energy removal will "turn off" the laser oscillation due to population build-up in the lower level.

An experimental measurement of energy transfer rates in SO must include a preparation step in which SO is produced in a desired energy level(s). A sensitive detection scheme must provide time-dependent concentrations of the SO molecules in each of the various energy levels following the preparation step. Finally, the rate constants must be extracted from the data by an appropriate mathematical analysis of the kinetic processes.

I have industrial and academic postdoctoral experience in experimental investigations of gas phase reaction kinetics. In kinetic studies of the chemical chain reactions and energy transfer processes involved in hydrogen halide chemical lasers, I used a sensitive infrared fluorescence technique to obtain time-dependent concentrations of molecules in specific vibrational energy levels. I developed a state-specific kinetic analysis of the data that yielded the desired rate constants.

This experience overlaps nicely with the requirements of the SO study and weighed heavily in my appointment as a UES Summer Fellow at AFWL.

II. OBJECTIVES OF THE RESEARCH EFFORT:

Dr. Ernest Dorko and I planned the research objectives during my pre-summer visit to AFWL. The long term objective was to design and execute a series of experiments that will yield accurate vibrational energy transfer (VET) rate constants for the lower ($v \leq 3$) energy levels of SO. It was expected that the steps to the final goal would include

1) a familiarization with the new diode laser,
2) assembly and evaluation of the apparatus,
3) execution of the experiments, and
4) mathematical analysis of results.

The full scope of this objective was realized to extend beyond the 10 week program, but we wished to progress as far as possible toward the final goal.

Felder et al (1988) demonstrated that 193 nm photolysis of sulfur dioxide (SO_2) generates SO radicals, predominately in the v=2 (67%) and v=1 (23%) energy levels. We elected to use this method to generate the "excited" SO radicals ($v \leq 3$) for our experiments.

Measurement of VET rates requires the ability to monitor specific vibrational states of "excited" SO radicals as they relax to lower energy levels through energy-exchanging collisions with other molecules. Two sensitive techniques are available for monitoring the SO radicals in various energy levels. The first is diode laser absorption spectrometry; the second is infrared fluorescence spectrometry.

The diode laser absorption technique was selected before my involvement because of its high spectral resolution. This technique is relatively new, more difficult to implement than the fluorescence technique, and more expensive. It will, however, yield a far more detailed picture of the energy flow in SO when the experiments are completed. The superior detail of the diode laser technique is amply demonstrated in previous work on SO by Kanamori et al (1985).

The infrared fluorescence technique is more readily implemented. Its lower resolution minimizes interference from rotational relaxation, and it is relatively insensitive to diffusion. These features enable the fluorescence method to yield a simpler view of the desired VET processes. The VET rates from such an investigation would be a valuable aid in analyzing the more complicated transient absorption signals and provide an independent check of the rate constants from the more detailed study. Being more easily obtained, the VET rate constants from fluorescence observations would be immediately useful in the evaluation of the SO chemical laser.

It became obvious, as the work progressed, that it will be some time before the diode laser experiments yield rate information. Consequently, as the diode laser work continues at AFWL, we are proposing to do the infrared fluorescence experiments at Wright State University (WSU) with partial funding from the Research Initiation Program. The combined results of these two studies should present a clear picture of the vibrational (and rotational) energy transfer processes in sulfur monoxide.

III.

a. While learning to use the diode laser, absorption scans of ammonia and sulfur dioxide were obtained in several spectral regions. Comparisons with other sources allowed the lines to be properly assigned.

b. This work became the primary responsibility of John McCord, who is finishing this project at Murray State University as a portion of his MS research. The assigned spectra will be returned to the AFWL research group to serve as wavelength calibration guides. Mr. McCord also wrote supplements to the diode laser manual in an effort to clarify some of our operational methods.

IV.

a. Assembly of the apparatus began with the positioning and plumbing of the excimer laser. Several optical configurations, requiring as many as five different glass photolysis cells, were evaluated.

b. A colinear geometry, using a 40 mm dia x 3 m cell and two passes of the infrared beam, was chosen. This configuration is similar to that used by Pasternack et al (1988). It combines ease of alignment and a long absorption path with low interference from intense HF emission from the exicimer laser.

Evaluation of the detection system was performed by executing preliminary experiments. Transient signals were obtained; however, the signal-to-noise ratio (S/N) was too low to allow any analysis of the data. Electrical interference from the excimer laser firing overwhelmed the amplifier at times. While the standard amplifier proved to be too slow, the "fast" amplifier did not have sufficient gain. The transient absorption signal level must be increased before experiments can begin in earnest. Problems of this nature are expected in new experiments, and their consideration has suggested several recommendations.

V. RECOMMENDATIONS:

a. A reduction of the excimer laser interference is required. We found that the coax line to the preamplifier was most sensitive and suggest the use of a shorter line that is well shielded. Using batteries to power the preamplifier may help to reduce the noise pick-up. Elimination of ground loops may also help. It is difficult to do a complete job, and it may be prevented by site safety regulations.

Improvements in signal levels may be obtained by increasing the (SO concentration) x (pathlength) product. A factor of three or four increase in 193 nm pulse energy may result from using an appropriate dielectric mirror in the excimer laser, leading to higher SO concentrations. Longer absorption paths would be provided by a multipass absorption cell with internal mirrors. More gain may be realized in the preamplifier by increasing the feedback resistance. We replaced the 500 ohm feedback resistor with one of 5000 ohm but did not have an opportunity to evaluate the response.

Most of the evaluation was performed with the diode laser tuned to SO lines in the 1107.4 cm^{-1} region. It may be that another spectral region would yield stronger signals. Future work will require a determination of SO line positions in regions of better laser performance.

b. Implementation of the recommendations will require a significant investment of effort at AFWL. After S/N improvements are made, a schedule of experiments will be executed. An analysis of the kinetic results must then be developed. Another determination of the VET rate constants will prove to be useful in guiding both the experimental design (suggested reagent concentrations) and the kinetic analysis (identifying VET contribution to signals with several time constants).

A fluorescence study of VET rates in SO is proposed to satisfy this need. A formal proposal will be made to the AFOSR RIP Program, for partial support of this work. The fluorescence technique will provide the VET rate constants, but cannot probe the finer details of rotational energy transfer. These experiments are performed and analyzed more easily than are the diode laser experiments. Results should be available in time to support the diode laser study.

REFERENCES

Felder, P., C. S. Effenhauser, B. M. Haas, and J. R. Huber, "Photodissociation of Sulfur Dioxide at 193 nm," Chem. Phys. Lett., 1988, Vol. 148, pp. 417-22.

Kanamori, H., J. E. Butler, K. Kawaguchi, C. Yamada, and E. Hirota, "Spin Polarization in SO Photochemically Generated from SO_2," J. Chem. Phys., 1985, Vol. 83, pp 611-15. and "Infrared Diode Laser Kinetic Spectroscopy of Transient Molecules Produced by Excimer Laser Photolysis: Application to the SO Radical," J. Mol. Spectrosc., 1985, Vol. 113, pp. 262-8.

Pasternack, L., R. J. Balla, and H. H. Nelson, "Study of Reactions of BH_3 with CO, NO, O_2, C_2H_4, and H_2O Using Diode Laser Absorption," J. Phys. Chem., 1988, Vol. 92, pp. 1200-3.

1988 USAF-UES SUMMER FACULTY RESEARCH PROGRAM/

GRADUATE STUDENT RESEARCH PROGRAM

Sponsored by the

AIR FORCE OFFICE OF SCIENTIFIC RESEARCH

Conducted by the

Universal Energy Systems, Inc.

FINAL REPORT

EVALUATING HOW LASER IRRADIATION DAMAGES LOADED COMPOSITE MATERIALS

Prepared by:	William M. Jordan, Ph.D.
Academic Rank:	Assistant Professor
Department and University:	Mechanical and Industrial Engineering Department Louisiana Tech University Ruston, LA 71272
Research Location:	AFWL/TAL Kirtland Air Force Base, New Mexico 87117
U.S.A.F. Researchers:	Dr. Pat Vail Jorge Beraun

Date:	September 2, 1988
Contract No.	F49620-87-R-0004

EVALUATING HOW LASER IRRADIATION DAMAGES LOADED COMPOSITE MATERIALS

by

William M. Jordan

ABSTRACT

This study was an analysis of how laser irradiation damages composite materials. Particular attention was placed on how lasers damage pressurized cylinders made from composite materials.

Three different models of laser damage of composite materials were examined. They were a viscoelastic model, a model developed by Southwest Research Institute, and Lockheed's 'Hybrid Model'. Each model's assumptions, advantages and limitations were analyzed. The viscoelastic model is not useful at the present time due to inadequate data and analysis. The Southwest Research Institute Model will predict when local failure occurs, while the 'Hybrid Model' is more useful in predicting when global failure will occur.

These last two models are too empirical at the present time and additional analysis and testing is required to determine more precisely under which conditions they will or will not work. Recommendations were made concerning changes on the next set of pressurized cylinder tests so that more useful data for these models could be obtained. Recommendations were made concerning additional mechanical tests whose results could help to examine the predictive capability of the models.

I. INTRODUCTION

Laser irradiation of composite materials is a concern to the Air Force because of the increased use of composites as structural parts in aerospace vehicles and the potential use of lasers as a weapon against the composite material. Various models of how laser irradiation damages composite materials have been proposed. Many of them have been largely empirical, able to predict what will occur in a specific system. Their capability to predict the amount of damage in different systems is less clear. This study was undertaken to evaluate the laser damage models to see if a more fundamental understanding of the damage process could be obtained.

My expertise lies in the area of composite materials and fracture mechanics. My Ph.D. research examined the delamination of graphite-epoxy composite materials, with emphasis on how to improve the composite toughness through modification of the resin. This research required a thorough knowledge of composite materials as well as a knowledge of the fundamentals of fracture mechanics. In this summer's work, I have attempted to apply my understanding of fracture mechanics and composite materials to this composite materials failure problem.

Some of my recent work has involved examining the effect of high velocity impact loading on composite materials and the effect of temperature cycling on the subsequent viscoelastic properties of composites. That study required an understanding of the viscoelastic nature of composite materials which was one of the proposed models to be evaluated in this study.

II. OBJECTIVES OF THE RESEARCH EFFORT

The initial plan was for this to be an analytical and experimental program to examine how laser irradiation damages composite materials. Due to circumstances beyond our control, the required composite material bottles were not ready to test this summer. This changed the work to an analytical one with the following three objectives. The first objective was to analyze the various proposed laser/composite damage models. A

key aspect of this was to understand what assumptions were made in the development of each model.

The second objective was to examine what sort of input data the models need in order to be able to make their predictions. This led to several suggested changes for the next set of pressurized bottle tests. There were also some suggested flat plate tests that could provide additional input data for the models. One of the problems with evaluating the present models is that not all of the required input data is known. Some of the material properties have to be 'assumed', which can lead to the temptation to assume values that will allow the model to predict the results that were already experimentally determined.

The third objective was to develop an experimental program that will yield the proper information so that the predictive capability of the models could be examined. The different models do not make the same starting assumptions and they cannot all be reasonably accurate. (There is still the possibility that none of them is reasonably accurate.) One of the problems with some of the current models is their empirical nature. For example, the 'hybrid model' appears to work satisfactorily for the specific systems used in its development. However it is not known what are the bounds of that model (or of the other models). For a model to be used confidently it must be known under which conditions it will function and which conditions it will not function. An analysis of six models was presented to my technical focal point in early August. This final report will place an emphasis on the three models still under development, the viscoelastic model, the Southwest Research Institute Model, and the 'Hybrid Model'. It is anticipated that this portion of the work would be continued in the minigrant that follows this summer effort.

III. ANALYSIS OF VARIOUS MODELS FOR LASER INDUCED COMPOSITE FAILURE

This section analyzes three of the various modelling approaches to laser damage of composite materials that have been attempted to this date. They are the ones currently being developed (and or refined).

(1) VISCOELASTIC ANALYSIS OF COMPOSITE/LASER INTERACTION

This is an attempt to model the viscoelatic behavior of the composite material bottles. This work, being performed by RDA, has three major tasks. The first task is to characterize the elastic-viscoelastic behavior of composite shells. Their second task is to develop a preliminary finite element based plate and shell model. Their third task is to apply this to a cylinder that has been radiated.

To accomplish the first task, the viscoelastic behavior of the pressurized composite cylinder needs to be determined. This involved analysis of the pressurization rate effect upon strain that was observed during the previous 10 inch bottle tests. Their first approach was a bilinear one, where the modulus of the resin was regarded as equal to zero once the resin strain to failure had been reached. This correlated well with the experimental data.

They represented the load as the sum of an elastic deformation component and a viscoelastic deformation component. The value of the viscoelastic stiffness, A_v, decreased with time which is not what was anticipated. So it was in turn represented in the following fashion as a product of a true viscoelastic function, $G(t)$, and a damage function, $F(\epsilon)$:

$$A_v(t) = G(t) \quad F(\epsilon) \qquad (1)$$

$G(t)$ increases with time up to a certain point and then levels off. The function $F(\epsilon)$ decreases with strain. As the composite is damaged, it is less able to withstand an applied load. This will increase the compliance (or decrease the stiffness) of the composite.

A problem developed when the calculated resin stiffness turned out to be higher than the fiber stiffness, which no one would really believe. The pressure was measured some distance away from the bottle and is apparently much larger than that which was in the bottle during the early portion of the pressurization run. R.D.A. is attempting to calculate the bottle pressure based on fluid flow concepts but has not yet been successful in doing so. Until this analysis can be made (or better pressure data obtained on the next set of bottle tests) it is

not possible to evaluate the significance of the viscoelastic effects on the laser damage of the composite material.

(2) SOUTHWEST RESEARCH INSTITUTE MODEL

Basis for Southwest Research Institute Failure Analysis Model

The authors developed a six stage scenario for the potential failure of pressurized composite cylinders subjected to laser irradiation. Their scenario is shown below:

A. Filament-wound vessel subjected to laser irradiation.

B. Time Dependent Cavity Growth

C. Through wall instability? (local instability?)

If yes, continue on to step D.

If no, go back to step B and grow the cavity some more.

D. Through wall penetration?

If condition C exists, then this will happen relatively quickly.

E. Global Vessel Failure?

If Yes, then vessesl bursts

If No, then vessel depressurizes (or vents)

The crucial issue was the determination of the critical cavity depth for perforation of the wall. The model will try to predict when this local failure would occur. It is not a model that will be used to predict a global failure criteria. This will still produce useful information for local failure is a necessary, though not sufficient, cause for global failure.

They reviewed seven 2-Dimensional models that had been developed by other researchers, as well as one model that had been developed by Southwest Research Institute. The major distinctions between these various models is the number and type of input information that is required. The authors of the report make the following statement (with which I wholeheartedly agree):

> 'Since each model is essentially a curve fit to the same set of experimental data, it is not surprising to find that the predictions are quite similar and that all

predictions agree with the experimental results. Thus, the distinction between the predictions of the 2-D failure models are relatively insignificant.

Since the differences between the 2-D model predictions appear to be insignificant, the question arises as to which model would be the most efficient to use in an engineering analysis application. This can be answered considering the testing required and the subsequent amount of data analysis necessary.

The Southwest Research Institute model is basically a 2-D model, although it does have a correction factor within it to partially account for the 3-D effects caused by the growth of the cavity. The input required for this model are the laminate fracture toughness and the initial crack length.

One very relevant observation was that the highest stresses do not necessarily occur in the outermost plies. This is because the composite is composed of plies both in the hoop direction and at an angle to the hoop direction (called helical). If the outermost plies at the cavity are in the helical direction, then the adjacent hoop plies will have the highest stresses. This is important in that it means that further cracking (such as delamination) might not begin at the surface.

Failure Analysis in Southwest Research Institute Model

The finite element models discussed above are not used to directly make failure predictions, they are used to determine the state of stress in the composite. The next issue is how to predict at which stress states failure will, in fact, occur.

There are several composite material failure analysis models. The authors chose to use one based on maximum allowable stress. As the laser removes more and more of the composite (thus growing the crack) the stress in the remaining plies will increase. When the stress reaches the ultimate tensile strength of the composite, then the system will have a local faillure.

The authors admit that they have ignored the issue of delamination crack growth around the edges of the thermally damaged region. It is not obvious that this was good thing to do at the present time. Whether

delamination is a big problem for this application I do not yet know, but it should not be ignored until it can be demonstrated that its effects are negligible.

The authors have made a very valid distinction between the processes involved with when considering the local instability (formation of a hole in the shell) and global instability (does the hole grow catastrophically or does the vessel depressurize?).

(3) LOCKHEED 'HYBRID MODEL'

Description of Research Modeling

This work is an attempt to deal with a problem that exists in the current modeling of laser induced damage in composite materials. The authors make the following statement (which I also believe to be very important):

> 'The inherent danger in using computational models that are derived in a predominantly empirical fahsion is the inappropriate extension of model parameters. Predictive failure techniques need to be improved and refined to the point of reliable confidence.'

The problem that exists is how to develop a model that is less empirically based. Their current model has three laser-target response variables, two of which are largely empirical. They are:

Q_D material/laser interaction damage parameter

D_D structural-response global failure parameter

X_D damaged depth parameter

It is claimed that X_D is less empirical than the others and is determined from a laminate model of the composite. When the depth of damage reaches X_D then mechanical damage is initiated and when the damage length reaches D_D then global failure will occur. The real problem with this model is the empirical nature of D_D and Q_D. The authors admit that 'bounds or constraints on the validity of the model are not clearly defined'. This is a major problem for if it is not possible to reliably determine when a model will work and when it will not work then the model has very limited usability.

Their continuing work concentrates on determining the values of Q_D and D_D in a more analytical fashion. Q_D will be evaluated using a composite-material thermal-response model. Their work uses a 2-D finite element code to analyze the calculation of composite layer failure initiation and accumuluation and the calculation of the fracture energy. This will be used to try to predict when global failure will occur. Both of the models will be analyzing the composite as a laminate, and not dealing with micromechanics of the fibers and resin.

The fracture energy, G_c, will be calculated from flat-plate data and from a few subscale cylinder tests. This will be compared with G_c calculated from a laminate finite-element analysis. This will be used to develop what they call a 'low-order model' that can be used to predict failure.

Discussion of 'Hybrid' Modelling Procedure

At this time I an not able to determine whether or not the calculation methodology of Q_D is an improvement over the current empirical approach. The calculation methodology for D_D is more clearly presented. I have some problems with the methods described to produce G_c from flat plate tests and from cylinder tests. The flat plate method appears to be a method to calculate the mode I delamination fracture toughness, while the toughness from the cylinders will be from tests that have a more complicated loading geometry. Even if the cylinders failed by delamination, it would probably not be only from mode I delamination (which is apparently what would be obtained from the flat plate tests). Since the plates and cylinders have different loading, and therefore a different state of stress, it would be expected that they would have a different fracture toughness.

In my opinion, the choice of which fracture toughness is needed for the model has not been carefully thought through. There is also the possibility that the fracture toughness of the composite will change during the length of its exposure to the laser. The resin near where the laser hits the target will be thermally damaged and will likely have a different fracture toughness than the resin that is some distance away from the thermally damaged area.

An accurate finite element model can be used to determine the state of stress near the defect but it still needs to have some sort of experimentally determined failure criteria applied to it. The current proposal of using what appears to be a mode I toughness as the failure criteria is rather simplistic. Some mixed mode failure criteria should be applied to the stress state analysis developed under this program.

IV. CONCLUSIONS

There are three main conclusion based on the analysis of the models:

(1) Usefulness of viscoelastic model cannot be determined at this time due to inadequate data and analysis.

(2) Southwest Research Model is useful as a predictor of when local failure will occur. This is a necessary, though not sufficient, cause for global failure.

(3) The 'Hybrid Model' is useful in predicting when global failure will occur (if the proper data has already been obtained).

All of the above models suffer from being too empirical at this time. The limits of their applicability are not yet known. More analysis and testing is required before they can be confidently used. Since the S.W.R.I. model appears to be best suited for predicting local failure and the 'Hybrid Model' for predicting when global failure will occur perhaps some combination of their best points into one model could be considered.

V. RECOMMENDATIONS: SUGGESTED MODIFICATIONS FOR THE NEXT SET OF PRESSURIZED BOTTLE TESTS

This research was initially intended to be an analytical and experimental program. However, due to circumstances beyond our control the required composite bottles will not be ready in time to test during this summer's program. This work's emphasis then shifted to an analysis of the various proposed laser/composite material failure models. The most important portion of this work are these recommendations about

future changes. In this section are the recommendations for changes in the experimental program on the next round of bottle tests. In Section VI will be the recommendations for an experimental program that can be used to better evaluate the predictive capability of the models.

(1) MODIFICATIONS TO AID IN THE REFINEMENT OF THE VISCOELASTIC MODEL

The proposed work by RDA appears to be based on a sound understanding of viscoelasticity. Since there was an apparent viscoelastic effect noticed on some of the 10 in bottle tests when they were pressurized at different rates, this project appears to have merit.

However, there was a problem with the data on the 10 inch bottle tests and the data is not considered very reliable. The pressure was measured at a distance significantly removed from the bottle and it gave erroneously high predictions for the stresses (and modulus) of the bottle. A better estimation of the bottle pressure needs to be obtained during the next round of tests. This could be obtained by placing a pressure gage adjacent to the bottle, rather than some distance away from it.

Even apart from the issue of the correct value of the pressure, the data from the 10 in bottle tests may not be sufficient to use as a basis for modelling. This is because the different pressurization rates also involved different stress levels. There may be some affect of the stress level that might obscure the significance of the pressurization rate. In addition to this, the pressurization rates within each test were not constant, which could lead to additional unpredicted results.

I would suggest that on the next set of bottle tests, several pressurization tests be performed to analyze the viscoelastic behavior of the composites. On the new set of 20 inch bottle tests, a method should be designed where a constant pressurization rate can be applied. This would remove any affects of the change in rate during pressurization. This system should be designed such that it could deliver different pressurization rates on different tests.

It is suggested that several tests be run at different pressurization rates but with the same maximum pressure. One problem with doing tests of this nature is that each bottle may be slightly different so it is difficult to compare results of different pressurization rates on different bottles.

One way to deal with the effect of bottle differences would be to pressurize a bottle at one rate, depressurize it, and then repressurize it at another rate. This removes the problem of differences between bottles but may produce an additional problem. It is possible that the first pressurization somehow damaged the composite, so that the repressurization would be done with a damaged bottle that might not behave the same. One way to deal with this would be to test two bottles. The first bottle should be pressurized at one rate, depressurized, and then repressurized at the same rate. Any differences between the two tests would be the result of the type of damage induced by the first pressurization. On a second bottle, pressurize it at one rate, depressurize it, and then repressurize it at a different rate. Using the data from the first bottle, the effect of any damage can be removed, leaving only the result of the viscoelastic behavior of the composite bottle. By having the two different rate tests done on one bottle, the effect of the different bottles can be minimized.

(2) MODIFICATIONS TO AID IN THE ANALYSIS OF THE SOUTHWEST RESEARCH INSTITUTE MODEL

This model assumes a maximum stress failure theory. For this theory to be successfully applied, the state of stress near the laser spot needs to be known. I think that a more experimental determination of the state of stress near the laser could help to provide better input data to the model. The high temperature resulting from the laser will also change the mechanical properties of the composite, and therefore how temperature damages the composite should be more precisely determined experimentally.

Measurement of State of Stress in Composite Material

I don't think that all of the strain gage locations chosen for the 10 inch bottle tests produced meaningful results. Strain gages that were away from the path of the delamination registered very little changes during heating up to the moment of bursting or venting. So it appears that if additional strain gages are going to be used, they should be placed in different locations. It is suggested that 9 strain gages to be placed in a cluster around the laser spot location. Two of them should be placed on each side of the spot in an attempt to measure strain in the path of the delamination. The remaining gages should be placed relatively close to the laser spot (but not on the path of expected delamination). It appears from the previous data on the 10 inch bottles that most of the deformation occurs very close to the laser spot, so this is the region where most of the strain gages should be placed. One strain gage should be placed at a position of 180 degrees from the laser spot so that an accurate measurement of the bottle (or system) response can be made.

On the last set of tests, the data acquisition rate was set to measure each parameter 1000 times per second. However, when the system was about ready to burst (or vent) a lot was happening in the 1 millisecond between each measurement. It would be very desirable in the next set of tests to measure the strain much more frequently so that the deformation occurring near the burst event can be determined with more precision.

Enough strain gages cannot be put onto the bottle to provide as much information as would be desirable. So other options should be explored that could also help to measure state of stress caused by the laser acting upon the surface of the pressurized composite cylinder.

One method to accomplish this would be to place a very fine grid on the outside surface of the bottle. As the composite bottle deforms, this grid will be distorted, and the amount of deformation can be measured. I have observed the failure of one of the 10 in bottles filmed at 2000 fps and think that this camera may be able to give us the resolution that is needed to accomplish this goal. I have been told that three cameras are available, two of them capable of running at 4000

fps and one of them at 2000 fps. They should be arranged so that deformation could be observed both at the laser spot region and a short distance away from it as well. One concern with this attempt is the effect of the very bright laser spot making any other observations nearby more difficult. The use of a neutral filter could lessen the effect of the bright spot, but it would make observation of everything else more difficult. One possibility would be to use a spot filter that would reduce the light coming from the laser spot region but would not reduce the light coming from nearby locations.

(3) MODIFICATIONS TO AID IN THE ANALYSIS OF THE LOCKHEED 'HYBRID' MODEL

This model is based on a determiniation of a critical damage parameter, D_D. Once the damage exceeds this value the system will fail. A more precise understanding of the mechanical damage near the laser spot could aid in the refinement of this model. An attempt should be made to determine it more precisely from experimental testing.

Measurement of Mechanical Damage in Composite Material

This discussion relates to how D_D is measured, and if D_D adequately represents all of the mechanical damage that needs to be evaluated. There are alternative methods that can be used to evaluate the extent of the mechanical damage. Some of these alternatives will be discussed below.

(1) The composite could be examined ultrasonically or with an X-ray unit. This could allow for internal cracking to be observed in the region surround the hole. This would work more easily with the vented samples, but still might be able to be accomplished in the region away from the burst site.

(2) Visual measurement of the delamination region on the composite cylinders. This could be done directly on some of the vented cylinders. On other vented cylinders, something needs to be added to make the the delaminated region more apparent. A dye penetrant could be used to penetrate into the damaged region after the test has been performed. This would need to be subsequently evaluated by either of the ultrasonic

or X-ray tests mentioned above. The penetrant could then be used to show the extent of the cracked region in the vicinity of the hole.

(3) Mechanical tests of the damaged region after the laser test. It would be expected that the damaged region would have internal cracks (and perhaps delamination) which would result in a lower stiffness. One difficulty with this approach, is that the samples would be curved, and they may be difficult to obtain (especially on burst tests where the macroscopic damaged region is quite extensive). This might be easier to accomplish by mechanically testing flat specimens which were irradiated while under the same tensile stresses as would be present in the pressurized cylinders.

VI. RECOMMENDATIONS: AN EXPERIMENTAL PROGRAM THAT COULD BE USED TO EVALUATE THE PREDICTIVE CAPABILITY OF THE MODELS

The goal of the analysis was to develop an experimental program that will yield the proper information so that the predictive capability of the various models can be examined. This experimental program should include tests that would allow discrimination to be made among the various models. It would be most desirable to design tests where one model would predict one result and another model would predict a different result.

Included in this program should be some materials characterization tests as well. These would be used to provide the proper toughness values to be input into the various models. This portion of the study would involve the determination of a mixed mode failure envelope for the materials in question. This type of work is absolutely necessary if the models are to be properly evaluated.

The following three sections are a discussion of the types of experimental tests that could be designed to help evaluate the three main models of interest.

(1) EXPERIMENTAL TESTS THAT COULD BE USED TO EVALUATE THE VISCOELASTIC MODEL:

These researchers appear to have a sound understanding of viscoelasticity. I have some questions about the quality of the viscoelastic data that has been provided to them to use as a basis for their evaluation. I think that more tests need to be made to provide them with better data for them to analyze. This will involve some bottle pressurization tests as well as flat plate tests.

The types of tests I would suggest are shown below:

(1) Viscoelastic bottle tests can be performed as was described in the recommendations section describing the next set of 20 inch bottle tests.

(2) Viscoelastic tests performed on a number of flat plate specimens to verify if there is a significant viscoelastic effect at the stress levels in question. The plates can be loaded up to the pressurization stresses at different rates and then held at those stress levels. The strain in the composite could then be monitored as a function of time.

(3) Tensile tests on unnotched specimens to determine the elastic constants of the material (may also be done using a 3 point test geometry). These tests should be performed both on samples that have been irradiated by the laser and on samples that have not.

(2) EXPERIMENTAL TESTS THAT COULD BE USED TO EVALUATE THE SOUTHWEST RESEARCH INSTITUTE MODEL:

This model uses fracture toughness and the maximum stress failure theory in an attempt to predict when local failure of the composite will occur. They used a modified 2-D model that takes into consideration the three dimensional nature of the stress state near the crack. They used maximum stress failure theory to predict when each individual ply would break. Part of their input requirements include the fracture toughness of the composite. They admit that they ignored the issue of delamination.

The experiments described below will attempt to analyze whether delamination is significant or not in the structures in question. The experiments will also attempt to determine the mixed mode fracture toughness of the composite to use as an input into the model. The use of an experimentally derived fracture failure criteria can be used to better evaluate the predictions of this model.

The types of tests I would suggest are shown below:

(1) The legitimacy of using the maximum stress failure theory (which has been assumed by several researchers) could be evaluated in the following fashion. Make up two sets of composites having the same layups (fiber orientations) and the same amount of fibers. Fabricate them in such a way that a different percentage of resin will result in the system. If maximum stress theory holds true then they should both have the same tensile strength when tested with a center crack (since almost all of the load is carried by the same amount of fibers). If they do not fail with the same amount of stress, then they probably have different amounts of delamination occurring in the systems. (This is because delamination toughness is usually very dependent upon the resin content, while tensile strength is usually relatively independent of resin content). Separate mode I and mode II delamination tests can be performed on these materials to verify that their delamination behavior is different.

An alternative method might be to cure two sets of composites differently such that one set has some small voids present. The presence of the voids would not change the tensile strength of a center cracked composite but would be expected to change the delamination toughness of the composite. This alternative method could also be used to evaluate the applicability using the maximum stress theory in this specific structural system.

(2) Tensile tests on unnotched specimens to determine the elastic constants of the material (may also be done using a 3 point test geometry). These tests should be done both on samples that have been irradiated and on samples that have not.

For some composite systems, a change in percentage resin content will also change the strength of the composite by affecting the bonding

between the fibers and the resin. By tensile testing both systems with unnotched samples, the effect of resin content (if any) can be separated from the effect of amount of delamination (for delamination would not be expected during the course of a tensile test on an unnotched specimen).

(3) Mixed mode delamination tests to evaluate the shape of the 'failure envelope' predicted from finite element model. These tests should be done both on samples that have been irradiated and on samples that have not. This will partially overlap with the delamination tests that will be done under (1) above. This is needed for these authors used fracture toughness as one of their input variables, but did not define which fracture toughness was required. It would be tempting to use whatever fracture toughness that would fit the data that was already obtained. Through the determination of a mixed mode fracture toughness, an independent value of the toughness could be used to evaluate how well the model predicted the experimentally observed results.

(4) Measurement of the extent of delamination during mechanical loading of the composite. This could be done with free edge delamination tests or on the center cracked tensile samples mentioned earlier. This might involve using a dye penetrant, followed by an ultrasonic analysis of the sample.

(3) EXPERIMENTAL TESTS THAT COULD BE USED TO EVALUATE THE 'HYBRID' MODEL:

This is a semi-empirical model that seeks to determine the critical value of damage that is required for bursting of the pressurized of cylinder to occur. They have attempted to predict when this occurs analytically. In their prediction of the critical damage parameter, D_D, they require as input the fracture toughness of the composite, K_c (or G_c), as well as a bulge correction factor, M_T. One problem with this model has been that K_c and M_T have not been known very precisely. They are either 'back-calculated' from the burst tests or 'typical' values are assumed. As long as these methods are used to determine the critical input parameters, this theory runs the risk of being considered only a curve fit to the data (and the limits of applicability of the

theory appear to be the systems that have already been tested). The experiments described below are an attempt to provide an independent source for the values of the fracture toughness so that the true predictive capability of the model may be examined.

This model assumed a typical value for the fracture toughness and does not appear to deal with the issue that there is mixed mode loading involved near the laser spot region. This means that some mixed mode fracture toughness failure envelope needs to be determined so that the appropriate fracture toughness value can be used as input to the theory. This model also uses the maximum stress failure theory, and the experiments described under the discussion of the Southwest Research Institute model also apply here.

It is suggested that flat plate tests be done on both Kevlar based composites as well as the graphite composites that will be used in the 20 inch tests. This will provide enough experimental data to evaluate whether this model did, in fact, predict the actual results obtained on the 10 inch bottle tests.

The types of tests I would suggest are shown below:

(1) Tensile tests on unnotched specimens to determine the elastic constants of the material (may also be done using a 3 point test geometry).

(2) Tensile tests on samples with center cracks to determine the load at which crack growth begins. This should be done for several different size of initial cracks. The size of the plastic zone could be calculated from a knowledge gained of the tensile properties.

(3) Load up some small samples with center cracks and measure the size of the damaged zone in a scanning electron microscope.

(4) Mixed mode delamination tests to evaluate the shape of the 'failure envelope' predicted from finite element model.

(5) Measurement of the extent of delamination during mechanical loading of the composite. This could be done with free edge delamination tests or on the center cracked tensile samples mentioned earlier. This might involve using a dye penetrant, followed by an ultrasonic analysis of the sample.

(6) The legitimacy of using the maximum stress failure theory (which has been assumed by several researchers) could be evaluated as described in the discussion under the Southwest Research Institute model.

(7) Perform tests (2), (3), (4), and (5) above on both an irradiated specimen and on a specimen that has not been irradiated.

ACKNOWLEDGEMENTS

I wish to thank the Air Force Systems Command and the Air Force Office of Scientific Research for the sponsorship of this research. I wish to thank Universal Energy Systems, Inc., for handling the administrative details of the program.

At the Air Force Weapons Lab I want to thank Dr. Pat Vail for his sponsorship of my time and his help along the way. I wish to thank Jorge Beraun and Lieutenants Ron Perry and Dan Hodgkiss for their many fruitful discussions about the ongoing experimental work at the Weapons Lab. Many of my suggestions about future work have been modified after discussion with them.

REFERENCES

No references to papers in the open literature were cited. A number of distribution limited reports were used in the analysis period. As such they are not cited in this 'open' report.

1988 USAF-UES SUMMER FACULTY RESEARCH PROGRAM

GRADUATE STUDENT RESEARCH PROGRAM

Sponsored by the

AIR FORCE OFFICE OF SCIENTIFIC RESEARCH

Conducted by the

Universal Energy Systems, Inc.

FINAL REPORT

RELATIVISTIC EFFECTS IN GPS TIME TRANSFER

Prepared by:	Arkady Kheyfets, Ph. D.
Academic Rank:	Assistant Professor
Department and University:	Department of Mathematics North Carolina State University
Research Location:	AWFL/AWPP Kirtland AFB Kirtland NM 87117
USAF Researcher:	Dr. Warner A. Miller
Date:	July 29, 1988
Contract No:	F49620-87-R-0004

RELATIVISTIC EFFECTS IN GPS TIME TRANSFER

by

Arkady Kheyfets

ABSTRACT

Precise global clock synchronization is an integral part of the Global Positioning System (GPS) operations. The GPS satellites clocks are moving with respect to the clocks of the surface stations observers at speeds sufficient to necessitate careful consideration of special relativistic effects on synchronization of the clocks. At the same time, the GPS satellites orbits radii are large enough to cause the difference between gravitational potentials at the satellites clocks and at the surface stations clocks sufficient to produce effect on the clocks synchronization of the same order of magnitude as the special relativistic effects. A consistent treatment of both effects can be done only in general relativity.

We have performed general relativistic analysis of the GPS time transfer effects using both traditional mathematical techniques and newly developed in general relativity technique of the null strut calculus. The obtained expressions for the effects, as we have shown, admit unambiguous physical interpretation of each term, which clarifies the physical origin of effects. The null–strut calculus technique illuminates the 4–geometry of the procedure. The null–strut calculus looks very promising as future common language in formulation of such kind of problems and developing a satellite–based Spacetime Common Grid (SCG).

ACKNOWLEDGMENTS

I wish to thank the Air Force Systems Command and the Air Force Office of Scientific Research for sponsorship of this research. Universal Energy Systems must be mentioned for their concern and help to me in all administrative and directional aspects of this program.

I am grateful to Norman J. LaFave of the University of Texas at Austin for many hours of discussions of different aspects of my work and for providing invaluable information on the null strut calculus.

I am especially thankful to Dr. Warner A. Miller. All my work was performed in close cooperation with him. This report contains the results of our joint efforts.

I. INTRODUCTION.

Proper operating of the satellite–based Global Positioning System (GPS) imposes increasingly demanding requirements on global clock synchronization. Such synchronization requires taking into account both special relativistic effects and effects caused by the earth's gravitational field. A consistent treatment of both kinds of effects can be performed only within the framework of general relativity.

Meanwhile, almost all previous attempts to resolve the problem were undertaken within the framework of special relativity. Besides, there was considerable difference in results obtained by different researchers evaluating the special relativistic effects, and some apparent confusion concerning formulation of the problem.

The 4–Geodesy Section of the Advanced Concept Branch of the USAF Advanced Weapons Laboratory at Kirtland Air Force Base recognized that general relativistic solution of the problem became necessity. It was also recognized that the language of 4–geometry and, particularly, newly developed null strut calculus could be most helpful in formulating the problem.

My research interests have been in the area of application of modern mathematical methods in field theories, foundational problems of physics, and, especially, classical and quantum gravity. I have very strong background in general relativity, both in foundational aspects and in applications. I owe it to the University of Texas at Austin (where I received my Ph. D. degree), and, particularly, to Prof. John A. Wheeler (with whom I worked for more than four years). My especially strong side is the ability to see clearly the geometric content of general relativistic problems. This geometric insight played very important role in performing my research this summer and, no doubt, can be used effectively in the future.

II. OBJECTIVES OF THE RESEARCH EFFORT

The requirements on global clocks synchronization are becoming increasingly demanding in GPS operations. Furthermore, when more satellites are added to the GPS constellation to form a spacetime common grid (especially with cross-link ranging between satellites), it is believed that the precision requirements will become crucial for the coherent functioning of the system as a whole.

The GPS constellation will someday contain 18 clocks (with 3 active spares) moving with respect to each other. The GPS satellites will have almost circular orbits of 4 earth radii, with 12-hour periods, which means that the satellite velocity will be ~ 8 times the velocity of the surface station observer originating from earth rotation. Therefore, the required precision of the clocks synchronization necessitates taking into account special relativistic effects on the rate of the clocks. In addition, all the activity of GPS occurs in the earth's gravitational field with clocks placed in positions with different gravitational potentials. The gravitational influence of the field on the clocks rate is determined by the parameter $\frac{M_\oplus}{r}$ which produces an effect of the same order of magnitude as the second order special relativistic effects. A consistent treatment of both effects together can be done only within the framework of general relativity.

The need in such general relativistic treatment of the GPS clock synchronization problem was recognized prior the 1988 SFRP[1] and confirmed during it[2]. Investigation of the general relativistic effects on clock rates was performed on several occasions[16]. The results have been implemented partially into the ranging procedure. But by the time the 1988 SFRP period started the matter became a subject of controversy[3]. Previous results were ignored (to such extent that we became informed about them only by the end of our work). Everything was started anew. Two schemes, one using the second order Doppler correction[4,5], and another one using the ranging data[2,6], were under consideration. There was considerable differ-

ence in the results of the calculations of the second order Doppler correction. Most of the new attempts[4,6] were undertaken within the framework of special relativity (with different results) with the only completely general relativistic attempt[5]. Almost all the results did not look intuitively satisfactory. Some of them contained nonlocal terms having no physical interpretation. Others look suspiciously symmetric with respect to transmitter and the receiver, even though the expression for the Doppler shift itself was not, and one would expect it to show up in the second order approximation. Only the results of Ashby[4] looked perfect in all intuitive respects but, unfortunately, were special relativistic. Overall impression was that different authors did not always quite understand each other and, possibly, tried to calculate different things.

My objectives for the research efforts within the SFRP could be formulated as follows:

(1) to find the correct general relativistic expression for the Doppler shift in the earth's gravity field up to the second order and to give the results physical interpretation;

(2) to formulate and solve (or, at least, to give one solution) a problem of global clock synchronization in the earth's gravitational field;

(3) To utilize maximally the 4-geometric language in formulating the problems and pictorial demonstrations of the problems peculiarities, having as a goal to avoid confusion in interpretation of the results in the future.

III. DOPPLER SHIFT IN THE SCHWARZSCHILD FIELD.

We use Schwarzschild geometry as the model of the earth's gravitational field. In doing so we neglect contribution of the earth rotation into the gravitational field. An enhanced model would involve the Kerr metric. However, the evaluation of

the Kerr model parameters shows that the produced effect of the inertial frames dragging would be of higher order than the effects caused by the parameters coming from the Schwarzschild model[7]. Meanwhile, the estimate of the Schwarzschild model parameters shows that the effect of $\frac{M_\otimes}{r}$ is of the same order as effects of the squares of the relevant velocities. Thus, to discuss Doppler shift up to the second order, we can use Schwarzschild geometry as a model of the earth's gravitational field and, provided that in all approximations terms proportional to $\frac{M_\otimes}{r}$ are retained (we can neglect higher powers of $\frac{M_\otimes}{r}$), we obtain a satisfactory expression for the Doppler correction up to the second order with respect to the velocities involved in the picture.

The Schwarzschild geometry is a static spherically symmetric geometry. Its metric in Schwarzschild coordinates is given by the expression[8]

$$ds^2 = -\left(1 - \frac{2M_\otimes}{r}\right) dt^2 + \left(1 - \frac{2M_\otimes}{r}\right)^{-1} dr^2 + r^2 \left(d\theta^2 + \sin\theta d\phi^2\right), \qquad (1)$$

where t, r, θ, and ϕ are Schwarzschild coordinates*, and $M_\otimes$ is the earth mass.

In the geometric picture (cf. Fig. 1) describing the Doppler shift of an electromagnetic signal sent from the transmitting satellite to the surface station observer, the free falling satellite has a geodesic world line, whereas the observer, being attached to the earth, has the world line with all three nonzero curvatures[9]. A Doppler shift arises since the 4–velocity of the satellite (at the moment of signal transmission) and the observer (at the moment of receiving) are not parallel. More precisely, the result of parallel transport of the satellite 4–velocity along the null geodesic connecting the event of transmitting and the event of receiving does not coincide with the 4–velocity of an observer.

The frequency shift can be expressed in terms of the 4–velocities of the satellite and the observer and the 4–momentum of the photon traveling from the satellite to

* We use throughout this report the system of units commonly accepted in general relativity with both the velocity of light and the gravitational constant equal to unity

the observer

$$\mathcal{D} = \frac{\nu_S - \nu_O}{\nu_S} = \frac{{}_SP_\mu V_S^\mu - {}_OP_\mu V_O^\mu}{{}_SP_\mu V_S^\mu}, \tag{2}$$

where V_S^μ, V_O^μ are the 4–velocities of the satellite and the observer and ${}_SP_\mu$, ${}_OP_\mu$ are the photon 4–momentum at the event of transmitting and the event of receiving, respectively. The 4–momentum of the photon is parallel transported along the null geodesic connecting the events of transmitting and receiving and is tangent to the null geodesic at all times.

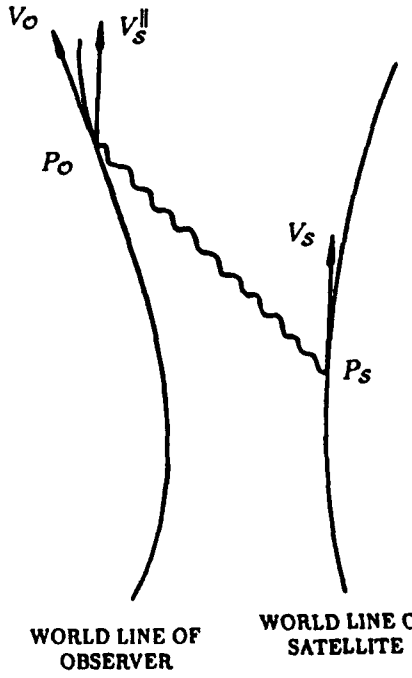

Fig. 1. Geometry of the Doppler shift. Vector $V_S^{\parallel}$ is the result of parallel transport of V_S along the null geodesic $P_S P_O$. Doppler shift is caused by $V_O \neq V_S^{\parallel}$.

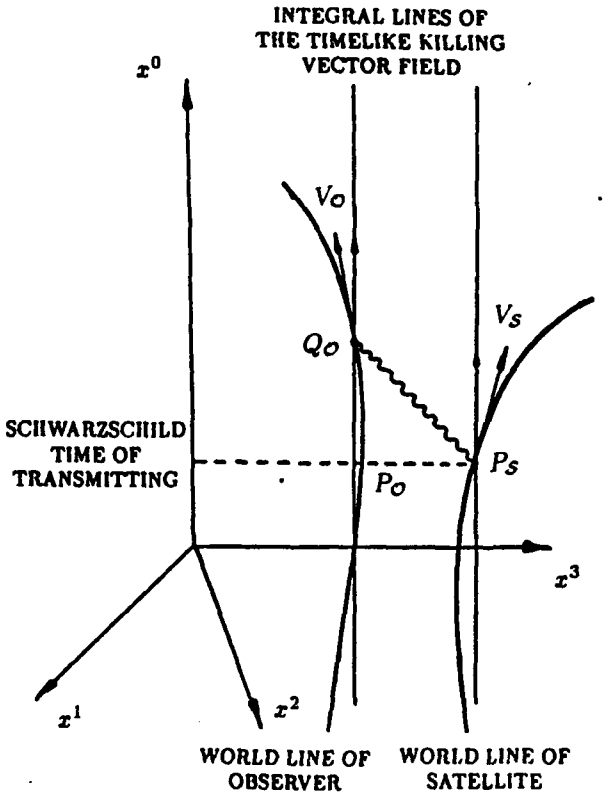

Fig. 2. The Doppler shift and its main contributing factors as viewed by observers resting with respect to Schwarzschild coordinates.

We have used for calculation of the Doppler shift up to the second order the techniques of the tensor series expansion of the world function[9], developed by J. L. Synge. Here we only describe and explain the result. Following J. L. Synge we introduce new coordinates $(x^\mu)_{\mu=0,1,2,3}$ related to the Schwarzschild coordinates

as follows

$$x^0 = t, \quad x^1 = r\sin\theta\cos\phi, \quad x^2 = r\sin\theta\sin\phi, \quad x^3 = r\cos\theta. \tag{3}$$

The metric tensor in these coordinates can be expressed as the sum $g_{\mu\nu} = \eta_{\mu\nu} + \gamma_{\mu\nu}$, where $\eta_{\mu\nu} = \mathrm{diag}(-1,1,1,1)$ and $\gamma_{\mu\nu}$ are small and static ($\gamma_{\mu\nu,0} = 0$). Coordinates (x^μ) are very convenient for a pictorial representation of the Doppler shift. In Fig. 2 these coordinates are used as coordinates of a Euclidean space. Of course, in this space the geodesics of the original Schwarzschild space do not always look as straight lines. The world line of the satellite in this picture is geodesic but looks curved. The vertical straight lines are the integral lines of the timelike Killing vector field of the Schwarzschild metric (described by the equations $x^i = \mathrm{const}$, $i = 1,2,3$). The satellite and the observer are moving with respect to Schwarzschild coordinates, so that the 4–velocities V_S, V_O are not parallel to the Killing vectors $\frac{\partial}{\partial t} = \frac{\partial}{\partial x^0}$. The angles between V_S, V_O and Killing vectors $\frac{\partial}{\partial t}$ (directed upward) are different and determined by the satellite and the observer orbital velocities. If the satellite and the observer were at rest with respect to Schwarzschild coordinates (in which case their world lines would be pictured as vertical straight lines), we would get for the Doppler shift

$$\mathcal{D} = \frac{M_\otimes}{R_S} - \frac{M_\otimes}{R_O}. \tag{4}$$

The right hand side of the Eq. (4) is often called the gravitational Doppler shift. It is of the second order of magnitude and should be expected to appear as one of the terms in the final result.

In fact, the final result for the Doppler shift up to the second order is

$$\mathcal{D} = (V_O^i - V_S^i)\frac{\Delta x^i}{\Delta t} + (V_O^i - V_S^i)\frac{\Delta x^i}{\Delta t}V_S^k\frac{\Delta x^k}{\Delta t} + \left(\frac{M_\otimes}{R_S} - \frac{M_\otimes}{R_O}\right) + \frac{1}{2}(V_S^iV_S^i - V_O^iV_O^i) \tag{5}$$

where$i, k = 1,2,3$, $\Delta x^i = x_O^i - x_S^i$, $\Delta t = x_O^0 - x_S^0$, and summation over repeating indices is assumed.

The first two terms in this expression are the first order Doppler shift and the second order correction to the first order term (note that the second term is not

symmetric with respect to V_O, V_S; it is related to the nonsymmetry of expression (2) with respect to ν_O, ν_S). The third term is the gravitational Doppler shift (cf. Eq. (4)). The last term can be called the centrifugal correction term, because, in a classical picture of circular orbits, the term can be thought of as the difference of potentials of centrifugal forces caused by angular velocities of the satellite and the observer orbital motion. The physical origin of the last term in the general case is motion of the satellite and the observer with respect to Schwarzschild coordinates.

We want to point out that in the case of circular orbits only the first two terms contain information about time delay between transmitting and receiving, and only these two terms are time dependent.

We also want to notice that Eq. 5 coincides with the expression obtained by Ashby[4], excluding the gravitational term having general relativistic origin (Ashby's calculations were special relativistic).

IV. GLOBAL CLOCK SYNCHRONIZATION IN SCHWARZSCHILD FIELD

The relation between the clock rates and the Doppler shift is established[5,6] via relation (cf. Fig. 3)

$$\mathcal{D} = \frac{\nu_S - \nu_O}{\nu_S} = 1 - \frac{\nu_O}{\nu_S} = 1 - \frac{d\tau_S}{d\tau_O} \tag{6}$$

or

$$d\tau_S = (1 - \mathcal{D})d\tau_O \tag{7}$$

However, closer look at this formula and at Fig. 3 makes it obvious that the infinitesimal interval of the satellite and the observer proper times ($d\tau_S$, $d\tau_O$) are measured at different Schwarzschild times. More precise form of (7) would look as follows

$$(d\tau_S)_{t_t} = (1 - \mathcal{D})(d\tau_O)_{t_r} \tag{8}$$

where t_t and t_r are Schwarzschild times of transmitting and receiving of the signal. The retardation of t_r compared to t_t is reflected in Eq. (5) by the structure of the first order term and the second order correction to the first order term. This circumstance was obviously the prime concern of H. Fligel[2] of Aerospace Corporation.

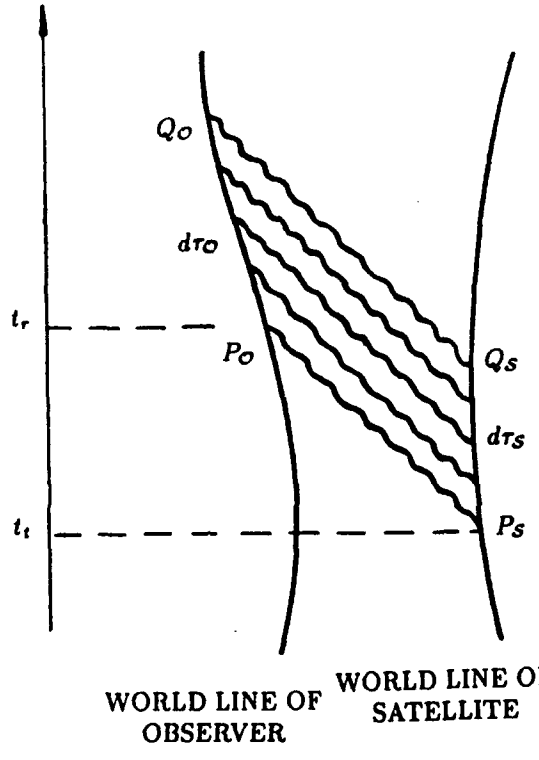

Fig. 3. Relation between the Doppler shift and and the rates of the moving clocks. Shown is the the set of null geodesics joining the world lines of the satellite and the observer. Each geodesic represents a wave crest. If there are n such crests and $d\tau_S$, $d\tau_O$ are the clock-measures of P_SQ_S and P_OQ_O respectively, then $n = \nu_S d\tau_S = \nu_O d\tau_O$.

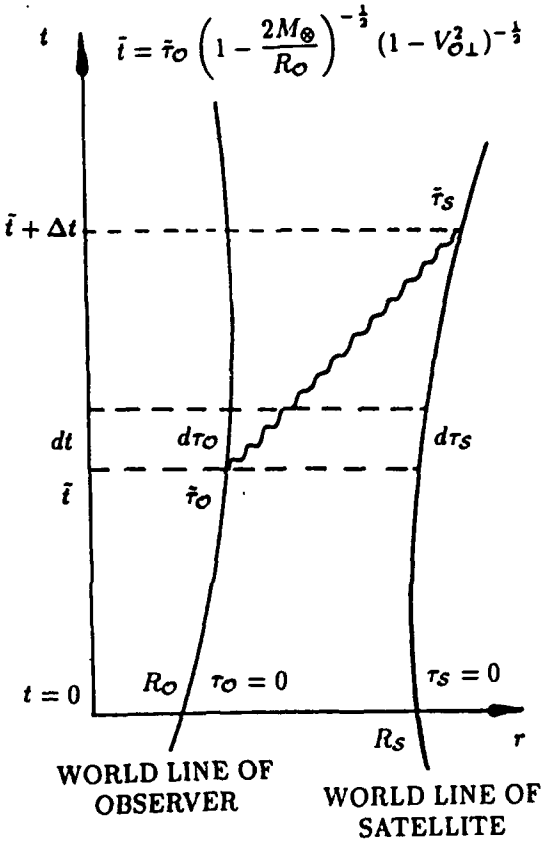

$$\Delta t = (R_S - R_O) + 2M_\otimes \ln \frac{R_S - 2M_\otimes}{R_O - 2M_\otimes}$$

Fig. 4. Relation between the satellite and the observer clock rates in a Schwarzschild simultaneity band and initial clock syncronization procedure.

The described above procedure of comparing the proper time rates of two clocks in general relativity is the only one (up to equivalence) that is correct for arbitrary gravitational fields. However, generally speaking, it will work only for two clocks (and under some reasonable conditions). In general enough gravitational field (with

no symmetries) it will not provide global synchronization for more than two clocks. It is not a drawback of this particular procedure. It is well known that in general relativity global synchronization of clocks in gravitational field with no symmetries is impossible in principle.

However, our model gravitational field of earth (Schwarzschild field) is very symmetric (static, spherically symmetric). One can convince himself easily that in this particular case our procedure will do the job. But so will many others. The task is to find the simplest one. For instance, one would like to minimize participation in the procedure of time dependent contributions like the first two terms of Eq. (5). It would be good idea to make all the clocks to show Schwarzschild coordinate time, i. e. the time of an observer placed at spatial infinity and resting with respect to Schwarzschild coordinates. Schwarzschild coordinate time is the closest possible analog of the time of the ECI frame (the special relativistic limit of the Schwarzschild coordinate frame coincides with the ECI frame).

The first step in this direction is to compare the rates of the clocks of the satellite and the observer with Schwarzschild clocks simultaneously with respect to Schwarzschild time (cf. Fig. 4). Elementary calculations show

$$(d\tau_S)_t = \left(1 - \frac{2M_\otimes}{R_S}\right)^{\frac{1}{2}} (1 - V_{S\perp}^2)^{\frac{1}{2}}\, dt \tag{9}$$

$$(d\tau_O)_t = \left(1 - \frac{2M_\otimes}{R_O}\right)^{\frac{1}{2}} (1 - V_{O\perp}^2)^{\frac{1}{2}}\, dt \tag{10}$$

where $V_{O\perp}$ ($V_{S\perp}$) is the component of the observer's (satellite's) 4–velocity V_O (V_S) orthogonal to the timelike Killing vector field of the Schwarzschild metric.

We will make the rest of our calculation highly idealized. Namely, we assume that R_O, $V_{O\perp}^2$, R_S, $V_{S\perp}^2$ are constant (the purpose of this idealization is to get rid of all the details of nonrelativistic origin). In this case both $d\tau_O$ and $d\tau_S$ are proportional to dt with constant proportionality coefficients. Thus one can take as fundamental any of them (the different choices are equivalent to the different

choices of time units). Dividing (9) by (10), we obtain

$$(d\tau_S)_t = \frac{\left(1-\frac{2M_\otimes}{R_S}\right)^{\frac{1}{2}}\left(1-V_{S\perp}^2\right)^{\frac{1}{2}}}{\left(1-\frac{2M_\otimes}{R_O}\right)^{\frac{1}{2}}\left(1-V_{O\perp}^2\right)^{\frac{1}{2}}}(d\tau_O)_t \tag{11}$$

or, in the usual second order approximation,

$$(d\tau_S)_t = \left[1-\left(\frac{M_\otimes}{R_S}-\frac{M_\otimes}{R_O}\right)-\frac{1}{2}\left(V_{S\perp}^2-V_{O\perp}^2\right)\right](d\tau_O)_t \tag{12}$$

which is interesting to compare with Eq. (5) (note the loss of the terms related to the time delay).

Integration of Eq. (11) yields

$$\tau_S = \frac{\left(1-\frac{2M_\otimes}{R_S}\right)^{\frac{1}{2}}\left(1-V_{S\perp}^2\right)^{\frac{1}{2}}}{\left(1-\frac{2M_\otimes}{R_O}\right)^{\frac{1}{2}}\left(1-V_{O\perp}^2\right)^{\frac{1}{2}}}\tau_O + C \tag{13}$$

The constant of integration C can be made equal to zero by employing an appropriate choice of the origin for τ_O, τ_S. We will show one way to do it for the particular case when the observer is placed on equator, the plane of the satellite orbit is equatorial, and the orbit period is shorter than the period of earth rotation. Let us suppose now that the ground observer is sending messages of his clock time continuously straight upward, so that the satellite receiver knows that the signals propagated along the radial null geodesics. Then, it is easy to figure out that the Schwarzschild travel time of the signal is

$$\Delta t = R_S - R_O + 2M_\otimes \ln\frac{R_S-2M_\otimes}{R_O-2M_\otimes} \tag{14}$$

Thus, if the satellite receives the ground station message sent at $\tau_O = \tilde{\tau}_O$ and, at the moment of receiving, sets on its clock time

$$\tilde{\tau}_S = \left(1-\frac{2M_\otimes}{R_S}\right)^{\frac{1}{2}}\left(1-V_{S\perp}^2\right)^{\frac{1}{2}}\left[\left(1-\frac{M_\otimes}{R_O}\right)^{-\frac{1}{2}}\left(1-V_{O\perp}^2\right)^{-\frac{1}{2}}\tilde{\tau}_O + \Delta t\right] \tag{15}$$

then the event on the world line of the satellite at $\tau_S = 0$ and on the world line of the observer at $\tau_O = 0$ become simultaneous with respect to Schwarzschild time, and, if we choose as $t = 0$ the Schwarzschild time hypersurface passing through both events, then at any Schwarzschild moment of time t the clock of the observer and the satellite will show

$$\tau_O = \left(1 - \frac{2M_\otimes}{R_O}\right)^{\frac{1}{2}} (1 - V_{O\perp}^2)^{\frac{1}{2}} t \tag{16}$$

and

$$\tau_S = \left(1 - \frac{2M_\otimes}{R_S}\right)^{\frac{1}{2}} (1 - V_{S\perp}^2)^{\frac{1}{2}} t \tag{17}$$

making it possible to tell Schwarzschild time looking at any of those clocks.

The constant C in Eq. (13) thus becomes equal to zero. It is clear that the described procedure allows to synchronize to Schwarzschild time as many clocks as one wishes and can be generalized easily to any placement of the observer on earth any satellite orbit inclination (only expression for Δt will become more complicated).

V. NULL-STRUT CALCULUS APPROACH.

As it has been mentioned above, our consideration is an idealized one. Main reason for this was to concentrate all the attention on general relativistic effects without getting into the details irrelevant for our present objectives. However, for practical applications these details can be very important. The orbits of the GPS satellites are not precisely circular, the satellites have non-equatorial orbits, etc. In more realistic problems one cannot possibly hope to be always able to find an analytic solution. The way out is, ordinarily, in using the numerical techniques. But numerical methods usually have a very essential drawback — the loss of the geometric interpretation, which in general relativity means the loss of clarity.

As far as we know there is only one exclusion to this rule — the newly developed null-strut calculus[10,11]. The null-strut calculus was developed originally

for numerical solving of geometrodynamic problems. We have shown, for the first time, that the null–strut calculus can be used also in chronogeometric problems, and, particularly, in the considered above GPS time transfer problems. It gave us a new stimulating boost in further development of the null–strut calculus, both in theory[12] and in applications[13,14,15].

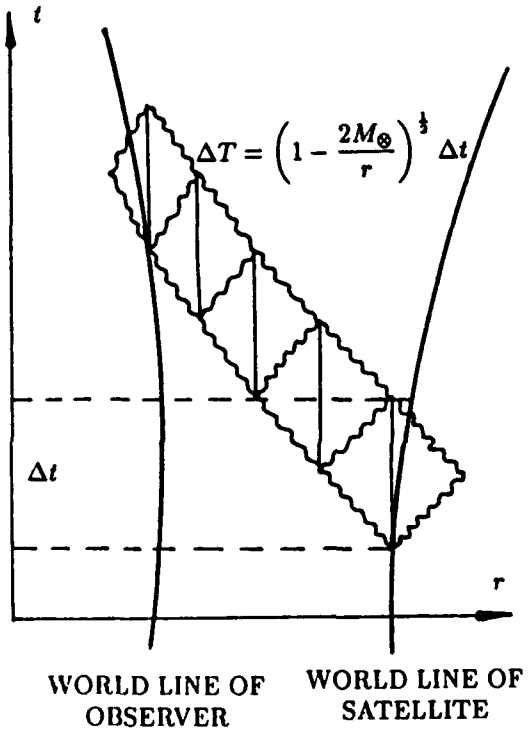

Fig. 5. The null–strut pictorial representation of the Doppler shift calculation in the Schwarzschild field. Vertical dimension Δt of all quasidiamonds is the same, but it corresponds to different proper time intervals intervals of clocks resting with respect to Schwarzschild coordinates $\Delta T = \left(1 - \frac{2M_\oplus}{r}\right)^{\frac{1}{2}} \Delta t$.

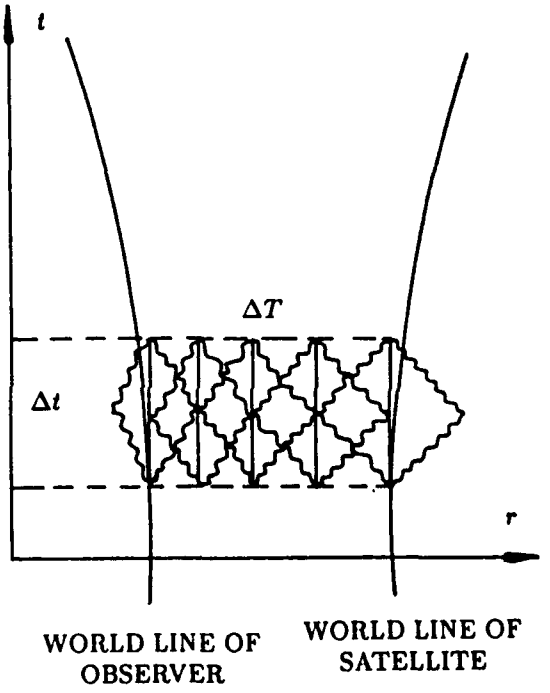

Fig. 6. The null–strut pictorial representation of the relation between the satellite and the ground observer clock rates in the Schwarzschild field. The quasidiamonds of Fig. 5. are dropped down to one level to form an interlocking Schwarzschild simultaneity band.

In the null–strut calculus spacetime is triangulated by internally flat simplexes (their size depends on desirable resolution). The chronogeometric relations inside of each simplex are these of special relativity. The general relativistic effects are taken

care of automatically by self – adaptation of the null–strut simplicial lattice to the geometry of spacetime. On Fig. 5 and Fig. 6 one can see a pictorial representation in the null–strut calculus of the Doppler shift(cf. Sect. III) and global synchronization (Sect. IV) in Schwarzschild field. The picture is made in the same space of coordinates as in Sect. III, IV. The apparent change in size and shape of quasidiamonds consisting of the null–struts (representing the light rays) and vertical timelike struts directed along the timelike Killing vector field of the Schwarzschild metric is reflecting the structure of the gravitational field. The quasidiamonds start from the square at spatial infinity and degenerate when approaching the Schwarzschild radius, thus adjusting to the symmetries of the gravitational field.

The results of the null–strut calculations in simple cases coincide with these of Sect. II, IV[13,14]. But the null-strut calculus automatically provides an algorithm to put in computer and allows to obtain numerical solutions in cases hard or impossible to handle analytically. No doubt that in the future development the null-strut calculus, as a unique approach having advantages of both numerical techniques an geometry, can become a major tool in solving and illuminating of chronogeometric problems and, in particular, navigational problems.

VI. RECOMMENDATIONS.

a. The general relativistic analysis of the Doppler shift and the global synchronization problems in the Schwarzschild field demonstrates clearly the following important features:

(1) The only experimentally measured parameters are the frequencies and the readings of the ground observer clocks and the satellite clocks (proper time);

(2) These parameters are determined at the events (points) of 4–dimensional spacetime, and not at points of the 3–dimensional proper space of a reference frame;

(3) Anything else depends on the point of view and the suggested synchronization scheme. It is a matter of interpretation and should be treated as such;

(4) For the Schwarzschild model of the earth's gravitational field, more than one global synchronization scheme, different in the degree of complexity, can be suggested. Synchronization scheme of Sect. IV is much simpler than the one based on the Doppler shift, Sect. III. This simplicity is achieved by maximal utilizing of the Schwarzschild metric symmetries and by eliminating the terms in the Doppler shift caused by time delay. The scheme is the result of careful analysis of the physical origin of each term in the Doppler shift expression;

(5) Not every interpretation leads to a global synchronization scheme. For instance, a try to interpret all the observations in the frame of reference of the ground observer[6] for the purpose of global synchronization is wrong. The world line of the ground observer is curved in such a way that the proper spaces of its frame corresponding to different moments of his proper time intersect each other, and consequently cannot be used for global synchronization, even in special relativistic limit. It is recommended to formulate the problems in four dimensions to avoid mistakes of such kind. In relativity only events are real, and not 3-dimensional positions.

b. It is recommended to compare the predicted relativistic corrections with the clock frequency and phase corrections currently accepted in GPS. Although it was not an objective of our SFRP research, it should be done in the future, especially for phase corrections (frequency corrections have been already taken into account). It is recommended to estimate possible contribution of the phase error (equivalent to the constant of integration error) in the final ranging error.

c. Looking at the currently used ranging procedures one can notice a striking inconsistency in treatment of two different parts of the problem. General relativity is used in an essential way in clock synchronization (at least in comparison of clock rates). But, when translating time data into ranging data, everything is currently

done using special relativity. It is recommended therefore to investigate the impact of general relativistic corrections on converting time measurements into ranging data.

d. Relativistic problems involving noncircular orbits and arbitrary satellite orbit inclinations should be also investigated in the future. Such an investigation should include not only clock rates comparison but also an evaluation of the integration constants and converting time data into ranging data.

e. The problem of cross linking based on satellite – to – satellite ranging should be taken into serious consideration. Equations (5) of Sect. III and (11)–(17) of Sect. IV indicate that such a system developed into Spacetime Common Grid will require much less maintenance than the current GPS as far as relativistic corrections are concerned.

f. Numerical methods adopted to the needs of spacetime navigation problems should be further investigated and developed. It is recommended to develop and to implement especially the null–strut calculus methods. Both basic and applied research in this area should be encouraged as much as possible.

REFERENCES.

1. W. A. Miller: Private communication.
2. H. Fligel: Private communication/letter.
3. "Performance Analysis Working Group (PAWG)", chaired by B. Winn, Aerospace Corporation, El Segundo, California, January, 1988.
4. N. Ashby: Private communication, presented at the January 1988 PAWG meeting.
5. R. Matzner: Private communication/letter.
6. C. Alley: Private communication/letter.
7. I. Ciufolini, R. E. Eanes, R. A. Matzner, J. C. Ries, and B. D. Tapley: Private communication.
8. C. W. Misner, K. S. Thorne, J. A. Wheeler: "Gravitation", W. H. Freeman and Co., San Francisco, 1971.
9. J. L. Synge:"Relativity: The General Theory", North-Holland Publishing Co., Amsterdam, 1966.
10. W. A. Miller and J. A. Wheeler:"4-Geodesy", Nuovo Cimento, 8 (1985) 418.
11. W. A. Miller:"Geometric Computation: Null-Strut Geometrodynamics and the Inchworm Algorithm", ed. J. Centrella, Cambridge University Press (1985) 256.
12. A. Kheyfets, N. J. LaFave, W. A. Miller: Pseudo - Riemannian Geometry on a Simplicial Lattice", in preparation.
13. A. Kheyfets, N. J. LaFave, W. A. Miller:"From Geodetic Triangulation to Spacetime Geodesy: Second Order GPS Time Transfer Effects", 16^{th} GGC, June, 1988.
14. A. Kheyfets, W. A. Miller: "Doppler Shift and Global Time Synchronization in the Schwarzschild field as Viewed through the Null-Strut Calculus", in preparation.

15. A. Kheyfets, W. A. Miller, J. A. Wheeler: "Null-strut Regge Calculus Geometrodynamics", submitted to Phys. Rev. Lett., May, 1988.

16. L. R. Gibson:"A Derivation of Relativistic Effects in Satellite Tracking", Report NSWC TR 83-55, April, 1983.

1988 USAF-UES SUMMER FACULTY RESEARCH PROGRAM/

GRADUATE STUDENT RESEARCH PROGRAM

Sponsored by the

AIR FORCE OFFICE OF SCIENTIFIC RESEARCH

Conducted by the

Universal Energy Systems, Inc.

FINAL REPORT

STOPPING POWER AND PENETRATION PHYSICS

Prepared by:	Leonard E. Porter, Ph.D.
Academic Rank:	Professor and Chairman
Department and	Physics and Astronomy
University:	University of Montana
Research Location:	AFWL/AWYS Kirtland AFB Albuquerque, NM 87117-6008
USAF Researcher:	Captain Greg S. Croon, USAF

Date:	19 Sep 88
Contract No:	F49620-87-R-0004

Stopping Power and Penetration Physics

by

Leonard E. Porter

ABSTRACT

The stopping power of matter for charged subatomic projectiles, a complex topic even for the specialist, often appears ominously complicated and perplexing for the uninitiated. The subject is of crucial importance in both target discrimination and target destruction aspects of particle beam physics. In the spirit of clarification basic stopping power theory and measurement were reviewed for all classes of projectile traversing elemental targets over the entire accessible interval of projectile energies. Extension of theory for composite target application was discussed in some detail. The concept of range was introduced, and methods of calculation and measurement were explained. Finally, various extant tabulations of range and stopping power were described, compared, and appraised.

Acknowledgments

I wish to express my appreciation to the Air Force Systems Command and the Air Force Office of Scientific Research for sponsorship of this research. Universal Energy Systems deserves recognition for the helpful attitude and remarkable administrative competence of the office staff.

My research experience proved productive and rewarding as a consequence of a thoroughly supportive climate within both the Particle Beam Assessment Section and the entire Space Applications Branch of the Applied Technology Division at the Air Force Weapons Laboratory. I am indebted to Major David Boyle for warm personal and professional hospitality, to Captain Greg Croon for administrative and technical support, to First Lieutenants Dan Topp, Mark Del Grande, and Don Lacasse, and to Mr. Charles Davis, for extraordinary patience and noteworthy expertise in providing assistance with preparation of the manuscript, and to Mr. Brian Conlon for perceptiveness and skill in preparing figures and tables. The quality of the research product was greatly enhanced by illuminating discussions with Dr. Ben Duran, Dr. Larry McKee, and Dr. Paul Nelson.

I. INTRODUCTION:

A major area of directed energy weapons research envisions a neutral particle beam impinging on a target with a view to either discrimination or destruction. The neutral projectile loses its electrons very soon after entering the target material, so that its fate thereafter depends on the stopping power of that target material for the specified projectile. Thus the subject of the stopping power of matter for charged subatomic projectiles is one of vital interest. The subject is enormously complex, and a novice seeking stopping power (or range) information would generally require considerable guidance.

The Particle Beam Assessment Section at the Space Applications Branch of the Applied Technology Division at the Air Force Weapons Laboratory intended to include a section devoted to stopping power and penetration physics in the Neutral Particle Beam Handbook then in preparation, and hence sought my assistance to write that section. My background in stopping power research served as the basis of selection for the task.

I first participated in stopping power measurements while a graduate student in low energy nuclear physics at the University of Wisconsin. When I subsequently served as a postdoctoral physicist at the University of California, Riverside under the tutelage of (the late) Professor Walter H. Barkas, I learned considerably more about stopping power studies and about higher-order projectile-charge corrections to the well-known Bethe-Bloch formula. My interest in stopping power calculation and measurement was rekindled when I conducted research at

the Los Alamos Scientific Laboratory, as a Visiting Summer Faculty Member, during the summer of 1969. At that time I initiated publication of some previous measurements, planned new experiments, and began modification of an existing computer code with a view to improvement of computational techniques. This work continued over many subsequent years at the University of Montana, and during five more Visiting Summer Faculty appointments, three at Los Alamos and two at Battelle Pacific Northwest Laboratory. Areas of study included composite material stopping powers and elemental stopping powers for heavy ions.

I have published widely in professional journals, as evidenced by a list of publications which includes more than fifty abstracts, proceedings papers and reports, and journal articles. My international stature in stopping power is indicated also by invitations to attend, and to participate through presentation of papers and chairing of sessions at, several workshops for specialists in the field. I was privileged to attend several of the Workshops on Penetration Phenomena, initially held at New York University. I was present at the 2nd (1978-NYU), 5th (1981-NYU), 6th (1982-Univ. of Hawaii), 7th (1983-ORNL), and the 9th (1985-ORNL). (I was forced to decline an invitation to attend the 8th (1984-ORNL) because of a conflict in dates with the Montana Science Fair.) I also accepted an invitation to attend the Workshop on Stopping Power at the University of Linz, Austria, September 20-21, 1984; my contribution appeared in a 1985 issue of Nuclear Instruments and Methods B. I declined an invitation to attend the Second Workshop on Stopping Power at the University of Linz (September

18-19, 1986) for want of travel funds. However, I attended the 10th Werner Brandt (i.e., NYU) Workshop on Penetration Phenomena, held in Alicante, Spain (January 7-9, 1987). Unfortunately, I could not attend the 11th Werner Brandt Workshop this past April because of a conflicting meeting, sponsored by DoE for consortia leaders, held at Argonne National Laboratory.

I have reviewed one or more manuscripts, upon request by the editor, for each of three prestigious journals (Nuclear Instruments and Methods, Journal of Applied Physics, and Radiation Research) in recent years.

II. OBJECTIVES OF THE RESEARCH EFFORT:

a. Preliminary Research Goals and Objectives

The preliminary goals and objectives that were agreeable mutually to Captain Greg Croon and me were:
The goal of the project is to provide a reliable but practical method of calculating the stopping powers of various prospective target materials for 200 - 300 MeV hydrogen ions (protons and deuterons). Since the incident beam consists of neutral hydrogen atoms, other aspects of penetration physics, such as the depth distribution of projectile states in the target material, are also pertinent.

The method of attaining this goal will be the assembly, appraisal, and synthesis of existing techniques for performing accurate calculations of energy loss for hydrogen ion projectiles at these intermediate energies. The resulting selection of a feasible method will focus on the best combination of simplicity and reliability. Special attention will be given to composite material targets.

b. Modifications of Preliminary Goals

The ancillary topic of depth distribution of projectile charge states in the target material proved to warrant relatively little interest for the purposes at hand. The incident hydrogen ion energy was selected as 100 MeV for the sake of argument, but calculations for the

higher energy interval originally selected could easily be accomplished with the guidance provided in the review paper.

c. Additional Research Goals and Objectives

Further assessment of the initial project goal led to an opinion that it was too restrictive in scope. Thus the scope was expanded to include all prospective projectile-target combinations that might be encountered in all potential aspects of the present or various speculative scenarios. Moreover, range calculational methods were included for the convenience of readers.

d. Final Research Objectives

The final research goal was to provide a reliable but practical method of calculating the stopping power of (and range in) any prospective target material for any charged subatomic projectile over the entire accessible kinetic energy interval. Conventional categories of projectile were utilized, so that implied objectives were to establish the calculational formalism for electrons and positrons, light projectiles (with masses from those of muons to alpha particles), and heavy ions (with masses greater than that of an alpha particle). Target materials were divided into elemental targets and composite material targets, so that the implied objectives theoretically doubled in number, but in practice this proliferation had no real impact because the methods described for application of stopping power theory to composite material targets pertained to all classes of projectile.

III. METHODS AND RESULTS:

a. The approach employed in realizing objectives remained essentially that described in the preliminary statement of research goals and objectives, namely, to assemble, appriase, and synthesize existing techniques for performing accurate calculations of energy loss for various classes of projectile in a given type of target material. My familiarity with the literature in the subject provided me with a great initial advantage, but it was nonetheless necessary to consult numerous new documents in the course of the study.

b. The resulting review paper provided the targeted calculational formalisms with state-of-the-art accuracy, which generally stands in need of improvement. Included at the end of the review paper was a subsection containing a description, comparison, and appraisal of various extant range and stopping power tabulations.

IV. RECOMMENDATIONS:

a. The review paper developed during the summer research project should serve very well as a source of referral information for a reader seeking assistance in calculating energy loss (or range) for given projectile-target combination. Should the tabular data described in the final subsection prove inadequate for the given purpose, some of the numerous references cited in the text can be consulted for further edification.

b. Deficiencies and shortcomings in existing methods for calculating stopping power were discussed briefly in the text. Areas of concentration in research which might lead to considerable improvement in the situation were also pointed out. Three of these areas were potential clarification of the proper form of the so-called projectile-z^3 correction term in the Bethe-Bloch stopping power formula, study of systematics in the effective charge parameters often used for calculation of heavy ion stopping powers, and a search for trends and patterns in stopping powers of composite materials for a given projectile (additivity studies). These areas represented the main thrust of research outlined in a mini-proposal already submitted for inclusion in the Research Initiation Program. Discussions of projectile effective charge and the proper form of the projectile-z^3 term can be found in a recent paper by Porter (1987). An excellent review of additivity studies has been provided by Thwaites (1983).

REFERENCES

Porter, L. E., Variations of Projectile Effective Charge in Analyses of Stopping Powers for Heavy Ions. Rad. Res., 1987, Vol. 110, pp. 1-18.

Thwaites, D. I., Bragg's Rule of Stopping Power Additivity: A Compilation and Summary of Results. Rad. Res., 1983, Vol. 95, pp. 495-518.

1988 USAF-UES SUMMER FACULTY RESEARCH PROGRAM/
GRADUATE STUDENT RESEARCH PROGRAM

Sponsored by the

AIR FORCE OFFICE OF SCIENTIFIC RESEARCH

Conducted by

Universal Energy Systems, Inc.

FINAL REPORT

Performance Models for Parallel Algorithms

Prepared by:	Michael D. Rice, PhD.
Academic Rank:	Associate Professor
Department and University:	Computer Science Department George Mason University
Research Location:	Super Computer Center Air Force Weapons Laboratory Kirtland Air Force Base Albuquerque, NM 87117-6008
USAF Researcher:	Captain Edward A. Carmona
Date:	15 September 88
Contract No:	F49620-87-R-0004

Performance Models for Parallel Algorithms

by

Michael D. Rice

ABSTRACT

New definitions of speedup and efficiency are used as the foundation for several models describing the performance of parallel algorithms. The new parameters introduced in these definitions provide improved interpretations of the "serial" and "parallel" fractions frequently used in the parallel computing literature. Moreover, they take into account the effects of problem size and number of processors and allow the formulation and proof of a number of basic laws in the models. These models provide the first sound basis for future theoretical and empirical studies of parallel algorithms. In particular, it is anticipated that the models will provide the foundation for understanding statistical aspects of parallel algorithms which will allow predictions of performance.

Acknowledgements

There are a number of individuals I wish to thank for a pleasant and rewarding ten week period at the Super Computer Center. These include Ken Summers and Col. Ed Oliver for recommending my participation in the program, Paul Mora and James Letterio for some interesting conversations, and the staff of General Atomics for their cheerfulness and the use of their facilities. Most of all, I wish to thank Capt. Ed Carmona for his fine efforts on my behalf and for the stimulating collaborative research work described in this report.

I. INTRODUCTION

The Parallel Computing Research Group at the Supercomputer Center performs basic research in the area of parallel computation. The overall objective of the group is the investigation of the feasibility of parallel computing technology for future scientific applications in the context of Air Force objectives. Current activities of the group include implementing fundamental numerical algorithms on parallel computers and assessing the work needed to implement large scale scientific simulation programs on parallel computers. In addition, recent activities of the group have included investigating aspects of performance evaluation for parallel algorithms.

My professional interests are concentrated in the areas of software development and parallel computation. In particular, my recent research interests have been in the areas of (i) models for concurrent computation, (ii) signal processing algorithms for parallel computers, and (iii) programming support environments for parallel computation. Therefore, my interests encompass both theoretical and applied topics in the area of parallel computation. This mixture of interests contributed to my assignment to the Parallel Computing Research Group. In particular, since I have a strong theoretical background in mathematics, I was able to make a significant contribution in my collaboration with this group.

II. OBJECTIVES OF THE RESEARCH EFFORT:

The preliminary goals of the research effort involved the design and implementation of Fourier Transform algorithms on parallel computers. In particular, the objectives were

(i) to summarize the theoretical and practical advantages and disadvantages of several designs for transform algorithms

(ii) to implement several of these designs on message passing parallel architectures

The first three weeks of the research effort were devoted to these objectives. The work performed on this topic is summarized in the initial brief report of effort (June 1 - June 28 , 1988) and in section III below.

The goals of the research effort for the remainder of the fellowship period were substantially altered by my collaboration with a member of the Parallel Computation Group, Capt. Ed Carmona. The main objective in this period was to formulate a model describing the performance of parallel algorithms based on new definitions of speedup and efficiency proposed by Capt. Carmona. The intention was that the model should reconcile several (apparently) conflicting definitions of speedup and efficiency found in the literature and also be able to predict the general behavior of fundamental performance evaluation parameters in a manner consistent with empirical data. Also, the model should clearly delineate the assumptions (axioms) from the consequences (derived laws).

During the latter portion of the fellowship period, Capt. Carmona and I jointly developed a model meeting the objectives outlined above. This work will be summarized in a technical report of the SuperComputer Center. Furthermore, work on the model has suggested a completely unexpected statistical approach for evaluating parallel algorithms that will form the basis for my future proposal to the AFOSR Mini Grant program.

III. WORK IN EARLY PERIOD (June 1 - June 28)

During this period, I finished a variety of work involving the Fourier Transform algorithm. First, I completed the development of a Fourier Transform algorithm for generic SIMD parallel computers with hypercube architectures. This algorithm is described in a data parallel specification language recently developed by the author and summarized in a draft paper that was also completed during this period. Secondly, I finished the specification of a program written in the occam2 language which computes the sixteen point kernel in a constant geometry algorithm for computing the Fourier Transform. This program is designed for execution on a four node INMOS Transputer system, but it could be implemented on a general message passing parallel computer.

IV. WORK ON MODEL (June 29 - August 12)

In brief, the objectives of the model were (i) to resolve apparent differences between predictors of parallel performance, (ii) to formulate axioms which are consistent with the observed behavior of performance parameters for parallel algorithms, and (iii) to derive consequences of these axioms. This section will be divided into three subsections which describe the approaches and results corresponding to these objectives.

Reconciliation

a. The approach involved the straightforward manipulation of algebraic definitions based on the new definitions of speedup and efficiency given by Capt. Carmona.

b. The above approach yielded the following results. First, the serial { s, s' } and parallel { p, p' } fraction parameters found in the parallel computing literature were expressed in terms of Carmona-Rice work parameters wa (work accomplished), we (work expended), and n_p (number of processors used). By expressing the serial and parallel fractions in these terms, greatly improved interpretations of the parameters were obtain- Secondly, the apparent dichotomy between two definitions of spee Barsis) : Speedup = $s' + p' n_p$ and (Amdahl) : Speedup = $1/(s + p/n_p)$ was resolved by establishing that the formulations are equivalent when s (resp. s') is expressed appropriately in terms of s' (resp. s) and n_p.

Finally, several fundamental laws were obtained using the above analysis. For example, it was established that (i) Speedup = s'/s, (ii) Efficiency (= Speedup/n_p) = p'/p, and (iii) assuming the existence of a constant C > 0 such that s > C for any n_p, then as n_p approaches infinity, s' approaches 1.

Axioms

a. The fundamental assumptions were determined by analyzing the behavior of the parameters described above based on a variety of theoretical models and empirical data on the performance of parallel algorithms. In particular, data compiled by Capt. Carmona based on the performance of Cholesky matrix factorization algorithms and data found in references 2 and 4 was used to understand the behavior of the parameters.

b. Three axioms were formulated which represent fundamental properties of the performance parameters. These are

(A1) Speedup and efficiency are absolute, not relative entities.
(all definitions of speedup are equivalent)

(A2) s is an increasing function of n_p.
(for a constant problem size n and sufficiently large n_p)

(A3) s is an decreasing function of n.
(for a constant n_p and sufficiently large n)

The graphs shown in Figure 1 illustrate axioms (A2) and (A3) for a variety of problem sizes and number of processors. These axioms also can be illustrated graphically using the following format. In a parallel system with n_p processors, assume that the total work wasted (ww) is initially grouped on the first n_p - 1 processors over the time period $0 \leq t \leq t_0 = ww/(n_p - 1)$ and the total work (we) is expended over the time period $0 \leq t \leq t_1 = we/n_p$. Then the parameters s, s', p, and p' can be interpreted in terms of relative areas as shown in Figure 2.

Consequences

a. Using basic properties of real valued functions involving limits and monotonicity, several consequences of axioms (A1)-(A3) were derived.

b. Consequences (C1)-(C3) were derived from (A1) and(A2):
(assume that all limits are relative $n_p \dashrightarrow +\infty$)

(C1) $\lim s = s^*$ exists and $\lim S = 1/s^*$
(C2) s' is an increasing function of n_p and $\lim s' = 1$.
(C3) E is a decreasing function of n_p and $\lim E = 0$.

Consequences (C4)-(C5) were derived from (A1) and(A3):

(C4) s' is a decreasing function of n
(C5) S and E are increasing functions of n

We have been unable to derive any general predictions regarding the values of lim s' or lim S, for example, as $n \dashrightarrow +\infty$. In the case of the Cholesky factorization algorithm implemented by Capt. Carmona, $\lim s' = 0$ was established.

Consequences (C1)-(C5) also have natural interpretations in terms of the graphical diagrams shown in Figure 2.

Finally, Figure 3 summarizes the most important formulas that were derived from the various definitions of speedup and efficiency for a parallel algorithm.

V. RECOMMENDATIONS:

a. The theoretical model cannot be implemented, but it can be partially validated by analyzing the performance parameters for a variety of test algorithms. In this direction, there are two possibilities. First, one can gather data on performance parameters from real implementations of algorithms on parallel computers. In the present work, this was done with data found in references 2 and 4. Secondly, one can generate test data from simple parallel computation models, such as fine-grain data flow graphs or cellular automata. For example, in the case of data flow graphs, one can construct a state chart which describes the execution strategy for a given number of processors. Using this type of chart, one can calculate the desired performance statistics.

b. The work on the performance model for parallel algorithms required a careful examination of the existing formulations of quantities such as speedup. In particular, the literature contains references (such as 3) to extended versions of Amdahl's law. However, these formulations are still too simplistic to provide good performance parameters for real parallel systems. The basic problems are, first, most models do not include time as a variable and, secondly, the performance parameters are based on the assumption that an algorithm executes on either exactly one processor or on all available processors. In other words, the current models are both too static and too restricted in nature.

The following material presents some ideas which may improve this situation.

Given an algorithm on a parallel system, define the random variable B as follows:

B(t) = (number of processors active at time t)/t*,

where $0 \leq t \leq t^*$ and t^* is the total execution time. For each $1 \leq k \leq n_p$ let b_k denote the fraction of total execution time when exactly k processors are active. Using the work parameters wa, ww, and we, one can show that

$$\text{Speedup} = \text{Expected Value[B]} = \sum \{ k\, b_k : 1 \leq k \leq n_p \} \quad (1)$$

Similarly, if w_k denotes the fraction of work accomplished when exactly k processors are active, one can establish that

$$\text{Speedup} = 1/(\sum \{ w_k/k : 1 \leq k \leq n_p \}) \quad (2)$$

Equations (1) and (2) are more complex versions of the Barsis and Amdahl formulations of speedup. Furthermore, the introduction of the random variable B provides the connection with time and the expected value provides the beginnings of a probabilistic point of view.

The performance parameters s, s', p, and p' also can be expressed in terms of the probability distributions { b_k } and { w_k }. These expressions show that the serial fractions s and s' depend on the values of <u>all</u> probabilities except wn_p and bn_p, respectively, while the parallel fractions p and p' depend on the values of <u>all</u> probabilities except w_1 and b_1, respectively. These facts support the idea that the probability distributions represent a <u>generalization</u> of the basic performance parameters. Furthermore, there exist valid analogues of the basic laws stated earlier in this report. For example, one can establish that

$$b_k = (\text{Speedup}/k)\, w_k \quad (1 \leq k \leq n_p) \quad (3)$$

The statistical nature of the work is reinforced by examining the following analogue of the usual standard deviation. Assume S = Speedup and define

$$d[B] = \sum\{ |k - S| \, b_k : 1 \le k \le n_p \}.$$

Then one can establish the following inequalities:

$$d[B]/(n_p - 1) < 2 \min\{ s', p' \} \qquad (4)$$

$$d[B] < 2 \min\{ S , n_p - S \} \qquad (4)'$$

Using (4)' and a weak version of Chebysheffs inequality satisfied by the d-statistic, one can state probabilistic conclusions of the form " the probability that more than ...processors are active is at least ... ".

To develop the theory outlined above, several lines of investigation should be explored. First, a variety of sample probability distributions need to be examined and analyzed. There are three potential sources for these distributions: (i) randomly generated based on probability distributions on the unit interval, (ii) computed using theoretical parallel computational models such as fine-grain dataflow graphs, systolic arrays, or cellular automata, and (iii) collected based on the execution of real parallel algorithms. The goal of the analysis will be to determine potential relationships between a parallel algorithm and the probability distributions $\{ b_k \}$ and $\{ w_k \}$. In particular, it will be important to identify potential limiting distributions which will permit performance predictions for certain classes of algorithms and large problem sizes and/or number of processors.

Secondly, one needs to integrate the statistical point of view with the model of parallel performance that has been summarized in earlier sections of this report. In particular, it will be necessary to understand the effects of changing the problem size n and the number of processors n_p on the distributions $\{ b_k \}$ and $\{ w_k \}$. Conversely, it will be necessary to understand how the random variable B changes as n and n_p are altered to permit constant values of the performance parameters. The later issue also involves

determining the approximate form of the level curves of the performance parameters.

In conclusion, the research outlined above has the aim of understanding the performance of algorithms on parallel systems by (i) examining performance parameters as a function of time, problem size, and number of processors, and by (ii) introducing random variables which will allow probabilistic interpretations. This increased understanding will contribute to the development of a more sophisticated model of parallel performance.

REFERENCES

Conference and journal publications :

1. Amdahl, G.M. Validity of the single-processor approach to achieving large scale computing capabilities, AFIPS Conference Proceedings, vol. 30 (Atlantic City, NJ, April 18-20). AFIPS Press, Reston, VA, 1967, pp. 483-485.

2. Benner, R.E., Gustafson, J.L., and Montry, R.E. Development of parallel methods for a 1024-processor hypercube, SIAM J. on Sci. and Stat. Computing, vol. 9, no. 4, July, 1988, pp. 1-32.

3. Kuck, D.J, Muroka, Y., and Chen, S. On the number of operations simultaneously executable in Fortran-like programs and their resulting speedups, IEEE Trans. on Computers, vol. C-21, no. 12, Dec., 1972, pp. 1293-1310.

Manuscripts :

4. Wamble, D.E., Allen, R.C., and Baca, L.S. Invariant imbedding and the method of lines for parallel computers, preprint Sandia National Laboratories, Albuquerque, NM, July, 1988.

LIST OF FIGURES

1 - Serial Fractions for Cholesky Factorization

2 - Graphical Illustrations

3 - Reference Formulas

Figure 1

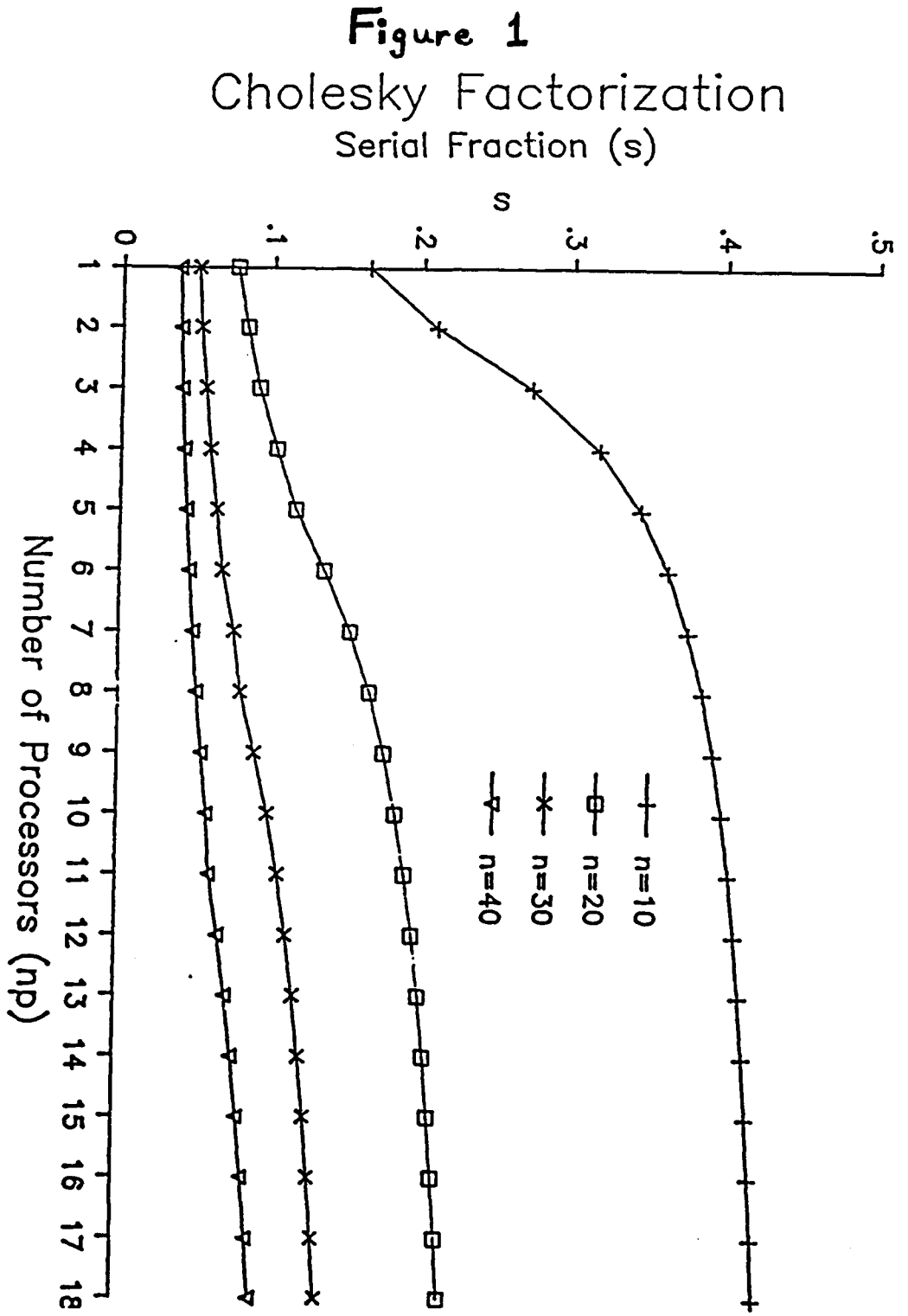
Cholesky Factorization
Serial Fraction (s)
s
0
.1
.2
.3
.4
.5
1 2 3 4 5 6 7 8 9 10 11 12 13 14 15 16 17 18
Number of Processors (np)
n=10
n=20
n=30
n=40

Figure 2

GRAPHICAL ILLUSTRATIONS

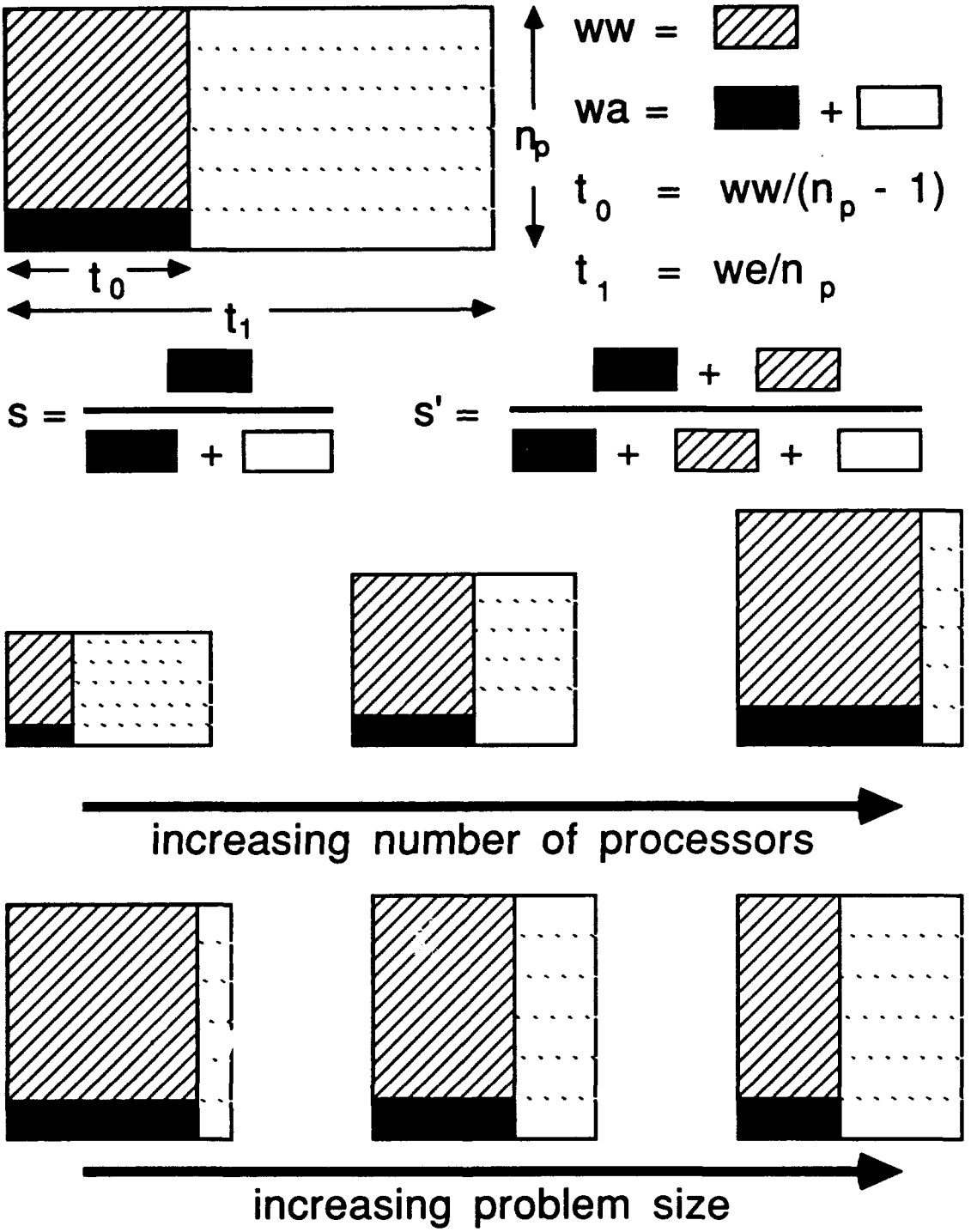

Figure 3
REFERENCE FORMULAS

General Definition of Speedup : $S = \text{Speedup} = S(n,n_p) = T(n,1)/T(n,n_p)$
[$T(n,n_p)$ = time needed to execute an algorithm of size n using n_p processors]

Definition of Efficiency : $E = \text{Efficiency} = \text{Speedup}/n_p$

Definition of Work Parameters : (Carmona / Rice)

ww = work wasted wa = work accomplished
we = work extended = wa + ww

Alternate Formulation of Speedup and Efficiency : (Carmona / Rice)

$E = wa/we$ $S = E\,n_p$

Definition : Serial and Parallel Fractions (Amdahl / Barsis)

s = fraction of time spent on the serial portion of a task
p = fraction of time spent on portions of a task that can be executed in parallel
s' = fraction of time spent performing serial work on the parallel system
p' = fraction of time spent performing parallel work on the parallel system
(Assumption is that $s + p = 1$ and $s' + p' = 1$)

Formulation of Speedup using Amdahl/Barsis fractions :

[Amdahl] $\text{Speedup} = 1/(s + p/n_p)$.
[Barsis] $\text{Speedup} = s' + p'n_p$

Formulas relating Amdahl/Barsis parameters : (Carmona/Rice)

(1) $S = s'/s$
(2) $E = p'/p$
(3) $s = (ww/wa)/(n_p - 1) = s'/(s' + (1-s')n_p)$ $(n_p > 1)$
(4) $s' = (ww/we)n_p/(n_p - 1) = s/(s + (1-s)/n_p)$ $(n_p > 1)$

Consequences of Above Formulas : (all limits are with respect to $n_p \to +\infty$)
(5) $\lim\ (s - 1/S) = 0$
(6) $\lim\ (E - p') = 0$
(7) If there exists $C > 0$ such that $s > C$ for all n_p, then
(i) $\lim s' = 1$ (ii) $\lim E = 0$